Solid State Lighting Technology and Application Series

Willem Dirk van Driel
Xuejun Fan
Guo Qi Zhang *Editors*

Solid State Lighting Reliability Part 2

Components to Systems

Solid State Lighting Technology and Application Series

Volume 3

Series Editors
Guo Qi Zhang, Eindhoven, The Netherlands
Wu Ling, Beijing, China

More information about this series at http://www.springer.com/series/8864

Willem Dirk van Driel • Xuejun Fan
Guo Qi Zhang
Editors

Solid State Lighting Reliability Part 2

Components to Systems

Editors
Willem Dirk van Driel
Philips Lighting
's-Hertogenbosch
Hertogenbosch
Noord-Brabant, The Netherlands

Delft University of Technology
EEMCS Faculty
Delft, Zuid-Holland
The Netherlands

Xuejun Fan
Lamar University
Beaumont, TX, USA

Guo Qi Zhang
Delft University of Technology
EEMCS Faculty
Delft, Zuid-Holland
The Netherlands

ISSN 2196-4203 ISSN 2196-4211 (electronic)
Solid State Lighting Technology and Application Series
ISBN 978-3-319-58174-3 ISBN 978-3-319-58175-0 (eBook)
DOI 10.1007/978-3-319-58175-0

Library of Congress Control Number: 2012943579

© Springer International Publishing AG 2018
This work is subject to copyright. All rights are reserved by the Publisher, whether the whole or part of the material is concerned, specifically the rights of translation, reprinting, reuse of illustrations, recitation, broadcasting, reproduction on microfilms or in any other physical way, and transmission or information storage and retrieval, electronic adaptation, computer software, or by similar or dissimilar methodology now known or hereafter developed.
The use of general descriptive names, registered names, trademarks, service marks, etc. in this publication does not imply, even in the absence of a specific statement, that such names are exempt from the relevant protective laws and regulations and therefore free for general use.
The publisher, the authors and the editors are safe to assume that the advice and information in this book are believed to be true and accurate at the date of publication. Neither the publisher nor the authors or the editors give a warranty, express or implied, with respect to the material contained herein or for any errors or omissions that may have been made. The publisher remains neutral with regard to jurisdictional claims in published maps and institutional affiliations.

Printed on acid-free paper

This Springer imprint is published by Springer Nature
The registered company is Springer International Publishing AG
The registered company address is: Gewerbestrasse 11, 6330 Cham, Switzerland

Preface

Human civilization revolves around artificial light. From its earliest incarnation as firelight to its most recent as electric light, artificial light is at the core of our living. It has freed us from the temporal and spatial constraints of daylight by allowing us to function equally well day and night, indoors and outdoors. It has evolved from open fire, candle, carbon arc lamp, incandescent lamp, and fluorescent lamp to what is now on our doorstep: solid-state lighting (SSL). SSL refers to a type of lighting that uses semiconductor light-emitting diodes (LEDs), organic light-emitting diodes (OLEDs), or light-emitting polymers. Unlike incandescent or fluorescent lamps, which create light with filaments and gases encased in a glass bulb, solid-state lighting consists of semiconductors that convert electricity into light. Technological developments in the last two decades have allowed LEDs to be used first in signal devices, like traffic lights and exit signs, and then in some limited illumination applications, such as flashlights; and are now on the doorstep of massive general illumination applications, from homes to commercial spaces to outdoor lighting. This penetration is mainly due to the promise of an energy-saving opportunity with an increased and improved reliability at low cost. According to the projections of the Department of Energy (DOE) of the United States, replacing incandescent lamps with SSL would save US $250 billion in energy costs, reduce the electricity consumption by nearly one half, and avoid 1,800 million metric tons of carbon emissions over the next two decades.

Nowadays, the lighting industry experiences the exponentially increasing impact of digitization, and connectivity of its lighting systems. The impact is far beyond the impact on single products, but extends to an ever larger amount of connected systems. Continuously, more intelligent interfacing with the technical environment, and with different kinds of users is being built-in by using more and different kinds of sensors, (wireless) communication and different kinds of interacting or interfacing devices.

An LED system is composed of an LED engine (or LED module) with a microelectronics driver(s) and control gears, integrated in a housing that also provides the optical, sensing, heat dissipation and other functions. Knowledge of

reliability at the component and system level is crucial for not only the business success of future SSL applications but also solving many associated scientific challenges. The increasing use of LEDs for intelligent applications will also pose additional reliability issues for SSL systems. It also means that system performance monitoring and further control options become more essential.

This book is part of the Solid State Lighting Technology and Application Series, with Prof Guo Qi Zhang as series editor. It is a continuation of *Solid State Lighting Reliability: Components to Systems* (published in 2013), with W.D. van Driel and X.J. Fan as editors. In that book, we presented the state-of-the-art knowledge and information on the reliability of SSL systems. The book soon became a reference book for SSL reliability from the performance of the (sub-)components to the total system. It was one of the top 25% most downloaded e-books in the relevant Springer eBook Collection in 2015 with up to 35,000 chapter downloads.

In the past 4 years, we have witnessed rapid development in technology and significant market penetration in many applications for LED systems. New processes and new materials have been introduced; new standards and new testing methods have been developed; new driver, control and sensing technologies have been integrated; and new and unknown failure modes have also been presented. In this book, *Solid State Lighting Reliability Part 2: Components to Systems*, we invited experts from the industry and academia to present the latest developments and findings in the LED system reliability arena. Topics in this book cover the early failures and critical steps in LED manufacturing, advances in reliability testing and standards, quality of color and color stability, degradation of optical materials and the associated chromaticity maintenance, characterization of thermal interfaces, LED solder joint testing and prediction, common failure modes in LED drivers, root causes for lumen depreciation, corrosion sensitivity of LED packages, reliability management for automotive LEDs, and lightning effects on LEDs. This book starts with a Quo Vadis and ends with a next frontier discussion in which the accomplishments so far are presented and what next hurdles need to be taken in order to make 100 % LED penetration an optional scenario.

Parts of the contents in this book are first-hand results from research and development projects. We would like to thank all the authors for their contributions to the book. We would like to acknowledge the contributions from the National High-Tech Research and Development Program of China (863 Program, Grant No.: 2015AA03A101), from which seven chapters in this book are supported. Dr van Driel and Prof Zhang would also like to make acknowledgments to many of their colleagues in Philips Lighting and Delft University of Technology who have contributed to this book in one way or another.

Personal Acknowledgments

Willem van Driel is grateful to his wife Ruth Doomernik; their two sons, Juul and Mats; and their daughter, Lize, for their support on writing and editing this book. Xuejun Fan is grateful to his wife, son, and parents for their unselfish support and love. Guo Qi Zhang is grateful to his wife and their two children.

Hertogenbosch, Noord-Brabant, The Netherlands — Willem Dirk van Driel
Beaumont, TX, USA — Xuejun Fan
Eindhoven, The Netherlands — Guo Qi Zhang
March of 2017

Contents

1 Quality and Reliability in Solid-State Lighting: Qua Vadis? 1
T. Vos, P. den Breeijen, and Willem Dirk van Driel

2 Chip-Level Degradation of InGaN-Based Optoelectronic Devices 15
Carlo De Santi, Matteo Meneghini, Gaudenzio Meneghesso, and Enrico Zanoni

3 LED Early Failures: Detection, Signature, and Related Mechanisms 49
B. Hamon, T. Merelle, and B. Bataillou

4 Advances in Reliability Testing and Standards Development for LED Packages and Systems 77
C. Qian, J.J. Fan, Xuejun Fan, and Guo Qi Zhang

5 Reliability and Lifetime Assessment of Optical Materials in LED-Based Products 115
M. Yazdan Mehr, Willem Dirk van Driel, and Guo Qi Zhang

6 The Influence of Phosphor and Binder Chemistry on the Aging Characteristics of Remote Phosphor Products 141
J.L. Davis, R. Yaga, M. Lamvik, K. Mills, and B. Fletcher

7 Thermal Characterization of Die-Attach Material Interface of High-Power Light-Emitting Diodes 159
Dae-Suk Kim and Bongtae Han

8 Color Quality 179
Y. Ohno

9 LED-Based Luminaire Color Shift Acceleration and Prediction 201
Guangjun Lu, Willem Dirk van Driel, Xuejun Fan, Jiajie Fan, and Guo Qi Zhang

10 Chromaticity Maintenance in LED Devices 221
J. Lynn Davis, Karmann Mills, Robert Yaga, Cortina Johnson, Monica Hansen, and Michael Royer

11 Fault Diagnostics and Lifetime Prognostics for Phosphor-Converted White LED Packages 255
Jiajie Fan, Cheng Qian, Xuejun Fan, Guo Qi Zhang, and Michael Pecht

12 Advances in LED Solder Joint Reliability Testing and Prediction 301
J. Zhang and Guo Qi Zhang

13 Online Testing Method and System for LED Reliability and Their Applications 353
Xiaobing Luo and Qi Chen

14 Degradation Mechanisms of Mid-power White-Light LEDs 381
Jianlin Huang, Dušan S. Golubović, Sau Koh, Daoguo Yang, Xiupeng Li, Xuejun Fan, and Guo Qi Zhang

15 Assessing the Reliability of Electrical Drivers Used in LED-Based Lighting Devices 433
J. Lynn Davis, Karmann Mills, Robert Yaga, Cortina Johnson, and Joe Young

16 Reliability Prediction of Integrated LED Lamps with Electrolytic Capacitor-Less LED Drivers 455
B. Sun, Xuejun Fan, Willem Dirk van Driel, and Guo Qi Zhang

17 Statistical Analysis of Lumen Depreciation for LED Packages 487
M. Schuld, Willem Dirk van Driel, and B. Jacobs

18 Long-Term Reliability Prediction of LED Packages Using Numerical Simulation 503
Sung-Uk Zhang

19 Corrosion Sensitivity of LED Packages 527
B.J.C. Jacobs, C. van der Marel, Willem Dirk van Driel, S.J. Lu, and X.P. Li

20 Reliability Management of a Light-Emitting Diode for Automotive Applications 549
C. Jung and Th. Zahner

21 Lightning Effects on LED-Based Luminaires 573
Adedotun Agbemuko, Johannes van Meurs, and Willem Dirk van Driel

22 The Next Frontier: Reliability of Complex Systems 585
D. Schenkelaars, Willem Dirk van Driel, and R. Duijve

Index 597

Chapter 1
Quality and Reliability in Solid-State Lighting: Qua Vadis?

T. Vos, P. den Breeijen, and Willem Dirk van Driel

Abstract In the past 4 years we have witnessed a change in quality and reliability to make the marked introduction of solid-state lighting (SSL) successful. LED penetration levels have reached values of 10–30%, depending on the application. The number and variety of LED packages and, thus, associated LED-based products, have significantly increased in the past years. Consequently, new processes and new materials are introduced which will introduce a new series of new and unknown failure modes in SSL products. The understanding of these failure modes is better understood, and the number has grown to beyond 50. The fingerprint is changing to failures that are due to interactions between components. First exercises with system level acceleration tests are presented, but it is important to derive acceleration models for these tests. Advanced reliability prediction capabilities are needed including algorithms and tools that couple the multi-physic and multiscale behavior of the SSL failure modes. The shift toward services will force the lighting industry to develop these capabilities in order to better address lifetime and reliability. Connected lighting will bring big data from live connections that can be used to determine the degradation level of the system. Both trends, service and connected, will bring yet another huge change in mind-set in the lighting industry when in concerns reliability: detailed understanding of failure mechanisms, usage scenarios, technology, and design will come together.

1.1 What We Predicted: A New Era in Lighting

In *Solid State Lighting Reliability: Components to System* we presented a chapter describing a brief history of quality and reliability, their interaction, and the impact for the change within the lighting industry into the solid-state era [1]. We mentioned

T. Vos • P. den Breeijen
Philips Lighting, HTC45, 5656 AE Eindhoven, The Netherlands
e-mail: tony.vos@philips.com; peter.den.breeijen@philips.com

W.D. van Driel (✉)
Philips Lighting, High Tech Campus, Eindhoven, The Netherlands

Delft University of Technology, EEMCS Faculty, Delft, The Netherlands
e-mail: willem.van.driel@philips.com

© Springer International Publishing AG 2018

W.D. van Driel et al. (eds.), *Solid State Lighting Reliability Part 2*, Solid State Lighting Technology and Application Series 3, DOI 10.1007/978-3-319-58175-0_1

that a huge mind-set change is needed in both quality and reliability to make the market introduction of solid-state lighting (SSL) applications a big success. Our final remark dealt with the challenge to embed known-good practices from industries such as semiconductors, automotive, military, and aerospace into the veins of the lighting designers. Let us in this paragraph reflect on what happened in the 4 years that elapsed; we focus on the reliability part and leave out the quality aspects of SSL. We first want to discuss three major observations from a market perspective that occurred in the past 4 years (our first chapter was published in 2013, see [1]).

First of all, in only 4 years of time we have seen a substantial change in the (traditional) lighting industry. The three major lighting companies in conventional technology, Osram, Philips Lighting, and General Electric (GE) Lighting, made substantial changes in their enterprise architectures. This is mainly due to the upcoming competition by other parties able to develop, manufacture, and sell LED-based products at competitive price levels. For example, the ascension of Chinese manufacturers in recent years has pushed down LED bulb prices considerably. The same trend occurred for professional luminaires, both for indoor and outdoor applications. In the past years GE, Osram, and Philips Lighting published a series of public announcements, just to highlight a few of them:

1. GE's 125-year-old lighting business has been the backbone of the organization's foundation since 1890 when Thomas Edison founded the company. In October 2015, GE announced it would be spinning off its commercial LED lighting business, solar energy, and energy storage devices into a new start-up company [2]. In 2016 GE said farewell to the compact fluorescent light, or CFL [3]. Here, the company announced in February 2016 that it would stop making and selling these bulbs by the end of the year.
2. German lighting giant Osram announced in 2015 to spin off of its lamps business into LEDVANCE. LEDVANCE encompasses Osram's lighting brand values in the conventional and LED lighting businesses sectors. Osram completed this organizational separation as of April 2016, while the legal separation was scheduled in July 2016 [4].
3. Royal Philips announced in 2015 to spin off its "historical" lighting business [5]. Effectively on January 2016, Philips Lighting ended up as an initial public offering (IPO), which will result in the listing of the lighting business on the Dutch bourse, and aims to sell at least 25% of its shares in the lighting company [6]. The Dutch conglomerate started making light bulbs 123 years ago, where Gerard Philips and his father Frederick founded one of the earliest makers of incandescent light bulbs in 1891. Besides this, Royal Philips also intends to divest in their LED components and automotive lighting business, named Lumileds.

These are just a few of the announcements we have seen passing in the past 4 years. It indicates that the transition from conventional lighting into SSL truly resulted into a new era for the lighting industry.

Secondly, SSL has the promise of an increased reliability with an energy-saving opportunity, and we mentioned in the first chapter that SSL applications are now at the doorstep of massive market entry. But what are then the current volumes and penetration levels of LED-based products in the different application domains, and

did they significantly increase? This question is answered by the DOE reports Energy Savings Forecast of Solid-State Lighting in General Illumination [7, 8]. There are seven iterations of the *Energy Savings Forecast of Solid-State Lighting in General Illumination*. Just recently, the 2016 report was published [8]. Here we only discuss this report and the one from 2014 [7]. LED lighting is projected to gain significant market penetration. Of the eight submarkets examined, they forecast that LEDs will grow most rapidly in the street and roadway and general service submarkets in terms of the percentage of total lumen-hour sales. Scenarios estimate the expected future adoption of LEDs based on historical data and the current trajectory for the technology. In the 2016 report, LEDs are predicted to comprise over 90% installed penetration by 2025 and nearly 100% by 2035. When one compares the 2016 forecast with the earlier one in 2014, it can be noted that the penetration is a bit slower. Take, for example, the street and roadway submarket, already a popular area for LED upgrades. In the 2014 report, LEDs are predicted to reach 83% market share of sales by 2020 and nearly 100% by 2030 [7]. In the 2016 report these values are 60% and 88%, with a 100% not to arrive before 2035 [8].

Penetration projections dating from December 2012 forecasted that LEDs will reach a level of 84% in 2020. This number represents the estimated LED market penetration between 2010 and 2020. In 2014, light-emitting diodes were expected to reach a penetration into the lighting market of approximately 11%.

Figure 1.1 depicts these three projections indicating the fact that LED penetration is growing rapidly but not as fast as one once thought. Following these

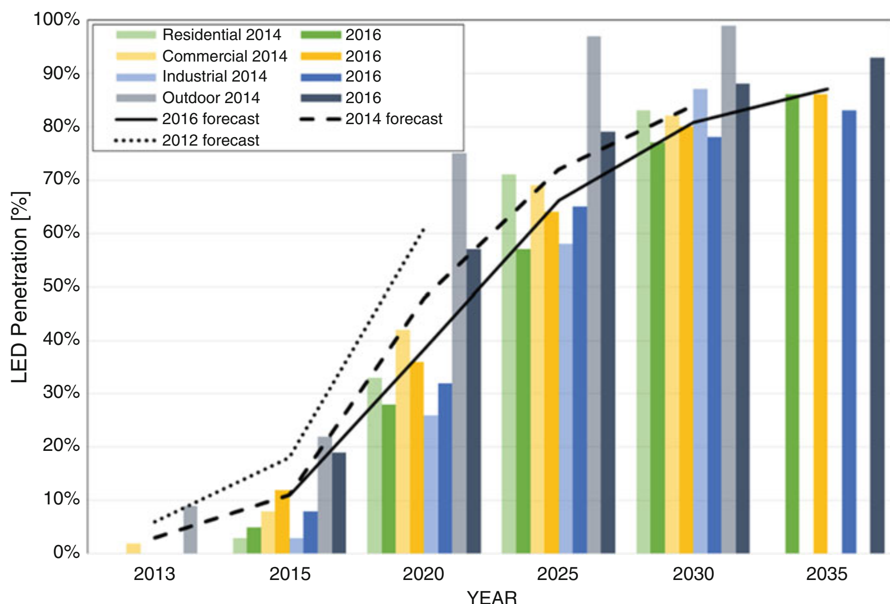

Fig. 1.1 LED penetration levels in four applications; *blue line* indicates overall trend (DOE data from [7, 8], 2012 data from [9]; with permission)

projections, the 2013 and 2017 numbers are <10 % and 20–30 %, respectively. It means a 2–3 times increase since 4 years. Remind that these are projections, and signals from countries and/or companies should underline them. For example, in June 2015 it was reported that Japan was the first country in the world to use LED lighting and with penetration rates for the home market exceeding 90 % [9]. GE's announced LED revenues soared 77 % during the second quarter in 2016 [3]. Philips Lighting announced LED lighting sales grew strongly by 27 % and now account for 50 % of the overall lighting sales [10]. But be aware that booming revenue figures in the LED business can be misleading as sharp price declines for LED-based products impact the margins on these products.

The third observation is the following one. The number and variety of LED packages and LED arrays have significantly increased in the past 4 years. This is mainly due to the fact that the LED supplier landscape is exploding; see Fig. 1.2 for just a snapshot. High-power LEDs are replaced by mid-power LEDs in the consumer products, chip-on-boards (COBs) were introduced, and low-power LEDs are currently introduced. The power consumption ranges from low-power LEDs that operate at less than 0.05 watts per package to COB that can consume over 50 watts per module. However, an agreed or standardized package outline for all these LED variants still does not exist. In the semiconductor industry, JEP95 is a compilation of some 1,800 pages of outline drawings for microelectronic packages including

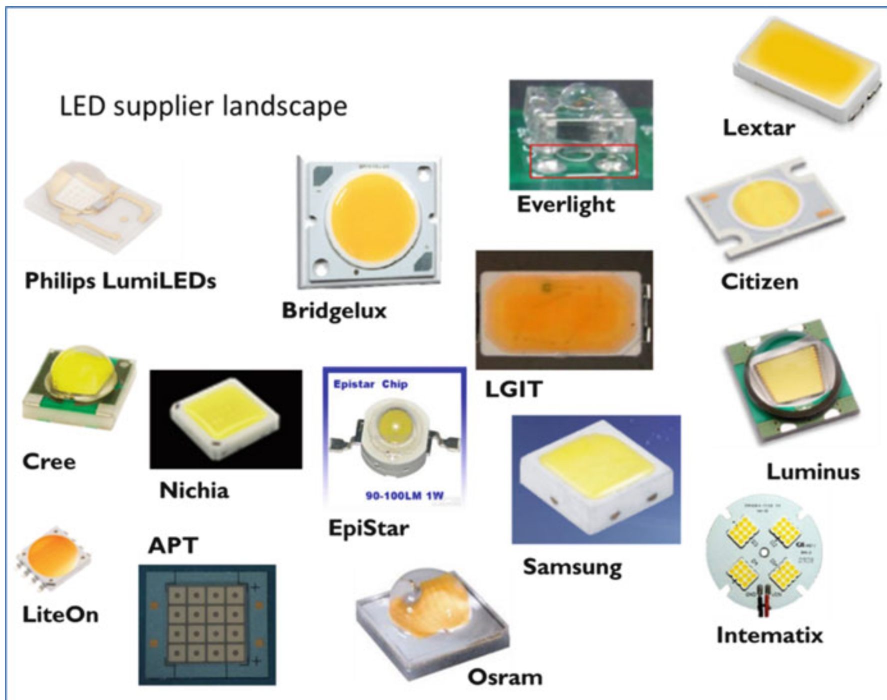

Fig. 1.2 The LED supplier landscape is exploding. Just a short list of companies providing LED packages. It resulted in an increased variety of LED packages

transistors, diodes, DIPS, chip carriers, and package interface BGA outlines in both inch and metric versions [11]. It facilitates easier product design and second sourcing of particular package types. In the LED industry the inexistence of such a standard (read, agreement) means that where one LED supplier offers a 2×3 mm ^{2} leadless package, it can completely differ from another supplier. The consequence of this is a corresponding increase in the number of LED replacement lamps and LED luminaires that are available. Also here, we see an explosion of offered solutions and products. And, consequently, new processes and new materials which will, as we wrote in [1], always introduce a series of new and unknown failure modes.

1.2 What Is the Current Status?

Since 2013, the understanding of the degree to which LED drive current and operating temperature affect product reliability is better understood. Failure modes, mainly originating from the semiconductor industry, are better understood and under control. Better designs are the positive outcome; however, still a wide range of design choices to meet specific application and market needs are required, hence a potentially wide range of product reliability. On top of that, other subsystems and components in a luminaire, e.g., sensors and controls, introduce other potential failure modes which will affect and may actually dominate the determination of its reliability. In 2014, the Lighting Industry Alliance LED Systems Reliability Consortium (LSRC) identified potential failure modes for SSL products. The LSRC members scored the failure modes they most frequently observed [12]; the resulting Pareto plot is shown in Fig. 1.3. Failure of the light source, in this case LEDs, is only 20 %. This result underlines our earlier statements:

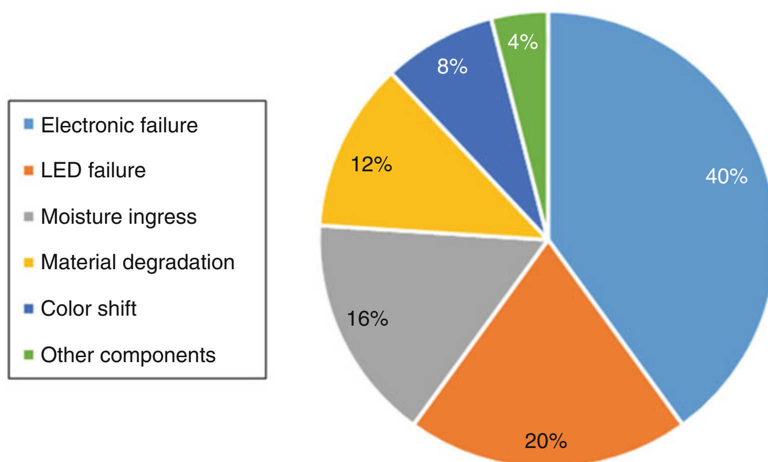

Fig. 1.3 Pareto plot of scored failure modes by the LSRC (Data from [11], with permission)

> There is a clear shift in the reliability budget for SSL applications: with the introduction of SSL it is no longer the light source that is the limiting factor for the product life.

In 2013, we mentioned that the amount of failure modes for SSL products would easily be larger than 30 [1]. They would partly be inherited from the semiconductor industry, as described in JEP122F [13]. In those days we did not know the effect of such failure modes on to the specifics of a SSL system. Simply due to the fact that the relation of them to the quality of light was unknown. Take, for example, the failure mode *wire bond fatigue*. In JEP122F [13] it is described as a:

> Wire bonds can break under temperature cycle, the mechanism are well modeled by Coffin-Manson or Paris power law models.

For LED-based products, however, we learned that the effect of a wire bond failure can have a more complex effect on a system level:

1. A wire bond failure leads to an open electrical structure.
2. It is quite common to design serial strings of LEDs; thus, if one fails, then the total string is giving no light.
3. In parallel designs with serial LEDs strings this will lead to black spots in the product.

Figure 1.4 schematically represents this situation in the middle picture: if single LEDs fail, the light distribution will be affected, either by showing blacks spots, by changing the color, or by a decreased lumen output. Other typical semiconductor failure modes, such as fatigue and/or interfacial failures, may lead to the same effects [14].

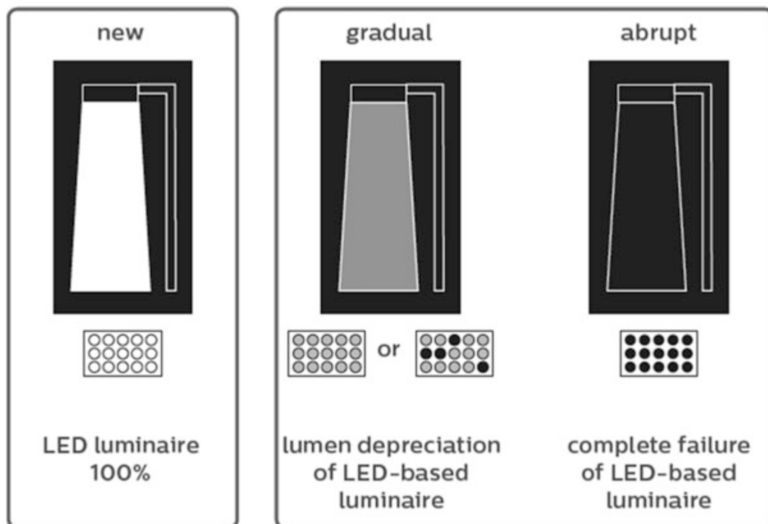

Fig. 1.4 Failures in LEDs can have unexpected effects on the lighting function

In the past 4 years, the industry learned how semiconductor failures interact within lighting products. Note that some of them could not be captured before affected products entered the market. This is quite logical if you consider the introduction of a totally new technology. The consumer product safety commission [15] lists the number of unsafe products that have entered the market. Searching for those that contain LEDs results in approximately 19 cases in the past 4 years. Main reasons are (i) impact hazard, (ii) burn hazard, or (iii) shock hazard. The largest one, that is, the one with the highest amount of affected products, comes from a large LED manufacturer, recalling >700,000 LED T8 lamps in the USA and Canada due to the risk of burn hazard [16].

Obviously plenty of failure modes do not lead to unsafe products. They are detected during the design phase of SSL products. Extensive testing, by using accelerated conditions, will reveal weaknesses in to-be-launched products [17]. Figure 1.5 depicts a so-called word cloud with failure modes in SSL products as seen in 2013 (gray) and appearing in the period after until 2016 (black). Here, the word size reflects the impact, which is common for such pictures. Figure 1.6 depicts the same

Fig. 1.5 Failure modes in SSL products: as seen in 2013 (*gray*) and appearing in the period after until 2016 (*black*). Word size reflects the impact

Fig. 1.6 Number of failure modes in SSL products versus the year detected

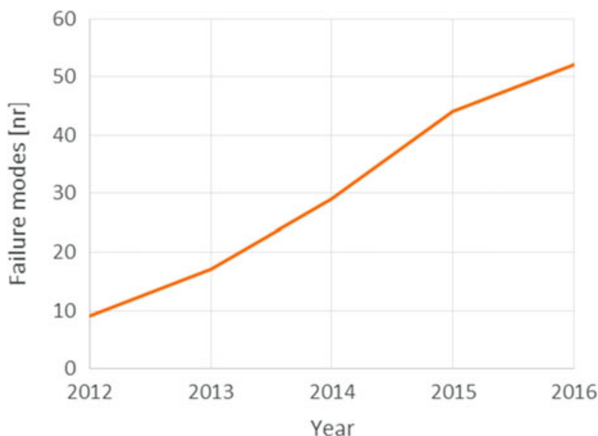

information in a more traditional kind of showing them: a line graph for the number of failure modes in SSL products versus the year detected. What can be seen in these figures is that since the past 4 years the amount of failure modes has more than doubled. Also our earlier forecast of >30 failure modes [1] was easily achieved, and a number of >50 are met. On average ten new failure modes per year were found, but this growth seems to decline in the last years. In semiconductor industry it is believed that one new failure mode is expected per year [18]. Here, the fingerprint changed from single mode failures to those that are due to interactions between components making it difficult to detect the root cause. Looking at the past 4 years, the SSL industry is slowly but gradually moving to that pace.

Finally we raised the question that the promising lifetime numbers of 50.000 and higher burning hours are great, but how does one cover that? It needs accelerated test conditions both on product and component level which is a totally new approach for the lighting industry. A first exercise in this direction was performed by the LED Systems Reliability Consortium [19] by conducting the so-called Hammer Tests. The Hammer Test was to serve as a highly accelerated stress test (HAST) method that would produce failures in SSL luminaires in a reasonable test period (defined as less than 2,000 h of testing). It was set up solely to provide insights into potential failure modes in SSL products. One loop of the Hammer Test consists of four stages of different environmental stresses, and each stage was modeled after common stress tests used in the microelectronics industry. Cumulatively, one loop of the Hammer Test lasted for 42 h, with each stage presenting a stress comprising variations in heat and humidity. Electrical power was cycled on and off during the Hammer Test and provided an extreme stress environment for the luminaires. The acceleration factor of the test was estimated at 30 or higher, depending on the actual application conditions. The testing protocol was exposed to seven commercial SSL luminaires. The results were very surprising [19]. The failures typically occurred in the driver circuit, and the 611 tested LEDs endured nearly 1 million hours of cumulative exposure with only four failures. These findings reinforce the need to consider a systems-level approach, including LEDs, drivers, optics, and other components.

1.3 What's Next: SSL Reliability, Qua Vadis?

Quo vadis is Latin for *where are you going?* According to the legend, it was the apostle Peter who first used these words, by then in a more religious meaning. Here we want to highlight the topics in the coming years that are important in the context of SSL reliability.

The first item worthwhile mentioning is acceleration models. There is a significant need for the creation of appropriate acceleration models for the SSL failure modes mentioned in the previous chapter. We can use the existing models, such as Arrhenius, Coffin-Manson, Norris-Landzberg, Peck, and/or Generalized Eyring, but they need to be tuned to lighting products. A working group in the International

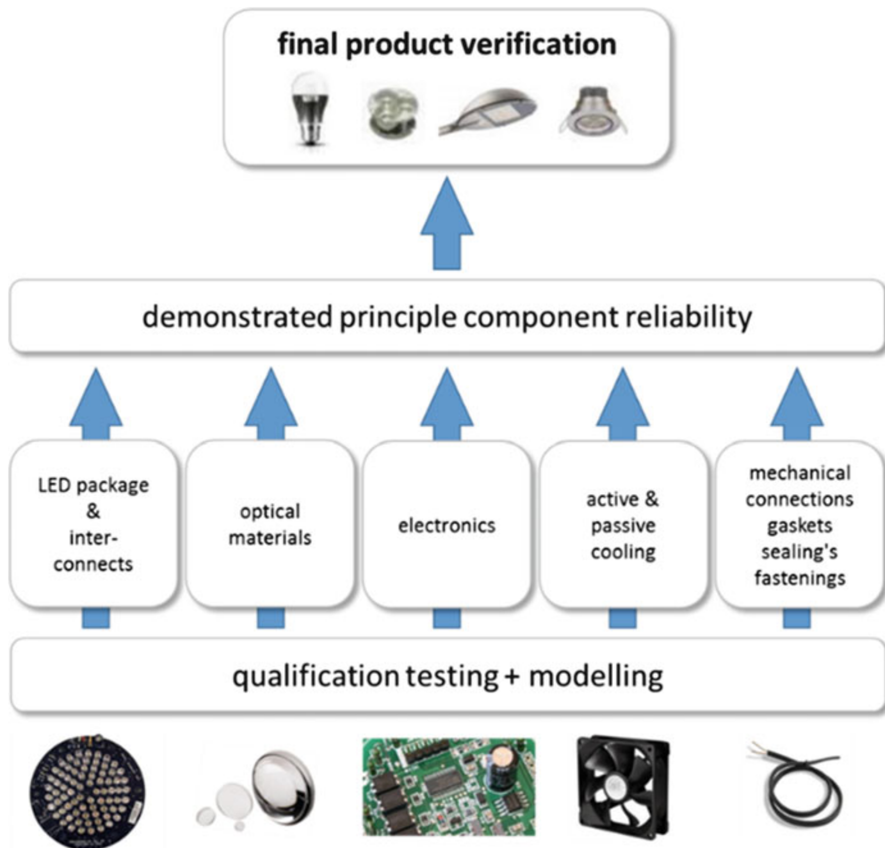

Fig. 1.7 Principal component reliability testing and demonstration on final product level

Electrotechnical Commission (IEC), known as IEC62861 [20, 21], has initiated the work to create a so-called guide to principal component reliability testing for LED light sources and LED luminaires. The group started in 2013, and a final version will appear in due time. Figure 1.7 depicts the principle behind this activity. The guide specifies minimum stress test-driven qualification and reliability requirements for the principal components of LED products. The purpose is to give guidance establishing a level of reliability for which a product is specified. What the exact level is depends on the product specification and depends on the application profile. Acceleration models are needed to project the accelerated test conditions to the application profiles. The publication of this document will certainly give a boost to the required creation of acceleration models.

A second point worthwhile to mention is concerning predictive reliability modeling capabilities. This does not only need advanced modeling theories, algorithm, and tools but also coupling of them and inclusion of the time factor in order to fulfill the reliability demand. Figure 1.8 depicts the currently available toolset for

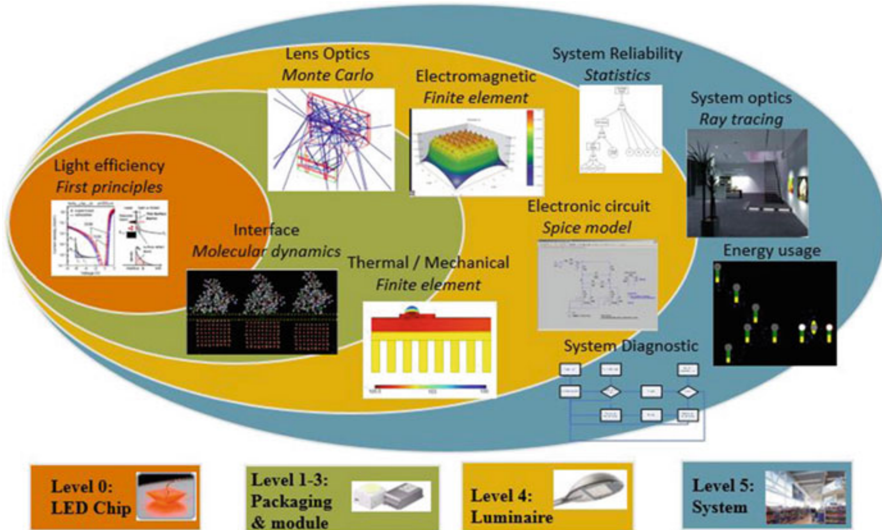

Fig. 1.8 The prediction landscape for SSL products. Coupling and inclusion of time are needed to cover reliability predictions (Courtesy by C.A. Yuan, [22])

SSL product reliability among the different levels from LED chip, package, to complete system. Clearly, tools do exist and are used by academia and industry, but direct coupling of them and inclusion of time need further attention.

Although finite element modeling (FEM) is a well-established technique for predicting thermomechanical behavior of product/process [18], they are not specifically developed for applications and needs of SSL systems. GaN chip is already manufactured to feature size down to several micrometer and nanometer, and also modeling the light output of GaN requires knowledge from across different field such as quantum efficiency and their interaction between different loading conditions. Hence, beyond-continuum mechanics modeling tools such as multiscale modeling tool that will incorporate both molecular dynamics and quantum mechanics need to be developed.

On top of this no coupling of available FEM techniques with traditional ray-tracing tools exists. For packaging and module-level modeling, FEM is a well-established technique for predicting thermomechanical behavior of the LED packages. However, since the performance of LEDs is highly dependent on the light quality, there is a need to develop techniques that could predict the light behavior in the optical system as the package degrades. The multiscale modeling platform (MMP) is part of the EU Multiscale Modeling Cluster of FP7-funded projects on multiscale modeling for nano-materials and systems by design [22]. This cluster unifies EU projects that have the ambition to develop an open, integrated, and multipurpose numerical nano-design environment. The cluster is intended to enable knowledge exchange, foster adoption of novel approaches for multiscale modeling and provide a platform for harmonizing standardization or interoperability. The first

results of this EU project were presented in 2016 at the EuroSimE conference [23, 24]. Tapaninen et al. [25] presented a test case for coupling two physical aspects of an LED, optical and thermal, using specific simulation models coupled through an open-source platform for distributed multi-physics modelling. They showed how to connect a Mie theory-based scattering calculator with ray tracing. Alexeev et al. [24] followed this approach by connecting a ray-tracing model for the light conversion in LightTools® to a thermal model in ANSYS®. Tarashioon et al. [26] introduced a multi-physics reliability simulation approach for solid-state lighting (SSL) electronic drivers. This work explored the system-level degradation of SSL drivers by means of applying its components' reliability information into a system-level simulation. An automatic coupling between electrical simulations in SPICE® with thermal simulations was established in order to perform thermal-electrical reliability predictions. Sun et al. [27] continued this work by improving the thermal part through automatic coupling with ANSYS®. These multi-physics modeling attempts are needed to cover the grand challenge for reliability modeling in SSL, simply because all failure modes and mechanisms, such as electronic drift, browning, coating degradation, color shift, lumen decay, water ingress, corrosion, etc., are results of strong multidisciplinary interactions. More effort should be spent on the development of sophisticated (multi-physics and multiscale) models, efficient numerical algorithms, and user interfaces, code integration methods, as well as advanced computational techniques.

A last important point is the fact that several lighting companies are shifting toward services and/or are increasingly integrating their products and services to offer "integrated solutions." Shifting toward services is attractive because they provide a continuous revenue stream. It has become the new way for some of the world's leading companies to achieve success, e.g., IBM, GE, and Ericsson [28]. Innovating with services brings challenges for high-technology industries or traditional goods industries [29, 30]. One of these challenges is related to reliability and lifetime [31]. Here, lifetime can be thought of as the time by which the product reaches end of life. As such, the service contract length is determined based on the product lifetime, and reliability is replaced by dependability: a measure of system's availability, reliability, and maintainability [32]. A high reliability will always lead to a high availability, but a system with low reliability can still have a very high availability. In the latter case, appropriate scheduling of maintenance will be key for the service overall performance and thus its success.

Next to the shift toward services, as a result of the continuous growth in the utility of disruptive technologies, companies are also enabled to shift more toward an information-based environment [33]. As a result of a radical transformation in the SSL industry – the adoption of digital technology and LED – traditional lighting is shifting toward connected lighting. Hardware is increasingly becoming a source of information with the introduction of, e.g., sensors. The use of information from all these sources can be described as a revolution named *big data*. Big data will cause a fundamental change in the basic reliability concepts. In a classical reliability approach the results from (accelerated) tests are used to obtain conservative bounds of failure rates. With big data, data analytics from live connections of

"intelligent" systems can be used to determine degraded performance. This will trigger scheduled maintenance and/or replacement of the (sub)system. Service in the lighting industry will move into the prognostics regime where a detailed understanding of failure mechanisms, usage scenarios, technology, and design comes together.

1.4 Final Remarks

In the past 4 years we have witnessed a substantial change in the lighting industry. Traditional companies have changed their strategy, and upcoming competition has pushed down prices for LED-based products considerably. LED penetration levels increased so as the diversity of commercially available replacement products. New processes and materials were introduced, and consequently new failure modes appeared. This trend will continue as the lighting industry is getting connected and large amounts of user data are being analyzed. New components are needed to deliver this functionality (sensors, actuator IoT modules), and, as such, the diversity from an architectural point of view will also increase. Gradually but slowly, the term reliability will be replaced by availability, and "smart" maintenance will distinguish good from bad products.

References

1. T. de Groot, T. Vos, R.J.M.J. Vogels, W.D. van Driel, in *Solid State Lighting Reliability: Components to System*, ed. by W.D. Van Driel, X.J. Fan. Quality and reliability in solid state lighting (Springer, New York, 2013); 978-1-4614-3067-4
2. GE's Metamorphizing Century Old Lighting Business, Announcement available at http://www.ledinside.com/news/2015/10/ges_metamorphizing_century_old_lighting_business. Last visited on 8/23/2016
3. G.E. to Phase Out CFL Bulbs, Announcement available at http://www.nytimes.com/2016/02/02/business/energy-environment/ge-to-phase-out-cfl-light-bulbs.html?_r=0. Last visited on 8/23/2016
4. Details of Osram Carve out of LEDVANCE to be announced by May 2016, Announcement available at http://www.ledinside.com/news/2016/4/details_of_osram_carve_out_of_ledvance_to_be_announced_by_may_2016. Last visited on 8/25/2016
5. Breaking with tradition, Philips splits off lighting, Announcement available at http://www.reuters.com/article/us-philips-spin-off-idUSKCN0HI0FV20140923. Last visited on 8/25/2016)
6. Philips Lighting IPO Announcement Leaves These Potential Acquisitors Heartbroken, Announcement available at http://www.ledinside.com/news/2016/5/philips_lighting_ipo_announcement_leaves_these_potential_acquisitors_heartbroken. Last visited on 8/25/2016).
7. Navigant Consulting, Inc., Energy Savings Forecast of Solid-State Lighting in General Illumination Applications, report prepared for the U.S. Department of Energy, Aug 2014.
8. Navigant Consulting, Inc., Energy Savings Forecast of Solid-State Lighting in General Illumination Applications, report prepared for the U.S. Department of Energy. Sept 2016.

9. Estimated LED penetration of the global lighting market from 2010 to 2020, available at http://www.statista.com/statistics/246030/estimated-led-penetration-of-the-global-lighting-market/. Last visited on 8/25/2016.
10. Philips' First Quarter Results 2016, Announcement available at http://www.philips.com/a-w/about/news/archive/corpcomms/news/press/2016/philips-first-quarter-results-2016.html. Last visited on 8/25/2016
11. JEP95: JEDEC Registered and Standard Outlines for Solid State and Related Products, JEDEC Publication No. 95, Jan 2000.
12. Next Generation Lighting Industry Alliance LED Systems Reliability Consortium, LED luminaire lifetime: recommendations for testing and reporting, 3rd edn. 2014
13. JEP122F, Failure mechanisms and models for semiconductor devices, JEDEC publication. Mar 2009
14. B. Hamon, W.D. van Driel, LED degradation: from component to system, Microelectron Reliabil xxx (2016) xxx–xxx
15. Recent Recalls, United States Consumer Product Safety Commission (CPSC), Available at: http://www.cpsc.gov/en/Recalls/. Last visited on 11/9/2016
16. Cree Recalls LED T8 Lamps Due to Burn Hazard, 2015, Available at: http://www.cpsc.gov/en/recalls/2015/cree-recalls-led-lamps. Last visited on 11/9/2016
17. W.D. van Driel, F.E. Evertz, J.J.M. Zaal, O. Morales Nápoles, C.A. Yuan, in *Solid State Lighting Reliability: Components to System*, ed. by W.D. Van Driel, X.J. Fan. An introduction to system reliability for solid state lighting (Springer, New York, 2013); 978-1-4614-3067-4
18. G.Q. Zhang, W.D. van Driel, X.J. Fan, Applications, **141**, ISBN: 1-4020-4934-X, 2006
19. LED Systems Reliability Consortium and the U.S. Department of Energy, *Hammer Testing Findings for Solid-State Lighting Luminaires*, RTI Project Number 0213159.002 (2013)
20. International Electrotechnical Commission (IEC)., Available at: www.iec.ch (n.d.)
21. IEC/TS 62861 Ed. 1: Guide to principal component reliability testing for LED light sources and LED luminaires, technical specification (available since March 2017)
22. Communication with Dr. C.A. Yuan, owner of Ichijouriki LS R&D Co., Ltd, http://www.ichijouriki.com/, 26-09-2016
23. MMP website http://mmp-project.eu/doku.php. Last visited on 9/04/2016
24. A. Alexeev, W. Cassarly, V. D. Hildenbrand, O. Tapaninen, A. Sitomaniemi Simulating Light Conversion in Mid-power LEDs, EuroSimE (http://www.eurosime.org/), 17th–20th of April 2016, Montpellier
25. O. Tapaninen, P. Myöhänen, A. Sitomaniemi, Optical and thermal simulation chain for LED package, EuroSimE (http://www.eurosime.org/), 17th–20th of April 2015, Montpellier
26. S. Tarashioon, W.D. van Driel, G.Q. Zhang, Multi-physics reliability simulation for solid state lighting drivers. Microelectron Reliab. (2014). doi:10.1016/j.microrel.2014.02.019
27. B. Sun, X. J. Fan, C. Qian, and G. Q. Zhang, *PoF-Simulation-Assisted Reliability Prediction for Electrolytic Capacitor in LED Drivers*, (IEEE Transactions on Industrial Electronics, in press 2016)
28. A. Davies, T. Brady, M. Hobday, Charting a path toward integrated solutions. MIT Sloan Manag. Rev. **47**(3), 39 (2006)
29. T. Tuunanen, H. Cassab, Service process modularization: reuse versus variation in service extensions. J. Serv. Res. **14**, 340–354 (2011)
30. Berry, L.L., Shankar, V., Turner Parish, J., Cadwallader, S. and Dotzel, T., Creating new markets through service innovation, Sloan Manag. Rev. **47**(2) (2006)
31. J. Björkdahl, M. Holmén, Editorial: business model innovation–the challenges ahead. Int. J. Prod. Dev. **18**(3/4), 213–225 (2013)
32. P. Jaramillo, A. Pruteanu, W.D. van Driel, W. van Kooten, J.P. Linnartz, in *Runtime Reconfiguration in Networked Embedded Systems: Design and Testing Practices*, ed. by Z. Papp, G. Exarchakos. Tools and methods for testing and verification, (Springer, Singapore, 2016), ISBN 978-981-10-0714-9
33. S. Ismail, *Exponential Organizations: Why New Organizations Are Ten Times Better, Faster, and Cheaper Than Yours (and What to Do About it)* (Diversion Books, New York, 2014)

Chapter 2
Chip-Level Degradation of InGaN-Based Optoelectronic Devices

Carlo De Santi, Matteo Meneghini, Gaudenzio Meneghesso, and Enrico Zanoni

Abstract This chapter reviews the main physical mechanisms responsible for the degradation of InGaN-based optoelectronic devices at chip level. The generation of defects caused by bias and temperature is frequent in modern devices, being responsible for the increase in non-radiative recombination and forward leakage current. Deep level enhancement related to diffusion will also be discussed. The investigation will then move to further processes, such as degradation of the ohmic contacts, electromigration, and device cracking due to mismatch. In addition, we described failure processes related to extrinsic factors, namely, electrostatic discharges and electrical overstresses, along with possible structure improvements that permit to increase device robustness. Finally, degradation caused by reverse bias will be investigated, a topic of growing interest for the design of AC-powered LEDs.

2.1 Defect Generation

The presence of defects in the device is one of the main factors that limit the optical performance. Defects may be native, when they originate from undesired arrangements of the crystal lattice, or extrinsic, when they are related to external impurities. Common native defects include missing gallium or nitrogen atoms in an expected position, called vacancies (V_{Ga}, V_N), presence of gallium or nitrogen atoms in locations that are not part of the lattice (interstitials Ga_i, N_i), and gallium or nitrogen atoms occupying the site of their counterpart (substitutionals Ga_N, N_{Ga}). These may be point defects, when only one atom is involved, or arranged in 2D or 3D configurations, giving birth to extended defects and dislocations. Typical external contaminants include impurities, such as silicon and magnesium that are introduced in order to achieve n- and p-type conductivity, respectively. Other elements present in the growth reactor may have a negative impact, such as hydrogen from the precursors (known for its passivating effect on p-type doping [1, 2]) and residual

C. De Santi • M. Meneghini • G. Meneghesso • E. Zanoni (✉)
Department of Information Engineering, University of Padova, Padova, Italy
e-mail: enrico.zanoni@unipd.it

© Springer International Publishing AG 2018

W.D. van Driel et al. (eds.), *Solid State Lighting Reliability Part 2*, Solid State Lighting Technology and Application Series 3, DOI 10.1007/978-3-319-58175-0_2

oxygen (which is probably involved in the strong yellow luminescence of GaN [3, 4]). Native and extrinsic defects may form bonds, creating several different kinds of complexes.

Defects can create allowed energy levels inside the forbidden bandgap, acting as non-radiative recombination centers according to the Shockley-Read-Hall (SRH) theory, and therefore they reduce the number of electron-hole pairs available for radiative recombination and emission of desired photons.

In a first-order approach, the overall efficiency of LEDs can be described by using the ABC model:

$$\eta_{\mathrm{EQE}} = \eta_{\mathrm{extr}} \times \eta_{\mathrm{inj}} \times \frac{\mathrm{B}n^2}{\mathrm{A}n + \mathrm{B}n^2 + \mathrm{C}n^3}$$

where η_{EQE} is the external quantum efficiency, η_{extr} the extraction efficiency, η_{inj} the injection efficiency, A the Shockley-Read-Hall coefficient, B the radiative recombination coefficient, C the Auger recombination coefficient, and n the carrier density. It is typically assumed that the radiative recombination coefficient does not change during stress, and experimental data obtained at low bias current have a negligible contribution from Auger recombination. At chip level, a variation in the extraction efficiency would require extensive modification in the device structure, since it is related to the reflectivity of the front and back surfaces. In summary, the analysis of the EQE at the various steps of the aging can provide useful information on the variation in SRH recombination and radiative efficiency. In the following, both processes will be analyzed.

2.1.1 Increase in Non-radiative Losses

A comprehensive study identifying the increase in the SRH coefficient as the cause for the optical degradation and its effects was carried out by La Grassa et al. [5]. The devices under test are single quantum well (SQW) LEDs grown on a silicon substrate. Stress caused a reduction in the external quantum efficiency, as shown in Fig. 2.1a. The effect is stronger in the low-moderate current regime, suggesting an increase in the SRH coefficient. The same effect may also be explained by an enhanced carrier escape or shunt leakage current contribution; therefore an additional experiment was designed. By using a highly focused laser diode with adequate peak wavelength, electron-hole pairs were created only inside the quantum well, and the photoluminescence (PL) and corresponding photocurrent were monitored during aging. Results, reported in Fig. 2.1b, show that the PL decreases and that this effect cannot be explained by a higher carrier escape because the corresponding photocurrent, shown in the inset, decreases. The reduction in both quantities can be explained by the additional e^-–h^+ loss process induced by the higher SRH recombination.

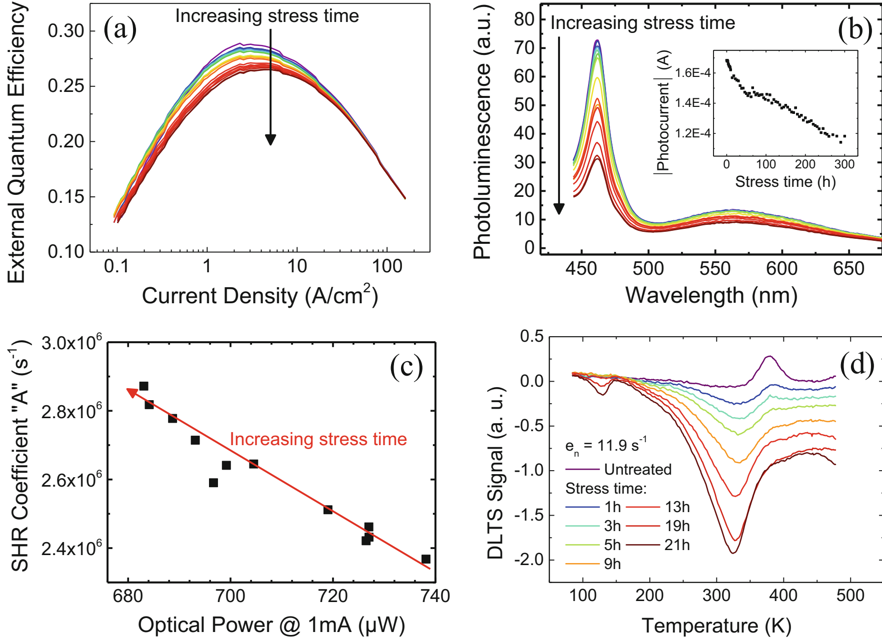

Fig. 2.1 The reduction in optical power at low-medium bias current (**a**) in SQW LEDs is associated to a lower photoluminescence (**b**). This effect is not caused by a higher leakage from the quantum well since the corresponding photocurrent does not increase (inset), but by an enhanced SRH non-radiative recombination, well correlated to the variation in optical power (**c**). The stronger C-DLTS signal (**d**) confirms the increased defect density (Reprinted from Microelectronics Reliability, vol. 55, no. 9–10, M. La Grassa, M. Meneghini, C. De Santi, M. Mandurrino, M. Goano, F. Bertazzi, R. Zeisel, B. Galler, G. Meneghesso, E. Zanoni, "Ageing of InGaN-based LEDs: Effects on internal quantum efficiency and role of defects,", pp. 1775–1778, Copyright (2015), with permission from Elsevier.)

Direct measurement of the SRH A coefficient is possible, thanks to the differential carrier lifetime technique [6]. In this case, an enhancement in non-radiative (SRH) recombination was experimentally found, well correlated with the reduction in the output optical power, as reported in Fig. 2.1c. By means of capacitance deep level transient spectroscopy (C-DLTS, [7]), an increase in defect density for a deep level located at E_c–0.61 eV was detected (see Fig. 2.1d), confirming that the measured increase in non-radiative recombination is supported by physical modification in the lattice and not caused by additional effects or measurement artifacts.

2.1.2 *Increase in Shunt Current*

Tracking changes in the injection efficiency is not an easy task, since there is no clear way to distinguish electron-hole pairs lost due to shunt conduction paths or to

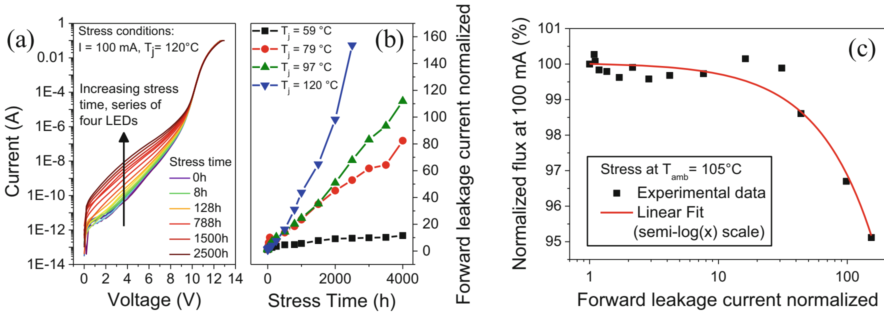

Fig. 2.2 (**a**) Aging causes an increase of the forward leakage current in the series of four white LEDs, (**b**) enhanced by the junction temperature during the stress at the same bias current. (**c**) The variation is well correlated with the decrease in output optical power (Reprinted from Microelectronics Reliability, vol. 55, no. 9–10, M. Buffolo, C. De Santi, M. Meneghini, D. Rigon, G. Meneghesso, E. Zanoni, "Long-term degradation mechanisms of mid-power LEDs for lighting applications", pp. 1754–1758, Copyright (2015), with permission from Elsevier.)

non-radiative recombination in the quantum well. A study involving the possible role of the forward leakage in the degradation of LEDs was presented by Buffolo et al. [8]. They tested the reliability of medium-power white LEDs stressed at nominal operating current and various junction temperatures, evaluated according to the forward-voltage technique [9].

Figure 2.2a reports the changes induced by the stress in the current-voltage characteristics of four LEDs connected in series configuration. A strong increase in the forward leakage current below 10 V is clearly visible, and its amount is influenced by the junction temperature during the stress (see Fig. 2.2b). Recent works correlate the current at low forward bias with the trap-assisted tunneling through mid-gap defects located in the quantum wells, the spacer, and the electron-blocking layer [10, 11]. Therefore, the experimental data are consistent with the creation of deep levels inside the device enhanced by the temperature. The increase in forward leakage is well correlated with the reduction in the output optical power, as described in Fig. 2.2c, possibly because the defect-related conductive path shunts the quantum wells, preventing part of the radiative recombination and lowering the injection efficiency. It is important to point out that, since the defects responsible for the increased forward leakage are located also in the quantum wells, it is possible that the lower optical flux is partly caused by the higher SRH recombination at this new defect and not only by the reduced injection efficiency.

2.2 Diffusion Processes

The defects responsible for the higher SRH recombination may be generated locally by the combined effect of current and temperature, or they can be originated by the diffusion of preexisting defects or impurities towards the active region.

In the literature, several models are available for describing the time dependence of the diffusion process. One of the most successful is the solution in one dimension of Fick's second law, as described by Orita et al. [12]. Assuming a constant N_0 concentration of impurities diffusing toward the active region, the amount of impurities N_{diff} at the position x after time t can be described as

$$N_{\text{diff}}(x,t) = N_0 \ \text{erfc}\left(\frac{x}{2\sqrt{\text{Dt}}}\right)$$

where D is the diffusion coefficient and erfc the error function. According to the SRH theory, a higher local defect concentration yields a faster recombination through deep levels and therefore a lower non-radiative lifetime τ_{nr}. Its variation therefore follows the equation:

$$\Delta\left(\frac{1}{\tau_{\text{nr}}}\right) = \frac{\text{KN}_0}{w}\int_0^w \text{erfc}\left(\frac{x}{2\sqrt{\text{Dt}}}\right)\text{dx}$$

where K is a coefficient that is related to carrier capture rate and w the width of the space charge region.

Diffusion is easier to detect in laser diodes (LD), owing to the linear relation between reciprocal carrier lifetime and threshold current I_{th}

$$I_{\text{th}} = \frac{\text{qV}}{\eta_{\text{inj}}}\frac{N_{\text{th}}}{\tau_{\text{nr}}}$$

where q is the absolute value of the electron electrical charge, V the volume of the active region, and N_{th} the carrier density at lasing threshold. Therefore, if a diffusion process is responsible for the degradation of a laser diode, the expected variation of the threshold current should follow a $\sqrt{t}$ dependence on stress time.

This model was successfully used by De Santi et al. to describe the threshold current variation in commercial green InGaN-based laser diodes submitted to accelerated lifetime tests [13]. The good fitting quality (not shown here) suggested the presence of a diffusion process, and in order to gain additional information, the authors carried out high-resolution spectrally resolved cathodoluminescence maps on the samples. This technique allows for selective excitation of electron-hole pairs in a limited volume of the device by means of a high-energy electron beam. The full emission spectrum is then recorded point by point and analyzed to detect the local composition and radiative efficiency.

Figure 2.3a shows the results at the front facet of an untreated LD. Each color represents the intensity recorded at a specific wavelength (emitted by a specific layer); color coding was done as described in Fig. 2.3b. The saturation level of the color is proportional to the CL signal intensity, i.e., a brighter color points out regions with high radiative efficiency and low defect-related non-radiative recombination. It can be clearly seen that the optical performances of the device are

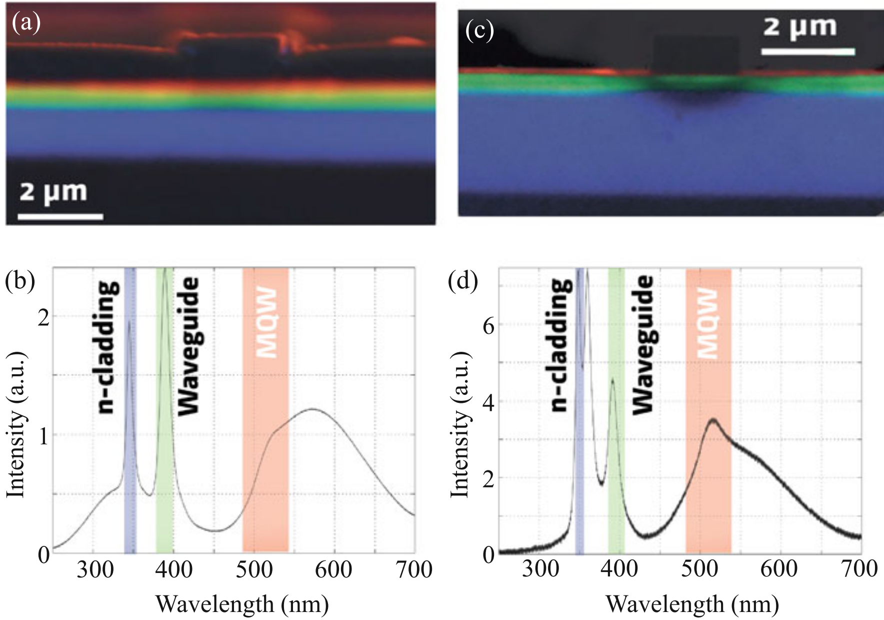

Fig. 2.3 Comparison between high-resolution cathodoluminescence maps at the front facet of an (**a**) untreated and (**c**) aged laser diode. The spectra integrated over the whole area, along with the explanation of the color coding, are shown in (**b**) and (**d**), respectively (Reprinted from De Santi et al. [13]. © 2016 IEEE)

uniform over the whole area under investigation. The intensity profile completely changes when a stressed device is tested (Fig. 2.3c, d). In this case, a dark zone identifies a local enhancement of the non-radiative recombination, affecting not only the quantum wells but also the waveguiding and cladding layers. It is worth noticing that the shape of the degraded region is semicircular and symmetrical along the axis from the p-side to the n-side (i.e., the direction of the current flow). This profile is compatible with a diffusion-related degradation originated from the p-side and moving toward the n-side. Possible culprits include magnesium and hydrogen, chemical elements present in the p-doped material in dopant-level concentration in a highly mobile interstitial position.

Additional information can be extracted by means of this innovative technique regarding the role of the yellow luminescence (YL) in the degradation of the device. The yellow luminescence is a parasitic radiative recombination path, involving gallium vacancies [14] and possibly enhanced by carbon [15–17] or oxygen [3, 4, 18]. In some cases the degradation of LEDs is associated to an increase in the yellow emission, and it is typically assumed that the reduction in optical power is caused by the higher SRH recombination at the defects responsible for the YL. In the case of the laser diodes under analysis, a stronger emission in the yellow spectral region was detected, but this was not the reason for the threshold current

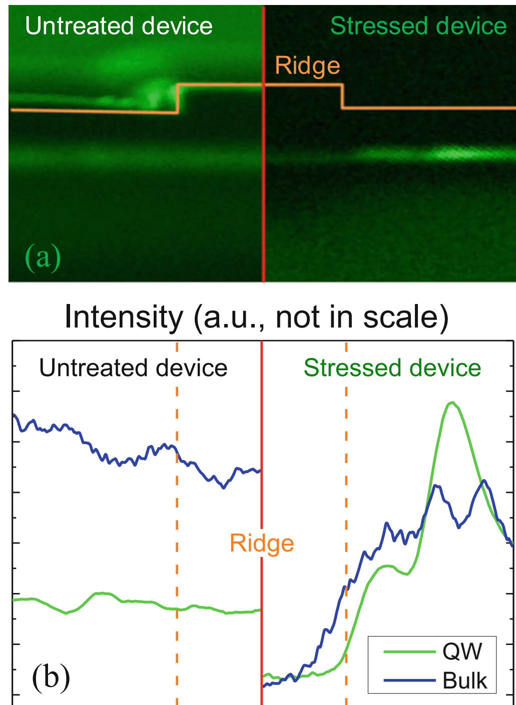

Fig. 2.4 (**a**) Monochromatic cathodoluminescence maps highlighting the spatial distribution of the yellow luminescence in an untreated and stressed device. The latter is affected by the same non-radiative reduction already described for the band-to-band emission. (**b**) Reports the intensity profile along the quantum wells and the bulk material for clearer comparison (Reprinted from De Santi et al. [13]. © 2016 IEEE)

increase. As can be seen in Fig. 2.4a, even the YL signal is affected by an intensity reduction, with the same semicircular shape already described for the band-to-band luminescence. Figure 2.4b reports the intensity profiles in the quantum wells and in the bulk material, allowing for a better understanding of the different intensity. The experimental data are compatible with the generation of an additional deep level, draining electron-hole pairs both from the main emission and from the parasitic yellow band.

A more extensive set of reliability tests on the same samples was carried out by De Santi et al. in [19], varying both the junction temperature and the bias current in order to understand the role of the two stress stimuli. The threshold current was chosen as the parameter used to monitor the degradation.

Figure 2.5a reports its variation during aging at the same bias current and six different junction temperatures, evaluated by means of the forward-voltage method [9], along with a stress at the highest temperature and no applied bias. It can be noticed that no degradation occurs if no current flows through the device and that the degradation is thermally activated. The dashed lines are the fits according to the diffusion model described at the start of this section; the very good agreement suggests that the degradation can be caused by a diffusion process. From the fits it is possible to extrapolate the value of the diffusion coefficient, whose values are summarized in Fig. 2.5b. At higher temperatures the degradation is faster and therefore the diffusion coefficient is higher, and an activation energy of 1.98 eV

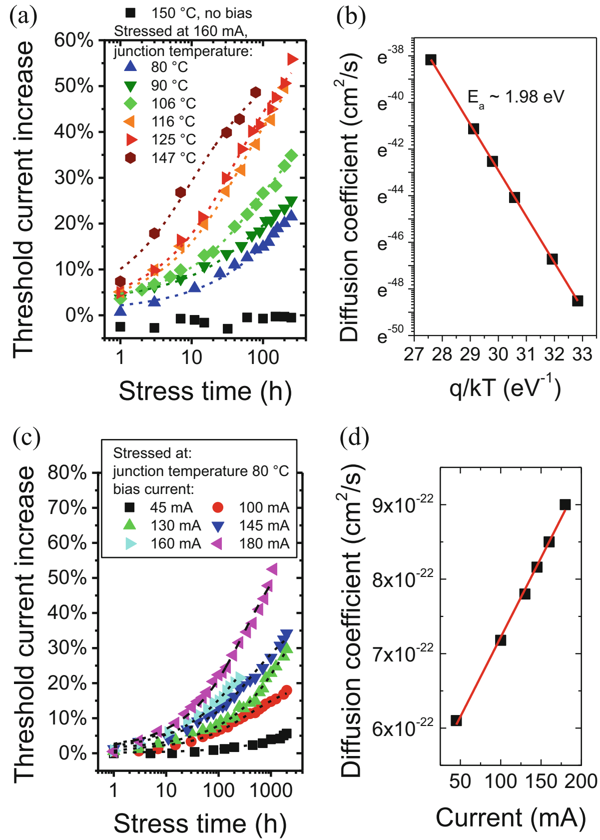

Fig. 2.5 (**a**) Variation in the threshold current of green laser diodes stressed at different junction temperature and fit according to the diffusion equations; the extrapolated values of the diffusion coefficient and its activation energy are in (**b**). (**c**) Presents the same data for devices stressed at different bias currents, the diffusion coefficients are summarized in (**d**) (Reprinted from Microelectronics Reliability, vol. 64, C. De Santi, M. Meneghini, G. Meneghesso, E. Zanoni, "Degradation of InGaN laser diodes caused by temperature- and current-driven diffusion processes", pp. 623–626, Copyright (2016), with permission from Elsevier.)

can be calculated. This value is similar to the 1.93 eV found by Seager et al. in p-n junctions for hydrogen diffusion and even closer to the theoretical 2.03 eV for the sum of the activation energies for diffusion and binding of H^+ to Mg acceptors [20].

The results of the tests at different bias current are shown in Fig. 2.5c. Even in this case, the diffusion equations are able to closely model the experimental data. The diffusion coefficient values in Fig. 2.5d suggest that the bias current level has an impact, even though few reports are available concerning a possible drift mechanism during diffusion [20]. A complete explanation of the whole dataset requires careful examination of the possible diffusing species, their charge state, and their position in the lattice. Possible additional mechanisms that need to be taken into account include the dopant activation, the transfer of kinetic energy from the carriers to the diffusing elements, the field-assisted drift of the impurities, and the diffusion of native defects. Additional details are given in [19]. Moreover, recent papers propose that, during operation of a device, a possible release of hydrogen from point defects can take place, in particular from gallium vacancies [21, 22]. This process can lead to an increased local concentration of hydrogen over stress time. In summary, the data suggest that the degradation could be related to the

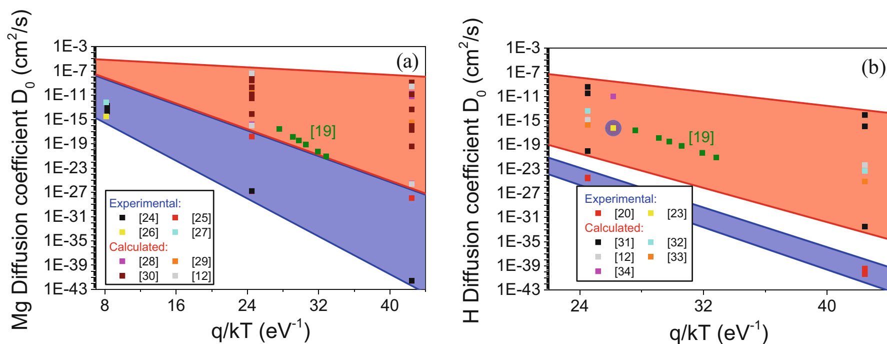

Fig. 2.6 Experimental (*blue region*) and calculated (*red region*) diffusion coefficients for (**a**) magnesium and (**b**) hydrogen from the literature [12, 19, 20, 23–34] (Reprinted from Microelectronics Reliability, vol. 64, C. De Santi, M. Meneghini, G. Meneghesso, E. Zanoni, "Degradation of InGaN laser diodes caused by temperature- and current-driven diffusion processes", pp. 623–626, Copyright (2016), with permission from Elsevier.)

diffusion of interstitial H^+ from the p-side toward the n-side. It is enhanced by temperature, as any diffusion process, and by current, due to the lower electric field in the space charge region that opposes the diffusion.

The analysis of the bias role in the diffusion process has important consequences for a correct understanding of the mechanism. Figure 2.6a, b reviews experimental and theoretical diffusion coefficients reported in the literature for Mg and H, respectively. A clear difference between experimental values and parameters computed from first principles can be noticed. This broad variation may point out that the theoretical basis of the diffusion mechanism for these impurities is not yet completely understood and that the electric field may be a likely candidate to include in the calculations.

2.3 Degradation of the Ohmic Contacts

The ohmic contacts are critical regions, since they strongly influence the injection efficiency of the devices. The metal-semiconductor interface may be affected by interdiffusion, and in GaN the lack of metals with high work function requires very high doping levels for obtaining a tunneling Schottky junction at the p-side. Even though as-grown devices usually suffer from no contact-related performance reduction, additional problems may appear during the lifetime of the device.

A degradation mechanism present in early LEDs is the partial or total detachment of the Ti-W contact and reflector layer from the n-side of the device, reported by Meneghini et al. [35]. Reliability tests carried out in DC and pulsed condition showed that it causes an increase in the series resistance of the device.

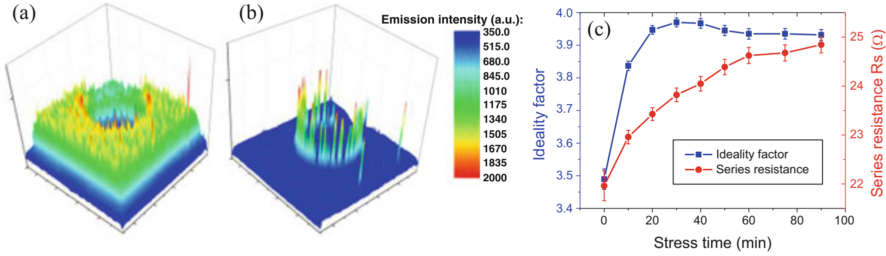

Fig. 2.7 Spatial distribution of the electroluminescence in a LED (**a**) before and (**b**) after thermal storage at 250 °C and no applied bias, showing significant current crowding. The increase in series resistance caused by the aging is shown in (**c**)

In addition to macroscopic mechanical damage, degradation may occur due to microscopic changes in the semiconductor, more common in the latest generations due to the improvements in contact deposition technology. The first demonstration of a degradation mechanism related to this problem was given by Meneghini et al. [36]. They submitted two series of multiple quantum well (MQW) LEDs grown on SiC substrate to accelerated lifetime tests at temperatures between 180 and 250 °C with no applied bias. The devices differ in the presence or lack of SiN passivation deposited by plasma-enhanced chemical vapor deposition (PECVD). They found a strong decrease in optical power only in passivated devices, along with a significant variation in the spatial distribution of the electroluminescence. Figure 2.7 shows that the luminescence, compared to the untreated device (a), is clearly localized near the bonding pad in a device aged for 90 min (b). The current crowding yields also a remarkable increase in the overall series resistance of the device (see Fig. 2.7c). The suggested degradation mechanism involves the transfer of hydrogen from the passivation (the SiN precursors in PECVD are SiH_4 and NH_3) to the p-GaN layer. The H atoms may bond with magnesium, reducing the effective doping level and therefore increasing the resistivity of the contact. This supports the strong current crowding under the bonding pad, since the metal prevents H diffusion from the passivation to the semiconductor.

These tests do not identify whether the contamination problem affects only the contact or also the p-GaN contact layer. In order to clarify this point, additional tests were carried out by Meneghini et al. by using the transmission line method (TLM) [37]. Circular TLM patterns passivated by H-rich PECVD with different radii were submitted to thermal storage at 250 °C. As shown in Fig. 2.8a, the stress caused an increase in series resistance, as previously reported, but also a rectifying behavior near 0 V. This last effect may be related to the Mg deactivation due to H diffusion from the passivation. A lower effective doping level causes a broadening of the Schottky barrier between the metal and the semiconductor, lowering the tunneling probability of the electrons and therefore moving the contact from an ohmic to a rectifying behavior. The TLM technique allows for estimate of both contact and sheet resistance, whose changes over stress are reported in Fig. 2.8b. The increase in contact resistivity is stronger compared to sheet resistance, proving that degradation

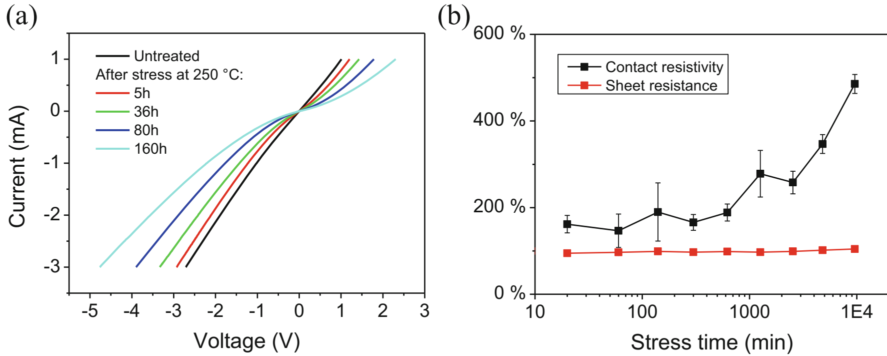

Fig. 2.8 (**a**) Change from ohmic to rectifying behavior of the TLM structure during stress at 250 °C and (**b**) comparison between the variation of the contact and sheet resistance

mainly affects the semiconductor in close proximity to the passivation but not the whole p-GaN layer. In this case, the degradation was found to be recoverable. Additional thermal storage after device depassivation was able to partly restore the initial characteristics, likely due to hydrogen outgassing from the surface. The use of low-H sputtered SiN (instead of PECVD deposition) was able to lower the amount of degradation.

The deposition method for the passivation is not the only parameter influencing the reliability of the contacts. The metal stack composition has a strong importance, due to the very high interdiffusion coefficient of Ni and Au (reported in the 400–600 °C range in [38]). A detailed study on the stability of conventional Ni/Au contacts and on the use of TiB_2 or Ir as an interdiffusion barrier in MQW LEDs was given by Stafford et al. [39]. They found that a strong increase in the turn-on voltage could be caused by thermal storage at the relatively low temperature of 200 °C. The leakage current and output optical power were negatively affected by the test. An improvement of the long-term stability was obtained through the use of TiB_2/Ti/Au or Ir/Au overlayers between the Ni/Au contact and the p-GaN.

2.4 Electromigration

Electromigration is the movement of atoms from the contact pads or the current spreading metal lines to the semiconductor. This process is aided by the current flow, due to the energy exchange between the electrons and the metal atoms, and by the temperature, since it follows the laws of diffusion.

Electromigration has detrimental effects for the reliability of the device: the movement of the metal causes a variation in the local resistance, leading to current crowding. The higher current density induces a stronger local self-heating, and the increased temperature reduces the resistance even more. If this positive feedback is

too strong, it may cause the device to fail due to thermal runaway. In addition, if there is a preferential path for electromigration, a continuous metal line could form from the p-side to the n-side, effectively shunting the active region and preventing correct device operation.

Barton et al. showed that strong electrical degradation, up to a short-circuit behavior, may be present in blue GaN-on-sapphire LEDs [40, 41]. The devices under test were submitted to short (100 ns) but intense current pulses, and no significant change in capacitance DLTS signal was detected. Electron beam-induced current (EBIC) imaging highlighted the presence of some small conductive paths shunting the active region, and scanning electron microscope (SEM) secondary images revealed damage to the p-side contact compatible with metal migration. An electromigration process was therefore identified as the mechanism responsible for the degradation.

Kim et al. analyzed multi-quantum well InGaN/GaN LEDs grown on a sapphire substrate, carrying out stress tests at different bias levels on unpackaged samples [42]. They found that the lifetime can be explained by the contact electromigration failure model of silicon devices, and the increase in forward and reverse current was consistent with the role of metal electromigration in the degradation. Optical photographs of the pad surface support this hypothesis.

Both papers suggested a correlation between the amount of electromigration and defect density in the lattice, since dislocations are believed to be preferential paths for the migration of the metal atoms. Decisive evidence was provided in the study by Hsu et al. who analyzed the effect of high temperature annealing in GaN-on-sapphire MQW LEDs with Ni/Au contact layer [43]. Devices were tested at different annealing temperatures, from 300 to 900 °C, and each annealing test lasted for 10 min in a furnace with continuous nitrogen flow. They found an increase of the forward and reverse leakage currents even at the lower temperatures and a clear short-circuit behavior at higher temperatures. The morphology of the electrodes changed during the test due to the creation of some bubbles on the surface, and in order to investigate the cause, they carried out a transmission electron microscope (TEM) investigation of the cross section directly below the bubbles. The result is summarized in Fig. 2.9. Figure 2.9a shows, for the LED annealed at 900 °C, a hollow region at the center of the bubble in the metal contact directly above a dislocation in the lattice, whereas in Fig. 2.9b, a dislocation in the LED annealed at 600 °C. The labels highlight the points where energy-dispersive X-ray spectroscopy (EDX) was carried out in order to investigate the chemical composition. As can be seen, the void in the bubble (EDS-1) contains some gallium, probably originated by Ga outdiffusion, and the corresponding gasification of nitrogen during GaN decomposition could be the cause for the formation of the bubbles. The most important finding comes from the comparison of EDS-2 and EDS-3. Along the dislocation it is possible to find contamination of nickel and gold, but the two elements are not present outside the dislocation in the p-GaN layer. This experiment confirms that metal from the contacts can be prone to electromigration, that dislocation are preferential paths, and that this mechanism could cause

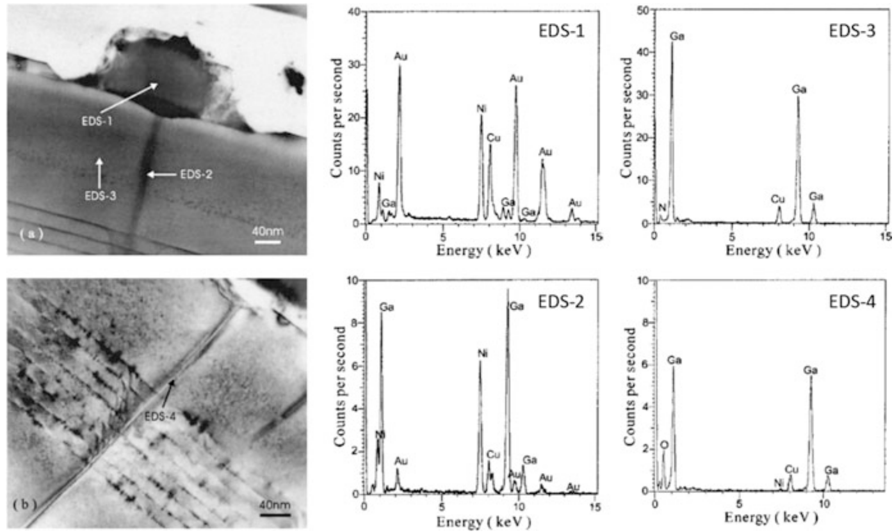

Fig. 2.9 Cross-sectional TEM image of an LED annealed at (**a**) 900 °C and (**b**) 600 °C. EDX spectra (EDS from one to four) confirm the presence of metal atoms from the contacts only inside the dislocations, as a consequence of electromigration (Reproduced from Hsu, Chin-Yuan and Lan, Wen-How and Wu, YewChung Sermon, Applied Physics Letters, 83, 2447–2449 (2003), with the permission of AIP Publishing [43])

shunting of the device. Metal atoms are present also in the dislocations of device annealed at a lower temperature, even if in lower concentration (EDS-4).

Liu et al. in a recent work suggested that electromigration and mechanical stresses can cause a broadening of the contact metal lines [44]. They suppose that dislocation-related failure may happen even without metal atoms migrating inside the dislocation, due to the de-trapping of space charges around threading dislocations caused by the higher electric field at the rough metal edges. Additional work is required in order to confirm this hypothesis.

2.5 Cracking Due to Mismatch

Gallium nitride substrates would be the best choice for device growth, but the technical difficulties involved in the creation of large area native substrates are not easy to overcome. Available GaN wafers have a small area and a remarkable cost, causing a high price for the final products. For this reason, sapphire substrates are commonly used, and a lot of effort is put into growth of efficient LEDs on cheaper silicon substrates.

Both sapphire and silicon have high thermal expansion coefficient and lattice constants mismatch with gallium nitride. For this reason, a high density of

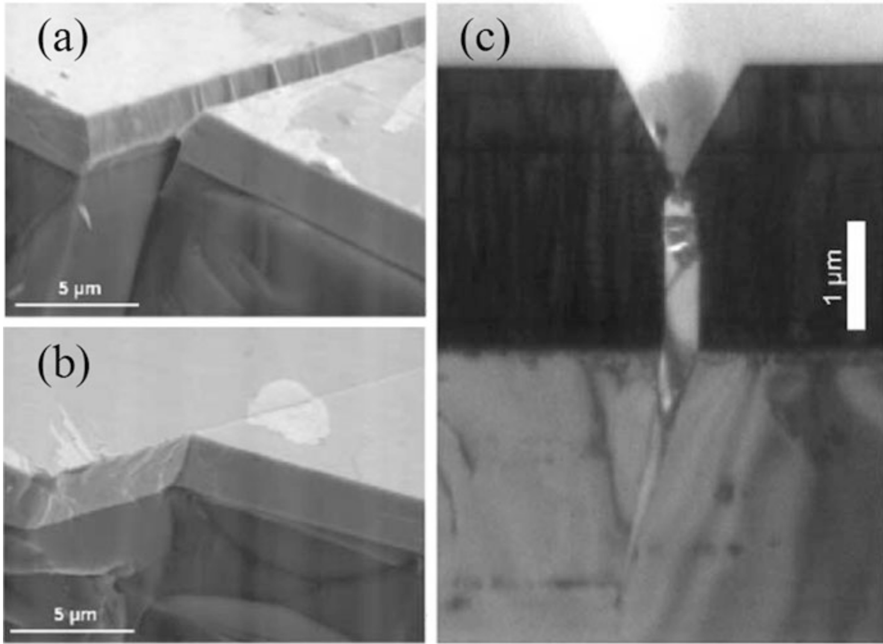

Fig. 2.10 Possible types of cracks for GaN on Si: (**a**) open groove with facets (occurs during heating); (**b**) closed crack (occurs during cooling). The cross section of an open crack is shown in (**c**) (Reprinted from Materials Science and Engineering: B, vol. 93, no. 1-3, A. Krost, A. Dadgar, "GaN-based optoelectronics on silicon substrates", pp. 77–84, Copyright (2002), with permission from Elsevier.)

dislocations forms at the interface between the substrate and the epitaxial layer, reducing the efficiency and the reliability of the devices. Moreover, the strain may relax through the creation of extended cracks during growth or device operation. For GaN on Si, two different types of cracks can be found: open grooves with facets occurring during growth (see Fig. 2.10a) and a crack without grooves, likely generated during the cooling process (see Fig. 2.10b). The cracks extend into the silicon substrate (see Fig. 2.10c).

The formation of cracks in both heating and cooling stages was confirmed by Sarua et al. even for $Al_{0.34}Ga_{0.66}N$ layers grown on GaN on sapphire [46]. By means of atomic force microscope (AFM), they detected the formation of cracks after sample cooling from growth temperature to room temperature and the creation of additional but smaller cracks after annealing above 900 °C. The variation of the position of the E_2(high) phonon mode measured by Raman scattering confirms that tensile stress is relieved near the cracks and that annealing reduces the overall stress, thanks to the formation of the additional cracks (and to the possible formation of dislocations).

Barton et al. studied the degradation of several GaN LEDs grown on sapphire substrate [47]. They used electron beam-induced voltage (EBIV) mapping to

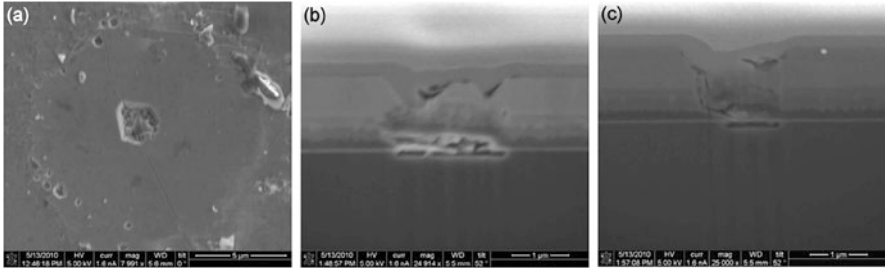

Fig. 2.11 SEM images of a microvoid (**a**) at the center of the plane view, (**b**) and (**c**) at a FIB cross section (Reproduced from Blake, Adam H. and Caselli, Derek and Durot, Christopher and Mueller, Jason and Parra, Eduardo and Gilgen, Joseph and Boley, Allison and Smith, David J. and Tsong, Ignatius S. T. and Roberts, John C. and Piner, Edwin and Linthicum, Kevin and Cook, James W. and Koleske, Daniel D. and Crawford, Mary H. and Fischer, Arthur J., Journal of Applied Physics, 111, 033107 (2012), with the permission of AIP Publishing [70])

correlate a sudden decrease in optical power with the formation of a crack in the device, isolating part of the active region from the contacts.

Various solutions are proposed in the literature to minimize the effects of mismatch, such as AlAs buffer layers [48, 49], AlN buffer layers [50–52], low-temperature AlN interlayers [53–55], AlGaN buffer layers [56], graded AlGaN buffer layers [57–59], superlattices [60–62], use of SiN interlayer [63], growth on patterned substrates [64–66], and growth on porous Si [67–69].

More recently, Blake et al. grew MQW InGaN/GaN LEDs on silicon substrate. The strain was relieved by means of ZrB_2 buffer layers and by an AlN/AlGaN/GaN transition layer [70]. Lateral cracks originated by microvoids were found on the surface of the LEDs (see in Fig. 2.11a a SEM image of a microvoid), completely quenching the electroluminescence from a vast area of the device. By means of cross-sectional transmission electron microscopy (XTEM) investigation, they showed that the presence of microvoids is not related to micropipes originating from the ZrB_2 buffer layer. A SEM analysis of a vertical focused ion beam (FIB) cross section revealed, under the microvoids, the presence of vertical cracks originating from thicker ZrB_2 regions, likely due to misoriented crystallites in the epitaxial ZrB_2 layer. Figure 2.11b, c is SEM cross sections of the region under the microvoid at two different steps of the FIB milling, showing cracks originating from distinctive features at the substrate interface. Devices without ZrB_2 buffer were not affected by this problem.

2.6 Electrostatic Discharge (ESD)

All electronic devices in every material system have a limited robustness to short and highly energetic stimuli, including GaN-based light-emitting diodes. These electrostatic discharge events (ESD) may last for a few hundreds of nanoseconds

and are originated from interaction with electrostatically charged manufacturing or handling equipment (machine model, MM), with installers or end users (human-body model, HBM), with ambient conditions in a typical operating environment (e.g., lightning for streetlight lamps), or with grounding connections when some residual charge is present on the device (charged-device model, CDM).

2.6.1 Role of Defects and Internal Capacitance

Critical regions for the reliability are defective parts and unwanted leakage paths, where the high energy of the discharge may cause a significant current to flow. Typical weak regions are the edges of the contact layer [71–73], the edge of the bonding pad [74, 75], and V-pits with threading dislocations [75, 76]. For this reason, LEDs are sensitive to ESD of both negative and positive polarity, even though the latter usually causes less damage, thanks to the ability of the diode to sustain very high forward currents for a short amount of time before thermal damage occurs [73, 75].

Two different parameters seem to play an important role in the failure mechanism of an LED submitted to electrostatic discharges: the presence of V-pits with threading dislocations and the overall internal capacitance of the device.

The first step in identifying the importance of V-shaped defects connected to threading dislocations was reported by Su et al. [75]. They designed InGaN/GaN MQW LEDs on a sapphire substrate with a Mg-doped GaN cap layer grown at two different temperatures, low temperature grown (LTG) at 900 °C and 1,000 °C, and high temperature grown (HTG) at 1,040 °C and 1,100 °C. The surface of the HTG devices was very smooth with almost no visible extended defects, whereas the LTG devices showed a very rough surface due to the presence of a high V-pit density. The difference was ascribed to the low migration speed of Ga atoms at lower temperatures, leading to a low lateral growth rate [77–79]. Even though all the LEDs showed similar robustness to positive polarity ESD, HTG devices were able to withstand an almost double voltage during negative discharges.

This work was further expanded by Tsai et al. [76]. They grew InGaN/GaN MQW LEDs on a sapphire substrate with different p-GaN growth conditions. A first set of samples, labeled LED-II, used a layer with low temperature grown at 850 °C, leading to a high concentration of V-pits connected to threading dislocations (see a SEM top-view image and a TEM cross section in Fig. 2.12a). In the second set of samples, LED-III, the Mg-doped layer, was grown in HTG conditions at 1,050 °C, preventing the formation of V-pits consistently with the previous paper but not affecting significantly the threading dislocation density (see Fig. 2.12b). The last set of samples, LED-I, was designed with a hybrid approach: a HTG layer is grown immediately above the quantum wells, followed by a LTG layer. This way, the surface of the sample is even rougher than LED-II due to the high concentration of V-pits, but the bottom of the pit is not connected to a threading dislocation, whose density was not reduced (see Fig. 2.12c). Figure 2.12d reports the results of the ESD

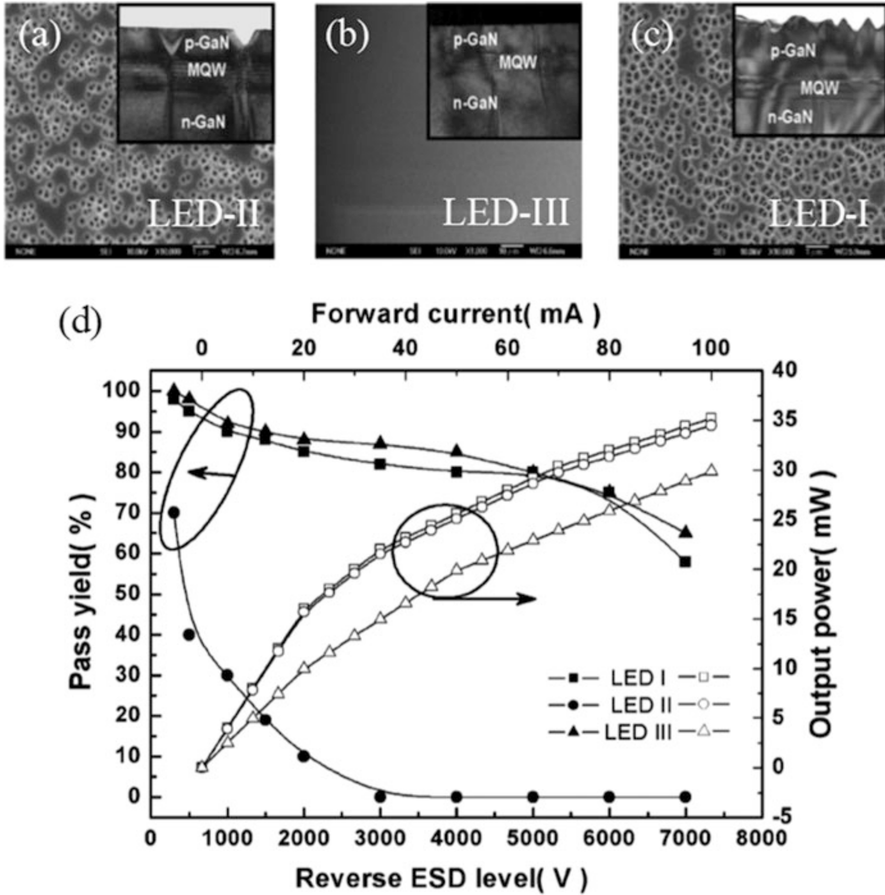

Fig. 2.12 SEM top-view image and TEM cross section of MQW LEDs with p-GaN layer (**a**) grown at 850 °C, (**b**) grown at 1,050 °C, and (**c**) composed of two subsequent layers grown at 1,050 °C and 850 °C. The ESD robustness and output optical power for the different growth conditions are reported in (**d**) (Reprinted from [76]. © 2016 IEEE)

tests. Devices with basic structure (LED-II) have a limited robustness, whereas HTG devices (LED-III) have a higher reliability, consistent with the paper by Su et al. [75]. Remarkably, LED-I samples have a pass yield comparable to LED-III devices, due to the suppression of threading dislocations connected to V-pits. Compared to LED-III set, LED-I devices have a higher output optical power, related to the better extraction efficiency at the rough surface.

Concerning the internal capacitance, its importance derives directly from general considerations on energy transfer during the discharge. Each ESD event is based on a rapid charge transfer, which is simulated through the charge and discharge of an external capacitance on the device under test. In this case, the average current I flowing through the LED is given by $I = Q/\tau$, where Q is the total

charge stored in the discharging capacitance C_d and τ the time constant of the discharge process, which in a simple RC circuit is given by $\tau = C_i(R_{LED} + R_{\text{par}})$, where C_i and R_{LED} are the parallel capacitance and the parallel resistance of the device under test, respectively, and R_{par} the parasitic resistances in the discharge circuit. When the LED resistance dominates in the time constant equation, the energy dissipation E_d in the LED can be evaluated as $E_d = R_{\text{LED}} I^2 \tau = Q^2/C_i$ [80]. For this reason, the higher the capacitance of the LED, the lower energy dissipation it has to sustain. This basic reasoning was experimentally confirmed by Jeon et al. [81]. They grew InGaN MQW LEDs on sapphire substrate with different Si doping concentration in the n-side. The higher doping level increases the capacitance of the device under reverse-bias condition, i.e., when the border of the space charge region is located deep in the doped contact layer. They detected a higher robustness for more highly doped devices.

A similar experiment was carried out by Jia et al. [82]. They grew three different sets of InGaN MQW LEDs on sapphire substrate. Set A has a common structure, whereas set B has a 15 nm thick Si-doped (carrier concentration 1.5×10^{19} cm^{-3}) InGaN layer between the bulk n-GaN and the MQWs. Additionally, set C has also a three-period modulation-doped p-InGaN/GaN hole injection layer between the p-GaN contact layer and the MQWs, where the GaN layers are unintentionally p-doped. The n-InGaN layer caused a small increase of the device capacitance, whereas a stronger effect was detected for devices with the p-superlattice. The ESD performances were improved by the higher internal capacitance.

A multilayer approach was exploited also by Li et al. at the n-side of InGaN MQW LEDs on sapphire substrate [80]. In this case, the improved devices possess three n-GaN/u-GaN pairs between the n-spacer layer and the active region. Experimentally, this additional insertion layer increased the capacitance of the device in the reverse-bias region and the ESD robustness.

2.6.2 ESD Effects

In order to understand the role of process and internal parameters in determining the ESD robustness, the simple pass-fail tests used in the previously reported papers are adequate. With the aim of explaining the effects of a discharge and the changes leading to the failure, more accurate and diverse tests are required.

SEM mapping of the samples is a good complementary technique, allowing for microscopic analysis of the differences between working and failed samples and for detection of most likely failure regions. This technique was used by Meneghini et al. during the tests of UV LEDs (see Fig. 2.13) [73]. The analysis of failed devices pointed out that the failure was located in a curved region of the contacts, where the mesa edge was irregular. This could lead to higher local electrical field and therefore to lower ESD robustness. As a consequence of the discharge, the region is affected by significant structural damage, preventing proper operation of the device.

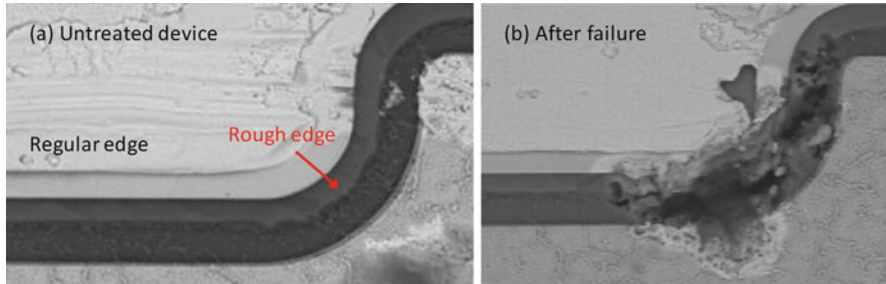

Fig. 2.13 SEM images of an (**a**) untreated and (**b**) failed device submitted to ESD discharges. The correlation between irregular borders of the mesa and failed regions can be noticed

An additional technique that can be used in order to understand the effect of the ESD events is the emission microscopy. The spatially resolved electroluminescence in reverse-bias condition, along with the reverse leakage, was monitored by Meneghini et al. during ESD events at increasing voltage simulated by a transmission line pulser (TLP) on green LEDs [83]. They found that, after the first discharges up to −60 V, the characteristics of the device remained stable. Any additional discharge then reduced the leakage current and emission intensity, until the strong increase in leakage and drop in EL associated to the catastrophic failure of the device. The spatial distribution of the reverse luminescence showed that the reduction is related to the disappearance of some of the "hot spots" composing the emission. The lower leakage current can therefore be associated to local destruction of conductive paths, rather than to processes affecting a wide area. This annihilation may be related to the high energy associated to the pulses, and therefore it is consistently present only when the voltage is higher than a threshold value. When the energy is too high, the conductive paths may melt leading to a short circuit rather than to a nonconducting behavior.

Emission microscopy can be used to detect and support the analysis of different failure modes caused by ESD discharges in devices with varying structure and indium content in the quantum wells, as reported by Dal Lago et al. [84]. They tested two different series of commercially available LEDs, blue with a grid-shaped metal contact and green with a simple bonding pad, monitoring the change in the device impedance and electroluminescence during the discharge. The failure of blue LEDs was identified by the instantaneous increase in the leakage current, related to the creation of a low-resistance conductive path caused by the high power dissipated during the ESD event. This conductive path can be detected by the increase in luminescence after the catastrophic breakdown, occurred at $V_{LINE} = 1{,}503$ V in the case of the representative sample of Figs. 2.14a and 2.15. Subsequent discharges cause a sudden decrease in the impedance of the device, highlighted by the increase in the current flowing through the device during the ESD pulse in Fig. 2.14a. The emitting area moves toward the edge of the damaged region after every additional event (see Fig. 2.15), suggesting a diffusion of the conductive path and more significant damage in the central region, where current

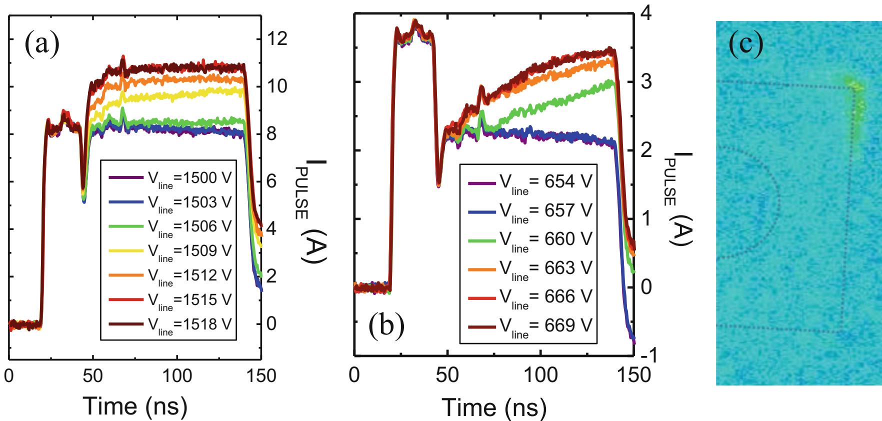

Fig. 2.14 Results of ESD tests on commercial *blue* (**a**) and *green* (**b**), (**c**) LEDs. (**a**, **b**) Current flowing through the device during the discharge, highlighting variation in the device impedance; **c** electroluminescence during the pulse, showing the location of the damaged area (Reprinted from Microelectronics Reliability, vol. 53, no. 9-11, M. Dal Lago, M. Meneghini, N. Trivellin, G. Mura, M. Vanzi, G. Meneghesso, E. Zanoni, ""Hot-plugging" of LED modules: Electrical characterization and device degradation", pp. 1524–1528, Copyright (2013), with permission from Elsevier.)

flows no more. After the test, the device appears melted in the region corresponding to the emitting area. Concerning green LEDs, the increase in leakage current is gradual, and modifications in the device impedance take place even during the pulse, as can be noticed by comparing Fig. 2.14a, b, representative of blue and green devices, respectively. In this case, the emission during the discharge comes from the edge of the device (see Fig. 2.14c), suggesting that an improvement in the defect concentration along the device perimeter could lead to a significantly enhanced ESD robustness.

2.6.3 Structure Improvements

Several solutions for improving the ESD robustness are available at device level and at circuit level. This chapter is focused on the reliability at chip level; therefore we will present only changes to the internal device structure and not designs requiring external components. For this reason, every possible design variation may cause also a positive or negative effect on the output optical power of the LED, other than an improvement of ESD robustness.

Chen et al. suggested a selective post-epitaxy etching and re-deposition in order to fabricate on-chip antiparallel GaN Schottky diodes [85]. Even if the etched areas were placed under the pads (to prevent loss of useful emitting area), in this case the emission from the protected LEDs was lower. The cause was ascribed to the increased non-radiative recombination at the defects generated by the etching process.

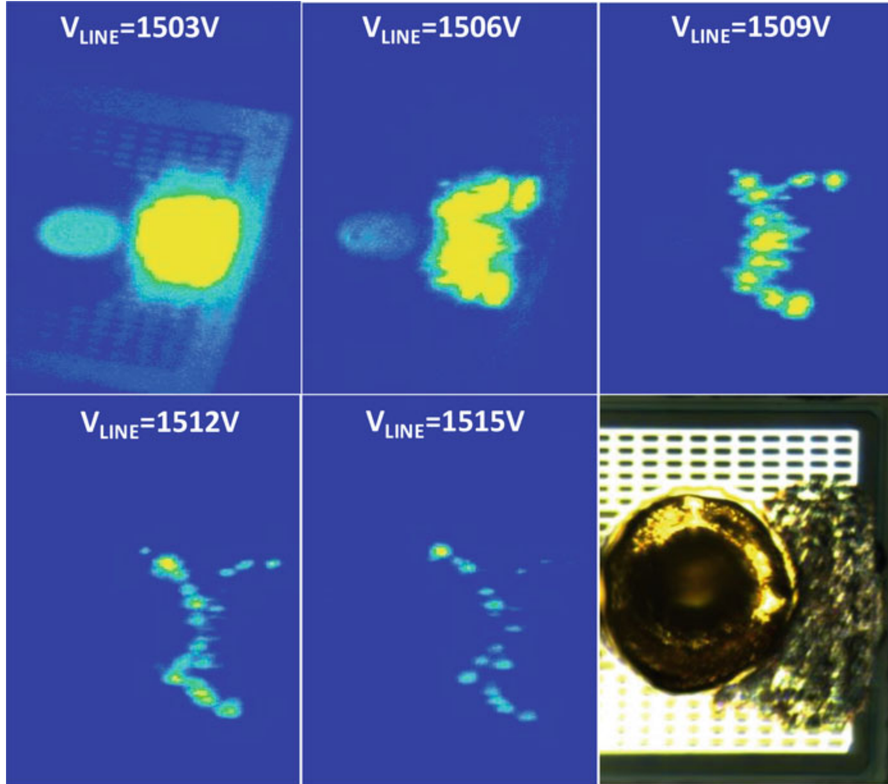

Fig. 2.15 Electroluminescence during the ESD test on the commercial *blue* LED of Fig. 2.14**a**, showing the location and time evolution of the damaged area. The last frame (*bottom right*) shows a photo of the failed device

Wen et al. used an $Al_{0.12}Ga_{0.88}N$/GaN superlattices for a better spreading of the ESD-related current [86]. The superlattices were placed between the active region and the Si-doped GaN substrate (on the n-side) or the Mg-doped GaN cap (on the p-side). They were modulation doped (Si or Mg) to reduce their resistivity, leading to a significant increase of the robustness under reverse-bias pulses. No variation was detected with forward bias tests. The superlattice approach was used also by Liu et al. [87]. In this case the superlattice was composed of p-GaN/i-InGaN layers placed between the multiple quantum wells and the p-GaN layer. The output optical power of the device with superlattice was higher, due to a more uniform current spreading and to a possible reduction in injection losses.

The higher robustness to positive polarity discharges of the GaN-based LEDs was exploited by Shei et al. [88] and by Jeong et al. [89]. By using a selective etching, they realized two independent LEDs with different area on the same epitaxial wafer. The LEDs were then connected in antiparallel configuration by the metal lines, allowing the lower area device to act as an internal shunt protection

diode. In this case, the output optical power is lowered, since part of the area is used for the protection structure.

Following the previously described approach by Tsai et al. [76], Jang et al. studied the effect of the p-AlGaN EBL thickness. They found an improvement of the ESD robustness when a thicker EBL is present in the structure, assuming that it may be related to the filling of the dislocation-related v-pits [90]. The corresponding increase in electroluminescence was related to the lower carrier losses due to overflow and/or tunneling mechanisms.

A creative solution was suggested by Park et al. [91]. They added an air gap in an Al film below the substrate, connecting one side to the anode and the other one to the cathode. If the width of the gap is correctly designed, when the bias pulse is applied, current flows not through the LEDs but through the air gap, due to the limited dielectric strength of air. For this reason, this structure is able to protect the device from both negative- and positive-polarity discharges. No indication was given on the effect of the air gap on the optical characteristics.

Tsai et al. manufactured an internal MOS capacitor by adding a SiO_2 layer in the n-GaN epilayer and extending the metal lines from the contacts [92]. They tested several line layouts and found that the capacitor increases the robustness of the device. Subsequent discharges may lead to damage and puncturing of the oxide and in some cases even damage to the device occurs. The authors do not report the variation of the optical power in the different structures, but it is probably lower due to the area used up by the protection structure.

Chen et al. demonstrated, by means of 3D simulations and experimental tests, the importance of the metal line layout even when a MOS capacitor is not present [93]. They found that current density and thermal dissipation peaks may be reduced by a more uniform distribution of the electric field during the electrostatic discharge. The improved contact structure with parallel extended electrodes theoretically offers the best uniformity of the electric field and was experimentally demonstrated as the most reliable solution against both forward- and reverse-polarity discharges. Even in this case, no indication was given on the variation of the optical power when different contact geometries are employed.

A different solution was used by Huang et al., involving accurate design of a patterned substrate [94]. They tested several devices with different values of fill factor and slanted angle. LEDs grown on substrates with lower fill factor showed a lower concentration of threading dislocations and therefore higher reliability. The most robust devices also have higher output optical power, due to the lower threading dislocation density and to the higher light extraction efficiency.

More recently, Lee et al. suggested the possibility of realizing patterned damage in the current-blocking layer by means of oxygen plasma treatment ion damage [95]. The patterned ion-damaged current-blocking layer (IDCBL) increases the robustness of the devices due to the better spreading of the current injected by the ESD event. Devices with IDCBL were found to have a higher electroluminescence level, thanks to the improved current injection and current spreading, and possibly to a better extraction efficiency.

2.7 Electrical Overstress (EOS)

Compared to ESD events, even electrical overstresses (EOS) can induce catastrophic damage due to stimuli beyond the safe operating area, but involve longer (in the millisecond-second range) and less energetic stresses.

A possible cause is the connection of a LED to a power supply with enabled output, for example, when a lamp is plugged to an energized driver. This event, called “hot plugging,” leads to a significant current flowing through the devices and to a possible degradation or failure. Dal Lago et al. carried out an extensive investigation of the mechanism and of its causes, testing several LEDs from various manufacturers, with varying peak wavelength, connected in series of different length, and even analyzing several drivers [96]. The current waveforms recorded during the hot plugging show that a significant overcurrent may flow through the devices and that its intensity is inversely proportional to the number of LEDs connected in series (see Fig. 2.16a). This behavior is consistent with the discharge of the output capacitance of the driver, charged up to the maximum allowed voltage value due to the lack of any load. This hypothesis was verified by simulation of the discharge time constant in a simple equivalent circuit composed of the output capacitance of the driver and a capacitance with a series resistance in order to

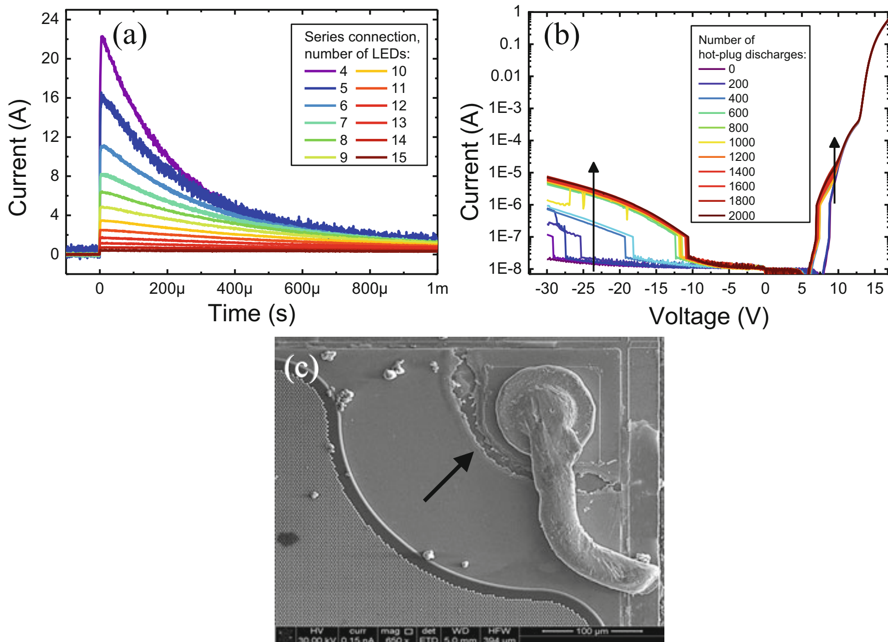

Fig. 2.16 (**a**) Current waveforms during the “hot plugging” event as a function of the number of LEDs connected in series configuration. (**b**) Variation of the current-voltage characteristic after several “hot plugging” connections. (**c**) SEM image showing localized damage around the bonding pad

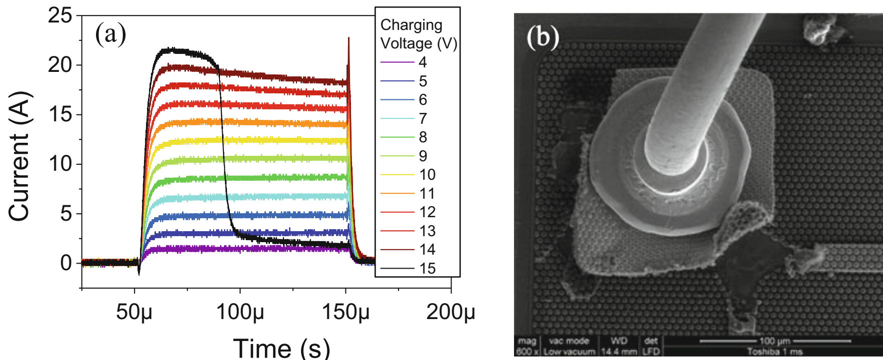

Fig. 2.17 (**a**) Current waveforms during an EOS event at several voltages. (**b**) SEM image showing localized damage at the bonding pad and metal lines

model each LED. Repeated tests on the same LED series showed that the main effect of the event is the creation of defects inside the lattice, acting as additional paths for current flow and therefore increasing the forward and reverse leakage (see Fig. 2.16b). Inspection of failed samples reveals a preferential damaged area near the bonding pad (see Fig. 2.16c). The melted appearance suggests the important role of the device heating during the discharge, possibly due to current crowding leading to thermal runaway.

Additional tests were carried out by Meneghini et al. by using a custom EOS simulator in order to prevent effects related to the specific driver model and manufacturer [97]. Figure 2.17a reports typical current waveforms measured during an EOS event at several voltages. Failure is highlighted by a sudden decrease in the current flowing through the device. The increase in the impedance may be related to damage to the bonding pad and/or to the metal lines (see Fig. 2.17b). The amount of current required for the failure was found to be several times the nominal operating current and to strongly depend on the pulse width, confirming the important role of temperature and the current crowding hypothesis.

2.8 Reverse-Bias Degradation

In the past, reliability studies of LEDs in reverse-bias operation were of limited interest since LEDs are designed for forward bias operation, but this is going to change in the next years. Several research centers and companies are currently developing LED lamps able to operate when directly connected to the mains wall plug, i.e., in AC condition. These lamps do not require an external driver and converter, and therefore they have no additional size, weight, and reliability issue related to additional electronic components. Moreover, they have no power conversion losses and a reduced price due to the lower number of components and to the lower design cost. These advantages have a drawback related to the specific

LED configuration used in the lamps: the reverse-bias degradation issue. Typical AC lamp structures are composed of two LED stripes connected in antiparallel configuration (which improves also the robustness to ESD, since every stripe protects its neighbor). When the lamp is biased, one strip emits light during the positive half of the mains wave, the other during the negative [98–101]. The “off” stripe has to sustain the entire negative mains voltage, and process variations in the equivalent reverse resistance may lead to significant voltage dropping on a limited set of LEDs. For this reason, the analysis of the stability under strong reverse bias is important for this application [102–104].

Chen et al. tested the reliability of green InGaN/GaN MQW LEDs on sapphire substrate when submitted to reverse bias in water vapor [105]. They report a strong increase in the reverse current and in the forward bias leakage current, up to the failure of the device due to the formation of a short circuit. The degradation caused the decrease in the EL in specific regions of the device and the increase in the reverse-bias emission in the same locations. EDX analysis revealed the presence of Au from the contacts near the quantum wells, which may cause a peak in the local electric field. The authors conclude that the catastrophic failure occurs due to the high electric field, but since the stress tests were carried out in water vapor, it is not clear if the same degradation mechanism may influence AC lamps.

An extensive experiment was carried out in air by Meneghini et al. on green MQW LEDs stressed at several constant reverse current and reverse voltage values [106]. They provide experimental evidence that, in reverse-bias condition, current flows through preferential localized paths due to a tunneling process and is correlated to the reverse-bias luminescence. The reliability tests cause a strongly correlated increase in both current and EL, not related to the small power dissipation. The degradation rate was found to depend linearly on the stress current and almost exponentially on stress voltage, suggesting an important role of hot carriers. Stresses at varying temperature showed that the enhancement in degradation rate is stronger for constant voltage tests rather than constant current, confirming that carrier density is the driving force for the increase in reverse current. Failure is therefore related to the generation or propagation of defects toward the active region due to the injection of hot carriers through defective states.

A similar analysis in more extreme conditions was carried out by De Santi et al. on MQW LEDs on sapphire [107]. The increase in reverse current during stress and in reverse EL intensity was confirmed even at higher reverse voltages, as was their correlation (see Fig. 2.18). They analyzed also the spatial distribution of the EL signal, which originates from localized conductive paths (“hot spots”). A novelty element is the fact that the number and intensity of “hot spots” increase over stress time (see the inset in Fig. 2.18) and that the failure point (which has a melted appearance) usually corresponds to the peak reverse EL position. This result suggests that catastrophic breakdown occurs due to the high-power dissipation under strong reverse voltage, driven by the increase in the current flowing in a localized region caused by generation and/or percolation of conductive paths created by the electric field.

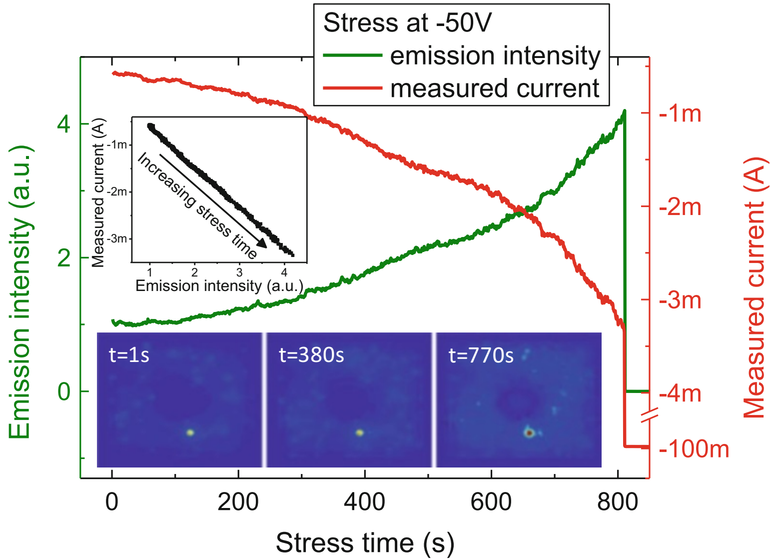

Fig. 2.18 Increase in leakage current and corresponding reverse-bias electroluminescence during stress test at high negative voltage. Insets show the correlation of the two quantities and the spatially resolved reverse electroluminescence maps at three different aging points

To confirm this hypothesis, they tested several devices at various stress voltages. Experimental results show that the time to failure is Weibull distributed (see Fig. 2.19), suggesting that GaN in deep depletion may behave as a dielectric and be affected by time-dependent dielectric breakdown (TDDB). Time-dependent dielectric breakdown is a time-dependent failure mechanism commonly found in insulating materials and consists in the generation/percolation of conductive paths through field-induced defects shunting the dielectric layer [108–110]. The detected exponential dependence of the failure time on stress voltage (see inset of Fig. 2.19) is a second common signature of TDDB. The fact that GaN itself can be affected by TDDB is an important result for a more clear understanding of the failure mechanism of electronic and optoelectronic devices under high electric fields [111–113].

2.9 Conclusions

In summary, the high reliability of GaN-based optoelectronic devices is one of the reasons of their high diffusion in the market of light-emitting devices. Thanks to several improvements in growth techniques and structure, commercial products are almost entirely free from some of the early degradation modes, such as electromigration and device cracking, and even contact robustness is strongly improved.

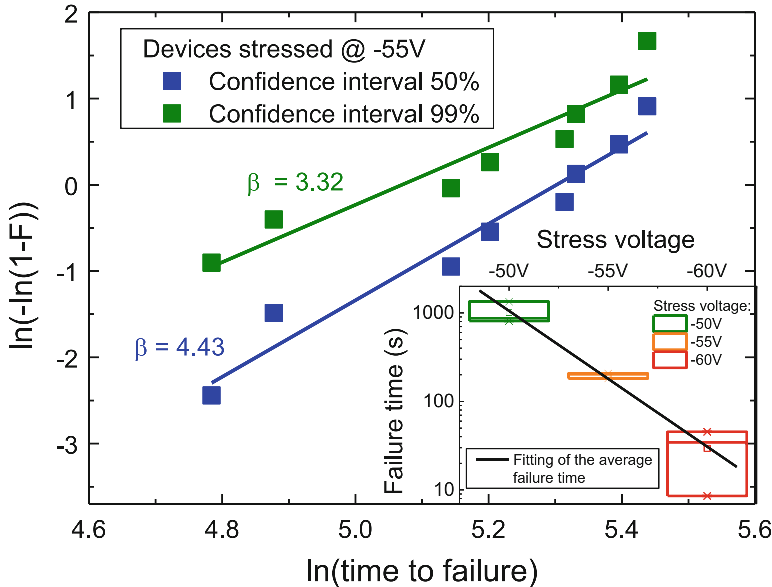

Fig. 2.19 Weibull plot of the distribution of eight devices stressed under high reverse bias and good agreement with the Weibull distribution. Inset: exponential dependence of the time to failure upon stress voltage

At the state of the art, the most critical aspect to be addressed is the generation of defects during the lifetime. They may lead to premature failure due to short circuiting of the active region, and even a moderate increase in their concentration can strongly affect the output optical power, enhancing the non-radiative recombination. To reach an even higher robustness and performance level, a lower defect density and defect generation rate is a mandatory task, and a more accurate analysis of the causes, impact, and improvements regarding the SRH recombination is required.

Out of the total number of failed luminaires in real applications, a large amount of devices exhibit the typical signatures of failure related to ESD or EOS. Even though the reliability at device level was strongly improved, an important role is played by electrical driver structure, mechanical design, and installation conditions. An analysis and careful planning at system level are therefore required to prevent early failures.

Finally, the very good robustness and performances of light-emitting devices enable creative and advanced solutions, such as AC-driven LEDs and new applications to the automotive field. Each of these is expected to create additional open reliability issues, ranging from the stability under reverse bias to operation at very high temperature and power density.

References

1. H. Amano, M. Kito, K. Hiramatsu, I. Akasaki, P-type conduction in mg-doped GaN treated with low-energy electron beam irradiation (LEEBI). Jpn. J. Appl. Phys. **28**., no. Part 2(12), L2112–L2114 (1989). doi:10.1143/JJAP.28.L2112
2. X. Li, J.J. Coleman, Time-dependent study of low energy electron beam irradiation of Mg-doped GaN grown by metalorganic chemical vapor deposition. Appl. Phys. Lett. **69** (11), 1605 (1996). doi:10.1063/1.117045
3. A. Sedhain, J. Li, J.Y. Lin, H.X. Jiang, Nature of deep center emissions in GaN. Appl. Phys. Lett. **96**(15), 5–8 (2010). doi:10.1063/1.3389497
4. D.O. Demchenko, I.C. Diallo, M.A. Reshchikov, Yellow luminescence of gallium nitride generated by carbon defect complexes. Phys. Rev. Lett. **110**(8), 1–5 (2013). doi:10.1103/PhysRevLett.110.087404
5. M. La Grassa, M. Meneghini, C. De Santi, M. Mandurrino, M. Goano, F. Bertazzi, R. Zeisel, B. Galler, G. Meneghesso, E. Zanoni, Ageing of InGaN-based LEDs: effects on internal quantum efficiency and role of defects. Microelectron. Reliab. **55**(9), 1775–1778 (2015). doi:10.1016/j.microrel.2015.06.103
6. D. Schiavon, M. Binder, M. Peter, B. Galler, P. Drechsel, F. Scholz, Wavelength-dependent determination of the recombination rate coefficients in single-quantum-well GaInN/GaN light emitting diodes. Phys. Status Solidi B **250**(2), 283–290 (2013). doi:10.1002/pssb.201248286
7. D.V. Lang, Deep-level transient spectroscopy: a new method to characterize traps in semiconductors. J. Appl. Phys. **45**(7), 3023–3032 (1974)
8. M. Buffolo, C. De Santi, M. Meneghini, D. Rigon, G. Meneghesso, E. Zanoni, Long-term degradation mechanisms of mid-power LEDs for lighting applications. Microelectron. Reliab. **55**(9), 1754–1758 (2015). doi:10.1016/j.microrel.2015.06.098
9. Y. Xi, E.F. Schubert, Junction-temperature measurement in GaN ultraviolet light-emitting diodes using diode forward voltage method. Appl. Phys. Lett. **85**(12), 2163–2165 (2004). doi:10.1063/1.1795351
10. M. Auf der Maur, B. Galler, I. Pietzonka, M. Strassburg, H. Lugauer, A. Di Carlo, Trap-assisted tunneling in InGaN/GaN single-quantum-well light-emitting diodes. Appl. Phys. Lett. **105**(13), 133504 (2014). doi:10.1063/1.4896970
11. M. Mandurrino, G. Verzellesi, M. Goano, M. Vallone, F. Bertazzi, G. Ghione, M. Meneghini, G. Meneghesso, E. Zanoni, Physics-based modeling and experimental implications of trap-assisted tunneling in InGaN/GaN light-emitting diodes. Phys. Status Solidi **212**(5), 947–953 (2015). doi:10.1002/pssa.201431743
12. K. Orita, M. Meneghini, H. Ohno, N. Trivellin, N. Ikedo, S. Takigawa, M. Yuri, T. Tanaka, E. Zanoni, G. Meneghesso, Analysis of diffusion-related gradual degradation of InGaN-based laser diodes. IEEE J. Quantum Electron. **48**(9), 1169–1176 (2012). doi:10.1109/JQE.2012.2203795
13. C. De Santi, M. Meneghini, D. Gachet, G. Mura, M. Vanzi, G. Meneghesso, E. Zanoni, Nanoscale investigation of degradation and wavelength fluctuations in InGaN-based green laser diodes. IEEE Trans. Nanotechnol. **15**(2), 274–280 (2016). doi:10.1109/TNANO.2016.2520833
14. P. Kamyczek, E. Placzek-Popko, V. Kolkovsky, S. Grzanka, R. Czernecki, A deep acceptor defect responsible for the yellow luminescence in GaN and AlGaN. J. Appl. Phys. **111**, 113105 (2012). doi:10.1063/1.4725484
15. T. Ogino, M. Aoki, Mechanism of yellow luminescence in GaN. Jpn. J. Appl. Phys. **19**(12), 2395–2405 (1980). doi:10.1063/1.115098
16. J.L. Lyons, a. Janotti, C.G. Van de Walle, Carbon impurities and the yellow luminescence in GaN. Appl. Phys. Lett. **97**(15), 152108 (2010). doi:10.1063/1.3492841

17. J.L. Lyons, a. Janotti, C.G. Van de Walle, Effects of carbon on the electrical and optical properties of InN, GaN, and AlN. Phys. Rev. B **89**(3), 035204 (2014). doi:10.1103/PhysRevB.89.035204
18. J. Neugebauer, C.G. Van de Walle, Gallium vacancies and the yellow luminescence in GaN. Appl. Phys. Lett. **69**(4), 503–505 (1996). doi:10.1063/1.117767
19. C. De Santi, M. Meneghini, G. Meneghesso, E. Zanoni, Degradation of InGaN laser diodes caused by temperature- and current-driven diffusion processes. Microelectron. Reliab. **64**, 623–626 (2016). doi:10.1016/j.microrel.2016.07.118
20. C.H. Seager, S.M. Myers, A.F. Wright, D.D. Koleske, A.A. Allerman, Drift, diffusion, and trapping of hydrogen in p-type GaN. J. Appl. Phys. **92**(12), 7246–7252 (2002). doi:10.1063/1.1520719
21. Y.S. Puzyrev, T. Roy, M. Beck, B.R. Tuttle, R.D. Schrimpf, D.M. Fleetwood, S.T. Pantelides, Dehydrogenation of defects and hot-electron degradation in GaN high-electron-mobility transistors. J. Appl. Phys. **109**(3), 034501 (2011). doi:10.1063/1.3524185
22. H. Nykänen, S. Suihkonen, L. Kilanski, M. Sopanen, F. Tuomisto, Low energy electron beam induced vacancy activation in GaN. Appl. Phys. Lett. **100**(12), 122105 (2012). doi:10.1063/1.3696047
23. S.J. Pearton, C.R. Abernathy, C.B. Vartuli, J.D. Mackenzie, R.J. Shul, R.G. Wilson, J.M. Zavada, Hydrogen incorporation in GaN, AlN, and InN during $Cl_2/CH_4/H_2/Ar$ ECR plasma etching. Electron. Lett. **31**(10), 836–837 (1995). doi:10.1049/el:19950558
24. Z. Benzarti, I. Halidou, Z. Bougrioua, T. Boufaden, B. El Jani, Magnesium diffusion profile in GaN grown by MOVPE. J. Cryst. Growth **310**(14), 3274–3277 (2008). doi:10.1016/j.jcrysgro.2008.04.008
25. C.J. Pan, G.C. Chi, The doping of GaN with mg diffusion. Solid State Electron. **43**(3), 621–623 (1999). doi:10.1016/S0038-1101(98)00289-5
26. H. Xing, D.S. Green, H. Yu, T. Mates, P. Kozodoy, S. Keller, S.P. Denbaars, U.K. Mishra, Memory effect and redistribution of mg into sequentially regrown GaN layer by metalorganic chemical vapor deposition. Jpn. J. Appl. Phys. **42**(1), 50–53 (2003). doi:10.1143/JJAP.42.50
27. J.C. Zolper, S.J. Pearton, R.G. Wilson, R.A. Stall, Implant activation and redistribution of dopants in GaN. Proc. 11th Int. Conf. Ion Implant. Technol. 705–708 (1996). doi:10.1109/IIT.1996.586515
28. K. Harafuji, K. Kawamura, Magnesium diffusion at dislocation in wurtzite-type GaN crystal. Jpn. J. Appl. Phys. **44**(9A), 6495–6504 (2005). doi:10.1143/JJAP.44.6495
29. K. Harafuji, T. Tsuchiya, K. Kawamura, Magnesium diffusion in wurtzite-type GaN crystal. Jpn. J. Appl. Phys. **0**(7), 2240–2243 (2003). doi:10.1002/pssc.200303298
30. K. Harafuji, T. Tsuchiya, K. Kawamura, Molecular dynamics of magnesium diffusion in Wurtzite-type GaN crystal. Jpn. J. Appl. Phys. **43**(2), 522–531 (2004). doi:10.1143/JJAP.43.522
31. S.M. Myers, A.F. Wright, G.A. Petersen, C.H. Seager, W.R. Wampler, M.H. Crawford, J. Han, Equilibrium state of hydrogen in gallium nitride: theory and experiment. J. Appl. Phys. **88**(8), 4676–4687 (2000). doi:10.1063/1.1309123
32. S.M. Myers, A.F. Wright, Theoretical description of H behavior in GaN p-n junctions. J. Appl. Phys. **90**(11), 5612–5622 (2001). doi:10.1063/1.1413950
33. W.R. Wampler, S.M. Myers, Hydrogen release from magnesium-doped GaN with clean ordered surfaces. J. Appl. Phys. **94**(9), 5682–5687 (2003). doi:10.1063/1.1616986
34. C.G. Van de Walle, N.M. Johnson, in *Semiconductors and Semimetals*, vol 57, ed. by J.I. Pankove, T.D. Moustakas. Hydrogen in III–V nitrides (Academic, Boston, 1999), pp. 157–184
35. M. Meneghini, S. Podda, A. Morelli, R. Pintus, L. Trevisanello, G. Meneghesso, M. Vanzi, E. Zanoni, High brightness GaN LEDs degradation during dc and pulsed stress. Microelectron. Reliab. **46**(9–11), 1720–1724 (2006). doi:10.1016/j.microrel.2006.07.050
36. M. Meneghini, L. Trevisanello, U. Zehnder, T. Zahner, U. Strauss, G. Meneghesso, E. Zanoni, High-temperature degradation of GaN LEDs related to passivation. IEEE Trans. Electron Devices **53**(12), 2981–2987 (2006). doi:10.1109/TED.2006.885544

37. M. Meneghini, L.-R. Trevisanello, U. Zehnder, G. Meneghesso, E. Zanoni, Reversible degradation of Ohmic contacts on p-GaN for application in high-brightness LEDs. IEEE Trans. Electron Devices **54**(12), 3245–3251 (2007). doi:10.1109/TED.2007.908900
38. H. Omiya, F.A. Ponce, H. Marui, S. Tanaka, T. Mukai, Atomic arrangement at the Au/p-GaN interface in low-resistance contacts. Appl. Phys. Lett. **85**(25), 6143 (2004). doi:10.1063/1.1840105
39. L. Stafford, L.F. Voss, S.J. Pearton, H.T. Wang, F. Ren, Improved long-term thermal stability of InGaN⁄GaN multiple quantum well light-emitting diodes using TiB_2- and Ir-based p-Ohmic contacts. Appl. Phys. Lett. **90**(24), 242103 (2007). doi:10.1063/1.2748306
40. D.L. Barton, J. Zeller, B.S. Phillips, Pei-Chih Chiu, S. Askar, Dong-Seung Lee, M. Osinski, K.J. Malloy, in *33rd IEEE International Reliability Physics Symposium*. Degradation of blue AlGaN/InGaN/GaN LEDs subjected to high current pulses (1995), pp. 191–199, doi:10.1109/RELPHY.1995.513674
41. M. Osiński, J. Zeller, P.-C. Chiu, B. Scott Phillips, D.L. Barton, AlGaN/InGaN/GaN blue light emitting diode degradation under pulsed current stress. Appl. Phys. Lett. **69**(7), 898 (1996). doi:10.1063/1.116936
42. H. Kim, H. Yang, C. Huh, S.-W. Kim, S.-J. Park, H. Hwang, Electromigration-induced failure of GaN multi-quantum well light emitting diode. Electron. Lett. **36**(10), 908 (2000). doi:10.1049/el:20000657
43. C.-Y. Hsu, W.-H. Lan, Y.S. Wu, Effect of thermal annealing of Ni/Au ohmic contact on the leakage current of GaN based light emitting diodes. Appl. Phys. Lett. **83**(12), 2447 (2003). doi:10.1063/1.1601306
44. L. Liu, L. Yin, D. Teng, J. Zhang, X. Ma, G. Wang, An explanation for catastrophic failures of GaN-based vertical structure LEDs subjected to thermoelectric stressing. J. Phys. D **48** (30), 305102 (2015). doi:10.1088/0022-3727/48/30/305102
45. A. Krost, A. Dadgar, GaN-based optoelectronics on silicon substrates. Mater. Sci. Eng. B **93** (1–3), 77–84 (2002). doi:10.1016/S0921-5107(02)00043-0
46. A. Sarua, S. Rajasingam, M. Kuball, C. Younes, B. Yavich, W.N. Wang, High temperature annealing of AlGaN: stress and composition changes. Phys. Status Solidi **1**, 568–571 (2003). doi:10.1002/pssc.200390115
47. D.L. Barton, M. Osinski, P. Perlin, C.J. Helms, N.H. Berg, in *1997 I.E. International Reliability Physics Symposium Proceedings. 35th Annual* . Life tests and failure mechanisms of GaN/AlGaN/InGaN light emitting diodes (1997), pp. 276–281. doi:10.1109/RELPHY.1997.584273
48. N.P. Kobayashi, J.T. Kobayashi, P.D. Dapkus, W.-J. Choi, A.E. Bond, X. Zhang, D.H. Rich, GaN growth on Si(111) substrate using oxidized AlAs as an intermediate layer. Appl. Phys. Lett. **71**(24), 3569 (1997). doi:10.1063/1.120394
49. A. Strittmatter, A. Krost, M. Straßburg, V. Türck, D. Bimberg, J. Bläsing, J. Christen, Low-pressure metal organic chemical vapor deposition of GaN on silicon(111) substrates using an AlAs nucleation layer. Appl. Phys. Lett. **74**(9), 1242 (1999). doi:10.1063/1.123512
50. H. Amano, N. Sawaki, I. Akasaki, Y. Toyoda, Metalorganic vapor phase epitaxial growth of a high quality GaN film using an AlN buffer layer. Appl. Phys. Lett. **48**(5), 353 (1986). doi:10.1063/1.96549
51. H. Lahrèche, P. Vennéguès, O. Tottereau, M. Laügt, P. Lorenzini, M. Leroux, B. Beaumont, P. Gibart, Optimisation of AlN and GaN growth by metalorganic vapour-phase epitaxy (MOVPE) on Si (111). J. Cryst. Growth **217**(1–2), 13–25 (2000). doi:10.1016/S0022-0248(00)00478-4
52. A.T. Schremer, J.A. Smart, Y. Wang, O. Ambacher, N.C. MacDonald, J.R. Shealy, High electron mobility AlGaN/GaN heterostructure on (111) Si. Appl. Phys. Lett. **76**(6), 736 (2000). doi:10.1063/1.125878
53. H. Amano, M. Iwaya, N. Hayashi, T. Kashima, S. Nitta, C. Wetzel, I. Akasaki, Control of dislocations and stress in AlGaN on sapphire using a low temperature interlayer. Phys. Status

Solidi **216**(1), 683–689 (1999). doi:10.1002/(SICI)1521-3951(199911)216:1<683::AID-PSSB683>3.0.CO;2-4

54. A. Dadgar, J. Bläsing, A. Diez, A. Alam, M. Heuken, A. Krost, Metalorganic chemical vapor phase epitaxy of crack-free GaN on Si (111) exceeding 1 μm in thickness. Jpn. J. Appl. Phys. **39**., no. Part 2(11B), L1183–L1185 (2000). doi:10.1143/JJAP.39.L1183
55. A. Reiher, J. Bläsing, A. Dadgar, A. Diez, A. Krost, Efficient stress relief in GaN heteroepitaxy on Si(111) using low-temperature AlN interlayers. J. Cryst. Growth **248**, 563–567 (2003). doi:10.1016/S0022-0248(02)01880-8
56. K. Cheng, M. Leys, S. Degroote, M. Germain, G. Borghs, High quality GaN grown on silicon (111) using a Si_xN_y interlayer by metal-organic vapor phase epitaxy. Appl. Phys. Lett. **92**(19), 192111 (2008). doi:10.1063/1.2928224
57. H. Marchand, L. Zhao, N. Zhang, B. Moran, R. Coffie, U.K. Mishra, J.S. Speck, S.P. DenBaars, J.A. Freitas, Metalorganic chemical vapor deposition of GaN on Si(111): stress control and application to field-effect transistors. J. Appl. Phys. **89**(12), 7846 (2001). doi:10.1063/1.1372160
58. K. Cheng, M. Leys, S. Degroote, B. Van Daele, S. Boeykens, J. Derluyn, M. Germain, G. Van Tendeloo, J. Engelen, G. Borghs, Flat GaN epitaxial layers grown on Si(111) by metalorganic vapor phase epitaxy using step-graded AlGaN intermediate layers. J. Electron. Mater. **35**(4), 592–598 (2006). doi:10.1007/s11664-006-0105-1
59. J. Lee, Y. Tak, J.-Y. Kim, H.-G. Hong, S. Chae, B. Min, H. Jeong, J. Yoo, J.-R. Kim, Y. Park, Growth of high-quality InGaN/GaN LED structures on (111) Si substrates with internal quantum efficiency exceeding 50%. J. Cryst. Growth **315**(1), 263–266 (2011). doi:10.1016/j.jcrysgro.2010.08.006
60. P. Saengkaew, A. Dadgar, J. Blaesing, T. Hempel, P. Veit, J. Christen, A. Krost, Low-temperature/high-temperature AlN superlattice buffer layers for high-quality $Al_xGa_{1-x}N$ on Si (111). J. Cryst. Growth **311**(14), 3742–3748 (2009). doi:10.1016/j.jcrysgro.2009.04.038
61. S.-H. Jang, C.-R. Lee, High-quality GaN/Si(111) epitaxial layers grown with various $Al_{0.3}Ga_{0.7}N$/GaN superlattices as intermediate layer by MOCVD. J. Cryst. Growth **253** (1–4), 64–70 (2003). doi:10.1016/S0022-0248(03)01015-7
62. E. Feltin, B. Beaumont, M. Laugt, P. de Mierry, P. Vennegues, M. Leroux, P. Gibart, Crack-free thick GaN layers on silicon (111) by metalorganic vapor phase epitaxy. Phys. Status Solidi **188**(2), 531–535 (2001). doi:10.1002/1521-396X(200112)188:2<531::AID-PSSA531>3.0.CO;2-V
63. L. Zhang, W.-S. Tan, S. Westwater, A. Pujol, A. Pinos, S. Mezouari, K. Stribley, J. Whiteman, J. Shannon, K. Strickland, High brightness GaN-on-Si based blue LEDs grown on 150 mm Si substrates using thin buffer layer technology. IEEE J. Electron Devices Soc. **3**(6), 457–462 (2015). doi:10.1109/JEDS.2015.2463738
64. Y. Honda, Y. Kuroiwa, M. Yamaguchi, N. Sawaki, Growth of GaN free from cracks on a (111)Si substrate by selective metalorganic vapor-phase epitaxy. Appl. Phys. Lett. **80**(2), 222 (2002). doi:10.1063/1.1432764
65. J. Xu, L. Chen, L. Yu, H. Liang, B.L. Zhang, K.M. Lau, Temperature dependence of cathodoluminescence spectra and stress analysis of a GaN layer grown on a mesa structured Si substrate. J. Appl. Phys. **102**(10), 104508 (2007). doi:10.1063/1.2817614
66. S.-J. Lee, G.H. Bak, S.-R. Jeon, S.H. Lee, S.-M. Kim, S.H. Jung, C.-R. Lee, I.-H. Lee, S.-J. Leem, J.H. Baek, Epitaxial growth of crack-free GaN on patterned Si(111) substrate. Jpn. J. Appl. Phys. **47**(4), 3070–3073 (2008). doi:10.1143/JJAP.47.3070
67. T. Boufaden, A. Matoussi, S. Guermazi, S. Juillaguet, A. Toureille, Y. Mlik, B. El Jani, Optical properties of GaN grown on porous silicon substrate. Phys. Status Solidi **201**(3), 582–587 (2004). doi:10.1002/pssa.200306740
68. K. Cheng, S. Degroote, M. Leys, B. Van Daele, M. Germain, G. Van Tendeloo, G. Borghs, Single crystalline GaN grown on porous Si(111) by MOVPE. Phys. Status Solidi **4**(6), 1908–1912 (2007). doi:10.1002/pssc.200674316

69. H. Ishikawa, K. Shimanaka, F. Tokura, Y. Hayashi, Y. Hara, M. Nakanishi, MOCVD growth of GaN on porous silicon substrates. J. Cryst. Growth **310**(23), 4900–4903 (2008). doi:10.1016/j.jcrysgro.2008.08.030
70. A.H. Blake, D. Caselli, C. Durot, J. Mueller, E. Parra, J. Gilgen, A. Boley, D.J. Smith, I.S.T. Tsong, J.C. Roberts, E. Piner, K. Linthicum, J.W. Cook, D.D. Koleske, M.H. Crawford, A.J. Fischer, InGaN/GaN multiple-quantum-well light-emitting diodes grown on Si(111) substrates with ZrB_2(0001) buffer layers. J. Appl. Phys. **111**(3), 033107 (2012). doi:10.1063/1.3684557
71. G. Meneghesso, A. Chini, A. Maschietto, E. Zanoni, P. Malberti, M. Ciappa, in *Electrical Overstress/Electrostatic Discharge Symposium, 2001. EOS/ESD '01* . Electrostatic discharge and electrical overstress on GaN/InGaN light emitting diodes (2001), pp. 247–252
72. S.-M. Kim, H.S. Oh, J.H. Baek, T.-Y. Park, G.Y. Jung, Negative-voltage electrostatic discharge characteristics of blue light-emitting diodes using an extended n-electrode onto plasma treated p-GaN. Appl. Phys. Express **4**(7), 072102 (2011). doi:10.1143/APEX.4.072102
73. M. Meneghini, A. Tazzoli, G. Mura, G. Meneghesso, E. Zanoni, A review on the physical mechanisms that limit the reliability of GaN-based LEDs. IEEE Trans. Electron Devices **57** (1), 108–118 (2010). doi:10.1109/TED.2009.2033649
74. M. Meneghini, A. Tazzoli, E. Ranzato, N. Trivellin, G. Meneghesso, E. Zanoni, M. Pavesi, M. Manfredi, R. Butendeich, U. Zehnder, B. Hahn, A study of the failure of GaN-based LEDs submitted to reverse-bias stress and ESD events. 2010 I.E. Int. Reliab. Phys. Symp. 522–527 (2010). doi:10.1109/IRPS.2010.5488776
75. Y.K. Su, S.J. Chang, S.C. Wei, ESD engineering of nitride-based LEDs. IEEE Trans. Device Mater. Reliab. **5**(2), 277–281 (2005). doi:10.1109/TDMR.2005.847197
76. C.M. Tsai, J.K. Sheu, P.T. Wang, W.C. Lai, S.C. Shei, S.J. Chang, C.H. Kuo, C.W. Kuo, Y.K. Su, High efficiency and improved ESD characteristics of GaN-based LEDs with naturally textured surface grown by MOCVD. IEEE Photon. Technol. Lett. **18**(11), 1213–1215 (2006). doi:10.1109/LPT.2006.875063
77. S. Kitamura, K. Hiramatsu, N. Sawaki, Fabrication of GaN hexagonal pyramids on dot-patterned GaN/sapphire substrates via selective metalorganic vapor phase epitaxy. Jpn. J. Appl. Phys. **34**., no. Part 2(9B), L1184–L1186 (1995). doi:10.1143/JJAP.34.L1184
78. D.I. Florescu, S.M. Ting, J.C. Ramer, D.S. Lee, V.N. Merai, A. Parkeh, D. Lu, E.A. Armour, L. Chernyak, Investigation of V-defects and embedded inclusions in InGaN/GaN multiple quantum wells grown by metalorganic chemical vapor deposition on (0001) sapphire. Appl. Phys. Lett. **83**(1), 33 (2003). doi:10.1063/1.1588370
79. S.M. Ting, J.C. Ramer, D.I. Florescu, V.N. Merai, B.E. Albert, A. Parekh, D.S. Lee, D. Lu, D.V. Christini, L. Liu, E.A. Armour, Morphological evolution of InGaN/GaN quantum-well heterostructures grown by metalorganic chemical vapor deposition. J. Appl. Phys. **94**(3), 1461 (2003). doi:10.1063/1.1586972
80. P. Li, H. Li, Y. Zhao, J. Kang, Z. Li, Z. Liu, X. Yi, J. Li, G. Wang, Excellent ESD resistance property of InGaN LEDs with enhanced internal capacitance. IEEE Photon. Technol. Lett. **27** (19), 2004–2006 (2015). doi:10.1109/LPT.2015.2448418
81. S.-K. Jeon, J.-G. Lee, E.-H. Park, J. Jang, J.-G. Lim, S.-K. Kim, J.-S. Park, The effect of the internal capacitance of InGaN-light emitting diode on the electrostatic discharge properties. Appl. Phys. Lett. **94**(13), 131106 (2009). doi:10.1063/1.3114974
82. C. Jia, C. Zhong, T. Yu, Z. Wang, Y. Tong, G. Zhang, Improvement of electrostatic discharge characteristics of InGaN/GaN MQWs light-emitting diodes by inserting an n^+-InGaN electron injection layer and a p-InGaN/GaN hole injection layer. Semicond. Sci. Technol. **27**(6), 065008 (2012). doi:10.1088/0268-1242/27/6/065008
83. M. Meneghini, A. Tazzoli, R. Butendeich, B. Hahn, G. Meneghesso, E. Zanoni, Soft and hard failures of InGaN-based LEDs submitted to electrostatic discharge testing. IEEE Electron Device Lett. **31**(6), 579–581 (2010). doi:10.1109/LED.2010.2045874

84. M. Dal Lago, M. Meneghini, C. De Santi, M. Barbato, N. Trivellin, G. Meneghesso, E. Zanoni, ESD on GaN-based LEDs: an analysis based on dynamic electroluminescence measurements and current waveforms. Microelectron. Reliab. **54**(9–10), 2138–2141 (2014). doi:10.1016/j.microrel.2014.07.122
85. C.-H. Chen, S.-J. Chang, Y.-K. Su, High electrostatic discharge protection of InGaN/GaN MQW LEDs by using GaN Schottky diodes. Phys. Status Solidi **200**(1), 91–94 (2003). doi:10.1002/pssa.200303496
86. T.C. Wen, S.J. Chang, Y.K. Su, L.W. Wu, C.H. Kuo, Y.P. Hsu, W.C. Lai, J.K. Sheu, Improved ESD reliability by using a modulation doped $Al_{0.12}Ga_{0.88}N$/GaN superlattice in nitride-based LED. Int. Semicond. Device Res. Symp. 2003 77–78 (2003). doi:10.1109/ISDRS.2003.1272004.
87. Y.J. Liu, C.H. Yen, L.Y. Chen, T.H. Tsai, T.Y. Tsai, W.C. Liu, On a GaN-based light-emitting diode with a p-GaN/i-InGaN superlattice structure. IEEE Electron Device Lett. **30** (11), 1149–1151 (2009). doi:10.1109/LED.2009.2030140
88. S.-C. Shei, J.-K. Sheu, C.-F. Shen, Improved reliability and ESD characteristics of Flip-Chip GaN-based LEDs with internal inverse-parallel protection diodes. IEEE Electron Device Lett. **28**(5), 346–349 (2007). doi:10.1109/LED.2007.895428
89. H.H. Jeong, S.Y. Lee, J.-H. Bae, K.K. Choi, J.-O. Song, S.J. Son, Y.-H. Lee, T.-Y. Seong, Improved electrostatic discharge protection in GaN-based vertical light-emitting diodes by an internal diode. IEEE Photon. Technol. Lett. **23**(7), 423–425 (2011). doi:10.1109/LPT.2011.2106204
90. C.-H. Jang, J.K. Sheu, C.M. Tsai, S.C. Shei, W.C. Lai, S.J. Chang, Effect of thickness of the p-AlGaN electron blocking layer on the improvement of ESD characteristics in GaN-based LEDs. IEEE Photon. Technol. Lett. **20**(13), 1142–1144 (2008). doi:10.1109/LPT.2008.924886
91. T.Y. Park, M.S. Oh, S.J. Park, Improvement of electrostatic discharge characteristics and optical properties of GaN-based light-emitting diodes. IEEE Electron Device Lett. **30**(9), 937–939 (2009). doi:10.1109/LED.2009.2025783
92. P.C. Tsai, W.R. Chen, Y.K. Su, Enhanced ESD properties of GaN-based light-emitting diodes with various MOS capacitor designs. Superlattice. Microst. **48**(1), 23–30 (2010). doi:10.1016/j.spmi.2010.04.006
93. S.L. Chen, Enhanced electrostatic discharge reliability in GaN-based light-emitting diodes by the electrode engineering. J. Disp. Technol. **10**(10), 807–813 (2014). doi:10.1109/JDT.2014.2321460
94. X.-H. Huang, J.-P. Liu, Y.-M. Fan, J.-J. Kong, H. Yang, H.-B. Wang, Improving InGaN-LED performance by optimizing the patterned sapphire substrate shape. Chinese Phys. B **21**(3), 037105 (2012). doi:10.1088/1674-1056/21/3/037105
95. K.H. Lee, Y.-T. Moon, S.K. Oh, J.S. Kwak, High efficiency and ESD of GaN-based LEDs with patterned ion-damaged current blocking layer. IEEE Photon. Technol. Lett. **27**(2), 149–152 (2015). doi:10.1109/LPT.2014.2362982
96. M. Dal Lago, M. Meneghini, N. Trivellin, G. Mura, M. Vanzi, G. Meneghesso, E. Zanoni, 'Hot-plugging' of LED modules: electrical characterization and device degradation. Microelectron. Reliab. **53**(9–11), 1524–1528 (2013). doi:10.1016/j.microrel.2013.07.054
97. M. Meneghini, C. De Santi, M. Buffolo, A. Munaretto, G. Meneghesso, E. Zanoni, in *2015 12th China International Forum on Solid State Lighting (SSLCHINA)*. Towards high reliability GaN LEDs: understanding the physical origin of gradual and catastrophic failure (2015), pp. 63–66. doi:10.1109/SSLCHINA.2015.7360690
98. H.-H. Yen, W.-Y. Yeh, H.-C. Kuo, GaN alternating current light-emitting device. Phys. Status Solidi **204**(6), 2077–2081 (2007). doi:10.1002/pssa.200674766
99. J. Cho, J. Jung, J.H. Chae, H. Kim, H. Kim, J.W. Lee, S. Yoon, C. Sone, T. Jang, Y. Park, E. Yoon, Alternating-current light emitting diodes with a diode bridge circuitry. Jpn. J. Appl. Phys. **46**(48), L1194–L1196 (2007). doi:10.1143/JJAP.46.L1194

100. H.-H. Yen, H.-C. Kuo, W.-Y. Yeh, Characteristics of single-chip GaN-based alternating current light-emitting diode. Jpn. J. Appl. Phys. **47**(12), 8808–8810 (2008). doi:10.1143/JJAP.47.8808
101. G.A. Onushkin, Y.-J. Lee, J.-J. Yang, H.-K. Kim, J.-K. Son, G.-H. Park, Y. Park, Efficient alternating current operated white light-emitting diode chip. IEEE Photon. Technol. Lett. **21** (1), 33–35 (2009). doi:10.1109/LPT.2008.2008204
102. H.H. Yen, H.C. Kuo, W.Y. Yeh, Particular failure mechanism of GaN-based alternating current light-emitting diode induced by GaO_x oxidation. IEEE Photon. Technol. Lett. **22**(15), 1168–1170 (2010). doi:10.1109/LPT.2010.2051424
103. W.Y. Yeh, H.H. Yen, Y.J. Chan, The development of monolithic alternating current light-emitting diode. SPIE OPTO 793910–793912 (2011). doi:10.1117/12.873668
104. Y. Gao, H. Zhang, X. Guo, F. Cao, J. Yu, A. Chen, N. Zou, Method to design alternating current light-emitting diodes luminous flux. Opt. Quant. Electron. **47**(12), 3715–3727 (2015). doi:10.1007/s11082-015-0241-z
105. H. Chen, B. Yun Huang, Y. Cheng Chu, Degradation mechanisms in GaN light-emitting diodes undergoing reverse-bias operations in water vapor. Appl. Phys. Lett. **103**(17), 8–11 (2013). doi:10.1063/1.4826254
106. M. Meneghini, U. Zehnder, B. Hahn, G. Meneghesso, E. Zanoni, Degradation of high-brightness green LEDs submitted to reverse electrical stress. IEEE Electron Device Lett. **30**(10), 1051–1053 (2009). doi:10.1109/LED.2009.2029129
107. C. De Santi, M. Meneghini, M. Buffolo, G. Meneghesso, E. Zanoni, Experimental demonstration of time-dependent breakdown in GaN-based light emitting diodes. IEEE Electron Device Lett. **37**(5), 611–614 (2016). doi:10.1109/LED.2016.2543805
108. R. Degraeve, G. Groeseneken, R. Bellens, J.L. Ogier, M. Depas, P.J. Roussel, H.E. Maes, New insights in the relation between electron trap generation and the statistical properties of oxide breakdown. IEEE Trans. Electron Devices **45**(4), 904–911 (1998). doi:10.1109/16.662800
109. J.H. Stathis, Percolation models for gate oxide breakdown. J. Appl. Phys. **86**(10), 5757 (1999). doi:10.1063/1.371590
110. T. Kauerauf, R. Degraeve, M.B. Zahid, M. Cho, B. Kaczer, P. Roussel, G. Groeseneken, H. Maes, S. De Gendt, Abrupt breakdown in dielectric/metal gate stacks: a potential reliability limitation? IEEE Electron Device Lett. **26**(10), 773–775 (2005). doi:10.1109/LED.2005.856015
111. D. Marcon, T. Kauerauf, F. Medjdoub, J. Das, M. Van Hove, P. Srivastava, K. Cheng, M. Leys, R. Mertens, S. Decoutere, G. Meneghesso, E. Zanoni, G. Borghs, in *2010 International Electron Devices Meeting*. A comprehensive reliability investigation of the voltage-, temperature- and device geometry-dependence of the gate degradation on state-of-the-art GaN-on-Si HEMTs (2010), pp. 20.3.1–20.3.4. doi:10.1109/IEDM.2010.5703398
112. M. Meneghini, O. Hilt, C. Fleury, R. Silvestri, M. Capriotti, G. Strasser, D. Pogany, E. Bahat-Treidel, F. Brunner, A. Knauer, J. Würfl, I. Rossetto, E. Zanoni, G. Meneghesso, S. Dalcanale, Normally-off GaN-HEMTs with p-type gate: off-state degradation, forward gate stress and ESD failure. Microelectron. Reliab. (2015). doi:10.1016/j.microrel.2015.11.026
113. M. Ťapajna, O. Hilt, E. Bahat-Treidel, J. Würfl, J. Kuzmík, Investigation of gate-diode degradation in normally-off p-GaN/AlGaN/GaN high-electron-mobility transistors. Appl. Phys. Lett. **107**(19), 193506 (2015). doi:10.1063/1.4935223

Chapter 3
LED Early Failures: Detection, Signature, and Related Mechanisms

B. Hamon, T. Merelle, and B. Bataillou

Abstract LED lifetime and reliability are strong differentiators for a luminaire assembler. An LED being more a system and not a single device means reliability analyses are complex. The different subparts constituting the LED present different failure modes and mechanisms, as well as different responses to stresses. In this chapter, the latest results of LED early failure investigation are presented. In a first part, an introduction to early failure management in reliability studies will be presented. In the second part of this chapter, the different critical steps in LED production and their variability and quality impact will be reviewed. The third part explains postproduction weak LED detection method at the LED assembly side as well as the modeling, characterization, and measurement techniques. Last part details early failure signatures, identified defects, and how they are linked to production process steps.

3.1 Introduction

In addition to their higher efficacy, the lifetime and the reliability of LEDs are strong differentiators for the technology on the lighting market. The fact that an LED cannot be considered only as a component but more as a system renders their reliability studies challenging. In fact, the different subparts constituting the LED present different failure modes and mechanisms as well as different responses to stresses. LED reliability and lifetime prediction is thus considered as a key point for solid-state lighting (SSL) massive adoption. Past studies have mostly focused on investigating the different failure mechanisms related to each subpart [1]. In the early years of LED lighting, reliability prediction efforts have been focused mostly on lumen maintenance predictions, as the flux depreciation over time was consid-

B. Hamon (✉)
Philips Lighting, Amsterdam, The Netherlands
e-mail: benoit.hamon@philips.com

T. Merelle • B. Bataillou
Pi Lighting, Avenue Ritz, 19, Sion, 1950, Switzerland
e-mail: thomas.merelle@pi-lighting.com; benoit.bataillou@pi-lighting.com

© Springer International Publishing AG 2018

W.D. van Driel et al. (eds.), *Solid State Lighting Reliability Part 2*, Solid State Lighting Technology and Application Series 3, DOI 10.1007/978-3-319-58175-0_3

ered as the main failure mode of LED components [1–6]. With the increase of the maturity of LED technology, an additional focus has been given to color maintenance models [7, 8] and end of life models such as wire bond fatigue models [9]. As a result, current modeling and investigations are focusing on predicting the performances and the behaviors of LEDs (or LED lighting systems) after thousands of hours of use.

In the process of building these long-term reliability models, the study of early failures and efforts to filter out components with initial weaknesses from the production appears to be a necessity.

The LED production process is composed of different steps from epitaxial growth to packaging [10]. Due to variability in production processes or to handling between manufacturing steps, defects and weaknesses in the component, which can lead to an early failure, cannot be entirely removed. Other defects such as lens crack or wire bond break can easily be filtered out from LED manufacturers' production through visual inspection processes or during binning process. In fact, at the end of the LED manufacturing process, components are measured in line and grouped by defined parameters (e.g., flux, color point, forward voltage), a step known as binning. Consequently, any abnormal component's behavior such as no light output due to anomaly in the wire bond process is then removed from the end products.

However, smaller defects which don't have directly observable consequences but which weakened the component are not necessarily identified in production. Therefore, efforts have been conducted to highlight these defects during the production of LED-based lighting systems.

The study of these defects requires knowledge on both component architecture and processes as well as an access to high LED quantity as these defects have an impact on a small percentage of the LED total production.

In the first part, device lifetime is defined, and an introduction to early failure management in reliability studies is presented.

In the second part of this chapter, the different critical steps in LED production, their variability, and the resulting impact on quality are reviewed. Small defects which don't have directly observable consequences but which weakened the component are not necessarily identified in the production phase. Efforts have then been conducted to highlight these defects during LED production. One can list three big families of variabilities: batch-to-batch variability, variability leading to hard fails, and variability leading to soft fails. Root causes for those three families are listed and discussed in this chapter.

The third part explains postproduction failing LED detection methods at the LED assembly side, as well as the modeling, characterization, and measurement techniques. Current modeling and investigation are focusing on predicting the performances and the behaviors of LEDs (or LED lighting systems) after thousands of hours of use.

The last part describes postproduction in-depth study of these defects, which requires knowledge on both component architecture and processes as well as an access to high LED volumes as these defects have an impact on a small percentage of the LED total production.

3.2 Early Failures in Reliability Studies

In reliability field, the lifetime of a population of any system is often graphically represented using the bathtub curve [11]. In this graphical representation (Fig. 3.1), lifetime is accessed to follow three regimes: an infant mortality (or early failure) regime, a random failure regime, and finally a wear out failure regime.

The failure rate in those three regimes can be described using the Weibull model [12]:

$$g_{\text{Weibull}}(x) = \frac{\alpha}{\beta}\left(\frac{x}{\beta}\right)^{\alpha-1}\exp\left(-\left(\frac{x}{\beta}\right)^{\alpha}\right) \tag{3.1}$$

In the Weibull model, the value of the parameter β allows to describe each regimes presented in Fig. 3.1. A parameter $\beta < 1$ is characteristic of a decreasing failure rate with time which characterizes the infant mortality regime. In the opposite, a parameter $\beta > 1$ is associated with an increasing failure rate representative of the wear-out failure regime.

Early failures can result from different failure causes, such as material or assembly defects. These defects, which cause the system to fail in a relatively short period of time, are highly undesirable as they cause warranty concerns and customer displeasure.

Early failures can be linked to initial material defects; consequently, they are linked to LED production variability and are then challenging to prevent. Therefore, LED productions have a population of “weak” (also called freak) components which present a lifetime below the one of the main population. An example of these main population and weak population lifetime distribution is displayed in Fig. 3.2.

From a probability point of view, the proportion of a lighting system (with several LEDs) to have a weak component is higher than the proportion of weak components within the LED production (see Eq. 3.2). Therefore, the impact of the weak population on a complete lighting system cannot be overlooked.

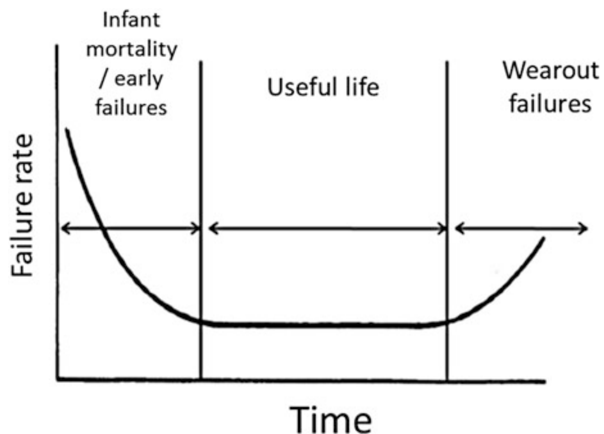

Fig. 3.1 The bathtub curve – failure rate vs. time [11]

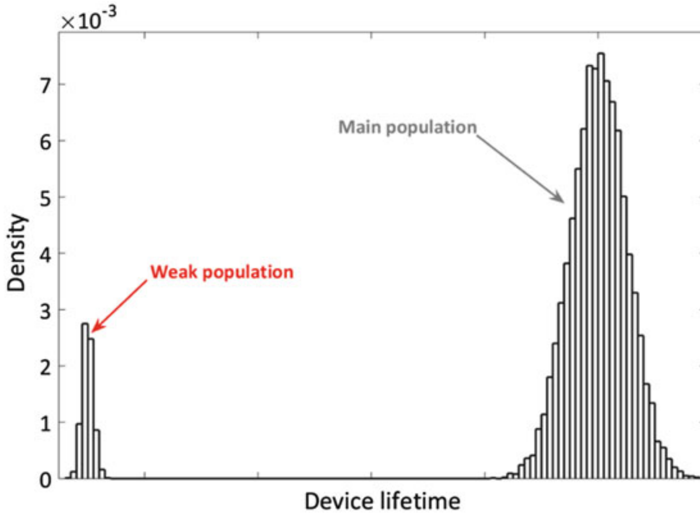

Fig. 3.2 Simulated production lifetime from a large LED population with a 10% ratio of weak components

$$F(f, n, k) = 1 - \sum_{i=0}^{k} \binom{n}{i} (1 - f)^{n-i*} f^{i} \tag{3.2}$$

With:

f: Probability of an LED component to be within the weak population
F: Probability of an LED system to have a weak component
n: Number of LED component in the LED system
k: Number of LED component early failure accepted in the LED system

Considering an LED system in which no early failure component is accepted ($k = 0$):

$$\begin{aligned} F(f, n, 0) &= 1 - (1 - f)^{n} \\ F(f, n, 0) &\geq f \qquad \forall n \end{aligned} \tag{3.3}$$

Using (3.2), it appears that the higher the number of LEDs in a luminaire, the higher the chance is to have a weak LED within the product. If one considers that an early failure on a single LED will result on a product early failure, the detection of these early failures as well as the necessity to filter the weak components out of the production appears to be a necessity in the LED-based lighting system industry. In the next part of this chapter, the root causes and the manufacturing variability which lead to this weak population will be discussed.

3.3 Early Failures from an LED Manufacturing Variability Point of View

Due to supplier-to-customer communication (with an understandable IP protection on the supplier side), it might be difficult for a customer to get a good insight on the real root cause for lifetime failure distributions such as the one presented in Fig. 3.2. However, three kinds of process variabilities capable of affecting the device lifetime can be highlighted:

- Batch-to-batch variability
- Soft defects
- Hard defects

Those three likely root causes are related to the production environment inside a semiconductor fabrication plant.

3.3.1 Batch-to-Batch Variability

On the customer side, LED forward voltage is being measured at fixed forward current conditions. The measured voltage can actually shift by hundreds of mV from one shipped LED batch to another. The reason is obviously due to changes in manufacturing process of the supplier fabrication plant.

3.3.1.1 Batch, Lot, Wafer, and Die Definitions

A given product follows a process route, constituted by all the specific process steps required for its manufacturing. A batch of LEDs sent to a customer is constituted by series of lots from the same process grade. A lot is constituted by a fixed number of wafers all located in a front-opening unified pod (FOUP). As it is displayed in Fig. 3.3, each wafer has been processed using photomasks several times on its surface, forming reticles containing several dies.

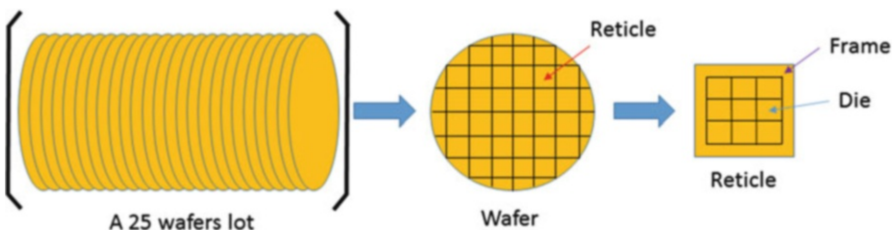

Fig. 3.3 Lot, wafer, reticle, and die definition

3.3.1.2 Lot-to-Lot, Wafer-to-Wafer, and Within-Wafer Variabilities

Standard deviation from lot to lot, from wafer to wafer, and from within a wafer can be measured. The equation summing the variances (3.4) holds true if the three variabilities are fully independent. In practice, lot-to-lot and wafer-to-wafer variances contain contributions from within-wafer variability.

$$\sigma^2_{\text{Total}} = \sigma^2_{\text{Lot2Lot}} + \sigma^2_{\text{Wafer2Wafer}} + \sigma^2_{\text{Within Wafer}} \tag{3.4}$$

Among those three variances, lot-to-lot variance is typically the dominant one. In fact, every wafer within a lot sees a similar environment. In the case of LEDs, it can be the same MOCVD reactor, for example. However, this is often not the case from one lot to another which explains this lot-to-lot variance.

On the other hand, a large wafer-to-wafer variance might indicate that the variation derives from the position of the wafers in a furnace or the sequence of processing through a single-wafer operation. Variability within a wafer is often a systematic "center-to-edge" drift especially observed when measuring an electrical parameter.

3.3.1.3 Tool-to-Tool Variability

In a fabrication plant, a given product follows a process route which lists every single process step an LED lot has to follow. For each family of tools (e.g., lithography tools, chemical mechanical polishing tools, MOCVD reactors, metal plating tools, etch tools, surface cleaning tools, etc.), a subset of tools (normally grouped by tool brand and generation) is attributed to a given product. However, depending on the plant load and on unavoidable dynamic changes in the different volume of products needed by each customer, tool attribution inevitably varies with time, and ideal process control can then be impacted. For an LED manufacturer, the best way to detect and correct rapidly such an issue can be separated in two steps.

- *Step 1*: To make Anova (analysis of variances) on electrical data to determine presence of distinct wafer populations on a SPC chart in a production flow. The principle of Anova is to calculate, within group, variance as well as the total variance and to test likelihood of having two distinct populations by comparing these two variances. The principle of Anova is described in Fig. 3.4.
- *Step 2*: If the existence of two or more distributions is confirmed, a tool commonality analysis needs to be performed to figure out which tool can be responsible for such a discrepancy between the different populations. Tool leading to the most off-target population is then inhibited for the corresponding product.

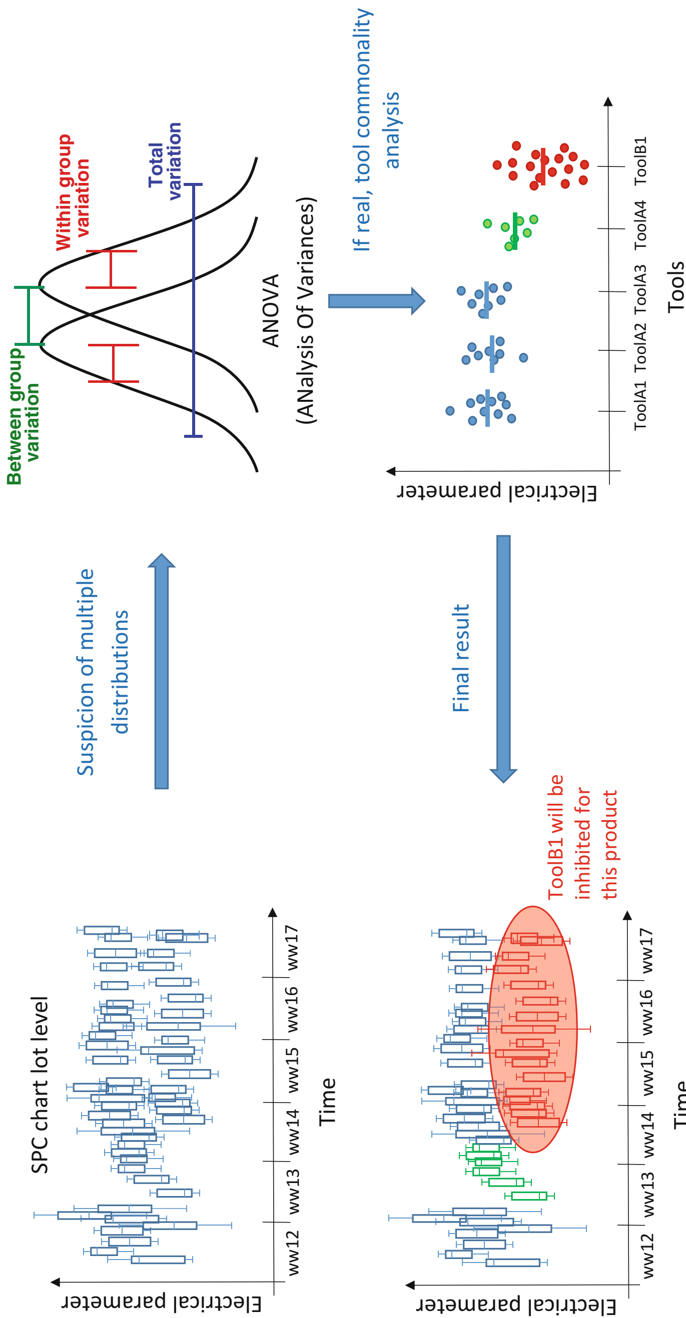

Fig. 3.4 Principle of Anova. Suspicion of several lot populations on a SPC chart leads to Anova. If true, tool commonality permits to detect maverick tools, which can then be inhibited

3.3.2 *Soft Fails*

The main population distribution in device lifetime in Fig. 3.2 is a consequence of the natural variation of the manufacturing process itself. Lower tail of this distribution is due to soft fails. A non-comprehensive list of the root causes for these soft fails is listed below.

3.3.2.1 Wafer Substrate

In order to prevent supply issues, a fabrication plant often has a first and a second source for wafer supply. For instance, even despite a preliminary chemical mechanical polishing process done within the plant, differences in thickness between wafer center and edge from one substrate supplier to another can be observed. This radial distribution can sometimes be seen on wafer electrical maps, at the very end of the process. These substrate differences will impact growth parameters and component variability.

3.3.2.2 Chemical Mechanical Polishing (CMP)

Control of the processing environment is challenging and can most of the time be criticized. In CMP, the wafer is pressed face down on a polishing pad, and a slurry is deposited onto the pad to grind and polish the surface. Therefore, obtaining access to the chemical and physical mechanisms which are taking place during processing is extremely difficult [13]. Pad aging and degradation can also affect polishing consistency as a function of time, though polishing rate is consistently monitored. In the case of LEDs, planarization (and cleaning) of a substrate should be as perfect as possible prior to epitaxy to avoid as much as possible defects at the crystalline interface when growing epitaxial layers. Hopefully, a buffer layer is used during the epitaxy phase to help relaxing constraints [10] prior to junction manufacturing (Fig. 3.5).

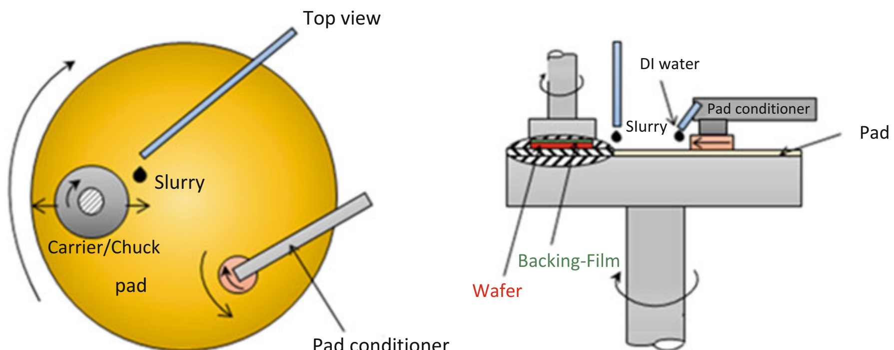

Fig. 3.5 Chemical mechanical polishing/planarization principle

3.3.2.3 Lithography Misalignment

From successive process steps, series of photomasks opened at key areas on the device have to be positioned above reticle onto the wafer under process. One photomask and its follower will be necessarily slightly misaligned. This misalignment can lead to overlay defects, though this is less critical for LED manufacturing (lithography is mostly used for front end) than in advanced CMOS technology processes where critical dimensions can be as small as a few tens of nanometers [14] (Fig. 3.6).

3.3.2.4 Chemicals Used in Lithography Developers, CMP or Etchants

These chemicals are used to develop resists or etch a specific area on a device. They are supplied by chemical compound companies. However, it may happen that impurities present in these chemical solutions affect desired chemical process or even remain on the device surface despite cleaning step which will affect the remaining process steps. It could also be that the chemical supplier changes its recipe affecting the chemical process itself. Moreover, in order to prevent supply issues, a fabrication plant often has a first and a second source for supplies. Despite rigorous specifications, minor differences in recipe from one supplier to another can have an additional impact on chemical process rate or post-process surface quality.

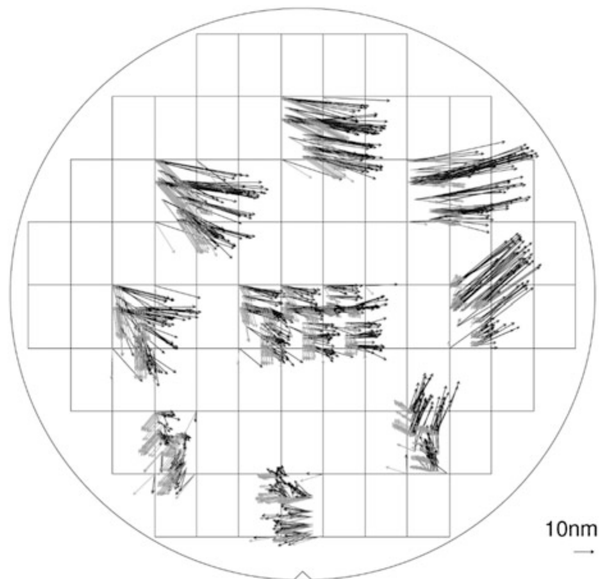

Fig. 3.6 Measured and simulated overlay on a wafer (each rectangle is a reticle) [15]

3.3.2.5 Standard Metrology Limitations

Critical dimensions and defectivity (impurities, scratches) are monitored at wafer level by metrology teams after each key process step. Scanning electron microscope (SEM) is the tool of choice for such an inspection. However, a limitation of this kind of microscopy is that it needs to operate in vacuum and dry conditions. Any wet residue such as chemical solutions used during etch or polymer resists applied prior to lithography will lead to electron charging and won't allow proper detection by a standard and systematic SEM inspection required in an industrial environment (though some methodologies exist at research level [16], which mostly consist of sputtering metal such as gold onto the surface of interest). This will bring challenges to understand, for instance, the direct root cause of an observed drift in time of a given electrical or yield SPC chart over a production period of several weeks. Nevertheless, standard inspection of any surface prior to epitaxy is critical in order to detect presence of defects and avoid their replication during growth, as illustrated in Fig. 3.7. These kinds of defects can lead to soft fails but also hard fails as discussed in part 3.2.3.

3.3.2.6 Crystal Growth

LEDs are grown by epitaxy in vapor phase (MOCVD, or MOVPE) [7]. This growth method consists of a slow deposit of well-controlled layers on a substrate. The LED die is grown from bottom to top. Any defect on a substrate will be found on the next grown layer. Defects can be limited by growing "buffer layers" (large thickness of material to cover defects). However, the current crystal quality of sapphire and the lattice mismatch with GaN do not allow for perfect crystal growth.

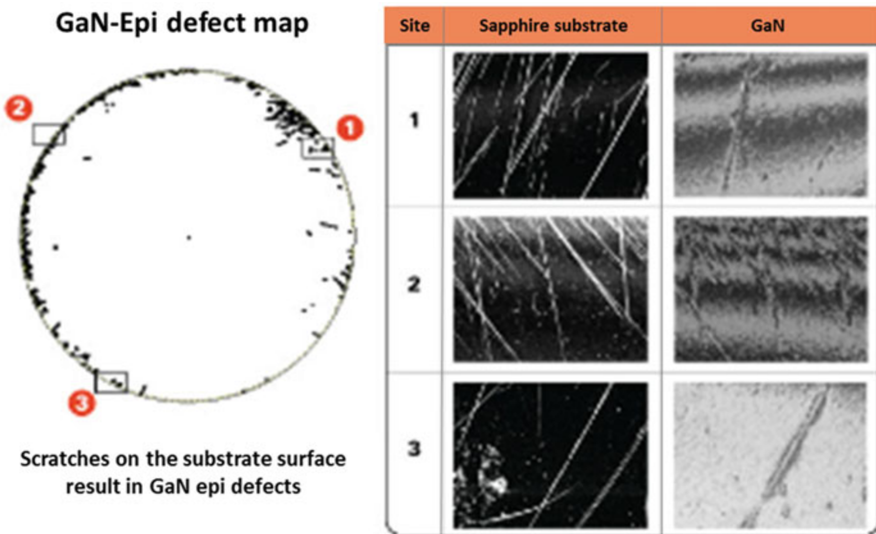

Fig. 3.7 GaN-Epi defectivity map at the edge of a wafer [17]

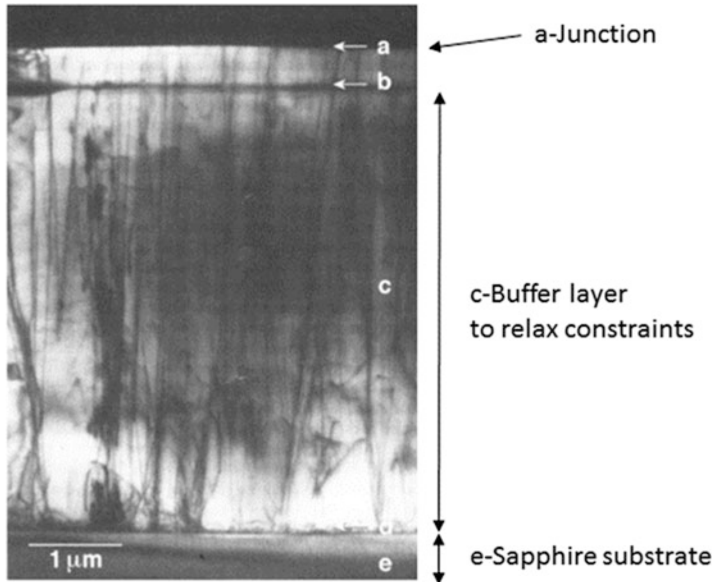

Fig. 3.8 InGaN LED TEM cross section

As a comparison, the number of crystal defects in electronic industry, in silicon growth, is about 0.1/cm^2, whereas in LED production, the best reported values are between 10^4/cm^2 and 10^8/cm^2 [10]. Those defects create current paths, leakage and parasitic junctions, impacting voltage, light output, and overall variability of the components. In addition, the MOCVD reactor production has been largely impacted by LED industry growth. The reactors have evolved tremendously on the last decade, and LED manufacturers have to deal with several generations of tools, with process differences, impacting lot-to-lot variability (Fig. 3.8).

3.3.3 Hard Fails

Weak population distribution in Fig. 3.2 is on the other hand directly related to hard fails due to serious process problems or accident hampering device functionality. Hard fail can, for instance, occur because of a process update initially intended to actually improve performance or yield, or because of human error in process recipe handling.

3.3.3.1 Process Improvement: Release to Manufacturing

Rigorous quality procedures are followed in order to validate a new process improvement prior to release to manufacturing. The common “good practice” in the vast majority of semiconductor manufacturers is every single change is reviewed by a quorum called the Program Change Review Board (PCRB).

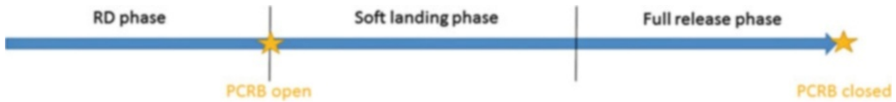

Fig. 3.9 A typical PCRB timeline

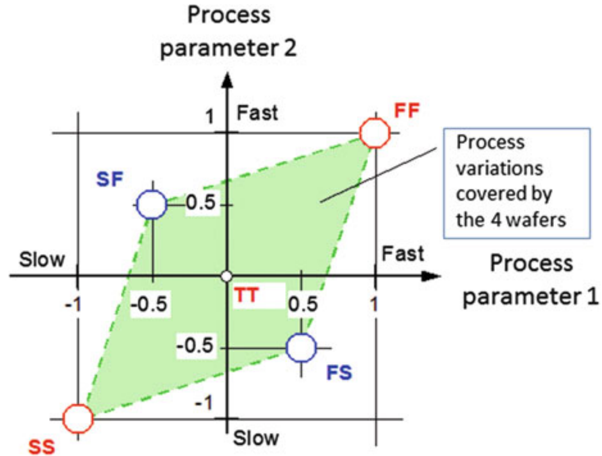

Fig. 3.10 Example of process corners made with four wafers. Process parameters could be, for instance, buffer layer thickness or MOCVD temperature

First, a few R&D lots are processed. Process changes, critical dimensions, and measured electrical and yield parameters (what is called a qualification plan) are carefully and thoroughly reviewed. POR wafers (process of reference) and GOTO wafers (new process) are systematically compared. If validated, the PCRB grants a limited portion of the production volume (the soft landing lots) to this new process.

Second, the PCRB meets again once soft landing lots were processed in order to reassess changes based on this larger sampling, with a higher confidence level on statistics. After technical data has been reviewed and validated for a second time, process change is fully released and the PCRB is closed (Fig. 3.9).

Nevertheless, it sometimes happens after PCRB closure that defects are detected in production due to this new process change at the tail of the distribution after PCRB closure, leading to hard defects. It means this tail was not sampled enough at the intermediate soft landing phase.

A good way to circumvent this problem is to run design of experiment (DOE) on R&D lots at the early step of a PCRB to test process corners far enough (in number of standard deviations) below or above the mean of what will be the new POR normal distribution in order to define the right process window (Fig. 3.10).

3.3.3.2 Process Recipe Error

Each product is not only attached to a tool but also to a specific process recipe (for instance, for an etch step: etch rate, temperature, required chemicals). Despite

thorough quality checks, it may happen that a mistake in recipe attribution occurs during a process update due to human error (technician, engineer) [18]. This often leads to hard defects. Other processes such as die singulation can also generate hard defects.

To conclude, in this second part, several causes for LED process variability have been presented. These causes are rarely disclosed outside the LED fab.

The race for performance and cost and the increasing LED volumes force manufacturers to deal with fast-changing and fast-evolving processes.

The LED variability can be envisioned to be something in the DNA of LEDs and not a “temporary situation.” As a consequence and despite the effort of LED manufacturer, LED assemblers have also to put efforts in removing weak LEDs from their production. In the next part of this chapter, a method is proposed to screen out weak LEDs from an LED assembly point of view. In the last part of this chapter, the screen-out samples will be analyzed in order to highlight signature and identified related defects.

3.3.4 Early Failure from an LED Assembly Side: Detection Methods

Once the component is purchased, the end user is limited to simple measurement methods. Detecting failures is a challenge, especially without early distribution information.

Different methods exist to reduce the early failure proportion by detecting and screening out the weak components. Two approaches can be used for this purpose. The first approach consists on testing the systems in normal or accelerated conditions for a given amount of time in order to force the early failures to occur. This method also called “burn-in” [19] needs to be conducted on the entire production to be effective. The second approach consists in investigating the root cause of the early failures in order to eliminate the defects. This second approach often uses results of the burn-in test and is considered as more effective and less costly.

For LEDs, duration of the early failure regime can be as long as several hundreds to a few thousands of hours of use. In theory, duration of industrially relevant tests will not make all the weak components failing. After a burn-in test, even weak LEDs can still emit light. Therefore, root causes and defects leading to lower lifetime LED have to be identified. An additional key point in the LED early failure detection is to identify one or more signatures of the defects which will cause the early failure. These signatures can be optical, electrical, or even thermal as long as they allow to easily screen out the weak components from the main population. For LED-based lighting systems, burn-in test is more to be used to trigger those signatures than to make the weak component fail.

3.3.5 Electrical Characterizations and Model

From a component architecture point of view, early failures are more likely to be linked to chip defects than optical package defects. In fact, optical package defects such as lens cracks do not cause early failure but more random/wear-out failure due to propagation of the lens crack which impact light path and can change color consistency of the device [1]. Defects related to die or die assembly are more likely to have consequences from an electrical point of view [1, 20]. As a consequence, investigating the electrical characteristic of the component is a good approach when looking for chip-related defects which can be the root cause of early failures.

A complete electrical characterization of the LED component brings useful information regarding its state. An electrical equivalent model of an LED can be described using the double diode model schematized in Fig. 3.11 [21]. This model assumes that the LED is made of a "radiative LED" in parallel with a "non-radiative diode" (a diode device which models all the losses). In addition to these two diodes, a series resistance allows to model contact/material resistances and a parasitic parallel resistance allows to model leakage paths.

The current-voltage characteristic of a perfect diode schematized in Fig. 3.11 has firstly been modeled by Shockley [21]:

$$I = \mathrm{eA}\left(\sqrt{\frac{D_p {n_i}^2}{\tau_p N_D}} + \sqrt{\frac{D_n {n_i}^2}{\tau_n N_A}}\right)\left(e^{eV/_{kT}} - 1\right) \tag{3.5}$$

$$I = I_s\left(e^{eV/kT} - 1\right) \text{ with } I_s = \mathrm{eA}\left(\sqrt{\frac{D_p {n_i}^2}{\tau_p N_D}} + \sqrt{\frac{D_n {n_i}^2}{\tau_n N_A}}\right) \tag{3.6}$$

With:

N_A: Acceptor concentration

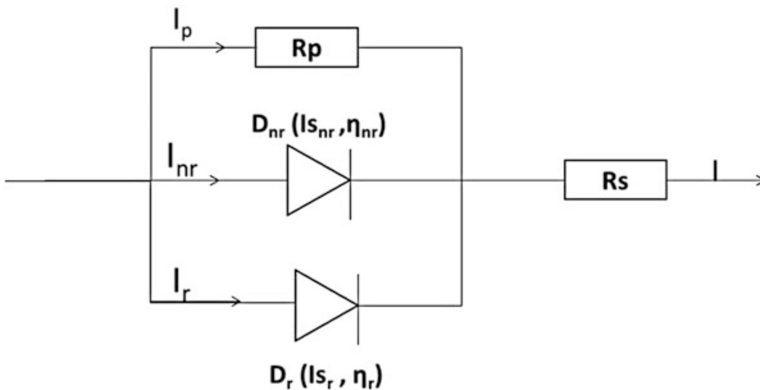

Fig. 3.11 Electrical equivalent model of an LED

N_D: Donor concentration
n_i: Intrinsic concentration
$D_{n,p}$: Electron and hole diffusion constants
$\tau_{n,p}$: Electron and hole minority carrier lifetimes
A: Cross-sectional area
I_s: Saturation current

Equation 3.7 has been proposed for ideal diodes. For real diodes, an ideality factor N is often added to the modeling [21].

$$I = I_s\left(e^{\mathrm{eV/NkT}} - 1\right) \tag{3.7}$$

From the electrical equivalent model displayed in Fig. 3.11, we can define the I–V equation of an LED:

$$I = I_p + I_{\mathrm{nr}} + I_r \tag{3.8}$$

With:

I_p: Leakage currents
I_{nr}: non-radiative currents
I_r: radiative current

Using the Shockley equation and the Ohms' law, the I–V curve of the LED can be modeled using Eq. 3.9.

$$I = \frac{V - R_s I}{R_p} + I_{s-\mathrm{nr}}\left(e^{(V - R_s I)/N_{\mathrm{nr}}\mathrm{kT}} - 1\right) + I_{s-r}\left(e^{(V - R_s I)/N_r kT} - 1\right) \tag{3.9}$$

As described in Eq. 3.9, the I–V characteristic of an LED can be separated into three parts. Each part is associated with one of the following currents: leakage, non-radiative, and radiative. According to the value of the LED model parameters, each current will be dominant on a different voltage range. Figure 3.12 displays a I–V curve of an LED in the semilog scale highlighting the three regimes (leakage, non-radiative, radiative).

Studies conducted by Chang M.H et al. in 2011 [1] have permitted to build a table of known failure mechanisms with associated failure modes and failure causes. Results show that failure mode related to electrical variations is associated with die and interconnects failure mechanisms. In addition, process variability presented in the previous part of this chapter, especially when speaking about hard defects, appears to have more impact and relationship with chip process. As a consequence, a first assumption of a relation between hard defects and electrical variations (caused by chip localized defects) has been considered.

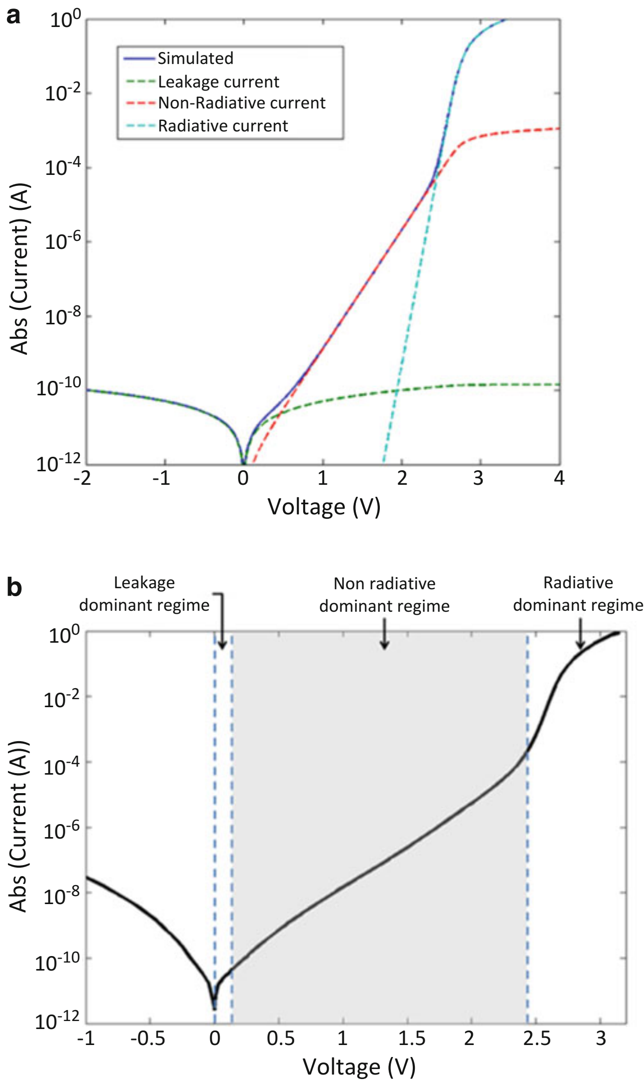

Fig. 3.12 I–V curve of an LED in semilog scale highlighting the three regimes (leakage, non-radiative, radiative)

3.3.6 Experiment

A burn-in test has been conducted on millions of high power white LEDs with $2mm^2$ die size. Two different die technologies from two major LED suppliers have been tested: vertical thin film (VTF, Fig. 3.13b) architecture and thin film flip chip (TFFC, Fig. 3.13c) architecture.

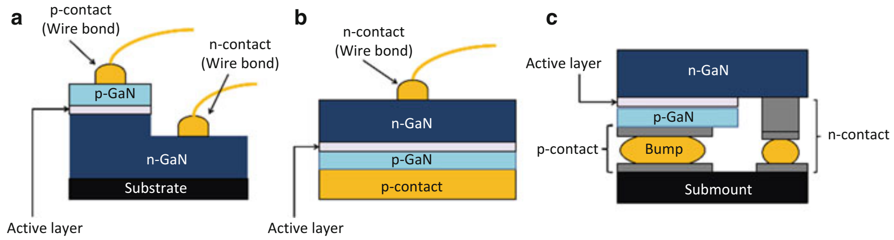

Fig. 3.13 Typical architecture of LED chips: (**a**) lateral, (**b**) vertical thin film (VTF), and (**c**) Thin Film Flip Chip (TFFC)

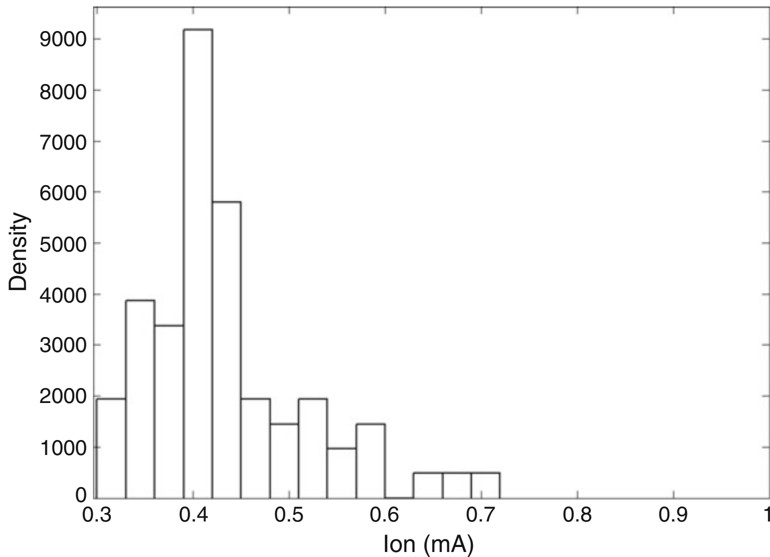

Fig. 3.14 Light up current distribution for a sample set of 2,000 samples from the main population

The conducted burn-in test consists of several hours of test in which the LEDs are driven at 700 mA with an 85 °C solder temperature.

In addition to this burn-in test, a control test has been defined. At the end of the burn-in test, a direct current is applied to the LED and a visual light up test is performed. Current value has been defined close to the early stage of the radiative regime. Therefore, any abnormal characteristic in the leakage or non-radiative regimes will immediately result as non-emission behavior for this particular currents.

Using I–V characteristics of samples from the main population, the distribution of transition current from the non-radiative regime to the radiative regime (Fig. 3.14) has been evaluated.

Based on Fig. 3.14, the light up current criteria have been set to 10 mA in order to avoid detection of false-positive samples. During several months, more than

2,000 selected samples presenting a "high light up current" have been collected and analyzed through complete electrical characterization, structural analysis, and stress in order to target a clear signature and evaluate the root cause of these early failures. As a first observation, none of the collected samples present an anomaly in application condition (optically or electrically). Results of this analysis are exposed in the last part of this chapter.

3.4 Early Failure: Signature and Related Defects

3.4.1 Electrical Signatures

Samples which did not pass the control test after burn-in have been collected and appear not to present any lower flux value or color point difference compared to the main distribution (i.e., samples which do pass the test) *in operating conditions*. Collected samples have been electrically characterized and compared to samples from the main distribution. I–V characteristics of both weak samples and samples from the main population are displayed in Fig. 3.15.

As it can be observed on Fig. 3.15, compared to the main population, collected samples have higher leakage and non-radiative currents. In most cases, modifications appear to be governed by a leakage current increase. For the collected samples, due to higher leakage currents, the radiative part of the I–V characteristic is modified. For example, on Fig. 3.15 for a driving current of 10 mA, the current flowing through the LED is entirely contributing to a non-radiative recombination process, and no light is emitted for these samples for the control light up test. Fitting the results using Eq. 3.9, we can extract the value of the leakage resistance for both

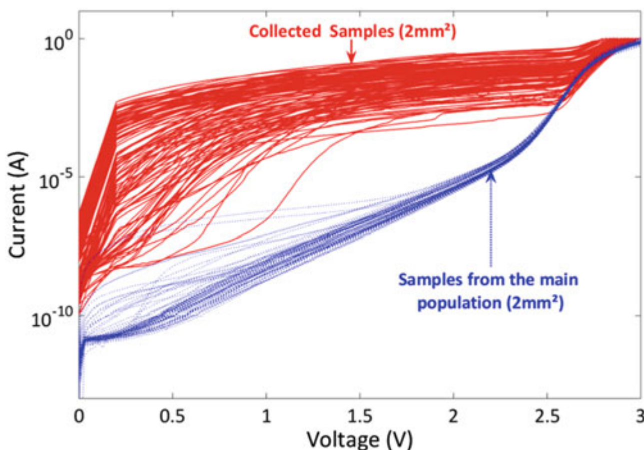

Fig. 3.15 Measured I–V characteristic of collected samples (from the weak population) and samples from the main population

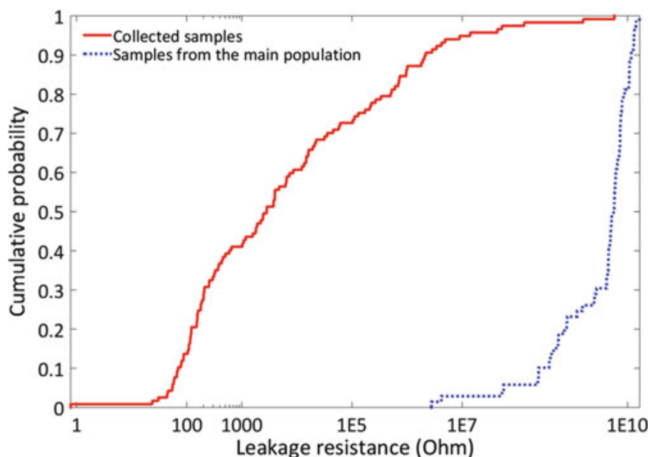

Fig. 3.16 Distribution of R_p – we find a median $R_p = 2800$ Ohm while samples from the main population present a median $R_p = 6e9$ Ohm

main and weak populations. The cumulative function distribution of the R_p values is displayed in Fig. 3.16.

From these results, an electrical signature for the samples which potentially present a higher probability of infant mortality (or at least an unusual low-current behavior) has been extracted. This electrical signature was found to be related to the leakage level of the devices. This leakage can be characterized by an increase of the minimum turn on current.

3.4.2 *Identification of Early Failure-Related Defects*

An early weakness associated to a higher leakage current has been identified. According to the list of known failure mechanisms for LEDs [1], this signature is more likely related to die defects. In fact, interconnect-related failure mechanisms are associated to open-circuit failure. But this is not the case in the present situation. As a matter of fact, investigation of the defects related to this early weakness has to focus on the die itself.

Localization of the defects can be done using high-resolution thermal imaging. As exposed, leakage current is by definition not used to produce light, and related defects will act as thermal generation centers through Joule effect. From an optical point of view, these defects will also act as non-radiative areas.

To localize defects, the optical package (lens + phosphor layers) has been chemically removed in order to characterize the die surface. Top surface of the die is observed using a high-resolution thermal camera highlighting hot spots (Fig. 3.17). The general localization of hot spots allows to efficiently target the

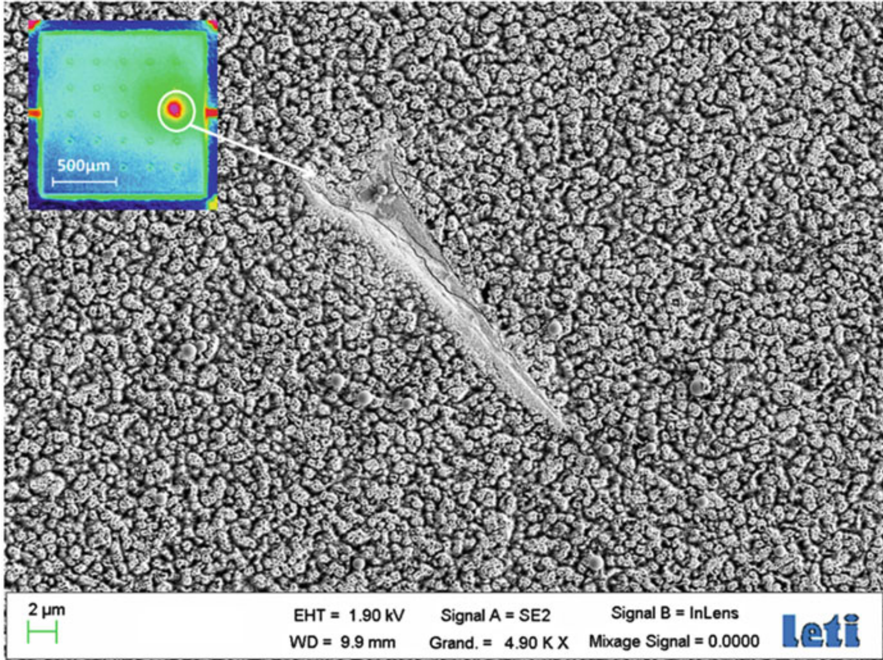

Fig. 3.17 IR measurement and *top-down* SEM observation of the hot spot localization (sample with $I_{on} = 15$ mA)

defected area. SEM images, as shown in Figs. 3.17 and 3.18, put in relief die defects in the hot spot areas. Presence of a hot spot already confirmed a weakness of these components. In fact the thermomechanical stress in this particular location will be much higher and might lead to a shorter lifetime of the component.

These local defects on top surface of the die can be related to local hot spot associated with leakage current characteristic of an initial weakness of the component. Surface of those defects (about 100 μm^2) explains the challenges to screen out these LEDs during production by using visual inspection.

In order to evaluate the impact on these defects on the components, defects have to be considered in three dimensions. Cross sections on defects have been conducted (Fig. 3.19) to evaluate their depth in order to identify the impacted layers (n-GaN, p-GaN, Quantum wells).

As it can be observed in Fig. 3.19c, the defect impacts the entire thickness of the epitaxial layers which explains the increase of leakage current which passes through the junction.

Investigation on multiple samples has highlighted two types of defects related to the identified electrical signature. All of these defects are considered as hard defects as described in the previous section.

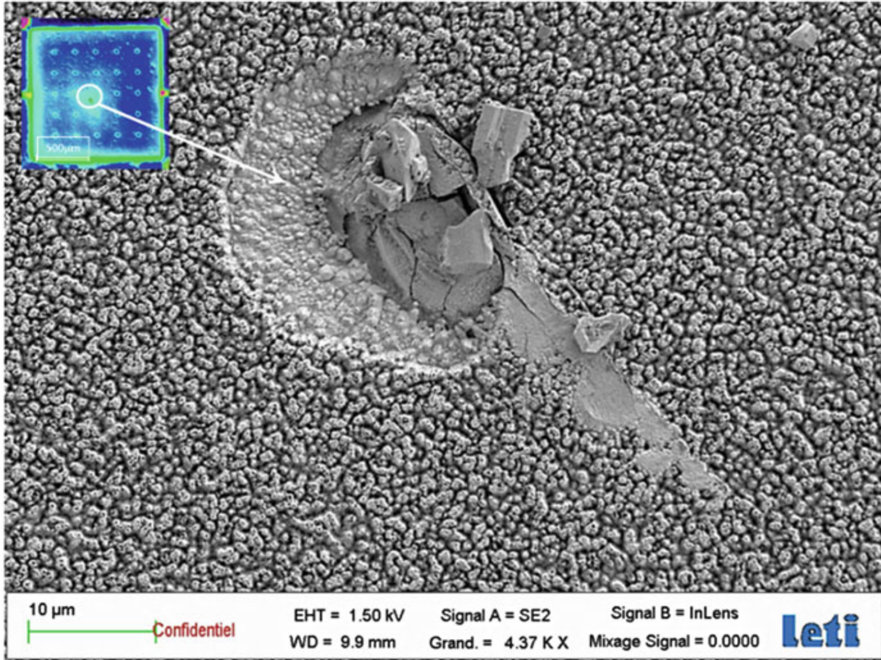

Fig. 3.18 IR measurement and *top-down* SEM observation of hot spot localization (sample with $I_{\mathrm{on}} = 12$ mA)

- Die defects such as the one observed in Figs. 3.17 and 3.18 can be related to hard defects from a process variability point of view. Depending on the defect localization, several process steps can be seen as a root cause. In the case presented in Fig. 3.19, defects on the edge of the chip might be associated to dicing variability. Other defects such as the one presented in Fig 3.17 or 3.18 are localized in the center of the chip and can be related to other steps in the process such as CMP or epitaxy. From a chip architecture point of view (technology presented in Fig. 3.13c), these defects are localized on the n-GaN layer (to the bottom of the chip from a growth point of view). As a consequence, this type of defects can occur during the epitaxial growth (non-planarized or unclean substrate) or during the laser lift-off phase. In the laser lift-off phase, sapphire substrate is removed using a laser-induced reaction. During this process step, particles of the removed substrate can mechanically damage the n-GaN.
- Larger die defects (Fig. 3.20) can be related to an improper die attach which cause abnormal stress leading to die cracks. These defects have been observed on different die attach technologies such as gold-gold interconnect. According to the die attach technology, this type of failure will be mostly observed in the center (for vertical die architecture (Fig. 3.13b)) or in the corner (GGI Bump) of the die. The stress generated during operation (thermomechanical) will cause the

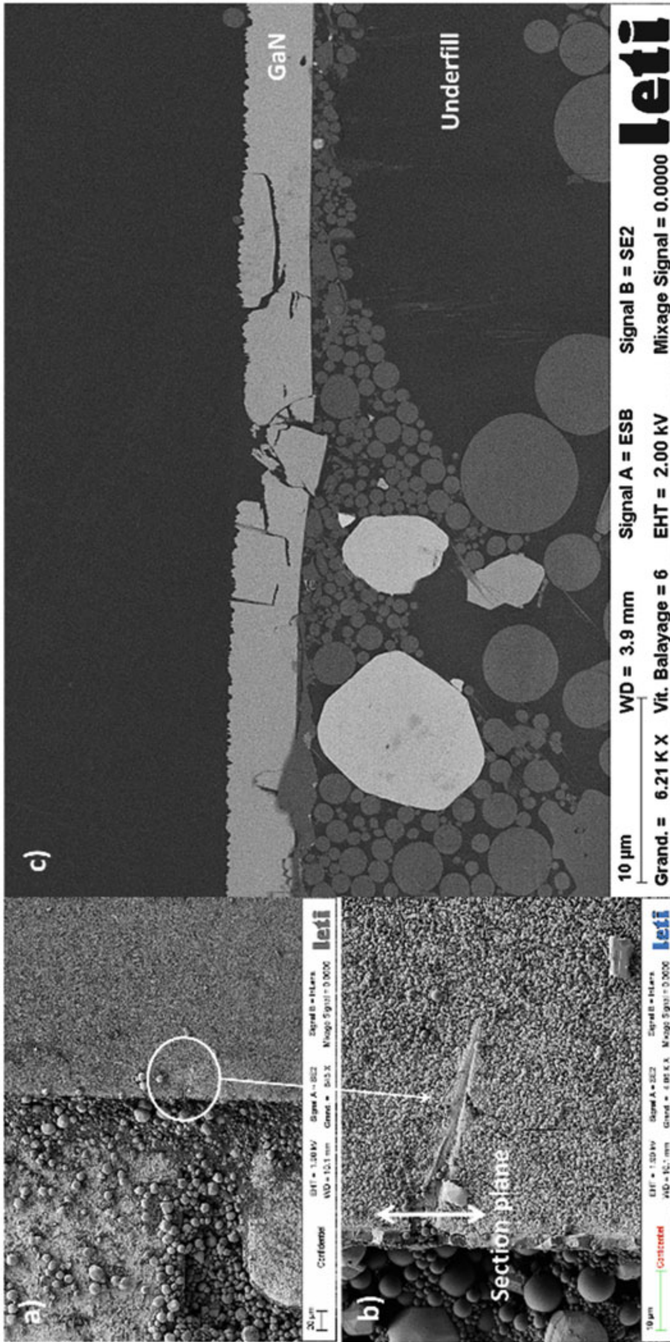

Fig. 3.19 (**a**, **b**) *Top-down* SEM observation of a local defect. **c** Cross-sectional SEM observation of the local defect following the section plane presented in (**b**)

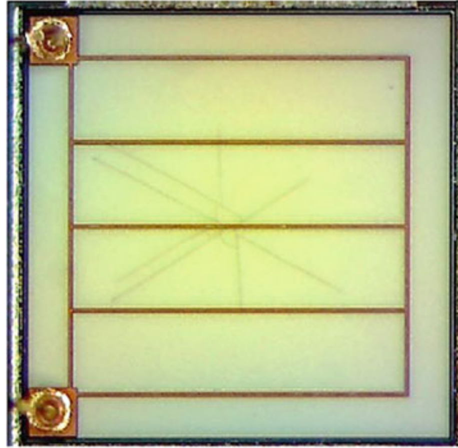

Fig. 3.20 Observation of large die cracks on a vertical thin film LED

die to break leading to a within-die leakage path. These defects are also related to hard fails from a variability point of view but have much more critical consequences as the die defects are much larger. It has been observed that this second type of defects is related to much larger leakage currents.

3.4.3 Relation Between Initial Defects and Lower Lifetime

In the previous section, early failure signatures as well as defects related to these early failures have been identified. To demonstrate a lower lifetime sample presented an abnormal low-current behavior, a series of experiments have been conducted.

Collected samples have been mounted on boards and submitted to surge stress. Test consists in applying 20 times (10 in direct – 10 in reverse) a 3 keV wave to the driver. This test is often used for outdoor luminaires as it simulates different phenomena which are representative from what a luminaire might face during operation (i.e., lightning). Figure 3.21 shows the evolution of turn on current of the LEDs. For the purpose of this experiment, six ranges of currents have been defined.

Figure 3.21 shows that leakage current of components presenting the identified signatures increase when stressed. This leakage increase is transcripted in this experiment by an increase of the turn on current of the LED. As this stress is representative from situations that can be observed during the LED lifetime, it is then proven that the identified defects have a negative impact on the component lifetime and then lead to early failures.

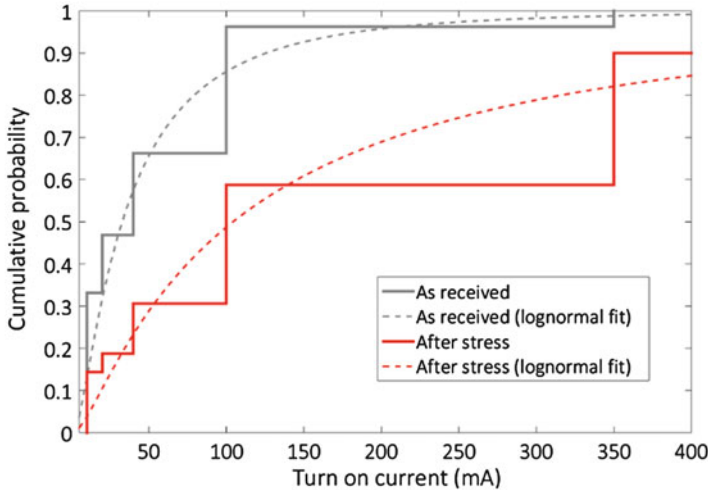

Fig. 3.21 CDF of Ion before and after surge test

Further tests have shown that the increase of leakage current with stress continues until a shortage of the component is occurring. Failure analyses of LEDs presenting short-circuit failures have been conducted. As it can be seen in Fig. 3.22, silver particles are found on the die top surface.

In this particular architecture (TFFC), the silver layer acts as a mirror and is in contact with the p-GaN layer. The presence of silver particles on the top surface of a die means that silver has migrated in the die cracks through the p-GaN, active, and n-GaN layers, leading the junction shunt and as a consequence to the device abrupt failure [22]. Electromigration of the silver atoms with reverse bias is assumed to be the root cause of this short circuit.

3.5 Conclusion

In this chapter, the subject of LED early failures has been discussed. These failures have an impact on the overall luminaire lifetime, and as a consequence, samples which are more likely to present these early failures have to be removed from production. Weak components cannot be entirely removed as it is dependent from manufacturing and process variabilities. The different variability root causes in the process have been presented. They can be sorted into soft fails and hard fails. On one hand, lower tail of main distribution of the LED lifetime is due to soft failures. On the other hand, weak components which will present early failure are linked to hard failure in the process, hampering device functionality.

Using a burn-in method, LEDs presenting an abnormal behavior at low driving currents have been filtered out from the assembly production. Analysis of sorted out

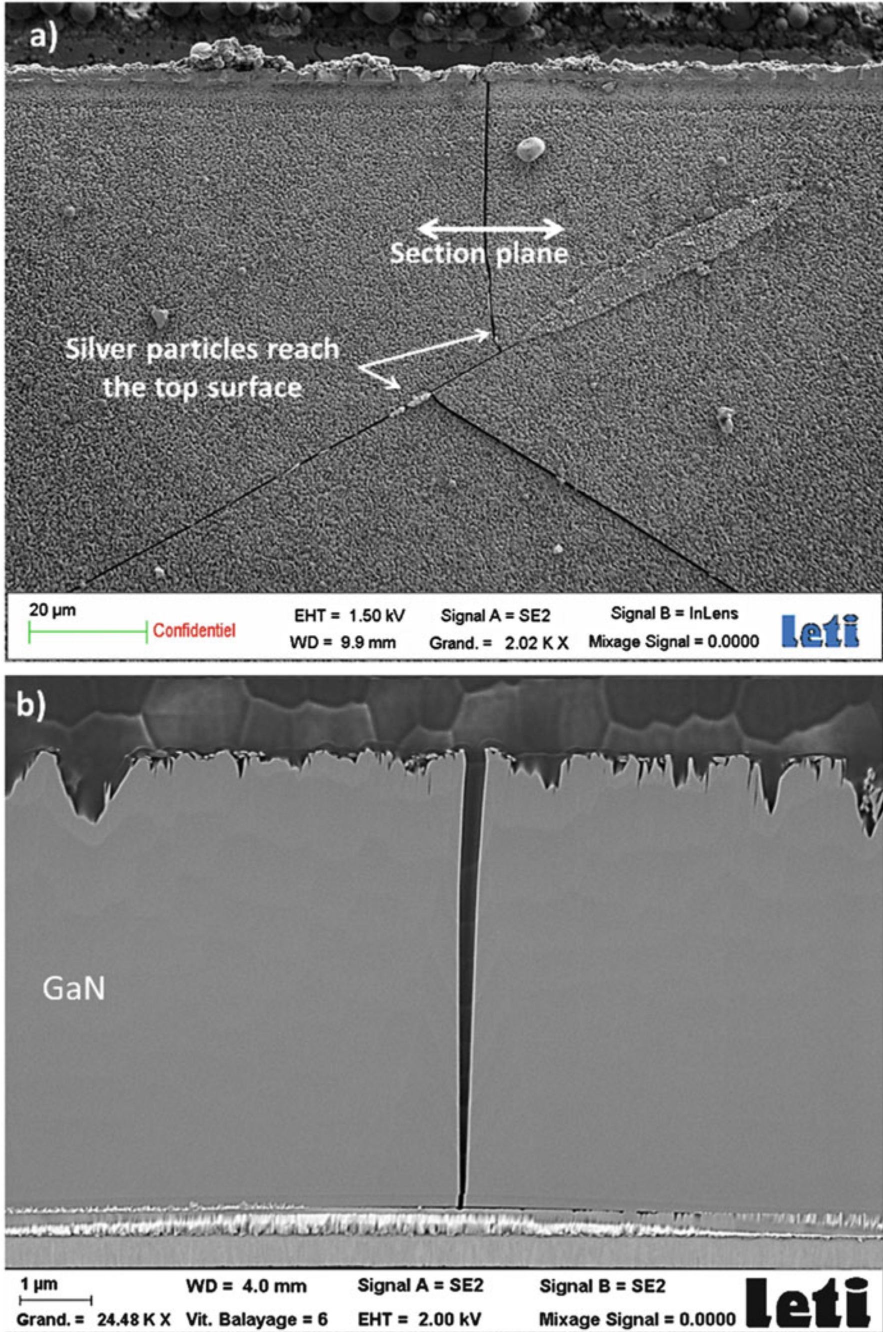

Fig. 3.22 (**a**) *Top-down* SEM observation of the surface of a weak sample. (**b**) Cross section following the section plane

LEDs, the ones which have failed the proposed low-current light up test, reveals a common signature of the "weak" population related to a higher value of leakage current. Further analyses have demonstrated that this electrical signature is linked to die damages. Those die damages cause a significant decrease of the device leakage resistance and consequently an increase of the leakage current responsible for the device not to turn on at low currents. Using stress tests such as surge testing, lower lifetime of the filtered out components has been demonstrated. It has been shown that electromigration of silver atoms from the mirror through the die crystalline defects is the mechanism responsible for the increase of the LED leakage current, leading to a short-circuit failure.

Knowledge about the defects and signatures related to this weak population are critical to improve screen-out efficiency for these components, and as a consequence, this expertise will help increase the overall lifetime of LED-based luminaires. From an LED manufacturer point of view, identification of those defects allows to focus control efforts on targeted process steps in order to reduce the weak component population.

As a general guideline, it seems important to focus on efficient measurements or methods to trigger the presented defects sooner in the LED process flow, preferably on the LED supplier side, in order to improve LED quality and ensure minimized test costs for the luminaire assembler.

References

1. M.-H. Chang et al., Light emitting diodes reliability review. s.1. Microelectron. Reliab. (2011). doi:10.1016/j.microrel.2011.07.063
2. N. Narendran et al., Performance characteristics of high-power light-emitting diodes. 3rd international conference on solid state lighting, proceedings of SPIE 5187 (2004), p. 267–75
3. Y. Deshayes et al., Long-term reliability prediction of 935nm LEDs using failure laws and low acceleration factor ageing tests. Qual. Reliab. Eng. Int. **21**, 571–594 (2005)
4. W.D. van Driel et al., Lumen maintenance predictions for LED Packages using LM80 data, EuroSimE (2015)
5. P. Lall et al., Bayesian Models for life prediction and fault-mode classification in Solid State Lamps, EuroSimE (2015)
6. J. Huang et al., Degradation modeling of mid-power white-light LEDs by using Wiener process. Opt Express **23**(15), A966–78 (2015)
7. S. Koh et al., Investigation of color shift of LEDs-based lighting products, EuroSimE (2014)
8. M. Royer et al., *Color Maintenance of LEDs in Laboratory and Field Applications, National Information Service*, (US Department of Energy, 2013)
9. S.-U. Zhang et al., Fatigue life evaluation of wire bonds in LED packages using numerical analysis. Microelectron. Reliab. **54**(12), 2853–2859 (2014)
10. C.A. Yuan et al., in *Solid-State Lighting Technology in a Nutshell,* ed. by W.D. van Driel, X.J. Fan. Solid state lighting reliability components to systems. s.l. (Springer, New York, 2013)
11. R.E. Barlow, F. Proschan, *Mathematical theory of reliability*. (Society for Industrial and Applied Mathematics, 1996)
12. P.D.T. O'Connor, A. Kleyner, in *Practical Reliability Engineering Fifth edition*. Chapter 2: Reliability mathematics. s.l. (Wiley, New York, 2011)

13. S. Wolf, in *Silicon Processing for the VLSI Era, Vol. 4: Deep-Submicron Process Technology*. Chapter 8: Chemical mechanical polishing. (Lattice Press, Sunset Beach, 2002), pp. 313–432
14. K. Yamazaki et al., Sub-10-nm overlay accuracy in electron beam lithography for nanometer-scale device fabrication. Jpn. J. Appl. Phys. **37**(Part 1, 12B) (1998). Copyright (c) 1998 The Japan Society of Applied Physics
15. N. Smith et al., For semiconductor manufacture, pattern alignment requires subnanometer uncertainty 26 February 2008, SPIE Newsroom. (2008). doi: 10.1117/2.1200702.1036
16. A. Nyska et al., A new method of wet scanning electron microscopy for the analysis of myelination in EAE mouse model of multiple sclerosis. Received 29 Sept 2005; accepted 22 Nov (2005)
17. R. Howland et al., The gleam of well-polished sapphire. Solid state technology. KLA-Tencor. http://electroiq.com. 8 Jan 2013
18. J. Moyne, E. del Castillo, M. Arnon, *Run-to-Run Control in Semiconductor Manufacturing*. (CRC Press, 2000)
19. F. Jensen, N.E. Petersen. *Burn-in An Engineering Approach to the Design and Analysis of Burn-in Procedures,* (Wiley, New York, 1982)
20. M. Meneghini et al., *A review on the Reliability of GaN-Based LEDs*. IEEE Trans. Device Mater. Reliab. **8**(2) (2008)
21. E.F. Schubert, Chapter 4: LED basics: electrical properties, in *Light Emitting Diodes -Second Edition. s.l*, (Cambridge Press, Cambridge, 2006)
22. H. Kim et al., Electromigration-induced failure of GaN multi-quantum well light emitting diode. Electron. Lett. **36**, 10 (2000)

Chapter 4
Advances in Reliability Testing and Standards Development for LED Packages and Systems

C. Qian, J.J. Fan, Xuejun Fan, and Guo Qi Zhang

Abstract Currently available reliability test standards (and specifications) for LED packages and systems have mainly been focused on the evaluation of lumen maintenance lifetimes. A brief review on these published standards is given in Sect. 4.1. Then some advanced methods for LED lumen maintenance lifetime estimation by taking into the statistical effects into account are discussed in Sect. 4.2. Afterward Sects. 4.3 and 4.4 in which part of the materials are excerpted from reference (Qian et al., Reliab. Eng. Syst. Saf. 147:84–92, 2016; Qian et al., Prediction of Lumen Depreciation and Color Shift for Phosphor-converted White Light-Emitting Diodes Based on a Spectral Power Distribution Analysis Method, IEEE Access, to Be Published, (n.d.)) present two of the hot topics in the reliability field. In Sect. 4.3, a temperature-driven accelerated test method within 2000 h is proposed instead of the 6000 h test methods to qualify the LED luminaires and lamps with an expected lumen maintenance lifetime of 25,000 h. And in Sect. 4.4, a spectral power

C. Qian (✉)
State Key Laboratory of Solid State Lighting, Institute of Semiconductors, Chinese Academy of Sciences, Beijing, China

State Key Laboratory of Solid State Lighting (Changzhou Base), Changzhou, China
e-mail: cqian@sklssl.org

J.J. Fan
State Key Laboratory of Solid State Lighting (Changzhou Base), Changzhou, China

College of Mechanical and Electrical Engineering, Hohai University, Changzhou, China
e-mail: jay.fan@connect.polyu.hk

X. Fan
State Key Laboratory of Solid State Lighting (Changzhou Base), Changzhou, China

Department of Mechanical Engineering, Lamar University, Beaumont, USA
e-mail: xuejun.fan@lamar.edu

G.Q. Zhang
State Key Laboratory of Solid State Lighting, Institute of Semiconductors, Chinese Academy of Sciences, Beijing, China

State Key Laboratory of Solid State Lighting (Changzhou Base), Changzhou, China

EEMCS Faculty, Delft University of Technology, Delft, The Netherlands
e-mail: g.q.zhang@tudelft.nl

© Springer International Publishing AG 2018

W.D. van Driel et al. (eds.), *Solid State Lighting Reliability Part 2*, Solid State Lighting Technology and Application Series 3, DOI 10.1007/978-3-319-58175-0_4

distribution (SPD) analysis-based method is proposed to simultaneously predict the lumen depreciation and color shift of phosphor-converted white LEDs (pc-LEDs). In the end, concluding remarks of this chapter are summarized in Sect. 4.5.

4.1 State of the Art of the Reliability Test Standards

As the mainstream of the fourth-generation light sources (after the incandescent lights, fluorescent lights, and high-intensity discharge lights), the light-emitting diode (LED) has gained numerous applications including home lighting, urban lighting, commercial lighting, industrial lighting, landscape illumination, display backlighting, communications, medical services, etc. [1, 2]. In the early 2000s, industrialization of the LED blue chips initializes the rapid development of LED lighting products. With the steady improvement in both lumen efficacy and color quality, it is expected that the market penetration of the LED lamps and luminaires will reach over 60–75% or even more by 2020 [3]. Meanwhile, consumers are always fond of the products with high cost-effectiveness and long lifetime. This pushes manufacturers to pay more attention on the reliability of their products before launching them into the market.

A LED light product is considered as a complicated system composing multiple levels, each of which suffers from a variety of catastrophic and degradation failures [1]. The catastrophic failure modes are omnifarious, including the die crack, ESD damage, wire bonding failure, phosphor thermal quenching, solder crack, electrical short, driver catastrophic failure, etc. [1]. These failures usually occur in the early stage of the operating lifetime and can be avoided with an improvement of the reliability design of the LED product. Detection of these catastrophic failures can be achieved by a batch of environmental tests such as High/Low Temperature Operating Life Test, Wet High Temperature Operating Life Test, Powered Temperature Cycle Test, Pulse Life Test, High/Low Temperature Storage Test, Solder Heat Resistance Test, Solderability Test, Thermal Shock Test, Mechanical Shock Test, Vibration Test, Corrosion Test (Salt Atmosphere), Dust Test, and Electrostatic Discharge Test. A discussion of these test methods is beyond the scope of this chapter. For more detailed information, the readers may refer to the relevant standards, for instance, JEDC22 series standards, JEITA ED-4701 series standards, GB/T-2423 series standards (in Chinese), etc.

Compared to the catastrophic failures, the degradation failure modes are relatively simpler and can be mainly categorized into two kinds, i.e., lumen depreciation and color shift, respectively. Generally, the lifetime for a LED lighting product refers to the expected operating hours until its light output (e.g., luminous flux) has depreciated to 70% of initial levels, indicating as L_{70}. The term “lumen maintenance” is often used to describe the degradation in light output during operation. The degradation failures are related to the material characteristics of the LED packages, and for this reason, they appear throughout the whole operating time of the LED products. To catch up the advancement of LED technology, standards (and specifications) on LED reliability/lifetime assessment are being developed by a number of organizations, such as Illuminating Engineering Society of North

America (IESNA), Energy Star, and International Electrotechnical Commission (IEC). In these standards, the samples are operated under specified ambient temperatures and operational time, depending on the situation of lifetime claim. Nevertheless, the requirement on the ambient humidity is not strict, as long as it is no more than 65%.

In 2005, IESNA launched TM-16-05 (in which "TM" is an abbreviation of "Technical Memorandum") to give a comprehensive introduction of the characteristics of LEDs [4]. In this document, the LED's lifetime is recommended no less than 50,000 h for illuminance applications based on a consensus in LED lighting industry at that time [5]. However, TM-16-05 did not provide any test methods nor qualifications for obtaining the lifetime of LEDs. A few years later, IESNA published LM-80-08 (in which "LM" is an abbreviation of "Lighting Measurements") and TM-21-11 for lifetime estimation of LED packages and modules [6, 7]. The test consists of a minimum of 6000 h (preferred 10,000 h or more) with data collection of at every 1000 h (at the maximum) intervals at three different temperatures (which are 55 °C, 85 °C, and a third temperature selected by the users). By far, LM-80-08 has been a widely accepted luminous flux depreciation test standard for the measurement of lumen maintenance of LED sources. With the test data provided by LM-80-08, TM-21-11 presents an exponential extrapolation method to predict the L_{70} lifetime of the test samples. In addition, a sample size-related multiplication law is employed to adjust the projected L_{70} lifetime within an accepted range. For a sample size of 20 units or more, the reported lifetime estimation is the minimum between the extrapolated L_{70} time and six times the total test duration. For a sample size of 10–19 units, the reported lifetime estimation is the minimum between the extrapolated L_{70} time and 5.5 times the total test duration, whereas, for a sample size of less than 10 units, it is totally nonsense to address a lifetime estimation.

In 2015, IES released a comprehensively revised edition of LM-80 test method, which is LM-80-15, together with American National Standards Institute (ANSI) [8]. This recently released test standard only focuses on the requirements of photometric and colorimetric measurement methods for LED sources (including LED packages, arrays, and modules). Compared to LM-80-08, LM-80-15 makes the following changes:

(a) Increasing requirements for the colorimetric measurement method
(b) Reducing the mandatory operating case temperatures T_s (sometimes also called solder temperatures) from three temperatures to two, one of which has to be 55 °C or 85 °C
(c) Removing requirements for the test duration which has to be at least 6000 h in LM-80-08

In addition, a number of tiny changes on measurement details (such as driving mode, T_s determination, failure definition) of the LED light sources provide an explicit description for the photometric and colorimetric measurements.

At the product level, IESNA published LM-84-14 and TM-28-14 standards for the lifetime estimation [9, 10]. With the test data provided by LM-84-14, TM-28-14 presents a method similar to TM-21-11 to estimate lifetimes of LED lamps, light

engines, and luminaires. There are two L_{70} lifetime estimation methods given in TM-28-14. In the situation that an LM-80 report (either LM-80-08 or LM-80-15) with at least 6000 h test data for the LED source is available, and the T_s temperature is exactly within the range of the temperatures provided in the LM-80 report, the operating time of the test samples can be shortened to 3000 h. The test data shall be collected at most in every 500 h after the initial 1000 h. Then, with the assistance of the LM-80 data, the L_{70} lifetime of the test samples can be estimated using the "combined" exponential extrapolation technique. Otherwise, at least 6000 h test data at 1000 h intervals are required, and the L_{70} lifetime of the test samples can be estimated using the "direct" exponential extrapolation technique, as used in TM-21-11. For avoiding excessive statistical weights to certain data points, TM-28-14 stipulates a uniform distributed time intervals after the initial 1000 h in the L_{70} lifetime calculation. The operating time in between a pair of two neighboring time points should be consistent within a ±48-h upper and lower bands. For instance, it is not allowed to collect data every 1000 h and occasionally 500 h and the other way around during the test.

In TM-28-14, the multiplication law is also applied to adjust the expected lifetime of the test samples, using the multiplication factors relevant to the extrapolation techniques. The minimum sample sizes for the "combined" and "direct" exponential extrapolation techniques are 5 and 3, respectively. By increasing the sample size, the multiplication factors are gradually raised up to 6, as shown in Table 4.1. Considering the impact of multiplication factors, the expected lifetime of the test samples might be extremely short by using the "combined" exponential extrapolation technique. Here is an example demonstrating the usage of multiplication factors. We suppose to estimate the lifetime of a LED lamp from the test results on a group of six samples. If the L_{70} lifetime is calculated based on 3000 h test data using the "combined" exponential extrapolation technique, the expected lifetime of the test samples is the minimum between the projected L_{70} lifetime and 6000 h. Otherwise, if the L_{70} lifetime is calculated based on 6000 h test data using

Table 4.1 Multiplication factors with respect to different sample sizes in the "combined" and "direct" exponential extrapolation techniques

Sample size	Multiplication factor used in the "combined" exponential extrapolation technique	Multiplication factor used in the "direct" exponential extrapolation technique
3	/	3
4	/	4
5	1.5	5
6	2	5
7	2.5	5.5
8	3	5.5
9	3.5	5.5
10	4	6
11	4.5	6
12	5	6
13–14	5.5	6
15	6	6

the "direct" exponential extrapolation technique, the expected lifetime of the test samples is the minimum between the projected L_{70} lifetime and 30,000 h.

For the purpose of regulating the LED lighting products, Energy Star, affiliated to Environmental Protection Agency of the United States, released a series of program requirements to qualify the LED lighting products, which are categorized into two types, i.e., LED luminaires and integral LED lamps, respectively [11–14]. Compared to a LED lamp, a LED luminaire is a more complex lighting system. In many circumstances, LED lamps can be regarded as the light source of a LED luminaire.

The program requirements for LED luminaires were launched in 2007 (last revised in 2010, version 1.3) [12]. This standard specifies the lumen maintenance requirements for LED luminaires at the light source level and luminaire level, respectively, and the test samples are required to satisfy either of the two. At the light source level, an effective LM-80 test report of the light source (i.e., packages, modules, arrays, etc.) has to be provided to show a lumen maintenance of at least 91.8% at 6000 h for residential indoor luminaires and 94.1% for residential outdoor luminaires and all commercial luminaires. In addition, the T_s temperature of the light source measured by a thermal couple should be no higher than the temperature specified in the LM-80 test report with the corresponding drive current or higher (but not beyond the manufacturer's specified operating current range). At the luminaire level, a test report similar to LM-80 report on the entire test samples has to be provided to show that the lumen maintenance at 6000 h is no less than 91.8% for residential indoor luminaires and 94.1% for residential outdoor luminaires and all commercial luminaires.

The program requirements for integral LED lamps were launched in 2009 (last revised in 2011, version 1.4) [11]. In this specification, the integral LED lamps are divided into nonstandard lamps, replacement lamps, decorative lamps, and directional lamps. The minimum L_{70} lifetimes of these LED lamps are required at least 25,000 h, except for the decorative lamps of which is at least 15,000 h. To claim such long period lifetime, an at least 6000 h aging test has to be performed on ten test samples, among which five samples are installed base-up and the other five base-down. Except for the decorative lamps, the test temperature has to be 25 °C when the power of the test samples is less than 10 W and 45 °C for the other cases, whereas the decorative lamps are always tested at 25 °C independent on the power of the test samples (Table 4.2).

Table 4.2 Luminous flux maintenance thresholds for the lifetime qualification [11]

Maximum L_{70} lifetime claim	Minimum lumen maintenance by 6000 h (%)	Minimum lumen maintenance by the test period/total test period (h)
15,000	86.7	86.7%/6000
20,000	89.9	89.9%/6000
25,000	91.8	91.8%/6000
30,000	93.1	91.2%/7500
35,000	94.1	91.5%/8750
40,000	94.8	91.5%/10,000
45,000	95.4	91.5%/11,250
50,000	95.8	91.8%/12,500

Table 4.3 Categories of the LED lighting products

Lumen maintenance after a minimum period between 6000 h and 25% of the rated lifetime (%)	Self-ballasted lamps	Modules	Luminaires[a]
90	Cat A	Code 9	Code 9
80	Cat B	Code 8	Code 8
70	Cat C	Code 7	Code 7
60	Cat D	–	–
50	Cat E	–	–

[a]For the LED luminaires using the modules which did not pass IEC/PAS 62717 at their t_p temperatures

Since 2011, Energy Star has reconstructed the program requirements on lighting products into two kinds, i.e., luminaire and lamps, respectively [13, 14]. For instance, the specifications for residential light fixtures and LED luminaires are merged into a comprehensive one for luminaires [13], and the specifications for compact fluorescent lamps and integral LED lamps are merged into another one for lamps [14]. Nevertheless, the lumen maintenance requirements of the LED luminaires and lamps remain the same with those in the abovementioned specifications.

The IEC standards relevant to the lumen maintenance are IEC/PAS 62612 (in which "PAS" is an abbreviation of "Publicly Available Specification") for self-ballasted LED lamps, IEC/PAS 61717 for LED modules, and IEC/PAS 62722 for LED luminaires [15–17] Unlike IESNA and Energy Star, IEC classifies the test samples into different categories according to the lumen maintenance measurement after 6000 h (or 25% of the rated lifetime if it is shorter than 6000 h) aging, instead of estimating their lifetimes. Table 4.3 indicates the categories of the LED lighting products stipulated in IEC standards. Note that the LED luminaires of which the modules have passed the IEC/PAS 62717 standard at their t_p temperatures are exempt from the IEC/PAS 62722 requirements. During the test, at least three ambient temperatures including 25 °C and another two performance temperatures (so-called t_p temperatures) are required for LED modules. For self-ballasted LED lamps and LED luminaires using the modules which did not pass the IEC/PAS 62717 standard at their t_p temperatures, the ambient temperature is simply required to be 25 °C. Meanwhile, the sample size requirement is at least 20 units for the LED modules and self-ballasted LED lamps, whereas 5 units for the LED luminaires using the modules without being proved by the IEC/PAS 62717 standard at their t_p temperatures.

Color shift over time, or color stability, is another degradation concern for LEDs and LED products [18–21]. At the LED source level, the color shift can arise from changes in the LED package such as the emitter, phosphor used to convert emitted blue light into white light, and clear encapsulant [18, 19]. At the lamp and luminaire level, the color shift is exaggerated by the degradation of optical lens and diffusers which are usually made by PC or PMMA materials [20, 21]. Unfortunately, there have not been standardized methods to claim the chromaticity lifetime caused by the color shift failure for LED packages, lamps, and luminaires. The commonly

used industrial qualification for the color shift of LED modules, lamps, and luminaires is referred to the requirements in Energy Star standards [11–14], in which the Euclidean distance $du'v'$ between the CIE 1976 color coordinates at origin and 6000 h should not exceed 0.007.

4.2 Advanced Lumen Maintenance Lifetime Estimation Methods

The lumen maintenance of a LED is defined as a maintained percentage of the initial light output over time. It is a general law that in most cases a LED will not experience a sudden death but gradual degradation on its lumen maintenance. Therefore the L_{70} lifetime defined by the time when the lumen maintenance drops to 70% is equivalent to the operational lifetime for LEDs in a long period [22–40].

Qiao et al. presented the analysis of a series of LED degradation models and recommend the exponential decay model shown by Eq. 4.1 as an appropriate empirical model to describe the luminous flux depreciation of the LED packages and modules [18].

$$\Phi(t) = \beta \exp(-\alpha t) \tag{4.1}$$

where $\Phi(t)$ denotes the luminous flux at the time t and β and α are the pre-factor and depreciation rate, respectively. Following Eq. 4.1, the lifetime estimation of LEDs is usually implemented by projecting the lumen maintenance measurements to a threshold value (for instance, L_{70}). TM-21 presented a least square extrapolation method (herein called TM-21 method) on a minimum of 6000 h degradation test data to estimate the lumen maintenance lifetime of LEDs [7]. Due to the simplicity and operability, the TM-21 method has been widely used for estimating the LED lifetimes up to now.

Being operated at higher stress levels, accelerated degradation tests (ADTs) quickly yield information on the lifetime distribution of a test unit [41, 42]. The accelerated loadings in LEDs are mainly focused on thermal and moisture stresses. Tan et al. studied the degradation physics in high-power LEDs under high temperature-humidity tests [43]. They found the dominant failures in the LEDs under high temperature-humidity conditions include Kirkendall voids formation, bondpad contamination, galvanic dissolution of Ag, phosphor dissolution, encapsulant delamination, and die attach delamination. For these reasons, they argued that the degradation physics of LEDs are completely different among the various RH levels from 95% to 70% and 85 °C. Luo et al. investigated the effects of moist environments on the reliability of high-power LEDs [44]. They observed that the moisture diffusion does aggravate the degradation of lumen maintenance. But it is also possible to cause an electronic failure and in this way to break the LED. Chan et al. applied unbiased highly accelerated temperature/humidity stress test (HAST)

on high-power LEDs [45]. They concluded the root cause of the lumen maintenance degradation of LEDs by the failure of silicon encapsulant, such as bubbling and discoloration. Similar phenomenon is found by Huang et al. from biased HAST of high-power LEDs. They observed silicon carbonization which they believed it was resulted from a very high temperature inside the silicon by a blue light over-absorption [18]. Meneghini et al. proposed a set of specific experiments, which is aimed at separately analyzing the degradation of the properties of the active layer, of the ohmic contacts, and of the package/phosphor system in LEDs [46]. As a result of the abovementioned results, it seems that the humidity-based ADTs are not suitable for high-power LEDs. For the mid-power LEDs, the negative impact of the humidity-based ADTs is alleviated to some extent. Huang et al. developed a wet-high temperature operation life test (WHTOL) for mid-power LEDs. They demonstrated that lumen degradation mechanism in WHTOL is similar to the failure in LM-80 test, although a discoloration failure mode is also found in the silicon encapsulant [19].

In addition to a theoretical degradation path (i.e., mean degradation curve), the lumen maintenance measurements of LEDs are also affected by a number of uncertainties caused by, for instance, measurement error, turbulence of test conditions, material defects, and some other unknown reasons. These uncertainties result in a random variation (i.e., error) in the degradation measurements of the LED lumen maintenances. In the TM-21 method, influence of such a variation is not considered, and because of this, the estimated LED lumen maintenance lifetime is questionable. For using the LM-80 test data more effectively, a number of advanced methods that take the error analysis into account are introduced to provide more accurate and reliable estimations for the lumen maintenance lifetimes of LEDs.

Taking the effect of random variation into account, the time-based lumen maintenance degradation path can be described by Eq. 4.2.

$$L(t) = M(t) + \varepsilon(t) \tag{4.2}$$

in which $L(t)$ denotes the actual degradation path of a LED under degradation, $M(t)$ denotes the mean degradation path, and $\varepsilon(t)$ denotes the error term caused by the random variation. Tseng and Peng summarized two approaches to deal with the situation where $\varepsilon(t)$ is involved [24]. The former one is called mixed effect model, in which a mixed effect between the $M(t)$ and $\varepsilon(t)$ is assumed and studied [25, 26]. The mixed effect model can provide an intuitive understanding of the random variation but on the other hand offer a computationally expensive algorithm due to a complicated model parameters estimation process. The alternative one is called stochastic process model, in which $\varepsilon(t)$ is described by using stochastic diffusion models such as the Gauss-Markov process and Wiener process [24, 27–33]. With the stochastic diffusion models, the lifetime distribution of LEDs is estimated to address the mean-time-to-failure (MTTF) and median lifetime (B50). Nevertheless, in both approaches, the lifetimes of LEDs are estimated from the test results under accelerated stress conditions, such as high temperature [25, 26], high temperature humidity [32], and temperature step stress [27, 33]. As a result, no

matter what approach is used, the $M(t)$ is assumed to follow the exponential degradation function such as Eq. 4.1 from a prospective of the ADT methodology.

Fan et al. and Wang et al., respectively, developed another degradation data-driven method to predict the lumen lifetime of high-power white LEDs [34, 35]. In details, Fan et al. applied a general degradation path model for LED's luminous flux depreciation, in which more reliability messages (e.g., MTTF, confidence intervals, and reliability function) could be estimated in addition to the lumen lifetime [34]. To improve the curve-fitting accuracy, Wang et al. used a bi-exponential model, replacing widely used exponential model, to fit the degradation curve of LEDs with the least square method [35]. Later on, as the least square method used before is a batch-processing estimation by minimizing the sum of the residuals between the actual measurements and the calculated values, it has a large estimation errors. Fan et al. updated their method with the consideration of measurement error using a nonlinear filter-based approach [22]. The result shows that the nonlinear filter approach can deliver a recursive and stochastic parameter estimation by dynamically updating measurements, which improved the accuracy of remaining useful lifetime estimation.

When using the degradation model to estimate the lifetime of LEDs, the estimation accuracy strongly relies on the sample size for curve fitting. Thus, a very practical problem is the determination of the test period for a reliable estimation of the lifetime. Tseng and Yu proposed a termination rule for both ordinary and accelerated degradation tests of LEDs [36, 37]. They traced the variation trend of the estimated mean lifetime (i.e., average of the estimated lifetimes of all test samples) extracted from the test results with an increasing time. Then they claimed that the test can be terminated at the time when the estimated mean lifetime is converged. By applying Tseng and Yu's method, van Driel et al. investigated five LM-80 test reports of high-power and mid-power LEDs and observed that for all of the five cases, convergence of the estimated mean lifetimes is reached after at least 6000 h testing [38].

In summary, as indicated in many studies, ADTs for high-power LEDs are too aggressive since extra failure modes are observed on such as silicon encapsulant, phosphor film, and die attach. For mid-power LEDs, these additional failure modes might be less apparent. This makes ADTs more workable for mid-power LEDs. Two approaches called the mixed effect model and stochastic process model are introduced, respectively, for the lifetime estimation of LEDs from the experimental results of ADTs with the consideration random variation. In addition, a few more statistics-based methods are discussed for the same reason. In the end, approaches to determine an appropriate time to terminate the aging tests or accelerated tests are talked about.

It has to be noted that the advanced methods mentioned in this subsection require sophisticated skills on statistics. Therefore it is an arduous task to develop a general lifetime estimation algorithm that is universal for a large variety of LEDs. Up to present, none of standards or specifications has been developed based on these methods.

4.3 A Temperature-Driven Accelerated Test Method

At the product level, the 6000 h aging tests for qualifying the luminous flux depreciation are vital for successful acceptance of the LEDs and LED products. For efficiently reducing the test period, an easy-to-handle ADT is developed to shorten the testing time from 6000 to 2000 h. The key point in the development of such method is to find a luminous flux depreciation "boundary curve," which is determined from a wide range of the known LM-80 data. Then exponential decay model for luminous flux degradation, together with the Arrhenius acceleration model, is applied to obtain the acceleration factor. At last, extensive verification studies based on the internal and external test data are presented.

4.3.1 Boundary Curve Definition

VDE standard VDE-AR-E2715-1, published and written in German, developed a so-called Border Function method for predicting the reduction in luminous flux of LEDs [47]. This method is based on the assumption that an exponential model is a conservative estimation (worst-case scenario) of the actual long-term luminous flux maintenance, as it is expected that most LEDs will show the long-term luminous flux maintenance better than the assumed exponential function. Therefore, the qualification accuracy for a LED package or system highly depends on the determination of the boundary curve. Following an exponential decay assumption, which is frequently used to describe the lumen maintenance decay characteristics of LEDs, the boundary curve is expressed by Eq. 4.1, when the $\Phi(t)$ is normalized by the initial value and the parameter β equals to unity. Meanwhile, the boundary curve pass the point (L_{70}, 70%), where L_{70} indicates the lifetime with respect to the 70% lumen depreciation [5]. An illustration of the boundary curve is shown in Fig. 4.1, in which a LED package or system is regarded as passing the qualification test when its luminous flux maintenance stays above the boundary curve.

Previous studies show that temperature plays a significant role on the luminous flux depreciation of LED packages and systems [34, 48]. It is possible to describe the temperature dependency by an Arrhenius model at luminaire level [49].

$$\alpha = A\exp\left(-\frac{E_{\mathrm{a}}}{kT_{\mathrm{s}}}\right) \tag{4.3}$$

where A and E_{a} are the pre-factor and activation energy, respectively, k is the Boltzmann constant (i.e., 8.617385×10–5 eV/K), and T_{s} stands for the solder temperature in Kelvin. For LED systems, the activation energy is defined as "equivalent activation energy" that considers the influences of other component devices such as secondary optical lens on the light output of the LED system. The

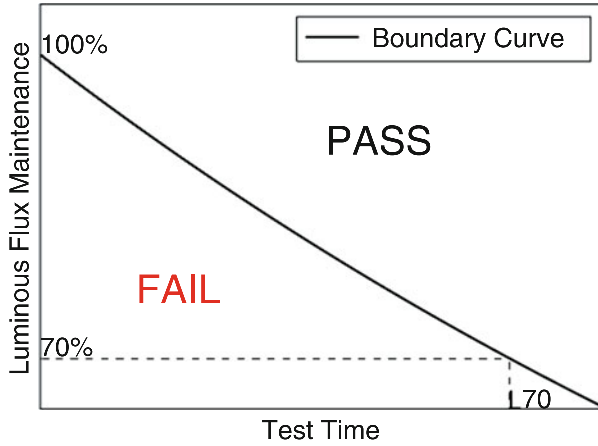

Fig. 4.1 Illustration of the boundary curve

relationship of luminous flux maintenances between a LED system and its light source (i.e., LED package or module) was expressed as follows [7]:

$$\Phi_{\mathrm{l}}(t) = \Phi_{\mathrm{p}}(t) \times C(t) \tag{4.4}$$

where $\Phi_{\mathrm{l}}(t)$ and $\Phi_{\mathrm{p}}(t)$ indicate the luminous flux maintenances of a LED luminaire and its light source, respectively. And $C(t)$ is the correlation function in terms of the time t. Assuming that both $\Phi_{\mathrm{l}}(t)$ and $\Phi_{\mathrm{p}}(t)$ follow Eq. 4.1, the correlation function $C(t)$ can be solved as:

$$C(t) = \frac{\beta_{\mathrm{l}}}{\beta_{\mathrm{p}}} \exp(-\Delta\alpha t) \quad \text{where} \quad \Delta\alpha = \alpha_{\mathrm{l}} - \alpha_{\mathrm{p}} \tag{4.5}$$

where β_{l}, β_{p}, α_{l}, and α_{p} are pre-factors and depreciation parameters for a LED luminaire (or lamp) and its light source, respectively. The parameter $\Delta\alpha$ determines the relationship of luminous flux depreciation rates between the LED luminaire and its light source. A positive $\Delta\alpha$ indicates that the luminous flux depreciation rate of a LED luminaire is faster than that of its light source. This could happen when the lumen depreciation originated from the LED light source is aggravated by additional failure mechanisms such as optical lens degradation and LED driver failures. On the contrary, a negative $\Delta\alpha$ means the LED luminaire behaves somehow a slower luminous flux depreciation rate compared to its light source. In the particular case that there is no additional degradation existing at the product level, $\Delta\alpha$ equals zero. It was reported that when the ambient temperature was below 80 °C, the influence of the driver and optical lens on LED luminaire lumen output is very limited [50]. Thus, $\Delta\alpha$ can be assumed to be zero. That means the equivalent activation energy can be treated as the activation energy of LED source.

According to Eq. 4.3, the luminous flux depreciation can be accelerated by increasing the T_s of the tested luminaire, and the acceleration factor AF can be calculated as:

$$\mathrm{AF} = \frac{\alpha|_{T_{s1}}}{\alpha|_{T_{s2}}} = \exp\left(-\frac{E_a}{k}\left(\frac{1}{T_{s2}} - \frac{1}{T_{s1}}\right)\right) \tag{4.6}$$

where T_{s1} and T_{s2} and $\alpha|_{T_{s1}}$ and $\alpha|_{T_{s2}}$ are the solder temperatures and depreciation parameters of the boundary curve obtained at room temperature and the accelerated ambient temperature, respectively.

4.3.2 Two-Stage Process

According to the abovementioned discussion, a two-stage process is utilized to reduce the testing time of qualifying the luminous depreciation of a LED lighting products at room temperature. As shown in Fig. 4.2, the sequence from Step 1 to 2 is used as an example to explain the two-stage process (same results can also be obtained for the process from Step 3 to 4). In the first stage, the exponential decay characteristic of the boundary curve is used to reduce the testing time. Referring to the requirement proposed by the Energy Star program [11, 14], the testing time should be at least 6000 h, and the luminous flux maintenance is required above 91.8%. With the ever-improving measuring techniques, it is possible to further shorten the test time by raising the luminous flux maintenance threshold to 95% [51]. Then the testing time is determined by calculating the $L_{95}|T_{s1}$ (the time when the luminous flux maintenance decays to 95% at a solder temperature of T_{s1}) on the boundary curve by Eq. 4.1, which is approximately 3595 h. Next, temperature acceleration is applied from T_1 to T_2 (ambient temperature, $T_2 > T_1$). Accordingly, the solder temperature T_{s2} is increased with the same ambient temperature

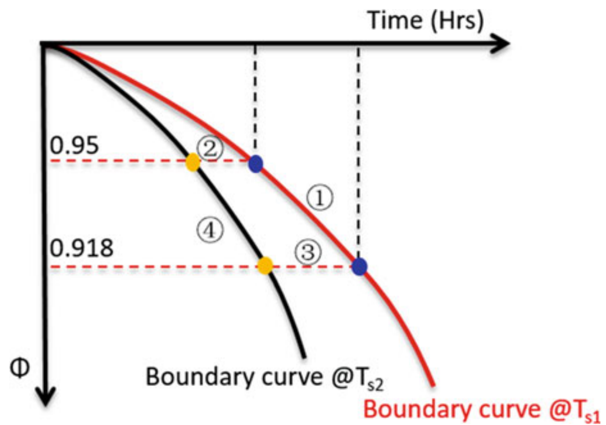

Fig. 4.2 Illustration of the two-stage process

increment. The final accelerated testing time $L_{95}|T_{s2}$ can be then calculated by dividing $L_{95}|T_{s1}$ by the AF as shown in Eq. 4.7. According to the calculation of AF in Eq. 4.6, the accelerated testing time $L_{95}|T_{s2}$ is eventually determined by parameters T_{s1} and T_{s2} and E_a.

$$L_{95} \mid T_{s2} = \frac{L_{95} \mid T_{s1}}{\mathrm{AF}} \tag{4.7}$$

4.3.3 Parameters Determination

A census and analysis on 30 LM-80 datasets of commercial phosphor-converted white LED sources from various sources such as internet, consortium, and vendor reports were conducted for properly extracting the parameters T_{s1} and T_{s2} and E_a. The selected LM-80 datasets originate from multiple sources. The Philips and Nichia published their LM-80 data on their web pages [52, 53], and other manufacturers will provide the data only to customers [54–57]. In addition, due to NDA arrangement with the suppliers, some of the LM-80 datasets are not provided in the reference. Each dataset contains the lumen depreciation data of about 25 LEDs, usually at CCT 2800–3500 K, tested under 55 °C, 85 °C, and a third temperature selected by manufacturers. The input currents range from 0.08A to 1A. Test times range from 6000 to 10,000 h.

Among the 24 out of 30 reports, the third case temperature is no more than 105 °C. Therefore, the T_{s1} is chosen as 105 °C which represents a worst reference T_s temperature in a LED luminaire working at 25 °C.

The determination of the T_{s2} is based on the consideration that there is no additional failure mode in the accelerated condition. In general, most of LED manufacturers allow their products to work under an ambient temperature of 55 °C (namely, 25 + 30 °C). Therefore, the T_{s2} in this paper is determined as 135 °C (namely, 105 + 30 °C).

Table 4.4 shows the parameters E_a, A, and β of the LED packages and modules, which were calculated from the test data at T_s of 55 °C and 85 °C using TM-21 method. As shown in Table 4.4, the calculated E_a spans in a large range from −0.226 to 0.702, covering the majority of LED luminaires in the market. A negative E_a indicates the test sample behaves a negative temperature effects on its depreciation parameter. That means, the luminous flux depreciation becomes less as the temperature rises. The root cause of a LED package having a negative E_a is still not clear. All calculated E_a were fitted in a Normal distribution as shown in Fig. 4.3. The 95th percentile of the distribution, equaling 0.396, is chosen as the E_a of the boundary curve. In general, the luminous depreciation rate of a LED luminaire with a larger E_a is more significantly affected by the rise of the ambient temperature. In the proposed method, the E_a of the boundary curve should be selected large enough to allow the luminaires being qualified at room temperature can pass the accelerated tests as well. However, an overestimated E_a will allow the luminaires not being qualified at room temperature but pass the accelerated tests.

Table 4.4 Parameters E_a, A, and β of the LED packages and modules obtained from 30 LM-80 test reports

No.	E_a [eV]	A	β	No.	E_a [eV]	A	β
1	−0.156	1.54E−08	1.014	16	0.702	6.03E+04	0.978
2	−0.033	1.12E−06	0.985	17	0.111	1.10E−04	1.008
3	0.190	1.67E−03	0.966	18	0.210	4.88E−03	0.993
4	0.120	1.34E−04	0.976	19	−0.226	1.17E−09	0.990
5	0.135	5.84E−04	1.001	20	0.179	1.31E−03	1.008
6	0.243	1.64E−02	1.006	21	−0.138	1.22E−08	0.986
7	0.061	4.11E−05	1.015	22	−0.097	7.88E−08	0.978
8	0.133	5.28E−04	1.015	23	0.065	1.61E−05	0.980
9	0.026	1.13E−05	0.990	24	0.040	2.17E−05	1.006
10	0.275	3.27E−02	0.992	25	0.088	1.16E−04	0.988
11	−0.121	5.03E−08	1.017	26	0.241	1.83E−02	1.013
12	−0.121	1.29E−08	0.995	27	0.367	5.52E−01	1.004
13	0.068	1.04E−04	1.030	28	0.028	2.08E−05	1.009
14	0.200	4.09E−03	1.006	29	0.151	5.69E−04	1.005
15	0.141	1.06E−03	1.018	30	0.082	9.42E−05	1.001

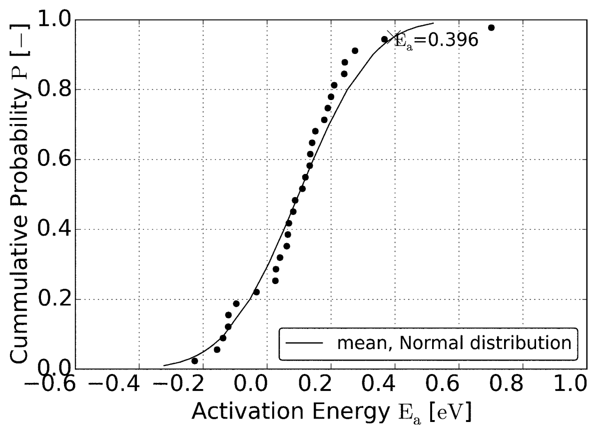

Fig. 4.3 E_a parameters fitted by a Normal distribution

Figure 4.4 shows the luminous flux maintenance of 12 LED packages operated at 105 °C from the LM-80 test reports. The boundary curve is calculated with a depreciation parameter α of 1.427e-5, which is marked by a black line. The result indicates that the selected boundary curve can envelope most of the test data.

4.3.4 *Determination of the Accelerated Time*

Due to the seasoning effect in LEDs, the luminous flux measurements of tested LED luminaires fluctuate in the initial stage. To minimize such effect, TM-21 and

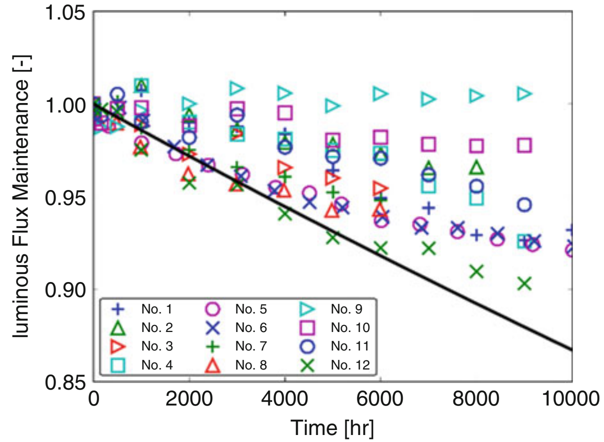

Fig. 4.4 Luminous flux measures of 12 LED packages operated at the T_s of 105 °C

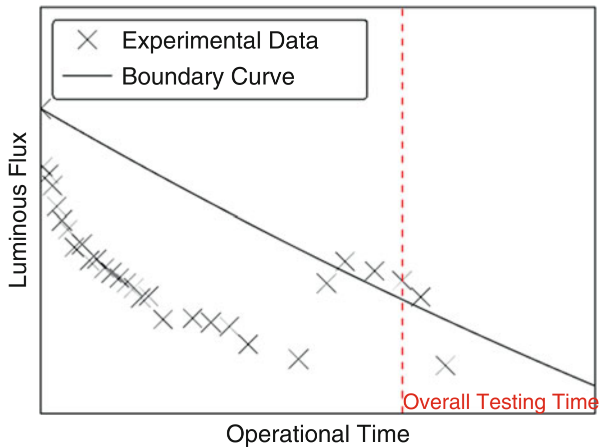

Fig. 4.5 An example of the luminous flux measurements of a LED luminaire

TM-28 methods recommend not to use the first 1000 h data in data analysis [7, 10]. In the accelerated test, the seasoning effect will be less than that at room ambient temperature. It is possible to use the obtained parameters T_{s1} of 105 °C, T_{s2} of 135 °C, and E_a of 0.396 for a first-order approximation of the acceleration factor *AF* for seasoning effect. After round-up, this gives an estimate of the seasoning time of 500 h at accelerated ambient temperature. Next, the overall testing time of the accelerated test is calculated from Eq. 4.7 as 1487 h, which has been rounded up to 1500 h.

Additionally, based on our previous experience, the fluctuation of luminous flux measurements could be also found during test time. Figure 4.5 shows an example that the luminous flux measurements decrease monotonically in the beginning but increase at the final testing time of 1500 h. Although this LED luminaire passes the 95% criterion threshold at 1500 h, it is not certain if the single data at 1500 h represent its true behavior. To solve this problem, two additional midpoint lumen

Table 4.5 Summary of the entire test condition

	Test temperature	Time	Lumen maintenance threshold
	[°C]	[Hours]	[%]
Seasoning	55	500	–
Accelerated test[a]	55	900	95
	55	1200	95
	55	1500	95

[a]The operational time is zeroed, and the lumen maintenance is normalized before the accelerated test

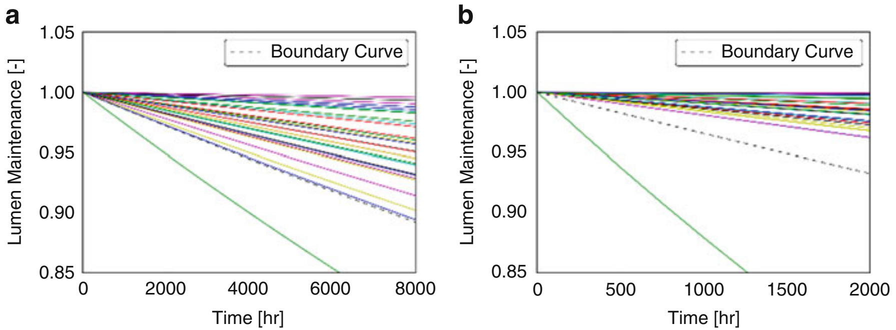

Fig. 4.6 Simulated luminous flux depreciation curves of the light sources, (**a**) $T_s = 105$ °C, (**b**) $T_s = 135$ °C

maintenance measurements at 900 h and 1200 h are recommended. In summary, Table 4.5 presents the entire test condition.

4.3.5 Verification

To verify the proposed boundary curve at LED light source level, we calculated the luminous flux depreciation curves at T_s of 105 °C and 135 °C, based on Eq. 4.6 with the parameters listed in Table 4.4. These calculated luminous flux depreciation curves are shown Fig. 4.6, together with a black dashed line indicating the boundary curve at the corresponding temperature. Comparing the calculated curves in Fig. 4.6 (a) (105 °C, 6000 h) and (b) (135 °C, 2000 h), it can be seen that those of which depreciation curves stay above the boundary curve at T_s of 105 °C, are also above the boundary curve at T_s of 135 °C, and vice versa. In other words, for every LED light source shown in Fig. 4.6, same qualification results can be obtained from both tests at T_s of 105 °C and 135 °C.

At product level, to demonstrate the relationship between the tests applied at ambient temperatures of 25 °C and 55 °C, numerical luminous flux depreciation simulation was performed on a number of virtual LED luminaires. A total of

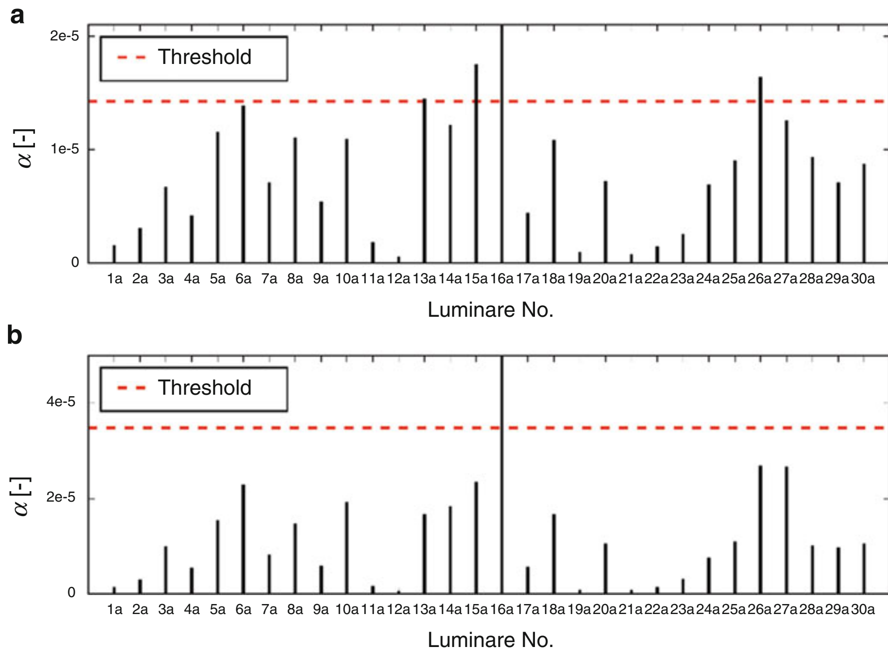

Fig. 4.7 Depreciation parameters of the virtual luminaires with a poorly designed heat sink, (**a**) $T_s = 125$ °C at an ambient temperature of 25 °C; (**b**) $T_s = 155$ °C at an ambient temperature of 55 °C

30 cases were studied that correspond to the 30 LM-80 data sets, where the E_a and A are shown in Table 4.1. In each case, two virtual luminaires with the same light source were created. The one labeled with "a" is equipped with a poorly designed heat sink, resulting in T_s of 125 °C and 155 °C when operated at ambient temperatures of 25 °C and 55 °C, respectively, whereas the other one labeled with "b" is equipped with a well-designed heat sink, resulting in T_s of 85 °C and 115 °C when operated at ambient temperatures of 25 °C and 55 °C, respectively. The calculated depreciation parameters α of these two kinds of virtual luminaires in all 30 cases are plotted in Figs. 4.7 and 4.8, in comparison with the thresholds (i.e., 1.427e-5 and 3.488e-5 at ambient temperatures of 25 °C and 55 °C, respectively) marked in red lines. The luminaires of which the value of α stays underneath the threshold line are regarded to pass the test.

The simulation results in Figs. 4.7 and 4.8 include four circumstances as follows:

1. The luminaires pass the tests at both 25 °C and 55 °C. This phenomenon occurs in the vast majority of the luminaires.
2. The luminaires fail the tests at both 25 °C and 55 °C. This phenomenon occurs on the luminaire 16a.
3. The luminaires pass the test at 25 °C but fail at 55 °C. This phenomenon occurs on the luminaire 16b.

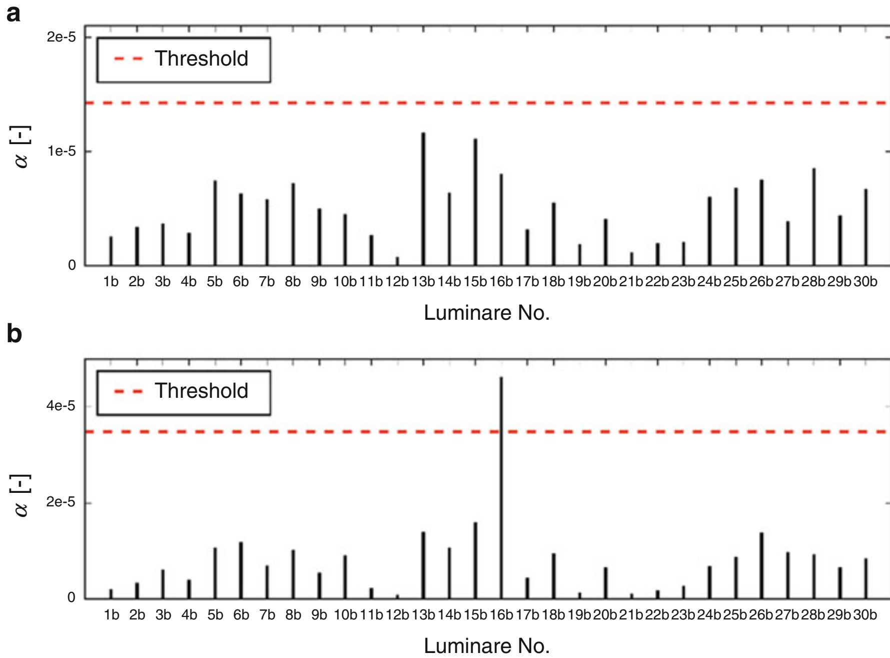

Fig. 4.8 Depreciation parameters the virtual luminaires with a well-designed heat sink, (**a**) $T_s = 85$ °C at an ambient temperature of 25 °C; (**b**) $T_s = 115$ °C at an ambient temperature of 55 °C

4. The luminaires pass the test at 55 °C but fail at 25 °C. This phenomenon occurs on the luminaires 13a, 15a, and 26a.

In summary, among more than 93% of the total 60 virtual luminaires, the qualification results obtained at both 25 °C and 55 °C are same. Furthermore, since the E_a of the light source in the luminaires 16a and 16b is as high as 0.702, the qualification results on these two luminaires are markedly dependent on the thermal design of the heat sink. For this reason, the luminaire with a poorly designed heat sink (for instance, luminaire 16a) cannot pass the test at either 25 °C or 55 °C. The luminaire with an improved heat sink (for instance, luminaire 16b) can pass the test at 25 °C but still fail at 55 °C. It can be imagined, by improving the heat dissipation capability of the heat sink further, the luminaire will pass the tests at both 25 °C and 55 °C. For the case (4) where the luminaires pass the tests at 55 °C but fail at 25 °C, Fig. 4.9 further illustrates the calculated luminous flux depreciation curves as function of time at T_s of (a) (125 °C, 6000 h) and (b) (155 °C, 2000 h). It can be seen that the depreciation curves of these three virtual luminaires stay above the boundary curve at T_s of 155 °C but below the boundary curve at T_s of 125 °C. As seen in the simulated luminous flux depreciation curves of the light sources at T_s of 105 °C and 135 °C for all 30 LED sources in Fig. 4.6, those of which depreciation curves stay above the boundary curve at T_s of 105 °C, are also above the boundary curve at T_s of 135 °C, and vice versa. This

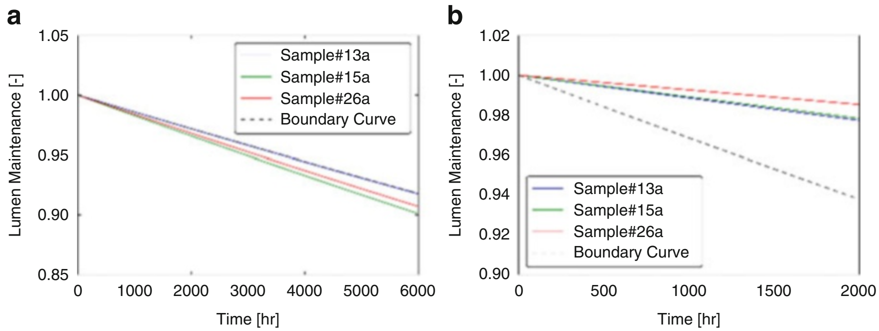

Fig. 4.9 Luminous flux depreciation curves of the virtual luminaires 13a, 15a, and 26a, (**a**) $T_s = 125$ °C; (**b**) $T_s = 155$ °C

indicates that the characteristics of the boundary curve α, in Eq. 4.3, depend not only on the activation energy but also the pre-factor A. The combination of these two parameters, as defined in the proposed two-stage model, may present a complex depreciation behavior for the lumen depreciation of 95% at the accelerating temperature, compared to that of 91.8% at non-accelerating temperature.

In addition, experimental results from both external and internal product level test were utilized to further prove the accelerated test method. In one of the latest US DOE CALiPER data [58], a batch of the accelerated life tests on 15 types of LED A lamps at 45 °C were conducted. Ten lamps from each type were tested simultaneously in a large automated long-term apparatus (ALTA) for 7660 h with a weekly in situ measurement recording. The lamps selected for the tests were expected to have at least 25,000 h rated lifetime. In order to apply the proposed model, the overall test time has to be recalculated in terms of the ambient temperature of 45 °C, which gives the test time approximately 2000 h. The data are processed in the following:

1. Considering the first 500 h as the seasoning period, the initialization of the luminous flux maintenance is selected at 500 h.
2. Calculate the luminous flux maintenance at 1200 h, 1600 h, and 2000 h from the initialization, respectively.
3. Plot lumen maintenance for each lamp and also plot the lumen maintenance at 6000 h by Energy Star requirement.

Figure 4.10a shows the lumen maintenance at 6000 h, and Fig. 4.10b shows the test results at 1200 h, 1600 h, and 2000 h, respectively. The corresponding criterion thresholds were indicated by black lines in both figures. The number of lamps whose lumen maintenance at 6000 h lower than the threshold (91.8%) was 6 (i.e., 13RT-03, 13RT-09, 13RT-11, 13RT-13, 13RT-14, and 13RT-58). Likewise, the number of lamps whose lumen maintenance at 1200 h, 1600 h, and 2000 h lower than the threshold (95%) was 5 (i.e., 13RT-03, 13RT-09, 13RT-11, 13RT-13, and 13RT-58), except one for 13RT-14. A further investigation on the lamp 13RT-14 reveals that the luminous flux of the tested samples at 6000 h was measured with a

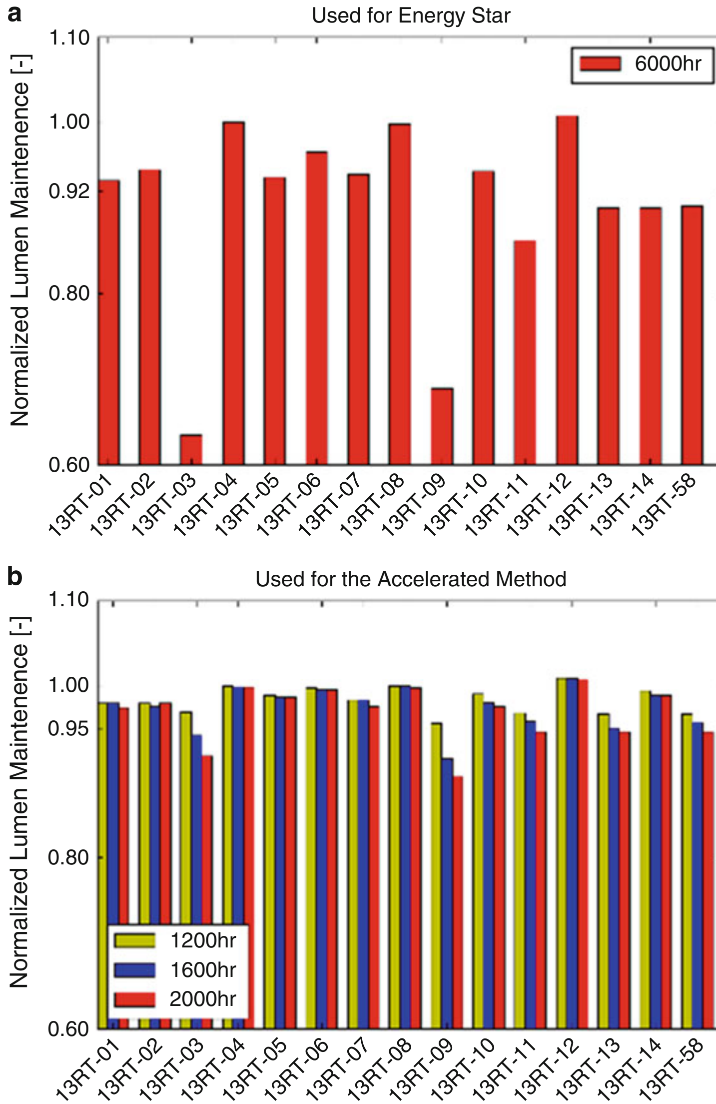

Fig. 4.10 Luminous flux maintenance of the LED A lamps operated at 45 °C, (**a**) for qualification by Energy Star requirements; (**b**) for qualification by the accelerated method

large variance and the average luminous flux was biased by the lowest measurement [58]. Therefore there is a very good correlation between the proposed accelerated test and traditional 6000 h test.

The internal validation tests were conducted on a batch of indoor LED luminaires at ambient temperatures of 25 °C and 55 °C, respectively. Six LED luminaires including Product 1 (12 W spotlight), Product 2 (8 W bulb), Product 3 (6 W

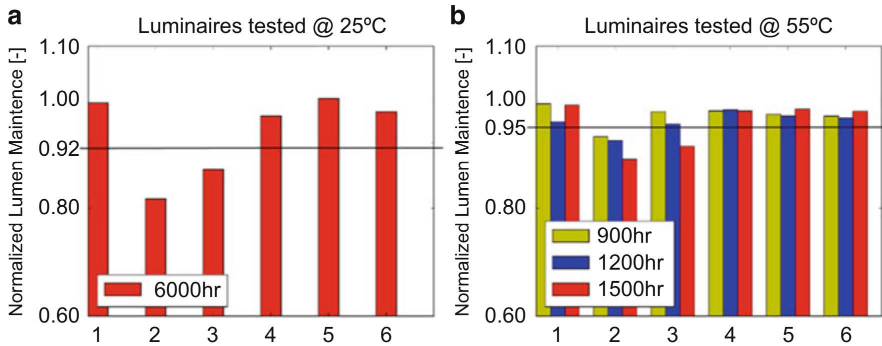

Fig. 4.11 Luminous flux maintenance of the indoor LED luminaires, (**a**) operated at 25 °C; (**b**) operated at 55 °C

bulb), Product 4 (6 W bulb), Product 5 (20 W downlight), and Product 6 (16 W downlight) were selected as test samples. At 25 °C ambient temperature, the luminaire was aged without seasoning, whereas at 55 °C, a 500 h seasoning was taken before aging. Figure 4.11a, b plots lumen maintenance at 6000 h aging at 25 °C ambient temperatures and lumen maintenance at 900, 1200, and 15,000 h aging at 55 °C ambient temperatures. Products 2 and 3 fall below the threshold (91.8%) in Fig. 4.11a. Similarly, in the accelerated test shown in Fig. 4.11b, Products 2 and 3 fall under the threshold (95%) after 1200 h aging.

4.4 A SPD-Based Degradation Prediction Method

Nowadays the LED products are faced with a new era of not only replacing but also exceeding their traditional counterparts (such as incandescent lamps and cold cathode fluorescent lamps). Under this circumstance, the requirements of the color consistence in LEDs become more important than those of lumen maintenance in many applications (such as supermarket, shopping mall, museum, and healthcare lightings). The formulation of the chromaticity lifetime qualification method for the LED products is based on an accurate prediction of the color shift propagation. However, the study on quantitative models of the color shift of LEDs is just beginning. Fan et al. proposed a nonlinear dual-exponential model to describe the chromaticity state shift process [22]. Then by using an unscented Kalman filter technique, they predict the growing trends of the color shift according to the historical data obtained from the aging tests of the LEDs. Huang et al. demonstrated that a linear model could also be applicable for the color shift of LEDs by analyzing both the experimental and simulation data [32]. Similar to Fan's work, they applied a modified Wiener process to predict the progression of the color shift of LEDs based on the acquired historical data. However, the algorithms in the

above two methods are purely empirical, without considering the color shift failure mechanism.

As a matter of fact, both the lumen depreciation and color shift of a LED are linked by the degradation of its spectral power distribution (SPD), since the photometric and colorimetric parameters of the LED such as luminous flux, color coordinates, correlated color temperature (CCT), and color rendering index (CRI) are originally calculated from its SPD [59–63]. Many studies related to the improvement of the photometric and colorimetric parameters are performed based on the design and optimization of SPDs. For instance, via the SPD analysis, Lu et al. [63] proved that RGB LEDs provide a wider color gamut and smaller color shift than cold cathode fluorescent lamps and therefore are more suitable to be used as the backlights of the liquid crystal displays. Lin et al. [64] performed a sensitivity study on the CRI parameters (for instance, Ra and R9) of LEDs with different SPDs by using a spectra-loss simulation method. They found that the CRI parameters were significantly sensitive with some certain wavelengths, for instance, 444 nm, 480 nm, 564 nm, and 622 nm for Ra, whereas 461 nm, 581 nm, and 630 nm for R9. As a result, they concluded that extra cautions should be paid on the shift around these wavelengths in the design of SPD for a LED. Song et al. [65] developed an approach to deconvolute the SPD of a phosphor-converted white LED (pc-LED) into blue and phosphor-converted peaks, each of which was formed by a superposition of several decomposed SPDs in a Gaussian form. Based on these two decomposed peaks, the radiant fluxes of the blue light and phosphor-converted light could be calculated for the investigation of the yellow-to-blue ratio and phosphor power conversion efficiency of the pc-LED.

Recently, the SPD analysis has been successfully applied to qualify the reliability of LEDs. Chang et al. [66] developed a similarity-based metric test method to detect the anomaly point where the color shift failure of the pc-LED is expect to occur. In their method, 24 features including the peak wavelengths, amplitudes, etc., were first extracted from the decomposed blue light and phosphor-converted light peaks of the LED. Then a k-nearest neighbor (KNN)-kernel density-based clustering technique was employed to partition the principle components of the 24 features under degradation. Finally, the anomaly was detected when the Euclidean distance from the centroid to the test data for each cluster was beyond the threshold value. Chang's method provides a fast way to detect the failure of the LEDs which could potentially fail during the early stage of operation; however, it is not able to estimate the lifetime of the LEDs.

In order to achieve the goal of lifetime prediction, this subsection proposes an SPD analysis-based method to predict the time dependency of the photometric and colorimetric parameters of the pc-LED. Firstly, the empirical curve-fitting models for describing the SPD of the pc-LED are discussed and a sensitivity study of the model parameters on the photometric and colorimetric parameters. Then the evolutionary process of the SPDs of the pc-LED under degradation testing is predicted for estimating the lifetimes of the pc-LED due to lumen depreciation and color shift, respectively.

4.4.1 Spectral Power Distribution Models

As a mixed light, the entire SPD of a white LED is regarded as a superposition of a couple of coincident "bell-shaped" spectra, as shown in Eq. 4.8.

$$\mathrm{SPD}_{\mathrm{LED}}(\lambda) = \sum_{i=1}^{n} \mathrm{SPD}_i(\lambda) \tag{4.8}$$

in which λ is the wavelength; $\mathrm{SPD}_{\mathrm{LED}}$ and SPD_i indicate the SPD of the entire LED and ith decomposed component, respectively; and n is the total number of the decomposed SPDs. Candidate models for describing the decomposed SPD include the Gaussian Function [64, 65, 67, 68], Asymmetric Gaussian Function [69], Asymmetric Double Sigmoidal (Asym2sig) Function [70], etc., as given in the following.

1. Gaussian Function

$$\mathrm{SPD} = a\exp\left(-\frac{(\lambda - \lambda_\mathrm{c})^2}{w^2}\right) \tag{4.9}$$

in which parameters a, λ_c, and w are the amplitude, peak wavelength, and full width at half maxima (FWHM), respectively.

2. Asymmetric Gaussian Function

$$\mathrm{SPD} = \begin{cases} a\exp\left(-\frac{(\lambda - \lambda_\mathrm{c})^2}{w_1^2}\right) & \lambda \le \lambda_\mathrm{c} \\ a\exp\left(-\frac{(\lambda - \lambda_\mathrm{c})^2}{w_2^2}\right) & \lambda > \lambda_\mathrm{c} \end{cases} \tag{4.10}$$

in which parameters a, λ_c, w_1, and w_2 are the amplitude, peak wavelength, and left and right FWHMs, respectively.

3. Asym2sig Function

$$\mathrm{SPD} = a\frac{1 - \frac{1}{1+\exp\{-(\lambda-\lambda_\mathrm{c}-w_1/2)/w_3\}}}{1 + \exp\{-(\lambda - \lambda_\mathrm{c} + w_1/2)/w_2\}} \tag{4.11}$$

in which parameters a, λ_c, w_1, w_2, and w_3 are the amplitude, peak wavelength, FWHM, and variance of the low-energy and high-energy sides, respectively. For decomposed SPDs of a LED, w_1 is always much lower than λ_c and therefore can be ignored. Then Eq. 4.11 is simplified into Eq. 4.12.

$$SPD = a\frac{1-\frac{1}{1+\exp\{-(\lambda-\lambda_c)/w_3\}}}{1+\exp\{-(\lambda-\lambda_c)/w_2\}} \tag{4.12}$$

By using the abovementioned models to describe a decomposed SPD, the SPD deformation is related into the change of the model parameters. For instance, Fig. 4.12 shows a comparison between the original and deformed SPDs drawn by Eq. 4.12. The deformed SPDs are created by increasing each of the parameters a, λ_c, w_3, and w_2, respectively. Among the four subplots in Fig. 4.12, it can be seen that:

1. The SPD stretches upward by an increase of 10% of a, as shown in Fig. 4.12a.
2. The SPD shifts to the right by an increase of 10% of λ_c, as shown in Fig. 4.12b.
3. The left half of the SPD shifts to the left by an increase of 50% of w_2, as shown in Fig. 4.12c.
4. The right half of the SPD shifts to the right by an increase of 50% of w_3, as shown in Fig. 4.12d.

The number of decomposed SPDs in Eq. 4.8 depends on the fitting accuracy. A superposition of numerous decomposed SPDs can give a high fitting accuracy but on the other hand tremendously increase the model complexity. From the standpoint of SPD modeling, it is not convenient to investigate the evolution of the SPDs of a LED under degradation by an overcomplicated model where each of the

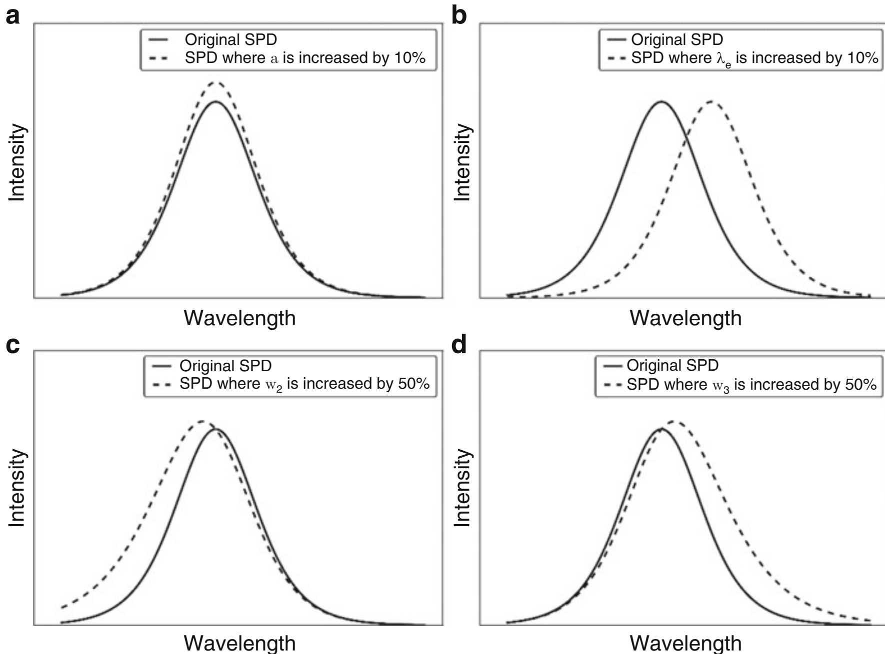

Fig. 4.12 Influences of Asym2sig parameters on the shape of a decomposed SPD

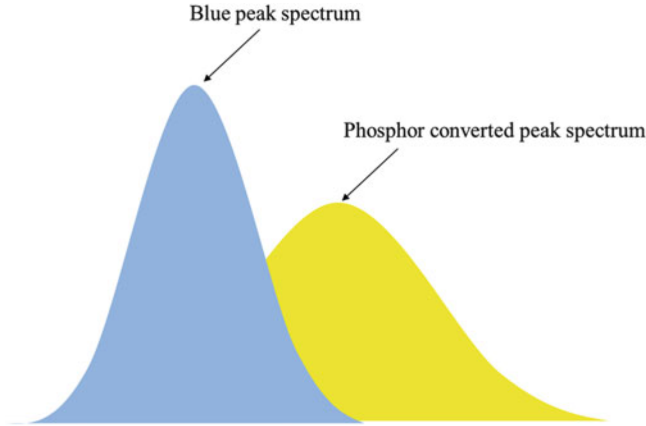

Fig. 4.13 Illustration of SPD of a typical pc-LED

parameters influences the SPD deformation in its own way. Thus, in order to reduce the model complexity, the following considerations are implemented:

1. Use the asymmetric model (such as Asymmetric Gaussian Function or Asym2sig Function [71]) in Eq. 4.8, since the decomposed peaks of a LED are usually asymmetric.
2. Reduce the number of decomposed SPDs as less as possible.

In our study, curve fitting of the SPD of a pc-LED is investigated since the pc-LED occupies a majority market share in white LED light sources. As illustrated in Fig. 4.13, the SPD of a typical pc-LED is formed by a superposition of a blue light and phosphor-converted light peaks. Therefore the simplest SPD model will be created by superposing two decomposed SPDs indicating the blue light and phosphor-converted light peaks, respectively. The models to describe the decomposed SPDs can be any one given in Eqs. 4.9, 4.10, 4.11, and 4.12, depending on their actual shapes. Equation 4.13 shows an expression of the SPD model where the decomposed SPDs are fitted by Eq. 4.12.

$$\mathrm{SPD_{LED}}(\lambda) = a_1 \frac{1 - \frac{1}{1+\exp\{-(\lambda-\lambda_{c1})/w_{31}\}}}{1 + \exp\{-(\lambda - \lambda_{c1})/w_{21}\}} + a_2 \frac{1 - \frac{1}{1+\exp\{-(\lambda-\lambda_{c2})/w_{32}\}}}{1 + \exp\{-(\lambda - \lambda_{c2})/w_{22}\}} \tag{4.13}$$

in which a_1, λ_{c1}, w_{31}, and w_{21} are the amplitude, peak wavelength, and variance of the low-energy and high-energy sides for the decomposed blue light peak and a_2, λ_{c2}, w_{32}, and w_{22} are for the decomposed phosphor-converted light peak. Next, a set of photometric and colorimetric parameters of the LED are calculated by Eqs. 4.14, 4.15, and 4.16.

(i) Luminous flux Φ

$$\Phi = 683 \int_{380}^{780} \text{SPD}_{\text{LED}}(\lambda) V(\lambda) \text{d}\lambda \tag{4.14}$$

in which Φ is the luminous flux and $V(\lambda)$ is the spectral luminous efficiency function for photopic vision that describes the visual sensitivity of the human eye in a bright environment and is shown in Fig. 4.14.

(ii) Chromaticity coordinates (x, y) in CIE1931 color space

$$\begin{aligned} & x = \frac{X}{X+Y+Z}, y = \frac{Y}{X+Y+Z} \\ & \text{where } X = \int_{380}^{780} \text{SPD}_{\text{LED}}(\lambda) \bar{x}(\lambda) \text{d}\lambda, \\ & Y = \int_{380}^{780} \text{SPD}_{\text{LED}}(\lambda) \bar{y}(\lambda) \times \text{d}\lambda \text{ and } Z = \int_{380}^{780} \text{SPD}_{\text{LED}}(\lambda) \bar{z}(\lambda) \text{d}\lambda \end{aligned} \tag{4.15}$$

in which X, Y, and Z are the tristimulus values corresponding to the red, green, and blue colors and^{-} $\bar{x}(\lambda), \bar{y}(\lambda)$, and $\bar{z}(\lambda)$ are the color matching functions shown in Fig. 4.15.

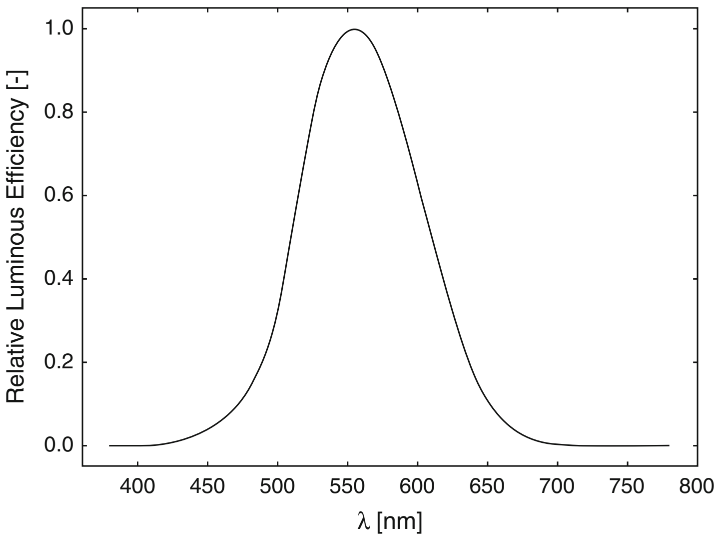

Fig. 4.14 Spectral luminous efficiency function for photopic vision [72]

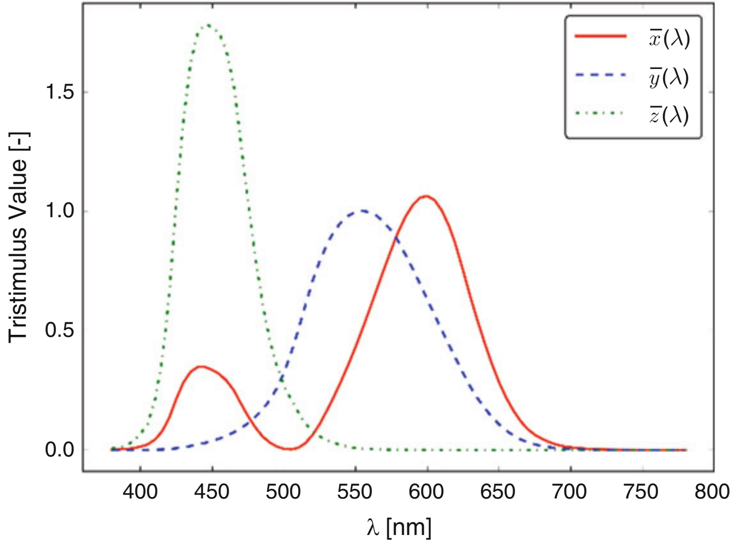

Fig. 4.15 Color matching functions [73]

(iii) Uniform chromaticity scales (u', v') in CIE 1976 color space

$$u' = \frac{4x}{-2x + 12y + 3}, v' = \frac{9y}{-2x + 12y + 3} \tag{4.16}$$

(iv) Color shift d$u'v'$

$$\mathrm{d}u'v' = \sqrt{\left(u' - u_0'\right)^2 + \left(v' - v_0'\right)^2}. \tag{4.17}$$

in which u_0' and v_0' are the initial values of u' and v', respectively.

To investigate the impacts of the SPD parameters on the calculated Φ, u' and v' values, a sensitivity study is performed by the following procedure:

1. Generate an artificial SPD with the parameters a_1, λ_{c1}, w_{31}, w_{21}, a_2, λ_{c2}, w_{32}, and w_{22} of 0.001, 450, 10, 10, 0.001, 600, 50, and 50, respectively. Based on such a SPD, the Φ, u' and v' values are calculated as 14.54, 0.2349, and 0.4741.
2. Increase a single SPD parameter to some extent, whereas the others remain the same to observe the changes on the calculated Φ, u', and v' values.

Figure 4.16 shows the results of the sensitivity study. For comparison purpose, all eight SPD parameters as well as the calculated Φ, u', and v' values are normalized by their initial values. From all subplots in Fig. 4.16, the parameters λ_{c1} and λ_{c2} are found the most sensitive to the calculated Φ, u', and v' values. This is because they determine the peak wavelengths of the blue light and phosphor-converted light

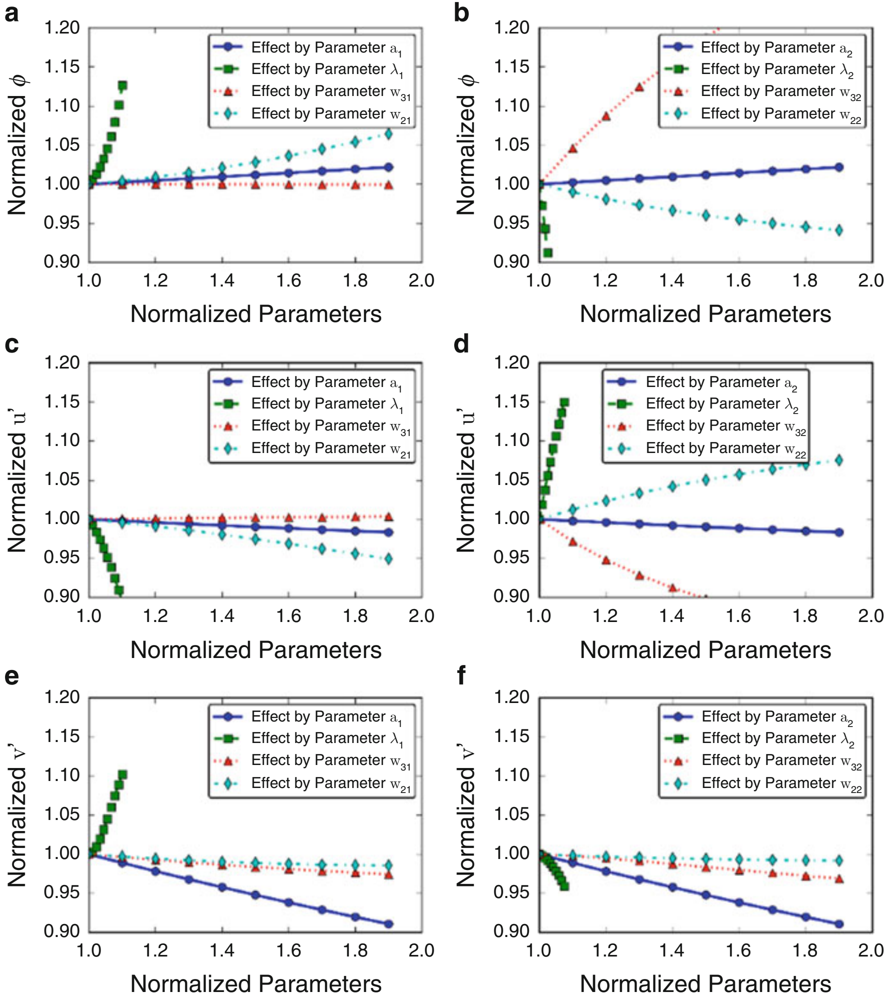

Fig. 4.16 Impacts of the SPD parameters on the calculated Φ, u', and v' values

peaks, respectively. As shown in Fig. 4.16b, a small change of the λ_c parameter yields a significant shift of the SPD, resulting in a great change on the photometric and colorimetric parameters as well. On the contrary, the parameters a_1 and w_{31} hardly affect the Φ and u' calculations, since the difference on the decomposed blue light SPDs caused by these two parameters, as shown in Fig. 4.16a, c, do not significantly contribute the calculation of the Φ and u' values. For the similar reason, the parameters w_{31}, w_{21}, w_{32}, and w_{22} also weakly affect the v' calculation, whereas the parameter a_1 weakly affects the u' calculation. To conclude, the impacts of the SPD parameters on the Φ, u', and v' calculations are summarized

Table 4.6 Summary of the sensitivity study results of the SPD parameters

	Φ	u'	v'
a_1	L	L	S
λ_{c1}	H	H	H
w_{31}	L	L	L
w_{21}	S	S	L
a_2	S	L	S
λ_{c2}	H	H	H
w_{32}	S	S	L
w_{22}	S	S	L

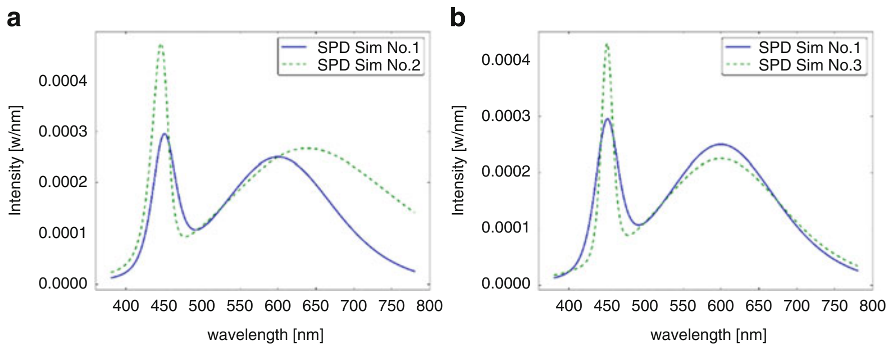

Fig. 4.17 Illustration of two special pairs of SPDs (**a**) resulting in same Φ but different u' and v'; (**b**) resulting in same u' and v' but different Φ

in Table 4.6, in which "H," "S," and "L" indicate "highly sensitive," "sensitive," and "less sensitive," respectively.

According to the abovementioned discussions, it is possible to theoretically find a pair of SPDs giving the same Φ but different u' and v', and vice versa. Examples of these two circumstances are illustrated by the SPDs Sim No.1 and No.2 in Fig. 4.17a and Sim No.1 and No.3 in Fig. 4.17b, respectively. Exact values of the SPD parameters and the calculated Φ, u', and v' values of the SPDs Sim No.1 to No.3 are given in Table 4.7.

4.4.2 Degradation Prediction

For verifying the proposed method, the entire SPD of a 3000 K pc-LED under a driving current of 180 mA was fitted by using Eq. 4.13. The goodness-of-fit was examined by the coefficient of determination r^2 calculated by Eq. 4.18

Table 4.7 SPD parameters and the calculated Φ, u', and v' values of the SPDs shown in Fig. 4.17

ID	a_1	λ_{c1} [nm]	w_{31}	w_{21}	a_2	λ_{c2} [nm]	w_{32}	w_{22}	Φ [lm]	u'	v'
Sim No.1	0.001	450	10	10	0.001	600	50	50	14.54	0.2349	0.4741
Sim No.2	0.0015	450	10	5	0.001	600	60	103	14.54	0.2441	0.4544
Sim No.3	0.0015	450	5	5	0.0009	600	56.5	56.5	13.56	0.2349	0.4741

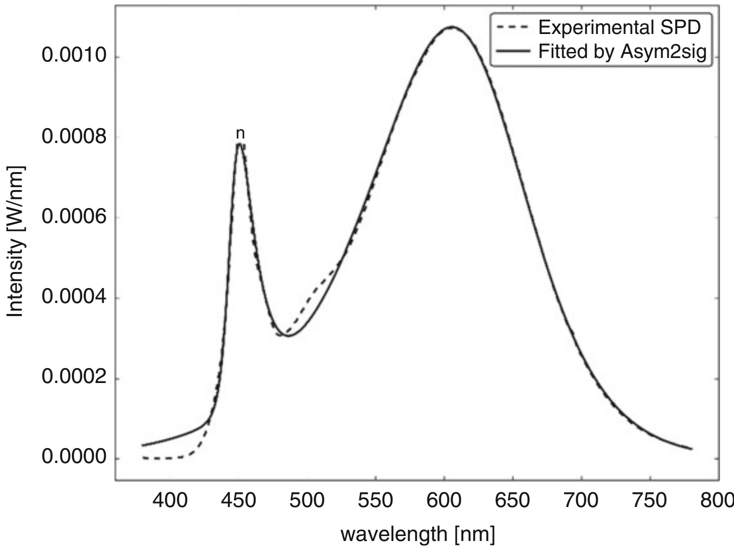

Fig. 4.18 Experimental and fitted SPDs of a 3000 K pc-LED test at initial time

$$r^2 = 1 - \frac{\sum_{i=1}^{n} \left(y_i - y_{i,\text{pred}}\right)^2}{\sum_{i=1}^{n} \left(y_i - y_{\text{avg}}\right)^2} \tag{4.18}$$

in which y_i and $y_{i,\text{pred}}$ are the ith value of the SPD and its fitting estimation and y_{avg} is the average of all values on the SPD. As shown in Fig. 4.18, a good agreement between the experimental and fitted SPDs is obtained through a high r^2, except for the left tail less than 430 nm caused by a broad width of the decomposed phosphor-converted peak. This fitting error has no effect on the prediction of Φ since the $V(\lambda)$ function less than 430 nm is nearly zero. However, it might give an overestimated X and Z tristimulus values to cause a high prediction on u' but a lower prediction on v'.

From both experimental and fitted SPDs, measurements and predictions of the Φ, u', and v' values of the pc-LED were calculated and compared in Table 4.8. It can

Table 4.8 Measurements and predictions of the initial photometric and colorimetric parameters

	Measurement	Prediction
Φ_v [lm]	55.05	55.02
u'	0.2498	0.2506
v'	0.5082	0.5078

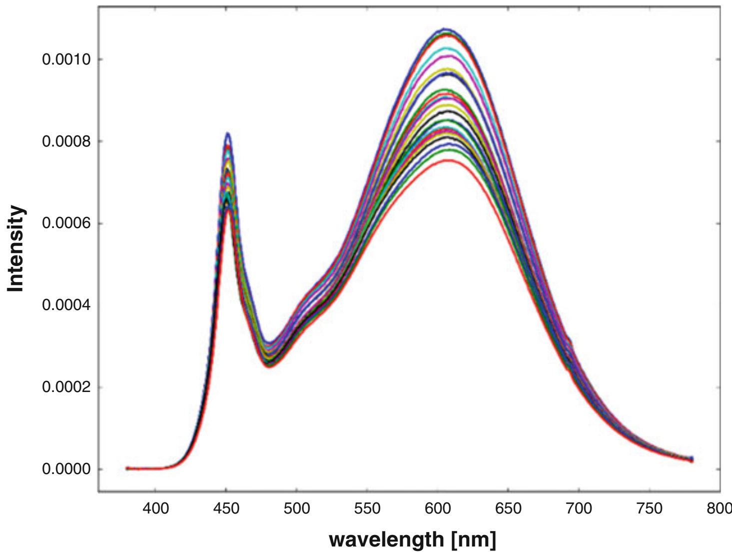

Fig. 4.19 Evolutionary SPDs of the test sample under degradation

be seen that a good agreement can be achieved in between the measured and predicted values. That means the influence of the fitting error at the left tail can be neglected in this case.

Then the test for the 3000 K pc-LED continued at a solder temperature of 105 °C for 4600 h, in which the SPD was measured after about every 200 h. As shown in Fig. 4.19, the SPD of the pc-white LED gradually degrades with the increase of the operational time from 0 to 4600 h. When using Eq. 4.13 to fit all of the degraded SPDs, the increase or decrease models of the eight parameters were supposed as an exponential form expressed by Eq. 4.19.

$$y = C_1 \exp(C_0 t) \tag{4.19}$$

in which y is one of the SPD parameters, t is the aging time, and C_0 and C_1 are the fitting parameters estimated by the Maximum Likelihood Estimation (MLE) method. Figure 4.20 shows the extracted values of all of the SPD parameters from the degraded SPDs and the corresponding exponential fitting curves.

After the pairs of the C_0 and C_1 values for each of the SPD parameters were determined, the evolutionary process of the SPDs of the pc-LED was predicted. Figure 4.21 displays the predicted SPDs at a few operational time points compared

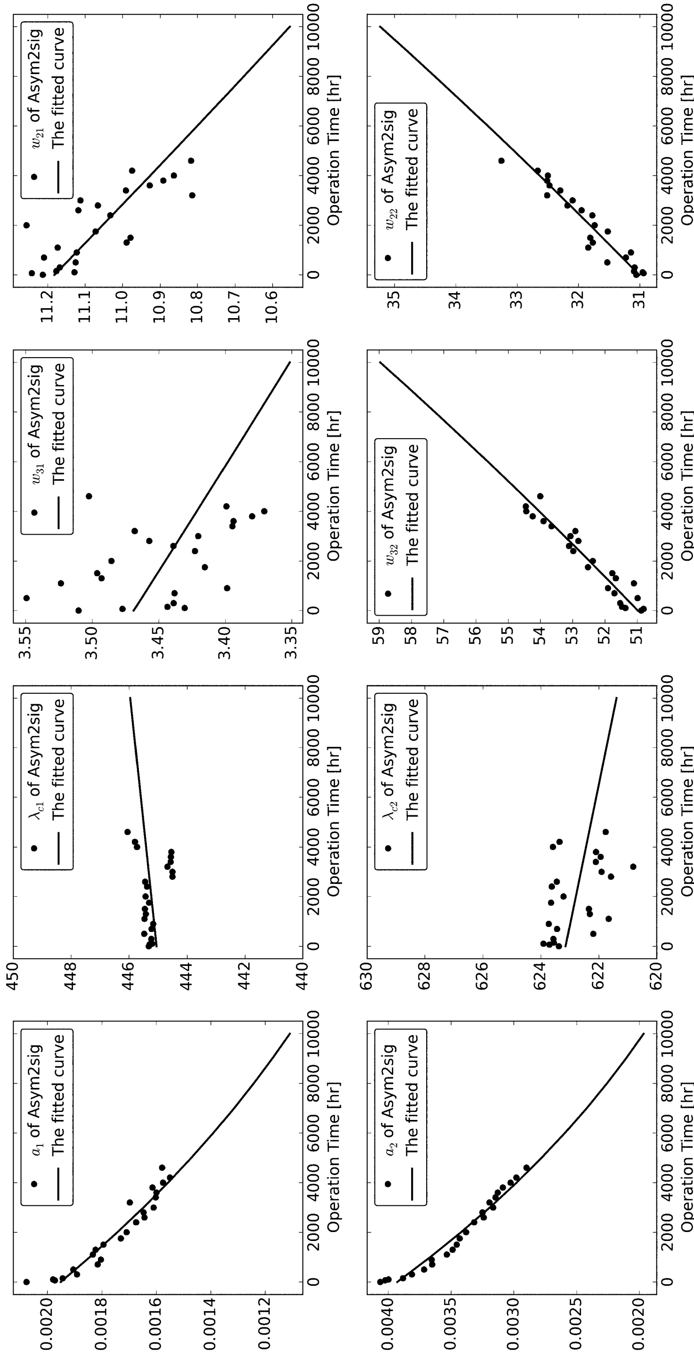

Fig. 4.20 Evolution of the eight SPD parameters extracted from the SPDs of the pc-LED under degradation and their fitting curves

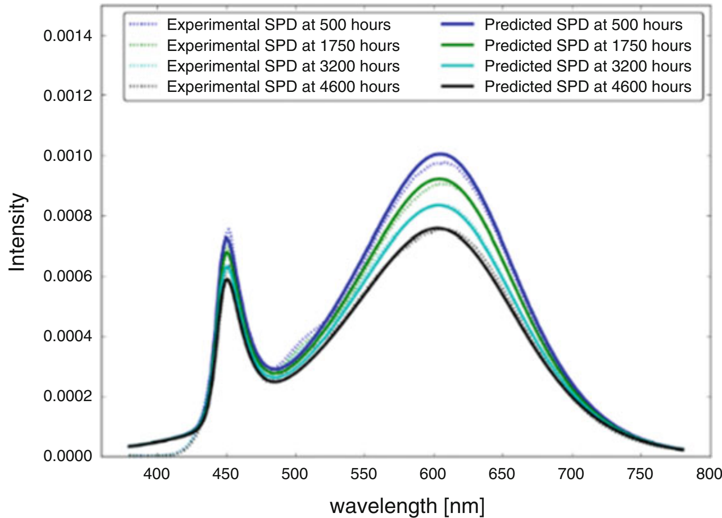

Fig. 4.21 Experimental and predicted SPDs of the pc-LED aged until 500 h, 1750 h, 3200 h, and 4600 h

with the experimental curves. A reasonable agreement can be observed in between the experimental and predicted SPDs, except for a bias at the left tail (less than roughly 430 nm).

Based on the predicted evolutionary process of the SPDs, the degradation curves of Φ, u', and v' of the pc-LED were predicted by using Eqs. 4.14, 4.15, and 4.16. Comparisons in between these predicted curves and the experimental measurements are shown in Fig. 4.22a–c, respectively. The predicted Φ and v' curves match the experimental measurements very well. Nevertheless, the predicted u' curve stays a little higher than the experimental measurements. This is mainly because of the matching error at the left tail of the SPDs as mentioned in Sect. 4.2. In addition, based on the predicted degradation curves of u' and v', the degradation curve of d$u'v'$ was further predicted and shown in Fig. 4.22d in comparison with the experimental measurements. Finally, according to the predicted degradation curves of Φ and d$u'v'$, the L_{70} lifetime (where the lumen maintenance decays to 0.7) is estimated as 5402 h, whereas the color maintenance lifetime (where d$u'v'$ grows to 0.007) as 5214 h.

4.5 Conclusions

The frequently used test standards and specifications for LED packages and systems are firstly reviewed in this chapter. In general, the luminous depreciation test requires a minimum of 6000 h testing period, which is comparable or even longer than the period for developing a new generation of LED lighting products. This

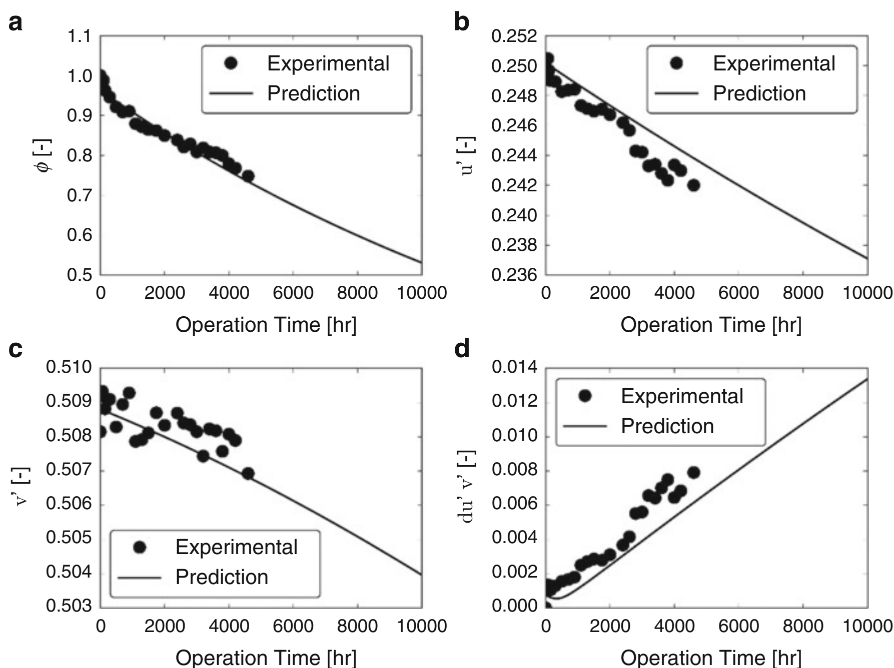

Fig. 4.22 Experimental measurements and predicted curves of Φ, u', v', and d$u'v'$ of the pc-LED

necessitates an urgent study on the development of ADTs for LED packages and systems. At the package level, a number of statistics-based approaches are discussed for lifetime estimation of LEDs with the consideration of random variation in the experimental results of ADTs. At the product level, a temperature-driven accelerated test method is developed to reduce the testing time within 2000 h. And this method serves as a quick and fast pass/fail luminous depreciation qualification test for LED lamps and luminaires with an expected lifetime of 25,000 h.

The color shift is another ordinary failure modes which has gained an increasing attention in LED lighting products. Unfortunately, the qualification standards and specifications for LED's color shift are very ambiguous, and none is related to the estimation of the color maintenance lifetime of LEDs. This is because a reliable and robust model for describing the growing trend of color shift is still missing. In this chapter, a SPD analysis-based method is proposed to simultaneously predict the drift curves of lumen maintenance Φ, color coordinates u' and v' (in CIE1976 color space), and color shift d$u'v'$. Then based on the predicted drift curves of Φ and d$u'v'$, lifetimes of the pc-LED due to lumen depreciation and color shift can be estimated, respectively. By directly predicting the evolutionary process of SPDs of a LED under degradation, this method provides a new insight into the estimation of both lumen and color maintenance lifetimes. Thus it has a great potential being used in the development of qualification standards for the color shift of LEDs in future.

Acknowledgment The authors would also like to acknowledge the support of the National High-Tech Research and Development Program of China (863 Program, Grant No. 2015AA03A101) and China Postdoctoral Science Foundation (Grant No. 2015M570133).

References

1. W.D. van Driel, X.J. Fan, *Solid State Lighting Reliability: Components to Systems* (Springer, New York, 2012)
2. S. Liu, X. Luo, *LED Packaging for Lighting Applications* (Wiley, Singapore, 2011)
3. McKinsey & Company, *Lighting the Way: Perspectives on the Global Lighting Market*, 2nd edn. (McKinsey & Company, 2012)
4. IESNA TM-16-05, *IESNA Technical Memorandum on Light Emitting Diode (LED) Sources and Systems* (Illuminating Engineering Society, New York, 2005)
5. ASSIST Recommendation, *LED Life for General Lighting* (Lighting Research Center, Troy, 2005)
6. IESNA LM-80-08, *IES Approved Method for Measuring Lumen Maintenance of LED Light Sources* (Illuminating Engineering Society, New York, 2008)
7. IESNA TM-21-11, *Projecting Long Term Lumen Maintenance of LED Light Sources* (Illuminating Engineering Society, New York, 2011)
8. IESNA LM-80-15, *IES Approved Method for Measuring Luminous Flux and Color Maintenance of LED Packages, Arrays and Modules* (Illuminating Engineering Society, New York, 2015)
9. IESNA LM-84-14, *Approved Method for Measuring Luminous Flux and Color Maintenance of LED Lamps, Light Engines, and Luminaires* (Illuminating Engineering Society, New York, 2014)
10. IESNA TM-28-14, *Projecting Long-Term Luminous Flux Maintenance of LED Lamps and Luminaires* (Illuminating Engineering Society, New York, 2014)
11. ENERGY STAR®, *Program Requirements for Requirements for Integral LED Lamps Eligibility Criteria – Version 1.4* (Energy Star, Washington, 2011)
12. ENERGY STAR®, *Program Requirements for Solid State Lighting Luminaires Eligibility Criteria – Version 1.3* (Energy Star, Washington, 2010)
13. ENERGY STAR, *Program Requirements – Product Specification for Luminaires (Light Fixtures) Eligibility Criteria – Version 1.1* (Energy Star, Washington, 2011)
14. ENERGY STAR, *Program Requirements – Product Specification for Lamps (Light Bulbs) Eligibility Criteria – Version 1.1* (Energy Star, Washington, 2014)
15. IEC/PAS 62612, *Self-Ballasted LED-Lamps for General Lighting Services – Performance Requirements, Edition 1.0* (International Electrotechnical Commission, Geneva, 2009)
16. IEC/PAS 62717, *LED Modules for General Lighting – Performance Requirements, Edition 1.0* (International Electrotechnical Commission, Geneva, 2011)
17. IEC/PAS 62722-2-1, *Luminaire performance – Part 2–1: Particular Requirements for LED Luminaires, Edition 1.0* (International Electrotechnical Commission, Geneva, 2014)
18. H.A. Qiao, T.C. Pulsipher, J.E. Hathaway, E.E. Richman, E. Radkov, A statistical method to analyze LED lumen depreciation and project useful LED product life, in *Proceedings of the IES 2010 Annual Conference, November 9, 2010, Toronto, Ontario*. J. Huang, D.S. Golubović, S. Koh, D. Yang, X. Li, X. Fan, G.Q. Zhang, Rapid degradation of mid-power white-light LEDs in saturated moisture conditions, IEEE Trans. Device Mater. Reliab. **15**:478–485 (2015)
19. J. Huang, D.S. Golubović, S. Koh, D. Yang, X. Li, X. Fan, G.Q. Zhang, Degradation mechanisms of mid-power white-light LEDs under high-temperature–humidity conditions. IEEE Trans. Device Mater. Reliab. **15**, 220–228 (2015)

20. G.J. Lu, M.Y. Mehr, W.D. van Driel, X.J. Fan, J.J. Fan, K.M.B. Jansen, G.Q. Zhang, Color shift investigations for LED secondary optical designs: comparison between BPA-PC and PMMA. Opt. Mater. **45**, 37–41 (2015)
21. G.J. Lu, W.D. van Driel, X.J. Fan, M.Y. Mehr, J.J. Fan, K.M.B. Jansen, G.Q. Zhang, Degradation of microcellular PET reflective materials used in LED-based products. Opt. Mater. Opt. Mater. **49**, 79–84 (2015)
22. J.J. Fan, K.C. Yung, M. Pecht, Prognostics of chromaticity state for phosphor-converted white light emitting diodes using an unscented kalman filter approach, IEEE Trans. Device Mater. Reliab. **14**:564–573, (2014). J.J. Fan, K.C. Yung, M. Pecht, Prognostics of lumen maintenance for high power white light emitting diodes using a nonlinear filter-based approach, Reliab. Eng. Syst. Saf. **123**:63–72 (2014)
23. J. Fan, K.C. Yung, M. Pecht, Physics-of-failure-based prognostics and health management for high-power white light-emitting diode lighting. IEEE Trans. Device Mater. Reliab. **11**, 407–416 (2011)
24. S.T. Tseng, C.Y. Peng, Stochastic diffusion modeling of degradation data. J. Data Sci. **5**, 315–333 (2007)
25. W.Q. Meeker, L.A. Escobar, C.J. Lu, Accelerated degradation test: modeling and analysis. Technometrics **40**, 89–99 (1999)
26. S.J. Bae, P.H. Kvam, A nonlinear random-coefficients model for degradation testing. Technometrics **46**, 460–469 (2004)
27. K.A. Doksum, A. Hóyland, Model for variable-stress accelerated life testing experiments based on Wiener processes and the inverse Gaussian distribution. Technometrics **34**, 74–82 (1992)
28. H.F. Yu, S.T. Tseng, Designing a screening experiment for highly reliable products. Nav. Res. Logist. **49**, 514–526 (2002)
29. S.T. Tseng, J. Tang, I.H. Ku, Determination of burn-in parameters and residuals life of highly reliable products. Nav. Res. Logist. **50**, 1–14 (2003)
30. J. Lawless, M. Crowder, Covariates and random effects in a gamma process model with application to degradation and failure. Lifetime Data Anal. **10**, 213–227 (2004)
31. X. Wang, N. Balakrishnan, B. Guo, Residual life estimation based on a generalized Wiener degradation process. Reliab. Eng. Syst. Saf. **124**, 13–23 (2014)
32. J. Huang, D.S. Golubović, S. Koh, D. Yang, X. Li, X. Fan, G.Q. Zhang, Degradation modeling of mid-power white-light LEDs by using Wiener process. Opt. Express **23**, A966–A978 (2015)
33. J. Huang, D.S. Golubović, S. Koh, D. Yang, X. Li, X. Fan, G.Q. Zhang, Lumen degradation modeling of white-light LEDs in step stress accelerated degradation test. Reliab. Eng. Syst. Saf. **147**, 152–159 (2016)
34. F.K. Wang, Y.C. Lu, Useful lifetime analysis for high-power white LEDs. Microelectron. Reliab. **54**, 1307–1315 (2014)
35. J.J. Fan, K.C. Yung, M. Pecht, Lifetime estimation of high-power white LED using degradation-data-driven method. IEEE Trans. Device Mater. Reliab. **12**, 470–477 (2012)
36. S.T. Tseng, H.F. Yu, A termination rule for degradation experiments. IEEE Trans. Reliab. **46**, 130–133 (1997)
37. H.F. Yu, S.T. Tseng, On-line procedure for terminating an accelerated degradation test. Stat. Sin. **8**, 207–220 (1998)
38. W.D. van Driel, M. Schuld, B. Jacobs F. Commissaris, Lumen maintenance predictions for LED packages using LM80 data, in *Proceedings of International Conference on Thermal, Mechanical and Multi-physics Simulation and Experiments in Microelectronics and Microsystems* (IEEE, 2015)
39. K.I. Hwu, W.C. Tu, Controllable and dimmable AC LED driver based on FPGA to achieve high PF and low THD. IEEE Trans. Ind. Inform. **9**, 1330–1342 (2013)
40. X. Tao, S.Y. Ron Hui, Dynamic photoelectrothermal theory for light-emitting diode systems. IEEE Trans. Ind. Electron. **59**, 1751–1759 (2012)

41. D. Han, Time and cost constrained optimal designs of constant-stress and step-stress accelerated life tests. Reliab. Eng. Syst. Saf. **140**, 1–14 (2015)
42. H. Oh, S. Choi, K. Kim, B.D. Youn, M. Pecht, An empirical model to describe performance degradation for warranty abuse detection in portable electronics. Reliab. Eng. Syst. Saf. **142**, 92–99 (2015)
43. T.C. Ming, P. Singh, Time evolution degradation physics in high power white LEDs under high temperature-humidity conditions. IEEE Trans. Device Mater. Reliab. **14**, 742–750 (2014)
44. X. Luo, B. Wu, S. Liu, Effects of moist environments on LED module reliability. IEEE Trans. Device Mater. Reliab. **10**, 182–186 (2010)
45. S. Chan, W. Hong, K. Kim, Y. Yoon, J. Han, J.S. Jang, Accelerated life test of high power white light emitting diodes based on package failure mechanisms. Microelectron. Reliab. **51**, 1806–1809 (2011)
46. M. Meneghini, L.R. Trevisanello, G. Meneghesso, E. Zanoni, A review on the reliability of GaN-based LEDs. IEEE Trans. Device Mater. Reliab. **8**, 323–331 (2008)
47. VDE-AR-E 2715-1, *Measurement and Prediction of Reduction in Luminous Flux of LEDs* (German Standard, Frankfurt, 2012)
48. J.L. Davis, M. Lamvik S. Shepherd, Insights into accelerated aging of SSL luminaires, Proc. SPIE Int. Soc. Opt. Eng. **8835**(1):88350L (2013)
49. W. Nelson, *Accelerated Testing: Statistical Methods, Test Plans, and Data Analysis* (Wiley, New York, 1990)
50. M.Y. Mehr, W.D. van Driel, K.M.B. Jansen, P. Deeben, G.Q. Zhang, Lifetime assessment of Bisphenol-A Polycarbonate (BPA-PC) plastic lens, used in LED-based products. Microelectron. Reliab. **54**, 138–142 (2014)
51. S. Koh, C. Yuan, B. Sun, B. Li, X.J. Fan, G.Q. Zhang, Product level accelerated lifetime test for indoor LED luminaires, in *Proceedings of Eurosime 2013, Wroclaw, Poland*, (2013)
52. Philips LM-80 Report – LUXEON Rebel (n.d.), http://www.lighting.philips.com/pwc_li/us_en/connect/tools_literature/downloads/LM-80.pdf
53. Nichia LM-80 Report (n.d.), http://www.arraylighting.com/DL/BR30LM-80.PDF
54. LM-80 Test Report, (Integrated Service Technology, 2012)
55. LM-80 Test Report, (Edison Opto Corporation, 2013)
56. LM-80 Test Report, (OSRAM Opto Semiconductors, 2010)
57. LM-80 Test Report, (Bay Area Compliance Laboratories Corp. (Dongguan), 2014)
58. CALiPER Report, *Retail Lamps Study 3.2: Lumen and Chromaticity Maintenance of LED A Lamps Operated in Steady-State Conditions* (US DOE, Washington, 2014)
59. H. Chen, S.Y. Hui, Dynamic prediction of correlated color temperature and color rendering index of phosphor-coated white light-emitting diodes. IEEE Trans. Ind. Electron. **61**, 784–797 (2014)
60. X. Feng, W. Xu, Q. Han, S. Zhang, LED light with enhanced color saturation and improved white light perception. Opt. Express **24**, 573–585 (2016)
61. P. Zhong, G. He, M. Zhang, Spectral optimization of the color temperature tunable white light-emitting diode (LED) cluster consisting of direct-emission blue and red LEDs and a diphosphor conversion LED. Opt. Express **20**, A684–A693 (2012)
62. K.H. Loo, Y.M. Lai, S.C. Tan, C.K. Tse, Stationary and adaptive color-shift reduction methods based on the bilevel driving technique for phosphor-converted white LEDs. IEEE Trans. Power Electron. **26**, 1943–1953 (2011)
63. R. Lu, Q. Hong, Z. Ge, S. Wu, Color shift reduction of a multi-domain IPSLCD using RGB-LED backlight. Opt. Express **16**, 6243–6252 (2006)
64. Y. Lin, Z. Deng, Z. Guo, Z. Liu, H. Lan, Y. Lu, Y. Cao, Study on the correlations between color rendering indices and the spectral power distribution. Opt. Express **22**, A1029–A1039 (2014)
65. B.M. Song, B. Han, Spectral power distribution deconvolution scheme for phosphor-converted white light-emitting diode using multiple Gaussian functions. Appl. Opt. **52**, 1016–1024 (2013)

66. M. Chang, C. Chen, D. Das, M. Pecht, Anomaly detection of light-emitting diodes using the similarity-based metric test. IEEE Trans. Ind. Inform. **10**, 1852–1863 (2014)
67. B.M. Song, B. Han, Analytical/experimental hybrid approach based on spectral power distribution for quantitative degradation analysis of phosphor converted LED. IEEE Trans. Device Mater. Reliab. **14**, 365–374 (2014)
68. K. Man I. Ashdown, Accurate colorimetric feedback for RGB LED clusters, Proc. SPIE Int. Soc. Opt. Eng., **6337**:633702-633702-8 (2006)
69. G. He, H. Yan, Optimal spectra of the phosphor-coated white LEDs with excellent color rendering property and high luminous efficacy of radiation. Opt. Express **19**, 2519–2529 (2011)
70. L. Marsich, L. Moimas, V. Sergo, C. Schmid, Raman spectroscopic study of bioactive silica-based glasses: the role of the alkali/alkali earth ratio on the Non-Bridging Oxygen/Bridging Oxygen (NBO/BO) ratio. Spectroscopy **23**, 227–232 (2009)
71. C. Qian, J.J. Fan, X.J. Fan, A.E. Chernyakov G.Q. Zhang, Lumen and chromaticity maintenance lifetime prediction for LED lamps using a spectral power distribution method, in *Proceedings of 12th China International Forum on Solid State Lighting* (SSLCHINA 2016)
72. 2° *Spectral Luminous Efficiency Function for Photopic Vision* (CIE, 1990)
73. CIE Colorimetry, 3rd edn (CIE, 2014)

Chapter 5
Reliability and Lifetime Assessment of Optical Materials in LED-Based Products

M. Yazdan Mehr, Willem Dirk van Driel, and Guo Qi Zhang

Abstract Lumen depreciation is one of the major failure modes in light-emitting diode (LED) systems. It originates from the degradation of the different components within the system, including the chip, the driver, and the optical materials (i.e., phosphorous layer). The kinetics of degradation in real-life applications is relatively slow, and in most cases, it takes several years to see an obvious deterioration of optical properties. A highly accelerated stress testing (HAST) setup and a methodology to extrapolate the results to real applications are therefore needed to test the reliability of LED package and lens materials. Employing HAST concept in LED industry is inevitable due to the necessity of assessing the reliability of new products in a short period of time. This chapter aims at briefly explaining the degradation mechanism of optical components in LED package and how they contribute to the lumen depreciation of the LED package. The concept of HAST and the way the reliability of LED packages can be assessed will also be explained.

M. Yazdan Mehr (✉)
EEMCS Faculty, Delft University of Technology, Delft, The Netherlands
e-mail: m.yazdanmehr@tudelft.nl

W.D. van Driel (✉)
Philips Lighting, High Tech Campus, Eindhoven, The Netherlands

Delft University of Technology, EEMCS Faculty, Delft, The Netherlands
e-mail: willem.van.driel@philips.com

G.Q. Zhang
State Key Laboratory of Solid State Lighting, Institute of Semiconductors, Chinese Academy of Sciences, Beijing, China

State Key Laboratory of Solid State Lighting (Changzhou Base), Changzhou, China

EEMCS Faculty, Delft University of Technology, Delft, The Netherlands
e-mail: g.q.zhang@tudelft.nl

© Springer International Publishing AG 2018

W.D. van Driel et al. (eds.), *Solid State Lighting Reliability Part 2*, Solid State Lighting Technology and Application Series 3, DOI 10.1007/978-3-319-58175-0_5

5.1 LED and the LED Landscape

Solid-state lighting (SSL) technology is known as a revolutionary invention in the history of lighting industry. Light-emitting diodes (LEDs) are used as source of illumination in solid-state lighting systems. The first practical LED, made from GaAsP semiconductor, was invented in 1962 [1]. The blue LED (GaN semiconductor) was then invented in 1993 [2]. The first commercial white LED was introduced to the market in 1997, using blue LED [3]. Since then the LEDs have become a credible alternative and competitor to incandescent and fluorescent lamps. Recently due to technological improvements of the LED designs, the high-brightness LEDs (HB LEDs) with higher output lumen flux are introduced to the market. The multiple benefits of LEDs, including compactness, output, and color adjustment, and the continuous increase in their performance have made them competitive to fluorescent lamps and tubes. One of the advantages of LEDs over conventional lighting systems is its relatively longer lifetime. A common incandescent lamp has an average lifetime of around 1,000 h, whereas the fluorescent lighting technology has an average lifetime of about ten times longer than incandescent light, which is around 10,000 h. The present LED lighting devices have an average lifetime of around 25,000 h with the potential of reaching up to 50,000 h lifetime. In addition LEDs are increasingly becoming an eco-friendly technology. Longer lifetime means less materials waste and less release of toxic materials. Another important environmental benefit of LEDs is their comparatively lower energy consumption. The electrical energy consumption for lighting in big cities is about 25% of the total consumed electrical energy. It is estimated that in 2013, the lighting industry was responsible for 17% of energy consumption in the USA. Figure 5.1 illustrates the prediction of the lighting energy consumption in the USA till 2030. One can see that the expected saving due to the replacement of LEDs will be 15% in 2020 and 40% in 2030 [4].

Due to the comparatively lower energy consumption of LEDs and their longer lifetimes, compared to traditional light sources, the total lifetime cost of LEDs will be much lower than the traditional lighting technologies. LEDs have also higher efficiency, compared to other light sources [5, 6]. This makes lighting systems, based on LEDs, a great new solution for lighting applications. The internal quantum efficiencies of green and blue LEDs are around 20–40% and 40–60%, respectively [7]. The maximum theoretical efficiency of combining blue LED and yellow phosphor is around 50% [8, 9]. However, the commercial white LEDs, used in different applications, have normally lower power conversion efficiency [2].

In order to define the quality of LED lighting, three qualitative measurements are usually applied. The first one is efficiency of light, known as efficacy, which is usually defined by lumens/watt (lm/W). Light sources with higher efficacy have obviously higher energy efficiency. The second measurement of the lighting quality is the color rendering index (CRI). CRI is a quantitative measure of the ability of a light source to reproduce the colors of various objects faithfully in comparison with an ideal or a natural light source. The last qualitative measurement is the lifetime

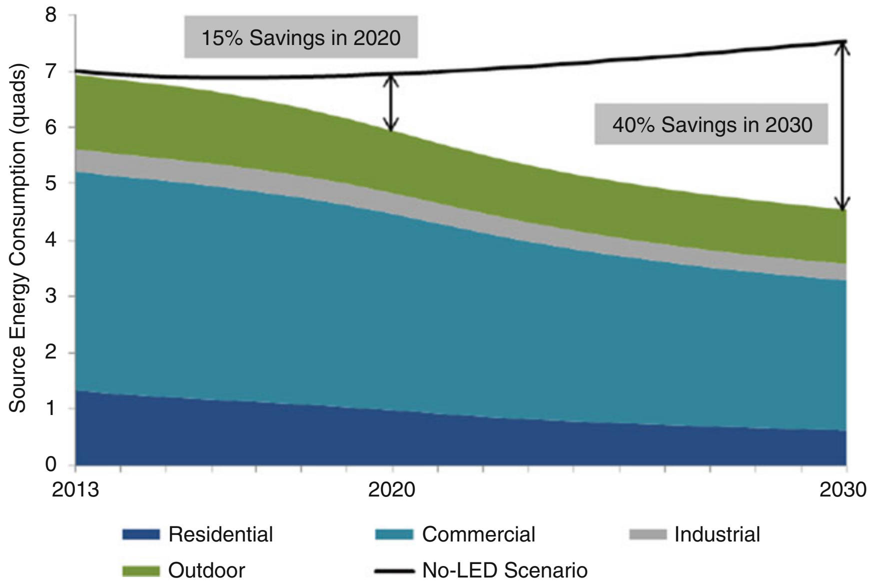

Fig. 5.1 Total US lighting consumption prediction (2013–2030) [4]

Table 5.1 Efficacy, CRI, and lifetime of common light sources [10]

Light source	Efficacy (lm/W)	CRI	Lifetime (hours)
Incandescent (120 V)	14.4	100	1,000
Compact fluorescent	51	80	10,000
High-pressure mercury	34	50	24,000
High-pressure sodium	108	22	24,000
LED	130–220	>80	50,000

which is a reliability parameter of the light source. It represents the working time of such light source within the lighting specification. Table 5.1 presents examples of the optical characteristics for common light sources. One can see that the overall properties of LED technology are better than those of other light sources.

Because of all benefits explained above, there can be a wide variety of applications for which LEDs are potentially perfect choices. This rapid progress in adopting LED lighting is well seen in the England's Palace in center room chandelier, where all 25 W tungsten lamps were removed and a low voltage system controlling 2.8 W LED lamps were installed initiating an energy saving in excess of 80% [5]. There are many more examples obviously. LED lighting is not only adopted for general indoor lighting applications. In fact, the largest applications of colored and white LEDs are for automobile interior and exterior lighting, backlighting for mobile devices and small- and middle-sized liquid crystal displays (LCD), single and traffic lighting, and LED display. These applications now

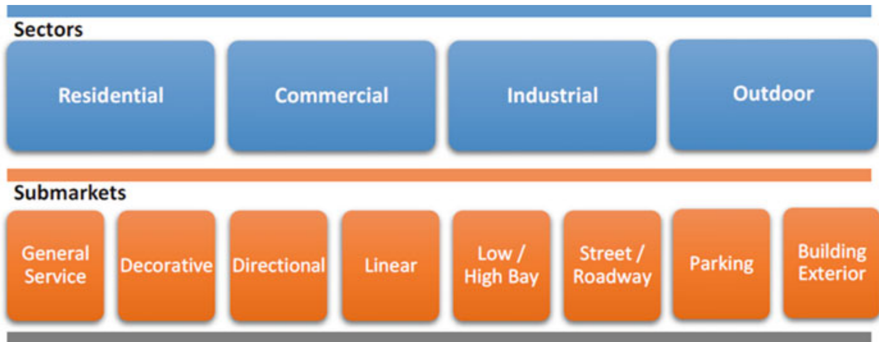

Fig. 5.2 Market domains for LED lighting [4]

Fig. 5.3 Three examples for different applications of LED-based products

account for about 90% of the LED needs. Figures 5.2 and 5.3 show some market domains and examples of the application for SSL devices for indoor lighting, outdoor/street lighting, and automotive lighting.

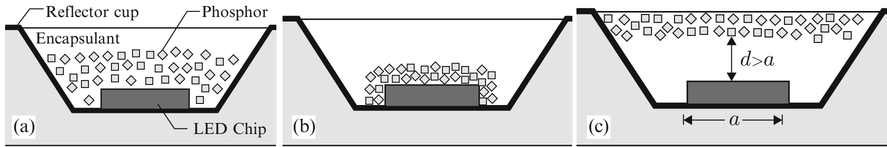

Fig. 5.4 (**a**) Proximate phosphor distributions, (**b**) conformal proximate phosphor distributions, and (**c**) remote phosphor distribution [9]

5.2 White Light LEDs

Currently there are several technologies, used to produce white light in high-power LED systems [11–13]. These methods are mainly based on combining different LED chips with different colors to generate high color rendering index (CRI) and tunable colors. These methods can be listed as follows:

- A blue chip and two color phosphors such as green and red phosphors
- An ultraviolet (UV) chip and three-color phosphors in which the UV light excites the three-color phosphors (red, green, and blue) to generate white light with a high CRI
- A blue chip and yellow phosphor in which the yellow phosphor is excited by a blue radiation, producing white light by mixing of nonabsorbed blue light

LEDs, made by combining the blue-emitting diode chips with phosphor, are the most commercially available white LEDs due to their high efficiency. In this system, the phosphor layer can be either deposited directly on the chip or incorporated into a lens disc [14–17]. The spatial phosphor distribution in white LED lamps strongly influences the color uniformity and efficiency of the lamp. One can distinguish between proximate and remote phosphor distributions [14–17]. In proximate phosphor distributions, the phosphor is located in close proximity to the semiconductor chip. In remote phosphor distributions, however, the phosphor is spatially removed from the semiconductor chip. Proximate phosphor distributions and remote phosphor distribution are schematically shown in Fig. 5.4a–c, respectively. A general weakness of proximate phosphor distributions is the absorption of light by the semiconductor chip. Phosphorescence emitted toward the semiconductor chip can be absorbed by the chip. The reflectivity of the semiconductor chip and metal contacts is generally not very high. This negative point of proximate phosphor distributions can be avoided by remote phosphor distributions in which the phosphor is spatially placed apart from the semiconductor chip. In such remote phosphor structure, it is less likely that phosphorescence is absorbed by the semiconductor chip due to the separation between the semiconductor chip and the phosphor.

5.3 Failure Mechanisms in LEDs

The failure of LEDs can be attributed to three regions in the system; semiconductors, interconnections, and the package [18–21]. The die-related failures include severe light output degradation, burned/broken metallization on the die, lattice

defects, die cracking, dopant diffusion, and electromigration. The interconnect failures of LED packages are electrical overstress-induced bond wire fracture, metallurgical interdiffusion, and electrostatic discharge, which leads to catastrophic failures of LEDs. Package-related failures are mostly due to the degradation of polymeric materials and result in an optical degradation, color change, and severe discoloration of the encapsulant/lens materials.

5.4 Aging of Optical Materials and Origins of Color Shift

There are many technical challenges for LEDs to be considered as viable lighting sources. Among them, the light extraction efficiency and the light output degradation are key issues, which turn out to be all related to the packaging materials. LEDs have to often operate in different temperatures and environments with high level of humidity. Moisture, ionic contaminants, heat, radiation, and mechanical stresses can also be highly detrimental to LEDs and may lead to device failures. Almost all microelectronic devices are encapsulated by plastics. LEDs are also encapsulated to prevent mechanical and thermal stress shock and humidity-induced corrosion and oxidation [22]. Details of package-related failures and the relative solutions are given in Table 5.2 and shown schematically in Fig. 5.5. Most important challenges for packaging materials to be dealt with are to increase the light extraction efficiency, minimize the heat generated, extract more heat out of the package, and make the package more heat and UV resistant.

To sum up, the below mentioned requirements are essentially needed to improve the performance of the packaging materials and therefore enhance the lifetime of LEDs:

- High refractive index
- Excellent electrical properties
- Good chemical resistance

Table 5.2 Materials challenges and solutions for packaging high-power LEDs [22]

Challenges	Problems	Packaging material solutions
Light extraction	Refractive index mismatch between LED die and encapsulant	High refractive index encapsulant
		Efficient lens/cup design
Thermal yellowing	Thermal degradation of encapsulants induced by high junction temperature between LED die and lead frame	Modified resins or silicone-based encapsulant
		Low thermal resistance substrate
UV yellowing	Photodegradation of encapsulants induced by UV radiation from LED dies and outdoor radiation	UV transparent encapsulant
Stress/ delamination	Failure of wire bond and die attach caused by the CTE mismatch among encapsulant, LED die and lead frame	Low CTE and modulus encapsulants
		Excellent adhesion and CTE matching materials between the surfaces

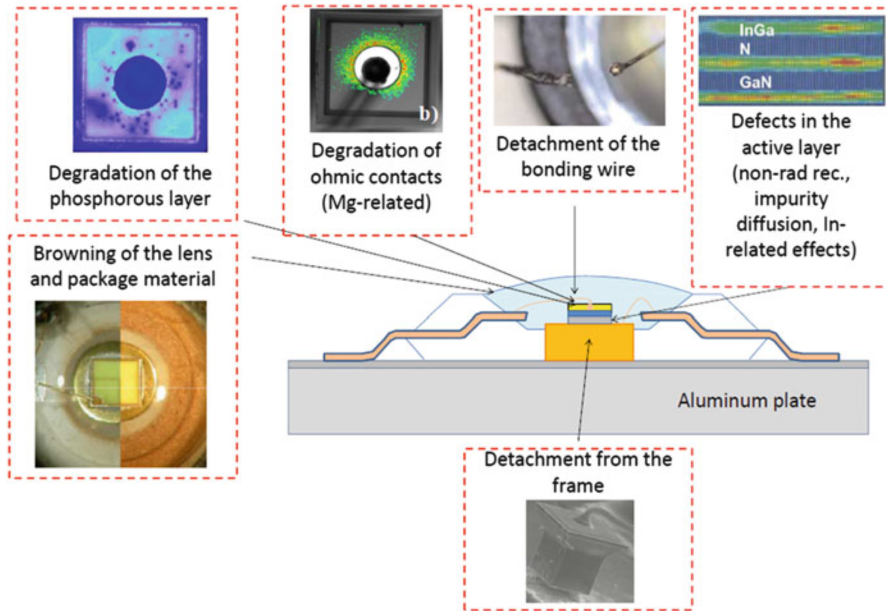

Fig. 5.5 Schematics of some common failure reasons in LED systems [11]

- Low water absorption (high resistance to moisture)
- Good adhesion to package components
- Mechanical strength
- Good UV and thermal resistance

Some of the most important degradation reasons of optical packages, which result in the aging of optical materials, will be explained in details here.

5.4.1 Contaminations

LEDs are susceptible to failures due to contaminations from several sources. A particular concern is the presence of sulfur-containing compounds which can cause darkening of the silver mirror that is frequently used beneath LEDs to increase package optical efficiency. Contamination and impurities can also accelerate the oxidation reaction of the polymer and therefore accelerate the kinetics of degradation.

5.4.2 Interface Delamination

Figure 5.6 shows the effects of the delamination of a phosphor coating applied directly to the LED in a high-power package. For case A, the phosphor has peeled

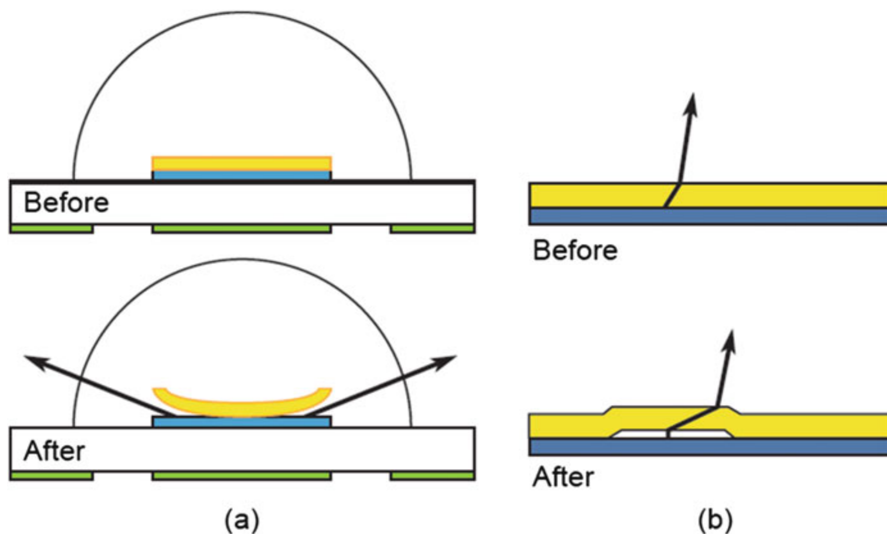

Fig. 5.6 Curling (**a**) and delamination (**b**) of phosphor-coated LED package [23]

up from the edges of the LED, allowing more blue light to escape and causing an overall shift toward blue. It may also cause spatial nonuniformity. Such an LED will emit more blue light to the sides and more yellow light on the optical axis. For case B, the phosphor has lifted from the LED in the non-edge portion of the device. In this case, the average path length for a blue photon through the phosphor increases. With longer path length, the chance of capture in the phosphor increases and more blue light is absorbed in the phosphor and converted to lower wavelengths, shifting the color toward yellow. Lamps using remote phosphor are less susceptible to many of the effects described above, because delamination is not a concern and because the remote phosphor is generally at a lower temperature than phosphors embedded in an LED package.

Mid-power LED packages can also show signs of delamination. Mid-power packages frequently use combinations of metals, silicones, and epoxies that have coefficients of thermal expansion. The adherence of these materials strongly depends on the process and on environmental stresses, including humidity and temperature. If any interface delaminates, the scattering internal to the package will change, and color shift is likely.

5.4.3 Discoloration

LEDs are encapsulated to prevent mechanical and thermal stress shock and humidity-induced corrosion [24–27]. Encapsulants, used in an LED packages, include plastics, epoxies, or silicones. These materials can discolor over time.

Fig. 5.7 BPA-PC plate after discoloration [24]

One example is shown in Fig. 5.7 in which the aged sample (in yellow) is compared with the as-received sample (in white) [24]. This is from a bisphenol-A polycarbonate (BPA-PC) plate of 3 mm thickness, used as a substrate in remote phosphor configuration. This yellowing will certainly shift color and deteriorates optical output of the system. Among different polymers that are commonly used as encapsulants and lenses, the details of three important ones are explained below.

Epoxy Resin. The majority of encapsulant/lens materials used today belongs to the thermosetting polymers, based on epoxy resins. Epoxy resins have been widely used as encapsulant materials in LED packages because of their combination of low cost, ease of processing, and excellent thermal, electrical, mechanical, and moisture barrier properties [28, 29]. Epoxies are also widely used as die-attach adhesives, laminates for printed wiring boards, and underfill adhesives for flip-chip and transfer-molding compounds for plastic-encapsulated microcircuits (PEMs). Epoxy resins are based on the epoxy group, a strained three-membered carbon-oxygen ring structure, as shown in Fig. 5.8a. Epoxy resins, however, have two disadvantages as LED encapsulants. One disadvantage is that cured epoxy resins are usually hard and brittle owing to their rigid cross-linked networks. The other one is that epoxy resins degrade under exposure to radiation and high temperatures, resulting in chain scission and discoloration, due to the formation of thermo-oxidative cross-links. Among different degradation mechanisms in epoxy in optical systems, discoloration and yellowing are the most common failure mechanisms, resulting in a reduction in the transparency of the encapsulants/lens and a decrease in the LED light output [29].

Silicone. Is a material with enhanced optical, toughness, and thermal stability properties that can be used to replace epoxy. Silicone is a unique type of polymer in the sense that its structure is semi-organic. Because of its combination of organic groups (methyl, vinyl, etc.) with an inorganic backbone (Si–O), silicone exhibits unique properties such as higher purity, stronger stress absorbing, better high and

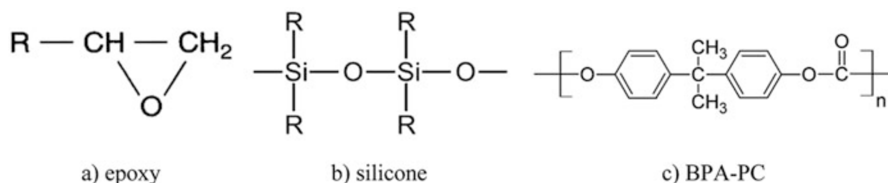

Fig. 5.8 The chemical structure of different polymers that are commonly used as encapsulants and lenses

low temperature stability, and more excellent biocompatibility than other polymers. Also, silicone maintains its excellent electrical properties at high temperatures and under humid environments [30]. The general formulation of silicone is shown in Fig. 5.8b. However, the disadvantages of silicone are its lower glass transition temperature (T_g), larger coefficient of thermal expansion (CTE), and poorer adhesion to the housing. One possible way to improve the thermal and mechanical properties of silicone is to use a siloxane-modified LED transparent encapsulant. The siloxane compounds improve the bond energy of the polymer chains to mitigate chain scission by increasing the cross-link density [31].

Polycarbonate. Is a thermoplastic and is the third most widely used material for LED encapsulants. It has high impact strength, high heat resistance, and high modulus of elasticity. It has been used in various applications, and its application in different domains has increased tremendously in recent years [31–33]. The general formulation of BPA-PC is given in Fig. 5.8c. Similar to epoxy resins and silicones, polycarbonate is prone to yellowing and discoloration under exposure to radiation at elevated temperatures. This results in a decreased light output due to decreased encapsulant/lens transparency. Polycarbonate degrades by an oxidation process that is strongly dependent on the exact composition of the polycarbonate, the presence of additives, and the loading (i.e., temperature and light). More information can be found in Refs. [35–43].

5.5 Yellowing of Encapsulant/Lens

In previous section the yellowing of polymeric materials and their sensitivity to yellowing were briefly explained. In this section the chemical reasons for the yellowing will be explained in more details. The main reasons of discoloration and yellowing are believed to be continued exposure to wavelength emission (blue/UV radiation), excessive temperature, and the presence of phosphor. Photodegradation of polymer materials usually takes place as a result of increasing the molecular mobility of the polymer as well as the introduction of chromophores as an additive into the molecule, both of which have absorption maxima in a region where the matrix polymer has no absorption band [41]. Photodegradation also depends on exposure time and the amount of radiation. The chemistry of degradation processes in

polycarbonates has been studied extensively over the past few decades [41–43]. In BPA-PC the reasons, underlying the photodegradation, have been attributed to two different mechanisms: photo-Fries rearrangement and photooxidation. Rivaton et al. [41] reported that the photo-Fries rearrangement reaction is more likely to occur at wavelengths shorter than 300 nm, whereas photooxidation reactions are more important when light of longer wavelengths (>340 nm) is used. On the other hand, Diepens et al. [44] argued that the photo-Fries rearrangement products are also formed, when samples are exposed to wavelength longer than 300 nm. Formation of both photo-Fries and oxidation products results in the yellowing and decrease in the transmission of BPA-PC plates [41–44]. In photo-Fries rearrangement reactions, carbonyl groups are rearranged to products of phenyl salicylate (L1), dihydroxybenzophenone (L2), and L3 which are shown in Fig. 5.9. L3 units are formed when CO–O band scission leads to decarbonylate or decarboxylate before further radical recombination or hydrogen abstraction. Rivaton et al. [41] postulated that at wavelengths longer than 340 nm, where the photooxidation reaction is dominant, side-chain oxidation, ring oxidation, and ring attack reactions are likely to take place. The side-chain oxidation in BPA-PC, however, is reported to be more probable [41–44]. To start the oxidation process, initiating of free radicals is required [42]. Lemaire et al. [43] and Factor et al. [45] demonstrated that photo-Fries products can be oxidized easily and act as a source of intrinsic photooxidation. Diepens et al. [44], however, showed that the increase in

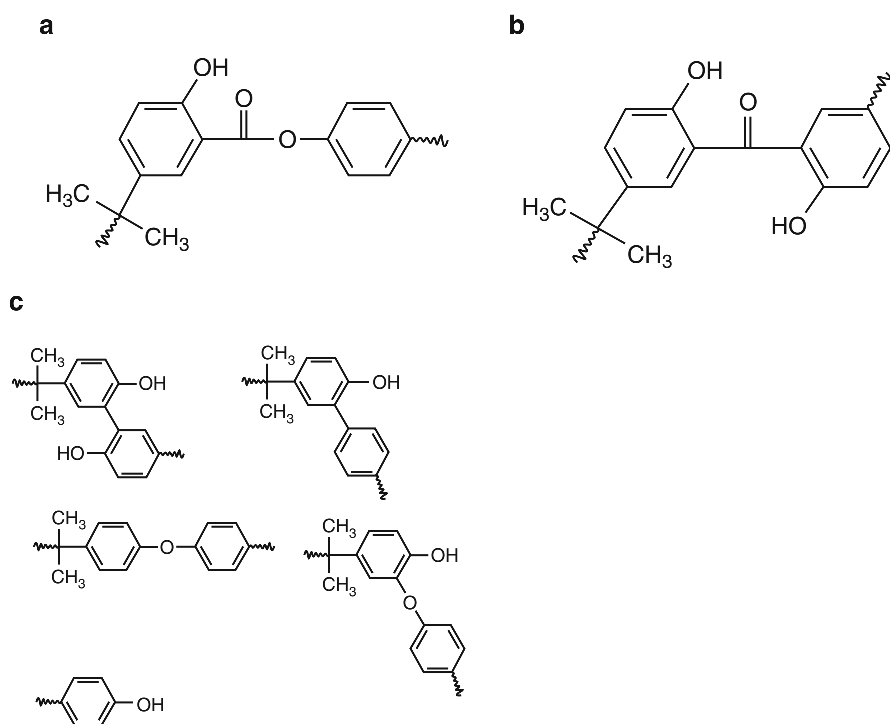

Fig. 5.9 Photo-Fries rearrangement products (**a**) L1, (**b**) L2, and (**c**) L3 [43]

photo-Fries rearrangement rate does not increase the oxidation rate, meaning that the photo-Fries reaction does not initiate the oxidation of polycarbonates.

Thermal degradation mechanisms and its effects on the optical and chemical properties of pure BPA-PC plates at 100, 120, and 140 °C are extensively studied by the author. Thermal aging of BPA-PC lens could significantly deteriorate the optical properties of LEDs. Rearrangement and oxidation in polycarbonate could result in discoloration and yellowing of BPA-PC encapsulant materials [35–38]. Discoloration due to the formation of oxidation products and rearrangement products or a combination of them could result in a decrease in the transmission of BPA-PC plates. Depending on the temperature, the degradation mechanism could be altered. It is believed that the higher the temperature, the more important the influence of rearrangement products on yellowing is [35]. Davis et al. [46] reported that the Fries rearrangement reaction is more likely to occur at high temperatures and under vacuum conditions. Rearrangement reaction in BPA-PC results in phenyl salicylate, diphenyl carbonate, phenol, and some other similar products [35]. Thermal oxidation products are more commonly reported as the main mechanism of yellowing of BPA-PC at low temperatures in the presence of oxygen [35–37]. Rivaton et al. [41] postulated that side-chain and ring oxidations are likely to take place during thermal degradation. Factor [45] showed that the main reason for discoloration and yellowing of thermally aged BPA-PC is the formation and subsequent oxidation of phenolic end groups, as is schematically shown in Fig. 5.10.

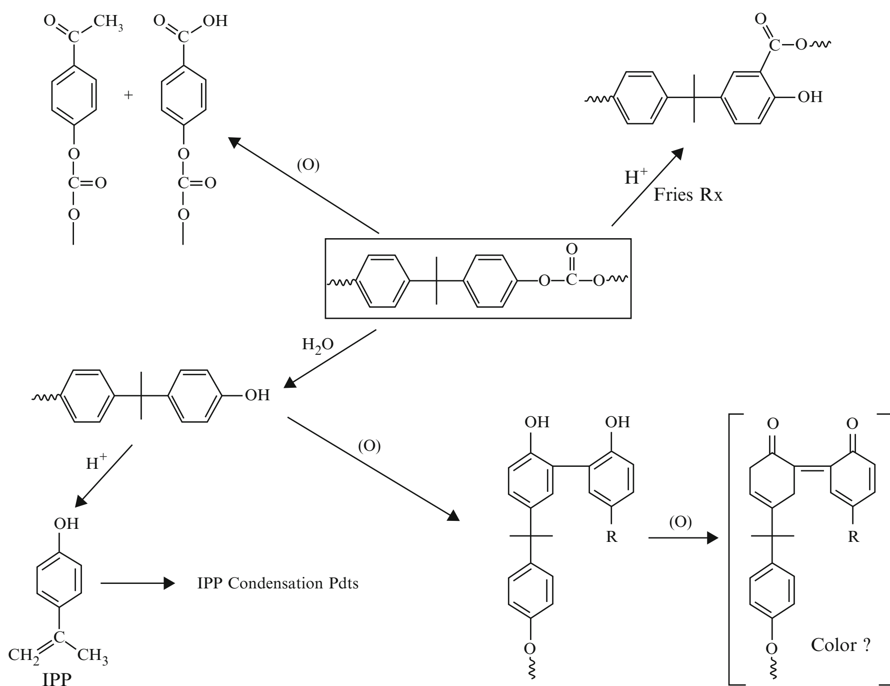

Fig. 5.10 Proposed pathway for the thermal oxidation of BPA-PC [43]

The temperature, leading to degradation, is a combination of junction temperature, ambient temperature, and LED self-heating [16]. Narendran et al. [16] reported that the degradation was affected by junction heat and the amount of short-wavelength emissions. It was shown that the thermal effect has greater influence on the yellowing than the short-wavelength radiation. Besides, it is revealed that a portion of the light circulated between the phosphor layer and the reflector cup would also contribute to the increasing of the temperature, causing yellowing [16]. Barton and Osinski [47] showed that a temperature of around 150 °C was sufficient to change the transparency of the epoxy and decreasing the light output of LEDs. Localized heating, produced by phosphor particles during light conversion, has also an effect on the encapsulant/lens discoloration [43]. It was shown that although phosphor is a necessary component to produce white light, the presence of phosphor causes a decrease in reliability. Phosphor thermal quenching decreases light output with the increase of the non-radiative transition probability due to thermally driven phosphorescence decay. Phosphor thermal quenching means that the efficiency of the phosphor is degraded when temperature rises. It is generally required that phosphors for white LEDs have low thermal quenching by a small Stokes shift to avoid changes in the chromaticity and brightness of white LEDs [34].

5.6 Terms and Definitions of Color Shifting

"Color maintenance" is analogous to lumen maintenance and is defined as the change in chromaticity of a light source with respect to the chromaticity at the beginning of the lamp's life. It is typically measured as Δxy or as $\Delta u'v'$ in the Commission Internationale de l'Eclairage (CIE) color coordinate systems. The chromaticity coordinates of a source provide a numerical representation of the color of the light. The three most common chromaticity diagrams, with their coordinates, are the CIE 1931 (x, y), the CIE 1960 (u, v), and the CIE 1976 (u', v'). The (x, y) coordinates are the most frequently reported. Figure 5.11 shows the CIE 1931 (x, y). Every color is represented by unique (x, y) coordinates. The CIE system is the most common method of characterizing the composition of any color in terms of three primaries [48, 49]. Artificial colors, indicated by X, Y, and Z coordinates, also called tristimulus values, can be added ($X + Y + Z = 1$), to produce real spectral colors. The chromaticity coordinates, x, y, and z [48], are the ratios of the X, Y, and Z coordinates of the light to the sum of the three tristimulus values. It is necessary only to consider the quantity of two of the reference stimuli in order to define a color, since the three quantities (x, y, z) are always made to sum to 1. Thus, the (x, y) coordinates are commonly used to represent a color [48, 49].

The (u', v') coordinates are related to the (x, y) coordinates by the following equations:

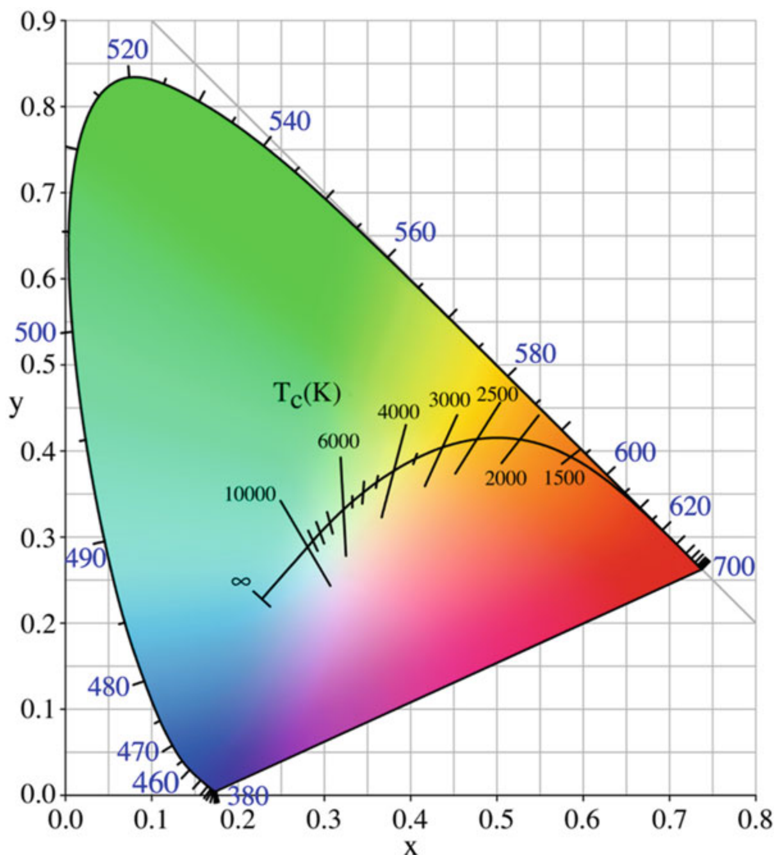

Fig. 5.11 The CIE 1931 x, y chromaticity space, also showing the lines of constant correlated color temperature

$$U' = \frac{4x}{-2x \times 12y \times 3} \tag{5.1a}$$

$$V' = \frac{9y}{-2x \times 12y \times 3} \tag{5.1b}$$

Based on Eq. 5.1a and 5.1b, the coordinates $\Delta u' v'$, which define the color shift at any two positions (0 and 1), can be calculated using the following formula:

$$\Delta u'v' = \sqrt{\left(u_1' - u_0'\right) + \left(v_1' - v_0'\right)} \tag{5.2}$$

Energy Star specifies that color maintenance must not exceed $\Delta u' v' = 0.007$ on the CIE (u', v') diagram, after 6,000 h of operation.

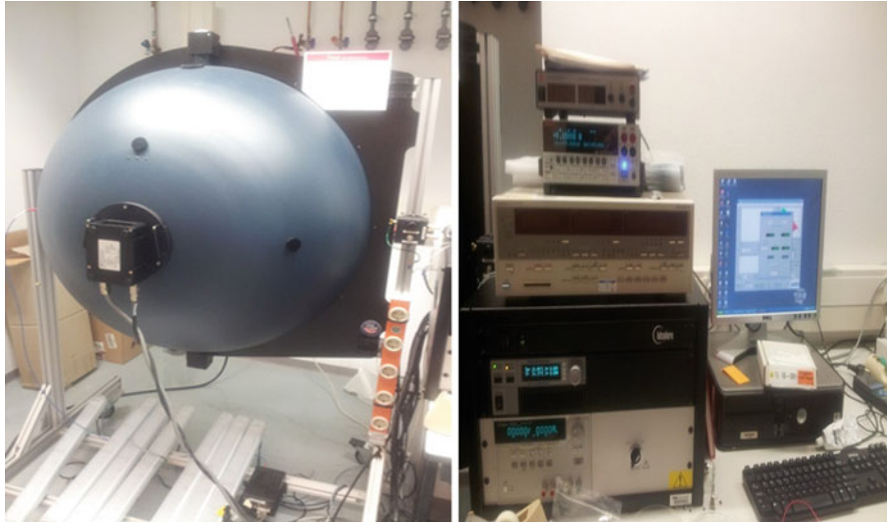

Fig. 5.12 Integrated sphere (IS), widely used to measure yellowing index

"Color consistency" is the variation in chromaticity at the start of a lamp's life among a population of products. For example, a product may be made from LEDs that are binned to fall within three *MacAdam* steps of a target chromaticity. These LEDs have a color consistency of three steps. Color consistency can also be defined in terms of (x, y) or (u', v'). The color consistency of lamps built from these LEDs may be worse than three steps because of temperature variations, current variations, or other factors.

The spectral power distribution (SPD) and the yellowing index (*YI*) of the aged plates, measured by integrated sphere, are always good measures of the yellowing extent in samples. The integrated sphere, shown in Fig. 5.12, is an optical device consisting of a hollow spherical cavity with its interior covered with a diffuse white reflective coating, with small holes for entrance and exit ports. It is typically used with some light source and a detector for optical power measurement. The yellowing index (YI) is calculated according to ASTM D1925 [50] with the following equation:

$$\mathrm{YI} = \frac{100\,(1.28X\ \ \mathrm{CIE} - 1.6Z\ \ \mathrm{CIE})}{Y\ \ \mathrm{CIE}} \tag{5.3}$$

where X and Y are the tristimulus values in (CIE) standard.

Figure 5.13 depicts the color shift ($\Delta u'v'$) of the BPA-PC specimens at different loading conditions as well as the yellowing index (YI) of BPA-PC plates as a function of exposure time under thermal and thermal plus blue light stress, as example. Obviously there is no major color shift during the incubation stage, whereas the color shift during the degradation stage is linearly proportional to the

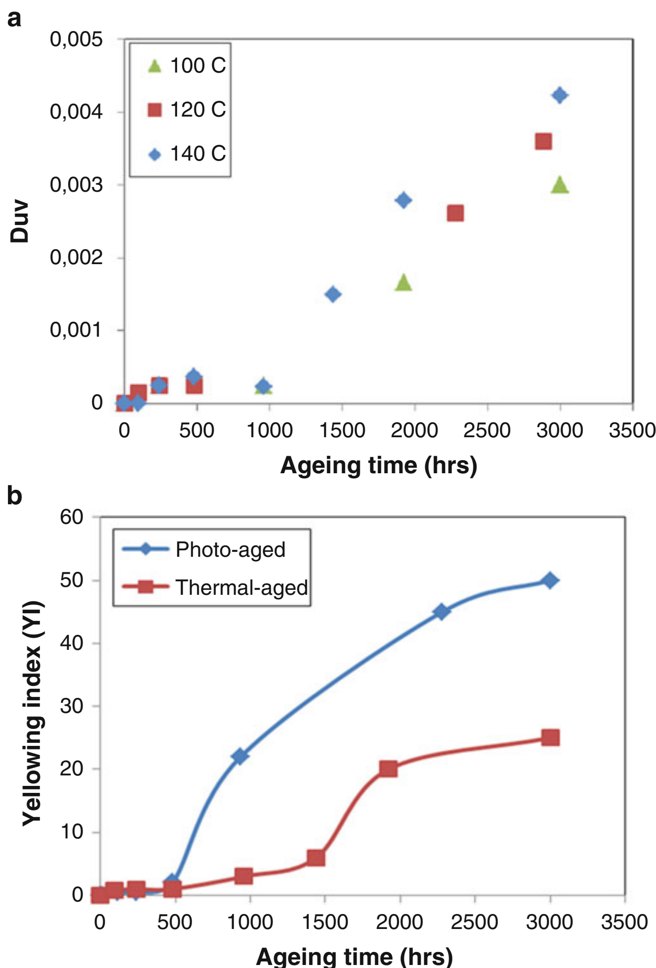

Fig. 5.13 Examples of (**a**) color shift of BPA-PC plate, aged at different temperatures, and (**b**) variation in YI of BPA-PC plates exposed to different stresses [37]

testing duration. Also Fig. 5.13b shows the temperature itself could cause the yellowing. However, one can see that the blue light has a significant contribution to the yellowing. The presented results in Fig. 5.13 are from the aging test, done on industrially pure BPA-PC, which is used as a lens and as a substrate for phosphor in remote phosphor LEDs. Details of the test are already published [37]. In commercial samples, the main reason for yellowing is thermal aging. For this reason, thermal aging can be used to accelerate degradation mechanisms in order to study color shift. It is already reported that by increasing the temperature, the kinetics of discoloration becomes faster [37–39].

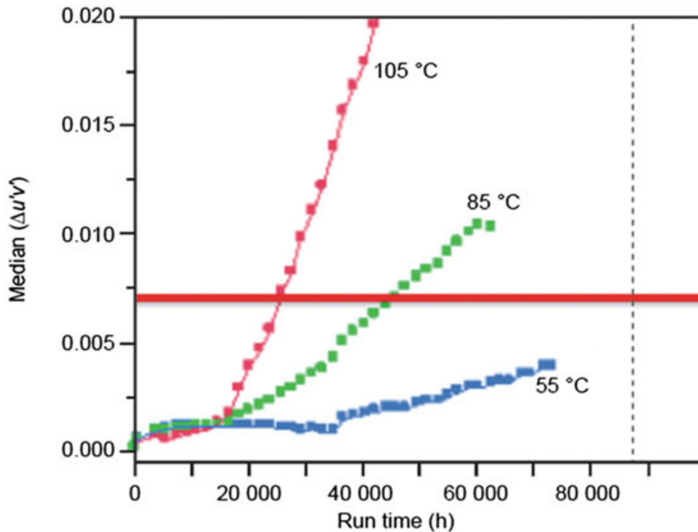

Fig. 5.14 Color shift in a high-power LED package [24]

Any of the degradation processes above is influenced by temperature and other stresses. Color shift will be accelerated by higher current or higher temperature. For example, Fig. 5.14 [24] shows a dramatic increase in the rate of color shift as the LED junction temperature is increased. In this particular case, the color shift begins only after about 15,000 h, so lamps, produced from these LEDs, would only begin to show strong color shift after being installed for about 2 years, if operated 24 h per day.

5.7 Reliability Performance of LEDs

Reliability is the probability that a system will perform its intended function under stated conditions for a specified period of time without failures [51]. By this definition, reliability is a measure as a function of time and, thus, a quantity. The LED domain, despite exciting innovations, motivated by technological developments, has still challenges regarding lack of information regarding the failure mechanisms and reliability. The relative low reliability information is an obstacle to the acceptance of LEDs in traditional applications. Consumers of LEDs expect that the industry guarantees the lifetime of LEDs in the usage conditions. LED lifetime is measured by lumen maintenance, which is how the intensity of emitted light tends to weaken over time. Other parameters such as chromaticity coordinate values (x and y) and correlated color temperature (CCT) are also important. The Alliance for Solid-State Illumination Systems and Technologies (ASSIST) defines LED lifetime based on the time to 50% or 70% of light output degradation at room temperature [25]. In order to increase the quality of LEDs, it is important to know the main reason of lumen depreciation in a reasonable experimental time periods.

LED manufacturers usually perform tests in the product development cycle during the design and development phases to predict the lifetime of LED. The term reliability prediction is historically used to denote the process of applying mathematical models and data for the purpose of estimating field reliability of a system before empirical data are available [52]. These predictions are used to evaluate design feasibility, compare design alternatives, identify potential failure areas, trade off system design factors, and track reliability improvement. In order to predict LED lifetime, it is needed to carry out accelerated life tests at high temperatures and monitor the light output during the test. Modeling of acceleration factors (*AF*) is generally used to predict the long-term lifetime of LED packages at specific usage conditions [18]. Typical qualification tests of LEDs are categorized into operating life tests and environmental tests by using industrial standards such as *JEDEC* or *JEITA* and *LM-803* [53–55].

5.8 Highly Accelerated Stress Test (HAST) Setup

A highly accelerated stress testing (HAST) setup was developed in our previous works to study the effects of both blue light intensity and the thermal stress on the lifetime and the kinetics of aging of phosphor plates used in SSL luminaires. This work is a significant step forward and an improvement of our previously applied accelerated test methodology [36], where the only applied stress factor was thermal stress. Application of both thermal stress and light intensity in HAST setup makes the kinetics of degradation much faster. Figure 5.15 shows an overview picture of the HAST system including all components. The core of the HAST consists of a blue light source with wavelength of 450 nm and a working surface. Blue light sources were Philips modules, with each module containing 18 high-power LED packages. Samples were placed on the working surface and were directly aged under blue light radiation. The working surface in this setup is a hot plate, and absorptive filters are placed between the samples and the hot plate in order to prevent the reflection of light by the surface of the hot plate. The hot plate should constantly be calibrated by an IR camera. The temperature on the surface of the hot plate should also be perfectly homogenous, with the difference not being more than 5 °C all over the plate. The blue light source is composed of a mechanical assembly that holds the light source at a desired distance from the hot plate. In order to change the light intensity, the distance between the samples and the blue light source can be changed. The homogeneity of the light source across the samples can be checked by photometer at different distances and times. In one set of experiments, three temperatures of 80, 100, and 120 °C are used and samples are aged up to 3,000 h. The samples were remote phosphor plates of 3 mm thick with correlated color temperature (CCT) of 4,000 K and color rendering index (CRI) of 80. The luminescent powder mix for this sample was made of YAG powder with 3.3% Ce content and 1.5% nitride red phosphor, doped with CaSN-Eu. The blue light in this study was radiated on the sample with different light intensities of 825, 3,300, and

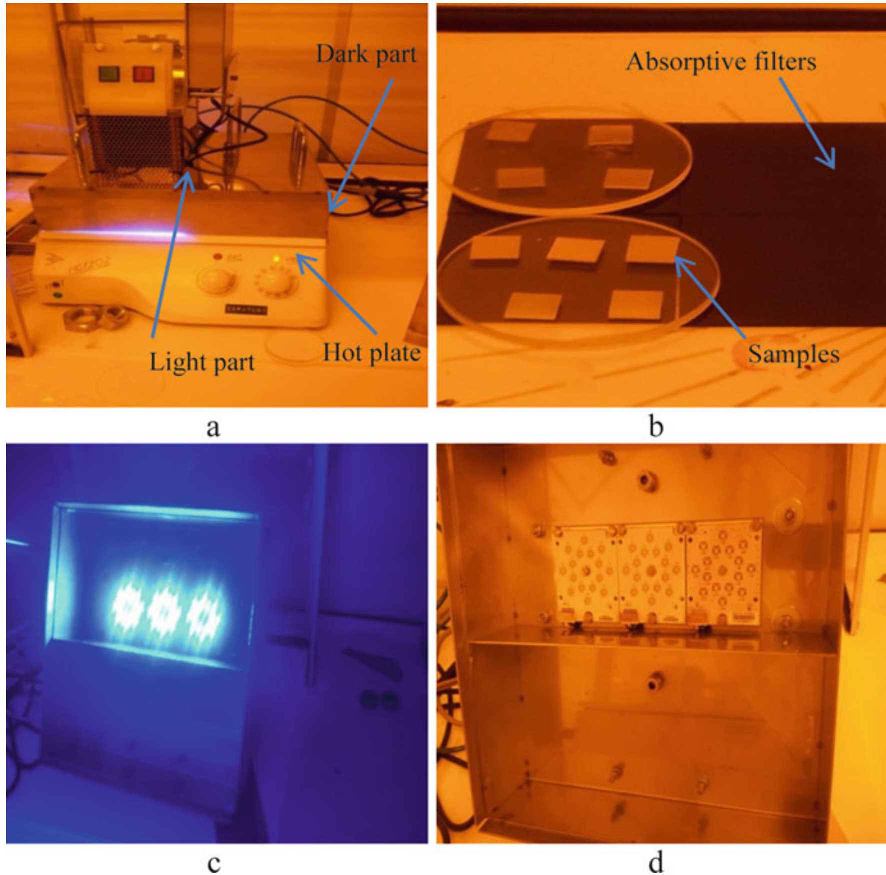

Fig. 5.15 Highly accelerated stress testing (HAST) setup, with (**a**) frontal view in off state (*top left*); (**b**) samples on the absorptive filter (*top right*); (**c**) the blue LED light source (*bottom left*); and (**d**) frontal view in off state (*bottom right*)

13,200 W/m^2. The change in the spectral power distribution (SPD) was used as a measure to monitor the optical degradation of remote phosphors.

Optical properties of photoaged plates, i.e., luminous flux depreciation and CCT of plates, were studied at room temperature, using an integrated sphere. In addition, color shifting in the aged specimens was also monitored. More details about the experiment and the results can be found in our previously published works [37].

5.9 Reliability Models

TM-21 is a Technical Memorandum being developed by an Illuminating Engineering Society (IES) technical committee. TM-21 does project the lumen maintenance of an LED source (package/array/module), which can then be used to project the

Table 5.3 Lumen maintenance life projections in standard TM-21 [55]

Model	Decay rate	Closed form solution	Comment
1	$\frac{dI_v}{dt} = k_1$	$I_v = I_v^0 + (t - t^0)$	
2	$\frac{dI_v}{dt} = k_2 I_v$	$I_v = I_v^0 \exp[k_2(t - t^0)]$	
3	$\frac{dI_v}{dt} = k_1 I_v + k_2 I_v$	$I_v\left(I_v^0 + \frac{k_1}{k_2}\right)\exp[k_2(t - t^0)] - \frac{k_1}{k_2}$	Model 1 + Model 2
4	$\frac{dI_v}{dt} = \frac{k_3}{t}$	$I_v = I_v^0 + k_3 \ln\left(\frac{t}{t^0}\right)$	
5	$\frac{dI_v}{dt} = k_1 + \frac{k_3}{t}$	$I_v = I_v^0 + k_1(t - t^0) + k_3 \ln\left(\frac{t}{t^0}\right)$	Model 1 + Model 4
6	$\frac{dI_v}{dt} = k_4 I_v^2$	$I_v = \frac{I_v^0}{1 + I_v^0 k_4 (t - t^0)}$	
7	$\frac{dI_v}{dt} = k_5 \frac{I_v}{t}$	$I_v = I_v^0 (t/t^0)^{k_5}$	
8	$\frac{dI_v}{dt} = k_2 I_v + k_5 \frac{I_v}{t}$	$I_v = I_v^0 \exp[k_2(t - t^0)](t/t^0)^{k_5}$	Model 2 + Model 7
9		$I_v = I_v^0 \exp\left[-\frac{(t-t^0)}{k_6}\right]^{k_7}$	

expected lumen output of the source as part of a system [55]. Table 5.3 shows the proposed reliability model in TM-21 for different applications.

The simplest form of ratability model, which can be applied in many cases for the lifetime assessment of remote phosphor plates, is based on an exponential luminous decay equation, where the Φ can be calculated as [55]:

$$\varnothing(t) = \beta \exp(-\alpha t) \tag{5.4}$$

with $\phi(t)$ being the lumen output, α is degradation reaction rate or depreciation rate parameter, t the aging time, and β a pre-factor. When lumen output, Φ, is equal to 70%, t is time to failure [12]. In the HAST experiments, where the light intensity is also used as an extra acceleration factor, the *Eyring* relationship, given below, is a more appropriate equation [55]:

$$R = \gamma_0 (I)^n \exp\left(\frac{-E_a}{\mathrm{KT}}\right) \tag{5.5}$$

where R is the reaction rate, γ_0 is the pre-exponential factor, I is the intensity of blue light, n is the constant factor, E_a is the activation energy (eV) of the degradation reaction, K is the Boltzmann gas constant (eV/K), and T is the absolute temperature (K). In one of our studies, the aging temperatures of the hot plate were adjusted at 80, 100, and 120 °C. However, by radiation of light, the temperature of phosphor plates increased up to 2, 10, and 20 °C for 825, 3,300, and 13,200 W/m^2 intensities, respectively. The increase of the temperature by radiation of light was measured by a thermometer with an accuracy of ±0.5 °C. This temperature increase should then be always taken into consideration in calculations.

Thermal stress tests have also some significant effects on the CCT. The variation of CCT during aging at high temperature stress test for remote phosphor plates is shown in Table 5.4. It is obvious that by increasing the thermal aging time, the CCT decreases.

Table 5.4 CCT for remote phosphor plates at a temperature of 80–120 °C after 3,000 h aging

Light intensity (W/m^2)	825	3,300	13,200
80	4,410	4,370	4,300
100	4,120	4,000	3,900
120	4,050	3,900	3,720

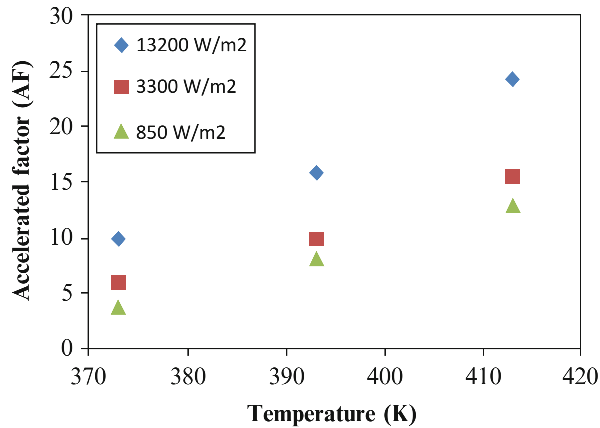

Fig. 5.16 Acceleration factor of photothermal-aged at 120 °C

5.9.1 *Effect of Light Intensity on the Acceleration of Aging Test*

Using generalized Eyring equation [37], the acceleration factor of the tests at different stresses can be calculated. Acceleration factor is a measure of how much faster the test is performed at a certain testing condition, compared to normal behavior at real working conditions. Obviously the higher the acceleration factor, the faster and the more efficient (in terms of needed time for the experiment) the experiments. This factor is defined by the following equation:

$$\mathrm{Af} = \left(\frac{I}{I_0}\right)^n \exp\left(\frac{E_a}{K}\left(\frac{1}{T_{\text{reference}}} - \frac{1}{T_{\text{test}}}\right)\right) \tag{5.6}$$

where $T_{\text{Reference}}$ is reference temperature, which is assumed to be 80 °C which is closer to reality, T_{test} is the testing temperature, I is the intensity of blue light which is 13,200 and 3,300 W/m^2, and I0 is the reference light intensity which is considered to be 850 W/m^2. The acceleration factors of remote phosphor at aging temperature of 80–120 °C with radiation of light with intensities 825, 3,300, and 13,300 W/m^2 are given in Fig. 5.16.

The radiation of light accelerates the kinetics of the aging of remote phosphor. The increase in the acceleration factor by the radiation of light indicates the effect of light intensity (see Eq. 5.5). Using Eq. 5.5, the power factor, n, is found to be equal to 0.2. The acceleration factors of remote phosphor at aging temperature of

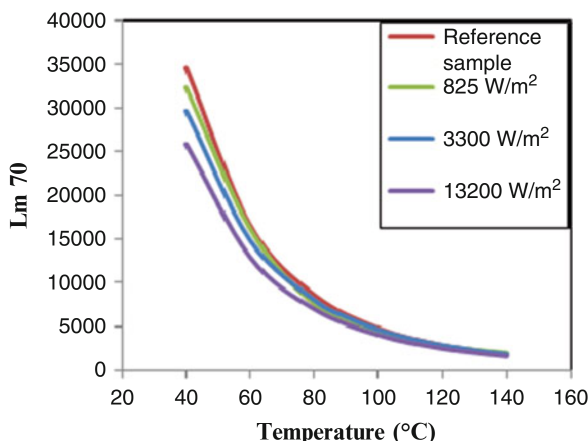

Fig. 5.17 Time to failure (70% lumen decay) of remote phosphor at different temperatures for light intensities of 825, 3,300, and 13,200 W/m^2

120 °C with radiations of 825, 3,300, and 13,300 W/m^2 light and dark experiment are 1.01, 1.2, and 1.9 for blue light radiations of 825, 3,300, and 13,200 W/m^2, respectively. The increase in acceleration factor by radiation of light indicates the effect of light intensity (see Eq. 5.5).

5.9.2 Effect of Light Intensity on the Time to Failure of Remote Phosphor

The temperature of phosphor during service can increase up to 100 °C [24]. However, it is more logical to use 80 °C as reference temperature, which is more an average value over the whole year. The kinetics of lumen depreciation to 30% of its initial value can be calculated using Eq. 5.1a and 5.1b, equating ϕ to 0.7, knowing that a can be obtained from Eq. 5.2. Figure 5.13 illustrates the time to failure (70% lumen decay) of remote phosphors, calculated at different temperatures for the photothermal aging, where the aging temperature was 120 °C. Data for the reference sample (thermally aged at 120 °C without light radiation) is added for the sake of comparison [36]. It is shown that the lifetime, defined as 30% lumen depreciation at 40 °C, is around 35 khrs, for the lowest energy power, which has almost the same lifetime as thermally aged phosphor. The lifetime of the phosphors with higher power energy is 25 khrs (Fig. 5.17).

5.10 Concluding Remarks

This chapter reviews the research done on the failure mechanisms and reliability of optical materials in LED systems. Different types of failures at the package level are discussed and introduced. Different operational and environmental stresses,

including junction temperature, contaminations, humidity, operation temperature, and UV light, might cause lumen decay and failure of LEDs. Among different failure modes, thermal degradation is the most severe one. If thermal management is insufficient in the remote phosphor, overheating and damage in the remote phosphor and its substrate can occur. For instance, the adhesives that bind the LED to the submount may degrade due to thermal weakening. Thermal loads result in thermal fatigue of solders in LED package as well. More importantly, thermal aging results in faster kinetics of yellowing and discoloration. With that said, thermal stress is frequently used for accelerated testing of LEDs. In this chapter a new acceleration test method for LED remote phosphors is introduced in which the effect of light intensity (in addition the temperature) on the kinetics of aging can be monitored. The results illustrated that there is a direct relation between the light intensity and the loss in conversion efficiency of remote phosphor. In fact, by increasing the light intensity, the conversion efficiency of remote phosphor decreases. Among different proposed lumen maintenance models, proposed in TM-21, the generalized Eyring equation is the right choice for the HAST setup. It is shown that the lifetime, defined as 30% lumen depreciation at 40 °C, is approximately 35 khrs, for the lowest energy power, which has almost the same lifetime as thermally aged phosphor. The lifetime of the phosphors with higher power energy is predicted to be 25 khrs. Although great effort was put into predicting lumen maintenance, resulting in the LM-80 and TM-21 standards, little has been done to address color maintenance. Few (or no) LED package manufacturers provide warranties on color maintenance. It is an absolute necessity to have a widely accepted method of predicting color maintenance and reliability of LED packages.

References

1. N. Jr, S.F. Bevaqua, Coherent light emission from GaAs(1-x)Px junctions. Appl. Phys. Lett. **1**, 82–83 (1962)
2. S. Nakamura, T. Mukai, M. Senoh, S. Nagahama, N. Iwasa, InxGa(1-x) N/InyGa(1-y)N superlattices grown on GaN films. J. Appl. Phys. **74**, 3911–3915 (1993)
3. S. Nakamura, G. Fasol, *The Blue Laser Diode: GaN Based Light Emitters and Lasers* (Springer, Berlin, 1997)
4. US DOE, Energy saving forecast of solid-state lighting in General Illumination Applications, prepared for US department of energy, prepared by Navigant Consulting, Inc., (2014)
5. Y.C. Lin, Y. Zhou, T. Nguyen, Tran, F.G. Shi, LED and optical device packaging and materials. Mat. Adv. Packag. **8**, 629 (2009)
6. Multi-year program plan, prepared for US department of energy. Technical report, Navigant Consulting, Inc., Radcliffe Advisors, Inc., and SSLS, Inc., March (2009)
7. D.A. Steigerwald, J.C. Bhat, D. Collins, R.M. Fletcher, M.O. Holcomb, M.J. Ludowise, P.S. Martin, S.L. Rudaz, Illumination with solid state lighting technology selected topics in quantum electronics. IEEE J. **8**, 310–320 (2002)
8. P. Schlotter, J. Baur, C. Hielscher, M. Kunzer, H. Obloh, J. Schmidt, R. Schneider, Fabrication and characterisation of GaN/InGaN/AlGaN double heterostructure LEDs and their application in luminescence conversion LEDs. Mater. Sci. Eng. **59**, 390–394 (1999)

9. J.K. Park, C.H. Kim, S.H. Park SH, S.Y. Choi, Application of strontium silicate yellow phosphor for white light-emitting diodes. Appl. Phys. Lett. **84**(10), 1647–1649 (2004)
10. A. Zukauskas, M.S. Shur, R. Gaska, *Introduction to Solid-State Lighting* (Wiley, New York, 2002)
11. X. Fan, Lamar University Beaumont, Presentation in ECTC 2016 Conference, 2016 IEEE 66th Electronic Components and Technology Conference (ECTC), Las Vegas
12. P. Mottier, *LEDs for Lighting Applications* (Wiley, London, 2009), p. 2
13. R. Mueller-Mach, G.O. Mueller, White light-emitting diodes for illumination. Proc. SPIE **3938**, 30–41 (2000)
14. M.H. Chang, D. Das, P.V. Varde, M. Pecht, Microelectron. Reliab. **52**(5), 762–782 (2012)
15. W.D. van Driel, X.J. Fan, *Solid State Lighting Reliability: Components to Systems*, (Springer, New York, 2012), ISBN 978–1–4614-3066-7
16. N. Narendran, Y. Gu, J.P. Freyssinier, H. Yu, L. Deng, Solid state lighting: Failure analysis of white LED. J. Cryst. Growth. **268**(3–4), 449–456 (2004)
17. N. Narendran, Y. Gu, J.P. Freyssinier-Nova, Y. Zhu, Extracting phosphor-scattered photons to improve white LED efficiency. Phys. Stat. Sol. (a) **202**(6), R60–R62 (2005)
18. S.I. Chan, W.S. Hong, K.T. Kim, Y.G. Yoon, J.H. Han, J.S. Jang, Accelerated life test of high power white light emitting diode based on package related failure. Microelectron. Reliab. **9-11**, 1806–1809 (2011)
19. X. Luo, B. Wu, S. Liu, Effects of moist environments on LED reliability. IEEE Trans. Dev. Mater. Relia. **10**(2), 182–186 (2010)
20. J.M. Kang, J.W. Kim, J.H. Choi, D.H. Kim, H.K. Kwon, Lifetime estimation of high power blue light-emitting diode chips. Microelectron. Reliab. **49**, 1231–1235 (2009)
21. M. Meneghini, L.R. Trevisanello, G. Meneghesso, E. Zanoni, A review on the reliability of GaN-based LEDs. IEEE Trans. Device Mater. Reliab. **8**(2), 323–331 (2008)
22. H. Ardebili, M.G. Pecht, *Encapsulation Techniques for Electronic Applications*, vol 57 (William Andrews, California, 2009), ISBN: 9780815519706
23. M. Royer, R. Tuttle, S. Rosenfeld, N. Miller, *Color Maintenance of LEDs in Laboratory and Field Applications, PNNL-22759* (Pacific Northwest National Laboratory, Richland, 2013)
24. U.S. Department of Energy, Solid State Lighting Technology Fact Sheet: LED Color Stability, PNNL-SA-101828 (US Department of Energy, 2014). http://apps1.eere.energy.gov/buildings/publications/pdfs/ssl/color-shift_factsheet.pdf
25. M.-H. Chang, D. Das, S.W. Lee, M. Pecht, Concerns with interconnect reliability assessment of high power light emitting diodes (LEDs). In: SMTA China south technical conference 2010, Shenzhen, 31st Aug–2nd Sept 2010, pp. 63–69
26. CIE. International commission on illumination. 2015-03-18. http://www.cie.co.at/index.php/Technical+Committees
27. J.J. Licari, *Coating Materials for Electronic Applications: Polymers, Processes, Reliability, Testing* (William Andrews, New York, 2003)
28. Tanabe S, Fujita S, Yoshihara S, Sakamoto A, Yamamoto S, in *SPIE Proceedings Vol. 5941: Fifth International Conference on Solid State Lighting*. ed. by I.T. Ferguson, J.C. Carrano, T. Taguchi, I.E. Ashdown. YAG glass ceramic phosphor for white LED (II): Luminescence characteristics (San Diego, California, 2005), p. 594112
29. N.Y.A. Shammas, Present problems of power module packaging technology. Microelectron. Reliab. **43**, 519–527 (2003)
30. Dow Corning Corporation, Silicone chemistry overview (Dow Corning Corporation, Midland, 1997). https://www.dowcorning.com/content/publishedlit/01-4027-01.pdf
31. D.G. LeGrand, J.T. Bendler, *N Handbook of Polycarbonate Science and Technology* (Marcel Dekker, New York, 2000)
32. H. Krimm, H. Schnell, L. Bottenbruch, Thermoplastic aromatic polycarbonates and their manufacture: US, 3028365 A. 1962-04-03
33. D.W. Fox, Polycarbonates of dihydroxyaryl ethers, US, 3148172 A. 1964-09-08

34. A. Factor, W.V. Ligon, R.J. May, The role of oxygen in the photoaging of bisphenol a polycarbonate. 2. GC/GC/high-resolution MS analysis of Florida-weathered polycarbonate. Macromolecules **20**(10), 2461–2468 (1987)
35. M. Yazdan Mehr, W.D. van Driel, K.M.B. Jansen, P. Deeben, G.Q. Zhang, Lifetime assessment of bisphenol-a polycarbonate (BPA-PC) plastic lens, used in LED-based products. Microelectron. Reliab. **54**(1), 138–142 (2014)
36. M. Yazdan Mehr, W.D. van Driel, G.Q. Zhang, Accelerated life time testing and optical degradation of remote phosphor plates. Microelectron. Reliab. **54**(8), 1544–1548 (2014)
37. M. Yazdan Mehr, W.D. van Driel, S. Koh, G.Q. Zhang, Reliability and optical properties of LED lens plates under high temperature stress. Microelectron. Reliab. **54**(11), 2440–2447 (2014)
38. M. Yazdan Mehr, W.D. van Driel, H. Udono, G.Q. Zhang, Surface aspects of discoloration in bisphenol a polycarbonate (BPA-PC), used as lens in LED-based products. Opt. Mater. **37**, 155–159 (2014)
39. M. Yazdan Mehr, W.D. van Driel, K.M.B. Jansen, B.M. Deeben, G.Q. Zhang, Photodegradation of bisphenol a polycarbonate under blue light radiation and its effect on optical properties. Opt. Mater. **35**(3), 504–508 (2013)
40. Solais Lighting Inc., *LED Color Shift—Causes and Management* (Solais Lighting, Stamford, 2014) http://www.solais.com/download.php?f=/var/chroot/home/content/19/10197719/html/uploadedFiles/download/pdf/LEDColorshift.pdf
41. A. Rivaton, Recent advances in bisphenol-a polycarbonate photodegradation Polym. Degrad. Stab. **49**(1), 163–179 (1995)
42. A. Rivaton, D. Sallet, J. Lemaire, The photochemistry of bisphenol-a polycarbonate reconsidered. Polym. Photochem. **3**(6), 463–481 (1983)
43. J. Lemaire, J.L. Gardette, A. Rivaton, A. Roger, Dual photo-chemistries in aliphatic polyamides, bisphenol a polycarbonate and aromatic polyurethanes—a short review. Polym. Degrad. Stab. **15**(1), 1–13 (1986)
44. M. Diepens, P. Gijasman, Photodegradation of BPA. Polym. Degrad. Stab. **92**(3), 397–406 (2007)
45. A. Factor, M.L. Chu, The role of oxygen in the photoageing of bisphenol-a carbonate. Polym. Degrad. Stab. **2**(3), 203–223 (1980)
46. A. Davis, J.H. Golden, Thermal rearrangement of diphenyl carbonate, J. Chem. Soc. (B), 40–45 (1968)
47. D.L. Barton, M. Osinski, Degradation mechanisms in GaN/AlGaN/InGaN LEDs and LDs, Proceedings of the 10th SIMC-X 259. Semiconducting and Insulating Materials 1998. Proceedings of the 10th Conference on Semiconducting and Insulating Materials (SIMC-X) (Cat. No.98CH36159) (1998)
48. G.R. Jones, A.G. Deakin, J.W. Spencer, *Chromatic Monitoring of Complex Conditions* (Taylor & Francis Group, London, 2008)
49. D.L. MacAdam, *Color Measurement: Theme and Variations*, 2nd edn. (Springer, New York, 1985)
50. American Society for Testing and Materials, *Test Method for Yellowness Index of Plastics. Annual Book of Standards, 8.01, ASTM D1925–70* (ASTM, Philadelphia, 1970)
51. G.Q. Zhang, *Shaping the New Technology Landscape of Lighting, Proceedings of Green Lighting Forum* (Shanghai, 2010)
52. Cree, *Cree Xlamp XR family LED Reliability*. CLD-AP06 Rev. 7 (Cree, Inc., 2009), pp. 1–5
53. Nichia, *Specifications for Nichia Chip Type White LED Model: NCSW119T-H3"*, Nichia STS-DA1-0990A (Nichia Corporation, 2009)
54. IES LM-80-08: Approved method for measuring maintenance of LED light sources
55. Illuminating Engineering Society of North America, *Projecting Long Term Lumen Maintenance of LED Light Sources,* IES Report TM-21 11 (Illuminating Engineering Society, New York, 2011)

Chapter 6
The Influence of Phosphor and Binder Chemistry on the Aging Characteristics of Remote Phosphor Products

J.L. Davis, R. Yaga, M. Lamvik, K. Mills, and B. Fletcher

Abstract The influence of phosphor and binder layer chemistries on the lumen maintenance and color stability of remote phosphor disks was examined using wet high-temperature operational lifetime testing (WHTOL). As part of the experimental matrix, two different correlated color temperature (CCT) values, 2,700 K and 5,000 K, were studied and each had a different binder chemistry. The 2,700 K samples used a urethane binder, whereas the 5,000 K samples used an acrylic binder. Experimental conditions were chosen to enable study of the binder and phosphor chemistries and to minimize photooxidation of the polycarbonate substrate. Under the more severe WHTOL conditions of 85 °C and 85% relative humidity (RH), absorption in the binder layer significantly reduced luminous flux and produced a blue color shift. The milder WHTOL conditions of 75 °C and 75% RH resulted in chemical changes in the binder layer that may alter its index of refraction. As a result, lumen maintenance remained high, but a slight yellow shift was found. The aging of remote phosphor products provides insights into the impact of materials on the performance of phosphors in an LED lighting system.

6.1 Introduction

Solid-state lighting (SSL) technologies are energy-efficient illumination sources that are found in lamps and luminaires. In building light engines for SSL devices, manufacturers typical use one of two approaches [1]. In proximate phosphor light-emitting diodes (LEDs), white light is generated by placing phosphors in close proximity to the LED. This structure has the advantage of being compact, but can also produce extreme temperatures in the phosphor layer, which can impact performance [2]. In the alternative remote phosphor configuration, the phosphor layer is remotely located from the LED to minimize direct heat transfer from the LED to

J.L. Davis (✉) • R. Yaga • M. Lamvik • K. Mills • B. Fletcher
RTI International, 3040 E. Cornwallis Road, P.O. Box 12194, Research Triangle Park, NC 27709, USA
e-mail: ldavis@rti.org

© Springer International Publishing AG 2018

W.D. van Driel et al. (eds.), *Solid State Lighting Reliability Part 2*, Solid State Lighting Technology and Application Series 3, DOI 10.1007/978-3-319-58175-0_6

the light conversion layer. In some cases, this approach has been shown to produce lower temperature rises in the phosphor layer, even at high flux levels [3].

Accelerated life testing (ALT) using high temperature alone or temperature and humidity environments can be used to investigate the aging characteristics of SSL devices. Previous studies have shown that accelerating environments such as 85 °C and 85% relative humidity (RH) can produce color shifts in proximate phosphor LEDs that increase the correlated color temperature (CCT) of the devices [4–6]. The extent of these color shifts appears to be related to the color of the LEDs with higher CCT values being more stable and exhibiting less propensity for large color shifts than LEDs with lower CCT values (i.e., warmer colors). This observation may be due to the higher intrinsic stability of cerium-doped yttrium aluminum garnet (Ce:YAG) phosphors used for cool white lighting compared to nitride phosphors used in warm white lighting [7].

Previous studies of accelerated aging of remote phosphors have typically concentrated on cooler CCT materials with higher Ce:YAG content. Dal Lago et al. examined the performance of 4,000 K remote phosphor plates in accelerated stress testing carried out at temperature levels between 85 and 145 °C [8]. This study, which also included irradiation of the samples with blue light power levels ranging from 40 to 350 mW/cm^2, found a degradation mechanism that significantly reduced luminous flux and produced a color shift. The primary degradation mechanism identified in this study was photooxidation of the polycarbonate substrates used for the remote phosphor disks. Mehr et al. also investigated the optical degradation of remote phosphor plates formed on polycarbonate substrates [9, 10]. This work examined samples with CCT values of 4,000 K and 5,000 K and observed degradation in luminous flux and color point stability when the polycarbonate samples were exposed to temperatures between 100 and 140 °C for prolonged periods. Higher temperatures produced faster degradation kinetics and consequently faster lumen depreciation and color shift.

We report herein results on accelerated aging of remote phosphor disks (RPDs) in temperature and humidity environments. This study was conducted at multiple CCT values to provide insights into the potential effects of different chemistries on lumen maintenance and color stability. In particular, this study examines both warm white (2,700 K) and cool white (5,000 K) remote phosphor samples to understand the impact of different phosphor and binder materials on lumen maintenance and color point stability. While this investigation focuses on remote phosphor configurations, the findings on phosphor stability in accelerated life tests may have implications for proximate phosphor LEDs as well.

6.2 Methods

The remote phosphor disk (RPD) samples used in this study were 61.5 mm polycarbonate disks (Intematix) coated on one side with a layer of dispersed phosphors in a binder medium. The samples were purchased from a commercial source around

Table 6.1 Physical characteristics of the remote phosphor samples used in this study

Intematix disks in WHTOL					
Intematix color series	Part number	CRI	Average initial CCT measurement	Diameter (mm)	Thickness (mm)
2,700 K	CL-927-LR-PC	90	2,687	61.5	2.12
5,000 K	CL-750-LR-PC	70	4,935	61.5	2.12

and in 2012. Two different CCT values, 2,700 K and 5,000 K, were used in this study. Fourier transform infrared (FTIR) spectroscopy identified the composition of the binder layer in the 2,700 K samples to be a polyurethane (61% match), while the binder layer of the 5,000 K RPD samples was a poly(methyl methacrylate) (PMMA) (83% match). X-ray diffraction was used to identify the phosphor composition in samples for both CCT values. The 5,000 K samples were found to contain a YAG phosphor, and the 2,700 K formulation used a mixture of YAG and silicon nitride phosphors. Thus, these samples provide the opportunity to investigate the impact of both binder and phosphor chemistry on remote phosphor performance. Table 6.1 gives the physical characteristics of the RPD samples as well as the average initial CCT measurement when used in a light engine. In addition to the RPD samples, blank polycarbonate disks were made from stock materials. The disks were cut to 61.5 mm and were used as controls in all experimental runs.

6.2.1 Wet High-Temperature Operational Lifetime (WHTOL) Test

Wet high-temperature operational lifetime (WHTOL) tests were used to accelerate aging of the RPD samples. One version of this test consisted of a continuous exposure to 85 °C and 85% RH (hereafter termed 85/85) following procedures outlined in JESD22-A101C. In addition, WHTOL tests were also performed on a second population of samples under conditions of 75 °C and 75% RH (hereafter 75/75).

WHTOL testing was conducted on the RPD samples in two different environmental chambers (Tenney T20RC-2.0 for 85/85 and Tenney TC10RS for 75/75). The RPD samples were exposed to WHTOL concurrent with luminaire testing. So, the RPD samples were placed on the top shelf in each chamber to avoid direct illumination from the luminaires. Since the rate of polycarbonate photooxidation is dependent upon the intensity of blue radiation exposure [11], this configuration minimized photooxidation of the polycarbonate substrates and allowed for this study to focus on the effects of temperature and humidity.

6.2.2 Testing the RPD Samples

After each 250 h of WHTOL exposure, the RPD sample populations, consisting of ten samples each of 2,700 K and 5,000 K CCT values, were removed from the environmental chamber and their performance measured in a light engine using a calibrated 65″ integrating sphere. The photometric properties of the RPD samples were measured by placing each sample in a light engine (Intematix) that contained six blue LEDs (emission wavelength maximum 450 nm). The light engine was not subjected to aging, but was maintained in pristine condition throughout. All samples were tested using the same light engine.

All integrating sphere measurements of the remote phosphor samples were performed using the 2π configuration with the light engine and RPD samples mounted on the exterior of the sphere with an adapter plate. Corrections to sphere readings were made for zero level and self-absorbance, as outlined in LM-79, and sphere calibrations were performed using a National Institute of Standards and Technology (NIST)-traceable forward flux standard from Labsphere (Model Number FFS-100-1000).

In all experiments, the light from the blue LEDs first traveled through the phosphor layer of the RPD samples, then through the polycarbonate substrate, and then into the sphere. The LEDs in the light engine were powered by a BK Precision 1,760 A lab power supply at a current-limiting setting of 200 milliamps.

In addition to photometric properties, the optical properties of the samples were measured after each 250 h WHTOL exposure. Total transmittance (%T) measurements were performed using a Cary 5000 UV-Visible-NIR (UV-Vis) spectrometer in conjunction with the Cary Diffuse Reflectance Accessory (DRA). The DRA contains an integrating sphere that is coated with a highly reflective diffuse reflector. All disk transmittance measurements were made with a double-beam optical bench and sample blank, and background corrections were applied. In performing %T measurements, the disks were placed on the exterior of the integrating sphere of the DRA in between the light source and integrating sphere. This configuration closely mimics the intended operation of the RPD samples in a light engine.

Fourier transform infrared (FTIR) spectroscopy was used to identify some of the RPD constituent materials and to follow their changes during WHTOL tests. FTIR spectra were acquired using the attenuated total reflection (ATR) technique by placing a sample on an ATR plate. The FTIR spectra were acquired using a Thermo Fisher Nicolet 6700 FTIR spectrometer in conjunction with a Thermo Fisher Nicolet “Smart Orbit” diamond ATR accessory. Identifications of materials were based on the spectral libraries installed in this FTIR system.

6.3 Results

Populations of cool white (5,000 K CCT) and warm white (2,700 K CCT) RPDs, each with ten samples, were subjected to both 85/85 and 75/75 WHTOL in increments of 250 h continuous exposure. Thus, a total sample set of 40 RPDs

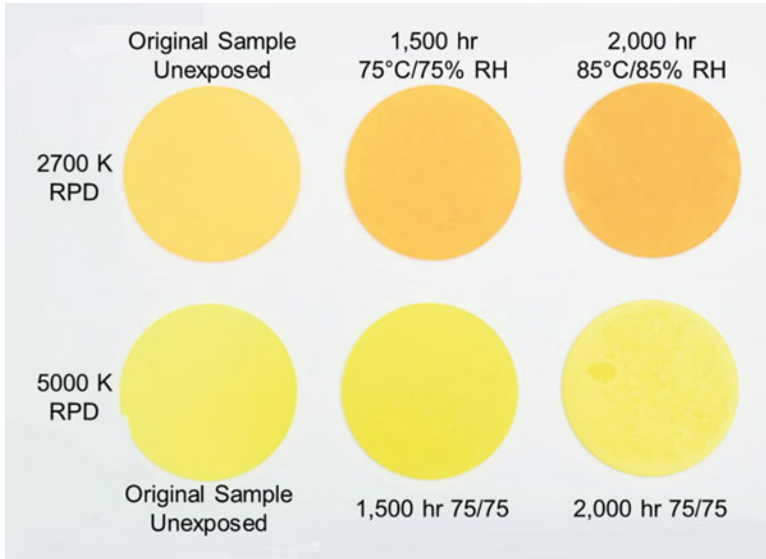

Fig. 6.1 Picture of representative RPD samples from this study. The 2,700 K RPD samples are shown in the *top row* with an unexposed sample on the *left*, a sample exposed to 1,500 h of 75/75 in the *center*, and a sample exposed to 2,000 h of 85/85 on the *right*. The 5,000 K RPD samples are shown in the *bottom row* with an unexposed sample on the *left*, a sample exposed to 1,500 h of 75/75 in the *center*, and a sample exposed to 2,000 h of 85/85 on the *right*

was studied. The study was terminated after 1,500 h for the 75/75 populations and after 2,000 h for the 85/85 populations. As shown in Fig. 6.1, the samples subjected to either WHTOL setting were darker than the original (i.e., unexposed) samples. This darkening of the RPD samples can be attributed to changes in the binder layer and is discussed below.

6.3.1 Cool White Remote Phosphor Samples

Despite the discoloration of the 5,000 K, cool white, RPD samples, the lumen maintenance of both the 75/75 and 85/85 populations remained high (Fig. 6.2). The lumen maintenance after 1,500 h of 75/75 was better, with only a 1–2% decrease in luminous flux. The 5,000 K RPD sample population subjected to the 85/85 test environment exhibited a sharper decline in lumen maintenance, but still maintained luminous flux levels well above 70% (i.e., L_{70}) in the test light engine, even after 2,000 h of 85/85. In general, the lumen maintenance standard deviation observed for the sample population in 75/75 was small (coefficient of variation (COV) was less than 1%), and the standard deviation was somewhat larger for the 85/85 sample population (COV ranged from 0.8% to 2.4%).

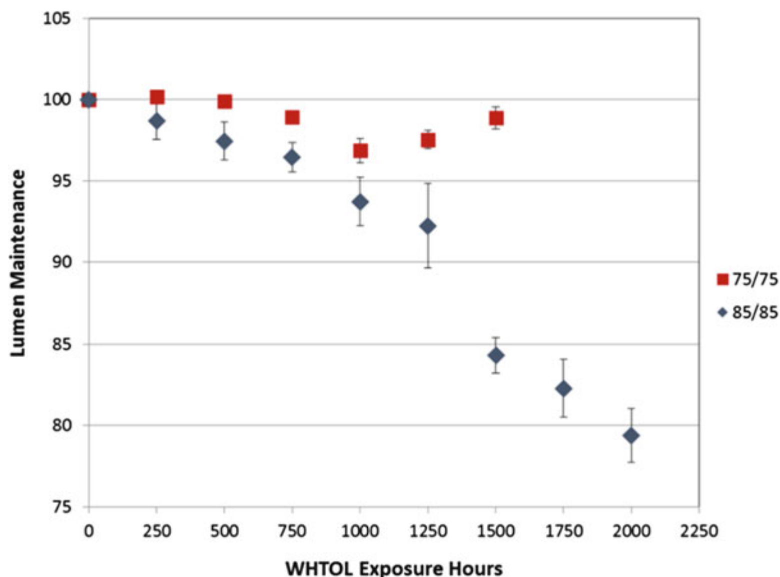

Fig. 6.2 Average lumen maintenance of two separate populations of 5,000 K RPD samples subjected to 75/75 (*red squares*) and 85/85 (*blue diamonds*). The *error bars* represent one standard deviation for measured values of the sample population at each measurement point

In contrast, the color shift behaviors of the 75/75 and 85/85 populations were completely different (see Fig. 6.3). The 75/75 populations exhibited a small color shift to yellow and plateaued after 750 h. A yellow color shift was indicative of either of (1) a relative increase in emission from the phosphor or (2) a relative reduction in blue emission from the LEDs. The color shift for the 85/85 populations was significantly larger and generally blue. As shown in Fig. 6.3, the color of the 85/85 RPD samples shifted steadily over the test period, and there was no indication of plateauing like that seen in the 75/75 populations. A blue color shift is indicative of either (1) a reduction in emissions from the phosphor (e.g., lower efficiency or increased absorption after conversion) or (2) an allowed increase in transmittance of blue light from the LEDs through the RPD sample.

This difference in behavior can be understood by examining the changes in the spectral power distribution (SPD) and diffuse transmittance (%T) for representative samples from both test populations, given in Fig. 6.4. The yellow shift observed for the RPD samples in 75/75 is small and occurred despite a slight drop in transmittance at the phosphor emission wavelengths (see Fig. 6.4a). Further, the transmittance of the samples was unchanged across the LED emission range (400–475 nm). However, there was a slight ($<1\%$) drop in overall SPD peak maximum for the blue emissions, which suggests that more blue photons were being converted by the phosphor. We, therefore, attribute the small yellow shift observed for the 5,000 K RPD samples in 75/75 to a drop in blue photon emission caused by an increase in phosphor conversion.

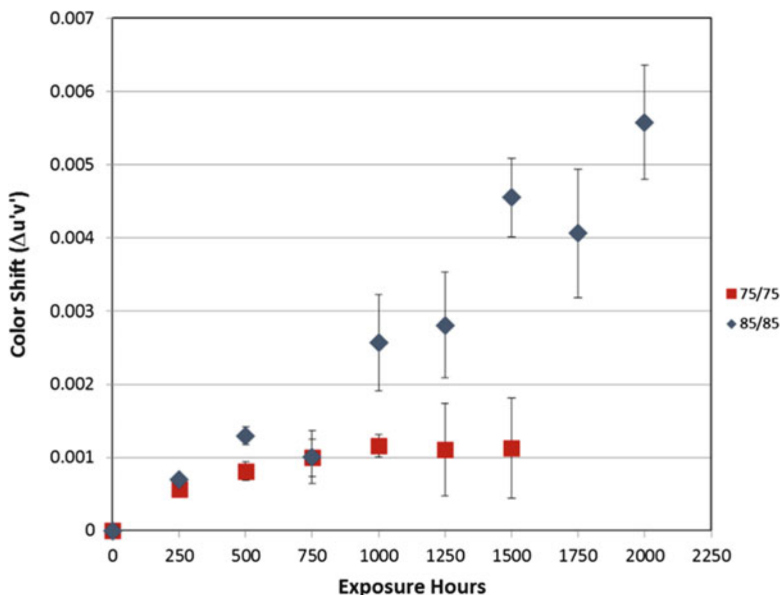

Fig. 6.3 Average color shift of two separate populations (ten samples in each set) of 5,000 K RPD samples subjected to 75/75 (*red squares*) and 85/85 (*blue diamonds*). The *error bars* represent one standard deviation for measured values of the sample population at each measurement point

The blue shift observed for the 85/85 RPD samples can be explained by the more dramatic reduction in phosphor emissions (the spectral region from 500 to 750 nm) compared to the emissions from the blue LED. Judging by the diffuse transmittance spectra given in Fig. 6.4b, it is clear that at least part of the decrease in observed phosphor emissions was due to increased absorption (i.e., reduced transmittance) by the polymer binder over the phosphor emission wavelengths. However, the impact of reduced phosphor efficiency (i.e., lower quantum efficiency) cannot be ruled out as a contributing factor. The Ce:YAG phosphor has been shown to be stable in WHTOL tests, so a reduction in conversion efficiency is deemed to be unlikely [4].

The experimental conditions for this study were chosen so as to minimize the extent of photooxidation of the polycarbonate substrate in order to concentrate on the impact of the phosphor and binder chemistries. We have previously reported on the changes in polycarbonate lenses under the combined influences of WHTOL testing and irradiation from a warm white light source [5]. These previous results demonstrated that photooxidation of polycarbonate in 85/85 changes lens transmittance from greater than 65% over the wavelength range of 350–400 nm to between 5% and 35% over the same wavelength range with as little as 1,250 h of 85/85 exposure. The transmittance change for these WHTOL-aged lens samples was highest at lower wavelengths, indicating that the 350–380 nm spectral region will show significant changes if photooxidation of the polycarbonate substrate is occurring. As shown in Fig. 6.4, this spectral region changed little during WHTOL

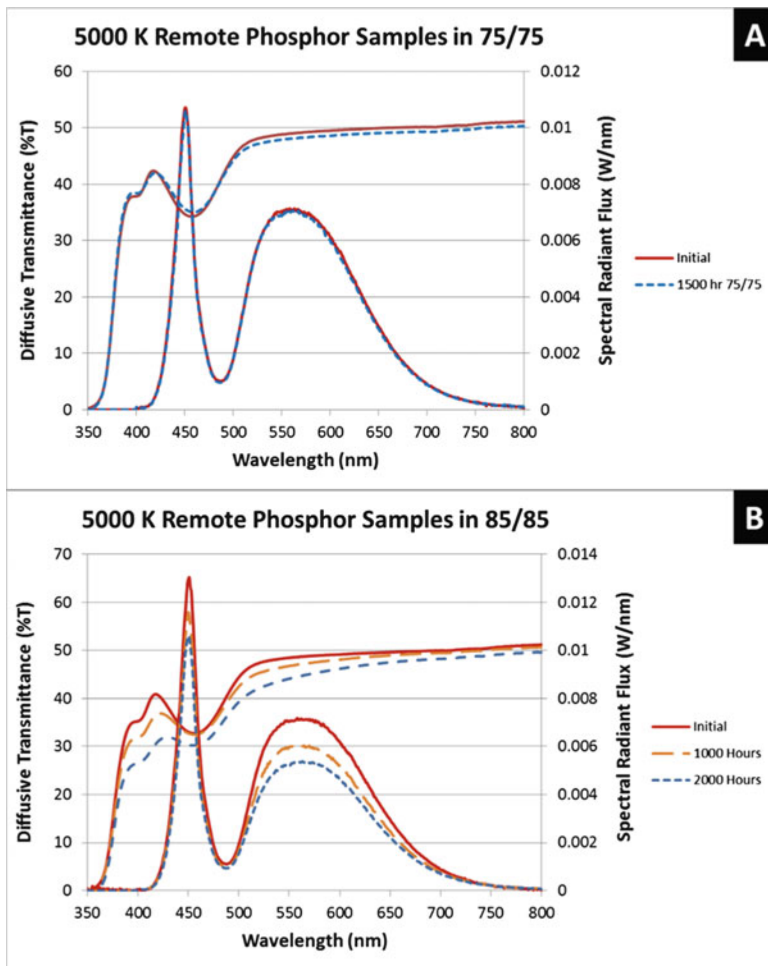

Fig. 6.4 Diffuse transmittance (%T) and spectral power distribution (SPD) of representative 5,000 K RPD samples. All samples in the test matrix were evaluated and exhibited similar behavior. Changes in %T and SPD for the representative sample as received and after 1,500 h of 75/75 exposure are shown in (**a**). Changes in %T and SPD for another representative sample as received, after 1,000 h of 85/85, and after 2,000 h of 85/85 are shown in (**b**)

testing under our experimental conditions, indicating that changes in the polycarbonate substrate had a negligible effect on the results observed in these tests.

6.3.2 *Warm White Remote Phosphor Samples*

The 2,700 K, warm white, RPD samples discolored during WHTOL (see Fig. 6.1), and the final lumen maintenance magnitudes were lower than that observed with the

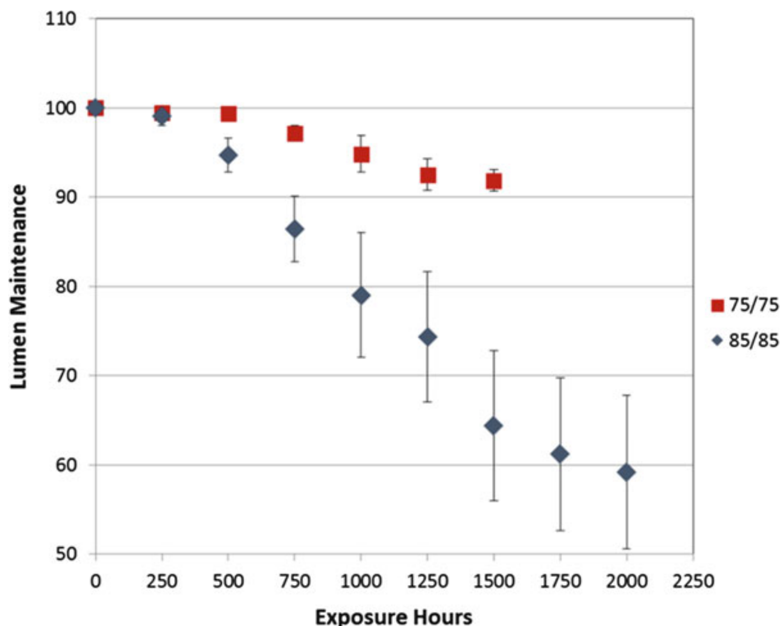

Fig. 6.5 Average lumen maintenance of two separate populations of 2,700 K remote phosphor samples subjected to 75/75 (*red squares*) and 85/85 (*blue diamonds*). The *error bars* represent one standard deviation for measured values of the sample population at each measurement point

5,000 K, cool white, RPD samples. As shown in Fig. 6.5, the lumen maintenance for the 2,700 K RPD samples in 75/75 declined to 92% after 1,500 h of testing, compared to a 98% lumen maintenance level for the 5,000 K RPD samples after the same test period. In addition, the 2,700 K RPD sample population subjected to the 85/85 test environment exhibited an even sharper decline in lumen maintenance with the average value dropping to below 60% after 2,000 h of 85/85. There was also a much larger standard deviation in the lumen maintenance measurements for the 85/85 sample population (coefficient of variation was greater than 10% after 1,000 h of 85/85) than observed for the 75/75 population. This finding suggests that the phosphor and binder mix used in the 2,700 K formulation is not as intrinsically stable as that of the 5,000 K formulation, in line with previous findings [4, 7].

The color shifts of the 75/75 and 85/85 populations of 2,700 K RPD samples were similar in magnitude (i.e., $\Delta u'v'$), as shown in Fig. 6.6. In testing on the standard light engine, the 75/75 RPD population exhibited a small color shift to yellow. The average color shift for the 2,700 K RPD samples plateaus after 750 h at a level slightly higher than observed for the 5,000 K samples. Each of the ten individual samples in the population exhibited the same behavior, although the magnitude of the plateau varied from 0.001 to 0.003.

When tested in the standard light engine, the magnitude of the color shift for the 85/85 population was similar to that of 75/75. However, the direction of the color shift was generally in the blue direction and there was more variation than seen

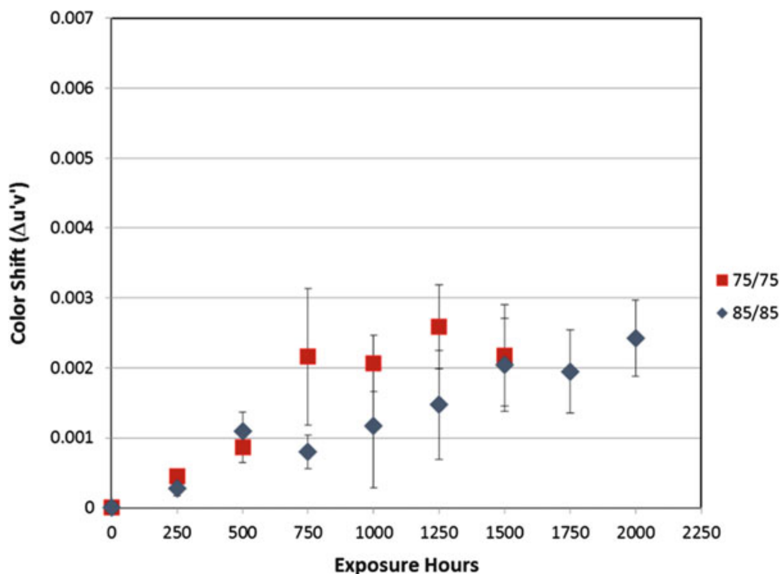

Fig. 6.6 Average color shift of two separate populations (ten samples in each set) of 2,700 K RPD samples subjected to 75/75 (*red squares*) and 85/85 (*blue diamonds*). The *error bars* represent one standard deviation for measured values of the sample population at each measurement point

from the other test samples. Forty percent of the warm white, 85/85 samples had a noticeable yellow shift for the first 500–750 h followed by a pronounced blue shift through the remainder of the test period (totaling 2,000 h). The other 60% of the samples had a consistent blue shift through the test period.

The SPD and %T profiles given in Fig. 6.7 for representative samples provide insights into the changes occurring in the 2,700 K RPD populations. For the representative 75/75 sample, the %T is virtually unchanged at the blue emission wavelengths throughout the exposure period (1,500 h); however, the SPD shows a drop in overall blue emission intensity. This suggests that more of the blue light is being converted by the phosphor, which will proportionally increase yellow emissions and decrease blue emissions, resulting in a yellow shift. This increase in down conversion could be due to increased scattering in the phosphor layer or a change in the optical properties of the sample [12].

Under 85/85 exposure, a proportionally larger absorption of light from 475 to 650 nm can be observed in the %T spectrum, suggesting that the urethane binder used for the 2,700 K samples is absorbing an increasing amount of emissions from the phosphor. The urethane binder also absorbs an increasing amount of blue radiation from the LED. As discussed above, absorption by the polycarbonate substrate can be judged to be no more than a minor contribution, since the spectral region of 350–380 nm is unchanged in all 85/85 measurement samples (see Fig. 6.7). If polycarbonate oxidation was occurring to an appreciable extent, this region would show increased absorbance (i.e., decreased transmittance) due to

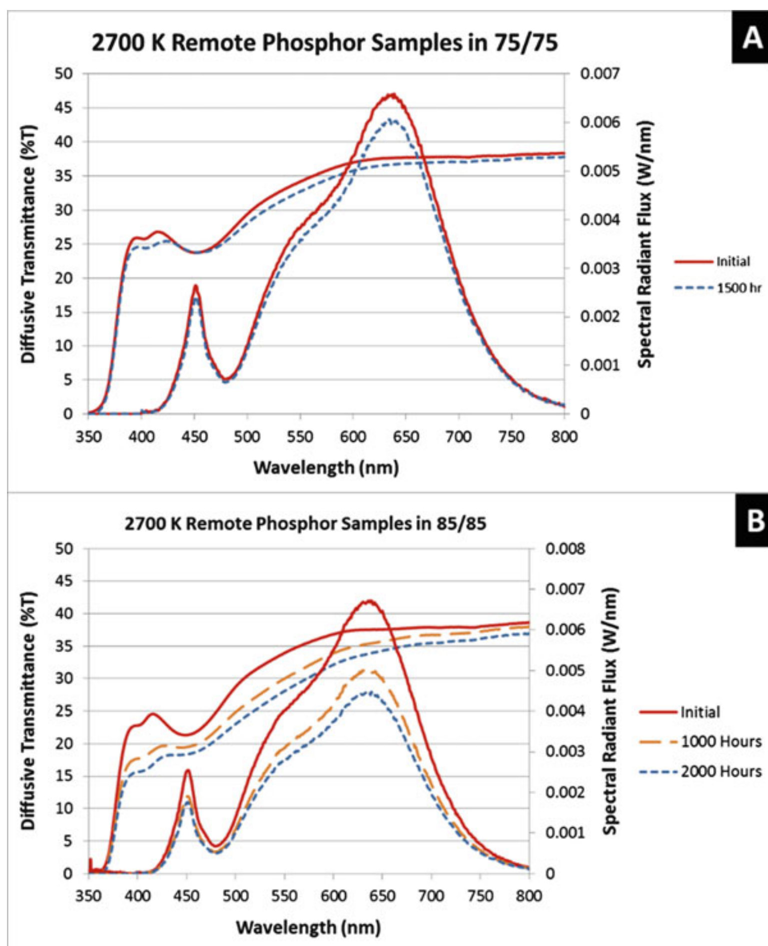

Fig. 6.7 Diffuse transmittance (%T) and spectral power distribution (SPD) of representative 2,700 K RPD samples. All samples in the test matrix were evaluated and exhibited similar behavior. Changes in %T and SPD for the representative sample as received and after 1,500 h of 75/75 exposure are shown in (**a**). Changes in %T and SPD for another representative sample as received, after 1,000 h of 85/85, and after 2,000 h of 85/85 are shown in (**b**)

polycarbonate photooxidation [5]. Therefore, the general trend of a blue shift in 85/85 appears to be due to urethane binder used for this phosphor formulation.

6.3.3 FTIR Studies of Binder Properties

FTIR was used to study the change in the binder properties before and after WHTOL and the results are shown in Fig. 6.8. For convenience, only the results

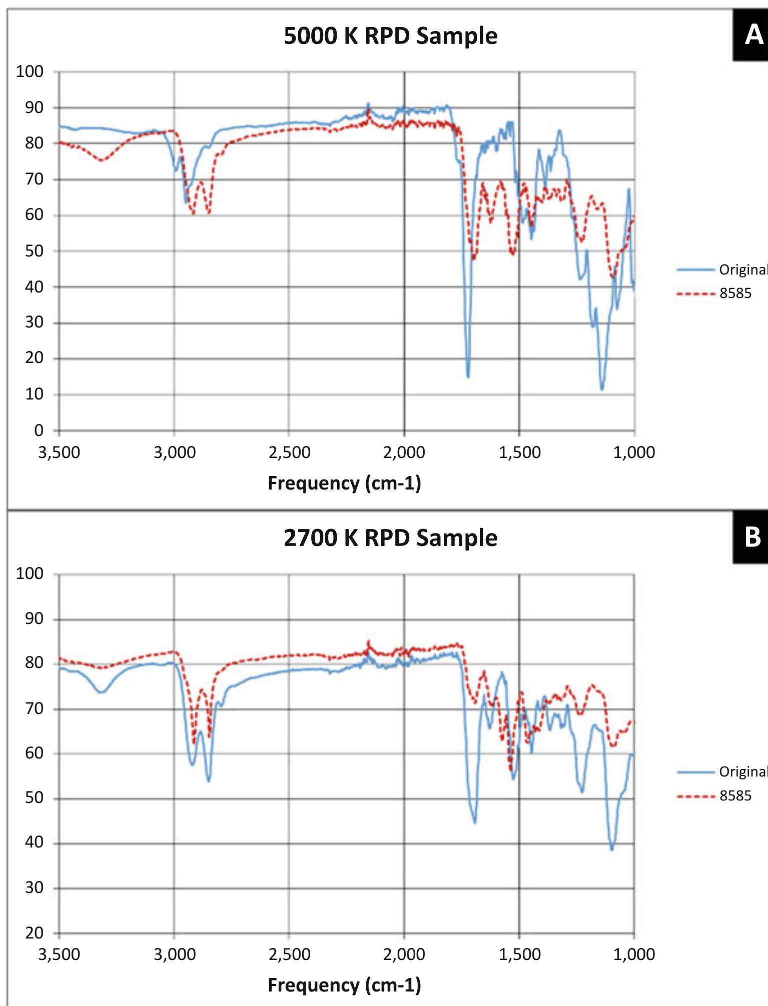

Fig. 6.8 FTIR spectra of the binder-phosphor layers for the 5,000 K and 2,700 K RPD samples. The *top panel* shows the spectra for representative 5,000 K RPD samples both as received and after 2,000 h of 85/85. The *bottom panel* shows the spectra for representative 2,700 K RPD samples both as received and after 2,000 h of 85/85

for an unexposed sample and a representative sample after 2,000 h of 85/85 are shown. The FTIR results provide clear evidence of changes in the chemical composition of the binder layers for both the 5,000 K and 2,700 K samples, and these changes may account for the discoloration that was observed after WHTOL exposure. These changes may be significant enough to alter the optical properties of the binder layer.

The 2,700 K RPD samples used a polyurethane binder. After 85/85, the spectrum of the binder layer underwent several significant changes. First, while the NH stretching (ν(NH)) mode at ~3,318 cm^{-1} was present in both the unexposed and 85/85 samples, the intensity of this peak dropped in the 85/85 samples. In both sample groups, the ν(NH) peak is superimposed on a broad peak that is likely due to the ν(OH) mode of hydrogen-bonded water. Second, the frequency of the urea carbonyl stretching mode (ν(CO)) at 1,693 cm^{-1} is consistent with significant hydrogen bonding in the film, and there was a change in intensity and a shift in peak location. This suggests additional hydrogen bonding in the film, introduced by the WHTOL environment. These spectral shifts provide an indication of the initial presence of water in the urethane film and the introduction of additional water into the film during 85/85 exposure [13]. There were also changes in peak locations and intensities in the 1,000–1,630 cm^{-1} region. The spectral changes occurring during WHTOL are characteristic of significant chemical changes in the binder layer, although the exact nature of these changes was not determined.

The 5,000 K RPD samples used a PMMA binder. As shown in Fig. 6.8, the most notable difference between the unexposed sample and the sample after 2,000 h of 85/85 was the introduction of OH groups, as evidenced by the appearance of a broad ν(OH) mode at 3,314 cm^{-1}. The width of this peak indicates that significant hydrogen bonding is occurring in the film, and this is supported by a noticeable red shift of the ν(C=O) peak from 1,722 to 1,697 cm^{-1}. Additional differences between the original and the WHTOL spectra were the emergence of another ν(CO) mode at 1,624 cm^{-1} and a significant change in the ester stretch vibrations (ν_s(OCO)) in the 1,140–1,179 cm^{-1} range [14]. Thus, while it is unclear whether water uptake is occurring within the phosphor particles or the binder, the spectral shifts observed for vibrational modes of the PMMA binder suggest that it *is* involved in the hydrogen bonding. The carbonyl oxygen of PMMA is most likely involved in the moisture uptake process [15]. These observed spectral changes are also indicative of chemical changes occurring in the binder layer, including an increase in hydrogen bonding and the possibility of water sorption into the film.

FTIR analysis was also performed on a representative polycarbonate substrate from this study. The analysis indicated minimal oxidation of the polycarbonate material, in line with the UV-Vis results discussed above.

6.4 Discussion

Remote phosphor structures have been used in a variety of SSL devices ranging from lamps to light engines for downlights. These products are advantageous because of their flexible designs and their potential ability to provide both high lumen maintenance and excellent color stability. A variety of materials and structures are also possible with remote phosphor devices. For example, the remote phosphor can be coated onto polycarbonate or glass disks or embedded into polymeric lenses during the molding process. However, achieving high luminaire

performance requires an understanding of the materials used to construct the remote phosphor plate as well as other substrates used in the SSL device.

Polycarbonate substrates can undergo photooxidation in the presence of blue radiation. This degradation process has been shown to have a significant impact on the performance of remote phosphor materials using polycarbonate substrates [8, 9, 11]. Polycarbonate photooxidation is characterized by the appearance of a yellow to amber color in the material and a significant reduction in transmittance that is especially pronounced at low wavelengths [5, 9]. The extent of this effect is clearly visible in the sample photos shown by Dal Lago [8] which appear much darker than the samples produced by these experimental protocols. Since this photooxidation process has been shown to be thermally activated in the absence of light [8], reducing blue irradiance to a low level and maintaining mild temperatures (<90 °C) can effectively shut down the polycarbonate oxidation pathway and enable the study of other effects in the phosphor layer.

In this study, we intentionally minimized the light exposure of the RPD samples to enable a focus on the effects of the binder and phosphor chemistries. There were significant differences in the chemical composition of the two sample groups, with the 2,700 K RPD samples using a urethane binder and a mix of nitride and YAG phosphors and the 5,000 K RPD samples using a PMMA binder and only YAG phosphors.

As shown in the FTIR analysis in Fig. 6.8, both binders undergo significant chemical changes during WHTOL, specifically in their polar groups, e.g., ester and urea linkages. Since the index of refraction of a material is determined in part by the concentration and orientation of polar groups [16], it is not unreasonable to assume that the chemical changes observed in the binder layer with FTIR can also change the refractive index of the polymer. Since the optical path length and light-scattering properties of phosphor particles embedded in a polymer matrix will be a function of the refractive indices of both the polymer and the phosphor [17, 18], the chemical changes observed in the binder layer can be expected to change the light emission properties of the RPG samples. We attribute the yellow shift observed in 75/75 to this effect.

As the chemical reaction proceeds, additional changes in the binder layer occur and the light absorption properties of the material change. This effect is illustrated in Figs. 6.4b and 6.7b. The increased absorption, especially in the 500–800 nm spectral region, will reduce overall emissions from the phosphor and account, at least in part, for the blue shift observed in both CCT groups exposed to 85/85.

The difference in phosphor chemistry also plays a significant role in the performance of the RPD samples in WHTOL. The Ce:YAG phosphor, which is often the only phosphor in cool white LEDs and a component of the phosphor mix for warmer colors, is known to be highly stable. In contrast, the red phosphors typically used in warm white LEDs are known to be less stable and can exhibit both color shifts and a reduction in quantum efficiency [7]. Therefore, the possibility of phosphor degradation should be examined, at least for the 2,700 K samples.

We have previously demonstrated that high-power LEDs (HPLEDs) using silicone encapsulants and Ce:YAG phosphors (for cool white colors) and doped

nitride phosphors (for warm white colors) exhibited significantly different behaviors [4, 19–21]. Cool white LEDs typically exhibit little color shift due to their chemical stability, and this study concurred, with the emission peak of Ce:YAG phosphors showing little change after WHTOL. In contrast, the emission peak of doped nitride phosphors underwent a significant green shift in WHTOL. Our work also demonstrated that the matrix material for the phosphor particles has a significant impact on the rate at which these changes will occur. Nitride phosphors combined with silicone binders and encapsulants will exhibit large color shifts in WHTOL, since silicone is permeable to water. In contrast, glass matrix materials, which are impervious to water, will not experience the water effect.

In the current study, the behavior of the Ce:YAG phosphors of the 5,000 K RPD samples was in agreement with our previous results for cool white HPLEDs in WHTOL. Therefore, the observed reduction in luminous flux and color shifts for the 5,000 K RPD samples is attributed to changes in the binder layer. However, no significant spectra shifts were observed for the warm white RPD samples (see Fig. 6.7), and the observed color shift was minimal. This contrasts greatly with our results with HPLEDs using silicone encapsulants in which $\Delta u'v'$ values as large as 0.02 (10$\times$ larger than observed here) were reported after 2,000 h of 85/85 [19–21]. However, warm white phosphors embedded in a water-impermeable glass were found to exhibit color stability levels comparable to those observed in the study. Since polyurethane has a significantly lower water permeability than silicone [13], the relative color point stability, including the absence of a shift in the phosphor emission maximum, is attributed to the polyurethane binder used in the 2,700 K samples. Since the polyurethane layer is preventing the degradation of the warm white phosphor, the observed loss of luminous flux is attributed mainly to light absorption in the binder layer. Secondary effects, such as the loss of quantum efficiency, may also be occurring but likely to a lesser extent.

Although this study has focused on remote phosphor samples, it provides insights into the properties of materials that may be used in LED devices. First, changes in the chemical properties of materials used in remote phosphor binders can not only reduce light emission through absorption effects but can also change the emission color if the chemical changes in the binder are significant enough to change the material's refractive index. Second, while red phosphors used in warm white LEDs may be subject to color point changes due to oxidation, these changes can be mitigated to some extent through proper material choices, such as the use of less water-permeable materials like polyurethane.

6.5 Conclusions

Understanding the chemical properties of materials used in LED devices is critical to developing products that meet or exceed lifetime expectations. Accelerated testing of remote phosphor disks (RPDs) was performed using wet high-temperature operational lifetime (WHTOL) testing. The results demonstrated that

the chemical properties of phosphors and binders used in RPDs have a significant impact on lumen maintenance, color stability, and the directions of color shifts. Chemical changes in the RPD polymer binder from WHTOL include increased absorption at certain wavelengths and altered index of refraction of the RPD. Both of these changes caused a color shift in the RPDs, although in different directions. The phosphor chemistry also had a big effect, with YAG phosphors exhibiting higher stability and better lumen maintenance than YAG/silicon nitride phosphor blends. In addition to providing insights into the performance of remote phosphor devices, these findings emphasize that understanding the properties of materials used in LED devices is critical to achieving high lumen maintenance and color point stability over the life of the product.

Acknowledgments Todd Ennis of RTI performed the x-ray diffraction analysis of the remote phosphor disks. Funding for this work was provided by the US Department of Energy under Award Number DE-EE0005124.

Disclaimer This report was prepared in part as an account of work sponsored by an agency of the US Government. Neither the US Government nor any agency thereof, nor any of their employees, makes any warranty, express or implied, or assumes any legal liability or responsibility for the accuracy completeness, or usefulness of any information, apparatus, product, or process disclosed, or represents that its use would not infringe privately owned rights. Reference herein to any specific commercial product, process, or service by trade name, trademark, manufacturer, or otherwise does not necessarily constitute or imply its endorsement, recommendation, or favoring by the US Government or any agency thereof. The views and opinions of authors expressed herein do not necessarily state or reflect those of the US Government or any agency thereof.

References

1. E. Fred Schubert, *Light-Emitting Diodes*, 2nd edn. (Cambridge University Press, Cambridge, UK, 2006)
2. S. Watzke, P. Altieri-Weimar, in *2014 15th International Conference on Thermal, Mechanical, and Multi-physics Simulation and Experiments in Microelectronics and Microsystems (IEEE EuroSimE)*. Degradation of silicone in white LEDs during device operation: a finite element approach to product reliability prediction (Ghent, 2014)
3. H. Luo, J. Kim, E. Schubert, J. Cho, C. Sone, Y. Park, Appl. Phys. Lett. **86**, 243505 (2005)
4. J.L. Davis, K. Mills, M. Lamvik, R. Yaga, S.D. Shepherd, J. Bittle, N. Baldasaro, E. Solano, G. Bobashev, C. Johnson, A. Evans, in *Proceedings of the 2014 15th International Conference on Thermal, Mechanical, and Multi-physics Simulation and Experiments in Microelectronics and Microsystems* (*IEEE EuroSimE*) System reliability for LED-based products (Ghent, 2014)
5. J.L. Davis, M. Lamvik, J. Bittle, S. Shepherd, R. Yaga, N. Baldasaro, E. Solano, G. Bobashev, Insights into accelerated aging of SSL luminaires. Proc. SPIE: LED Based Illumination Syst. **8835**, 88350L-1–88350L-10 (2013)
6. S.D. Shepherd, K.C. Mills, R. Yaga, C. Johnson, J.L. Davis, in *Proceedings of the SPIE 9190*. New understandings of failure modes in SSL luminaires (2014)
7. C.W. Yeh, W.T. Chen, R.S. Liu, S.F. Hu, H.S. Sheu, J.M. Chen, H.T. Hintzen, J. Am. Chem. Soc. **134**, 14108–14117 (2012)

8. M. Dal Lago, M. Meneghini, N. Trivellin, G. Mura, M. Vanzi, G. Meneghesso, E. Zanoni, Phosphors for LED-based light sources: thermal properties and reliability issues. Microelectron. Reliab. **52**, 2164 (2012)
9. M.Y. Mehr, W.D. van Driel, G.Q. Zhang, Accelerated life time testing and optical degradation of remote phosphor plates. Microelectron. Reliab. **54**, 1544 (2014)
10. M.Y. Mehr, W.D. van Driel, G.Q. Zhang, in *Proceedings of the 2014 15th International Conference on Thermal, Mechanical, and Multi-physics Simulation and Experiments in Microelectronics and Microsystems* (*IEEE EuroSimE*). Reliability and accelerated test methods for plastic materials in LED-based products (Ghent, 2014)
11. M.Y. Mehr, W.D. van Driel, K.M.B. Jansen, P. Deeben, M. Boutelje, G.Q. Zhang, Photodegradation of bisphenol A polycarbonate under blue light radiation and its effect on optical properties. Opt. Mater. **35**, 504 (2013)
12. R. Tuttle, LED system lifetime and reliability: LED components, presented at Strategies in Light. Las Vegas, 24 Feb 2015
13. M. Shibaya, Y. Suzuki, M. Doro, H. Ishihara, N. Yoshihara, M. Enomoto, J. Polym. Sci. B **44**, 573 (2006)
14. M.O. Bensaid, L. Ghalouci, S. Hiadsi, F. Lakhdari, N. Benharrats, G. Vergoten, Molecular mechanics investigation of some acrylic polymers using SPASIBA force field. Vib. Spectrosc. **74**, 20 (2014)
15. W.J. Lee, J.G. Chang, S.P. Ju, Hydrogen bond structure at the interface between water/poly(methyl methacrylate), water/poly(methacrylic acid), and water/poly(2-aminoethylmethacrylamide). Langmuir **26**, 12640 (2010)
16. J. P. Runt, J. J. Fitzgerald (eds.), *Dielectric Spectroscopy of Polymeric Materials: Fundamentals and Applications* (American Chemical Society, Washington, DC, 1997)
17. H.C. van de Hulst, *Light Scattering by Small Particles* (Dover, New York, 1981)
18. C.F. Bohren, D.R. Huffman, *Absorption and Scattering of Light by Small Particles* (Wiley-VCH, New York, 1983)
19. J.L. Davis, Color shift in LEDs and SSL luminaires, presentation at the 2014 DOE Solid-State Lighting Manufacturing R&D Workshop, San Diego, 8 May 2014
20. J.L. Davis, Solid-state lighting luminaire reliability, presentation at Delft University, Delft, 10 Apr 2014
21. J.L. Davis, K. Mills, R. Yaga, C. Johnson, S. Shepherd, The impact of material properties on the reliability of LED lighting systems, presentation at the 2014 I.E. Conference of Reliability Science for Advanced Materials and Devices (RSAMD), Golden Colorado, 8 Sept 2014

Chapter 7
Thermal Characterization of Die-Attach Material Interface of High-Power Light-Emitting Diodes

Dae-Suk Kim and Bongtae Han

Abstract An advanced inverse approach, based on the transient junction temperature behavior, is proposed and implemented to quantify the resistance of the die-attach thermal interface (DTI) in high-power light-emitting diodes (LEDs). After describing the unique transient behavior of high-power LEDs associated with the forward voltage method, a hybrid analytical/numerical model is utilized to determine an approximate transient junction temperature behavior, which is governed predominantly by the resistance of the DTI. Then, an accurate value of the resistance of the DTI is determined inversely from the experimental data over the predetermined transient time domain using numerical modeling. The proposed inverse approach is capable of determining the DTI to an accuracy of 0.01 K/W, which is sufficiently high to evaluate die bonding manufacturing processes.

7.1 Introduction

Under a given operating current, the light output as well as the lifetime of high-power LEDs decreases as the junction temperature increases [1–3]. A die-attach layer often creates the most significant resistance to the flow of heat from the junction to the heat spreader in high-power LEDs [4–7]. Thus, characterization of the die-attach thermal interface (DTI) in high-power LEDs is one of the most important tasks for assessing performance range and reliability.

The thermal resistance of the die-attach layer is governed by the bond line thickness (BLT), the thermal conductivity of the die-attach material, and the contact resistance at the die-attach interfaces [8]. In addition, the existence of undesired but inevitable voids created by the die bonding processes serves to increase the thermal resistance between the die and the substrate and thus gives rise to a further junction temperature increase [9–13].

D.-S. Kim • B. Han (✉)
Mechanical Engineering Department, University of Maryland, College Park, MD 20742, USA
e-mail: bthan@umd.edu

© Springer International Publishing AG 2018

W.D. van Driel et al. (eds.), *Solid State Lighting Reliability Part 2*, Solid State Lighting Technology and Application Series 3, DOI 10.1007/978-3-319-58175-0_7

It is well known that interfacial thermal resistance can be evaluated using the transient behavior of the device junction temperature [3–5, 14–19], which can be expressed analytically using a model based on the thermal resistance and the thermal capacitance by proceeding carefully through a series of empirical steps. In the approach, the transient junction thermal behavior is determined first from the forward voltage measured during the transient period [15, 20–22]. Next, the thermal impedance curve is obtained by dividing the transient junction temperature change by the power dissipation. The spectral distribution of the observed thermal time constants is, then, extracted from the thermal impedance curve by numerical differentiation and deconvolution. As a next step, the LED structural function is obtained from the one-dimensional Cauer network, by discretizing the time constant spectrum into 100–200 peaks [18], and the thermal capacitance is calculated by dividing the thermal resistance from the time constants at each peak. The sum of the thermal capacitances can then be plotted as a function of the sum of the thermal resistances, which is the cumulative structure function, and the interfacial thermal resistance can be determined from the differential structural function.

Commercial equipment utilizing this principle is available and has been actively used to compare relative changes of the thermal resistance produced by different die-attach materials and/or thicknesses [4, 16, 23]. This approach does not require the thermal properties of the materials used in the device, which is a very attractive advantage in practice. Yet, the mathematically complex process used in this approach (i.e., differentiation and deconvolution) can lead to considerable measurement uncertainties, especially for the thermal resistance of the die-attach layers [24]. Moreover, it is worth noting that the lateral heat spreading resistance in a high-power LED is significant and not easily captured by a 1-D model, as used in this approach [25, 26].

In this chapter, an advanced inverse approach is proposed and implemented to more accurately determine the effective DTI resistance of high-power LEDs. A hybrid analytical/numerical model is first used to determine the approximate transient junction temperature behavior, which is governed predominantly by the resistance of the DTI. Then, a more accurate value of the DTI resistance is determined inversely from the experimental data using numerical modeling.

7.2 Transient Behavior of LED Junction Temperature

The junction temperature of an LED can be measured by the well-known forward voltage method [15, 20–22]. The method is based on the theory that the forward voltage of a semiconductor device has a negative linear relationship with the junction temperature. This negative linear relationship (called a calibration curve) is obtained at a very low probe current to avoid any undesired junction temperature increase while obtaining the calibration curve. In the actual measurements, the probe current is suddenly applied after an LED reaches the steady-state condition under high operating currents. This section is devoted to describing the unique transient behavior of a high-power LED during the application of the probe current.

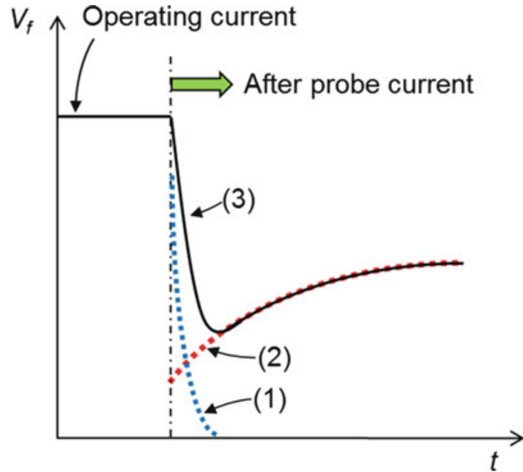

Fig. 7.1 Schematic illustration of (1) the RC delay, (2) the thermal delay, and (3) the combined behavior of the forward voltage from the high operating current to the low probe current

7.2.1 Transient Voltage Behavior of LED

During the transition period (when the forward current changes from the high operating current to the low probe current), the forward voltage, V_f, shows the combined behavior of "diode delay" and "thermal delay." This is illustrated schematically in Fig. 7.1. When the probe current is applied, the ideal diode voltage shows a behavior known as the "RC delay" due to the resistance of an LED and the capacitance of a current source (the blue dotted line (1)). At the same time, the junction temperature starts to decrease due to the small probe current. This gradual reduction of the junction temperature causes the voltage to increase since the junction temperature has the negative linear relationship with the forward voltage (the red dotted line (2)). In actual voltage measurements, the combined effect is observed (the black line (3)). The forward voltage decreases first but starts to increase after the thermal effect overrides the RC delay effect. After the RC delay effect diminishes, the voltage represents the thermal behavior only, and it can be used to measure the resistance of the DTI.

7.2.2 Measurement of Transient LED Junction Temperature

Figure 7.2 shows the schematic illustration of a measurement setup. The junction temperature of the LED was controlled by a high-power thermoelectric cooler (TEC) (LB320: Silicon Thermal), which had a temperature control resolution of ±0.1 °C. When a desired junction temperature was reached, the spectral power distribution (SPD) was measured by an integrating sphere equipped with a spectrometer (SMS–500: SphereOptics). The LED was operated by a source meter (2401: Keithley Instruments). A data acquisition (DAQ) module (USB-6212:

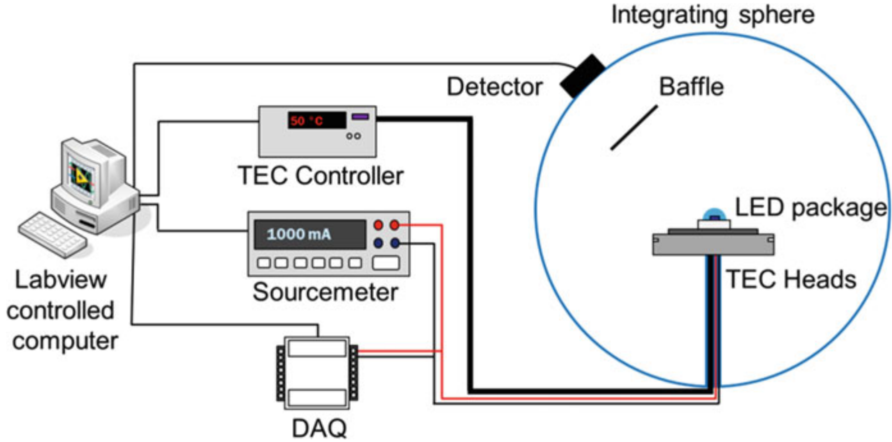

Fig. 7.2 Schematic illustration of the measurement setup

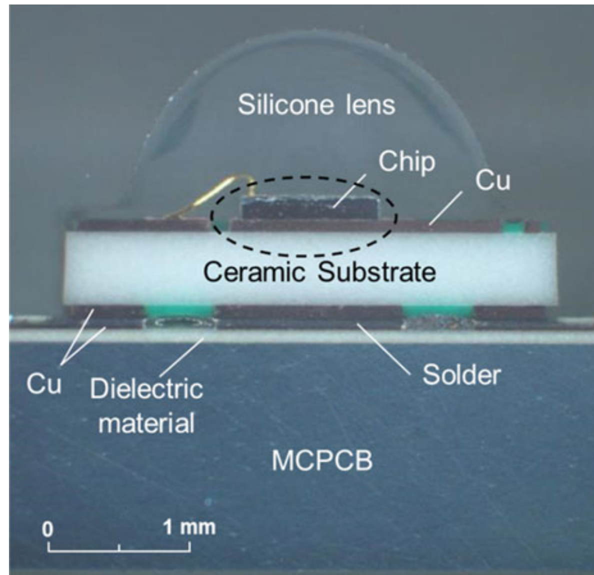

Fig. 7.3 Cross-section image of the high-power blue LED

National Instruments) measured the forward voltage of the LED at the resolution of 16-bits. In order to control the TEC, the source meter, and the DAQ simultaneously, the control routines were integrated by a LabVIEW program.

A cross-section image of a high-power blue LED tested in the study is shown in Fig. 7.3. It is a typical high-power LED with a DTI for lighting applications, which has a total thermal resistance of 10 K/W. The high-power blue LED chip is mounted on a ceramic substrate to form a package, which is subsequently mounted on a metal core printed circuit board (MCPCB) using solder connections. Figure 7.4 also

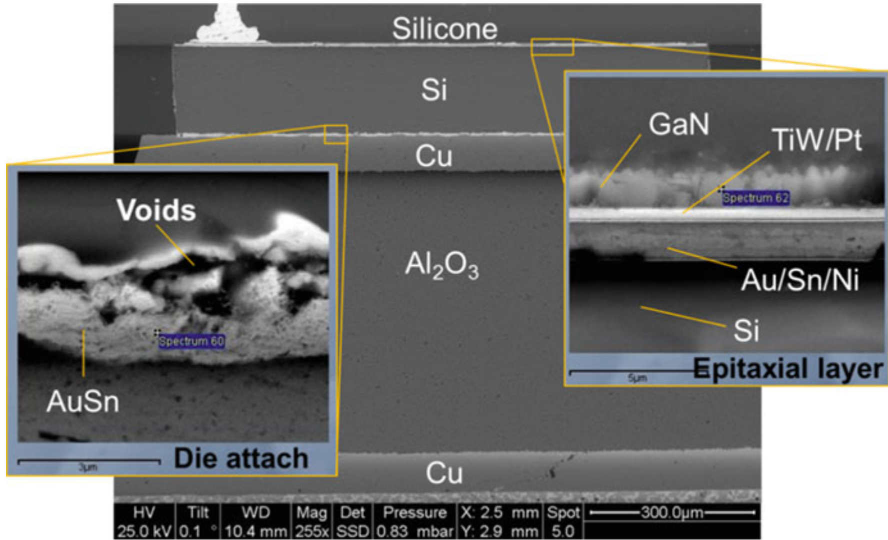

Fig. 7.4 SEM image of the epitaxial layer, the die attach, and the LED package

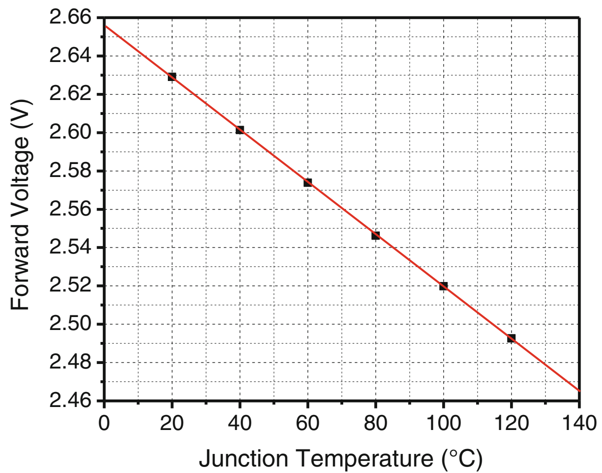

Fig. 7.5 Calibration curve of the blue LED

shows the SEM picture of a region marked by a dashed ellipse in Fig. 7.3, containing the epitaxial layer, the die attach, and the ceramic substrate. There is virtually no defect in the epitaxial layer, but many voids appear in the interfacial region between the silicon substrate and the die attach.

The calibration curve was obtained by measuring the forward voltage under a low injection current of 10 mA, which showed the highest R^2 value (0.999), at different temperatures. The low current was applied only for 10 ms to ensure that the effect of the heat generated by the current on the junction temperature was negligible. The results are shown in Fig. 7.5, from which the slope and the

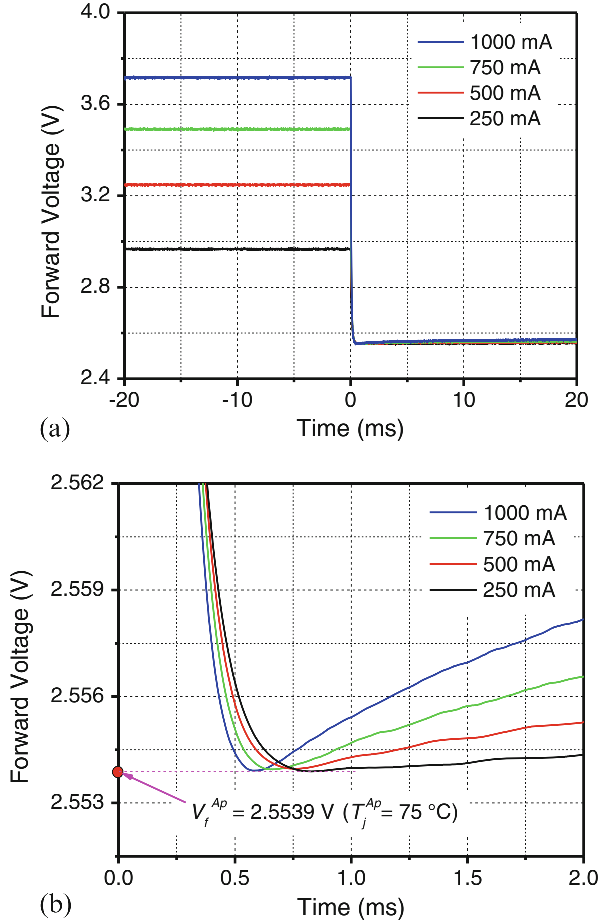

Fig 7.6 Transient voltage behaviors under four different operating currents in (**a**) the total history and (**b**) the zoomed-in view

y-intercept were determined to be −1.36 mV/K and 2.6559 V, respectively, which is close to the theoretical slope of GaN (−1.7 mV/K) [20].

The transient voltage behavior, under four different operating currents, is shown in Fig. 7.6. The TEC was controlled to produce the same minimum voltage value (2.5539 V) for all four operating currents, which corresponded to 75 °C in the calibration curve. This temperature will be referred to as the "apparent junction temperature (T_j^{Ap})." The well-known Savitzky-Golay smoothing filter was employed to reduce the random noise of the experimental data. The experimental data have repeatability within 0.14 mV (corresponding to 0.1 °C). The total history is shown in Fig. 7.6a, and the zoomed-in view containing the minimum voltage is shown in Fig. 7.6b.

The power dissipation at each current can be determined from the following equation:

$$P_h = I_f V_f - P_r \tag{7.1}$$

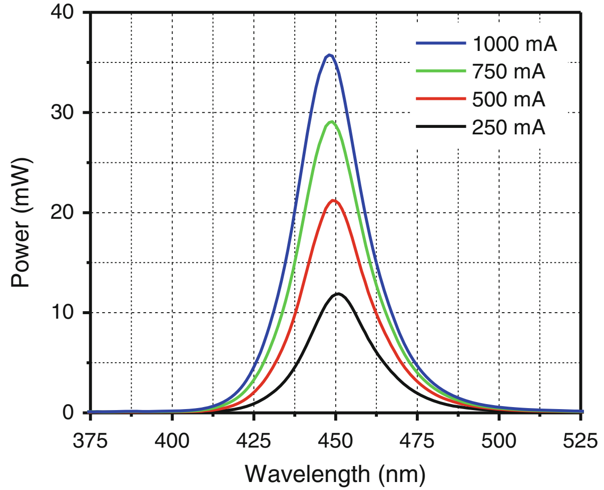

Fig. 7.7 SPDs under the different operating currents at $T_j^{Ap} = 75^\circ$C

Table 7.1 Experimental data of blue LED using the AuSn solder die attach

I_f (mA)	V_f (V)	Electrical power (W)	Radiant flux (W)	Power dissipation (W)	T_s (°C)
250	2.934	0.733	0.316	0.417	69.6
500	3.194	1.597	0.593	1.004	63.8
750	3.428	2.571	0.835	1.736	57.5
1000	3.648	3.648	1.009	2.639	49.8

where P_h is the power dissipation [W], I_f is the forward current [A], V_f is the forward voltage [V], and P_r is the radiant flux [W] [27]. The above equation requires the forward voltage and current, as well as radiated light power, to yield the power dissipation at each current.

The SPD's obtained at the four operating currents are shown in Fig. 7.7. The emitted light power was determined from the SPD's, and it was subtracted from the total electrical power to calculate the power dissipation. The electrical power, the radiant flux, the power dissipation, and the surface temperature of the TEC are summarized in Table 7.1.

The transient junction temperature behavior can be obtained from the transient voltage behavior using the calibration curve. The transient junction temperature behavior is shown in Fig. 7.8.

7.3 Transient Domain for Inverse Approach

The transient thermal behavior is affected by various layers in the LED device. In order to determine the DTI resistance accurately, it is first necessary to define the transient domain that is governed predominantly by the resistance of the DTI. This

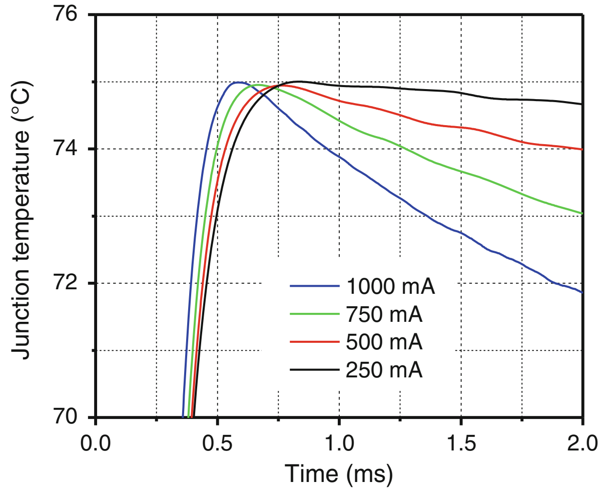

Fig. 7.8 Transient junction temperature behavior at $T_j^{Ap} = 75^{\circ}C$

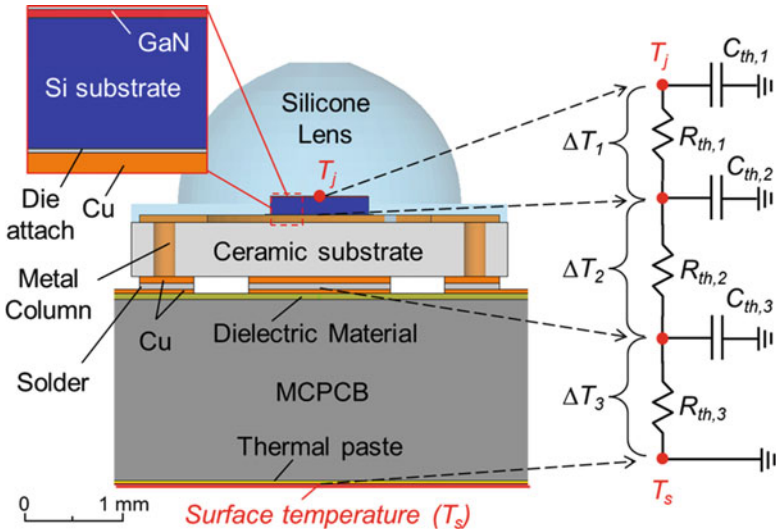

Fig. 7.9 Schematic illustration of the hybrid analytical/numerical model

section describes a hybrid analytical/numerical model of multiple conduction thermal time constants that is utilized to determine the DTI dominant region.

7.3.1 Hybrid Analytical/Numerical Model

The hybrid analytical/numerical model used in the analysis is shown in Fig. 7.9. The model consists of three main layers: the layers produce temperature differences

(1) between the junction and the bottom surface of the die attach (ΔT_1), (2) between the bottom surface of the die attach and the bottom surface of the solder (ΔT_2), and (3) between the bottom surface of the solder and the bottom surface of the thermal paste (ΔT_3). Only the heat transfer in the downward conduction is considered in the model because the upward heat transfer through the lens, as well as the thermal radiation and convection, is assumed to be negligible (less than 1% of the total heat transfer) [28].

The thermal resistance and the thermal capacitance of each layer can be expressed as [15, 18]

$$R_{\mathrm{th}} = \frac{d}{k_{\mathrm{s}} A} \tag{7.2}$$

$$C_{\mathrm{th}} = c_{\mathrm{p}} \rho d A \tag{7.3}$$

where R_{th} and C_{th} are the thermal resistance [K/W] and the thermal capacitance [J/K], d is the thickness along the heat transfer direction [m], A is the cross-section area [m^2], K_{s} is the thermal conductivity [W/(m·K)], c_{p} is the specific heat [J/(kg·K)], and ρ is the density [$\mathrm{kg/m}^3$].

The product of the thermal resistance and the thermal capacitance is called thermal time constant, τ_{th} [s], which is defined as the heating or cooling time required to produce a temperature change equal to 63.2% of the total temperature difference between the initial and the final body temperature. It can be expressed as [15, 18]

$$\tau_{\mathrm{th}} = R_{\mathrm{th}} C_{\mathrm{th}} = \frac{c_{\mathrm{p}} \rho}{k_{\mathrm{s}}} d^2 = \frac{d^2}{\alpha} \tag{7.4}$$

where α is the thermal diffusivity [m^2/s].

The Eqs. 7.2 and 7.4 are valid only when the heat generated at the junction conducts along one dominant path. In an LED structure, however, additional heat spreading paths exist due to the large lateral dimensions of the heat generation layer and package layers, and thus, one-dimensional conduction, as represented in (7.2) and (7.4), is not directly applicable [29].

A supplementary numerical analysis was conducted to more accurately determine the LED thermal resistances, including the spreading resistances in various layers. The numerical model (ANSYS Icepak 15.0) used in the analysis is shown in Fig. 7.10a. In the model, the epitaxial layers, typically just 1 μm thick, were modeled as a single effective layer to reduce the element count in the numerical model. The volume fraction and the mass fraction were used to determine the effective density and the effective specific heat, respectively, while the thermal resistance network equation was used to obtain the effective thermal conductivity of this layer. The effective density, specific heat, and conductivity used in the model are summarized in Table 7.2. The experimentally determined power of 2.639 W at 1 A (Table 7.1) was used in the analysis.

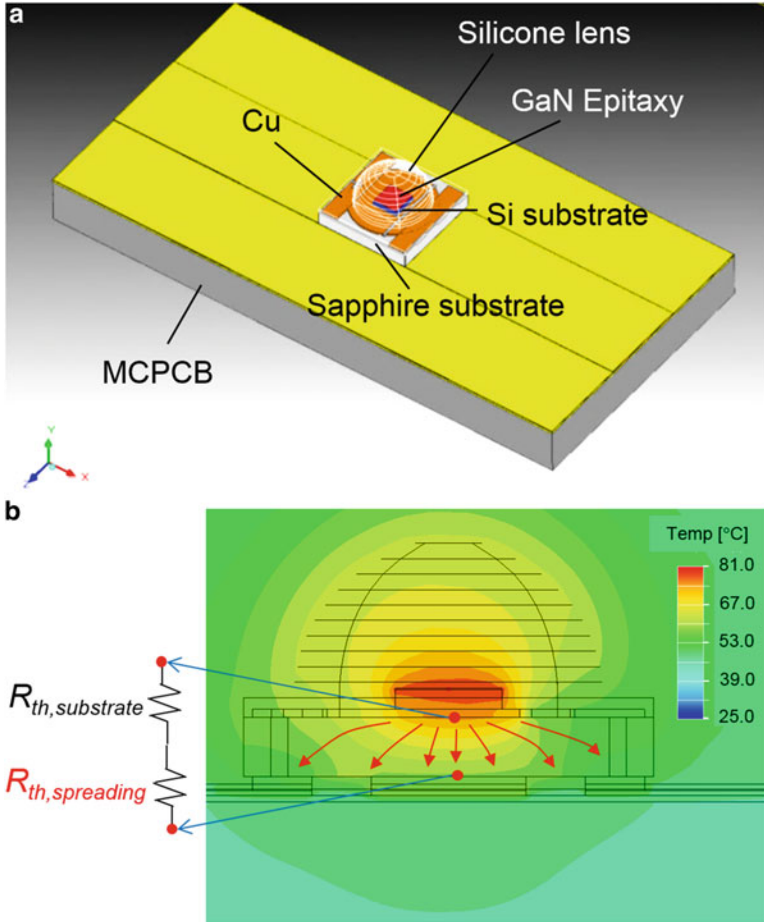

Fig. 7.10 (**a**) 3D model and (**b**) temperature distribution at the steady state

Temperature distribution obtained at the steady-state condition is shown in Fig. 7.10b, where the ambient temperature is 25 °C. The effective thermal resistances, including the spreading resistances, were calculated by

$$R_{\mathrm{th},i} = \frac{\Delta T_i}{P_\mathrm{h}} \quad \text{for} \;\; i = 1, 2, 3 \tag{7.5}$$

where ΔT_i and $R_{\mathrm{th},i}$ are the temperature difference and the corresponding effective thermal resistance of each layer, respectively. The corresponding thermal capacitance, $C_{\mathrm{th},i}$, and thermal time constant, $\tau_{\mathrm{th},i}$,were calculated from Eqs. 7.3 and 7.4; the values are summarized in Table 7.3.

Table 7.2 Material properties used in the numerical model and the analytical solution [30–35]

Name and materials	Density (kg/m^3)	Specific heat (J/kg·K)	Conductivity (W/m·K)
Silicone lens (DOW OE6630)	1170	1512	0.2
Metal column (W, Mo)	14,750	176	150
MCPCB (solder mask)	1250	1300	0.4
Effective Epi (GaN)	10,494	261	70
Chip substrate (Si)	2330	713	124
Die attach (AuSn)	14,500	150	52
Die attach (Ag paste)	1820	882	2.3
Cu layers	8933	385	401
Ceramic substrate (Al_2O_3)	3960	880	22.3
Solder (PbSnIn)	8690	239	56.9
MCPCB (dielectric material)	1900	795	2
MCPCB (Al)	2710	900	140
Thermal paste	2270	1000	2.3

Table 7.3 Thermal resistance, thermal capacitance, and time constant used in the hybrid analytical numerical solution

Layer	Thermal resistance (K/W)	Thermal capacitance (mJ/K)	Time constant (ms)
First layer	1.40	0.26	0.37
Second layer	6.77	42.30	286.24
Third layer	4.64	1683.02	7809.83

7.3.2 *DTI Dominant Domain*

The transient total junction temperature rise relative to the surface temperature, ΔT_{j}, can be described by a multiple exponential function with the π network (Cauer network) [15, 18], which can be expressed as

$$\Delta T_j(t) = P_{\mathrm{h}}\left(\sum_{i=1}^{3} R_{\mathrm{th},i}\cdot \mathrm{e}^{-t/\tau_{\mathrm{th},i}}\right) = \sum_{i=1}^{3} \Delta T_i \cdot \mathrm{e}^{-t/\tau_{\mathrm{th},i}} \quad \text{for } i = 1,2,3 \tag{7.6}$$

where $R_{\mathrm{th},i}$ and $\tau_{\mathrm{th},i}$ are the thermal resistance and the thermal time constant of the ith layer, respectively. Each ΔT_i is calculated simply by multiplying the power dissipation and the thermal resistance of the ith layer.

The transient junction temperature behavior of the LED operated at the maximum allowable forward current (1 A) is plotted in Fig. 7.11a. The y-axis shows the temperature difference between the top and bottom of each layer, and the x-axis shows the time in a log scale. The sum of all three differences is equal to the temperature difference between the junction and surface temperatures; it is denoted as "Total ΔT_j" in the plot (the black line).

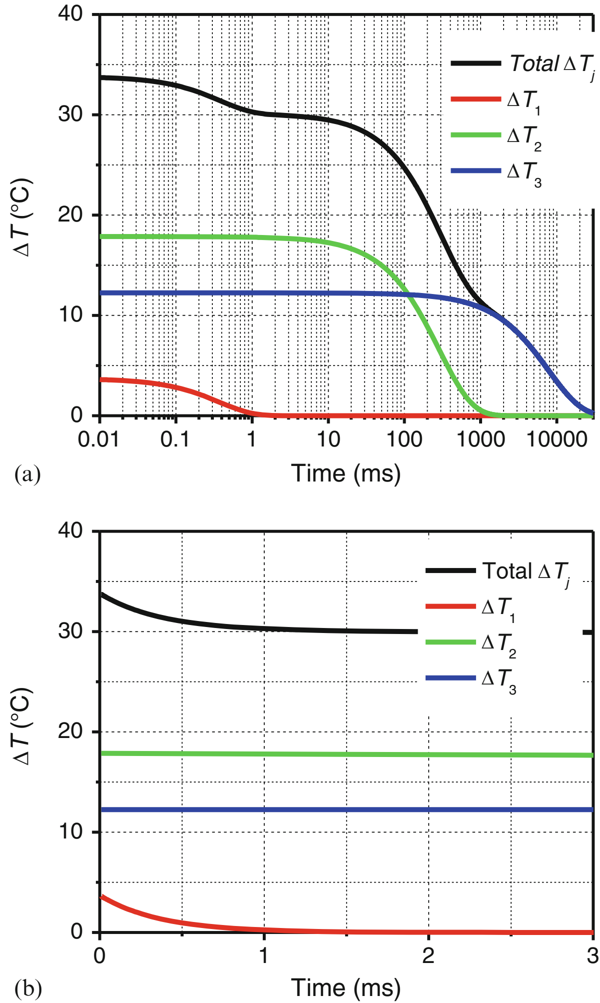

Fig. 7.11 Transient behavior of ΔT for (**a**) 30,000 ms in the log scale and for (**b**) 3 ms in the linear scale

As expected from the extremely small value of the first layer's thermal time constant (Table 7.3), the transient behavior of the LED is governed only by the first layer for the first few milliseconds ($\approx 5 \cdot \tau_{\text{th},i}$). This is illustrated in Fig. 7.11b, where the transient behavior of each layer is plotted in the linear scale only for the first three milliseconds. The effect of the second and the third layer on the transient behavior of the total ΔT_j was also investigated. The thermal resistance of the second and the third layer was altered by $\pm 10\%$. The normalized ΔT_2 and ΔT_3 are plotted in Fig. 7.12. As expected, the normalized temperatures are virtually unchanged for the first 3 ms due to the large time constants. This confirms that the transient behavior over $\approx 5 \cdot \tau_{\text{th},i}$ can be used effectively to characterize the DTI. Considering the range of the thermal resistance of the DTI, the DTI dominant transient time domain was chosen as 2.0 ms, and it will be used for the following analysis.

Fig. 7.12 Normalized transient behavior of ΔT under the different thermal resistance of (**a**) second layer and (**b**) third layer

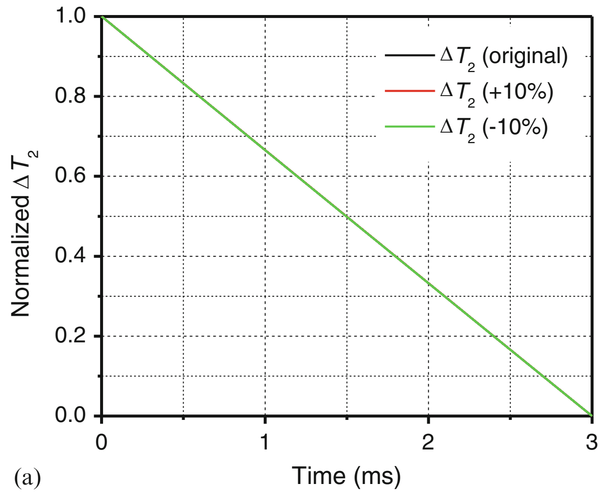

(a)

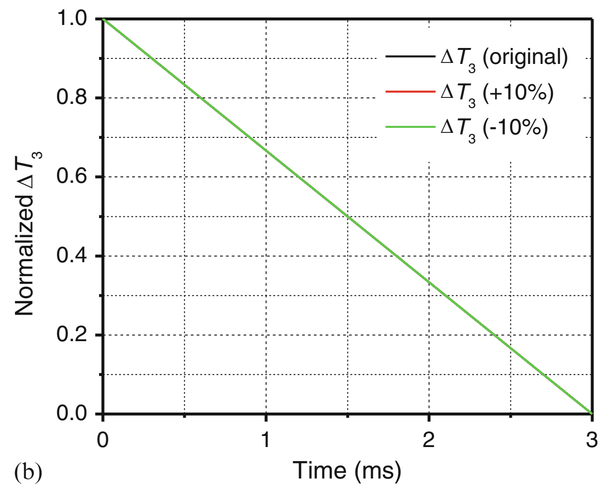

(b)

7.4 Inverse Approach to Determine the Resistance of DTI

In Step 1, a numerical simulation is conducted to determine the steady-state temperature distribution under an operating current. In Step 2, a transient numerical simulation is conducted after switching the power dissipation from the operating condition to the probing condition (determined from Eq. 7.1) while using the results from the previous analysis as the initial condition. The result of Step 2 provides the transient junction temperature behavior. The steady-state temperature distribution under an operating current of 1 A is shown in Fig. 7.13a (Step 1), and the corresponding transient temperature distribution at $t = 2$ ms is shown in Fig. 7.13b (Step 2).

The next step is an iteration process, in which a small resistance that takes account of the DTI is continuously added to the bulk property of the die-attach material until the numerical results match the experimental data.

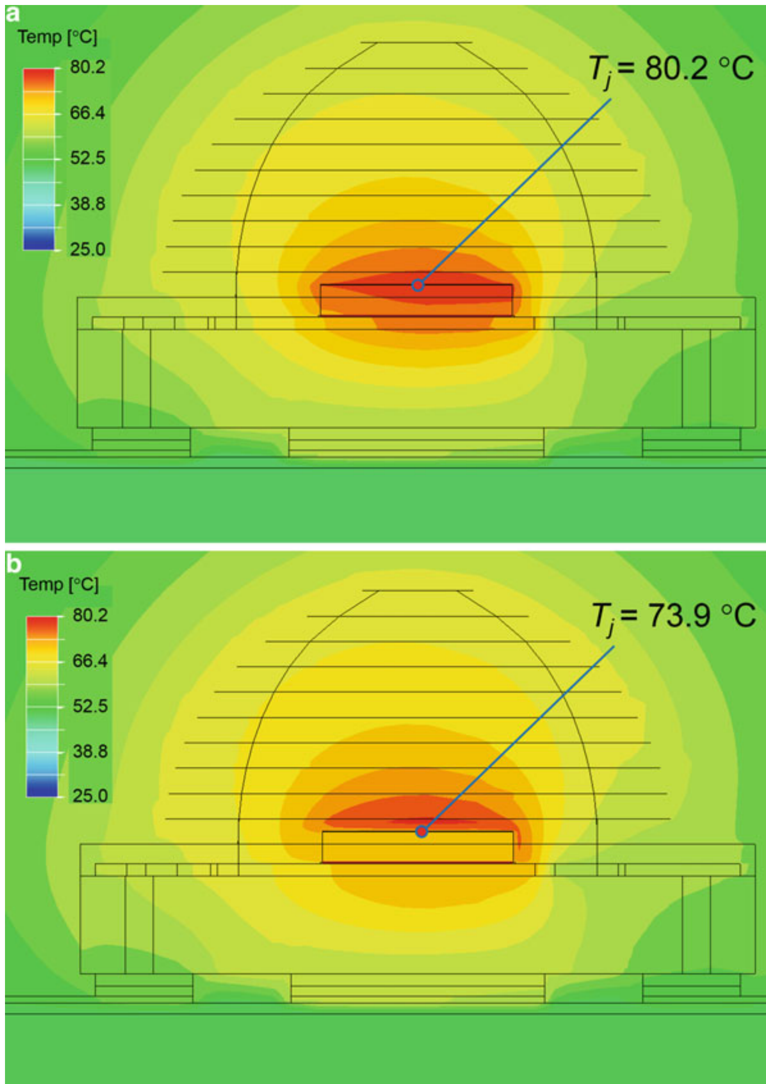

Fig. 7.13 Temperature distribution at (**a**) 0 ms and (**b**) 2 ms

It is important to note that the bulk thermal conductivities of the packaging materials were not known accurately, which affected the junction temperature at $t = 0$. Before the iteration process began, the bulk thermal conductivities were adjusted until the numerical prediction matched to the experimental value at the end of the DTI dominant transient time domain, i.e., $t = 2$ ms. The temperature-dependent properties did not have to be considered because the transient behavior of the junction temperature in the DTI dominant region was not affected by the bulk thermal conductivities and the chip temperature was nearly constant (around 75 °C).

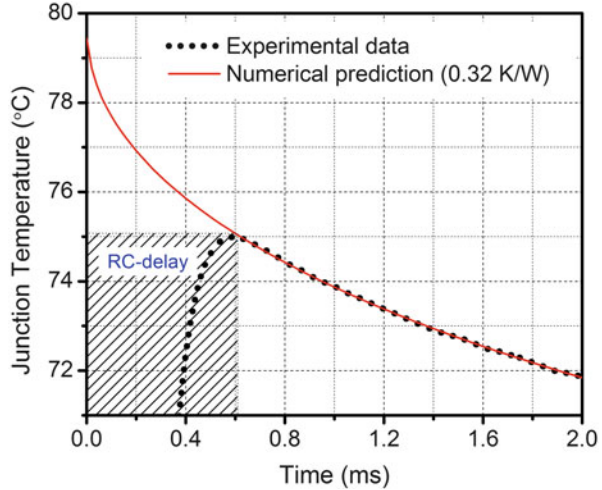

Fig. 7.14 Experimental data is compared with numerical prediction after the iteration

The iteration was conducted in a two-step process: (1) a coarse increment of 0.1 K/W and (2) a finer increment of 0.01 K/W. The final result after the iteration is shown graphically in Fig. 7.14, where the zone affected by the RC-delay is marked as a shaded area. The DTI resistance was determined to be 0.32 K/W.

7.5 Validity of DTI Resistance

The same LED used in Sect. 7.4 was tested under three other operating currents (250 mA, 500 mA, and 750 mA) to validate the DTI resistance obtained from the inverse approach. For each case, the power dissipation and the TEC surface temperature required for the apparent temperature of 75 °C were determined first. The values for the three operating currents are also summarized in Table 7.1.

The experimental results are compared with the modeling results obtained with the DTI resistance of 0.32 K/W in Fig. 7.15. They match each other very well with the temperature difference within 0.05 °C in the calibration region, which is a clear indication that the DTI resistance determined by the proposed inverse approach is valid.

The representative cross-section images of the AuSn die-attach layer are shown in Fig. 7.16, which were taken at (a) 200× and (b) 1000× magnification. The random and contiguous void area in the die attach (more than 50% of the total die attach area) is evident. It is worth noting that the measured DTI resistance was 3.5 times larger than the thermal resistance calculated from the bulk property available in the literature (0.09 K/W). The large void area was attributed to the increase in the DTI resistance.

The same procedure was implemented for a different die-attach material. It consisted of silver paste and AuSn solder. The nominal thickness of the die attach

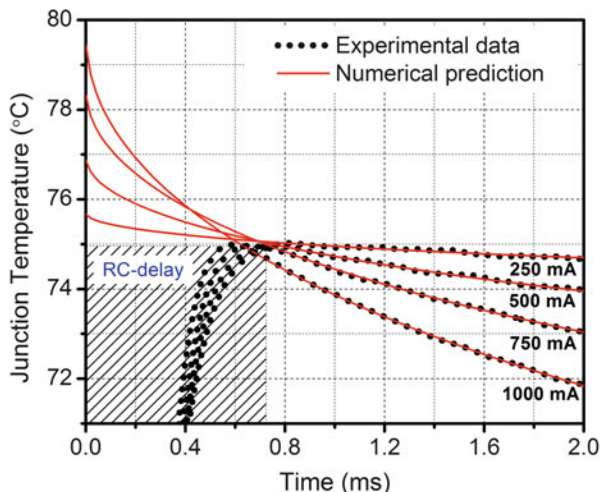

Fig. 7.15 Predicted transient behavior of AuSn die attach at different forward currents is compared with experimental data, where the DTI resistance obtained from Fig. 7.14 is used in the numerical simulation

was about 10 μm. The electrical power, the radiant flux, the heat generation rate, and the TEC surface temperature are summarized in Table 7.4.

The DTI resistance was determined using the data obtained under an operating current of 1 A. It was 0.22 K/W and its accuracy was validated under three other operating currents (250, 500 and 750 mA). The results are shown in Fig. 7.17. The excellent agreement between the experimental data and the prediction not only proves the validity of the measurements but also supports a fact that the proposed scheme can be used for a wide range of die-attach materials.

7.6 Conclusion

An inverse approach was proposed to determine the resistance of the DTI in high-power LEDs. The transient time domain governed predominantly by the resistance of the DTI was selected first using the hybrid analytical/numerical solution. Then, the resistance of the DTI was determined inversely from the experimental data over the predetermined transient time domain using numerical modeling.

Supplementary experiments at various forward currents were conducted to verify the validity of the proposed method. The validity was further confirmed by measuring the actual voids in the die-attach layer. The same procedure was implemented for a different die-attach material. The results confirmed that the proposed approach offered a measurement accuracy of 0.01 K/W for various types of die-attach materials.

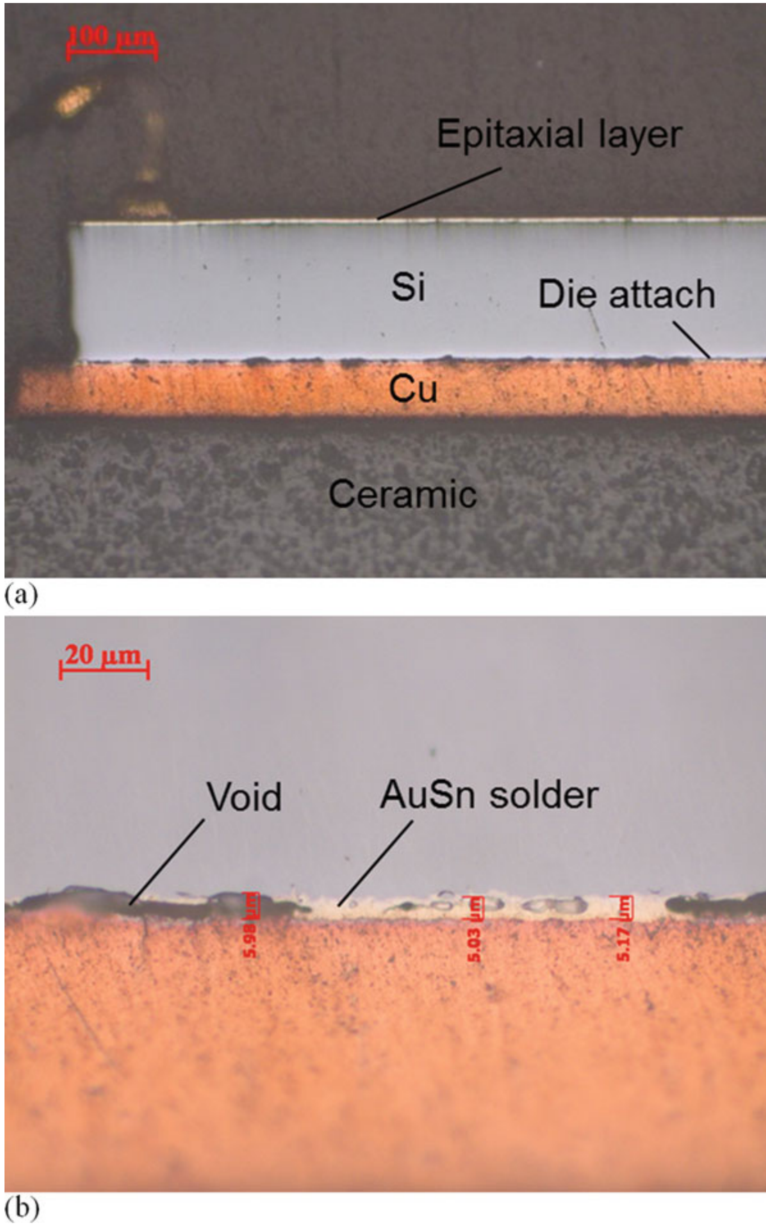

Fig. 7.16 Cross-section image of the AuSn die-attach layer at (**a**) 200× and (**b**) 1000× magnification

Table 7.4 Experimental data of blue LED using the AuSn solder and Ag paste die attach

I_f (mA)	V_f (V)	Electrical power (W)	Radiant flux (W)	Heat generation rate (W)	T_s (°C)
250	2.891	0.723	0.300	0.423	67.5
500	3.139	1.569	0.550	1.020	58.9
750	3.358	2.519	0.788	1.731	48.8
1000	3.563	3.563	0.988	2.575	36.5

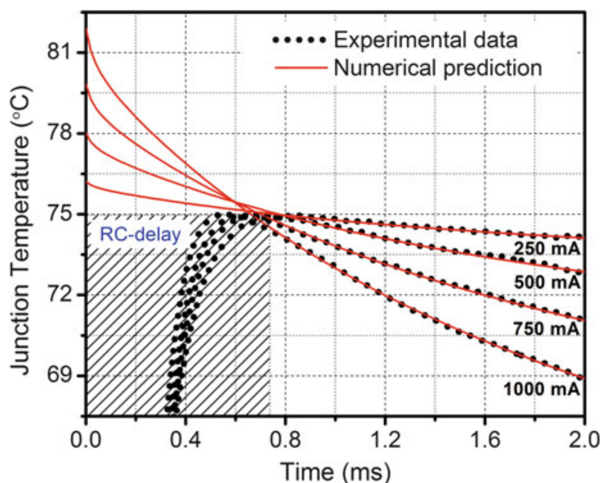

Fig. 7.17 Predicted transient behavior of AuSn and Ag paste die attach at different forward currents is compared with experimental data, where the DTI resistance obtained from the 1000 mA case is used in the numerical simulation

References

1. X.A. Cao, S.F. LeBoeuf, L.B. Rowland, C.H. Yan, H. Liu, Temperature-dependent emission intensity and energy shift in InGaN/GaN multiple-quantum-well light-emitting diodes. Appl. Phys. Lett. **82**(21), 3614–3616 (2003). doi:10.1063/1.1578539
2. L. Trevisanello, M. Meneghini, G. Mura, M. Vanzi, M. Pavesi, G. Meneghesso, E. Zanoni, Accelerated life test of high brightness light emitting diodes. IEEE Trans. Device Mater. Reliab. **8**(2), 304–311 (2008). doi:10.1109/tdmr.2008.919596
3. C.-P. Wang, T.-T. Chen, H.-K. Fu, T.-L. Chang, P.-T. Chou, M.-T. Chu, Analysis of thermal characteristics and mechanism of degradation of flip-chip high power LEDs. Microelectron. Reliab. **52**(4), 698–703 (2012). doi:10.1016/j.microrel.2011.11.009
4. H.-H. Kim, S.-H. Choi, S.-H. Shin, Y.-K. Lee, S.-M. Choi, S. Yi, Thermal transient characteristics of die attach in high power LED PKG. Microelectron. Reliab. **48**(3), 445–454 (2008)
5. B. Pardo, A. Gasse, A. Fargeix, J. Jakovenko, R.J. Werkhoven, X. Perpina, X. Jorda, M. Vellvehi, T. Van Weelden, P. Bancken, Thermal resistance investigations on new lead frame-based LED packages and boards. Microelectron. Reliab. **53**(8), 1084–1094 (2013). doi:10.1016/j.microrel.2013.02.016
6. B. Han, C. Jang, A. Bar-Cohen, B. Song, Coupled thermal and thermo-mechanical design assessment of high power light emitting diode. IEEE Trans. Components Packag. Technol. **33** (4), 688–697 (2010). doi:10.1109/tcapt.2010.2044413

7. D. Yang, Y.C. Chan, B.Y. Wu, M. Pecht, Electromigration and thermomigration behavior of flip chip solder joints in high current density packages. J. Mater. Res. **23**(9), 2333–2339 (2008). doi:10.1557/jmr.2008.0305
8. R. Prasher, Thermal interface materials: historical perspective, status, and future directions. Proc. IEEE **94**(8), 1571–1586 (2006). doi:10.1109/jproc.2006.879796
9. M. Montano, J. Garcia, W. Shi, M. T. Reiter, U. Vadakkan, K. L. Phillippe, B. Clark, M. Valles, C. Deppisch, J. D. Ferrara-Brown, S. G. Jadhav, E. Bernal, M. K. Kuan, in *ASME 2005 Summer Heat Transfer Conference*, ed by D. Walsh. Asme novel process techniques to reduce voids in solder thermal interface materials used for flip-chip package applications, (American Society of Mechanical Engineers (ASME), New York, 2005), pp. 2369–2374)
10. D. S. Kim, Q. Yu, T. Shibutani, N. Sadakata, T. Inoue, in *Thermal and Thermomechanical Phenomena in Electronic Systems, 2004. ITHERM ' 04 '04. The Ninth Intersociety Conference, 1--4 June 2004*, ed. by R. Jacob Baker. Effect of void formation on thermal fatigue reliability of lead-free solder joints, vol 322 (Institute of Electrical and Electronics Engineers (IEEE), New York, 2004), pp. 325–329. doi:10.1109/itherm.2004.1318300.
11. K. C. Otiaba, R. S. Bhatti, N. N. Ekere, S. Mallik, E. H. Amalu, M. Ekpu, in *Adaptive Science and Technology (ICAST). 3rd IEEE International Conference, 24–26 Nov 2011*, ed. by R. Jacob Baker. Thermal effects of die-attach voids location and style on performance of chip level package, (Institute of Electrical and Electronics Engineers (IEEE), New York, 2011), pp. 231–236). doi:10.1109/ICASTech.2011.6145176
12. R. O. Carlson, A. J. Yerman, J. F. Burgess, C. A. Neugebauer, in *Reliability Physics Symposium, 21st Annual. Apr 1983*, ed. by R. Jacob Baker. Voids, cracks, and hot spots in die attach, (Institute of Electrical and Electronics Engineers (IEEE), New York, 1983), pp. 138–141. doi:10.1109/irps.1983.361974.
13. A.S. Fleischer, L.-h. Chang, B.C. Johnson, The effect of die attach voiding on the thermal resistance of chip level packages. Microelectron. Reliab. **46**(5–6), 794–804 (2006.) doi:http://dx.doi.org/10.1016/j.microrel.2005.01.019
14. EIA/JEDEC, Transient dual interface test method for the measurement of the thermal resistance junction to case of semiconductor devices with heat flow through a single path. vol JESD51–14. (2010)
15. Q. Shan, Q. Dai, S. Chhajed, J. Cho, E.F. Schubert, Analysis of thermal properties of GaInN light-emitting diodes and laser diodes. J. Appl. Phys. **108**(8), 084504–084501.–084508. doi:084504 (2010). doi:10.1063/1.3493117
16. P. Szabo, A. Poppe, M.Rencz, Studies on the possibilities of in-line die attach characterization of semiconductor devices, in *Electronics Packaging Technology Conference*. EPTC. 9th, 10–12 Dec 2007 (2007), pp. 779–784. doi:10.1109/eptc.2007.4469707
17. M.R. Rencz, V. Szekely, Measuring partial thermal resistances in a heat-flow path. Components Packag. Technol. IEEE Trans. **25**(4), 547–553 (2002). doi:10.1109/tcapt.2002.808003
18. V. Szekely, A new evaluation method of thermal transient measurement results. Microelectron. J. **28**(3), 277–292 (1997). doi:10.1016/s0026-2692(96)00031-6
19. V. Szekely, Identification of RC networks by deconvolution: chances and limits. Circ. Syst. I Fundam. Theory Appl. IEEE Trans. **45**(3), 244–258 (1998). doi:10.1109/81.662698
20. Y. Xi, E.F. Schubert, Junction temperature measurement in GaN ultraviolet light-emitting diodes using diode forward voltage method. Appl. Phys. Lett. **85**(12), 2163–2165 (2004)
21. Y. Xi, J.Q. Xi, T. Gessmann, J.M. Shah, J.K. Kim, E.F. Schubert, A.J. Fischer, M.H. Crawford, K.H.A. Bogart, A.A. Allerman, Junction and carrier temperature measurements in deep-ultraviolet light-emitting diodes using three different methods. Appl. Phys. Lett. **86**(3), 031907–031901.–031903. doi:031907 (2005). doi:10.1063/1.1849838
22. Q. Chen, X. Luo, S. Zhou, S. Liu, Dynamic junction temperature measurement for high power light emitting diodes. Rev. Sci. Instrum. **82**(8), 084904–084901 (2011.) 084907
23. W.J. Hwang, T.H. Lee, J.H. Choi, H.K. Kim, O.H. Nam, Y.J. Park, M.W. Shin, Thermal investigation of GaN-based laser diode package. IEEE Trans. Components Packag. Technol. **30**(4), 637–642 (2007). doi:10.1109/tcapt.2007.906346

24. A. Vass-Varnai, J. Parry, G. Toth, S. Ress, G. Farkas, A. Poppe, M. Rencz, in *Electronics Packaging Technology Conference (EPTC). IEEE 14th*, ed. by R. Jacob Baker. Comparison of JEDEC dynamic and static test methods for the thermal characterization of power LEDs, (Institute of Electrical and Electronics Engineers (IEEE), New York, 2012), pp. 594–597. doi:10.1109/eptc.2012.6507151
25. M. Rencz, V. Szekely, Structure function evaluation of stacked dies. Paper presented at the 20th Annual IEEE Semiconductor Thermal Measurement and Management Symposium. (2004)
26. D.L. Saums, *Advances in Thermal Interface Materials for Power LED Applications*, Thermal Management for LED Applications, vol 2 (Springer, New York, 2014). doi:10.1007/978-1-4614-5091-7_8
27. A. Poppe, A step forward in multi-domain modeling of power LEDs, in *Semiconductor Thermal Measurement and Management Symposium (SEMI-THERM)*. 2012 28th Annual IEEE, 18–22 Mar 2012 (2012), pp. 325–330. doi:10.1109/stherm.2012.6188868
28. B.-M. Song, B. Han, A. Bar-Cohen, R. Sharma, M. Arik, Hierarchical life prediction model for actively cooled LED-based luminaire. IEEE Trans. Components Packag. Technol. **33**(4), 728–737 (2010)
29. Y.S. Muzychka, J.R. Culham, M.M. Yovanovich, Thermal spreading resistance of eccentric heat sources on rectangular flux channels. J. Electron. Packag. **125**(2), 178–185 (2003). doi:10.1115/1.1568125
30. R.B. Ross, *Metallic Materials Specification Handbook*, 4th edn. (Chapman & Hall, London, 1992)
31. M.W. Shin, J.P. Kim, *Introduction to LED Packaging Technology* (Bookshill, Seoul, 2008)
32. J.R. Davis, Properties and Selection: Nonferrous Alloys and Special-Purpose Materials, in *Metals Handbook*, vol. 2, 10th edn., (ASM International, Novelty, OH, 1990)
33. C. Qian, in *Electronic Packaging Technology. ICEPT. 8th International Conference on, 14–17 Aug 2007*, ed. by R. Jacob Baker. Thermal management of high-power white LED package, (Institute of Electrical and Electronics Engineers (IEEE), New York, 2007), pp. 1–5
34. A. Nayer, *The Metals Databook* (McGraw-Hill, New York, 1997)
35. D.R. Lide, *CRC Handbook of Chemistry and Physics*, 80th edn. (CRC Press, Boca Raton, 1999)

Chapter 8
Color Quality

Y. Ohno

Abstract This chapter deals with the quality of color. Good color quality is essential for any light source that is used for general illumination. It is important to ensure that solid-state lighting (SSL) sources at least give equal color quality as seen with conventional light sources such as fluorescent lamps. Even more, with the lifetime extension that SSL technology provides, the color characteristics should be maintained over the economic life of the product. This chapter provides the fundamentals of color quality in general and, more specific, to SSL sources.

8.1 Introduction

Good color quality is essential for solid-state lighting (SSL) sources for general illumination. It is important to ensure that SSL sources have acceptable color quality suitable for intended applications and that the color characteristics are maintained over the lifetime of the products. In this chapter, the fundamentals of color quality characteristics related to SSL sources are described, including information on standards and recent studies on color quality. There are two aspects in the color quality of light sources for lighting: chromaticity and color rendering. These characteristics are treated separately but closely interrelated.

The chromaticity of light sources is expressed by chromaticity coordinates, $(x\ y)$ or (u', v') and is often plotted on the (x, y) or the (u', v') chromaticity diagram, which are defined by the International Commission on Illumination (CIE) [1, 2]. The chromaticity coordinates of light sources are normally chosen to be around the Planckian locus, which is generally considered as the central region for white light. Shifts of chromaticity along the Planckian locus result in changes in correlated color temperature (CCT). Shifts of chromaticity across the Planckian locus are specified by the term, Duv [3], and make the lights appear yellowish or greenish in the region above the Planckian locus, and pinkish in the region below the Planckian locus. Section 8.2 introduces the fundamentals of chromaticity, CCT, Duv, and

Y. Ohno (✉)
National Institute of Standards and Technology, 100 Bureau Drive, Gaithersburg, MD 20899-8442, USA
e-mail: yoshi.ohno@nist.gov

© Springer International Publishing AG 2018

W.D. van Driel et al. (eds.), *Solid State Lighting Reliability Part 2*, Solid State Lighting Technology and Application Series 3, DOI 10.1007/978-3-319-58175-0_8

color difference specifications, and, in addition, some recent studies on perception of white light chromaticity are introduced.

Another important aspect of color quality is color rendering, which is a property of a light source that determines how natural the colors of objects appear under the illumination. The current international standard for color rendering is the color rendering index (CRI) [4]. The CRI has been widely used for many years. However, problems have been raised on the CRI when it is used for light-emitting diode (LED) sources [5]. To solve the major problems of the CRI, preference and perception aspects of color quality need to be considered. There are many studies published recently to address such aspects. Section 8.3 explains the object color specification, which is important to understand color quality, then Sect. 8.4 provides the details of the CRI, color preference, and perception aspects of color quality, with information on related recent research on color quality.

Color rendering depends on the spectrum of the light source, which also affects the energy efficiency of the light source. Color rendering is generally excellent if the spectrum is broadly distributed over the visible region. However, such broadband spectra are generally less energy efficient, thus the spectra of white LEDs are designed to balance these two factors for intended applications. Section 8.5 describes the definitions of the terms related to energy efficiency of light sources, in particular luminous efficacy of radiation (LER), which is important in designing LED sources for lighting.

Section 8.6 introduces the definitions of the color-related terms used for single color LEDs including dominant wavelength, centroid wavelength, and peak wavelength.

8.2 Chromaticity

8.2.1 Chromaticity Coordinates and Chromaticity Diagrams

The CIE 1931 (x, y) and CIE 1976 (u', v') chromaticity coordinates and corresponding diagrams are defined by the CIE [2]. Both are widely used to specify chromaticity of light sources. These diagrams are shown in Fig. 8.1. The curved boundary line is formed by the chromaticity coordinates of monochromatic radiation. Any color of light lies within this boundary. The (x, y) diagram is significantly spatially nonuniform in terms of color differences. Figure 8.1 also shows the plots of MacAdam ellipses (just noticeable color differences) [6] on these diagrams, with the ellipses' sizes magnified by ten. For the same difference in (x, y) values, the perceived color differences in the green region would be much smaller than in the blue region. The (u', v') diagram is more spatially uniform and is preferred, especially to specify chromaticity of colored sources including single color LEDs.

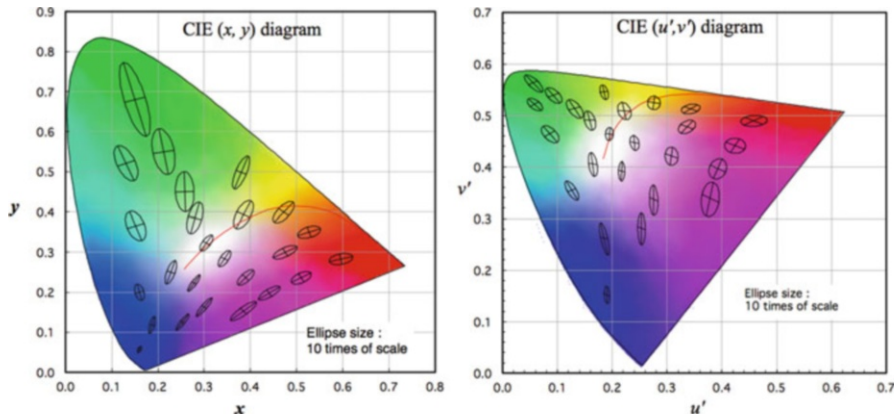

Fig. 8.1 CIE 1931 (x, y) chromaticity diagram (*left*) and CIE 1976 (u', v') chromaticity diagram (*right*) with MacAdam ellipses plotted

The chromaticity coordinates of a light source are calculated from its spectral power distribution $\phi(\lambda)$. The tristimulus values X, Y, Z are first calculated as

$$
\begin{aligned}
X &= k\int_{\lambda}\varphi(\lambda)\bar{x}(\lambda)d\lambda \\
Y &= k\int_{\lambda}\varphi(\lambda)\bar{y}(\lambda)d\lambda \\
Z &= k\int_{\lambda}\varphi(\lambda)\bar{z}(\lambda)d\lambda
\end{aligned}
\tag{8.1}
$$

where $\bar{x}(\lambda), \bar{y}(\lambda), \bar{z}(\lambda)$ are the CIE 1931 color matching functions (Fig. 8.2). The CIE also specifies the color matching functions $\bar{x}_{10}(\lambda), \bar{y}_{10}(\lambda), \bar{z}_{10}(\lambda)$ for the 10° field of view [2] (also plotted in Fig. 8.2), but these 10° functions are mainly used for specification of object colors and generally not used of light sources.

The values of these functions at 5 nm intervals and 1 nm intervals are available in Refs. [2, 7]. The chromaticity coordinates (x, y) and (u', v') are calculated by

$$
x = \frac{X}{X+Y+Z}, \quad y = \frac{Y}{X+Y+Z} \tag{8.2}
$$

$$
u' = \frac{4X}{X+15Y+3Z}, \quad v' = \frac{9Y}{X+15Y+3Z} \tag{8.3}
$$

The (u', v') coordinate can also be calculated from (x, y)

$$
u' = \frac{4x}{(-2x+12y+3)}, \quad v' = \frac{9y}{(-2x+12y+3)} \tag{8.4}
$$

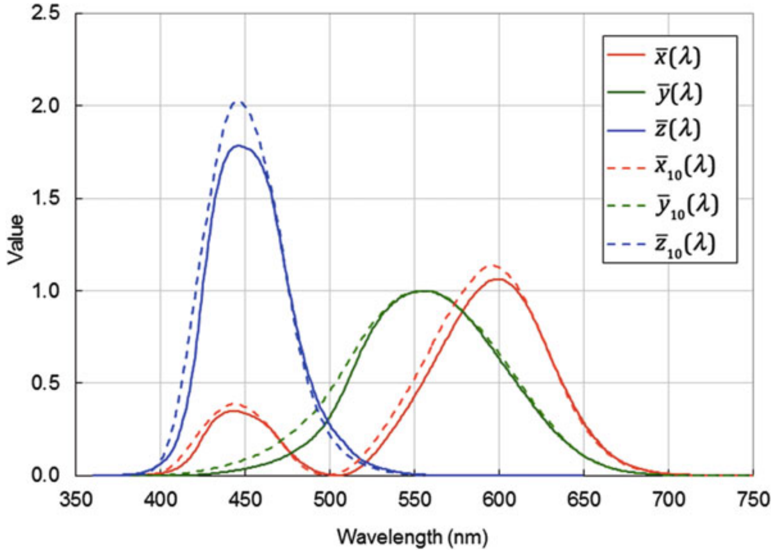

Fig. 8.2 CIE 1931 color matching functions (*solid lines*) and CIE 1964 10° color matching functions (*dashed lines*)

Likewise, (x, y) coordinate can be converted from (u', v') by

$$x = \frac{9u'}{(6u' - 16v' + 12)}, \quad y = \frac{2v'}{(3u' - 8v' + 6)} \tag{8.5}$$

The CIE 1960 (u, v) coordinates (now obsolete) are introduced here only for the purpose of calculating CCT and Duv and are obtained by

$$u = u', \quad v = \frac{2}{3}v' \tag{8.6}$$

The (u, v) coordinates should not be used for calculations other than for CCT and Duv. The curve formed by the plots of the chromaticity coordinates of monochromatic radiation at various wavelengths is called *spectrum locus* (this forms the horseshoe shape of the diagram), and the curve formed by the plots of Planckian radiation at various blackbody temperatures is called *Planckian locus* (also often called *blackbody locus*) as depicted in Fig. 8.3 on the (x, y) diagram. The straight line connecting both ends of the spectrum locus is called the *purple line*.

The curve formed by the plots of phases of daylight at varied CCTs is called *daylight locus*, also plotted in Fig. 8.3. The Planckian locus and the daylight locus are often used as the central curves for white light for sources at lower and higher CCT ranges, respectively. The formula to calculate the daylight locus is available in [2]. The phase of daylight at 6500 K is defined as CIE standard illuminant D65 [8],

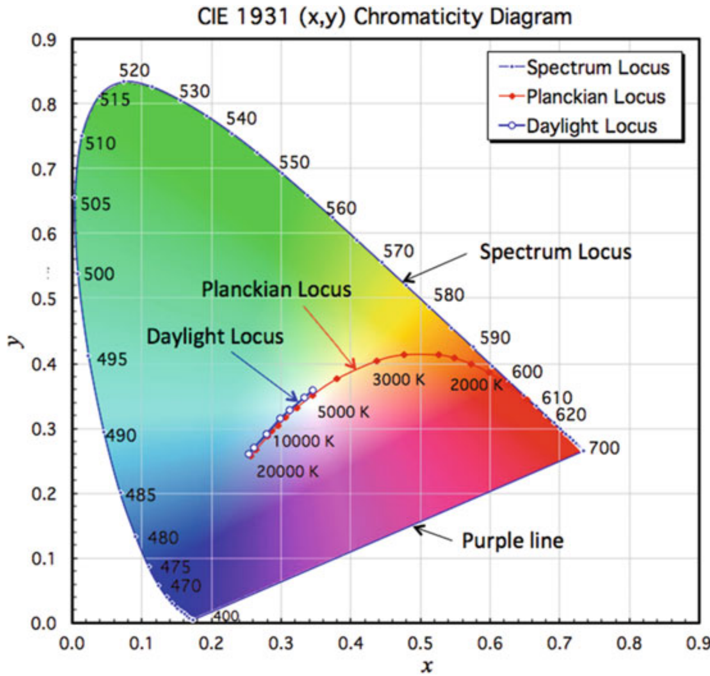

Fig. 8.3 The spectrum locus and the Planckian locus on the (x, y) diagram

and those at 5000 K, 5500 K, and 7500 K, are described as daylight illuminants D50, D55, and D75 [2]. In the calculation of CRI [4], the transition from Planckian locus to daylight locus occurs at 5000 K for a procedural purpose only.

8.2.2 Chromaticity Specifications for Lighting Products

Light sources for general lighting need to have acceptable white light chromaticity. The chromaticity specifications for fluorescent lamps have been available for many years [9, 10]. Figure 8.4 (upper) shows the specifications by International Electrotechnical Commission (IEC) [9]. For SSL sources, American National Standards Institute (ANSI) published C78.377 chromaticity specifications for SSL products, first in 2008 and the latest version in 2015 [3]. Figure 8.4 (lower) shows the specifications of this ANSI standard for SSL products. ANSI C78.377 is widely used internationally and is often used as the basis for color binning of white LED products. There are ten nominal CCTs in this standard from 2200 to 6500 K, and the Flexible CCT specification is provided as an option, in which nominal CCTs can be specified at every 100 K in the CCT range above.

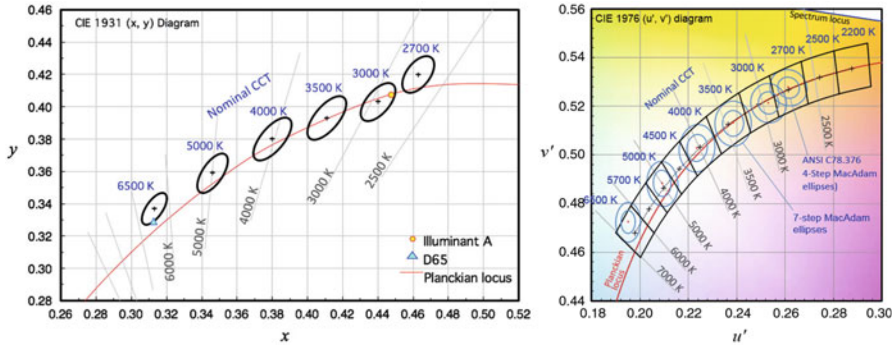

Fig. 8.4 The chromaticity specifications for fluorescent lamps by IEC 60081 on the CIE (x, y) diagram (*left*) and those for SSL products by ANSI C78.377-2015 on the CIE (u', v') diagram (*right*)

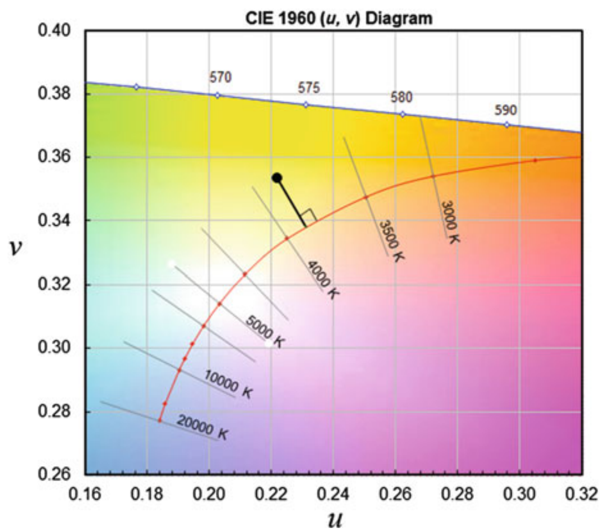

Fig. 8.5 Illustration of the definition of CCT on the 1960 (u, v) diagram (now obsolete)

8.2.3 Correlated Color Temperature

Correlated color temperature (CCT, Symbol: T_{cp}) is defined as the temperature of the Planckian radiator having the chromaticity that is closest to the chromaticity of the given light source, on the CIE (u', 2/3 v') coordinate, as illustrated in Fig. 8.5. A more official definition is available elsewhere [1, 2]. The (u', 2/3 v') coordinate is the same as the CIE 1960 (u, v) coordinate, which is now obsolete, and the expression, 2/3 v' is used because (u, v) it should not be used in official documents. Note that the term *color temperature* is defined as the temperature of the Planckian

radiator having the same chromaticity as that of the given light source. Thus, color temperature is used only for blackbody sources and thermal radiation sources such as incandescent lamps.

The Planck's equation used for the calculation of CCT is given in the form

$$L_{e,\lambda}(\lambda, T) = \frac{c_1 n^{-2} \lambda^{-5}}{\pi} \left[\exp\left(\frac{c_2}{n \lambda T} \right) - 1 \right]^{-1} \tag{8.7}$$

where L is the spectral radiance, T is the temperature [K], and n is the refractive index of the medium. For historical reasons, $n = 1$ (exactly 1) has been used and must be used for calculation of CCT. The parameters c_1, c_2 are the radiation constants; but only c_2 is relevant to the value of CCT. The value of c_2 used in the calculation of CCT must follow the value adopted in the current International Temperature Scale (ITS-90), namely, $c_2 = 1.4388 \times 10^{-2}$ m·K. See Appendix E of CIE 15:2004 [2] for the details of these constants used for calculation of CCT. Some examples of calculation algorithms for CCT are available in [11].

8.2.4 Duv

The two numbers of a chromaticity coordinate are not intuitively indicative of the color of a light source. The CCT is used to express the chromaticity of white light by one number, on condition that its chromaticity is close to the Planckian locus. However, it is not always the case. The shift of chromaticity across the Planckian locus is a critical factor that affects acceptability of lighting.

To specify this shift, the term *Duv* (symbol: D_{uv}) is defined in the ANSI standard [3]. Duv is defined as the closest distance from the Planckian locus on the CIE (u', $2/3v'$) coordinates, with plus sign (+) for above and minus sign (−) for below the Planckian locus. The distance is measured on the CIE 1960 (u, v) diagram[1]. A positive value of Duv indicates a shift in yellowish or greenish directions, and a negative value indicates a shift in pinkish directions. Figure 8.6 shows the scales of Duv depicted on the (u, v) diagram.

Duv can normally be calculated in the process of calculating CCT, which requires determination of the closest point on the Planckian locus to the (u, v) chromaticity coordinates of the light source being tested.

If it needs to be calculated separately, and if the CCT of the light source is known, Duv can be obtained by calculating the spectral distribution of

[1]CIE 1960 (u, v), now obsolete, is used in this paper only for the convenience of describing Duv and some other color quantities.

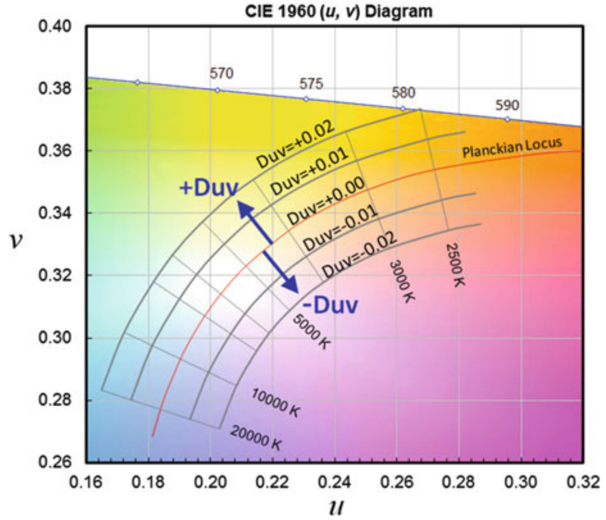

Fig. 8.6 The scales of Duv shown on the 1960 (u, v) diagram

Planckian radiation at the CCT of the source using the Planck's equation (Eq. 8.7), then calculate $\left(u'_0, \frac{2}{3}v'_0\right)$ of that Planckian spectral distribution, then Duv is given by

$$D_{\mathrm{uv}} = \left[\left(u' - u'_0\right)^2 + \left(\frac{2}{3}v' - \frac{2}{3}v'_0\right)^2\right]^{\frac{1}{2}} \cdot \mathrm{SIGN}\left(v' - v'_0\right) \tag{8.8}$$

where $\mathrm{SIGN}(z) = 1$ for $z \geq 0$ and $\mathrm{SIGN}\ (z) = -1$ for $z < 0$. Further information on practical calculation of Duv is available in [11].

8.2.5 *Perception of White Light Chromaticity*

Light sources for general lighting, including SSL sources, have been traditionally designed to have their chromaticity around Planckian locus based on the standards [3, 9, 10], as shown in Fig. 8.4. However, it has been anecdotally known for many years that light sources having their chromaticity below Planckian locus are preferred. For example, neodymium lamps[2], popularly sold in the USA and Japan, have Duv ≈ -0.005. This effect is recently gaining high attention as a part of color quality study for SSL sources. Several studies [12–16] are reported, which all

[2]Incandescent lamp with its glass envelope doped with neodymium, which absorbs much of the yellow portion of the lamp spectrum.

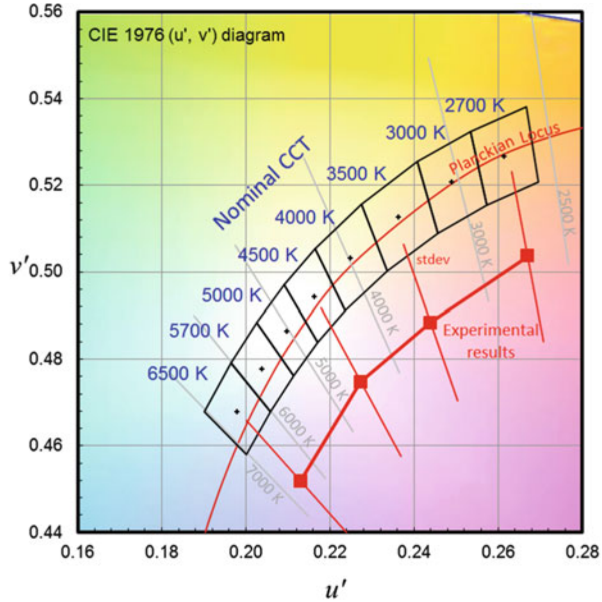

Fig. 8.7 The results of the NIST's study [13] plotted over the ANSI C78.377 specifications, showing the chromaticity points (*red filled squares*) that were perceived most natural on the average by 18 subjects

indicate that lights on the Planckian locus and the daylight locus are not perceived as the most natural or most neutral white light.

The studies [12–14] show that chromaticity in a certain range below Planckian locus is preferred or perceived natural in typical indoor lighting conditions. The result of a study by National Institute of Standards and Technology (NIST) [13] is shown in Fig. 8.7. This experiment used a real room size spectrally tunable lighting facility, which was set for a typical interior room with some furniture and common fruits and vegetables on the table, and 18 subjects participated. The results showed that chromaticity points at Duv ≈ -0.015 (on the average), much below the ANSI specifications, were perceived most natural. The study [14] is the same experiment using a different set of spectra, and nearly the same results were obtained. The study [12] used a miniature of an office and shows similar results as the NIST's studies.

The studies [15, 16] are different from the above studies in that they investigated perceived whiteness of illumination, and experiments were done using white booths with no colored objects inside. The results of these studies indicate that the chromaticity points of white light that appear as most neutral white lie below Planckian locus, which is in the same direction as the results of the other studies [12–14]. These studies are gaining high attention in the SSL community, and ANSI is preparing an addition of chromaticity specifications in C78.377 for the white light region below Planckian locus.

8.2.6 Color Difference of Light Source

Color difference of light sources need to be specified in many cases, for example, for angular color uniformity, color shifts during lifetime (color maintenance), and color tolerances of lighting products. The color difference of light stimuli, in general, are expressed by the distance on CIE (u', v') diagram, which is the uniform color space for light stimuli officially recommended by the CIE. The term "color difference" should not be confused with that of object colors, which are specified differently (see Sect. 8.3).

Color differences of light sources (any colors) are generally expressed by the distance in (u', v') coordinates, which is denoted as $\Delta_{u',v'}$ and is calculated as the distance between two points $\left(u'_1, v'\right)$ and $\left(u'_2, v'_2\right)$ on the (u', v') diagram by

$$\Delta_{u',v'} = \sqrt{\left(u'_2 - u'_1\right)^2 + \left(v'_2 - v'_1\right)^2} \tag{8.9}$$

The color differences of light sources (e.g., chromaticity tolerances for lighting products) have often been specified by the size of MacAdam ellipses [6]. For example, the ellipses included in Fig. 8.4 (left) are five times the size of MacAdam ellipses, so-called five-step MacAdam ellipses, used for specifications of compact fluorescent lamps in the USA [17]. The chromaticity specifications for linear fluorescent lamps in the USA [10] use four-step MacAdam ellipses. Similar expressions occasionally used are SDCM (standard deviation of color matching) or JND (just noticeable difference), meaning the color difference corresponding to one-step MacAdam ellipses. However, these are not internationally defined standard metrics. While these terms served for many years for fluorescent lamps, which have only six nominal CCTs, this method is not convenient for new lighting technologies, which are more versatile. The shape and size of the MacAdam ellipses change depending on the location of chromaticity coordinate, and they need to be interpolated between the original 25 points measured by MacAdam [6] (Fig. 8.1). Such interpolation formulae are not specified in any international standard. This is a problem for LED light sources that do not follow the traditional nominal CCTs of fluorescent lamps. For example, the 4500 K and 5700 K nominal CCTs or any of the flexible CCTs in the ANSI specification [3] do not have corresponding MacAdam ellipses defined. Even if interpolation of ellipses is possible, it would be complicated and not practical.

The CIE recently published TN 001 [18], which recommends using circles in the (u', v') diagram to replace MacAdam ellipses for white region. In this method, only the radius of the circle needs to be specified to express chromaticity tolerances, and it is called *$u'v'$ circle*. The size of (one-step) MacAdam ellipses (in the white region) corresponds to $u'v'$ circles with a radius of 0.0011. TN 001 also defines *n-step $u'v'$*

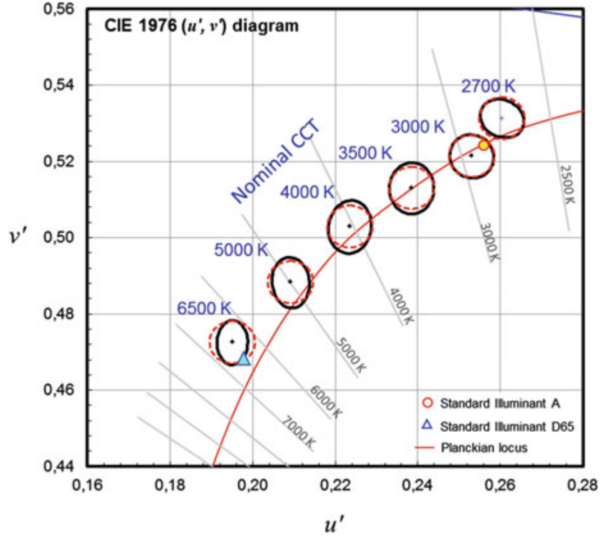

Fig. 8.8 Five-step MacAdam *ellipses* in IEC 60081 [9] and *circles* (radius 0.0055) in the CIE 1976 (u', v') chromaticity diagram

circle, as a circle in the (u', v') diagram with a radius of n times 0.0011. For a center point $\left(u'_c, v'_c\right)$, the n-step $u'v'$ circle is expressed by the equation

$$\left(u' - u'_c\right)^2 + \left(v' - v'_c\right)^2 = (0.0011 \cdot n)^2 \tag{8.10}$$

and corresponds to a n-step MacAdam ellipse. As an example, Fig. 8.8 shows the five-step MacAdam ellipses for the fluorescent lamp specifications [9] plotted on the (u', v') diagram, on top of which $u'v'$ circles with a radius of 0.0055 (red dashed line) are plotted. As shown, these ellipses and the circles are closely overlapped, which means that circles can be used to replace MacAdam ellipses in this white region on (u', v') diagram.

There are small differences between the circles and MacAdam ellipses, but it is considered insignificant in practical applications. Additionally, the experimental uncertainty of MacAdam ellipses measured 75 years ago with only one subject is not well known.

8.3 Object Color Specifications

Color rendering is a phenomenon in which colors of objects appear differently under illumination having different spectra. Thus, in discussing color rendering, it is important to understand how object color is specified and how their differences are evaluated. The general approach for evaluating color rendering is to measure or

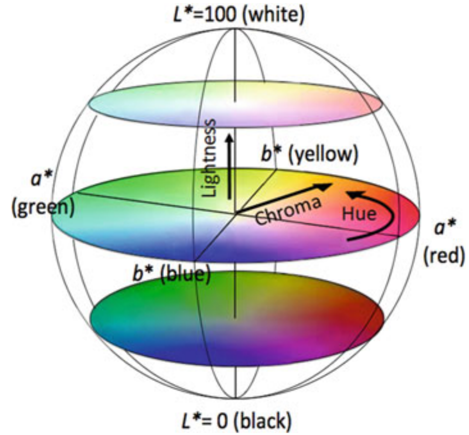

Fig. 8.9 Illustration of CIELAB object color space

calculate color differences of objects under given illumination, and this approach is used in CRI and other new proposed metrics. Unlike light source colors, which have two dimensions, object color requires another dimension, lightness – a scale from black, gray, to white. For example, there is no brown or black in the (x, y) diagram, while such colors exist for object colors. Brown color has the same chromaticity as red but has a different lightness. Therefore, a three-dimensional color space is needed for object colors.

There are two standardized object color spaces defined by CIE, which are $L^*a^*b^*$ (CIELAB) [2, 19] and $L^*u^*v^*$ (CIELUV) [2, 20]. CIELAB is commonly used in lighting research as well as imaging applications and is illustrated in Fig. 8.9. The two horizontal axes, a^* and b^*, determine *hue* and *chroma*, and the vertical axis L^* gives *lightness*. The center is gray, and the further the position is shifted outside horizontally, the more colorful the object is. The three coordinates L^*, a^*, b^* of an object surface are calculated by.

$$
\begin{aligned}
L^* &= 116\ (Y/Y_n)^{1/3} - 16 \\
a^* &= 500\ \left[(X/X_n)^{1/3} - (Y/Y_n)^{1/3}\right] \\
b^* &= 200\ \left[(Y/Y_n)^{1/3} - (Z/Z_n)^{1/3}\right] \\
&(\text{when } X/X_n, Y/Y_n, Z/Z_n > 0.008856)
\end{aligned}
\tag{8.11}
$$

where X, Y, Z are the tristimulus values of the object surface, and X_n, Y_n, Z_n are the tristimulus values of the white reference (perfect diffuser) under a given illumination. Note that there are further formulae for samples with very low reflectances, but these are practically not needed. To specify object colors, CIE standard illuminants

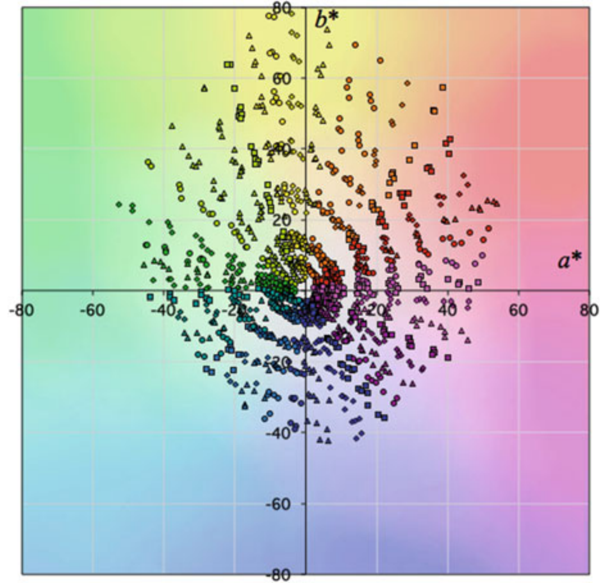

Fig. 8.10 The CIELAB (a^*, b^*) plots of 1269 Munsell color samples under D65

D65 [8] is normally used to calculate the tristimulus values. The color difference between two objects are calculated by

$$\Delta E^*_{\mathrm{ab}} = \left[(\Delta L^*)^2 + (\Delta a^*)^2 + (\Delta b^*)^2 \right]^{1/2} \tag{8.12}$$

For evaluation of color rendering of light sources, object colors are calculated with the spectrum of a reference illuminant and that of a given light source, and the difference ΔE^*_{ab} between them are evaluated. Since it is not convenient to draw three-dimensional diagram, only (a^*, b^*) is often plotted as a two-dimensional graph. As an example, Fig. 8.10 shows (a^*, b^*) plots of 1269 Munsell color samples [21] under D65.

8.4 Color Rendering Characteristics

8.4.1 Color Rendering Index

Color rendering is defined by the CIE [1] as "effect of an illuminant on the color appearance of objects by conscious or subconscious comparison with their color appearance under a reference illuminant." The CIE color rendering index (CRI) [4]

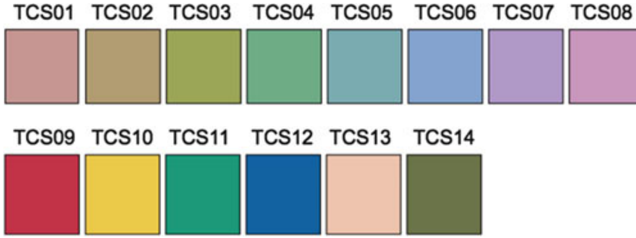

Fig. 8.11 The 14 test color samples used in the calculation of CRI

is widely used and the only internationally accepted metric for assessing the color rendering performance of lighting products. The details of procedure for the calculation are available in Ref. [4], but a brief introduction is provided in this section. The first step of the calculation is to calculate the color differences ΔE_i (in the 1964 $W^*U^*V^*$ object color space – now obsolete) of 14 test color samples (Munsell samples) when illuminated by a reference illuminant and when illuminated by a given light source. The first eight test samples are medium-saturated colors, and the last six include four highly saturated colors (red, yellow, green, and blue), skin complexion, and leaf green. These samples are shown in Fig. 8.11. The reference illuminant should have the same CCT as that of a test light source and is Planckian radiation for a correlated color temperature (CCT) $<$5000 K, or a phase of daylight (one of daylight spectra at varied CCT; the formula is available in [2]) for CCT $\geq$5000 K of the test light source. The chromaticities of the test samples are adjusted by the von Kries chromatic adaptation transform. The *special color rendering indices* R_i for each test color sample are obtained by

$$R_i = 100 - 4.6\Delta E_i \ ; \ (i = 1, \ldots, 14) \tag{8.13}$$

This gives the evaluation of color rendering for each test color sample. The *general color rendering index* R_a is calculated as the average of R_i for the first eight color samples:

$$R_a = \sum_{i=1}^{8} \frac{R_i}{8} \tag{8.14}$$

The score for perfect color rendering (zero color differences) is 100, and the values of R_i or even R_a can be below zero (negative) if color differences are extremely large. Note that the term CRI is often used referring to R_a, but the CRI actually consists of 15 numbers: R_a and R_i ($i = 1$ to 14).

The values of $R_a \geq 80$ are generally considered acceptable for indoor lighting, and $R_a \geq 90$ is generally considered excellent color rendering. The special color

rendering indices R_i are not often used except R_9 (index for the saturated red sample), which is often examined as red is critical for skin tone and overall color rendering and also to supplement R_a to address some of its problems. Note that color rendering is often not critical for outdoor lighting, and $R_a < 80$ can be well acceptable for such applications.

8.4.2 *Color Preference and Perception*

The CRI is designed to measure how close the object colors appear under a given illumination to those under the reference illuminant thus is a metric of color fidelity, which is only one aspect of color quality. Another important aspect of color quality is color preference. For example, some light spectra can increase the chroma of objects, which appear more vivid than under a reference illuminant and tend to be preferred. Such a preference effect is known for many years [22–24]. Some examples of such light sources are shown in Fig. 8.12, in which their color gamut is larger than those of the reference illuminant. Neodymium lamps are popularly sold in the USA, which is an evidence that such light sources are preferred by many people.

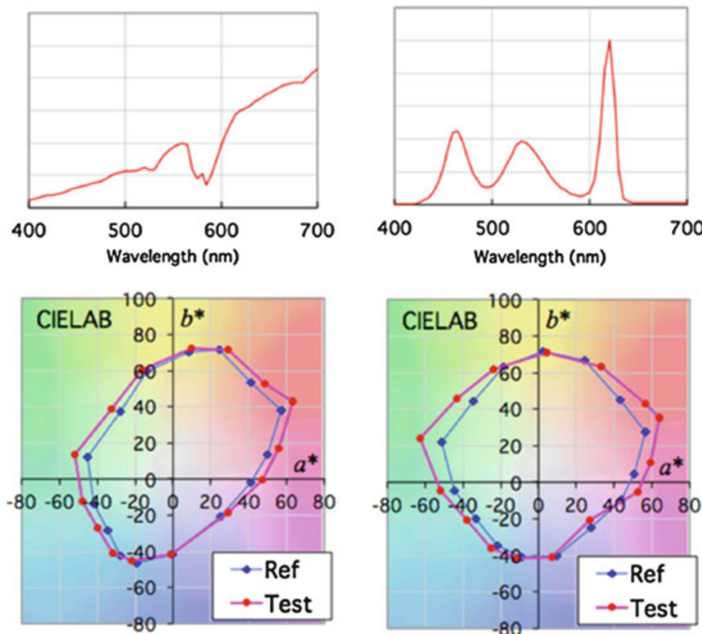

Fig. 8.12 Examples of color enhancement by a neodymium lamp (*left*) and an experimental RGB LED source (*right*). Plotted are the CIELAB (a^*, b^*) coordinates of the 15 color samples of CQS [28] under the given light spectra (*red line*) and the reference illuminant (*blue line*)

Also, it has been verified by a recent experimental study [25] that such illumination with slightly increased chroma is generally preferred in a typical indoor lighting environment. The CRI R_a score for the neodymium lamp shown in the figure is only 77, though it may be more preferred than a normal incandescent lamp, which has R_a score of 100.

Currently, such preferred light sources are penalized or discouraged by CRI, and very few products of such characteristics are available, except some RGB products may have such characteristics. Though such sources with increased chroma are not common in the current market, it is considered that such sources may become popular when the standard is revised.

There have been many studies recently to address such preference effects related to increased chroma and various metrics have been proposed, for example, feeling of contrast index [26], gamut area index [27], color quality scale [28], and memory color index [29]. The color quality scale (CQS) addresses the preference of such light sources while maintaining the color fidelity aspect of the CRI. It is also known that perceived chroma of objects is reduced at lower light levels (Hunt Effect) [30]. If this is proved to be effective for the light levels in typical indoor lighting conditions compared to the level of outside daylight, a slightly increased gamut may produce color rendering closer to daylight, leading to higher color fidelity.

As discussed in 8.2.5, the chromaticity of white light below Planckian locus may be generally preferred. The CRI R_a score, however, does not reflect such perception effects of Duv and penalizes such shifts of chromaticity below Planckian sources. As an example, Fig. 8.13 (right) shows CIE R_a values for an example of an LED source with shifts of Duv from -0.02 to 0.02 (varied by only changing the ratios of four peaks). The figure shows that R_a value decreases as the Duv moves to a negative direction, while this direction is reportedly preferred, and R_a value stays high in the positive Duv region up to Duv $\approx$ 0.015, while positive Duv shifts (yellowish shifts) are disliked as reported in the studies [13, 14]. Though this is not always the case, this is another example where CRI R_a, being a color fidelity metric,

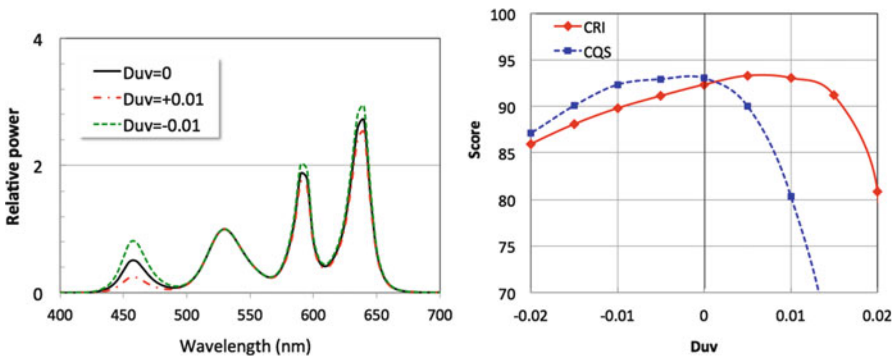

Fig. 8.13 The spectra of an experimental RGBA source (*left*), and the change of CRI R_a score (*red solid line*) and CQS Q_a score (*blue dashed line*) of this source as a function of Duv shift (*right*)

does not agree with the perception of white light. Figure 8.13 (right) also shows the plots of the CQS values, which shows a much improvement on this aspect.

The need for updating the CRI has been long recognized. CIE concluded that the CRI needs to be updated for SSL sources [5]. CIE recognizes that, the color preference or perception aspects, beyond color fidelity, are very important in the evaluation of overall color quality and continues efforts to develop a set of color quality metrics including improved color fidelity and color preference metrics that can update CRI in the future [32, 33].

8.5 Luminous Efficacy

The spectrum of a light source affects not only color rendering but also the energy efficiency of the light source; thus, color rendering is closely related to energy issues. The terms related to energy efficiency of light sources are introduced below.

The energy efficiency of a light source or a lighting product is evaluated by *luminous efficacy of a source* (often called simply *luminous efficacy*), which is the ratio of *luminous flux* (lumen) emitted by the source to the input electrical power (watt) to the source. Thus, the unit is lumen per watt (lm/W). The luminous efficacy of a source, η_v(lm/W), is determined by two factors:

$$\eta_v = \eta_e K \tag{8.15}$$

where η_e is the *radiant efficiency* of the source, which is the ratio of radiant flux output to input electrical power. *External quantum efficiency* is also used for the same meaning for LED devices. K is the *luminous efficacy of radiation*, which is the ratio of luminous flux to radiant flux, denoted as LER in this chapter and is determined only by the spectral distribution $S(\lambda)$ of the source as given by

$$K = \frac{K_m \int_\lambda V(\lambda) S(\lambda) d\lambda}{\int_\lambda S(\lambda) d\lambda} \tag{8.16}$$

K_m is the *maximum spectral luminous efficacy of radiation*, and its value, 683 lm/W (for monochromatic radiation at 555 nm), comes from the international definition of the candela [34]. While various other terms are used in the LED industry, the terms introduced above are the ones officially defined internationally [1].

Figure 8.14 illustrates the calculation of the LER. This LED spectra has an LER value of $K = 294$ (lm/W). The LER of common discharge lamps range from ~250 to ~380 lm/W. The maximum LER for white light with acceptable color rendering ($R_a \approx 80$) is considered to be around 400 lm/W. The LER is entirely dependent on the SPD of the light source and represents the luminous efficacy that would be possible if the conversion of electricity to light could happen without any losses.

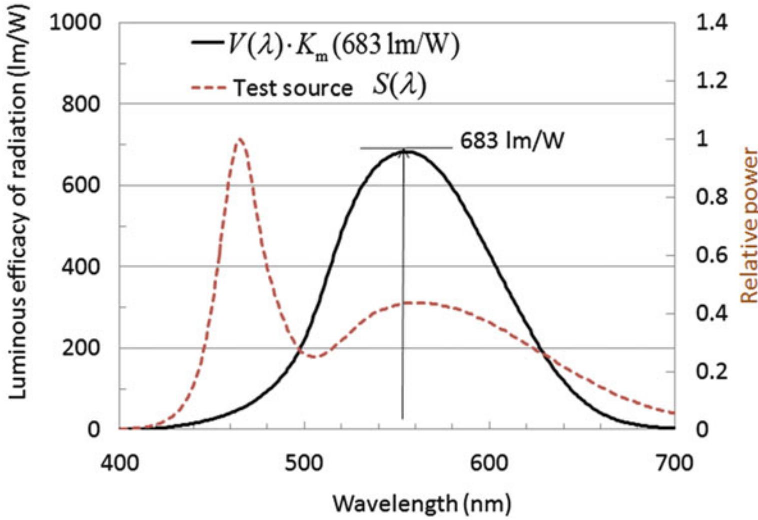

Fig. 8.14 Luminous efficacy of monochromatic radiation (*solid line*), plotted with an example of LED spectrum (*dashed line*)

8.6 Color Characteristics of Single Color LEDs

Chromaticity, as described in 8.2.1, is used for all LED devices including white and single color LEDs. In addition to chromaticity, the characteristics below are often used for single color LEDs.

8.6.1 Dominant Wavelength λ_d

The dominant wavelength is commonly used to specify the color of single color LEDs. It is defined in [1] as follows.

The wavelength of a monochromatic stimulus that, when additively mixed in suitable proportions with the specified achromatic stimulus, matches the color stimulus considered in the 1931 x, y chromaticity diagram.

This is illustrated in Fig. 8.15. For characterizing LEDs, the reference achromatic stimulus should be an equal-energy spectrum (sometimes called Illuminant E), which has the chromaticity coordinates $x_E = 0.3333$, $y_E = 0.3333$ [35]. It should be noted that dominant wavelengths of red LEDs are shorter than their peak wavelengths as shown in Fig. 8.16, and longer for blue LEDs. This is due to the slope of the color matching functions in the red and blue regions, where deeper red and blue portion of the spectrum contribute less to chromaticity. The difference can be greater than 10 nm for deep red and deep blue LEDs.

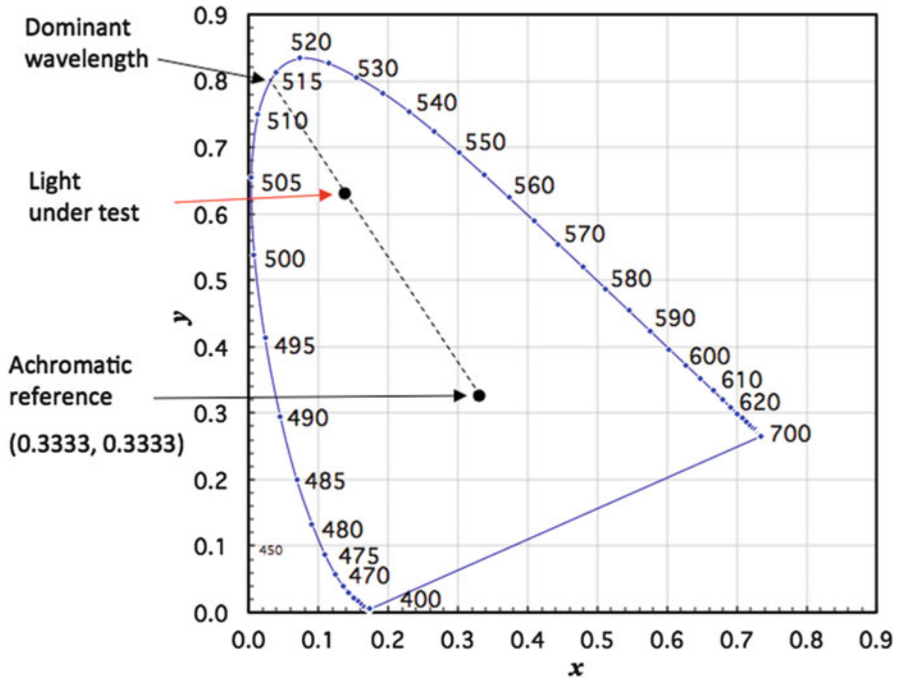

Fig. 8.15 Illustration of dominant wavelength

Fig. 8.16 An example of dominant wavelength and peak wavelength

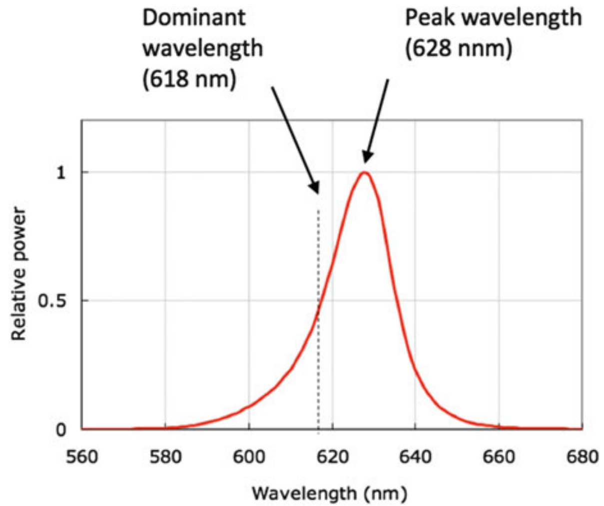

8.6.2 Centroid Wavelength λ_c

The centroid wavelength λ_c is defined in [35] and is calculated as the "center of gravity wavelength" by

$$\lambda_c = \int_{\lambda_1}^{\lambda_2} \lambda \cdot S(\lambda) d\lambda \Big/ \int_{\lambda_1}^{\lambda_2} S(\lambda) d\lambda \tag{8.17}$$

The diminishing tails of an LED spectrum (including noise and stray light) may affect the value of centroid wavelength significantly, which should be considered as an uncertainty in a given measurement.

8.6.3 Peak Wavelength λ_p

As described in Ref. [35], the wavelength at the maximum of the spectral power distribution is known as the peak wavelength λ_p. The (absolute) spectral distribution is usually normalized at this wavelength rather than at an arbitrary wavelength, to give a relative spectral power distribution with a maximum value of unity.

References

1. CIE S 017/E:2011, *ILV: International Lighting Vocabulary*, and its on-line version at http://eilv.cie.co.at. International Commission on Illumination
2. CIE 15:2004, *Colorimetry*, 3rd edn. International Commission on Illumination
3. ANSI_NEMA_ANSLG C78.377-2015, *Specifications for the Chromaticity of Solid State Lighting Products* (American National Standard for Electric Lamps, 2015)
4. CIE 13.3-1995, *Method of Measuring and Specifying Colour Rendering of Light Sources,* 3rd edn. International Commission on Illumination
5. CIE 177: 2007, *Colour rendering of white LED light sources* (International Commission on Illumination, 2007)
6. D.L. MacAdam, Visual sensitivities to colour differences in daylight. J. Opt. Soc. Am. **32**, 247 (1942)
7. ISO 11664-1:2007(E)/CIE S 014–1/E:2006: Joint ISO/CIE Standard: Colorimetry – Part 1: CIE Standard Colorimetric Observers
8. ISO 11664-2:2007(E)/CIE S 014-2/E:2006: Joint ISO/CIE Standard: Colorimetry – Part 2: CIE Standard Illuminants for Colorimetry
9. IEC 60081 Double-capped fluorescent lamps – Performance specifications, Annex D (1997)
10. ANSI C78.376 Specifications for the Chromaticity of Fluorescent Lamps (2001)
11. Y. Ohno, Practical use and calculation of CCT and Duv. LEUKOS **10**(1), 47–55 (2013). doi:10.1080/15502724.2014.839020
12. E.E. Dikel, G.J. Burns, J.A. Veitch, S. Mancini, G.R. Newsham, Preferred chromaticity of color-tunable LED lighting. LEUKOS **10**(2), 101–115 (2013). doi:10.1080/15502724.2013.855614

13. Y. Ohno, M. Fein, Vision experiment on acceptable and preferred white light chromaticity for lighting, CIE x039:2014, (2014), pp. 192–199
14. Y. Ohno, Semin Oh, Vision experiment II on white light chromaticity for lighting, Proc., CIE 2016 LQ&EE, Melbourne, CIE x042:2016, (2016), pp. 175–184
15. M.S. Rea, J.P. Freyssinier, White lighting. Color. Res. Appl. **38**(2), 82–92 (2013)
16. M. Perz, R. Baselmans, D. Sekulovski, Perception of illumination whiteness, CIE x043:2016, (2016)
17. Department of Energy. *ENERGY STAR® Program Requirements for CFLs ENERGY STAR Eligibility Criteria Energy-Efficiency Criteria – Version 4.1* (Department of Energy, Washington, 2008)
18. CIE TN 001: 2014, *Chromaticity Difference Specifications for Light Sources*
19. ISO 11664-4:2008(E)/CIE S 014-4/E:2007: Joint ISO/CIE Standard: Colorimetry – Part 4: CIE 1976 L*a*b* Colour Space
20. ISO 11664-5:2009(E)/CIE S 014-5/E:2009: Joint ISO/CIE Standard: Colorimetry – Part 5: CIE 1976 L*u*v* Colour Space and u′, v′ Uniform Chromaticity Scale Diagram
21. http://en.wikipedia.org/wiki/Munsell_color_system
22. D.B. Judd, A flattery index for artificial illuminants. Illum. Eng. (N.Y.) **62**, 593–598 (1967)
23. W.A. Thornton, A validation of the color preference index. J. Illum. Eng. **4**, 48–52 (1974)
24. W.A. Thornton, Color-discrimination index. J. Opt. Soc. Am. **62**, 191–194 (1972)
25. Y. Ohno, M. Fein, C. Miller, Vision experiment on chroma saturation for color quality preference, Proc. 28th Session of CIE, CIE 216:2015, (2015), pp. 60–69
26. K. Hashimoto, T. Yano, M. Shimizu, Y. Nayatani, New method for specifying color-rendering properties of light sources based on feeling of contrast. Color. Res. Appl. **32**, 361–371 (2007)
27. Lighting Research Center, guide to light and color in retail merchandising. ASSIST Recommends **8**(1), (2010). http://www.lrc.rpi.edu/programs/solidstate/assist/pdf/AR-ColorGuideforRetailLighting-March2010.pdf
28. W. Davis Y. Ohno, Color quality scale. Opt. Eng. **49**(3), 033602-1 to 15 (2010)
29. K. Smet, S. Jost-Boissard, W.R. Ryckaert, G. Deconinck, P. Hanselaer, Validation of a colour rendering index based on memory colours, CIE x035:2010, Proc., CIE 2010 Lighting Quality and Energy Efficiency (2010), pp. 136–142
30. R.W.G. Hunt, Light and dark adaptation and the perception of color. J. Opt. Soc. Am. **42**, 190–199 (1952)
31. M.S. Rea, J.P. Freyssinier, White lighting. Color. Res. Appl. **38**(2), 82–92 (2013)
32. CIE, *CIE Position Statement on CRI and Colour Quality Metrics*, (2015), http://www.cie.co.at/index.php?i_ca_id=981
33. CIE, *CIE Research Strategy*, 2nd topic, (2016), http://www.cie.co.at/index.php/Research+Strategy
34. BIPM, *SI Brochure: The International System of Units (SI)*, 8th edn. (2014), http://www.bipm.org/en/publications/si-brochure/
35. CIE 127:2007, *Measurement of LEDs,* 2nd edn

Chapter 9
LED-Based Luminaire Color Shift Acceleration and Prediction

Guangjun Lu, Willem Dirk van Driel, Xuejun Fan, Jiajie Fan, and Guo Qi Zhang

Abstract Color stability is of major concern for LED-based products. Currently, much effort is done on lumen maintenance, and for color shift, no agreed method currently exists, be it from testing or from prediction side. To investigate the physics of color shift, we present experiments of each individual part failure of each individual part that are present in LED-based products. In order to develop a color shift prediction method, it is imperative to investigate the color shift contribution by each individual part. We present a new method to predict color shift on a system level, which we named the *view factor approach*. We compare this

G. Lu (✉)
Beijing Research Centre, Delft University of Technology, Beijing, China

EEMCS Faculty, Delft University of Technology, Delft, The Netherlands

State Key Laboratory of Solid State Lighting, Changzhou, China
e-mail: lv-guangjun@163.com

W.D. van Driel
Philips Lighting, High Tech Campus, Eindhoven, The Netherlands

Delft University of Technology, EEMCS Faculty, Delft, The Netherlands
e-mail: W.D.vanDriel-1@tudelft.nl

X. Fan
State Key Laboratory of Solid State Lighting, Changzhou, China

Department of Mechanical Engineering, Lamar University, Beaumont, TX 77710, USA
e-mail: xuejun.fan@lamar.edu

J. Fan
Beijing Research Centre, Delft University of Technology, Beijing, China

State Key Laboratory of Solid State Lighting, Changzhou, China

College of Mechanical and Electrical Engineering, Hohai University, Changzhou, China
e-mail: jay.fan@connect.polyu.hk

G.Q. Zhang
EEMCS Faculty, Delft University of Technology, Delft, The Netherlands

Institute of Semiconductors, Chinese Academy of Sciences, Beijing, Haidian, China
e-mail: g.q.zhang@tudelft.nl

© Springer International Publishing AG 2018

W.D. van Driel et al. (eds.), *Solid State Lighting Reliability Part 2*, Solid State Lighting Technology and Application Series 3, DOI 10.1007/978-3-319-58175-0_9

prediction method with experiments on luminaire level to conclude that we have taken satisfactory first steps in the field of color shift predictions for LED-based systems.

9.1 Introduction

Luminous flux maintenance and color stability are two important factors to evaluate the lighting quality. While much research efforts have been done on the former and even some standards have been generated for lumen decay acceleration, research activities and achievements on the latter have lagged behind [1–3]. With increased adoption and accumulation of hours of use, awareness is growing that color shift is an issue for some products, especially in some important application fields, such as museums, patient examination rooms, urban scene illumination occasions, offices, street lighting, and so on [4, 5].

DOE Energy Star Program requires that the change of chromaticity over the lifetime of the product should be within 0.007 on the CIE 1976 (u',v') diagram [6]. Unlike traditional lighting products, the color shift mechanism of LED lighting is complex due to its much more comprehensive structure, generally composed of LED die, phosphor, silicone, reflector, diffusers, and so on, all of which may contribute to the color shift during operation, and each individual component has its own degradation mechanism [7]. Some studies have been done on some failure mechanisms of package level color shift, such as color shift to the blue end of spectrum caused by phosphor settle for the combination of "blue" LED and "yellow" phosphor, color shift caused by the discoloration of the plastic (PPA) or polycarbonate (PC) used in the package, color shift toward yellow end resulting from mean free path of the blue photons through the phosphor increase caused by delamination, and so on [8–17]. Mehr et al. experimentally investigated the color shift of remote phosphor plates made from Bisphenol-A polycarbonate (BPA-PC) and some other materials [18–21]. However, studies on the LED-based luminaire level color shift reliability are little publicly available except some based on the statistical (data-driven) method. This chapter will investigate LED-based luminaire level color shift mechanisms based on a breakdown method and introduce a novel approach for investigation of color shift contribution by each individual component. Finally, we propose a color shift acceleration and prediction approach.

9.2 Breakdown Method for Color Shift and Mechanism Investigation

9.2.1 Materials and Methods

A commercially widely used downlight with size of 4 in, power of 10 W, correlated color temperature (CCT) of 4000 k, was chosen as a representative, as shown in Fig. 9.1.

Fig. 9.1 Representative of downlight for color shift investigation

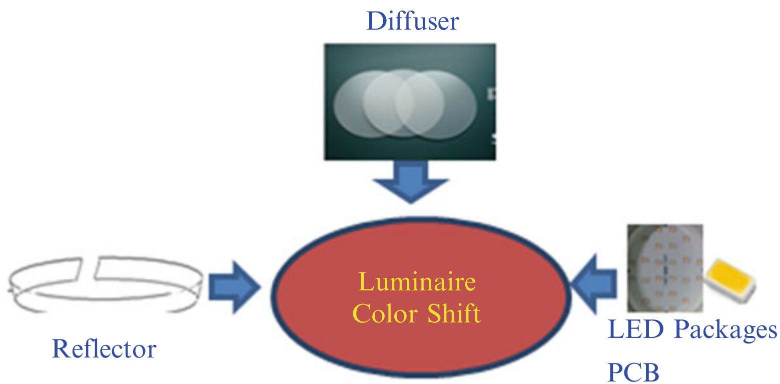

Fig. 9.2 Breakdown of downlight color shift

In terms of color shift in the study, an entire downlight can be divided into three individual parts, reflectors, diffusers, and LED packages. The color shift of each individual part adds up to the color shift of the entire downlight. Such a breakdown method can be simplified as shown in Fig. 9.2.

In the investigation, diffuser material used in the downlight is PMMA, which is widely used in indoor lighting application due to comparatively low cost and mature manufacturing process. Reflective material for the reflector is the novel microcellular PET material. Compared with the traditional metal-based reflective material, the microcellular PET has many advantages, such as high total reflectivity, high diffuse reflectivity, and lightweight. LED package is the mid-power 5630 which has comparatively high luminous efficiency and is flexible in combination for downlight application. Figures 9.3 and 9.4 show the molecular structures of PMMA and PET materials, respectively.

To investigate the physics of color shift failure of each individual part, experiments were done as follows.

Rectangular pure PMMA plates with a thickness of 3 mm and dimension of 30 mm × 50 mm and rectangular microcellular PET reflective sheets with a thickness of 0.51 mm and the same dimension of 30 mm × 50 mm were subjected to the following three experimental conditions, respectively: (1) Thermal aging in an

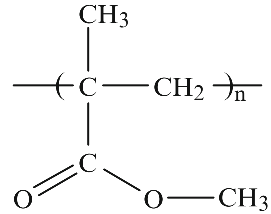

Fig. 9.3 Molecular structure of PMMA

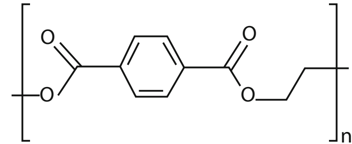

Fig. 9.4 Molecular structure of PET

aging test oven with a temperature setting of 85 °C for more than 3000 h; (2) Blue light irradiation at 85 °C for more than 3000 h (The specimens were placed inside the oven at 85 °C and exposed to blue light through the oven glass window generated by the blue light LEDs outside the oven). The wavelength of blue light used is 450 nm, the distance between blue light source and the specimens is 40 cm, and the blue light intensity that the specimen received is around 40 k lux; (3) Humidity reliability test (Specimens were put in the isothermal oven for more than 3000 h at 85 °C and 85% RH). In addition, PMMA specimens of the same type and thickness with a dimension of 100 mm × 100 mm were put separately in two ovens with a temperature of 100 °C for 3000 h and 150 °C for 360 h, respectively.

While subjected to the aging conditions: room temperature, 85 °C and 85 °C and 85% RH, the LED packages were separately mounted to small hexagonal heat sink plates and lighted up via a jig with the same current as that normally used in the downlight luminaire.

Transmittance spectra of PMMA plates and reflectance spectra of microcellular PET specimens with different aging conditions were recorded in the range 380–740 nm with a step of 5 nm with the Lambda 950 spectrophotometer (PerkinElmer 950). Relative reflectance mode other than the absolute mode is chosen to do the measurement with a universal reflectance accessory as the light spectral reference.

Stress-strain curves were also measured with a DMA Q800 to characterize the mechanical properties of Microcellular PET specimens with different aging conditions. Infrared spectra of specimens were measured for chemical analysis in the range of 900–1800 cm^{-1} using a Perkin–Elmer Spectrum 100 series spectrometer in the attenuated total reflection (ATR) mode for 180 scans at a resolution of 5 cm^{-1}.

In addition, in order to quantify the color shift effects of microcellular PET specimens after aging, a downlight LED luminaire was used and measured by an integrating sphere with a diameter of 2 m at 2 pi mode. The LED packages subjected to different aging conditions for a different aging time were also measured by another integrating sphere with a diameter of 0.5 m at 2 pi mode too. For more details, please refer to [22–25].

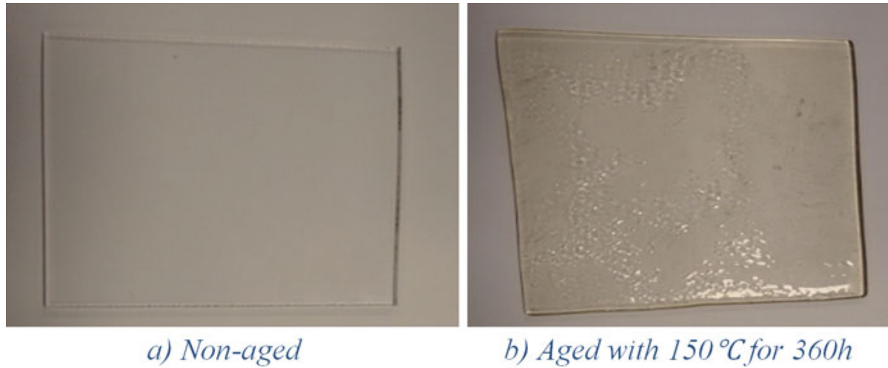

Fig. 9.5 Discoloration of PMMA after aging. (**a**) Nonaged. (**b**) Aged with 150 °C for 360 h

9.2.2 Results and Discussions

9.2.2.1 PMMA

Discoloration was not observed for any sample subjected to aging of 85 °C for 5000 h, or with additional blue light irradiation for 5000 h, or with additional humidity of 85%RH for 5000 h, or even with aging of 100 °C for 3000 h. By contrast, after 360 h of thermal aging at 150 °C in the oven, the color in the surface of PMMA specimen tends to be slightly yellowing. Pictures of the specimen before and after aging are shown in Fig. 9.5.

Note that the aging temperature 150 °C is above Tg (around 110 °C) and below melting point (around 200 °C) of the PMMA material, and we didn't observe any color change of the surface during the first day of aging.

Transmittance spectra of PMMA under different aging conditions were also measured. The transmittance of specimen aged at 150 °C for 360 h is lower than that of any subjected to other aging conditions in the wavelength range from 360 to 760 nm, and the specimens subjected to other aging conditions have almost the same spectra as that of the nonaged specimen. Furthermore, as shown in Fig. 9.7, the transmittance reduction (calculated on the difference of transmittance between lines of nonaged and aged at 150 °C shown in Fig. 9.6) of the specimen aged at 150 °C is wavelength dependent, and the reduction of transmittance at around 450 nm (blue light area) is much higher than that at around 590 nm (yellow light area) (Fig. 9.7).

FTIR analysis implies oxidation occurred to that specimen. There are three steps involved in the aging. The first step is the splitting off of the acrylate group, whereas the second step is the actual oxidation and followed by hydrogenation. Such chemical mechanism can be described in Fig. 9.8.

It should be pointed out here the experiments found that PMMA will exhibit yellowing only at high temperatures (150 °C) which are well above the glass transition temperature of the polymer. This temperature is also above the accepted

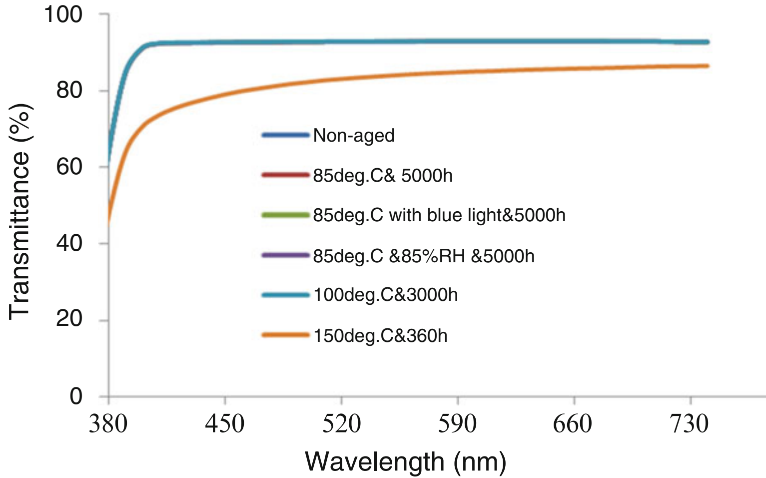

Fig. 9.6 Transmission spectra after being subjected to different aging conditions (Note: the 85 °C and 100 °C lines coincide with the nonaged line)

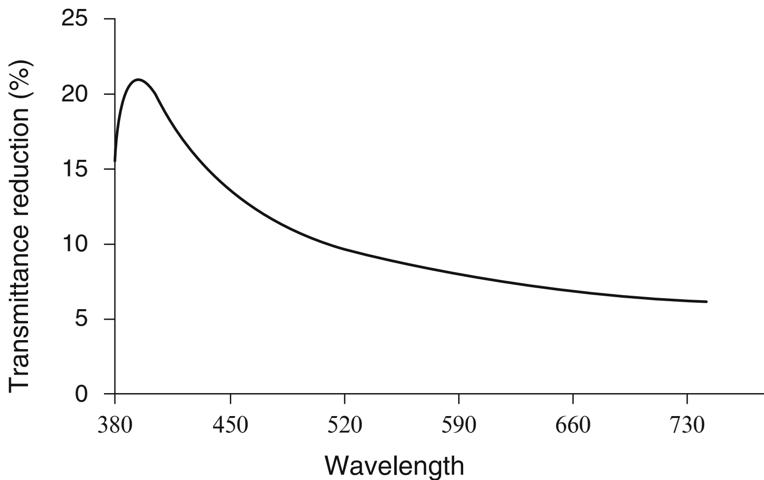

Fig. 9.7 Transmittance reduction for the PMMA subjected to 150 °C for 360 h

use temperature of PMMA and is unlikely to be used in a practical luminaire. Therefore, the risks on introducing a new failure mode is high since the experiments were performed above Tg and chain mobility will be increased.

The nonuniform reduction of transmittance in the transmission spectrum caused by aging could induce the change of radiant flux intensity ratio of blue light to yellow light, which gives rise to the color shift in perception and chromaticity change in the CIE1976 diagram. In order to quantify color shift effects of the specimen subjected to 150 °C for 360 h, as aforementioned, a downlight LED

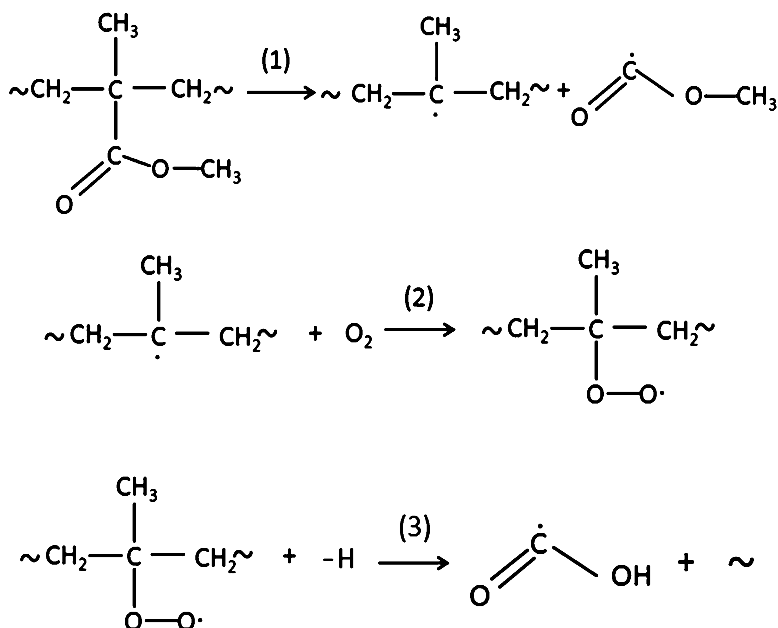

Fig. 9.8 Chemical mechanisms of oxidation and hydrogenation during aging

luminaire mounted with such an aged sample and a nonaged one of identical size was measured by an integrating sphere. Normalized spectral power distributions are shown in Fig. 9.9.

The results of color coordinates in the CIE1976 diagram by such measurement are also given, as shown in Fig. 9.10. As can be found in Fig. 9.9, the peak wavelength neither at blue light area (around 450 nm) nor at yellow light area (around 590 nm) changed; however, the peak intensity at blue light area has a more severe reduction than that at the yellow light area, which causes the reduction of radiant flux intensity ratio of blue light to yellow light and hence induces the color shift to yellow as confirmed in Fig. 9.10.

9.2.2.2 Microcellular PET

After 4000 h of aging for the microcellular PET reflective material, discoloration was not observed to any specimen. However, during manually handling when we took out the samples from the humidity test oven, one specimen broke. Hence, the stress-strain measurement was conducted on all the specimens to investigate the possible changes of mechanical property. Only the sample subjected to humidity test fractured, and this fracture occurred at a strain of 0.38% (1.1 Mpa). The samples of the nonaged and 4000 h thermally aged did not fracture during the test. The reflectance spectra of specimens after 4000 h of aging were measured and recorded

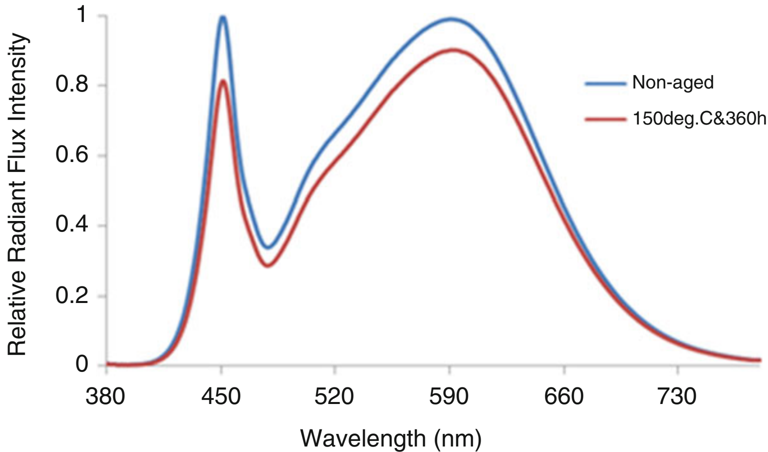

Fig. 9.9 SPDs of LED-based luminaire mounted with aged PMMA specimen

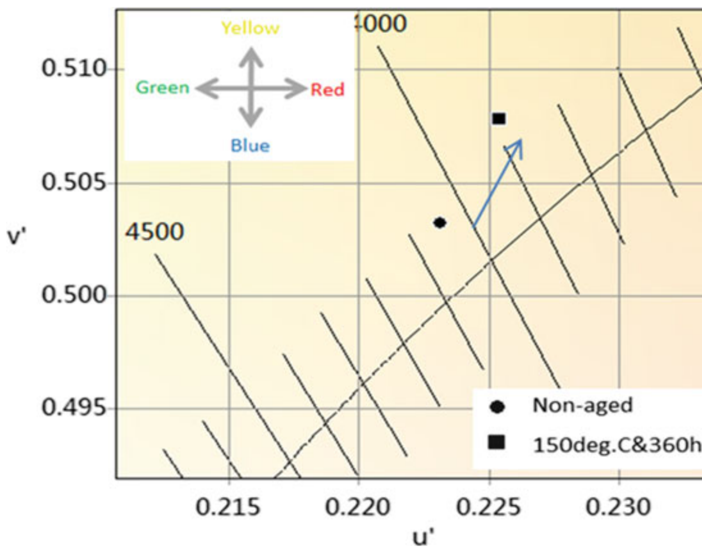

Fig. 9.10 Color coordinates in the CIE 1976 Diagram for the LED-based luminaire mounted with PMMA specimens

by a Lambda 950 spectrophotometer in a wavelength range from 380 to 800 nm with a step of 5 nm. Reflectance spectra of microcellular PET with different aging conditions are shown in Fig. 9.11. The reflectance spectrum of the 85 °C aged specimen is nearly the same as that exposed to additional blue light irradiation. Furthermore, the reflectance spectrum of the 85 °C aged specimen is higher than the nonaged one in the wavelength range from 380 to 430 nm. The specimen which was

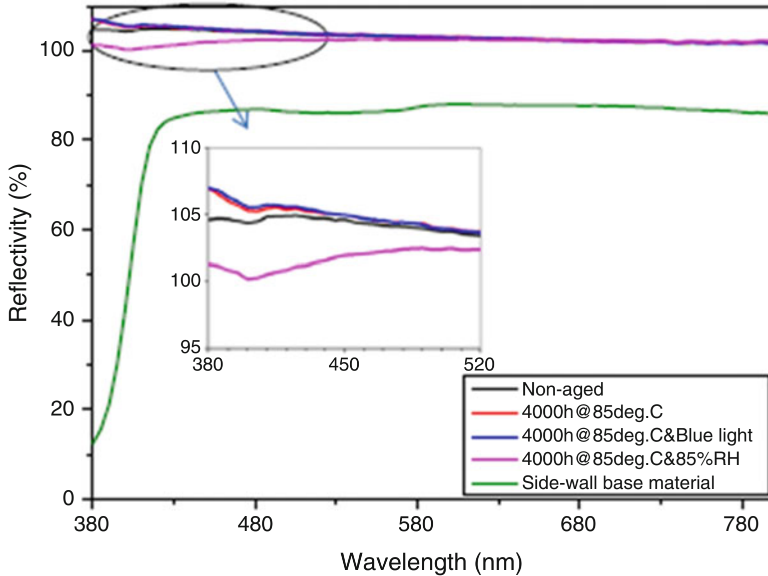

Fig. 9.11 Reflectance spectra of microcellular PET with different aging conditions and side-wall base material

subjected to humidity test has an obvious reflectivity decrease in the range from 380 to 520 nm compared to the nonaged sample.

FTIR studies were performed in order to chemically explain the abovementioned optical and mechanical property changes after aging. Compared to the slower oxidation in the thermal aging test, the hydrolytic degradation in the humidity test induces chemical structure change of the specimen, which causes the remarkable changes of optical and mechanical properties.

In order to quantify color shift effects of those specimens after aging under different conditions, a downlight LED luminaire with aged and nonaged specimens was measured by an integrating sphere, respectively. The specimen subjected to 4000 h of thermally aged test has a color shift of 0.0001 due to a reduction of u' by 0.0001, while 4000 h of humidity test causes a color shift of 0.0004 with an equivalent reduction of u' and v' of 0.0003, which is far less than 0.001 (or 1 sdcm). Note that embrittlement of the microcellular PET after 4000 h of humidity test will make it so fragile that when it is disturbed (e.g., for repair or ceiling maintenance), the material may crumble exposing the underlying paint reflector. Consequently, during the color shift investigation for 4000 h of humidity test, the microcellular PET was not mounted, during which the side-wall base material, which has a lower reflectivity, acted as a reflector. Color shift by PET was attributed to the change of flux intensity ratio of blue light to yellow light, similar to the PMMA.

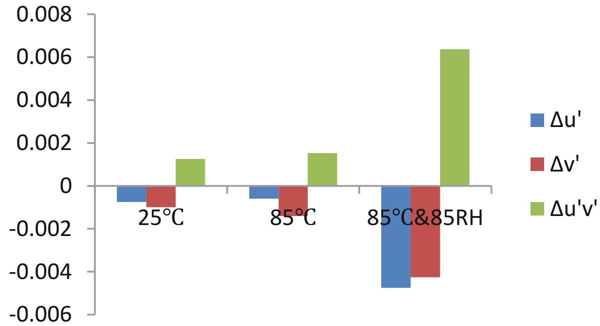

Fig. 9.12 Color shift of LED packages subjected to different aging conditions

9.2.2.3 LED Package

Color data of 5630 LED packages which were subjected to different aging conditions have been measured. Color shift results ($\Delta u^{'}, \Delta v^{'}, \Delta u^{'}v^{'}$) of the specimen subjected to different aging conditions for ~6000 h were shown in Fig. 9.12. First 2000 h of data was not used due to unstable degradation. It can be found that the specimen after humidity aging test has the maximum color shift $\Delta u'v'$, and the color shift tends to blue light area for both thermal aging conditions and humidity test. Some studies implied that the moisture entrapment to the inside of silicone bulk caused a localized extremely high temperature (around 300 °C), which accelerates the degradation of LED package.

As a summary, in the color shift study, the downlight can be divided into three parts, the diffuser, the reflector, and the LED packages, which have different color shift failure physics or mechanisms and contribute differently to the total color shift. Optical properties will be changed under thermal aging conditions, which will contribute color shift for diffuser and reflectors. LED packages have a color shift toward blue during thermal aging and humidity test. Humidity test demonstrates a strong acceleration in color shift.

9.3 A Novel Approach for Color Shift Investigation on LED-Based Luminaires

9.3.1 Materials and Methods

In order to develop the color shift acceleration and prediction method, it is important to investigate the color shift contribution by each individual part. Hence, a novel approach for color shift investigation based on view factor method was proposed in this section. The downlight to be investigated was aged at 85 °C in an oven and lighted on for around 4000 h. Measured the soldering temperature Ts is around 105 °C with a thermal couple. To quantify the color and lumen change of the

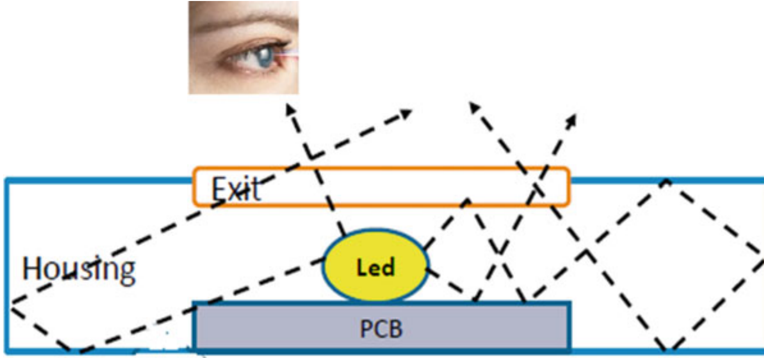

Fig. 9.13 Schematic diagrams of light paths

LED packages mounted in the downlight during aging, same type of LED packages also from same suppliers was separately mounted and placed in the same oven and lighted on with equivalent current. The Ts of LED package measured is also around 105 °C. The light flux, color, and SPDs (spectrum power distributions) of those LED packages were measured and recorded by an integrating sphere before and after aging. The diffuser used in the downlight is a type of commercial misty PMMA with a thickness of 2 mm. The transmittances of diffuser before and after aging were measured. The reflective material used in the downlight is one type of commercial PET, whose reflectivity before and after aging were also measured. Refer to [26] for more details.

To help illustrate this approach, a schematic diagram of light paths for the downlight investigated is shown in Fig. 9.13. Each exchange of light in the light paths can be considered as a contribution to color shift. The matrix Eq. 9.1 shown below can be used to describe the exchange.

$$\begin{pmatrix} \Phi_{\text{itoLEDs}} \\ \Phi_{\text{itopcb}} \\ \Phi_{\text{itohousing}} \\ \Phi_{\text{itoexit}} \end{pmatrix} = \begin{pmatrix} F_{L-L} & F_{P-L} & F_{h-L} & F_{e-L} \\ F_{L-P} & F_{P-L} & F_{h-p} & F_{e-p} \\ F_{L-h} & F_{P-h} & F_{h-h} & F_{e-h} \\ F_{L-e} & F_{P-e} & F_{h-e} & F_{e-e} \end{pmatrix} \begin{pmatrix} \Phi_{\text{ifromLEDs}} \\ \Phi_{\text{ifrompcb}} \\ \Phi_{\text{ifromhousing}} \\ \Phi_{\text{ifromexit}} \end{pmatrix} \tag{9.1}$$

Where Φ stands for the light flux and the number *i* denotes the number of reflections undergone. *F* is the so-called view factor (conservation of light: sum of each matrix column =1). The software LightTools is used to extract the view factor *F* and light flux Φ. For the physics of reflection, it can be described as the Eq. 9.2:

$$\begin{pmatrix} \Phi_{i+1\text{fromLEDs}} \\ \Phi_{i+1\text{frompcb}} \\ \Phi_{i+1\text{fromhousing}} \\ \Phi_{i+1\text{fromexit}} \end{pmatrix} = \begin{pmatrix} R_L & & & \\ & R_p & & \\ & & R_h & \\ & & & R_e \end{pmatrix} \begin{pmatrix} \Phi_{\text{itoLEDs}} \\ \Phi_{\text{itopcb}} \\ \Phi_{\text{itohousing}} \\ \Phi_{\text{itoexit}} \end{pmatrix} \tag{9.2}$$

Each reflection is accompanied with a small color change $\Delta u_i{}'$, $\Delta v_i{}'$, depending on part L, p, h, and e.

The equation for the exit transmission can be described in Eq. 9.3, as shown below. It also accompanies with a small color change during transmission. Φ_{toexit} is the light flux to exit for transmission, which can be calculated via Eq. 9.4:

$$\begin{aligned}\Phi_{\text{fromexit=}} &= (1 - R_e - A)\Phi_{\text{toexit}} \\ \Phi_{\text{toexit}} &= \sum_i \Phi_{\text{itoexit}}\end{aligned} \tag{9.3}$$

$$= F_{L-e}\sum_i \Phi_{\text{ifromLEDs}} + F_{h-e}\sum_i \Phi_{\text{ifromhousing}} + F_{p-e}\sum_i \Phi_{\text{ifrompcb}} + F_{e-e}\sum_i \Phi_{\text{ifromexit}} \tag{9.4}$$

Color shift $\Delta u'$, $\Delta v'$, $\Delta u'v'$ of the flux to exit Φ_{toexit} in the downlight could be estimated via below Eqs. 9.5, 9.6, and 9.7. $\Delta u'_L$, $\Delta u'_p$, $\Delta u'_h$, and $\Delta u'_e$ denote the color changes of fluxes exchanged on the part L, p, h, and e. r is the ratio of the flux returned to the exit after a cycle of reflections in the downlight. All of them could also be captured by Monte Carlo simulation with the software LightTools. The color change caused by the transmission of exit diffuser can be also got via Monte Carlo simulation.

$$\Delta u' = w_{\text{LED}} \bullet \Delta u_L{}' + w_{\text{pcb}} \bullet \Delta u_P{}' + w_{\text{housing}} \bullet \Delta u_h{}' + w_{\text{housing}} \bullet \Delta u_e{}' \tag{9.5}$$

$$\Delta v' = w_{\text{LED}} \bullet \Delta v_L{}' + w_{\text{pcb}} \bullet \Delta v_P{}' + w_{\text{housing}} \bullet \Delta v_h{}' + w_{\text{housing}} \bullet \Delta v_e{}' \tag{9.6}$$

$$\Delta u'v' = \sqrt{(\Delta u')^2 + (\Delta v')^2} \tag{9.7}$$

Where $w_{\text{LED}}, w_{\text{pcb}}, w_{\text{housing}}$ and w_{exit} could be described as below:

$$\begin{aligned}w_{\text{LED}} &= \frac{F_{L-e}\sum_i \Phi_{\text{ifromLEDs}}}{\Phi_{\text{toextt}}} \\ w_{\text{pcb}} &= \frac{F_{p-e}\sum_i \Phi_{\text{ifrompcb}}}{\Phi_{\text{toexit}}} \\ w_{\text{housing}} &= \frac{F_{h-e}\sum_i \Phi_{\text{ifromhousing}}}{\Phi_{\text{toexit}}} \\ w_{\text{exit}} &= \frac{r\sum_{i-1} \Phi_{\text{ifromexit}}}{\Phi_{\text{toexit}}}\end{aligned}$$

To perform the simulations for extraction, initial condition is shown in equation:

$$\begin{pmatrix} \Phi_{0\text{fromLEDs}} \\ \Phi_{0\text{frompcb}} \\ \Phi_{0\text{fromhousing}} \\ \Phi_{0\text{fromexit}} \end{pmatrix} = \begin{pmatrix} \Phi_{\text{LEDs}} \\ 0 \\ 0 \\ 0 \end{pmatrix} \tag{9.8}$$

Some assumptions were made as follows. The LED is top emitting, and light exits from LEDs, and there is no bouncing back and forth from them.

9.3.2 *Results and Discussions*

9.3.2.1 Measured Results for Color Shift of Downlights After Aging

The SPD, lumen, and color data of the downlight before and after aging were measured and recorded by an integrating sphere with a diameter of 2 m at 2 pi mode. Figure 9.14 shows the SPD of the downlight before and after aging. Obvious degradation of the flux intensity could be found both in the yellow light area (around 590 nm) and blue light area (around 450 nm). Table 9.1 shows the lumen and color changes for this downlight.

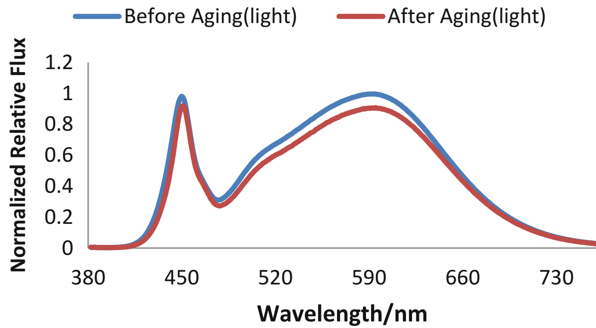

Fig. 9.14 SPDs of downlight before and after aging

Table 9.1 Lumen and color data measurement before and after aging

			Before aging	After aging
Power		(W)	10.1	10.1
Luminous flux		[lm]	936.65	838.66
Lumen degradation		[–]	10.46%	
Color point	u'	[–]	0.2229	0.2248
	v'	[–]	0.5026	0.5041
Color shift	$\Delta u'$	[–]	0.0019	
	$\Delta v'$	[–]	0.0015	
	$\Delta u'v'$	[–]	0.0024	

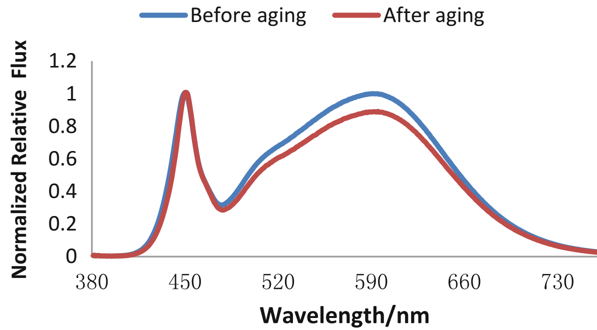

Fig. 9.15 SPDs for LED packages before and after temperature aging

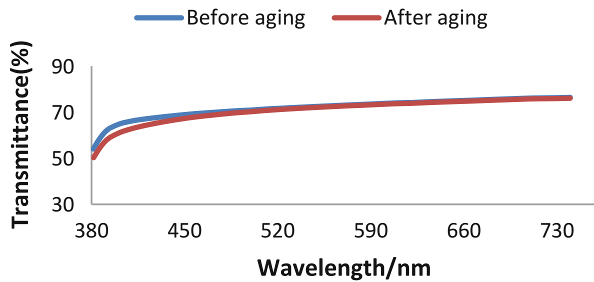

Fig. 9.16 Transmittance measured for PMMA diffuser before and after aging

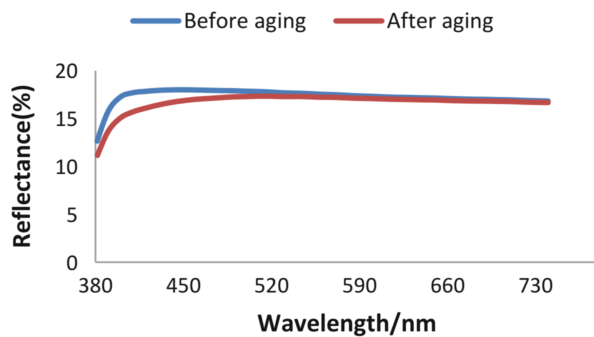

Fig. 9.17 Reflectance measured for PMMA diffuser before and after aging

9.3.2.2 Inputs for Simulation

The averages of SPDs for LED packages before and after aging are shown in Fig. 9.15, which will be used as inputs for simulation.

Both the transmittance and reflectance before and after aging were measured for the diffuser, shown in Figs. 9.16 and 9.17, respectively, which will be used as input for simulation.

PET was not only mounted on the side-wall used as the housing reflective material but also covered the PCB surface. So the housing and PCB's contribution on the color shift depends on the change of PET's reflectance. Figure 9.18 shows the reflectance measurement before and after aging, which will be used as inputs for simulation.

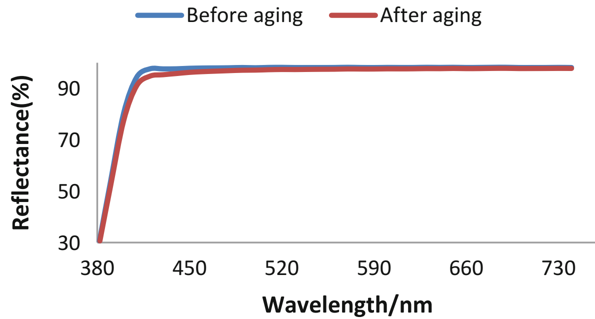

Fig. 9.18 Reflectance measured for PET material before and after aging

Table 9.2 View factor Table for 0 h

t0		From LEDs	PCB	Housing	Exit
To	LEDs	0.00000	0.00000	0.00000	0.00000
	PCB	0.00000	0.00000	0.24526	0.53365
	Housing	0.21378	0.21378	0.00000	0.46635
	Exit	0.78622	0.78622	0.75474	0.00000

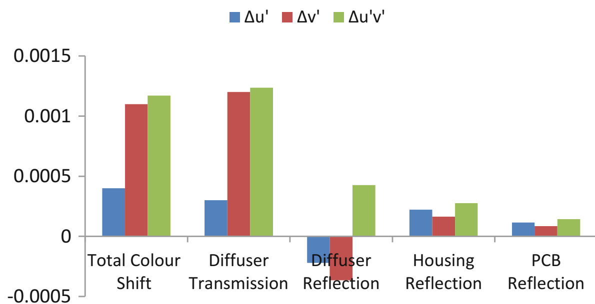

Fig. 9.19 Color shift of downlight at 0 h

9.3.2.3 Color Shift Results

1. *Color shift before aging (0 h).*

View factors were extracted by Monte Carlo simulation as shown in Table 9.2 for the downlight before aging. Color shift of each individual part could be also got via simulation. Accordingly, the color shift of downlight could be calculated. Figure 9.19 shows the color shift of downlight at 0 h and contribution by each individual part. Even nonaged (at 0 h), the light coming out of the downlight has a color change of ~0.001 compared with the color of light emitted from the LED packages. The diffuser has a major contribution. When the light goes through the diffuser, the ratio of blue light to yellow light in the SPD has a change due to the transmittance difference between wavelengths, which leads to the color change.

Table 9.3 View factor Table for 4000 h

t = 4000 h		From			
		LEDs	PCB	Housing	Exit
To	LEDs	0.00000	0.00000	0.00000	0.00000
	PCB	0.00000	0.00000	0.23939	0.53598
	Housing	0.21378	0.21378	0.00000	0.46402
	Exit	0.78622	0.78622	0.76061	0.00000

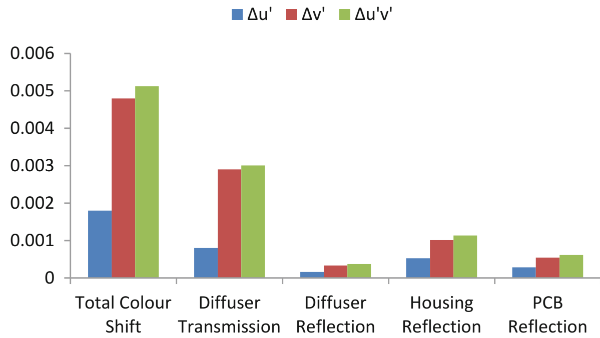

Fig. 9.20 Color shift of downlight at 4000 h

2. *Color shift after aging (4000 h)*

Similarly, we got the view factor table (shown in Table 9.3) for the downlight after aging for 4000 h. Color shift of each individual part and accordingly the color shift of downlight could be calculated. Figure 9.20 shows the color shift of downlight after aging for 4000 h and contribution by each individual part.

9.3.2.4 Comparison and Discussion

Note that color change shown in Figs. 9.19 and 9.20 does not include the color shift of LED packages. Figure 9.21 shows the color shift and contribution of each individual part including LED packages caused by aging.

According to results from the simulation and calculation method, after aging for 4000 h, the downlight has a total color shift of ~0.002, even less than the color shift of LED packages, which is around 0.0025. This is because the two major contributors LED package and diffuser have an opposite contribution in the color shift component of $\Delta v'$. The component $\Delta v'$ of LED package has a decrease of 0.0026, compared to the increase of around 0.0017 caused by diffuser transmission change during aging. Color shift induced by aging of LED packages is quite different from that of diffuser. LED packages' relative flux degradation in SPD occurred obviously in the yellow light area, which induces the color shift to blue. By contrast, the color will shift to yellow for aging of the diffuser since there is much more degradation of flux in the blue light area.

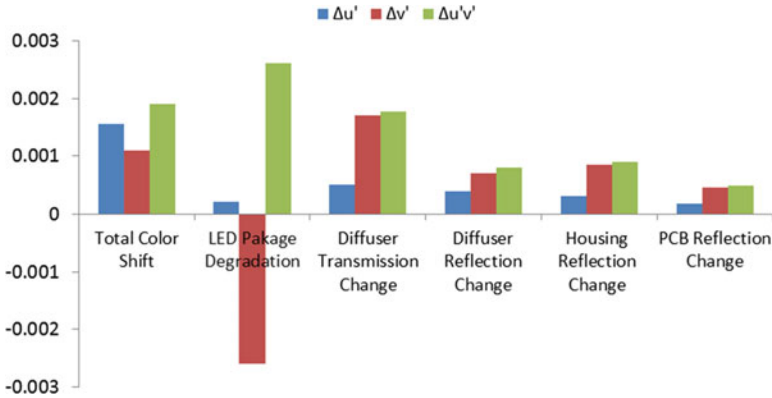

Fig. 9.21 Color shift contribution after aging

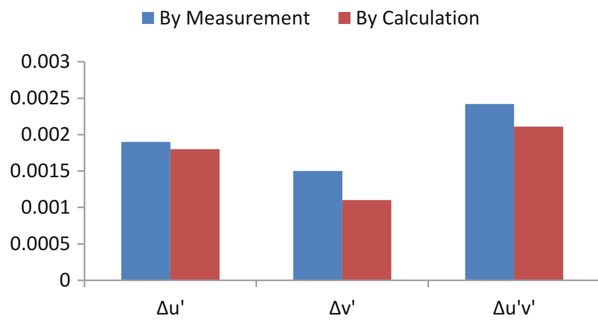

Fig. 9.22 Downlight color shift comparison between measurement and proposed approach

Figure 9.22 shows the comparison between measurement and proposed approach. It could be found that the results are comparable. Errors for the approach proposed in this section could be attributed to several factors. One is the assumption: we assumed there is no bouncing back and forth from LED packages, which would slightly decrease the color change. The other factor is measurement error of optical parameters as inputs for simulation.

9.4 Luminaire Color Shift Acceleration and Prediction

Based on the above investigation, we can breakdown the total color shift $\Delta u'v'$ into component $\Delta u'$ and component $\Delta v'$ for acceleration and prediction. Since each individual part has different contribution and mechanism, we can add up the contribution by each individual part to the color shift component, and acceleration can be performed individually. If we only consider the temperature aging for acceleration, the prediction could be described as below Eqs. 9.9, 9.10, and 9.11.

$$\Delta u'(t,T) = \Delta u'_{\text{led}}(t,T) + \Delta u'_{\text{diffuser}}(t,T) + \Delta u'_{\text{reflector}}(t,T) \tag{9.9}$$

$$\Delta v'(t,T) = \Delta v'_{\text{led}}(t,T) + \Delta v'_{\text{diffuser}}(t,T) + \Delta v'_{\text{reflector}}(t,T) \tag{9.10}$$

$$\Delta u'v'(t,T) = \sqrt{\Delta u'^2(t,T) + \Delta u'^2(t,T)} \tag{9.11}$$

We could follow below steps for luminaire color shift acceleration and prediction.

Step1 For LED packages, determine the SPDs as *F* (time, temperature) by integrating sphere measurement, and for other components, determine the optical parameters as *F* (time, temperature) by optics measurement.

Step2 Using Step 1 as inputs, determine the Du' and Dv' as *F* (time, temperature) for each component by simulation. Meanwhile, determine the view factor matrix as *F* (time, temperature).

Step3 For each component, fit the acceleration model (linearity, Arrhenius + Weibull/lognormal).

Step4 Calculate system level color shift based on Eqs. 9.9, 9.10, and 9.11.

9.5 Conclusions

In this chapter, we present experimental results for components in LED-based products which have color shift concern. We use this test data as input for a newly developed system level prediction method that we name the view factor approach. We verified the new method with experiments with luminaires to conclude that we have taken satisfactory first step in the field of color shift predictions for LED-based systems.

References

1. Illuminating Engineering Society, *LM-80-08 Standard- Approved Method for Measuring. Lumen Maintenance of Led Lighting Sources* (IES, New York, 2008)
2. Illuminating Engineering Society, *TM-21-11 Standard-Projecting Long Term Lumen Maintenance of LED Light Sources* (IES, New York, 2011)
3. China Solid State Lighting Alliance, *CSA-020 Standard-Accelerating Depreciation Test Method for Light Emitting Diode (LED) Lighting Products*, (CSAS, Beijing, 2013)
4. M. Royer, R. Tuttle, S. Rosenfeld, N. Miller, *Color Maintenance of LEDs in Laboratory and Field Applications, Gateway demonstrations, Prepared for Solid-State Lighting Program,* (Wiley, New York, 2013)
5. J. Lynn Davis, K. Mills, M. Lamvik, R. Yaga, S.D. Shepherd, J. Bittle, N. Baldasaro, E. Solano, G. Bobashev, C. Johnson, A. Evans, System reliability for LED-based products, in *15th International Conference on Thermal, Mechanical and Multi-Physics Simulation and Experiments in Microelectronics and Microsystems*, (EuroSimE, Belgium, 2014)

6. Eligibility Criteria – Version 1.3, ENERGY STAR Program Requirements for Solid State Lighting Luminaires., http://www.energystar.gov/ia/partners/product_specs/program_reqs / Solidstate_Lighting_Program_Requireme-nts.pdf
7. W.D. Van Driel, X.J. Fan, *Solid State Lighting Reliability:Components to Systems* (Springer, New York, 2013)
8. S. Chhajed, Y. Xi, Y.-L. Li, T. Gessmann, E.F. Schubert, Influence of junction temperature on chromaticity and color-rendering properties of trichromatic white-light sources based on light-emitting diodes. J. Appl. Phys. **97**, 054506 (2005)
9. T. Yanagisawa, T. Kojima, Long-term accelerated current operation of white light-emitting diodes. J. Lumin. **114**, 39–42 (2005)
10. L.-R. Trevisanello, M. Meneghini, G. Mura, C. Sanna, S. Buso, G. Spiazzi, M. Vanzi, G. Meneghesso, E. Zanoni, Thermal stability analysis of high brightness LED during high temperature and electrical aging, seventh international conference on solid state lighting, Proc. SPIE. 6669, 666913-3, (2007)
11. J. Huang, D. S. Golubović, S. Koh, D. Yang, X. Li, X. Fan, G.Q. Zhang, Rapid degradation of mid-power white-light LEDs in saturated moisture conditions, IEEE Trans. Device Mater. Reliab. **99**, 478–485 (2015)
12. N. Narendran, Y. Gu, J.P. Freyssinier, H. Yu, L. Deng, Solid-state lighting: failure analysis of white LEDs. J. Cryst. Growth **268**, 449–456 (2004)
13. J. Huang, D.S. Golubović, S. Koh, D. Yang, X. Li, X. Fan, G.Q. Zhang, Degradation modeling of mid-power white-light LEDs by using Wiener process. Opt. Express **23**, A966–A978 (2015)
14. J. Fan, K.C. Yung, M. Pecht, Physics-of-failure-based prognostics and health management for high-power white light-emitting diode lighting. IEEE Trans. Device Mater. Reliab. **11**(3), 407–416 (2011)
15. M.H. Chang, D. Das, P.V. Varde, M. Pecht, Light emitting diodes reliability review. Microelectron. Reliab. **52**, 762–782 (2012)
16. P. Lall, J. Wei et al, *L70 Life Prediction for Solid State Lighting Using Kalman Filter and Extended Kalman Filter Based Models*, Proceeding ECTC conference Las Vegas USA, (2013) pp. 1454–1465
17. M. Buffolo, C. De Santi, M. Meneghini, D. Rigon, G. Meneghesso, E. Zanoni, Long-term degradation mechanisms of mid-power LEDs for lighting applications. Microelectron. Reliab. **55**, 1754–1758 (2015)
18. M. Yazdan Mehr, W.D. van Driel, H. Udono, G.Q. Zhang, Surface aspects of discoloration in bisphenol a polycarbonate (BPA-PC), used as lens in LED-based products. Opt. Mater. **37**, 155–159 (2014)
19. M. Yazdan Mehr, W.D. van Driel, K.M.B. Jansen, P. Deeben, G.Q. Zhang, Lifetime assessment of plastics lenses used in LED-based products. Microelectron. Reliab. **54**, 138–142 (2014)
20. M. Yazdan Mehr, W.D. van Driel, K.M.B. Jansen, P. Deeben, M. Boutelje, G.Q. Zhang, Photodegradation of bisphenol A polycarbonate under blue light radiation and its effect on optical properties. Opt. Mater. **35**, 504–508 (2012)
21. M. Yazdan Mehr, W.D. van Driel, G.Q. Zhang, Progress in understanding color maintenance in solid-state lighting systems. Engineering **1**, 170–178 (2015)
22. G. Lu, M. Yazdan Mehr, W.D. van Driel, X. Fan, J. Fan, K.M.B. Jansen, G.Q. Zhang, Color shift investigations for LED secondary optical designs- comparison between BPA-PC and PMMA. Opt. Mater. **45**, 37–41 (2015)
23. G. Lu, W.D. van Driel, X. Fan, M. Yazdan Mehr, J. Fan, K.M.B. Jansen, G.Q. Zhang, Degradation of microcellular PET reflective materials used in LED-based products. Opt. Mater. **49**, 79–84 (2015)
24. G. Lu, W.D. van Driel, X. Fan, M. Yazdan Mehr, J. Fan, C. Qian, K.M.B. Jansen, G.Q. Zhang, et al., Opt. Mater. **54**, 282–287 (2016)
25. G. Lu, W.D. van Driel, X. Fan, M. Yazdan Mehr, J. Fan, C. Qian, G.Q. Zhang, *A POF Based Breakdown Method for LED Lighting Color Shift Reliability* (SSL, China, 2015)
26. G. Lu, W.D. van Driel, J. Fan, C. Qian, H. Ye, X. Fan, G.Q. Zhang, *A Novel Approach for Color Shift Investigation on LED-based Luminaires*, (Eurosime, France, 2016) (On line publication)

Chapter 10
Chromaticity Maintenance in LED Devices

J. Lynn Davis, Karmann Mills, Robert Yaga, Cortina Johnson, Monica Hansen, and Michael Royer

Abstract With the recent improvements in LED luminous efficacy that have been achieved by the lighting industry, greater attention is being devoted to understanding the long-term performance of LEDs. Specifically, there is a need to understand and predict the ability of LEDs to maintain luminous flux and chromaticity over time. The issue of chromaticity maintenance (aka, chromaticity stability and color shift) is especially important for LED devices since they may be used for 10 years or more without replacement of the light source. The characteristics of LEDs have a significant impact on chromaticity maintenance for LED-based lamps and luminaires. However, other components of an LED device, including lenses, reflectors, and device design, can also have an impact on chromaticity. Understanding the aging characteristics of LEDs, lenses, and reflectors is critical to designing and building LED-based products for long-term use.

10.1 Introduction

The luminous efficacy of light-emitting diode (LED)–based lighting products continues to improve rapidly, and performance in excess of 150 lumens per watt (lm/W) with long lumen maintenance times are achievable with commercially available LEDs. When these high-efficiency LEDs are incorporated into luminaires, the luminous efficacy of the complete system is lower because of various losses in the luminaire. Nonetheless, LED-based lighting products generally exceed the efficacy available in most lighting products that use conventional lamp tech-

J. Lynn Davis (✉) • K. Mills • R. Yaga • C. Johnson
RTI International, 3040 Cornwallis Road, PO Box 12194, Research Triangle Park, NC 27709-2194, USA
e-mail: ldavis@rti.org

M. Hansen
LED Lighting Advisors, Santa Barbara, CA, USA

M. Royer
Pacific Northwest National Laboratory, 620 SW 5th Avenue, Suite 810, Portland, OR 97204, USA

© Springer International Publishing AG 2018

W.D. van Driel et al. (eds.), *Solid State Lighting Reliability Part 2*, Solid State Lighting Technology and Application Series 3, DOI 10.1007/978-3-319-58175-0_10

nologies (e.g., fluorescent, halogen, and metal halide lamps). The ready availability of high-efficiency, LED lighting products with good lumen maintenance is causing a shift in the LED lighting industry from a focus solely on efficacy to a broader focus on light quality, including balancing efficacy, lumen maintenance, and chromaticity maintenance.

By analogy to lumen maintenance, chromaticity maintenance can be defined as the change in light source chromaticity from the original chromaticity values. A change in light source chromaticity can also be termed a chromaticity shift when expressed as a difference in coordinates of a chromaticity diagram, such as the Commission Internationale de l'eclairage (CIE, the International Commission of Lighting) 1976 (u', v') chromaticity diagram, which gives rise to the quantity $\Delta u'v'$. Chromaticity shifts have always occurred in lighting technologies, and the amount of shift that can be tolerated varies widely depending on the application, the position of the light source in the field of view, and the proximity to other light sources [1]. Chromaticity shifts have historically been less of an issue with other lighting technologies given that relamping occurred every 2–5 years. However, because the same LED lighting devices may be used for 10–20 years, chromaticity stability can be a significant concern over the life of the product. Some examples of applications where chromaticity maintenance could be of importance include:

- Lobbies of office buildings where some LED lamps are operated 12 h per day and others are on an emergency circuit and operated 24 h per day. The longer operating times and the higher setbacks used for building temperature and ventilation controls in off-peak hours result in significantly different usage profiles for luminaires on the two different circuits [2].
- Applications in museums, retail, and commerce when light source quality may be important to the presentation of merchandise [1].
- Applications in health care where the appearance and color of tissue are affected by illumination.
- Installations where a single LED lamp or luminaire is replaced while many "aged" LED luminaires are already in place.
- Different aging characteristics for equivalent products from different manufacturers. The differing designs may lead to variations in long-term lumen and chromaticity maintenance.

The nature of chromaticity shifts in LED lighting devices has been the subject of limited studies to date. One of the first publicly available long-term studies of chromaticity maintenance was performed by Pacific Northwest National Laboratory (PNNL) as part of the evaluation of the Philips L-Prize® 60-W equivalent A-lamps. The average chromaticity change observed for these lamps, as measured by $\Delta u'v'$, was less than 0.001 after 40,000 h of continuous operation [3]. This chromaticity shift corresponds to a one-step MacAdam ellipse. The chromaticity shift for the worst performing lamp in this test, as measured by $\Delta u'v'$, was only 0.003, which is better than the pre-determined performance requirements. These samples were specially made for the L-Prize tests and may not be a representative of mass-produced samples, and they were operated continuously instead of

undergoing on/off cycling as normal products would. Nonetheless, these findings do indicate that long chromaticity maintenance times are possible with well-designed LED lighting products. A follow-up study conducted by PNNL on commercially available 60-W equivalent A-lamps demonstrated that there were many products with minimal chromaticity shift during the 7000 h test, but there were also some commercial products that displayed large shifts in excess of 0.004 [4]. In contrast, the average chromaticity shift of compact fluorescent, halogen, and ceramic metal halide lamps was found to be larger that of the average LED product in the same study.

10.2 Representing Chromaticity Shifts

The color appearance of a light source can be represented by using several different approaches, including chromaticity coordinates based on established color spaces or the combination of correlated color temperature (CCT) and distance from the black body locus (D_{uv}). Because chromaticity coordinates, CCT, and D_{uv} are calculated directly from spectral power distributions (SPD) of a source, they provide a greatly condensed representation of spectral changes [5], with some of the information available in the SPD lost. One of the more common representations of color are the u' and v' chromaticity coordinates that form the CIE 1976 chromaticity diagram. This chromaticity diagram has emerged as the de facto standard for industry reports such as LM-80-15 [6] given that it provides a more uniform presentation of chromaticity differences compared with older schemes [7].

Most commercial white LEDs generate white light by combining the primary emissions from a blue LED with secondary emission from a phosphor such as cerium-doped yttrium aluminum garnet (Ce:YAG) or cerium-doped lutetium aluminum garnet (Ce:LuAG). These blue (i.e., LED) and yellow (i.e., phosphor) emitters can be represented by the appropriate chromaticity coordinates in the CIE 1976 chromaticity diagram. As shown in Fig. 10.1, any color along the line connecting these chromaticity points can be produced by the appropriate combination of these blue and yellow emissions. For a white LED package, an increase in blue emissions from the LED or a decrease in yellow emissions from the phosphor will produce a shift in the blue direction from the initial chromaticity point. Likewise, a decrease in blue emissions or an increase in yellow emissions will produce a yellow shift. As shown in Fig. 10.1, blue shifts are characterized by a decrease in both u' and v', whereas yellow shifts are characterized by an increase in both u' and v'. In general, the magnitude of the change in v' is greater than the change in u' for both blue and yellow chromaticity shifts especially at CCT values often encountered in lighting (2750–5000 K) [7].

If the specific emission characteristics, such as the peak wavelength or full width at half maximum (FWHM) of the blue or yellow spectrum components change, then other shifts in chromaticity are possible. As shown in Fig. 10.2, these shifts can generally be in either the green or red directions. In general, a green shift is

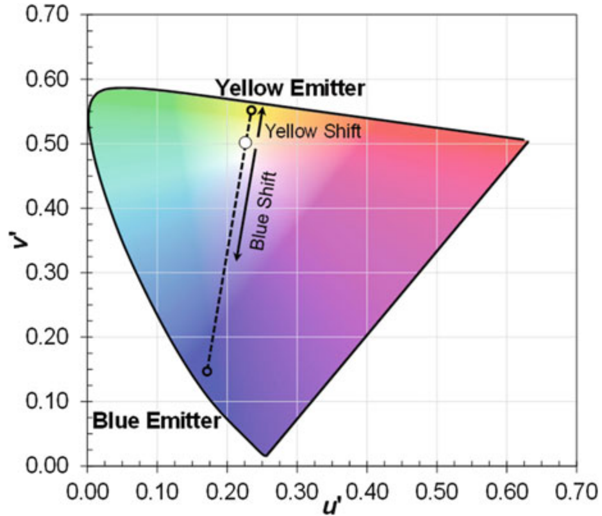

Fig. 10.1 Representation of color in the CIE 1976 color space. The combination of *blue* and *yellow* emitters in the proper proportions will produce *white* light. From this initial chromaticity point, increasing *blue* emissions relative to *yellow* will produce a *blue* shift. Likewise, increasing *yellow* emissions relative to *blue* will produce a *yellow* shift

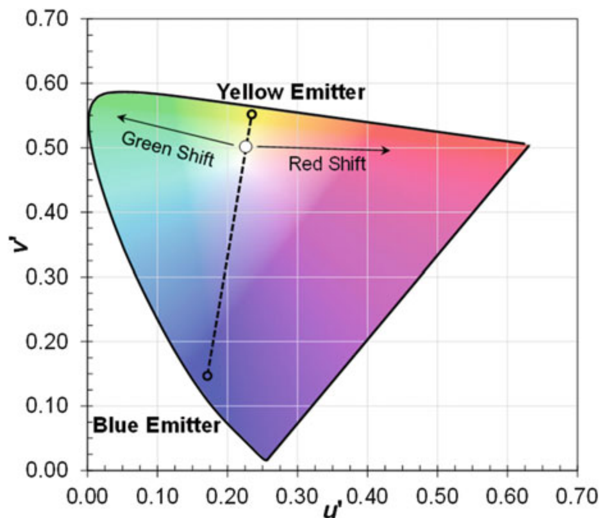

Fig. 10.2 Representation of color in the CIE 1976 color space. An initial *white* chromaticity can be produced by the appropriate blend of a *blue* and *yellow* emitter. A change in the spectral properties of either emitter can result in a *green* shift or a *red* shift relative to the initial chromaticity point. In pcLED devices, *green* shifts are more common and typically occur due to changes in the phosphor emission peak shape

indicated by a decrease in u' with minimal change in v'. Assuming that the blue emission remains unchanged, one example of a green shift is a change in either the peak emission wavelength or the FWHM of the phosphor emissions [8]. In a similar manner, a red shift is generally indicated by an increase in u' with minimal change in v'.

In addition to changes in the emission from the blue LED and the phosphor, several other changes in the LED package are known to have an effect on chromaticity stability. Tuttle and McClear [9] demonstrated that first-generation resins such as polyphthalamide (PPA) and polycyclohexylenedimethylene terephthalate

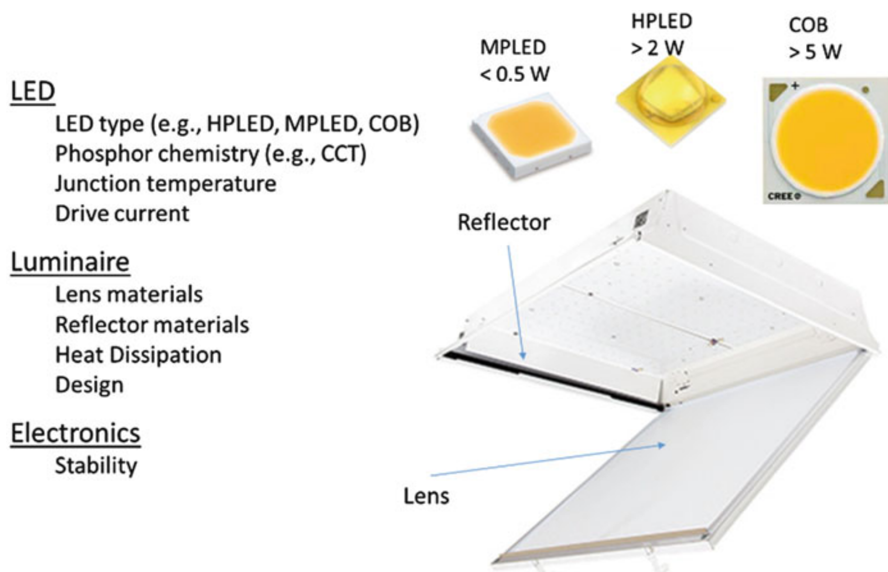

Fig. 10.3 A variety of factors can affect the chromaticity maintenance of LED-based luminaires and lamps

(PCT) that are used in mid-power LEDs (MP-LEDs) can yellow over time, resulting in a blue shift in chromaticity. In addition, oxidation of exposed silver-plated lead frames in MP-LEDs can also produce a blue shift in chromaticity [10]. Changes in the silicone binder used with the phosphor can result in yellowing of the material, which increases blue absorption and produces a yellow color shift [7, 11].

As the primary light source, LEDs play a significant role in determining the chromaticity maintenance of LED-based lamps and luminaires. However, LEDs are not the only factor affecting performance. As illustrated in Fig. 10.3, material selection for lenses and reflectors in combination with the luminaire design can have a significant impact on the chromaticity stability of a lamp or luminaire. In addition, the stability of electronic drivers can also impact chromaticity, especially in LED lighting devices that blend multiple LED colors, which can age at different rates. Each of these factors is discussed together with approaches to model color shift in LED devices.

10.3 LED-Induced Chromaticity Shifts

In most instances, the behavior of the LEDs will have the greatest impact on the chromaticity stability of any components in LED-based lamps and luminaires. There are a few published studies about chromaticity shift at the LED package level [8, 12–18], but significant amounts of proprietary data are available from LED

manufacturers in the form of reports generated using the LM-80 method. Most of these data were acquired under LM-80-08, which requires that chromaticity shift, as measured by $\Delta u'v'$, be reported for each measurement but does not require that individual chromaticity coordinates be given [19]. Although $\Delta u'v'$ provides the magnitude of a chromaticity shift, it does not provide the direction. In addition, data acquired using methods described in LM-80-08 are often considered to be proprietary by manufacturers, so the data are not openly available. Therefore, data collected according to LM-80-08 are of limited use when trying to understand chromaticity shift in LEDs. This situation could be alleviated if the individual chromaticity coordinates or the SPDs were reported for each measurement. The reissue of this standard, LM-80-15, requires that chromaticity coordinates be reported for each reading, but it will take time for the LED manufacturers to acquire data under this revised standard and make it available to the market [6].

10.3.1 Experimental Studies

Perhaps the most complete, publicly accessible data acquired using the LM-80-08 method is for the Philips Lumileds Luxeon Rebel LED [20]. Among the data contained in this report are $\Delta u'v'$, u', and v' values for each tested LED at each time interval. Although these data pertain only to older versions of the Luxeon product with the Lumiramic phosphor layer, they do provide some insights into chromaticity shifts that may occur at the LED package level.

The $\Delta u'v'$ data at one ampere drive current taken from the Luxeon LM-80 data given in reference [20] are presented in Fig. 10.4. The LED populations at all three ambient temperature settings (i.e., 55 °C, 85 °C, and 105 °C) show a rapid shift in chromaticity ($\Delta u'v'$) followed by a plateau region of varying duration depending on temperature and then a decrease in $\Delta u'v'$. At the highest temperature (i.e., 105 °C), the $\Delta u'v'$ value begins to increase again after 6000 h. The test interval for the other temperatures was not long enough to observe a similar rise in $\Delta u'v'$. The data found in all LM-80-08 reports provides information about the magnitude of the color shifts but no information about the direction of the shifts.

A vastly different perspective on the nature of the chromaticity shift in these LEDs can be gained by analyzing the change in the individual chromaticity coordinates (i.e., $\Delta u'$ and $\Delta v'$), and these results are shown in Fig. 10.5. At all three ambient temperatures, the initial, rapid rise in $\Delta u'v'$ corresponds to a decrease in both u' and v' (i.e., both $\Delta u'$ and $\Delta v'$ are negative), which indicates that the initial chromaticity shift is in the blue direction. At all temperatures tested, the $\Delta u'$ value for these LEDs decreases to a minimum value and then begins to increase, in contrast to the $\Delta u'v'$ data where there was a plateau region of minimal change. Once $\Delta u'$ begins to increase from the minimum value, it continues for an extended period in an approximately linear manner. In contrast, the $\Delta v'$ value at all temperatures decreases to a minimal value for these LEDs and then stays relatively constant for the remainder of the test period. The combination of an increase in u'

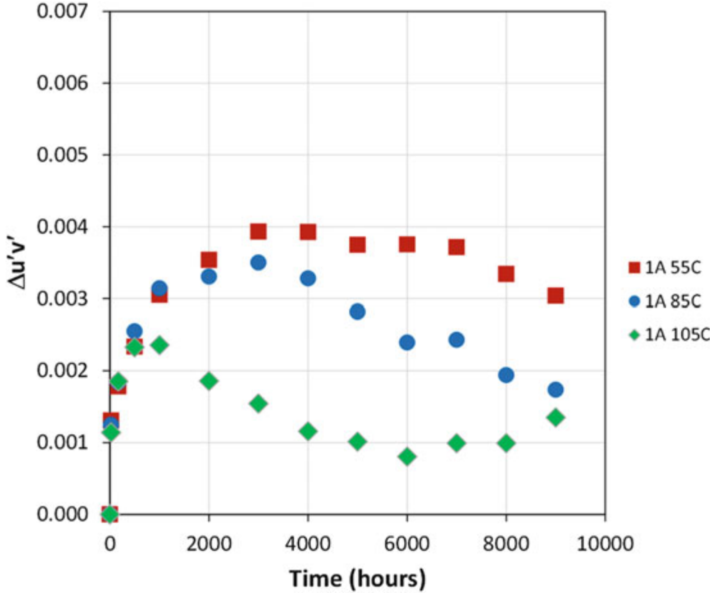

Fig. 10.4 Average chromaticity shift ($\Delta u'v'$) versus time for a population of Luxeon LEDs operated at 1 amp in the indicated ambient temperature. Each population consisted of 25 different LEDs (The data is taken from Ref. [20])

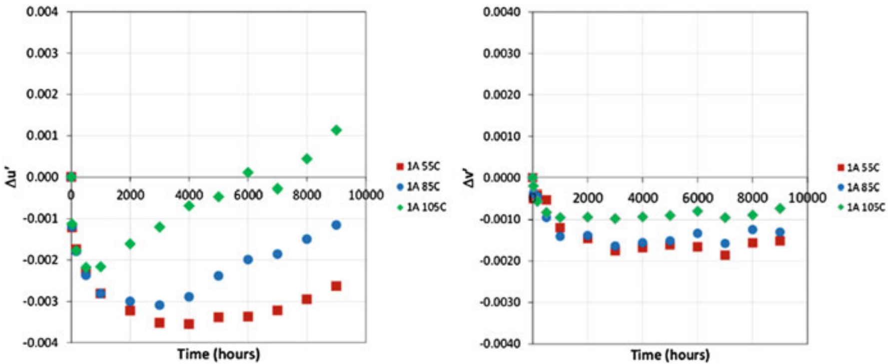

Fig. 10.5 Average change in chromaticity coordinates of a population of Luxeon LEDs operated at 1 amp in the indicated ambient temperature. Each population consisted of 25 different LEDs. (*Left*) Change in u' chromaticity coordinates (i.e., $\Delta u'$) versus time. (*Right*) Change in the v' chromaticity coordinates ($\Delta v'$) versus time (The data is taken from Ref. [20])

and minimal change in v' can be shown to be a red shift by examination of Fig. 10.2. Thus, the color shift found in the LEDs is an initial blue shift followed by a prolonged shift in the generally red direction.

Using the information in Fig. 10.5 to reexamine Fig. 10.4, several significant observations can be made. First, using the 105 °C data as an example, the behavior

in $\Delta u'v'$ observed between 1000 and 9000 h (i.e., $\Delta u'v'$ decreases between 1000 and 6000 h followed by an increase after 6000 h) is marked by a steady change in one parameter, $\Delta u'$. The shape of the $\Delta u'v'$ curve is because the chromaticity significantly shifts from the original value in the blue direction for the first 1,000 h but then moves back toward the original chromaticity point as the red shift occurs, so $\Delta u'v'$ decreases. As the chromaticity passes the initial value (which occurs at approximately 6000 h for the 105 °C data), $\Delta u'v'$ will begin to increase again. The second point to be considered is that there is still a significant change in the individual chromaticity points occurring during the time when $\Delta u'v'$ is plateaued. For example, at an ambient temperature of 55 °C, $\Delta u'$ begins increasing as early as 4000 h, but $\Delta u'v'$ does not begin to change until 8000 h of 55 °C, when a decrease in $\Delta u'v'$ begins. This delay in $\Delta u'v'$ change is because when these chromaticity reversals occur, they generally happen along an arc (as shown in Fig. 10.6), which results first in a decrease and then an increase in $\Delta u'v'$ as the chromaticity shifts with aging. In short, $\Delta u'v'$ is a limited measure for tracking chromaticity change over time.

Although this analysis was conducted on a specific LED, similar trends can be found for other LED products, although red shifts are generally less common in LEDs. Hansen and Davis [18] examined more than 200 data sets acquired using the LM-80-08 method and found a tendency for most, but not all, HP-LEDs to initially shift in the blue direction followed by a prolonged shift in either the green, blue, or yellow directions. Tuttle also previously reported prolonged yellow shifts for high-power LEDs (HP-LEDs) at various temperatures [21].

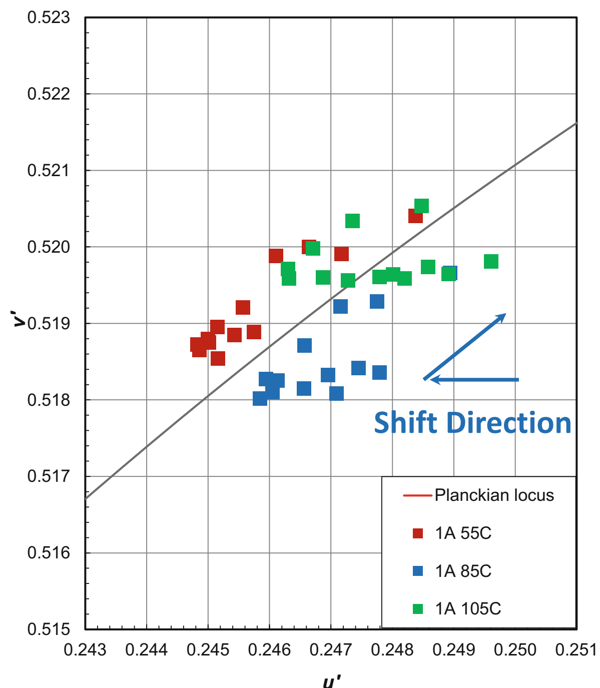

Fig. 10.6 Chromaticity plot for the Luxeon LED operated at 1 ampere forward current at various ambient temperatures (The data is taken from Ref. [20])

10.3.2 LED Chromaticity Shift Mechanisms

Although data acquired using the LM-80-08 method is not readily available, information about chromaticity changes in LEDs can be gathered by examining specific lamp and luminaire types. Recently, the US Department of Energy (DOE) published a report about the lumen and chromaticity maintenance of PAR38 lamps built before 2013 [22]. In this report, five samples of 32 different commercial PAR38 LED lamps were continuously operated at an ambient temperature of 45 °C, and their SPDs were measured weekly. In a follow-up report, RTI International and PNNL conducted additional analyses of the 160 PAR38 samples, including a detailed examination of the chromaticity changes across the different LED lamp models [7]. Given that the PAR38 lamps were operated at a mildly elevated ambient temperature of 45 °C, minimal changes in the lenses and other optical materials in the lamps were seen, as expected, with one exception. Because of the design of PAR38 LED lamps and the minimal changes in optical materials, the chromaticity shifts observed in this study were attributed to changes in the LEDs [7].

Another advantage of this analysis is that the 32 different PAR38 lamp products used as variety of different LED packages (as shown in Table 10.1), including HP-LEDs, plastic leaded chip carriers (PLCC), chip-on-board (COB)-LEDs, and hybrid LEDs. HP-LEDs generally consist of a ceramic base that is soldered to a printed circuit board (PCB), and the maximum operational power of these devices is greater than 2 W. PLCCs consist of one or more LED die in the base of a molded plastic chip carrier with the LED attached to a silver-plated lead frame overmolded with a polymer resin such as PPA, PCT, epoxy molding compound (EMC), or silicone molding compound (SMC). The operational power range of PLCCs can vary widely depending on the number of LEDs in the package. MP-LEDs are a special class of PLCCs that often contain a single die and are operated at power levels below 0.5 W. COB-LEDs consist of multiple LEDs mounted on a common substrate (i.e., often ceramic) and covered with a common phosphor layer. Hybrid LEDs consist of LEDs with different emission characteristics that are mixed together. In this study, the hybrid LED package consisted of three slightly greenish phosphor-converted HP-LEDs (pc-LED) and a single red direct emitter in the same package.

Based on this analysis, DOE CALiPER 20.5 reported four primary chromaticity shift modes (CSMs) within the PAR38 lamp population, and an examination of this

Table 10.1 Breakout of the LED package types found in the 32 different LED PAR38 lamps examined in CALiPER 20.5 [7]

LED package types	Number of PAR38 lamps in CALiPER 20.5
High-power LEDs	18
Mid-power LEDs	7
Chip-on-board LEDs	6
Hybrid LEDs	1
Total	32

Table 10.2 Primary CSMs observed in PAR38 samples [7]

CSM	Direction of shift	Changes in u' and v'
CSM-1	Blue	During the blue shift, both u' and v' decrease
CSM-2	Green	During the green shift, u' decreases, but v' changes a little or may increase slightly
CSM-3	Yellow	Both u' and v' decrease during the blue shift, and both u' and v' increase during the yellow shift
CSM-4	A complex shift consisting of first blue, then yellow, then a second blue shift	During both blue shifts, both u' and v' decrease. During the yellow shift, both u' and v' increase
CSM-5	Red	During the red shift, u' increases, but v' changes a little or may increase slightly

report and other data have identified a fifth CSM [7]. More than 90% of the PAR38 lamp models studied exhibited the behavior of one of these CSMs, suggesting that this approach is a convenient way to classify chromaticity shift in simple SSL devices and that it could possibly be extended to more complicated devices such as A-lamps and luminaires. The primary CSMs are presented in Table 10.2, and examples of each CSM are found in Fig. 10.7.

As shown in Fig. 10.8, there is a clear difference in CSM behavior between the different LED packages. Lamps with HP-LEDs predominantly demonstrated CSM-3 behavior, with 72% of the sample population changing chromaticity via this mode or the closely affiliated CSM-5 during the test period (approximately 14,000 h). If testing for these lamp models were terminated sooner, then the terminal mode of chromaticity shift may not be observed and either CSM-1 or CSM-2 behavior may be found. This is a constraint of the experimental design more than an indication of the long-term behavior of the LED package. In addition, there were five PAR38 lamp models with HP-LED packages representing 28% of the lamp samples with HP-LED demonstrated either CSM-1 or CSM-2 population during the test period. These lamp models contained HP-LEDs that were operated at low-stress conditions as indicated by the LED board temperature and power per LED in the device. It was speculated in DOE CALiPER 20.5 that operating these lamps for longer periods of time or at higher stress levels may result in the appearance of CSM-3 behavior. This hypothesis suggests that in some LEDs, there is a progression in CSMs from CSM-1 to CSM-2 and then to CSM-3, with the timing of these changes dependent on the construction of the LED, the junction temperature, and the drive current [7].

In contrast, only lamps containing PLCC LEDs exhibited CSM-4 behavior, and this was the dominant shift mode found for PLCC LEDs in this study [7]. A similar observation has also been made for A-lamps in a separate study suggesting that the CSM-4 behavior only occurs in PLCC packages [23]. This type of chromaticity shift has previously been attributed to browning of the molding resin (i.e., especially PPA and PCT) used in molded packages [9].

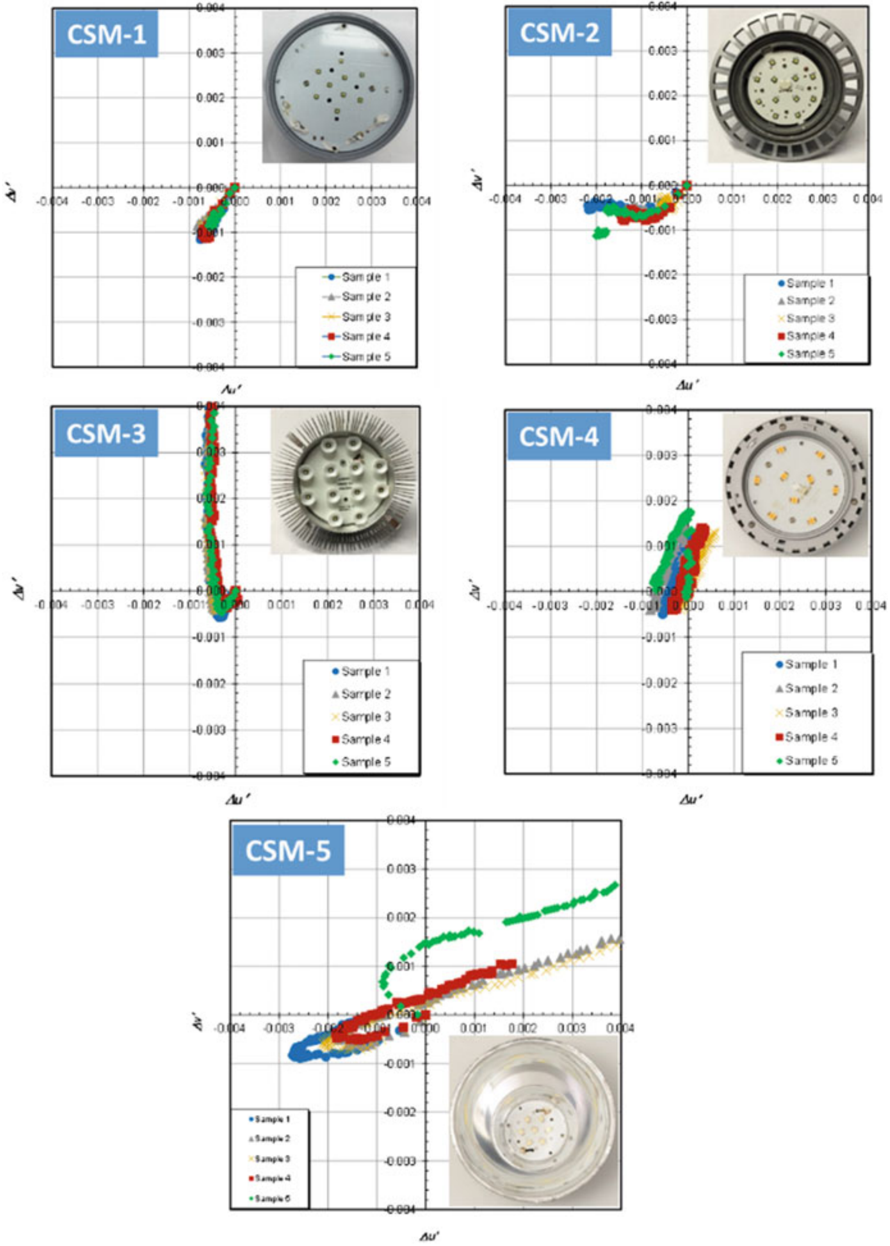

Fig. 10.7 Plots of chromaticity changes, as measured by Dv′ versus Du′ for four PAR38 LED lamp products. There are five samples for each product (The data is taken from Ref. [7])

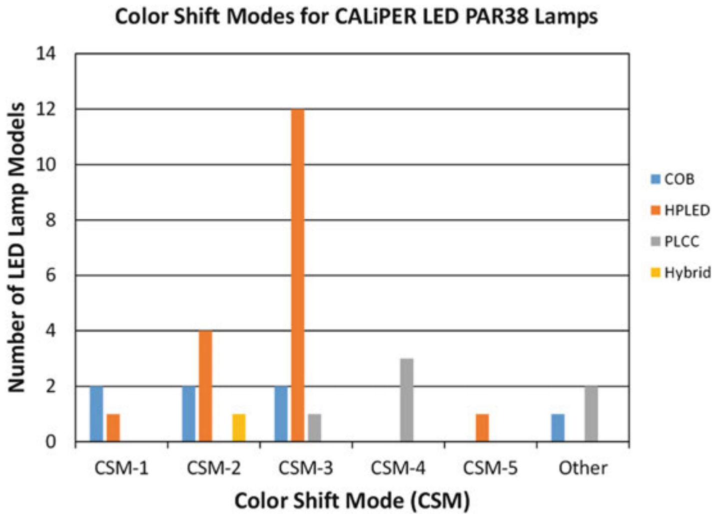

Fig. 10.8 Chromaticity shift modes exhibited by different LED packages (From Ref. [7])

10.3.3 Causes of Chromaticity Shifts in LEDs

A variety of factors, including packaging materials, manufacturing methods, and the environmental operating conditions, will have an impact on chromaticity shifts in LED packages. When evaluating package options for an LED-based lighting product, several LED and environmental issues should be examined for their impacts on chromaticity stability. These issues include LED packaging materials such as the substrate and molding compounds; phosphor layer construction, which includes the phosphor chemistry and binder materials such as silicones or glass; and LED encapsulants. Manufacturing methods to be considered include the stability of the epitaxial layer, phosphor application methods, and interconnects between the die and substrate. Environmental conditions, especially the presence of contaminants (e.g., volatile organic carbons [VOCs]) or humidity, can also have an impact.

10.3.3.1 LED Structures

LEDs are available in a variety of die architectures and package types. Despite this variety in structures, a few fundamental elements are found in all LED constructions, including the epitaxial layer forming the light-emitting pn junction, a means of providing electrical power to the anode and cathode of the pn junction, and a means of conducting heat from the pn junction to the package exterior. When an LED is first energized, heat produced by non-radiative processes can cause annealing of the epitaxial layer, and this process can, in turn, reduce the defect density and increase light emission. Likewise, annealing of the electrical

interconnects can lower the resistance of the LED and reduce the forward voltage [24, 25, 26]. Both of these factors improve the efficiency of the LED and will often increase the number of blue photons produced at a given current. This increase in efficiency may be at least partially responsible for the initial blue shift that is often observed when LEDs are first energized. As the LED ages, one potential cause of the yellow shift in emissions (i.e., CSM-3 behavior) is due to dielectric breakdown and increased contact resistance. This effect can be minimized by improved manufacturing processes and is less common in LEDs manufactured today than in earlier products [24, 25].

10.3.3.2 LED Package Substrates

As shown in Fig. 10.9, different materials and construction practices are used in Level 0 packaging of LEDs depending on the package type. HP-LEDs typically use ceramic substrates such as alumina or aluminum nitride. These substrates are stable in the normal LED operating environments. COB-LEDs typically use either ceramic or metal-core PCBs (MCPCBs), and the stability of MCPCBs will depend on the chemistry of the organic dielectric layers and solder masks used in the MCPCB. Substrates used in PLCCs often consist of a silver-plated lead frame overmolded with a resin such as PPA, PCT, EMC, or SMC. The stability of these resins varies depending on temperature and blue light flux with SMC and EMC having higher stability compared with PPA and PCT [17, 18]. Oxidation of PPA and PCT resins is a potential cause of CSM-4 behavior [9]. In addition, oxidation of exposed lead frames, such as reported by Lall et al. [8], may also produce CSM-4 behavior in LEDs.

10.3.3.3 Phosphors

By far, the most common LED structure used in lighting is the pcLED consisting of a phosphor layer on top of a blue LED. The phosphor converts a portion of the blue emissions from the LED into broadband emissions covering much of the visible spectrum. The combination of unconverted blue emissions and secondary emissions from the phosphor produce white light of a desired chromaticity. A variety of phosphor chemistries can be used in this application with Ce:YAG, Ce:LuAG, and doped silicon nitrides and silicon oxynitrides being commonly used [27–31].

In the pcLED structure, a phosphor and a binder are applied on top of the LED using a variety of methods. Typically, the binder material is a silicone, but occasionally glasses or ceramics are used. The phosphor-binder composite used in pcLEDs must be very stable because of the high-temperature and high-photon-flux environment in which this material operates. Failure of the binder to withstand the heat and/or photon exposure that occurs during LED operation usually results in increased light absorption in the blue, which will cause a yellow shift [7]. The temperature of the phosphor-binder layer typically exceeds the junction

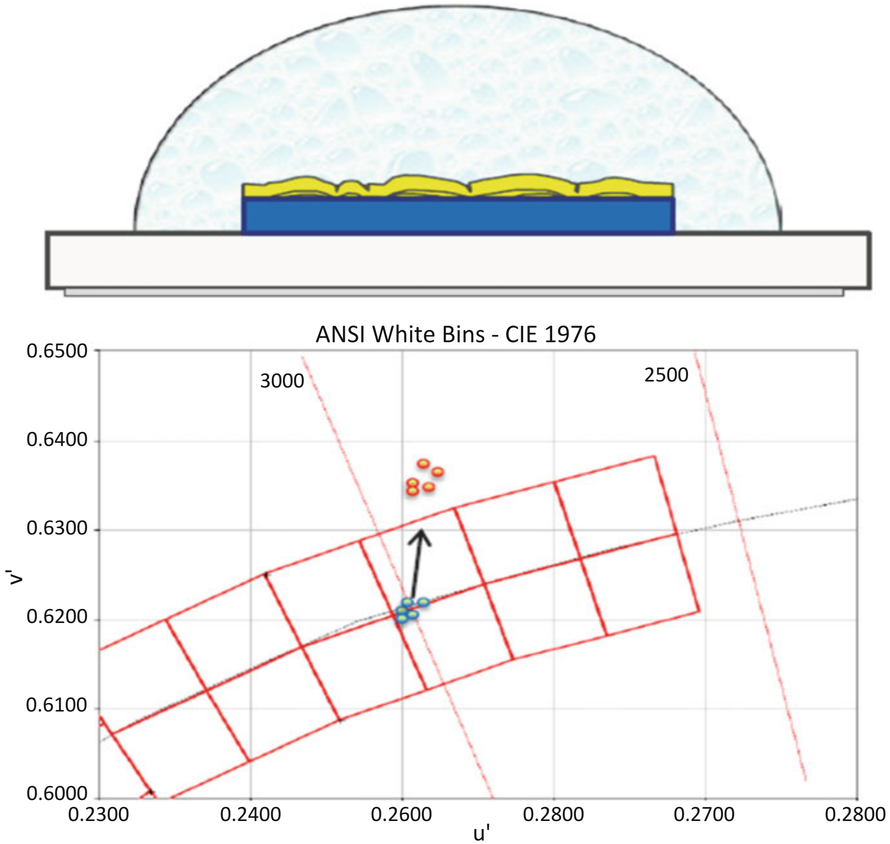

Fig. 10.9 Cracks and delamination within the phosphor-binder layer of a pcLED and at the interface of the die will introduce a material with a low index of refraction into the phosphor layer and change the propagation of light through the material (From Ref. [7] with permission)

temperature of the LED because of the combined effects of radiative heating from the pn junction, energy dissipated in the phosphor through the Stokes shift, and the poor thermal conductivity of the binder [11]. Glass binders have been shown to be significantly more stable under these conditions than silicone binders [32–34]. However, glass binders introduce additional manufacturing difficulties and are not as widely used as silicones.

Some aspects of the various CSM behaviors can be directly traced to changes that occur in the phosphor-binder layer as the package ages. Potential causes for the initial blue shift that is observed when most LEDs are first energized include changes in the index of refraction of the binder layer or a drop in phosphor quantum efficiency as the photon flux increases during early operation of the LED.

CSM-2 behavior can be attributed to changes in the phosphor, particularly nitride and oxynitride phosphors. Yeh et al. [35] demonstrated that doped nitride phosphors will undergo oxidation resulting in a green shift of the emission peak. Ce:YAG phosphors are generally more stable and will not undergo a green shift as

readily as nitride-containing phosphors [10, 12]. Peak wavelength shifts of less than 5 nm have also been shown to produce green shifts in LED lamps [7].

CSM-3 behavior has been attributed to changes in the phosphor-binder layer, resulting in delamination and cracks at the die-phosphor interface, which are caused by loss of mechanical compliance of the silicone binder with aging and thermal stresses at the die-phosphor interface [9, 22, 29]. As shown in Fig. 10.9, these cracks and delaminations introduce a material (i.e., air) with a low index of refraction into the pcLED structure. Photons encountering these imperfections will be refracted through the phosphor layer at more shallow angles than when the LED is new and these defects are not present. As a result, the optical path of the average blue photon through the phosphor is increased, resulting in greater conversion of blue photons to phosphor emissions. The net result is a yellow shift. In addition, such defects can also impact the overall light extraction efficiency of the LED, resulting in a drop in luminous flux maintenance [36–39]. Several examples of this behavior, including a spectral analysis to support this mechanism, are provided in literature [7, 25]. The appearance of cracks and delamination at the die-phosphor/binder interface can be attributed to the thermal stresses at the interface caused by the differences in coefficients of thermal expansion [48], as well as molecular changes in the silicone composition over time, which degrade its mechanical properties.

10.3.3.4 Encapsulants

Encapsulant materials are used to encase the LED and provide some measure of protection against external environmental conditions. Early encapsulants used in white-light LEDs were epoxy materials, and many studies have demonstrated that these materials often yellow under heat and high photon flux, resulting in a yellow shift for the emitted light [34, 40–44]. The lighting industry began using silicone encapsulants in approximately 2008, and two different silicone chemistries (i.e., methyl silicones and phenyl silicones) may be used, with a methyl-phenyl hybrid material recently appearing on the market. Phenyl silicones have a high index of refraction ($n \sim 1.54$), which can help improve light extraction efficiency, but they have a lower thermal stability than methyl silicones ($n \sim 1.41$) [21, 45]. As with many organic molecules, when encapsulants age, they begin to absorb blue light preferentially which will produce a yellow shift. This shift can be differentiated from other causes of CSM-3 behavior given that increased absorption in the blue will alter the peak wavelength or FWHM of the blue emission.

10.3.3.5 Contaminants

Although the silicones used as encapsulants and binders in LEDs have improved thermal stability, compared to epoxy materials, silicones also possess increased permeability to moisture, VOCs, and corrosive chemicals, making contaminant ingress a potential factor in chromaticity and lumen maintenance. Moisture

penetration results in delamination at the phosphor-die interface, which produces a yellow shift that is indicative of CSM-3 behavior [12, 23, 36–39]. In addition, there is at least one report of moisture ingress increasing the thickness of the phosphor-binder layer, which will reduce phosphor density and produce a blue shift [10]. The penetration of VOCs and potentially corrosive materials such as sulfur into the LED package has been shown to reduce lumen maintenance and produce a yellow chromaticity shift [46, 47]. This process can be reversible if the source of the contamination is removed

10.4 Projecting Chromaticity Shifts in LEDs

Methods such as TM-21-11 currently exist for projecting lumen maintenance in LEDs and are based on data taken at set operating conditions and are not necessarily indicative of product lifetime. While such methods for lumen maintenance projection can be useful, similar methods do not currently exist for projecting chromaticity maintenance. Since chromaticity shift directions can change over time, as observed for CSM-3 and CSM-5, projection of chromaticity shift can be more complicated than projecting a gradual decay phenomenon such as luminous flux depreciation. Standards committees are evaluating this situation, and projection methods may become available in the next several years. Until then, a high-level estimate of chromaticity change under set operating conditions can be made using existing LM-80-08 data [18, 23]. As shown in Fig. 10.7, CSM-3, CSM-4, and CSM-5 behaviors result in a region of nearly linear chromaticity change once the device chromaticity has shifted away and then back past the original chromaticity. This situation is demonstrated in Fig. 10.10 for two LED products that exhibit CSM-3 behavior. This linear increase in $\Delta u'v'$ enables an estimation of the time required to achieve a predetermined chromaticity shift (e.g., $\Delta u'v' = 0.007$) at a given current and temperature. With this information, a plot of the expected time for a given chromaticity shift can be created for a variety of operating conditions, as shown in Fig. 10.11, thereby allowing for the identification of LED operating conditions necessary to achieve a desired chromaticity maintenance level.

10.5 Optical Materials and Chromaticity Shifts

As shown in Fig. 10.3, the LED packages play a major role in the chromaticity maintenance of LED-based lighting devices. However, the behavior of other components, including polymeric optical materials used for lenses and reflectors, can also have a significant impact on chromaticity maintenance. An example of this effect is shown in Fig. 10.12 where the aging of the lens and reflector in a downlight

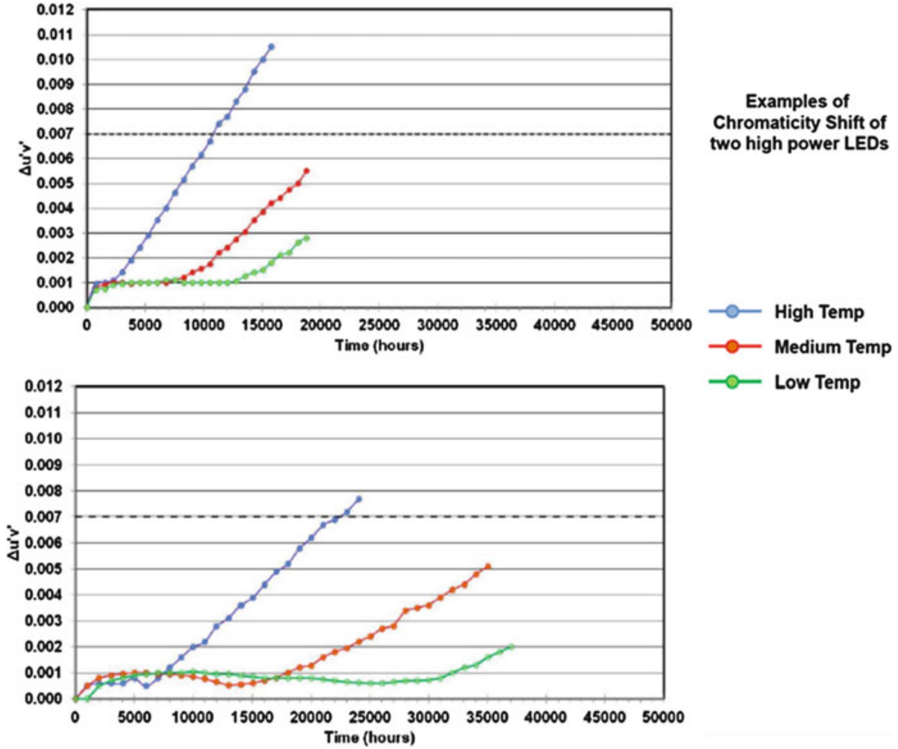

Fig. 10.10 Chromaticity shift plots for LEDs exhibiting *yellow* chromaticity shifts. The nearly linear increase in chromaticity provides a means to estimate time required to achieve a predetermined shift (Data is reproduced from Ref. [21] with permission)

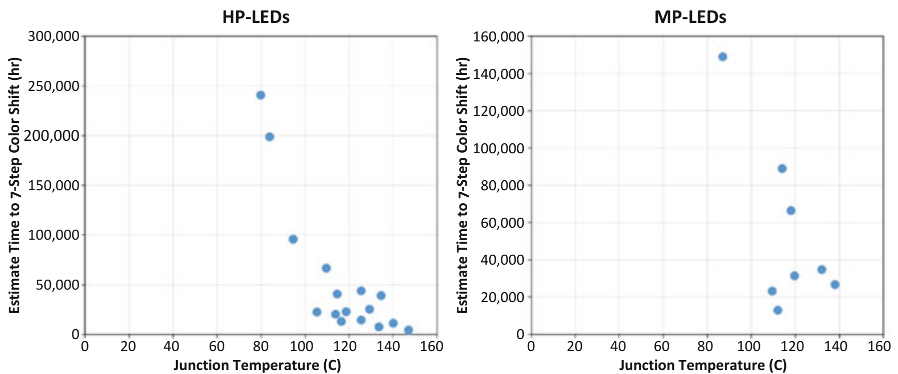

Fig. 10.11 Estimates of the time required for a seven-step chromaticity shift for HP-LEDs and MP-LEDs [23]

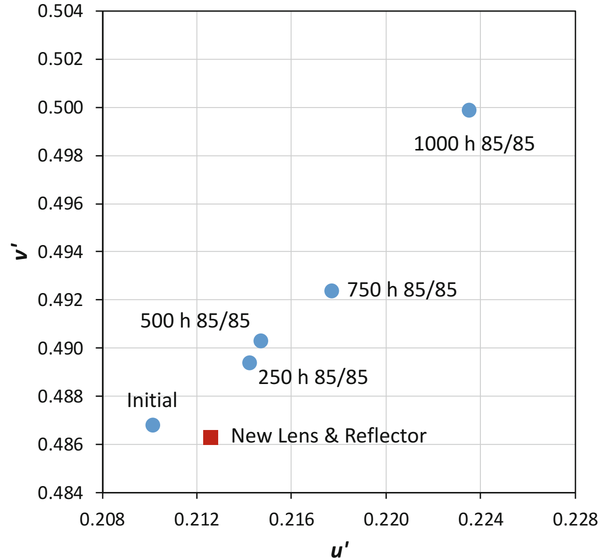

Fig. 10.12 Chromaticity change of cool white downlight (Initial CCT ~ 5000 K) subjected to operational lifetime test in an ambient environment of 85 °C and 85% RH. After 1000 h of exposure, the lens and reflector were replaced and the chromaticity moved close to the original value

can be seen to cause a yellow shift in chromaticity. Replacing the aged lens and reflector with new ones moves the chromaticity value close to the original point. In addition, as shown in Fig. 10.13, the appearance of the SPD is increasingly attenuated at lower wavelengths as the lens and reflector change resulted in a 40% drop in luminous flux, an increase in $\Delta u'v'$ of 0.030, and a 900 K reduction in CCT. This type of chromaticity shift is a consequence of polymer oxidation which typically affects blue wavelengths before others [12, 49–56].

The timescale for the degradation of these optical materials can vary widely as demonstrated by Davis et al. [12, 49]. During these studies, the optical properties of some materials such as polymethyl methacrylate (PMMA) lenses and polyethylene terephthalate (PET) reflectors changed little during exposure to 85 °C and 85% relative humidity (RH) [12, 49, 57]. This behavior suggests that such materials would be relatively stable in many environments used with SSL devices. In contrast, as shown in Figs. 10.12 and 10.13, other materials such as polycarbonate lenses quickly turned yellow in this environment, producing significant lumen depreciation and chromaticity shifts [12, 39]. This finding suggests that some materials may not be appropriate for use in specific environmental conditions but may function fine in others. Understanding the aging characteristics of common optical materials, such as polycarbonate PMMA, and PET, in different environments, is important in the lighting industry because of their ubiquitous use.

10.5.1 Lens Aging

Polycarbonate lenses are used in many LED luminaires due in part to the high optical clarity, excellent mechanical properties, and relatively low material costs.

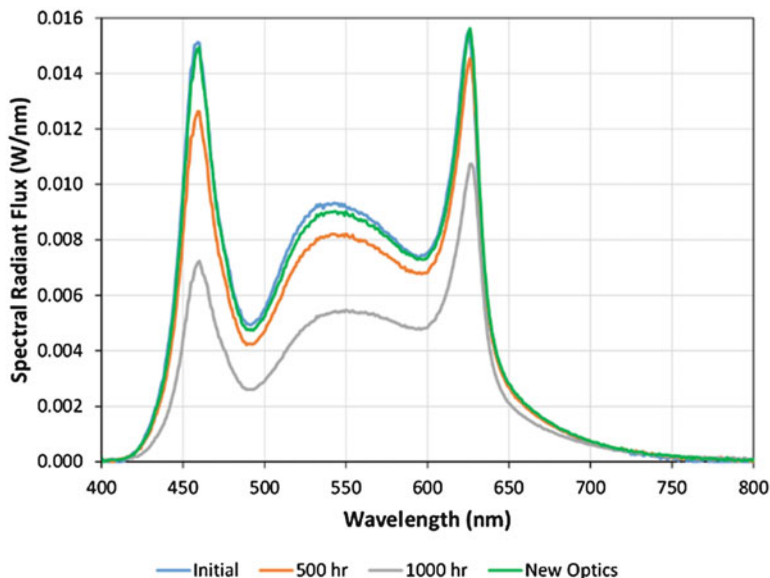

Fig. 10.13 SPD of cool white downlights (Initial CCT ~ 5000 K) subjected to accelerated aging at 85 °C and 85% RH. After 1000 h of 85 °C and 85% RH, both the lens and reflector were replaced and the SPD moved close to the initial measurement

However, it is known that the optical properties of polycarbonate change under various environmental stresses [49–54]. Polycarbonate has been shown to undergo a photooxidation reaction with the rate of the reaction impacted by temperature, humidity, and the wavelength of incident radiant flux. Temperature alone can also cause photooxidation of polycarbonate, but the reaction proceeds much faster in the presence of humidity and blue irradiance [52] than with temperature alone. An induction period has been observed for polycarbonate photooxidation, so the impact of this chemical reaction is not observed immediately [50–54].

For LED-based products containing polycarbonate lenses, the photooxidation reaction results in several significant changes in the emission spectra of the device including:

1. Increased absorption of visible radiation by the polycarbonate lens, with absorption of blue photons being higher than that of other colors, as shown in Fig. 10.14
2. Reduction in luminous flux from the device [49, 52–54]
3. Shift in chromaticity generally in the yellow or yellow-red direction [52–54]

In extreme cases of polycarbonate photooxidation, degradation of the mechanical properties resulting in increased brittleness can occur [55]. In addition, the photooxidation reaction is primarily a surface process that can cause increased haze in a lens [55], which may change the light distribution properties of an LED-based device with polycarbonate lenses.

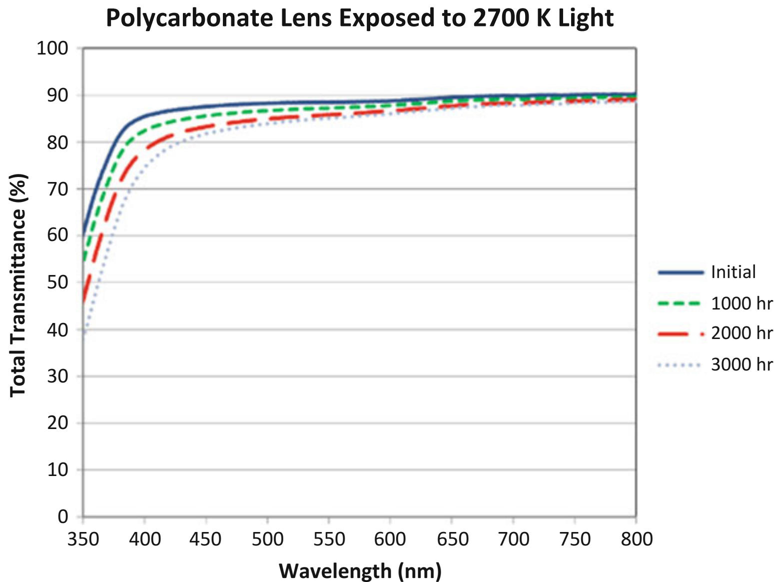

Fig. 10.14 Total transmittance of polycarbonate lenses subjected to 75 °C and 75% RH while being irradiated with warm white light in downlight test vehicles. These transmittance spectra are the average from four samples, and the coefficient of variation (COV) at each wavelength over the range 400 nm to 800 nm was less than 3% in all cases

PMMA is another commonly used lens material in luminaires, including those containing LED sources. PMMA is widely used in optical applications because of its clarity and resistance to change – even under sunlight and ultraviolet radiation. Although few studies have been performed regarding the effects of temperature, humidity, and blue photon irradiance on PMMA degradation, the studies performed to date clearly indicate that the material is optically stable under most use environments used for LED devices [49, 54, 56, 57]. During these studies, PMMA has been shown to be virtually unchanged, even after significant exposure to 85 °C and 85% RH [49, 56, 57]. However, some conditions such as extreme temperatures or very high blue photon flux can result in some discoloration of PMMA, and the appearance of a yellow color that absorbs some blue radiation and causes a chromaticity shift in the yellow direction [56].

10.5.2 Modeling the Degradation of Lens Materials

During use, lens transmittance at each wavelength ($\%T_{\lambda}$) changes in a linear manner, which allows the transmittance at any given time to be calculated by using the following equation:

$$\%T_{\lambda}(t) = \%T_{\lambda}(0) + \frac{\mathrm{d}(\%T_{\lambda})}{\mathrm{d}t} \times t \tag{10.1}$$

where

t = Time

$\%T_{\lambda}(0)$ = Initial lens transmittance (i.e., $t = 0$) for wavelength λ

$\%T_{\lambda}(t)$ = Lens transmittance at time t for wavelength λ

$\mathrm{d}(\%T_{\lambda})/\mathrm{d}t$ = Change in lens transmittance with time (experimentally derived)

The values for $\mathrm{d}(\%T_{\lambda})/\mathrm{d}t$ of each lens material can be best determined by conducting accelerated life tests (ALTs) under controlled conditions that can be related back to the expected operational environment. This methodology is demonstrated here for polycarbonate lenses under warm white (~3000 K) light, but the same procedures can be used for other lens materials and for other light exposures.

A typical result for the aging of polycarbonate lenses in an ALT of 75 °C and 75% RH (75/75) is shown in Fig. 10.14. A close examination of the transmittance spectra demonstrates that the rate of change in polycarbonate lens transmittance is dependent upon wavelength. This finding is consistent with previous studies of the kinetic analysis of polycarbonate photooxidation [52, 53].

The rate of change in lens transmittance at each wavelength can be determined by analyzing the transmittance spectrum as a function of exposure time in 75/75. As shown in Fig. 10.15, this change is highly linear at each wavelength, with the slope of this line corresponding to $\mathrm{d}(\%T_{\lambda})/\mathrm{d}t$. As can be expected, the value of $\mathrm{d}(\%T_{\lambda})/\mathrm{d}t$ decreases as wavelength increases, which is consistent with the preferential absorption of lower wavelengths.

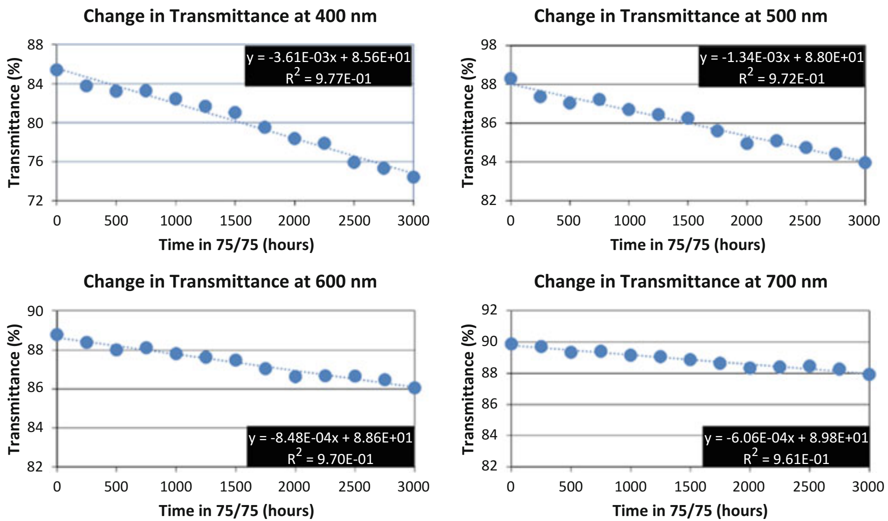

Fig. 10.15 Change in lens transmittance under warm white irradiation at selected wavelengths during 75/75 exposure. The reported values represent the average from the four samples

The slopes of the linear fits in Fig. 10.15 provide information about the rate of change [d(%T_λ)/dt] of polycarbonate transmittance with time in 75/75. Mehr et al. previously demonstrated that the photooxidation of polycarbonate proceeded at a consistent rate, after a short induction period, in a high-temperature environment [52, 53]. Because of the higher acceleration factor (AF) of the 75/75 ambient environment, a minimal induction period was observed during these tests compared to tests using elevated temperature alone. Consequently, a linear model is a good fit for the rate of change in lens transmittance.

By examining the linkage between the slopes for the linear models at each wavelength, an estimation of the change in transmittance at each wavelength can be made over the visible spectrum. Because slope has an inverse relationship with wavelength, the reciprocal of the slope (1/[d%T/dt]) should have a linear relationship with wavelength. Figure 10.16 shows the high degree of linearity in the relationship 1/[d%T/dt] and wavelength, and a high degree of linearity is found in the relationship. Consequently, the d(%T_λ)/dt values are expected to vary in a predictable manner, which allows the transmittance change to be determined at any visible wavelength.

A similar analysis for polycarbonate can also be performed under cool white (CCT ~ 5000 K) light. In this instance, the polycarbonate lenses exhibited a steeper decline in transmittance during 75/75 exposure, which is indicative of higher levels of photooxidation and is in agreement with previous results. This increased rate of yellowing can be attributed to the higher blue content of the cool white light based on the known dependence of polycarbonate photooxidation on blue light intensity [51–54].

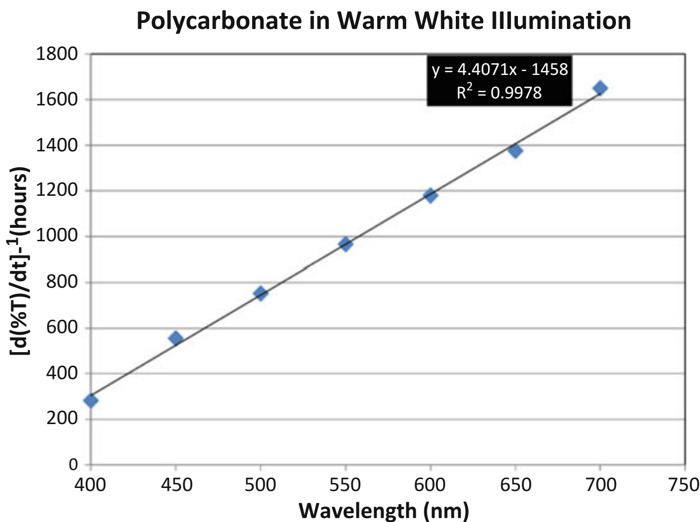

Fig. 10.16 Change in $[d(\%T_l/\mathrm{dt})]^{-1}$ under warm white irradiation at selected frequencies during 75/75 exposure. The reported values at each wavelength represent the average from the four samples

To link experiment data from various ALTs to aging under actual use conditions, an AF for the ALT must be calculated. This value can be determined if both the expected operational conditions and the ALT experimental conditions are known using the following equation:

$$t_{op} = t_{ALT} \times \mathrm{AF} \tag{10.2}$$

where

t_{op} = Operational time of the device in the normal operating environment
t_{ALT} = Operational time in the ALT environment used to build the models

10.5.3 Modeling the Degradation of Reflectors

Another element of the change in luminaire chromaticity during aging is the degradation of optical components such as reflectors. In general, reflectors can be classified as being specular (i.e., mirror-like), diffuse, or combination reflectors (i.e., containing both specular and diffuse components).

Depending upon the type of reflector, a variety of different materials can be used. The initial reflectance values for specular reflectors can range between 0.70 and 0.99. Specular reflectors are often used in products such as high-bay luminaires and parabolic reflector lamps where a well-defined beam shape is required. Examples of common specular reflectors include polished metal sheet and metal sheet with a thin silver coating, with silver-coated metal sheets usually exhibiting the highest specular reflectance.

In contrast, reflectors with an appreciable diffuse component are preferable in many indoor luminaire types, such as troffers and downlights, where the ability to diffuse light from LED point sources is needed. Initial reflectance values for diffuse reflectors can range from 0.70 to 0.98, with the lowest reflectance values generally being achieved with low-cost paints and the highest reflectance values achieved in specially made organic films. Diffuse reflectors typically achieve high reflectance by using either inorganic pigments such as rutile-phase titanium dioxide (TiO_2) or manipulating the index of refraction of the material by introducing pores (i.e., as occurring in foams [57, 58, 59] or biaxially stretched films [60, 61, 62]). The latter type of diffuse reflectors are often based on Teflon® or PET resins, whereas other polymers such as polycarbonate, polyolefins, and silicones require the addition of pigments to make TiO_2-polymer composites for reflector applications. Examples of common diffuse reflectors found in LED devices include surface-roughened metals, paints, coil coatings, high-performance paints, TiO_2-polymer composites, and PET films, coatings, and foams.

To date, there have been fewer studies regarding the changes of reflector materials used in LED devices than with lenses. Because diffuse reflectors often contain a significant polymeric component, oxidation of the polymer can be expected to occur, resulting in increased light absorption at lower wavelengths,

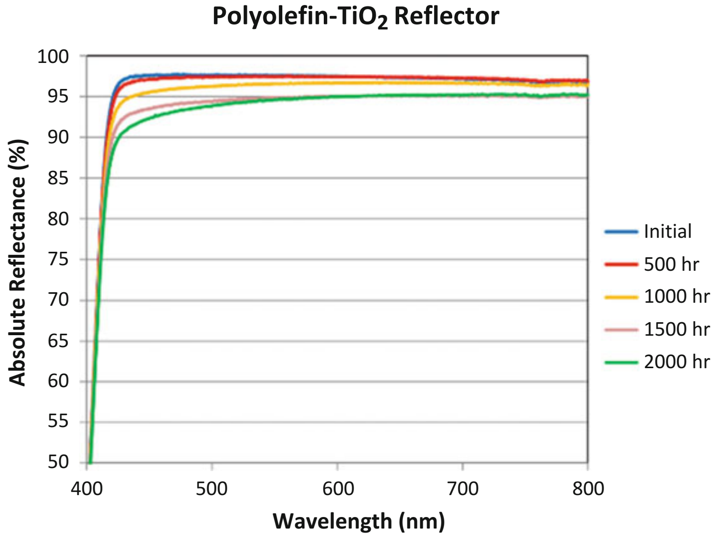

Fig. 10.17 Total absolute reflectance of polyolefin-TiO_2 reflectors subjected to 75 °C and 75% RH while being irradiated with warm white light in downlight test vehicles. These reflectance spectra are the average from four samples, and the coefficient of variation (COV) at each wavelength over the range 400–800 nm was less than 3% in all cases. Absolute reflectance is measured relative to a calibrated Spectralon reflectance standard

which may produce a yellow shift in chromaticity. Experimental results shown in Fig. 10.17 confirm this hypothesis. Davis et al. demonstrated that the blue emissions from a pcLED will overlap with the leading edge of the rutile-phase TiO_2 pigment, resulting in the photooxidation reactions and possible discoloration of the reflector [12, 49]. The effect was only observed under combinations of temperature, humidity, and blue light flux. In some instances, the interior of the reflector, which is exposed to blue light, will discolor, but the exterior will not (as shown in Fig. 10.18). In contrast, limited ALT tests performed on TiO_2-filled silicone reflectors demonstrated that the reflectance actually improves slightly, even after 1000 h of testing at 75 °C and 75% RH under high-intensity blue irradiance (0.46 W/cm^2 at λ_{max} at approximately 453 nm). These results, which are shown in Fig. 10.19, demonstrate that the chemistry of the polymer controls the reflectance stability of the polymer-TiO_2 composite and that some composites are very stable under extreme conditions. An analogous effect has also been observed with molding resins used in MP-LEDs [9].

The absence of TiO_2 fillers in polymer reflectors made with either Teflon or PET can be expected to result in different behavior for films and foams made with these materials than for filled polymers. Lu et al. demonstrated that PET reflectors are robust and will retain high reflectance, even under severe ALTs [57]. However, the PET-based reflectors were found to become brittle with prolonged exposure to accelerating conditions, which may ultimately result in breakage of the reflector, loss of luminous flux, and change in chromaticity because of exposure of the light beam to the support structure behind the reflector [57].

Fig. 10.18 Picture of a diffuse reflector formed from a sheet of a TiO_2-polyolefin composite. The edge of the *blue* emission band from the LED overlapped with the absorption of the TiO_2 pigment resulting in discoloration of the interior of the reflector cone. The exterior of the cone remained *white* due to lower *blue* photon flux

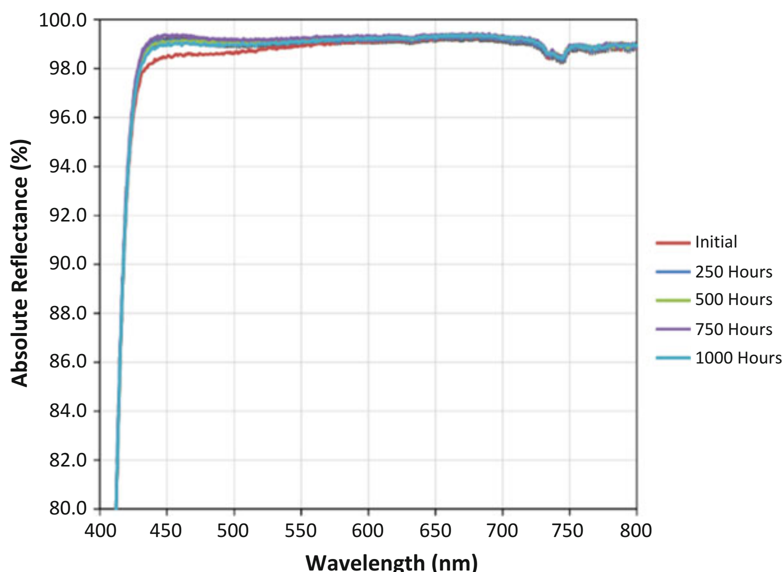

Fig. 10.19 Reflectance spectra for silicone reflector materials after exposure to an ambient environment of 75 °C and 75% RH. The samples was constantly irradiated with high intensity *blue* LEDs (0.46 W/cm^2 at l_{max} ~ 453 nm). Absolute reflectance is measured relative to a calibrated Spectralon reflectance standard

10.5.4 Modeling the Degradation of Lens Materials

The change in the reflectance of most common reflector materials can be modeled using procedures similar to those discussed for lenses. In this approach, the

reflectance at each wavelength ($\%R_\lambda$) changes in a linear manner and can be calculated at any given time by using the following equation:

$$\%R_\lambda(t) = \%R_\lambda(0) + \frac{\mathrm{d}(\%R_\lambda)}{\mathrm{d}t} \times t \tag{10.3}$$

where

t = Time

$\%R_\lambda(0)$ = Initial reflectance (i.e., $t = 0$) for wavelength λ

$\%R_\lambda(t)$ = Reflectance at time t for wavelength λ

$\mathrm{d}(\%R_\lambda)/\mathrm{d}t$ = Change in lens transmittance with time (experimentally derived)

The values for $\mathrm{d}(\%R_\lambda)/\mathrm{d}t$ of each reflector material can be best determined through ALTs, and these findings can be related to normal use environments provided that the AF is known. By recording the reflectance at periodic intervals, a graph of the reflectance versus time can be created as shown in Fig. 10.20. Because this reflector material contains rutile-phase TiO_2 pigment, a strong absorbance occurs below 420 nm, and the uncertainty in this model increases significantly below 420 nm because of the rapid change in reflectance.

To model the change in the reflectance of a material, graphs of reflectance versus exposure time must be created at each wavelength of interest; the calculated slope corresponds to the first derivative of reflectance (i.e., $\mathrm{d}(\%R_\lambda)/\mathrm{d}t$). In some cases, a plot of the first derivative values versus wavelength can also be shown to vary in a predictable, linear manner, for spectral regions where high light absorption does not

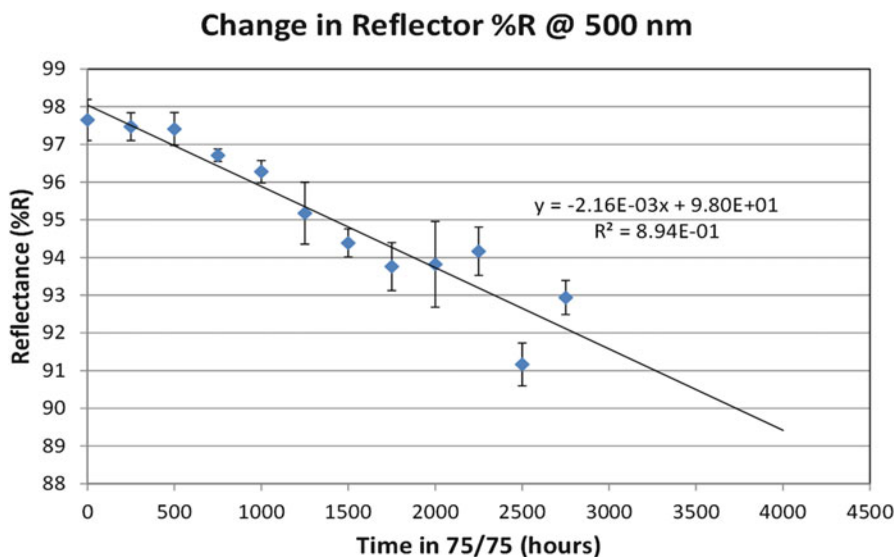

Fig. 10.20 Change in reflectance at 500 nm for a polyolefin-TiO_2 composite under warm white irradiation at selected frequencies during 75/75 exposure. The reported values represent the average from the four samples

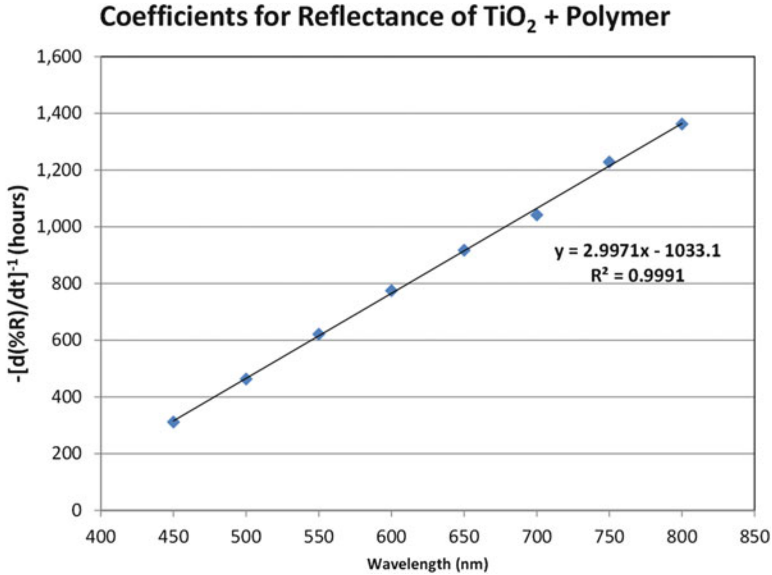

Fig. 10.21 Change in $[d(\%Rl)/dt]^{-1}$ between 450 and 800 nm for a polyolefin-TiO_2 composite under warm white irradiation during 75/75 exposure. The reported values at each wavelength represent the average from the four samples

occur, the reciprocal of $d(\%R_\lambda)/dt$ versus time is linear, as shown in Fig. 10.21. The value of $d(\%R_\lambda)/dt$ can be determined at any wavelength for which the model is valid by using a linear relationship such as the one shown in Fig. 10.20. By determining $d(\%R_\lambda)/dt$, the change in optical properties of the luminaire elements (i.e., reflectors) can be calculated at any time for the test environment. If the measurement was performed during an accelerated test, then these values can be correlated to expected changes in the actual usage environment, provided that the AF has been determined by using the following equation:

$$t_{op} = t_{ALT} \times AF \tag{10.4}$$

where

t_{op} = Operational time of the device in the normal operating environment
t_{ALT} = Operational time in the ALT environment used to build the models

10.6 Luminaire Design Effects

When a luminaire is new, its luminaire efficiency, which is defined as the ratio of luminous flux (lumens) emitted by a luminaire to that emitted by the light source (e.g., LEDs or lamps used therein), is at its maximum value. As the optical

components of the luminaire age, the luminaire efficiency will degrade in a systematic manner which can change the chromaticity point. Thus, when considering the chromaticity maintenance of LED-based lighting source, changes in the LEDs and the optical components (i.e., lenses and reflectors) of the luminaire need to be considered. In addition, the relative impacts of lens and reflector degradation will depend on the design of the luminaire [12]. This phenomenon can be studied by using optical simulation tools for nearly any luminaire design. This simulated or "virtual" luminaire approach, which is illustrated here, involves designing a luminaire in the simulation tool that includes the selection of the initial optical properties of the lenses and reflectors. Then, the properties of these materials can be degraded in a systematic manner, and the impacts on luminaire performance can be determined.

For this analysis, any luminaire design can be modeled for any expected physical parameters, including size and optical cavity depth. Aging of materials used in luminaire could be easily accommodated in the simulation by attenuating the optical properties of the materials. For example, the impact of a 10% drop in lens transmittance can be simulated by reducing normalized lens transmittance by 10%. Transmittance is normalized by the initial transmittance of the pristine material. By systematically changing the design parameters and simulating aging of the optical surfaces by introducing new values for normalized transmittance and reflectance, a model can be created to determine the change in luminous flux produced by the luminaire during aging. A simple power-law model of the form shown in Eq. 10.5 captures the impact of optical material degradation on lumen maintenance for the LED device:

$$\Phi_{\text{tot}}(t) = \Phi_{\text{init}} F_{\text{LEDs}} [L(t)]^m [R(t)]^n \tag{10.5}$$

where

Φ_{tot} = Total luminous flux from the luminaire at time t.

Φ_{init} = Initial luminous flux from the luminaire at time zero. This value is also the product of the luminous flux from the light engine and the luminaire efficiency.

F_{LEDs} = Lumen maintenance factor of the LED at time t.

$L(t)$ = Change in the normalized lens transmittance $[\%T(t)/\%T(t = 0)]$ at time t.

m = Design-dependent factor for the lens.

$R(t)$ = Change in the normalized reflector reflectance $[\%R(t)/\%R(t = 0)]$ at time t.

n = Design-dependent factor for the reflector.

An example of the output from a typical simulation for a 2 × 2 ft troffer with a 3-in. optical mixing cavity in shown in Table 10.3. In this simulation, the light engine for the luminaire consisted of 121 MP-LEDs. The luminaire lens was a common PMMA lens material, and the reflector was a high-performance PET reflector. As shown in Table 10.3, various "virtual luminaires" were created by attenuating the lens transmittance and reflector reflectance in 5% increments from their normalized initial values. The impact of these materials changes affect luminaire efficiency and will likely change the luminaire chromaticity as well. Ignoring

Table 10.3 Optical ray tracing simulation inputs, outputs, and comparison to a model for a virtual 2 × 2 troffer with a 3-in. deep optical mixing cavity

	Test 1	Test 2	Test 3	Test 4	Test 5	Test 6	Test 7	Test 8	Test 9
Reflector % (of original reflectance)	100%	100%	100%	95%	95%	95%	90%	90%	90%
Lens % (of original trasmittance)	100%	95%	90%	100%	95%	90%	100%	95%	90%
Cavity Height	3"	3"	3"	3"	3"	3"	3"	3"	3"
Photopia Calcuated Values									
Efficiency	94.2%	84.8%	75.9%	91.6%	82.5%	73.9%	89.3%	80.5%	72.1%
Output Lumens	2279	2052	1838	2217	1997	1789	2161	1947	1745
Intensity at Nadir (candela)	839.2	746.3	675.2	816.1	736.3	663.0	801.0	714.1	644.3
Full Beam Angle (90-270° plane)	107.3	108.0	107.7	107.4	107.5	107.0	107.0	107.2	107.1
Spacing Criterion (90-270° plane)	1.26	1.27	1.27	1.27	1.26	1.26	1.26	1.27	1.26
RTI Model Prediction	94.2%	84.8%	76.0%	91.7%	82.6%	74.0%	89.2%	80.3%	71.9%
Difference Between RTI and Photopia	0.0%	0.0%	0.1%	0.1%	0.1%	0.1%	-0.1%	-0.2%	-0.2%
Percent	0.0%	0.0%	0.1%	0.2%	0.1%	0.1%	-0.1%	-0.2%	-0.2%
Absolute Value	0.0%	0.0%	0.1%	0.2%	0.1%	0.1%	0.1%	0.2%	0.2%

Inputs to the optical simulation tool are provided in the yellow boxes, outputs from the simulation are given in the green boxes, and the model prediction using Eq. 10.6 with $m = 2.04$ and $n = 0.52$ are given in the blue boxes

the effects of LED lumen depreciation, Eq. 10.5 can be recast into a model for luminaire optical efficiency degradation as shown in the following equation.

$$\mathrm{LE}(t) = \mathrm{LE}(t = 0)[L(t)]^m[R(t)]^n \tag{10.6}$$

where

$\mathrm{LE}(t)$ = Luminaire efficiency at time t
$\mathrm{LE}(t = 0)$ = Initial luminaire efficiency
$L(t)$ = Change in the normalized lens transmittance $[\%T(t)/\%T(t = 0)]$ at time t
m = Design-dependent factor for the lens
$R(t)$ = Change in the normalized reflector reflectance $[\%R(t)/\%R(t = 0)]$ at time t
n = Design-dependent factor for the reflector

The parameters m and n take into account the impact of the luminaire design on the relative contributions of lens and reflector aging upon degradation in luminaire efficiency, and their values can be determined from a least squares analysis of data like that shown in Table 10.3. For example, in the 2 × 2 troffer design shown in Table 10.3, m is approximately 2 and n is approximately 0.5, indicating that the degradation of the lens has a much greater impact on changes in luminaire efficiency and by extension chromaticity stability than the degradation of the reflectors. However, for luminaires with smaller apertures and proportionally deeper optical mixing cavities, the value of n can equal or surpass the value of m, indicating that reflector degradation has a significant impact on overall luminaire efficiency changes in some designs [12].

Conceptually, the value of n can be thought of as being proportional to the likelihood that light emitted by an LED at the base of an optical cavity will strike the reflector in that optical cavity and be impacted by reflector degradation. For example, with a 6-in. downlight with a 3-in. optical mixing cavity with tapered

walls (i.e., the aperture is 6 in., and the optical mixing cavity depth is 3 in. for a 6:3 ratio), there is an increased likelihood that aging of the reflector will impact luminaire efficiency and chromaticity stability, so the value of n is high. In contrast, for a 6-in. downlight with a 1-in. optical mixing cavity (i.e., the aperture is 6 in., and the optical mixing cavity depth is 1 in. for a 6:1 ratio), the impact of reflector aging on luminaire efficiency is reduced, so n is less. In either case, the light must pass through the lens so the impact of its degradation on luminaire efficiency and chromaticity stability is significant. Consequently, the impact of reflector degradation on lumen maintenance and chromaticity stability can be reduced by shrinking the optical mixing cavity, but this may also change the distribution and homogeneity of the light emitted by the luminaire.

10.7 Conclusions

The increased emphasis on color quality from LED light sources has placed greater scrutiny on the chromaticity shift characteristics of LED lamps and luminaires. When used in integrated lamps and luminaires, LED packages are key contributors to chromaticity shift but are not the only cause. The materials used in luminaire components such as lenses and reflectors must be chosen wisely to ensure that the device maintains good chromatic stability.

LEDs are a leading component of chromaticity shift, and the magnitude and direction of this chromaticity shift can be traced to the LED package design and its materials. There appears to be at least five different chromaticity shift modes (CSMs) in LEDs, with chromaticity shifts generally occurring in either the blue, green, or yellow directions. Shifts in the red direction can occur as well but are generally less common. Chromaticity shifts can be caused by chemical changes in LED components (e.g., phosphor oxidation or encapsulate yellowing) or mechanical changes in the LED construct (e.g., delamination of the phosphor-binder layer).

Optical components in luminaires and lamps can also degrade during use, which can impact chromaticity stability and luminous flux maintenance. For example, light absorption by lenses increases over time with the absorption changes being larger for blue wavelengths and progressively less for green, yellow, and red wavelengths. However, some lens chemistries are more resistant to these changes than others. Likewise, the absorption of reflector materials also increases with time with a wavelength-dependent behavior. The combined effects of lens and reflector aging not only result in contributions to lumen depreciation but also contribute to chromaticity shift. The relative impact of lens and reflector aging is dependent upon luminaire design, and these factors change in a predictable manner, allowing models of the impact of aging to be constructed.

Understanding the causes of chromaticity shift at the LED, lens, and reflector level is important to designing and building LED products that maintain good chromaticity stability. Since LED-based devices are often expected to be used

much longer than similar luminaires employing conventional lamp technologies, this insight is critical to maintaining customer satisfaction and growing the industry.

Acknowledgments The Photopia simulations were performed by Eric Frydendall of LTI Optics, Inc. Mike Lamvik of RTI also assisted with the Photopia simulations.

Funding for this work was provided by the US Department of Energy under Award Number DE-EE0005124.

Disclaimer This report was prepared in part as an account of work sponsored by an agency of the US Government. Neither the US Government nor any agency thereof, nor any of its employees, makes any warranty, express or implied, or assumes any legal liability or responsibility for the accuracy completeness, or usefulness of any information, apparatus, product, or process disclosed, or represents that its use would not infringe privately owned rights. Reference herein to any specific commercial product, process, or service by trade name, trademark, manufacturer, or otherwise does not necessarily constitute or imply its endorsement, recommendation, or favoring by the US Government or any agency thereof. The views and opinions of authors expressed herein do not necessarily state or reflect those of the US Government or any agency thereof.

References

1. Next Generation Lighting Industry Alliance and LED Systems Reliability Consortium, LED Luminaire Lifetime: Recommendations for Testing and Reporting. Prepared for the U.S. Department of Energy. September 2014. (2014). Available at http://energy.gov/sites/prod/files/2015/01/f19/led_luminaire_lifetime_guide_sept2014.pdf
2. Talley Robert “Solid State Lighting: An Owners Perspective” presentation at the 2016 DOE SSL Research and Development Workshop, Raleigh, NC. (2016)
3. M.E. Poplawski, M.R. Ledbetter, M.A. Smith, L-Prize: stress testing of the Philips 60W replacement lamp entry. (2012). Available at http://www.lightingprize.org/pdfs/lprize_60w-stress-testing.pdf
4. Pacific Northwest National Laboratory, CALiPER retail lamps study 3.2: lumen and chromaticity maintenance of LED A lamps operated in steady state conditions. (2015). Available at http://energy.gov/sites/prod/files/2015/02/f19/caliper_retail-study_3-2.pdf
5. O. Noboru, A.R. Robertson, *Colorimetry Fundamentals and Applications* (Wiley, West Sussex, 2005)
6. Illuminating Engineering Society, LM-80-15: IES approved method: measuring luminous flux and color maintenance of LED packages, arrays, and modules. (2015)
7. Davis J. Lynn, Young Joe, Michael Royer, CALiPER report 20.5: chromaticity shift modes of LED PAR38. Lamps operated in steady state conditions. (2016). Available at http://energy.gov/sites/prod/files/2016/03/f30/caliper_20-5_par38.pdf
8. P. Lall, H. Zhang, J.L. Davis, A comparison of temperature and humidity effects on phosphor converted LED packages and the prediction of remaining useful life with state estimator” 2016 Intersociety Conference on thermal and thermomechanical phenomena in electronic systems, in press. (2016)
9. Tuttle Ralph, McClear Mark, Understanding the true cost of LED choices in SSL systems. LEDs Magazine (February 2014). (2014)
10. Lall Pradeep, Zhang Hao, Davis Lynn, “Phosphor converted LED failure mechanisms that relate to the phosphor layer area” presentation at the SMTA LED Assembly Reliability and Testing Symposium Atlanta, GA. (2015)

11. Watzke S., Altieri-Weimar P, Degradation of silicone in white LEDs during device operation: a finite element approach to product reliability prediction, 2014 15th International Conference on Thermal, Mechanical, and Multi-Physics Simulations and Experiments in Microelectronics and Microsystems (EuroSimE). (2014). doi: 978-1-4799-4790-4/14
12. Davis J. Lynn, K. Mills, M. Lamvik, R. Yaga, S.D. Shepherd, J. Bittle, N. Baldasaro, E. Solano, G. Bobashev, C. Johnson, A. Evans, "System-reliability for LED-based products," 2014 15th international conference on thermal, mechanical and multi-physics simulation and experiments in microelectronics and microsystems (EuroSimE). (2014)
13. C.K.Y. Wong, S.Y.Y. Leung, X.J. Xiong, C.C.A. Yuan, G.Q. Zhang, A model in predicting color of LED packages with different phosphor layers dimensions, 2014 15th international conference on thermal, mechanical and multi-physics simulation and experiments in microelectronics and microsystems (EuroSimE). (2014)
14. M. Buffolo, C. DeSanti, M. Meneghini, D. Rigon, G. Meneghesso, E. Zanoni, Long-term degradation mechanisms of mid-power LEDs for lighting applications. Microelectron. Reliab. **55**(2015), 1754–1758 (2015)
15. P. Lall, J. Wei, L. Davis, "Prediction of L70 lumen maintenance and chromaticity for LEDs using extended Kalman filter models", in *Proceedings of SPIE: LED-based Illumination Systems*, 8835 (2013), 88350M-1–88350M-10. (2013)
16. J. Fan, K.C. Yung, M. Pecht, Lifetime estimation of high-power white LED using degradation-data-driver method. IEEE Trans. Device Mater. Reliab. **12**(2), 470–477 (2012)
17. M. Hansen, Davis J. Lynn "The true value of LED packages" presented at Strategies in Light Las Vegas, NV. (2015)
18. M. Hansen, J. Lynn Davis "Package impact on color shift in LEDs" presented at Strategies in Light March 1, 2016 Santa Clara, CA. (2016)
19. IESNA LM-80-08, *IESNA Approved Method for Measuring Lumen Maintenance of LED Light Sources* (Illuminating Engineering Society, New York, 2008)
20. P. Lumileds, *IESNA LM-80 Test Report for Luxeon Products, Design Resource DR05-1* (Philips Lumileds of San Jose, California, 2012)
21. Tuttle Ralph "LED System Lifetime and Reliability: LED Components" presented at Strategies in Light Las Vegas, NV. (2014)
22. PNNL, *CALiPER Report 20.4: Lumen and Chromaticity Maintenance of LED PAR38 Lamps Operated in Steady-State Conditions* (U.S. Department of Energy, Washington, D.C., 2015)
23. Davis J. Lynn, Yaga Robert, Johnson Cortina, Mills Karmann, "The Causes of Color Shift in LED Devices," presentation at the 2016 Phosphor Global Summit Newport Beach, CA. (2016)
24. M. Meneghini, L.R. Trevisanello, G. Meneghesso, E. Zanoni, A review on the reliability of GaN-based LEDs. IEEE. Trans. Device Mater. Reliab. **8**(2), 323–331 (2008)
25. E. Zanoni, M. Meneghini, N. Trivelin, M. dal Lago, G. Meneghesso, GaN-based LEDs: State of the art and reliability-limiting mechanisms. 2014 15th international conference on thermal, mechanical and multi-physics simulation and experiments in microelectronics and microsystems (EuroSimE). (2014)
26. M. Royer, C. Stalker, R. Tuttle, LED Color Stability: 10 important questions DOE Webinar (April 15, 2014). (2014)
27. W.M. Yen, A. Shionoya, H. Yomamoto, *Phosphor Handbook: Second Edition CRC Press* (Taylor and Francis Group, Boca Raton, 2007)
28. R.-J. Xie, N. Hirosak, Silicon-based oxynitride and nitride phosphors for white. LEDs. Rev. Sci. Technol. Adv. Mater. **8**(2007), 588–600 (2007)
29. L.M. Dal, M. Meneghini, N. Trivellin, G. Mura, M. Vanzi, G. Meneghesso, E. Zanoni, Phosphors for LED-based light sources: thermal properties and reliability issues. Microelectron. Reliab. **52**(2012), 2164–2167 (2012)
30. Wang, Chen, Li, Wang, Sheu, Liu, Neighboring-cation substitution tuning of photoluminescence by remote-controlled activator in phosphor lattice. J. Am. Chem. Soc. **135**, 12504–12507 (2013)

31. M. Raukas, J. Kelso, Y. Zheng, K. Bergenek, D. Eisert, A. Linkov, F. Jermann, Ceramic phosphors for light conversion in LEDs. ECS. J. Solid State Sci. Technol. **2**(2), 3132–3137 (2013)
32. J. Wang, C.-C. Tsai, W.-C. Cheng, M.-H. Chen, C.-H. Chung, W.-H. Cheng, High thermal stability of phosphor-converted white light-emitting diodes employing Ce:YAG-doped glass. EEE J. Sel. Top. Quantum Electron. **17**(2001), 741–745 (2011)
33. W. Koh van Driel, G.Q. Zhang, High humidity resistance of high power white-light-emitting diode modules employing Ce:YAG doped glass 2011 Electronics Components and Technology Conference. (2011)
34. J.-S. Wang, C.-C. Tsai, J.-S. Liou, W.-C. Cheng, S.-Y. Huang, G.-H. Chang, W.-H. Cheng, Mean time-to-failure evaluations of encapsulation materials for LED package in accelerated thermal tests. Microelectron. Reliab. **52**(2012), 813–817 (2012)
35. C.-W. Yeh, W.-T. Chen, R.-S. Liu, S.-F. Hu, H.-S. Sheu, J.-M. Chen, H.T. Hintzen, Origin of thermal degradation of Sr2-XSi5N8:Eux phosphors in air for light-emitting diodes. J. Am. Chem. Soc. **134**(2012), 14108–14117 (2012)
36. B. Wu, X. Luo, S. Liu, Effect mechanism of moisture diffusion on LED reliability 2010 3rd Electronic System-Integration Technology Conference (ESTC). (2010)
37. X. Luo, B. Wu, S. Liu, Effects of moist environments on LED module reliability IEEE. Trans. Device Mater. Reliab. **10**(2010), 182–186 (2010)
38. B. Wu, X. Luo, Z. Zhao, S. Liu, Effect investigation of delamination on optical output of high power LEDs 2011. International conference on electronic packaging technology and high density Packaging. (2011)
39. C.M. Tan, B.K.E. Chen, G. Xu, Y. Liu, Analysis of humidity effects on the degradation of high-power white LEDs. Microelectron. Reliab. **49**(2009), 1226–1230 (2009)
40. N. Narendran, Y. Gu, J.P. Freyssinier, H. Yu, L. Deng, Solid-state lighting: failure analysis of white LEDs. J. Cryst. Growth **268**. (2004, 449–456 (2004)
41. P. Appaiah, N. Narendran, I.U. Perera, Y. Zhu, Y.-W. Liu, Effect of thermal stress and short-wavelength visible radiation on phosphor-embedded LED encapsulant degradation. Opt. Mater. **46**(2015), 6–11 (2015)
42. L. Lantz, S. Hwang, M. Pecht, Characterization of plastic encapsulant materials as a baseline for quality assessment and reliability testing. Microelectron. Reliab. **42**(2002), 1163–1170 (2002)
43. S. Koh, W. van Driel, G.Q. Zhang, Degradation of light emitting diodes: a proposed methodology. J. Semicond. **32**.(2011, 014004 (2011)
44. Tan, Khai, Chen, Xu, Liu, Analysis of humidity effects on the degradation of high-power white LEDs. Microelectron. Reliab. **49**, 1226 (2009)
45. J. MacDonald, “Advanced silicone materials for LED lighting” presentation at the 2015 DOE SSL R&D Workshop, San Francisco, CA. (2015)
46. J. S. Tonge, M. Mohamen, N. E. Shepherd, B. M. Ketola, Reliability of silicone encapsulants in high pollution environments 21st Annual Meeting of the IEEE Lasers and Electro-Optics Society p. 658–659. (2006)
47. P. Lall, H. Zhang, J. L. Davis “Failure mechanisms and color stability in light-emitting diodes during operation in high-temperature environments in presence of contamination” Electronic Components and Technology Conference (ECTC) Orlando, FL. P. 1624. (2015)
48. P. Lall, J. Wei, X-ray micro-CT and digital-volume correlation based three-dimensional measurements of deformation and strain in operational electronics 2015 Proceedings of the Electronics Component and Technology Conference (ECTC) p. 406–416. (2015)
49. J.L. Davis, M. Lamvik, J. Bittle, S. Shepherd, R. Yaga, N. Baldasaro, E. Solano, and G. Bobashev, “Insights into accelerated aging of SSL luminaires” Proceedings of SPIE: LED-based Illumination Systems, 8835 (2013), 88350L-1–88350L-10
50. M. Diepens, P. Gijsman, Photodegradation of bisphenol A polycarbonate. Polym. Degrad. Stab. **92**, 397–406 (2007)

51. M. Diepens, P. Gijsman, Influence of light intensity on the photodegradation of bisphenol a polycarbonate. Polym. Degrad. Stab. **94**, 34–38 (2009)
52. M.Y. Mehr, W.D. van Driel, K.M.B. Jansen, P. Deeben, M. Boutelje, G.Q. Zhang, Photodegradation of bisphenol A polycarbonate under blue light radiation and its effect on optical properties. Opt. Mater. **35**, 504–508 (2013)
53. M.Y. Mehr, W.D. van Driel, H. Udono, G.Q. Zhang, Surface aspects of discolouration in bisphenol A polycarbonate (BPA-PC) used as lens in LED-based products. Opt. Mater. **37**, 155–159 (2014)
54. G. Lu, M.Y. Mehr, W.D. van Driel, X. Fan, J. Fan, K.M.B. Jansen, G.Q. Zhang, Color shift investigations for LED secondary optical designs: comparison between BPA-PC and PMMA. Opt. Mater. **45**, 37–41 (2015)
55. G.F. Tjandraatmadja, L.S. Burn, M.C. Jollands, Evaluation of commercial polycarbonate optical properties after QUV-A radiation – The role of humidity in photodegradation. Polym. Degrad. Stab. **78**(2002), 435–448 (2002)
56. E. Estupinan, P. Wendling, M. Kostrun, R. Garner, Accelerated optical polymer aging studies for LED luminaire applications. Proc. SPIE. **8835**, 883502–883501 (2013)
57. G. Lu, W.D. van Driel, X. Fan, M.Y. Mehr, J. Fan, K.M.B. Jansen, G.Q. Zhang, Degradation of microcellular PET reflective materials used in LED-based products. Opt. Mater. **49**, 79–84 (2015)
58. G.L. McGregor, R.B. Minor, G.E. Hannon, U.S. Patent 5,892,621 "Light reflectance surface for luminaires."1999)
59. Trocellen, MCPET – Microcellular PET Sheet" available at www.trocellen.com. (n.d.)
60. K. Miyakawa, K. Tsunashima, S. Aoki, U.S. Patent 5,672,409 "Polyester film reflector for a light source surface. (1997).
61. G. Lu, W.D. van Driel, X. Fan, M.Y. Mehr, J. Fan, C. Qian, K.M.B. Jansen, G.Q. Zhang, Colour shift and mechanism investigation on the PMMA diffuser used in LED-based luminaires. Opt. Mater. **54**, 282–287 (2016)
62. J.L. Davis, M. Lamvik, J. Bittle, S. Shepherd, R. Yaga, N. Baldasaro, E. Solano, G. Bobashev, "Insights into accelerated aging of SSL Luminaires" Proceedings of SPIE: LED-based Illumination Systems, 8835, 88350M-1–88350M-10. (2013)

Chapter 11
Fault Diagnostics and Lifetime Prognostics for Phosphor-Converted White LED Packages

Jiajie Fan, Cheng Qian, Xuejun Fan, Guo Qi Zhang, and Michael Pecht

Abstract Traditionally, the photometric measurement methods for LEDs during aging tests are usually done by collecting performance degradation data offline, thus incurring measurement errors and significant testing costs. Additionally, owing to the long lifetime and high reliability of LEDs, estimating the lumen maintenance life by using traditional destructive life testing methods is time-consuming and expensive. Even the IESNA TM-21 standard, which is widely accepted by many LED manufacturers, has weaknesses in terms of guaranteeing life prediction accu-

J. Fan (✉)
College of Mechanical and Electrical Engineering, Hohai University,
Changzhou 213022, China

Beijing Research Center, Delft University of Technology, Beijing, China

Changzhou Institute of Technology Research for Solid State Lighting,
Changzhou 213161, China
e-mail: jay.fan@connect.polyu.hk

C. Qian
Changzhou Institute of Technology Research for Solid State Lighting,
Changzhou 213161, China

Institute of Semiconductors, Chinese Academy of Sciences, Haidian, Beijing 100083, China
e-mail: cqian@sklssl.org

X. Fan
Changzhou Institute of Technology Research for Solid State Lighting,
Changzhou 213161, China

Department of Mechanical Engineering, Lamar University, Beaumont, TX 77710, USA
e-mail: xuejun.fan@lamar.edu

G.Q. Zhang
Beijing Research Center, Delft University of Technology, Beijing, China

EEMCS Faculty, Delft University of Technology, Delft, The Netherlands

Institute of Semiconductors, Chinese Academy of Sciences, Haidian, Beijing 100083, China
e-mail: g.q.zhang@tudelf.nl

M. Pecht
Center for Advanced Life Cycle Engineering, University of Maryland, College Park, MD, USA
e-mail: pecht@calce.umd.edu

© Springer International Publishing AG 2018

W.D. van Driel et al. (eds.), *Solid State Lighting Reliability Part 2*, Solid State Lighting Technology and Application Series 3, DOI 10.1007/978-3-319-58175-0_11

racy, because it relies on the least-squares regression (LSR) method without considering measurement dynamics and uncertainties. The theory of prognostics and health management (PHM) has been widely used in many electronics that originates the idea that the "unhealthy" (anomaly) of electronics could be detected and the reliability (and remaining useful life) of electronics could be predicted by using an in situ sensing approach and data-driven methods. In this chapter, a detail review of current reliability testing and qualification methods for LEDs and general PHM methodologies are introduced in advance. Then an online anomaly detection and lumen maintenance life prediction method based on the PHM methodology are proposed for phosphor-converted white LED packages.

11.1 Introduction

Nowadays, artificial lighting consumes around 19% of the world's total energy, which produces approximately 10% of all carbon emitted in the world [1, 2]. In the long lighting history, traditional lighting sources (i.e., incandescent bulbs and fluorescent lamps) rely on thermal radiation or fluorescence to convert electricity to light, which are very inefficient. For example, an incandescent bulb converts only about 5% of electrical energy into visible light, and its luminous efficacy is only ~10 lm/W, while the luminous efficiency of fluorescent lamp is only 20% [3]. By contrast, light-emitting diodes (LEDs) produce visible light via electroluminescence which converts electricity to light without relying on heat for radiation (luminous efficacy >200 lm/W, luminous efficiency >30% [4]). Therefore, LED is much more efficient, and it has become a comparatively low-energy consuming, long-lasting, and environmentally friendly alternative to traditional lighting sources. Now LED is primed to play a critical role in the future of TVs and commercial displays/backlighting, mobile communications, and medical applications [5]. Thus, the 2014 Nobel Prize in Physics was awarded for inventing of blue LEDs.

However, the mass application of LEDs in our daily lives still has many barriers, such as high cost, time- and cost-consuming qualification tests, and unreliable lifetime predicted by current methods. This can be attributed to the limitations of the conventional qualification testing and reliability prediction methods applied in LEDs [6]. In the current LED market, there is often a large gap between the warranted life and the real application life [7]. For example, Xiamen City in China has been installing high-power LEDs for street lighting since 2008. The manufacturer promised a system lifetime of 100,000 h (over 5 years of reliable operation), but the city government discovered the lights failed within 2–3 months after installation [8]. In 2014, Lights of America Inc. was fined US$21M, because their LED lamps lasted no more than a few thousand hours, which was claimed a 30,000 h life (15 times longer than 2000 h incandescent bulbs) [9]. From 2008 to 2010, Taiwan installed 20,000 LED streetlamps (demand is for 1.7 million units); the failure rates of these units were about 8.2% and could be 6% after excluding

problems such as aging electrical wiring [10]. Otherwise, due to its longer lifetime, higher reliability, and different failure mechanisms compared to traditional light sources, it is difficult to qualify LEDs with traditional reliability assessment approaches which record only failure time data. Sometimes the duration of the qualification testing is longer than the time between product updates, which may delay technology innovation and development. Generally, a major hurdle for getting new LED products to the market quickly is the amount of time it takes to qualify them. Conventional LED testing and qualification processes do not meet the needs of quick and cost-effective qualification. The key issues and problems with current LED qualification testing include: firstly, current qualification testing methods based on lumen maintenance (as a failure mode) do not distinguish between failure mechanisms of LEDs since all failures affect light output degradation. Therefore, the current product qualification does not provide appropriate information on the failure modes, failure mechanisms, and failure sites of LEDs. Chang et al. [11] investigated and grouped 13 failure mechanisms of LEDs in terms of three failure sites: semiconductors, interconnects, and package. Each failure mechanism is associated with failure cause, effect on device, and failure mode. It is confirmed that there are multiple types of failure modes beyond the light output degradation in terms of electrical, thermal, and color features such as reverse leakage current, parasitic series resistance, short circuit, open circuit, forward voltage, discoloration of the encapsulant, broadening of spectrum, color coordinate shift, and color temperature shift [11, 12]. Fan et al. [13] developed a physics-of-failure-based PHM approach to assess the reliability of high-power white LED lighting from the chip level to the system level, which includes an analysis of materials and geometries; failure modes, mechanisms, and effects analysis (FMMEA); and failure models built for the prioritized failure mechanisms. Three failure modes, catastrophic failure (lighting sudden off), chromaticity shift, and luminous flux degradation, were firstly categorized to the whole system. The potential failure mechanisms and their contributing loads were presented by the "bottom-up" method. A new product qualification method is required to consider all of these failure modes which tell the difference among failure mechanisms more clearly.

In addition, qualification test time varies depending on the manufacturer, and test results do not offer reliability information about the product when the tests do not include failures. It can take several months to complete operating life tests even when the tests are time-terminated [14]. An accelerated test to reduce the qualification test time is used to predict the lifetime of LEDs by multiplying the light output (i.e., lumen) degradation projection by an acceleration factor, often based on the Arrhenius model [15, 16]. However, there is no relationship to relate the time under accelerated test conditions to the time under field conditions with the consideration of actual LED failure mechanisms. Additionally, the extrapolation of LED lifetime based on lumen maintenance under the accelerated test condition is affected by factors such as the number of samples tested, the assumed activation energy, possible failure mechanism shift, and the length of testing [17–19]. Current life prediction method does not perform remaining useful life estimation during operation.

Table 11.1 Environmental tests for LEDs

No.	Names	
1	Room temperature operating life test (RTOL)	Operating test
2	Low-temperature operating life test (LTOL)	
3	High-temperature operating life test (HTOL)	
4	Wet high-temperature operating life test (WHYOL)	
5	Powered temperature cycle test (PTC)	
6	Pulse life test (PL)	
7	High-/low-temperature storage test (H/LTS)	Nonoperating test
8	Solder heat resistance test (SHR)	
9	Thermal shock (TS)	
10	Mechanical shock (MS)	
11	Vibration test (VT)	
12	Corrosion test (salt atmosphere) (CT)	
13	Dust test	

Moreover, major LED manufacturers such as Cree, Lumileds, OSRAM, and Nichia evaluate LED failure criteria in terms of light output maintenance, forward voltage shift, and $u'v'$ shift [20–22]. As there is not yet a specific standard referring to the environmental testing for LEDs, many LED manufacturers prefer to use the environmental tests referring to the electronic devices testing standards designed by both JEDEC (Joint Electron Device Engineering Council) and JEITA (Japan Electronics and Information Technology Industries Association).Typically, the environmental tests used to simulate the application environments for LEDs can be categorized as operating tests and nonoperating tests. For the operating test, it means that the devices under test (DUT) are driven by an electrical supplier when being tested under a selected environmental condition. According to the different environmental conditions designed by JEDEC and JEITA standards, the typical environmental tests recommended for LEDs are summarized in Table 11.1.

Table 11.2 lists some environmental testing conditions selected by some leading LED manufacturers (such as Cree, Lumileds, OSRAM, and Nichia). These LED companies choose their own qualification specifications for their products according to JEDEC or JEITA standards. For instance, Cree and OSRAM use the JESD22 serial environmental testing methods, which includes the JESD22-A108C for RTOL, HTOL, and LTOL tests [23], JESD22-A101B for WHTOL test [24], JESD22-B104Cfor MS test [25] ,and JESD22-A107B for CT [26]. On the other hand, Nichia selects some Japanese standards from JEITA for the environmental testing of their products. For example, EIAJ ED-4701/100-105 is used as a specification for the LED TS test [27]. The failure threshold for each parameter varies depending on the manufacturers, applications, and materials. Due to the variability and complexity of these failure thresholds, it is difficult to evaluate and perform product qualification for different products at the same time. The acceptance criteria are usually a binary pass or fail in terms of those parameter thresholds. Manufacturers do not fully analyze the degradation trends and results by utilizing

Table 11.2 Environmental testing conditions selected by LED manufacturers

Test methods		Environmental testing conditions			
		XLamp at Cree [28]	K2 at Lumileds [29]	OS at OSRAM [30]	NCSW119T-H3 at Nichia [31]
RTOL	Ambient temperature	45 °C	55 °C	25 °C	25 °C
	Forward current	Maximum	Maximum	Maximum	700 mA
	Test period	1008 h	1000 h	1000 h	1000 h
HTOL	Ambient temperature	85 °C	85 °C	85 °C	100 °C
	Forward current	Maximum	Maximum	Maximum	300 mA
	Test period	1008 h	1000 h	1000 h	1000 h
LTOL	Ambient temperature	−40 °C	−55 °C	N.A.	−40 °C
	Forward current	Maximum	Maximum		350 mA
	Test period	1008 h	1000 h		1000 h
WHTOL	Ambient temperature	85 °C	121 °C	85 °C	60 °C
	Forward current	Maximum	N.A.	5 mA/10 mA	600 mA
	Humidity	85% RH	60% RH	85% RH	90% RH
	Test period	1008 h	120 h	1008 h	500 h
TS	Temperature range	−40–125 °C	−40–110 °C	−40–100 °C	−40–100 °C
	Dwell time	15 min	15 min	15 min	30 min
	Transfer time	<20 s	<20 s	N.A.	N.A.
	Cycles	200 cycles	1000 cycles	300/500/ 1000 cycles	100 cycles
MS	Shock	1500 G	1500 G	N.A.	N.A.
	Pulse width	0.5 ms	0.5 ms		
	Direction	5 each; 6 axis	5 each; 6 axis		
CT	Ambient temperature	35 °C	35 °C	N.A.	N.A.
	Sault deposit	30 g/m^2/day	N.A.		
	Test period	48 h	48 h		

the failure criteria for the qualification tests which require the anomaly detection and the prediction of remaining useful life to reduce the qualification test time.

Last but not least, the Illuminating Engineering Society (IES) recommends that LED manufacturers collect color shift data over 6000 h of operations [32]; however, a life prediction method in terms of color failure of LEDs has not been developed. Color shift is difficult to extrapolate because of differences in the

LED designs, materials, manufacturing processes, optics applied to the LED, and use conditions of LED operation. LED color change has been studied under different current loads [33–35]. There is no model that provides detailed information on color degradation.

Therefore, a new product qualification method is needed that not only reduces the time needed for the qualification process but also improves life prediction and ensures the reliability of LEDs over their lifetimes. An approach is needed to enable LED manufacturers to quickly qualify LED prototypes during the development phase (e.g., 100 h) under wear-out performance degradation and an unknown failure distribution. This is a benefit because market pressures demand a short qualification testing cycle. A prognostic-based qualification process will evaluate the product reliability in test conditions that accelerate potential failure mechanisms at associated sites, to assess LED degradation, detect anomalies, and estimate the remaining useful life (RUL). By employing such a methodology, both the qualification test time and costs will be reduced from those in traditional qualification testing allowing LED manufacturers to meet customer requirements based on the intended application and application conditions. The ability of manufacturers to undertake a fast, accurate, and effective qualification testing method for highly reliable LED is a critical economic and business barrier to LED adoption.

11.2 Prognostics and Health Management

Prognostics and health management (PHM) has been proven as an effective solution in diagnosing failures, predicting the residual lifetime, and estimating the reliability for electronic products and systems, which includes machinery systems, electronic devices and systems, hybrid systems, and so on [36–38]. PHM method always solves engineering problems (e.g., failure diagnostics, lifetime estimation, and reliability prediction) with multiple discipline approaches which includes physics, mathematics, and engineering. It applies physics-of-failure modeling and in situ monitoring techniques to detect the deviation or degradation of health and predict the reliability (and remaining life) for electronic products and systems under field operation. Typically, PHM methodology can be categorized into three different methods: (i) physics-of-failure (PoF) methods, (ii) data-driven (DD) methods, and (iii) fusion methods which incorporate the advantageous features from both PoF and data-driven methods.

11.2.1 PoF-Based PHM

The PoF method is an approach for designing for and assessing reliability by utilizing knowledge of a product's life cyclic loading and failure mechanisms, which is based on the understanding that failures occur due to the fundamental

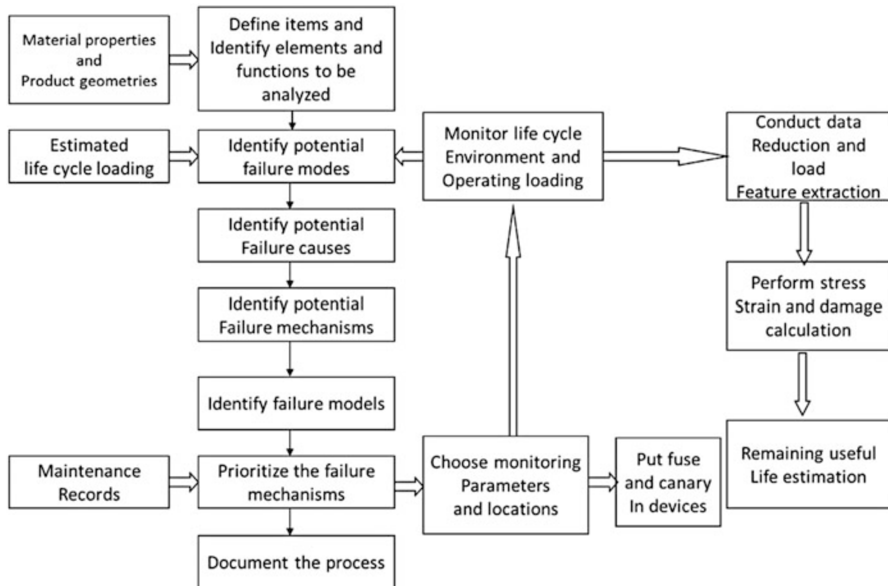

Fig. 11.1 PoF-based PHM methodology [38]

mechanical, chemical, electrical, thermal, and radiation processes [39]. Based on the PoF method, the potential failure modes, failure mechanisms, and failure sites of the product are identified as a function of the product's life cycle loading conditions. As shown in Fig. 11.1, the PoF methodology can be summarized in the following five steps:

Step 1: Identify the potential failure modes and mechanisms and failure sides merging in the selected device with FMMEA (failure modes, mechanisms, and effects analysis) methods.

Step 2: Monitor the life cycle loads that may lead to performance or physical degradation.

Step 3: Extract load features that represent damage characteristics of the critical failure mechanisms identified at step 1.

Step 4: Assess damage and calculate remaining life using the PoF models of the critical failure mechanisms identified at step 1.

Step 5: Predict the reliability by calculating the time to failure, or predict the likelihood of failure happened with considering the geometries, material construction, and environmental and operational conditions.

Most damage models are empirical-based models that are widely used for electronic components and systems. Some of these empirical damage models are reviewed below:

1. Arrhenius model

The Arrhenius model can be used to establish the time to failure model for an electronic device when the failure is induced by temperature factors. It is always used as a relationship between chemical reaction and temperature with the activation energy parameter E_a. Thus the acceleration factor AF between accelerated temperature stress and condition of usage is expressed by the Arrhenius equation [40]:

$$t_f \propto e^{\frac{E_a}{kT}} \tag{11.1}$$

$$\mathrm{AF} = e^{\frac{E_a}{k}\left(\frac{1}{T}-\frac{1}{T_{use}}\right)} \tag{11.2}$$

where k is Boltzmann's constant, T is the operating temperature in Kelvin, and T_{use} represents the temperature of use condition.

2. Eyring model

The Eyring model calculates the time to failure by taking both temperature stress and other nonthermal stresses (such as humidity and mechanical and electrical stresses) into account. This model can be considered as an extension of the Arrhenius approach, which imports the theoretical concepts (molecular collisions, activation energy). The time to failures can be expressed as follows:

$$t_f = \mathrm{AT}^{\alpha} \cdot e^{E_a/\mathrm{kT}} \cdot e^{(\beta_1 + C/T)S_1} \cdot e^{(\beta_2 + D/T)S_2} \tag{11.3}$$

where S_1 and S_2 represent the functions of the nonthermal stresses and β_1, β_2, C, and D are the constants related to stress.

3. Black's model

Black's model is an empirical relationship to estimate the time to failure of an electronic device because of electromigration. The failure mode assumption is a complete open circuit of the metallization:

$$t_f = (t_m \cdot w_m) / \left[j^n \cdot A \cdot e^{-E_a/kT}\right] \tag{11.4}$$

where t_m is the thickness of metallization, w_m is the width of metallization, j represents the current density (A/cm^2), n is experimentally determined exponent ($n = 2$), and A is a constant depending on geometry, substrate, protective coating, and film.

4. Coffin-Manson model

To modeling the thermomechanical fatigue failure in a solder joint or other metals under a thermal cycle condition, the Coffin-Manson model was established and can be used to express the relationship between the number of cycles to failure and the environmental conditions and is given by [41, 42]:

$$N_{\mathrm{f}} = Af^{-\alpha}\Delta T^{-\beta}G(T_{\max}) \tag{11.5}$$

where N_{f} is the number of cycles to failure; f is the thermal cycling frequency, α and β are the cycling frequency exponent and temperature range exponent, respectively; and $G(T_{\max})$ is the Arrhenius term evaluated at the maximum temperature.

Compared to the traditional handbook-based reliability prediction methods, PoF methods have several advantages in increasing the prediction accuracy, detecting root causes contributing to failures, and understanding potential failure mechanisms, which are helpful for manufacturers in understanding their products and improving them. Table 11.3 lists the performance comparisons between MIL-HDBK-217 and the PoF method, which indicates that the PoF method can be an alternative to traditional reliability prediction handbooks. Based on the PoF methodology, there are some computer-aided modeling and simulation software

Table 11.3 Comparison of MIL-HDBK-217 and physics-of-failure methods [45, 46]

Issues	MIL-HDBK-217	Physics of failure
Model development	Models cannot provide accurate design or manufacturing guidance since they were developed from assumed constant failure rate data, not root cause, time to failure data	Models based on science/engineering first principles. Models can support deterministic or probabilistic applications
Device design model	The MIL-HDBK-217 assumption of perfect designs is not substantiated due to lack of root-cause analysis of field failures. MIL-HDBK-217 models do not identify wear-out issues	Models for root-cause failure mechanisms allow explicit consideration of the impact that design, manufacturing, and operation have on reliability
Device defect modeling	Models cannot be used to (1) consider explicitly the impact of manufacturing variation on reliability and (2) determine what constitutes a defect or how to screen/inspect defects	Failure mechanism models can be used to (1) relate manufacturing variation to reliability and (2) determine what constitutes a defect and how to screen/inspect
Device screening	MIL-Hdbk-217 promotes and encourages screening without recognition of potential failure mechanisms	Provides a scientific basis for determining the effectiveness of particular screen or inspections
Device coverage	Does not cover new devices for approximately the first 5–8 years. Some devices, such as connectors, were not updated for over 20 years. Developing and maintaining current design reliability models for devices are an impossible task	Generally applicable – applies to both existing and new devices, since failure mechanisms are modeled, not devices
Operating temperature	Explicitly considers only steady-state temperature. Effect of steady-state temperature is inaccurate because it is not based on root-cause and time to failure data	The appropriate temperature dependence of each failure mechanism is explicitly considered
Cost of analysis	Cost is high compared with value added	Costs are flexible

developed by companies and universities. For example, computer-aided design of microelectronic packages (CADMP-II) is a set of integrated software programs that assist in assessing the reliability of microelectronic packages [43]. The calcePWA is a PoF-based tool designed by the University of Maryland, which can be used to perform simulation-based failure assessment of printed wiring assemblies, which combines thermal analysis, vibration analysis, and failure assessment [44]. However, because it requires comprehensive knowledge of the materials and geometries of a product and the thermal, mechanical, electrical, and chemical life cycle environment as well as processes leading to failures in the field in advance, the PoF method requires significant time resources to collection sufficient information, which also increases the operation cost of reliability prediction for manufacturers.

11.2.2 Data-Driven-Based PHM

To solve the problems mentioned above, such as expensively conducting a PoF on a complex system, data-driven methods have been proposed to determine anomalies and make predictions about the reliability of systems using historical information. The data-driven methods can intelligently provide valuable decision-making information based on learning from historical data. As shown in previous studies [47–49], these data-driven approaches always include (1) multivariate statistical methods (e.g., static and dynamic principle component analysis (PCA), linear and quadratic discriminates, partial least squares (PLS), and canonical variated analysis (CVA)), (2) black box methods based on neural networks [50] (e.g., probabilistic neural networks (PNN), decision trees, multilayer perceptions, radial basis functions, and learning vector quantization (LVQ)), (3) graphical models (Bayesian networks [51], hidden Markov models [48]), (4) self-organizing feature maps, (5) signal analysis (filtering, auto-regressive models, FFT, etc.), and (6) fuzzy rule-based systems and so on.

Generally, most of data-driven approaches are based on statistical and learning techniques from the theory of pattern recognition. Therefore, the data-driven methods for PHM can be classified into (1) statistical approaches and (2) learning approaches.

1. Statistical approach

Usually, the statistical approaches are composed of parametric methods and nonparametric methods. Where the parametric methods assume that the collected population data follow a certain statistical distribution (like normal, exponential, Weibull, or lognormal), the parameters of the distribution can be estimated by fitting the collected data. While the nonparametric methods are not based on the assumption of statistical distributions for the population data, they are just based on their inherent features. In this section, two representative statistical data-driven methods proposed for predicting the reliability (remaining useful life) (general

degradation path model as a parametric method and Mahalanobis distance (MD) as a nonparametric method) are reviewed.

(a) General degradation path model

For the devices with long lifetimes, most of the traditional reliability prediction handbook approaches require failure data that are time-consuming and expensive to obtain. In this condition, using degradation data to do reliability assessment appears to be an attractive alternative to deal with traditional failure time data. The general degradation path model as a parametric statistical method was first proposed by Lu and Meeker [52] who modeled the degradation as a function of time and multidimensional random variables and estimated the failure time distribution with analytical methods by using the relationship between the failure time distribution and the random variable distribution. Usually, several statistical methods have been proposed to estimate reliability based on the degradation data. The degradation path can be registered as time-performance measurement pairs $(t_{i1}, y_{i1}), (t_{i2}, y_{i2}), \ldots\ldots, (t_{imi}, y_{imi})$, for $i = 1, 2, \ldots\ldots, n$, and m_i represents the test time points for each unit:

$$y_{ij} = D\left(t_{ij}; \alpha; \beta_i\right) + \varepsilon_{ij} \tag{11.6}$$

where a random sample size is n and the measurement times are $t_1, t_2, t_3, \ldots\ldots t_s$. The performance measurement for the ith unit at the jth test time is referred to as y_{ij}. $D(t_{ij}; \alpha; \beta_i)$ is the actual degradation path of unit i at the measurement time t_{ij}; α is the vector of fixed effects which remains constant for each unit; β_i is a vector of random effects which varies according to the diverse material properties of the different units and their production processes or handing conditions; ε_{ij} represents the measurement errors for the unit i at the time t_{ij}, which is supposed to be a normal distribution with zero mean and constant variance.

To estimate the time to failure distribution, $F(t)$, based on the degradation data, this data-driven method involves two basic steps which involved (1) estimating the parameters for degradation path model and (2) evaluating the time to failure distributions, $F(t)$. Here, a hypothesis needs to be proposed first on the distribution of the random effects parameter β_i. For example, Wu and Shao [53] assumed the random effects parameter β_i followed a normal distribution. Wu and Chang [54] thought it was an exponential distribution, and Yu [55] designed it as a reciprocal *Weibull* distribution.

(b) Mahalanobis distance (MD)

In 1936, P.C. Mahalanobis first proposed MD to represent a single measure of the degree of divergence in the mean values of different characteristics of a population by considering the correlations between the variables [56, 57]. This method has been applied successfully over the years in several cases such as anomaly detection, classification, and pattern recognition. MD is superior to other

distance measures, such as Euclidean distance (ED), because it considers the correlations of the points:

$$Z_{ij} = \frac{\left(X_{ij} - \overline{X_{ij}}\right)}{S_i} \tag{11.7}$$

$$\overline{X_i} = \frac{1}{m}\sum_{j=1}^{m} X_{ij} \tag{11.8}$$

$$S_i = \sqrt{\frac{\sum_{j=1}^{m}\left(X_{ij} - \overline{X_i}\right)^2}{(m-1)}} \tag{11.9}$$

$$\mathrm{MD}_j = \frac{1}{p} Z_j^T C^{-1} Z_j \tag{11.10}$$

$$C = \frac{1}{(m-1)}\sum_{j=1}^{m} Z_j Z_j^T \tag{11.11}$$

where $\overline{X_i}$ and S_i are the mean and standard deviation, respectively, of data matrix, C is the correlation matrix, Z_j is a normalization of raw data matrix, and Z_j^T is the transpose of Z_j.

MD has two advantages in detecting differences: first, it reduces a multivariate system to a univariate one; second, MD is more sensitive in detecting changes) by taking into account the correlation of several parameters. Thus, MD methods are widely used as a fault alarm to detect anomalies before failure occurs. For example, Niu et al. [58] incorporated the MD method with a Weibull distribution to monitor the health of notebook computers. Kumar et al. [59] used MD as a health indictor to detect the gradual health degradation of electronic products. Sutharssan et al. [60] developed the distance measure techniques (both MD and ED) for a real-time prognostic system, including assessing the reliability, detecting failures, and estimating remaining useful life, for LED lighting.

2. Learning approach

The learning approach is based on machine learning algorithms for recognizing patterns in raw data and in making decisions on the state of the system based on the data. The data collected is analyzed with learning approaches using a variety of techniques depending on the type of data: (a) supervised learning approach, which is for data representing healthy and faulty states of the system, and (b) unsupervised learning approach, which is suitable for the unlabeled data.

(a) Supervised learning approach

Supervised learning is an algorithm to label the outputs of a set of inputs, where healthy and failure datasets are available. Thus, the first step of this approach is training the proposed algorithm with available healthy and unhealthy datasets and

in finding boundaries to distinguish them. The next step is to detect any anomaly for a new input dataset with the trained algorithm. Three basic supervised learning approaches are reviewed below (artificial neural network, support vector machine, and relevance vector machine).

The artificial neural network (ANN) is a graph-based model that establishes a set of interconnected functional relationships between inputs and outputs [61]. It always consists of input nodes, hidden layers, and output nodes. The inputs of neural networks can include process variables, condition monitoring indicators, asset characteristics, and maintenance history features. The outputs depend on the aim of the modeling process, which may be the desired maintenance action or the remaining useful life [62]. As supervised learning, the ANN model is trained with a set of training data to adjust and optimize the associated parameters of the functional relationship [63]. Typically, there are two application areas of ANN in prognostics: (1) estimations and classifications, which work as a nonlinear function approximator to predict system's failure features and trends, and (2) prognostics, which model the dynamic processes of system's degradation and predict the remaining useful life [64, 65]. There are several types of neural network architectures used for prognostics, such as self-organized maps (SOM), recurrent neural networks (RNN), dynamic wavelet neural networks (DWNN), and so on. For example, an SOM neural network was used by Zhang et al. as a multivariable trend indicator of fault development to estimate the remaining useful life of a bearing system [66]. Connor et al. [64] proposed recurrent neural networks for time series predictions. Vachtsevanos and Wang [67] used dynamic wavelet neural networks to predict the failures of a bearing system.

The support vector machine (SVM) is a supervised learning method used as a maximum margin classifier with the ability of simultaneously minimizing the empirical classification error and maximizing the geometric margin. Given a problem of binary classification with a set of training data, $(x_1, y_1); (x_2, y_2); \ldots;$ $(x_M, y_M), y_i = 1$ or $-1, i = 1, 2, \ldots, M$, a linear separating plane expressed as the Eq. 11.12 is established to distinguish the input data space:

$$f(x) = w^T x + b = \sum_{j=1}^{m} w_j x_j + b = 0 \tag{11.12}$$

$$y_i f(x_i) = y_i \left(w^T x_i + b \right) \geq 1 \tag{11.13}$$

where w is a weight vector and b is a scalar. Both these two parameters are trained with a training dataset. The training process uses the training dataset to satisfy the constraints which can be described as Eq. 11.13.

Figure 11.2 explains the classification process with SVM methodology. In this figure, the solid squares and the solid circles are support vectors and the two dash lines cross the support vectors representing two parallel planes and are called boundaries. The distance between the boundaries is called the margin. To get the

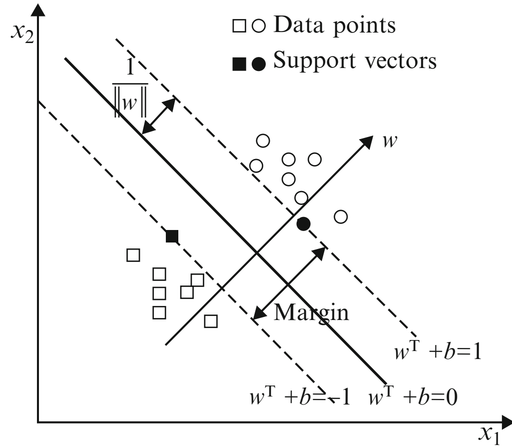

Fig. 11.2 Support vector machines used for classification [68]

optimal separating plane, an optimization process with maximizing margin $\frac{2}{\|w\|}$ (minimizing $\|w\|^2$) is used.

As a supervised learning approach, SVM is typically applied to detect any anomaly by distinguishing the features between healthy and unhealthy. For example, a hybrid two-stage one-against-all support vector machine (SVM) approach was proposed by Gryllias et al. [69] for the automated diagnosis of defective rolling element bearings. In the first stage, an SVM classifier was built to separate the normal condition signals from the faulty signals, and then the type of the fault is recognized and categorized by an SVM classifier at the second stage.

Recently, because SVM was challenged by the lack of probabilistic outputs that make more sense in health-monitoring application, another supervised learning approach (relevance vector machine (RVM)) was proposed within a Bayesian framework. It also uses fewer kernel functions for comparable generalization performance [70]. Given a set of input vectors $[x_n]$ with their corresponding targets $[t_n]$, the learning process is undertaken to infer the parameters of the relationship function between input vectors and the corresponding targets, $F(x)$. Then the likelihood of complete data is built for the next step prediction with the Bayesian framework:

$$t_n = F(x_n; w) + \varepsilon_n \tag{11.14}$$

$$p\left(t/w, \delta^2\right) = \left(2\pi\delta^2\right)^{-N/2} \exp\left\{-\frac{1}{2\delta^2}\|t - \Phi w\|^2\right\} \tag{11.15}$$

$$p(t^*/t) = \int p\left(t/w, {\delta_{\mathrm{MP}}}^2\right) p\left(w/t, \eta_{\mathrm{MP}}, {\delta_{\mathrm{MP}}}^2\right) \mathrm{d}w \tag{11.16}$$

where ε_n is the Gaussian noise with mean 0 and variance δ_2, w is the weight vector, and η is the hyperparameter vector.

(b) Unsupervised learning approach

The unsupervised learning approach deals with unlabeled data and finds clusters by itself. It is used to discover similar groups within the data based on clustering techniques and separates the data into different groups. Therefore, this approach also can be used to detect any anomaly in the new observation and can predict the reliability and remaining useful life. Here, two popular unsupervised learning approaches according to the different functions in PHM (anomaly detection and prediction) are reviewed.

Principal component analysis (PCA) is an unsupervised learning approach used for dimension reduction, data compression, feature extraction, data classification, and mapping. The singular value decomposition (SVD) tool is used in this approach to map higher-dimension data into lower-dimension data while maximizing the variance of the mapped data. Jiang et al. [71] improved a principal component analysis (PCA)-based chemical process monitoring performance and proposed a sensitive principal component analysis to detect and diagnose the faults in chemical processes. Liang et al. [72] combined PCA with a statistical control chart to reduce the multivariate variables for an industrial rolling mill reheating furnace.

The filter approach has been widely accepted as one of the unsupervised learning approaches for estimating and predicting the state of electronic devices or systems by using a state-space model [73–75]. The most widely used filter is the Kalman filter (KF), which has effective solutions on estimating the state of linear system with additive Gaussian noise. As shown in Fig. 11.3, KF is a recursive method to estimate the state of linear system based on prior knowledge of the state of the system and the measured information. However, for most nonlinear cases, KF loses its efficacy. Therefore, it is necessary to establish a nonlinear filter to solve state estimation problems in nonlinear systems. Up to now, there have been some

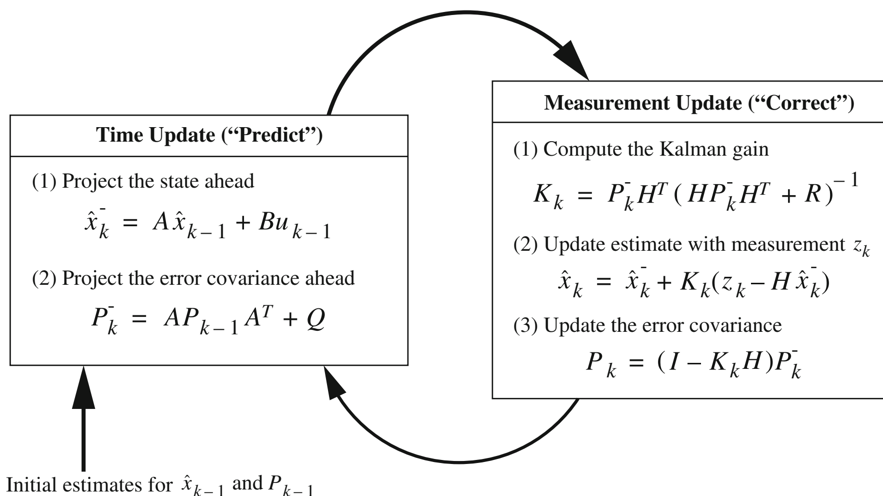

Fig. 11.3 Recursive operation of Kalman filter [77]

approximate nonlinear filters, such as the extended Kalman filter (EKF), unscented Kalman filter (UKF), and the particle filter (PF) [76], that have been used to deal with nonlinear problems.

Among these three nonlinear filters, the EKF linearizes both the state and measurement models by using a first-order Taylor approximation. The PF, known as the sequential Monte Carlo method, approximates the state distribution using a set of discrete, weighted samples, called particles. PF approaches have been widely used for state estimation and remaining useful life prediction for battery systems [78, 79]. The UKF approach was first proposed by Julier et al. and developed by Wan et al. [80–82] to estimate the state of nonlinear systems by using a deterministic sampling approach (sigma point sampling) to capture the mean and covariance estimates with a minimal set of sample points. Several previous literature studies have shown that the UKF is considered to be a useful approach for state-space prognostics and estimations for nonlinear systems. For instance, Santhanagopalan et al. [83] used the UKF method to estimate the state of charge for lithium-ion cells. Lall et al. [84] applied the UKF algorithm to predict the remaining useful life of electronic systems under mechanical shock and vibration conditions. Jafarzadeh et al. [85] developed a UKF-based approach to estimate the nonlinear state of induction motor drives.

In summary, compared to the PoF approaches, the advantages of data-driven approaches are as follows: (1) they do not need know system-specific information and can learn the behavior of the system, like black box models, based on the monitored data; (2) they can be used in complex systems with considering the correlation between parameters and the interactions between subsystems; and (3) they can be used to analyze the intermittent faults by detecting the sudden changes in system parameters. However, data-driven approaches have some limitations, as they require historical or operational data to train model. In some cases, there are insufficient training data to obtain health estimates and to determine trend thresholds from failure prognostics. Therefore, the solution to this problem is to incorporate PoF approaches with data-driven approaches.

In this situation, the fusion approach is proposed by absorbing the advance features of both data-driven and model-based approaches. As shown in Fig. 11.4, the fusion PHM method develops an accurate mathematical model of the system by using both the physical-based failure models and data-driven prognostic models. The aim of the fusion approach is to overcome the limitations of both the model and data-driven approaches for estimating the remaining useful life (RUL). Cheng et al. [86] demonstrated the fusion PHM method to predict the RUL of multilayer ceramic capacitors (MLCCs). The fusion PHM method uses the PoF approach to identify the critical parameters, identify and prioritize the potential failure mechanisms, identify the failure models, and define the failure criteria in terms of the isolated parameters or the function of isolated parameters and applies the data-driven method to extract the features from the monitored parameters, create a healthy baseline, and compare the monitored parameters with the baseline to conduct anomaly detection and trend the isolated parameters. Xu et al. [87] also implemented fusion-based PHM into avionic system to predict RUL, which shows that fusion-based PHM can provide a more accurate and more robust RUL

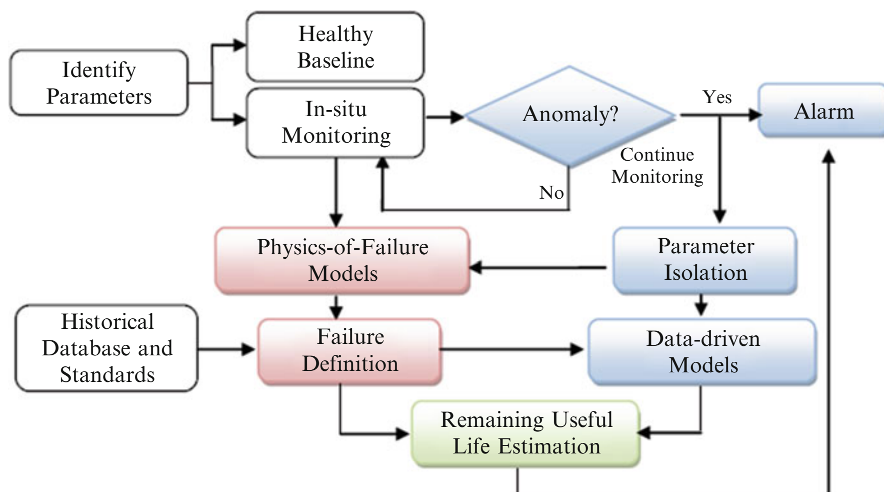

Fig. 11.4 Fusion PHM method [36]

estimation than either algorithm alone. Vasan et al. [88] developed a generic fusion PHM approach that combines stochastic differential models with a recursive nonlinear filtering approach to allow systems to self-assess performance and recursively estimate RUL, which was validated with a case of power systems using insulated-gate bipolar transistors (IGBTs).

11.3 In Situ Monitoring and Anomaly Detection for Phosphor-Converted White LED Packages

To establish new effective reliability assessments and lifetime prediction methods for LEDs, researchers have already proposed several mathematical approaches. For instance, Liao and Elsayed [89] developed a statistical inference procedure to predict the reliability of LEDs using accelerated lumen degradation data. Their results show that the proposed method could be applied to predict the reliability of LEDs in real applications by considering the stress variations. Moreover, Tsaing and Peng [90] also proposed a stochastic diffusion process to model the LED light output degradation path and predicted its lifetime distribution. With these proposed approximate methods, the LED's lumen lifetime (i.e., mean time to failure, MTTF, and median life, B50) could be estimated by using the light output degradation data. Fan et al. [91] also used a degradation data-driven method to estimate the lumen lifetime of high-power white LEDs while considering the variance of test samples. In 2011, the Illuminating Engineering Society of North America (IESNA) released the standard IES-21-11 to predict the lumen lifetime for LED light sources based on the lumen maintenance data collected from the IES LM-80-08 test report [92]. However, in these studies, the degradation data of LEDs during the aging test were

usually collected offline through the photometric measurement systems (e.g., integrating sphere or goniophotometer) [93], which not only might introduce many measurement errors from manual operations but also increase the total testing cost.

Therefore, an in situ monitoring system with sensing techniques is proposed to detect the health of LEDs under an aging test. Then, a data-driven method with a Mahalanobis distance (MD) approach is employed as a real-time health indicator to reflect the LED's degradation. By monitoring the MD values, early anomalies of LEDs can be detected before failures happen.

11.3.1 Test Vehicle, Experimental Setup, and Data Collection

The test vehicle selected in this study is a high-brightness, phosphor-converted white LED with an InGaN chip from Avago (type: 3W mini power white LED light source with the part number ASMT-JN31-NTV01 [94]). Figure 11.5a shows the packaging structure of the test vehicle, which indicates that the mechanism for generating white light is a combination of blue light emitted by an InGaN chip (Fig. 11.5b) and excited yellow light emission from a phosphor layer. The typical optical characteristics of the test vehicle at the recommended test conditions (I_c: 350 mA, V_F: 3.2 V, and T_j: 25 °C) are listed as follows: (i) luminous flux is around 85 lm; (ii) correlated color temperature (CCT) is 3500–4500 K with neutral white color; and (iii) luminous efficiency is 76 lm/W.

In this study, an accelerated aging test with an in situ monitoring technique was designed for the selected test vehicle. The 3W mini power white LEDs were soldered on a metal core printed circuit board (MCPCB) test board, which were electrically driven by the same DC current ($I_c = 200$ mA) provided by a DC power supply (Agilent E3611A). As shown in Fig. 11.5b, the thermal chamber provided a constant aging temperature for this test ($T_a = 90$ °C). After finishing a period of aging, the test vehicles were removed from the thermal chamber to be cooled to the ambient temperature for testing. The direct performance data of the LEDs (such as optical characteristics such as luminous flux, chromaticity coordinates, CCT, CRI, SPD) were manually measured by a Gigahertz-Optik BTS256-LED tester. When the test for the LEDs was finished, the test board was returned to the thermal chamber to undergo the next round of aging. With the online sensing technique, the indirect performance data of LEDs (such as lead temperatures, input-driven current, and forward voltage) were in situ monitored and collected every hour by a data acquisition mainframe (Agilent-34970A).

11.3.2 Theory and Methodology

To overcome the limitations of current lifetime prediction methods for LEDs, a fusion-based prognostics and health management (PHM) methodology framework

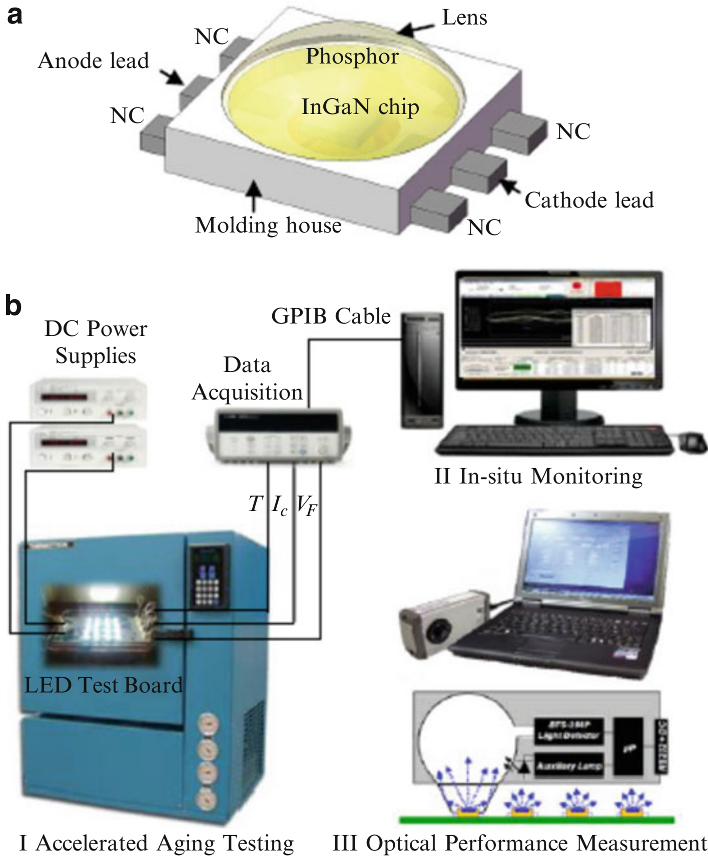

Fig. 11.5 Test vehicle: (**a**) schematic packaging structure; (**b**) experimental setup and data collection [95]

is proposed in this work. This methodology incorporates both failure modes, mechanisms, and effects analysis (FMMEA) and a data-driven method.

As shown in Fig. 11.6, the FMMEA is conducted firstly to identify the selected test vehicle's potential failure mechanisms, sites, and effects. With these results, the parameters are identified and categorized as either direct or indirect performance parameters. The direct performance parameters are always the optical characteristics of LEDs, whereas the indirect performance parameters are selected as in situ monitored data to indicate the performance degradation of LEDs. Then, the anomalies of LEDs during the aging process are detected by dealing with the in situ monitored data using the data-driven methods. Finally, the degradation of a selected direct performance parameter, lumen flux, is used to verify the proposed method.

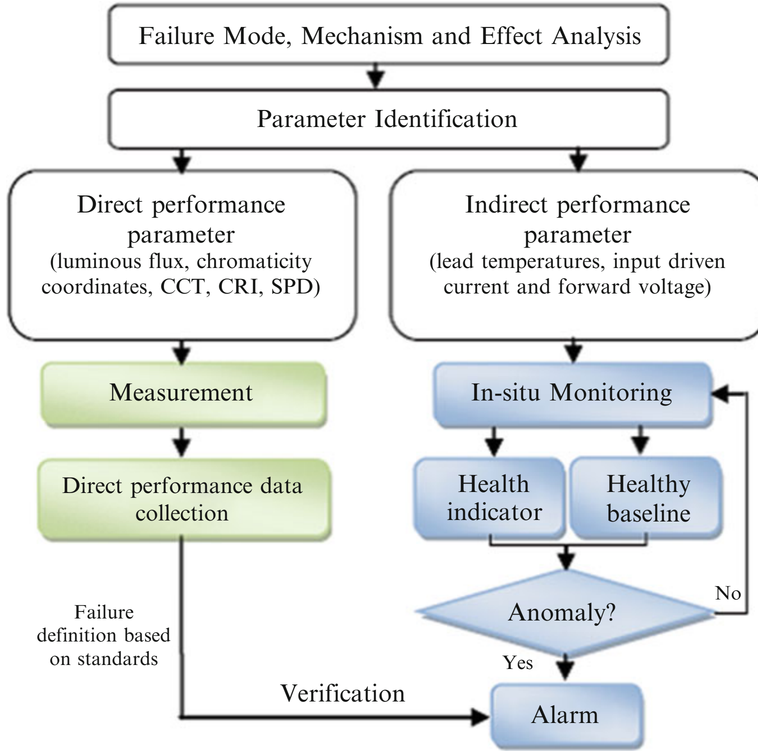

Fig. 11.6 Proposed fusion-based PHM methodology

(A) *Failure Modes, Mechanisms, and Effects Analysis*

FMMEA is a widely used approach to identify the potential failure modes, sites, mechanisms, and effects for electronic devices and systems under expected uses [96]. The FMMEA for package-level LEDs has been done by many researchers. As summarized, the failure modes of LED packages can be divided into three types: (i) catastrophic failure, (ii) lumen degradation, and (iii) chromaticity shift [13]. The failure sites in the package level are the InGaN chip, packaging materials (such as lens, silicon encapsulation, phosphors, chip attachments, thermal pads, and molding house), and interconnections (such as wire bonds and anode and cathode leads). The main mechanisms and impact factors that contribute to the above three failure modes are summarized in Table 11.4, which shows that the temperatures, input-driven current, and forward voltage are three major factors that determine the failure modes and mechanisms of package-level LEDs.

(B) *Parameter Identification*

In this step, the parameters, including environmental loads and performance parameters, should be identified and selected to reflect the state of health of LEDs

Table 11.4 FMMEA for HBWLEDs package [11]

Failure sites	Failure modes	Failure mechanisms	Impact factors
InGaN chip	Catastrophic failure	Chip crack	$\triangle T$, I_c, V_F
	Lumen degradation and chromaticity shift	Chip defects propagation (dislocation, dark lines, and spots)	T_a, I_c, V_F
	Lumen degradation	Chip dopant diffusion	T_a, I_c, V_F
Packaging materials	Lumen degradation	Lens crack	$\triangle T$, CM
	Lumen degradation and chromaticity shift	Silicon encapsulation darkening	T_a, I_c
	Lumen degradation and chromaticity shift	Phosphor degradation	T_a, I_c
	Lumen degradation	Delamination	$\triangle T$, CM, CTEs
Interconnections	Catastrophic failure	Wire crack	$\triangle T$, I_c
	Catastrophic failure	Wire ball bond fatigue	$\triangle T$, CTEs
	Catastrophic failure	Lead crack	$\triangle T$, CTEs

where CM and CTE represent the moisture concentration and coefficient of thermal expansion, respectively

during the long-term aging process. As recommended by the IES LM-79-08 measurement standard, the direct performance parameters, such as luminous flux, chromaticity coordinates, CCT, CRI, and SPD, are measured to characterize the optical performance of LEDs. However, these direct performance parameter data are required to be collected offline through the photometric measurement systems (e.g., integrating sphere or goniophotometer), and it is difficult to realize in situ monitoring using these systems. Thus, according to the FMMEA results, some indirect performance parameters, including lead temperature, input-driven current, and forward voltage, can be used to indicate the performance degradation of LEDs during aging. Meanwhile, these indirect performance parameters can be monitored and acquired with some proper online built-in sensing techniques (i.e., thermal and electric sensors).

(C) *Anomaly Detection*

After collecting the monitored data by sensors, the anomaly detection step uses data-driven methods to detect whether the test vehicles are healthy or not. This includes the establishment of health indicators and a health baseline. A health indicator is an index extracted from the in situ monitored data to represent the state of health for LEDs. It can also be defined as the quantitative deviation between healthy and unhealthy states. Because the collected data from sensors are always complicated and multidimensional, the purpose of health indicators is to extract the features from data and reduce data dimensions. The widely used approaches to

establish a health indicator with collected data include (i) distance measurement approach (i.e., Euclidean distance and Mahalanobis distance), (ii) statistical and probabilistic methods (i.e., mean, standard deviation, correlations, covariance, residuals, etc.), and (iii) Eigen values (i.e., peak, skewness, kurtosis, etc.) [36].

With the capability of condensing the multivariate system to a univariate one and detecting changes by taking into account the correlation of several parameters, the MD method has been widely used as a health indicator to monitor gradual performance degradation of electronic products and to detect anomalies before failure occurs [59, 97]. Therefore, in this work, we developed a method to construct a health indicator to represent the performance degradation of LEDs based on the MD method. The detailed procedure is presented as follows.

Firstly, the $p \times m$ in situ monitored indirect performance parameter data were collected for each test vehicle and denoted as X_i, where $i = 1, 2, \ldots, p$. The experiment setup and collected data are from Sect. 11.3.1. Thus, the number of parameters p equals 3 (i.e., lead temperature, input-driven current, and forward voltage). X_{ij} denotes the ith parameter vector on the jth observation, where $j = 1, 2, \ldots, m$. As the first 200 observations were selected as healthy data which corresponded to approximately the first 199 h of the accelerated aging test, $m = 200$ (Fig. 11.7).

Then, after the data in the performance parameter dataset on the jth observation are normalized by Eq. 11.7, the MD_j value can be calculated using Eq. 11.10.

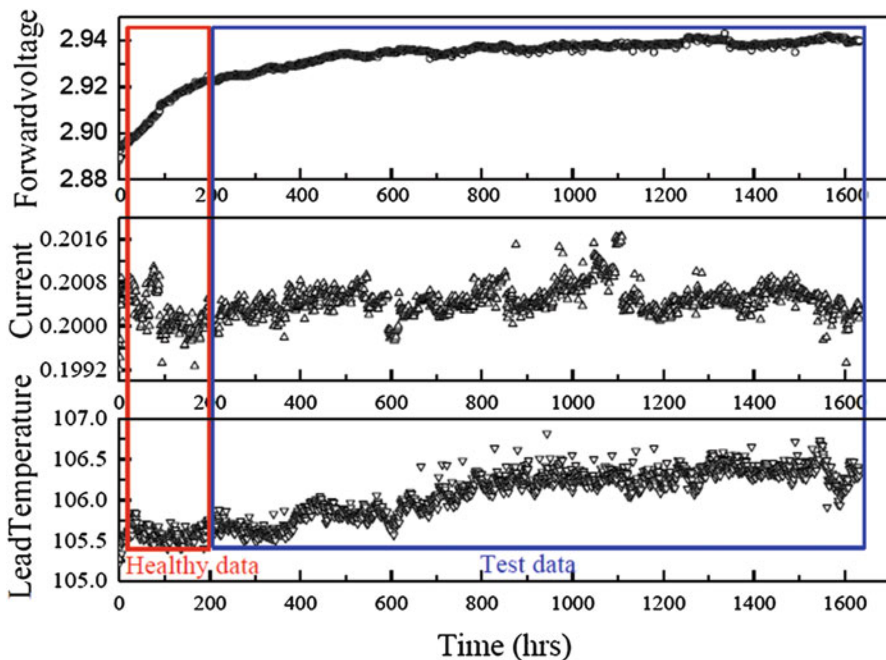

Fig. 11.7 In situ monitored indirect performance parameters of test LED 1#

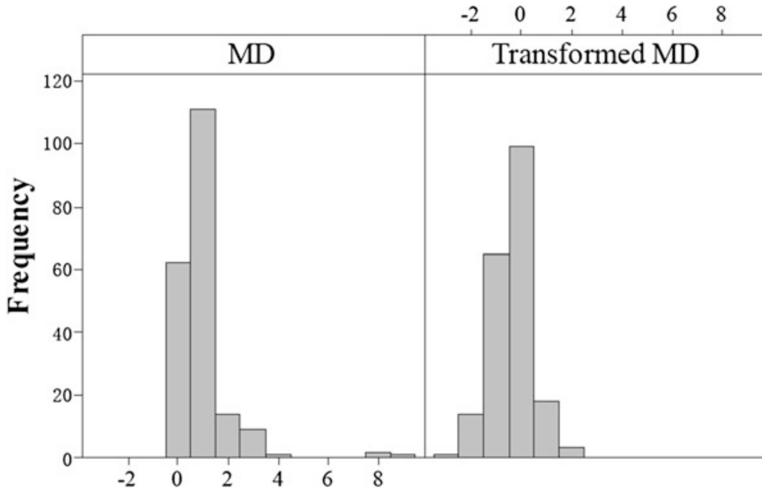

Fig. 11.8 Histograms of healthy MD for test LED 1# before and after the Box-Cox transformation

Next, as shown in the left-hand side of Fig. 11.8, the healthy MD values obtained did not follow a normal distribution. Therefore, a Box-Cox power transformation was used to transform the healthy MD values into a normal distribution. By using the Box-Cox transformation with Eq. 11.17, the transformed healthy MD values distribute normally, as shown in Fig. 11.8.

$$y(\lambda) = \begin{cases} \left(y^{\lambda} - 1\right)/\lambda & \lambda \neq 0 \\ \log\ y & \lambda = 0 \end{cases} \tag{11.17}$$

Finally, the control chart technique, frequently used in quality engineering, was implemented to find an anomaly detection threshold for LEDs. The mean μ and standard deviation σ of the transformed healthy MD values were used to obtain 3σ bounds about the mean. The upper bound ($\mu + 3\sigma$) was used as a threshold for anomaly detection, as increasing MD values indicate degradation in the LEDs. Thus, the transformed MD values at each observation can be selected as the health indicator of LEDs. When the transformed test MD values crossed the threshold, an anomaly occurred and was detected.

11.3.3 Implementation Results and Discussion

In this section, the in situ monitored indirect performance parameters from five tested LEDs as shown in Sect. 11.3.1 were calculated to the transformed MD values as their health indicators. The anomaly detection time of each test LED was obtained when its transformed MD value exceeded the defined threshold.

Meanwhile, one of the direct performance parameters, lumen flux, was measured to indicate the LED's actual failure time and was used to verify the proposed method. For the lumen degradation failure mode in general lighting applications, the Alliance for Solid-State Illumination Systems and Technologies (ASSIST) recommends using L70 to represent the LED's lifetime, which means the time at which the luminous flux declines by 30% from the initial value (or time to 70% lumen maintenance) [98].

As shown in Fig. 11.9, the anomaly times of five test LEDs were detected online at 666, 626, 638, 705, and 705 h, respectively. The lumen maintenance degradation curves indicate that the actual lumen degradation failure times of all test LEDs were detected as 1518, 1518, 1518, 1518, and 1472 h when the curves crossed the 70% lumen maintenance threshold. The detailed results are listed in Table 11.5, which shows that the early anomaly warning can be achieved at around 45% of lifetime before actual failure happens. Thus, this anomaly detection time can be considered as a starting time to predict the remaining useful life (RUL) for LEDs.

11.4 Prognostic of Lumen Maintenance Lifetime for Phosphor-Converted White LED Packages

Owing to the long lifetime and high reliability, few or any failures should occur in LED light sources during a short-term life test, even in an accelerated life test [6, 11]. Thus, it is time-consuming and expensive for LED developers to estimate the life for LEDs using traditional destructive life testing, which records failure data. Therefore, the capability to explore an expert system by conducting short-term and cost-effective qualification tests to predict long-term remaining useful life (RUL) is a critical economic and business requirement to new LED adoption, and it is the motivation of this research topic.

Apart from the traditional destructive life test, predicting RUL with a degradation test appears to be an attractive alternative for qualifying highly reliable products, bringing benefits by shortening the testing time, identifying the degradation path, and providing effective maintenance methods before failures occur [48, 52, 100]. When applied to LEDs, many previous RUL prediction methods based on degradation data rely on the least-squares regression (LSR) approach. For instance, the IESNA released the TM-21 standard in 2011 to predict the lumen maintenance life for LED light sources based on the collected lumen maintenance data from the IES LM-80-08 test report. In the TM-21 standard, the LSR method is used to estimate the parameters involved in the lumen degradation model, and the degradation curve is then projected to the failure threshold to get the lumen maintenance life. Currently, many LED manufacturers have accepted the TM-21 standard to predict the lifetime for their LED products (such as Philips Lumileds [101] and Cree [102]. Additionally, our previous work [91] proposed a degradation data-driven method to estimate the lumen lifetime of high-power white LEDs

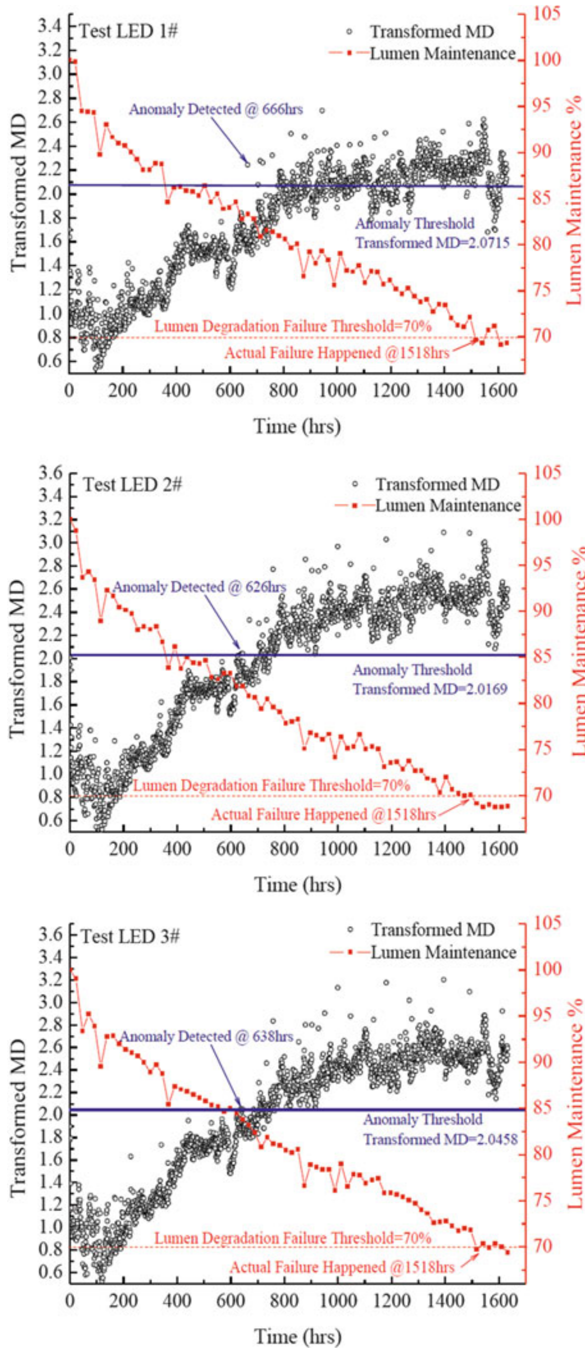

Fig. 11.9 Anomaly detection results of five test samples [99]

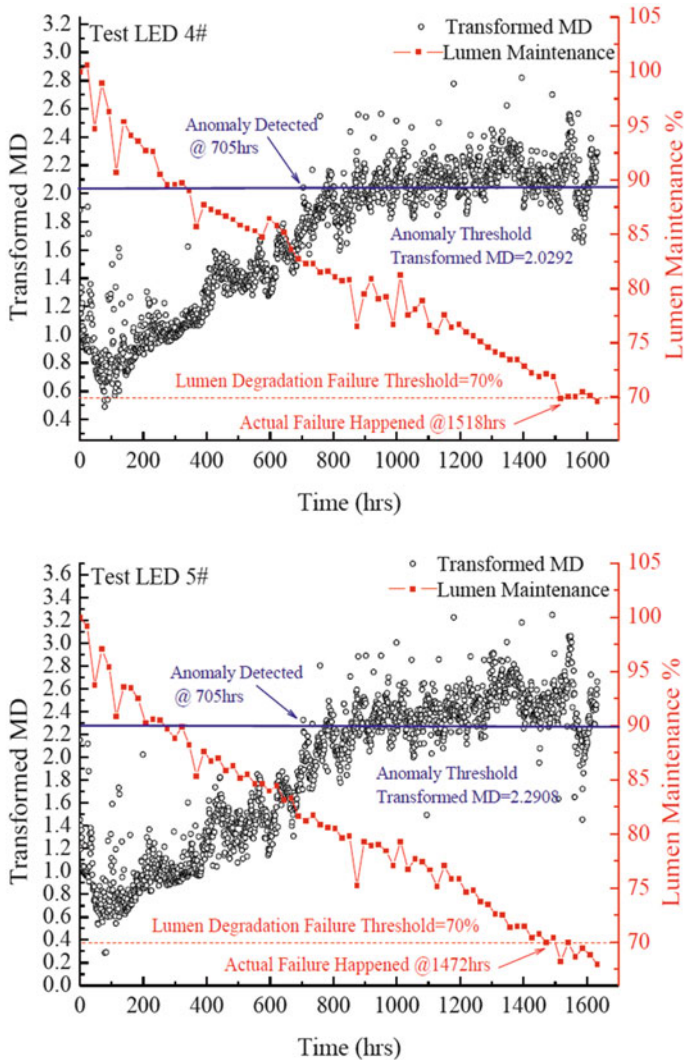

Fig. 11.9 (continued)

wherein the parameters of the lumen degradation model were estimated by using an ordinary LSR fitting method. Zhang et al. applied statistical distribution functions (such as a lognormal function [103] and the Weibull function [104]) to describe the relationship between OLED's lumen degradation and time, and the parameters of both statistical functions were calculated with the least-squares method. Wang and Lu [105] presented a bi-exponential model to fit the lumen degradation data for LEDs, and the model parameters were also estimated by the nonlinear LSR. However, previous studies [91, 106, 107] have shown that using the LSR method to estimate parameters for the lumen degradation curve has many weaknesses in

Table 11.5 Summary of anomaly detection results

Test LED	Healthy MD μ	Healthy MD σ	Anomaly threshold	Detection time (h)	Failure time (h)
1#	−0.3441	0.8052	2.0715	666	1518
2#	−0.3534	0.7901	2.0169	626	1518
3#	−0.3371	0.7943	2.0458	638	1518
4#	1.182	0.2824	2.0292	705	1518
5#	−0.5502	0.947	2.2908	705	1472

terms of guaranteeing prediction accuracy, because it does not consider the measurement dynamics and uncertainties. This can result in a large gap between the product lifetime estimated by LED manufacturers and the actual application life.

To improve the accuracy of lifetime prediction, this work proposes a dynamic recursive particle filter-based (PF-based) approach to model the lumen degradation data of LED light sources by taking measurement dynamics and uncertainties into consideration. As a nonlinear filtering approach, the PF prognostic approach has been widely used in state estimation and prediction for nonlinear/non-Gaussian systems [78, 108]. Normally, PF uses a set of weighted particles simulated by the sequential Monte Carlo (SMC) method [109] to approximate the state as a posterior probability density distribution and then dynamically update it and predict the future state with measurement data within a Bayesian framework [110–112].

This section focuses on modeling the dynamic nonlinear lumen degradation process of phosphor-converted white LED packages in an accelerated degradation test with considering the measurement uncertainties. Firstly, we selected the exponential degradation model recommended in the TM-21 standard to describe the lumen degradation process of LED light sources. The PF method, which replaces the LSR method used in the TM-21 standard, was then used to track the lumen degradation process by estimating and adjusting the model parameters from updated measurements. Finally, when the measurements terminated, the RULs with prediction confidence intervals were predicted by extrapolating the updated model with measurement noise to the failure threshold.

11.4.1 Methodologies and Algorithms

In this section, the methodologies and algorithms of both the TM-21 standard method and the proposed PF prognostic approach are introduced to predict the lumen maintenance life of LED light sources.

(A) *IES-TM-21 Projecting Method*

Lumen degradation, which refers to the decrease in light output during the aging process, is recognized as a critical failure mode in LED light sources [113]. In the lumen degradation process, the lumen maintenance (LM) of LED light sources is

defined as the maintained percentage of the initial light output. According to different applications, the Alliance for Solid-State Illumination Systems and Technologies (ASSIST) uses lumen maintenance to define the lumen maintenance lifetimes of LED light sources. For example, L50 for decorative lighting means the time at 50% lumen maintenance, and L70 for general lighting means the time at 70% lumen maintenance.

The TM-21 method is a lumen maintenance life prediction standard published by the IESNA in 2011. It is used to determine the operating lifetime of LED light sources based on the lumen maintenance data collected from the IES LM-80-08 test report. The main procedure of the TM-21 method is implemented as follows:

1. Normalize the collected luminous flux data as lumen maintenance data. Luminous flux data is used to represent the optical performance of LED light sources. Luminous flux data is normalized as lumen maintenance data to determine when the failure occurs. Lumen maintenance can be defined as the maintained percentage of the initial luminous flux over time:

$$\mathrm{LM}(t) = \frac{\Phi(t)}{\Phi(0)} \times 100\% \tag{11.18}$$

where $\Phi(0)$ is the initial luminous flux and $\Phi(t)$ is the luminous flux at time t.

2. Curve-fit the lumen maintenance data with the LSR method. The exponential expression, as shown in Eq. 11.19, is well proven and is a widely used model to describe the lumen degradation path of LED light sources. Therefore, exponential curve fitting is applied to the collected lumen maintenance degradation data, and the model parameters are estimated by the LSR (Eq. 11.20):

$$\mathrm{LM}(t) = B \cdot \exp(-\alpha \cdot t) \tag{11.19}$$

$$\min_{B,\alpha}\left\{\frac{1}{m}\sum_{i}^{m}[y_i - \mathrm{LM}(t_i;B,\alpha)][y_i - \mathrm{LM}(t_i;B,\alpha)]^T\right\} \tag{11.20}$$

where B is the initial constant and α is the degradation rate constant, both of which are derived by the least-squares curve fitting; and m is the number of collected lumen maintenance degradation data points for each test sample.

3. Project the lumen maintenance life, L_p. As introduced before, the LED lumen maintenance life is defined as the time when the lumen maintenance data decreases below the failure threshold ($\mathrm{LM}_\mathrm{threshold} = 70\%$ is defined for LED light sources used as general lighting). Thus, L_p can be predicted by projecting the degradation model with the estimated model parameters to the defined failure threshold:

$$L_\mathrm{p} = \ln\left(\frac{100 \times B}{p}\right)/\alpha \tag{11.21}$$

where p is the maintained percentage of the initial luminous flux ($p = 70$ is used in this chapter).

(B) *PF Prognostic Approach*

PF is widely known as a state estimation and prognostic approach for nonlinear/non-Gaussian systems. It integrates sequential Monte Carlo computation with Bayesian estimation [76, 110]. Usually, most dynamic processes of systems can be described by a state-space model, with both state and measurement (or observation) models (Eqs. 11.22 and 11.23). Differing from other nonlinear filtering approaches [107], PF simulates a set of particles with the sequential Monte Carlo technique to approximate the system state at the kth cycle as a probability density function (PDF), $x_k \sim p(x_k | z_{1:k})$:

$$\text{State model}: x_k = f(x_{k-1}, v_{k-1}) \tag{11.22}$$

$$\text{Measurement model}: z_k = h(x_k, \omega_k) \tag{11.23}$$

where $f(\cdot)$ and $h(\cdot)$ are the nonlinear state and measurement functions, respectively; x_k and z_k are the state and measurement, respectively; and v_k and ω_k denote the white noise of the state and measurement, respectively.

The procedure for predicting the lumen maintenance life with the proposed PF prognostic approach can be separated into six steps (see Fig. 11.10): (1) model definition, (2) parameter initialization, (3) parameter sampling and prediction, (4) dynamic update with the Bayesian algorithm, (5) particle weighting and resampling, and (6) RUL prediction.

1. Model definition

The state model used in this section is derived from the lumen degradation exponential model used in the TM-21 standard (Eq. 11.19). For simplicity, the initial constant B is assumed to be 1. The state noise v_k can be integrated into the uncertainty of the degradation model parameters [114]. The measurement model helps in mapping the actual states with the measured lumen maintenance data and measurement noise.

$$\text{State model}: x_k = \exp[-\alpha_k(t_k - t_{k-1})]x_{k-1} \tag{11.24}$$

$$\text{Measurement model}: z_k = x_k + \omega_k \quad \omega_k \sim N(0, \delta^2) \tag{11.25}$$

2. Parameter initialization

As shown in Eqs. 11.24 and 11.25, the parameter vectors for both the state and measurement models can be expressed as θ, and each parameter will be initialized by assuming a distribution drawn by the Monte Carlo simulation, with N particles:

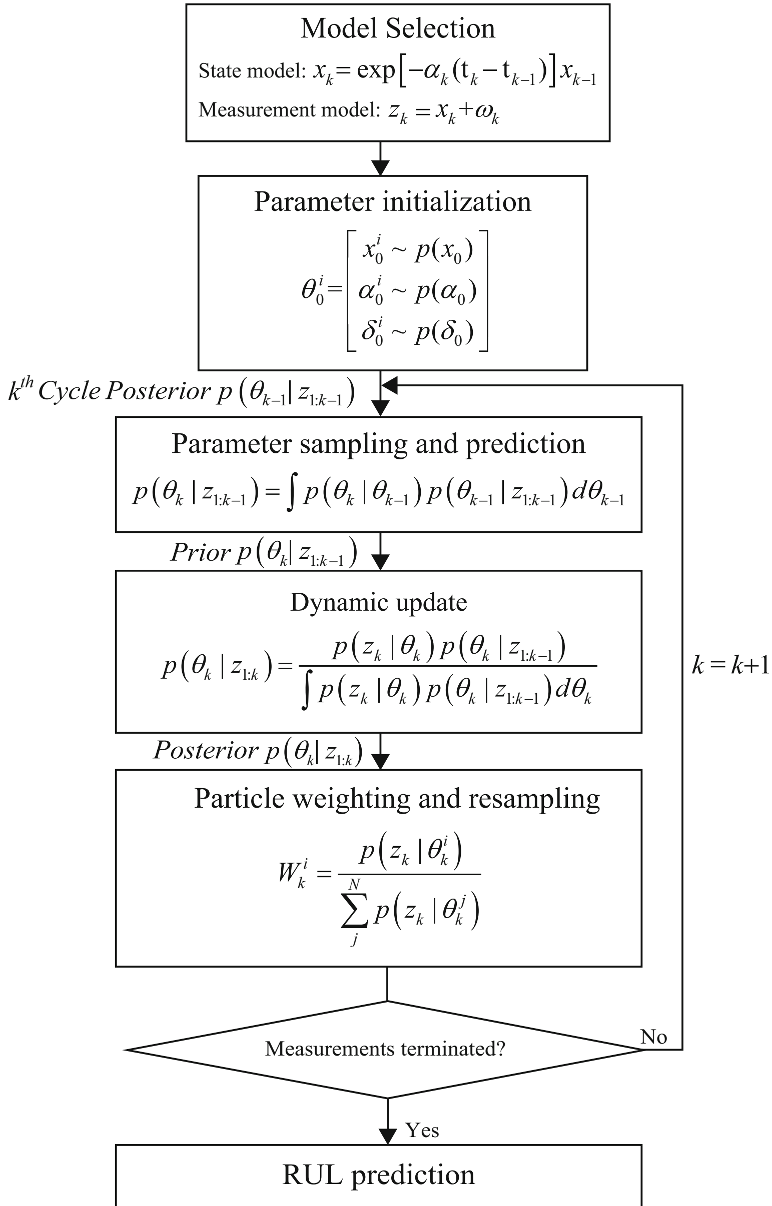

Fig. 11.10 Flowchart of implementation of PF prognostic approach

$$\theta_0^i = \begin{bmatrix} x_0^i \sim p(x_0) \\ \alpha_0^i \sim p(\alpha_0) \\ \delta_0^i \sim p(\delta_0) \end{bmatrix} \quad \text{where} \quad i = 1, 2, \ldots, N \tag{11.26}$$

3. Parameter sampling and prediction

Before receiving knowledge of the measurement z_k, given a posterior probability density function at the k–1th cycle as $p(\theta_{k-1}| z_{1:k-1})$, the prior probability density function of the parameter vector at the kth cycle, $p(\theta_k| z_{1:k-1})$, can be calculated based on the state model with the Chapman-Kolmogorov equation:

$$p(\theta_k|z_{1:k-1}) = \int p(\theta_k|\theta_{k-1})p(\theta_{k-1}|z_{1:k-1})d\theta_{k-1} \tag{11.27}$$

where $p(\theta_{k-1}|\theta_k)$ is the transition probability distribution defined by the state model (Eq. 11.24).

4. Dynamic update with the Bayesian algorithm

As shown in Eq. 11.28, with the new input measurement, z_k, the posterior probability density function at the kth cycle, $p(\theta_k| z_{1:k})$, can be updated by using the Bayesian algorithm and the Markov assumption:

$$p(\theta_k|z_{1:k}) = \frac{p(z_k|\theta_k, z_{1:k-1})p(\theta_k|z_{1:k-1})}{p(z_k|z_{1:k-1})} = \frac{p(z_k|\theta_k)p(\theta_k|z_{1:k-1})}{\int p(z_k|\theta_k)p(\theta_k|z_{1:k-1})\mathrm{d}\theta_k} \tag{11.28}$$

where $p(z_k|\theta_k)$ is the likelihood function of the measurement model. Since the measurement noise, ω_k, follows a Gaussian distribution, the likelihood function of the ith particle at cycle k, $p\left(z_k|\theta_k^i\right)$, can be formulated as follows:

$$p\left(z_k|\theta(x, b, \delta)_k^i\right) = \frac{1}{\sqrt{2\pi}\delta_k^i}\exp\left[-\frac{1}{2}\left(\frac{z_k - x_k^i\left(b_k^i\right)}{\delta_k^i}\right)^2\right] \tag{11.29}$$

5. Particle weighting and resampling

Based on the likelihood function of the measurement z_k at the kth cycle, the ith particle can be weighted as shown in Eq. 11.30 [76]. The particle weight is proportional to the PDF value of the likelihood function.

$$W_k^i = \frac{p\left(z_k|\theta_k^i\right)}{\sum_j^N p\left(z_k|\theta_k^j\right)} \tag{11.30}$$

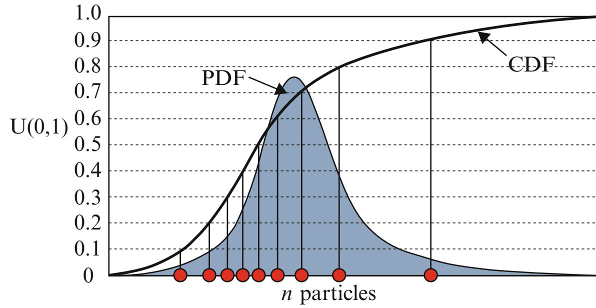

Fig. 11.11 Resampling with inverse CDF method [114]

To avoid the degeneracy problem in the iteration process [110, 115], resampling is always used to eliminate low-weight particles and condense high-weight particles. In this study, the inverse cumulative density function (CDF) method, based on the likelihood function, is used to resample particles [76, 114].

As illustrated in Fig. 11.11. Firstly, the CDF of the likelihood function is established based on Eq. 11.29. Next the uniform distributed random values are assumed as the CDF values, for instance, U(0,1). Then a particle with the CDF value can be found for the parameter distribution. Finally, by repeating n times, the resampled n particles, with the calculated CDF values, are selected as the posterior probability density function at the kth cycle, $p(\theta_k | z_{1:k})$.

Next, if $k \leq p$ (where t_p is the prediction time when the measurement is terminated), let $k = k + 1$, set the posterior $p(\theta_k | z_{1:k})$ at the kth cycle as the prior distribution at the $k + 1$th cycle, and repeat steps (iii) to (v) until the measurement is terminated (see Fig. 11.12).

6. RUL prediction

As shown in Fig. 11.12, when the measurement is terminated at the pth cycle, the parameter vector finishes the updating as θ_p, and the future lumen maintenance can be predicted by extrapolating the state model based on the estimated degradation parameter and measurement noise (α_p and δ_p). The time when the predicted lumen maintenance reaches the failure thresholds defined by ASSIST ($LM_{threshold} = 70\%$) is the time to failure, t_f. The RULs can then be obtained by calculating the distance between the time to failure and the time at the pth cycle.

11.4.2 Implementation Results and Discussion

The lumen maintenance degradation data of selected phosphor-converted white LED packages were collected from the accelerated degradation test as shown in Sect. 11.3.1, and they were used to demonstrate the prediction algorithm and methodology of the proposed PF prognostic method and to validate its feasibility, accuracy, and robustness. Following the methodology implementation steps

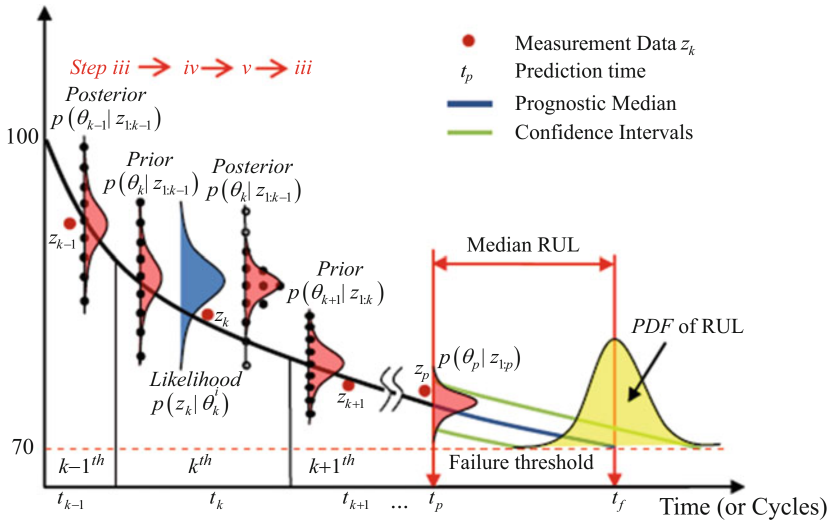

Fig. 11.12 PF prognostic approach [95]

introduced previously, the validation process of the PF prognostic method can be separated into three major steps: (1) method training, (2) method testing, and (3) robustness study.

1. Method Training

Normally, method training is a step to initialize the parameter vector of the selected state-space model with the historical database. However, for new products without historical records, either a calibration test [106] or an assumption [116] is always required for initializing the parameters. In this study, we selected five out of nine DUTs as training samples to collect initialization information for testing. As shown in Fig. 11.13, the lumen maintenance degradation data of these five training samples were exponentially curve-fitted with the lumen degradation model, and the model parameters were estimated by means of the nonlinear least-squares regression approach. According to the curve-fitting results of the training samples listed in Table 11.6, the standard deviation (SD) of the measurement noise was represented by the standard deviation of the curve-fitting residuals, and the estimated parameters from the training samples were averaged to initialize the parameter vector. The initial distributions of the parameters defined in Eq. (11.16) were assumed to be uniform distributions, which were represented as follows:

$$\theta_0^i = \begin{bmatrix} x_0^i \sim U(0.9, 1.1) \\ \alpha_0^i \sim U\left(1.8^* 10^{-4}, 2.2^* 10^{-4}\right) \\ \delta_0^i \sim U(0.01, 0.02) \end{bmatrix}$$

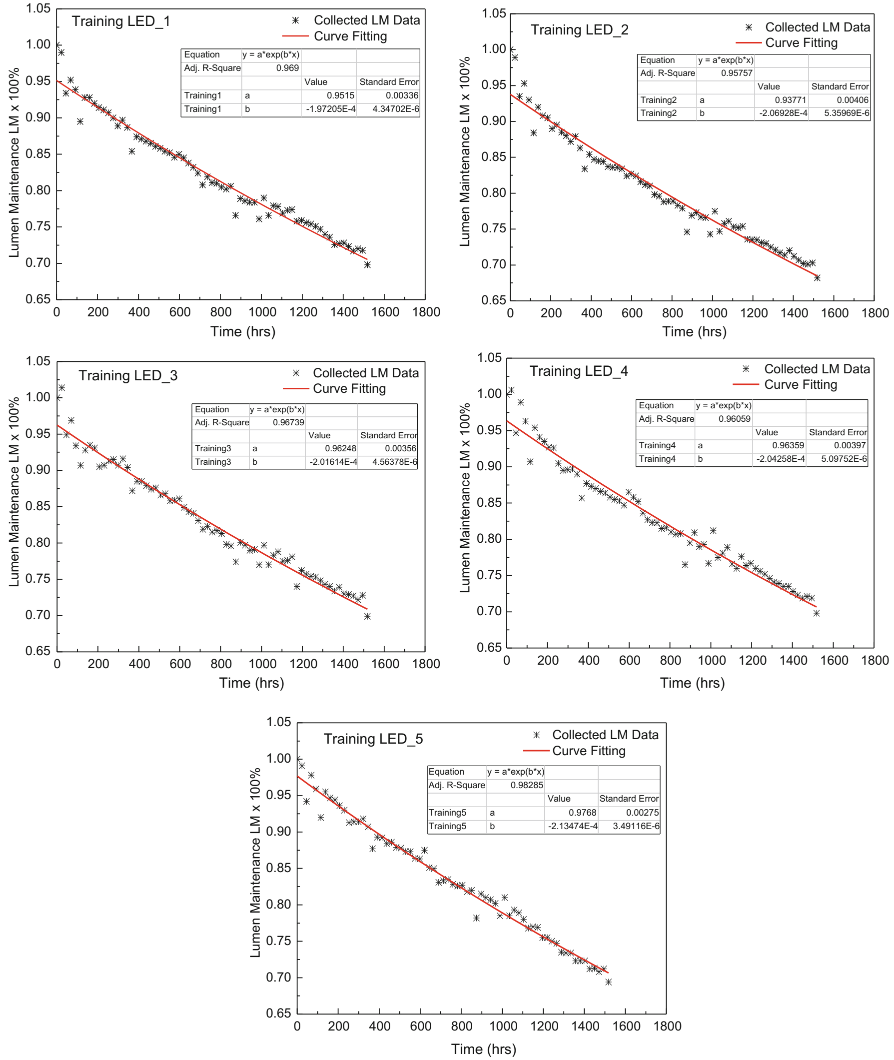

Fig. 11.13 Curve fitting for full lifetime data of training samples [95]

2. Method testing

In method testing, the remaining four DUTs were chosen as test samples to validate the feasibility and accuracy of the proposed PF prognostic approach. The lumen maintenance life prediction results of the four test samples based on both the PF prognostic approach and TM-21 standard method are shown in Fig. 11.14. The prediction time was chosen to be 690 h (30 cycles, approximately 45% of the full lifetime profile of DUTs). The results in Fig. 11.14 show that the median lumen

Table 11.6 Parameter initialization with training samples

Training samples	B	α*10^{-4}	Adjust R^2	SD of curve-fitting residuals
Training LED_1	0.95150	1.97	0.96900	0.012848
Training LED_2	0.93771	2.07	0.95757	0.015493
Training LED_3	0.96248	2.02	0.96739	0.013598
Training LED_4	0.96359	2.04	0.96059	0.015175
Training LED_5	0.97680	2.13	0.98285	0.010460
Averaged values	0.95842	2.05	0.96748	0.013515

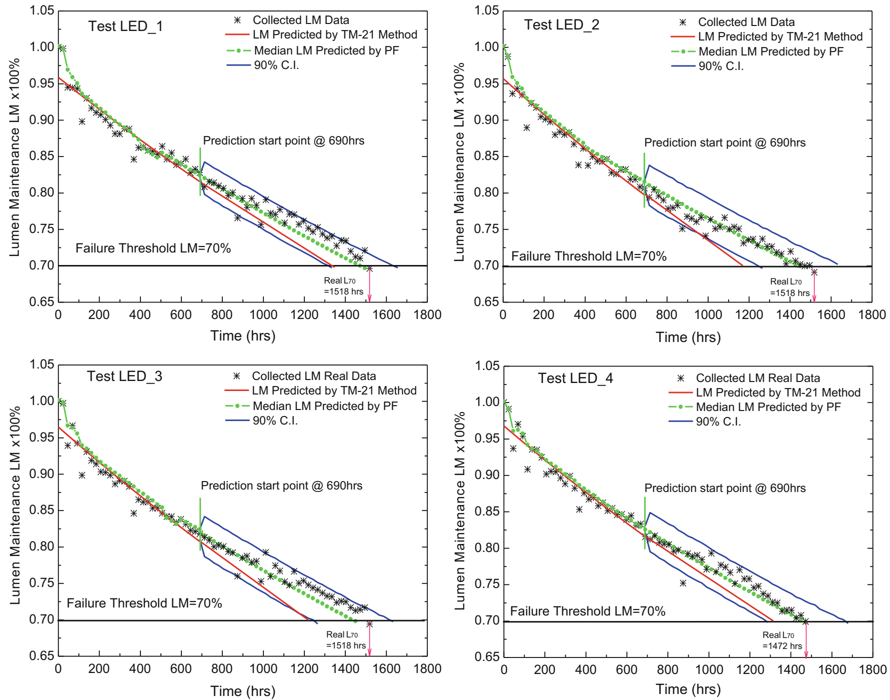

Fig. 11.14 Lumen maintenance life prediction: PF prognostic approach vs. TM-21 method [95]

maintenance lives of the four test samples predicted by the PF approach were close to the actual lifetimes, with a prediction error of less than 5%, while the prediction errors using the TM-21 method were larger than 10%.

As introduced in the PF methodology and algorithm, the initial distributions of the parameters of both the state and measurement models were first simulated by Monte Carlo simulation with N particles. Based on the Bayesian estimation, the periodical measurement data from 0 to 690 h were used to recursively update and adjust the parameter vector via the likelihood function. After 690 h, the lumen maintenance values of the test samples were estimated by extrapolating the updated degradation model with the measurement noise. When the estimated lumen

Table 11.7 Theoretical comparison of LED life prediction methods. (The proposed PF approach vs. TM-21 standard)

TM-21 standard with least-squares regression	Proposed PF prognostic approach with sequential Monte Carlo simulation
1. Batch least squares on finite data span	1. Recursive solution on unlimited data span
2. Periodic execution	2. Real-time processing suitable for online prediction
3. Deterministic model	3. Stochastic model with consideration of measurement dynamics and uncertainties
4. Solution for both linear and nonlinear processes	4. Solution for nonlinear/non-Gaussian problems
5. No requirement of prior information	5. Requires prior estimation (or initial assumptions)

maintenance reached the failure threshold ($LM_{threshold} = 70\%$), the lumen maintenance life could be predicted. Table 11.7 compares the theoretical differences between the proposed PF approach and the TM-21 standard in LED life prediction. The PF approach estimates and updates the parameter vector dynamically by absorbing new measurements with considering the measurement noise. Thus, the PF approach can take measurement dynamics and uncertainties into consideration. As shown in Eq. 11.20, the LSR used in the TM-21 method only depends on the minimization of the sum of the residuals between the actual measurements and the calculated values by using batch processing.

Figure 11.15 shows the RUL prediction results at different prediction times for both the PF approach and the TM-21 method. In addition to 690 h, some other prediction times, such as 960 h (40 cycles, approximately 63% of the full lifetime profile), 1150 h (50 cycles, approximately 76% of the full lifetime profile), and 1380 h (60 cycles, approximately 91% of the full lifetime profile), were also designed in this study. Compared to the TM-21 method, the predicted median RULs from different prediction times predicted by the PF approach were closer to the actual RULs, especially at lower prediction times (such as 690 h with the long-term prediction distance). This indicates that the accuracy of the PF approach is better than the TM-21 method in predicting long-term lumen maintenance life for LEDs.

With increasing prediction times, the accuracy of the RUL prediction by the TM-21 method improved, because the LSR method can track the real lumen maintenance degradation trajectory of LEDs by dealing with sufficient measurement data. However, the TM-21 method requires a longer test time to predict the lifetime than the PF approach. A comparison of the prediction performances of the PF approach and the TM-21 method is given in Table 11.8. Among all test samples, the prediction errors of the PF approach can be controlled within 7% for all prediction times (under 5% when applied to long-term prediction). The widths of the prediction confidence intervals (90% C.I.) become narrower with increasing measurement time, which means the prediction uncertainties are reduced.

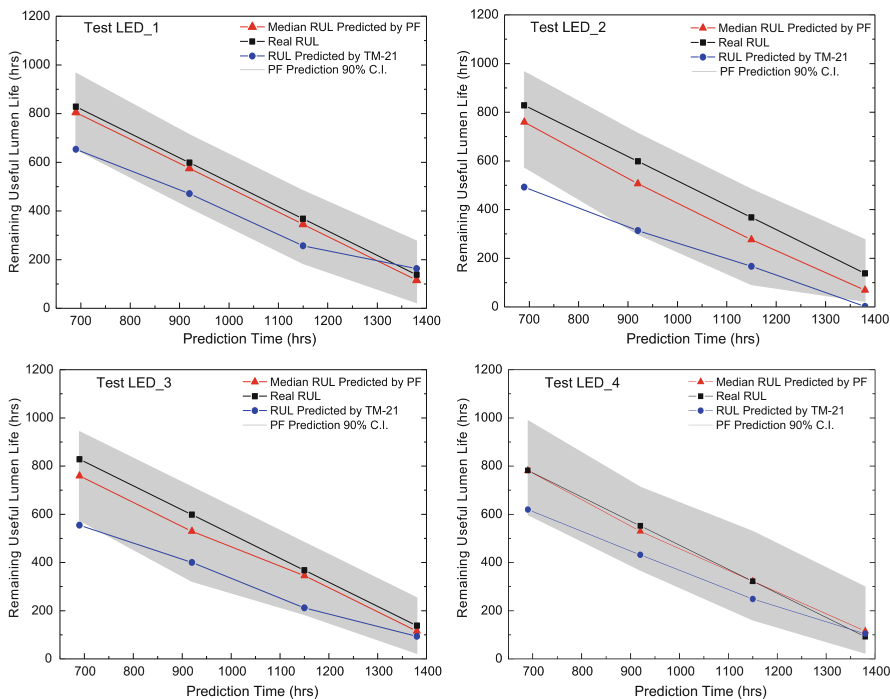

Fig. 11.15 Remaining useful life prediction: PF prognostic approach vs. TM-21 method [95]

3. Robustness study

Referring to previous studies [106, 116], the prognostic performances of filtering techniques are always related to the selection of the initial parameters. Thus, the effect of parameter initialization was studied to validate the robustness of the proposed PF prognostic approach in actual applications. As introduced before, the degradation rate of the lumen maintenance degradation model α and the standard deviation of the measurement noise δ are two critical parameters to determine the lumen degradation trajectory and the state updating process in the implementation of the PF approach. Except for the full lifetime training test (1518 h), the assumptions of the initial distribution for the degradation rate were based on the curve-fitting results from some other calibration tests for training samples, which included a 91% of full lifetime test (1380 h), a 76% of full lifetime test (1150 h), a 63% of full lifetime test (920 h), and a 45% of full lifetime test (690 h). The initial distributions of the two parameters were also assumed to be uniform distributions, as listed in Table 11.9.

Based on the assumed initial parameter vectors listed in Table 11.9, the prediction results for lumen maintenance life obtained by the PF prognostic approach are

Table 11.8 Comparison of prediction results: PF prognostic approach vs. TM-21 method

Test samples	Prediction time (h)	Prediction error of LM life %	
		TM-21	PF (the widths of 90% C.I.)
Test LED_1	690	11.52	1.52(312 h)
	920	8.38	1.52(299 h)
	1150	7.32	1.52(299 h)
	1380	−1.66	1.52(253 h)
Test LED_2	690	22.12	4.55(391 h)
	920	18.73	6.06(414 h)
	1150	13.29	6.06(391 h)
	1380	8.94	4.55(253 h)
Test LED_3	690	18.03	4.55(368 h)
	920	13.06	4.55(391 h)
	1150	10.32	1.52(299 h)
	1380	2.95	1.52(230 h)
Test LED_4	690	11.03	0.00(391 h)
	920	8.19	1.56(345 h)
	1150	5.01	0.00(368 h)
	1380	−0.80	−1.56(276 h)

shown in Fig. 11.16. Among all four test samples, the prediction errors of the PF approach from a shorter-term calibration test are larger than those from tests with a longer calibration time. The widths of the prediction confidence intervals mainly depend on the assumptions for the measurement noise. As shown in the time listed besides the prediction error in Fig. 11.16, with increases in the standard deviation of measurement noise, the widths of the prediction confidence intervals in the lumen maintenance life prediction by the PF approach increased, indicating that the prediction uncertainties were raised.

In a brief summary, the main contributions of the proposed method in this section are: (i) a recursive solution of PF, replacing the batch processing of LSR, is first proposed to deal with lumen degradation data of LED light sources and estimate the parameters of the lumen degradation model dynamically; (ii) with consideration of measurement uncertainties, an SMC method is employed in the PF to predict RUL as a life distribution with a confidence interval; and (iii) a robustness study is conducted to analyze the initialization of parameters impacting the prediction accuracy and the uncertainties of the proposed PF method.

11.5 Conclusions

PHM is a framework of methodologies that integrate part of component lifetime estimation and reliability prediction, and it permits the reliability of a system to be evaluated in its actual life cycle conditions, to determine the event of failure and

Table 11.9 The assumption of parameter initialization for robustness study

No.	Initial distribution assumption for degradation rate, α *10^{-4}	No.	Initial distribution assumption for SD of measurement noise, δ
1	U(1.8, 2.2) assumed from full lifetime training data	1	U(0, 0.01)
2	U(1.9, 2.3) assumed from 1380 h training data	2	U(0.01, 0.02)
3	U(2.0, 2.4) assumed from 1150 h training data	3	U(0.02, 0.03)
4	U(2.1, 2.5) assumed from 920 h training data		
5	U(2.2, 2.6) assumed from 690 h training data		

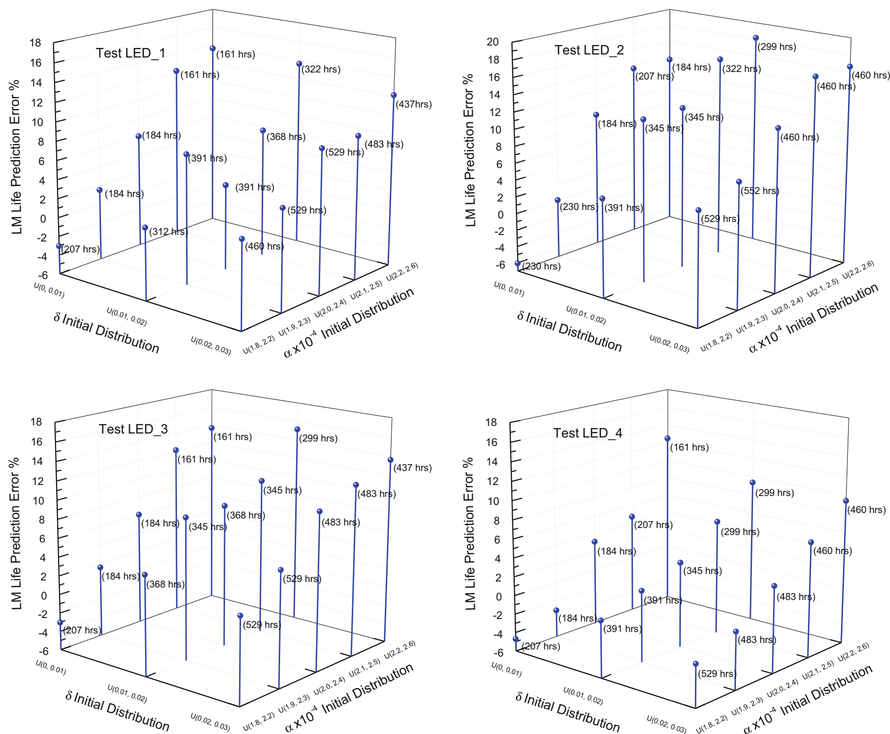

Fig. 11.16 Robustness study of PF prognostic approach (LM life prediction error with the width of 90% C.I. in *brackets*) [95]

mitigate the system risk. A successful PHM relies on the selection of an appropriate prognostic approach and algorithm. Currently, there are many prognostic techniques and their usage must be tuned for each application. This chapter develops the online anomaly detection and lumen maintenance life prediction methods for phosphor-converted white LED packages based on the PHM methodology.

Firstly, this section presents an in situ monitoring method with sensing techniques to detect the health of LEDs under an accelerated aging test. The transformed MD values were used as a real-time health indicator to reflect the LED's degradation. The results show that, according to the verifications with actual

lumen degradation failure times, the proposed MD-based anomaly detection approach can provide an early anomaly warning at around 45% of lifetime before actual failure happens for all test LEDs evaluated. Thus, this anomaly time can be a starting point for online remaining useful lifetime prediction for LEDs.

Moreover, in order to improve the accuracy of long-term lumen maintenance life prediction for LEDs and shorten the qualification test time, we developed a PF-based prognostic approach to replace the LSR method applied in TM-21 standard. Our PF-based prognostic approach dynamically estimates and adjusts the lumen degradation model parameters by absorbing new measurements with consideration of the measurement noise. Theoretically, there are at least two advantages of the PF approach in RUL prediction. Firstly, the PF approach delivers a recursive and stochastic parameter estimation by dynamically updating measurements, while the LSR used in the TM-21 standard conducts batch-processing estimation by minimizing the sum of the residuals between the actual measurements and the calculated values. Secondly, the SMC simulation in PF can predict a RUL distribution with a confidence interval by taking measurement uncertainties into consideration, whereas the TM-21 standard can only extrapolate the estimated curve to a deterministic lifetime. The results show that the PF approach possesses higher prediction accuracy (with an error of less than 5%) than the TM-21 method when applied for long-term lumen maintenance life prediction for LED light sources. In addition, the prediction uncertainties of the PF approach can be lowered by increasing the measurement time. The robustness study on the proposed PF method indicates that the prediction accuracy and uncertainties are related to the initialization of the parameters. This may be a limitation of proposed PF approach when it is applied to qualify new products. To guarantee the advantages of the PF method, a reasonable initialization process for the parameters based on historical databases (for used products) or calibration testing (for new products) is needed.

Finally, the future research directions of this topic are supposed as follows: firstly, a method for online RUL prediction by integrating the proposed recursive PF approach with in situ monitoring can be developed to qualify LEDs, with the goal of reducing the measurement errors from the offline data collection process and increasing prediction accuracy. Secondly, a system-level prognostics and health management expert system based on the sequential data-processing function of PF approach can also be designed for LED lighting systems (e.g., street lighting, indoor lighting) to achieve the system level real-time anomaly detection, RUL prediction, and reliability assessment.

References

1. T. Baumgartner, F. Wunderlich, A. Jaunich, T. Sato, G. Bundy, N. Grießmann, J. Kowalski, S. Burghardt, J. Hanebrink, Lighting the way: Perspectives on the global lighting market, Second edition. European Journal of Social Sciences **10**(1), 161–181 (2012)
2. W.D. van Driel, X.J. Fan, *Solid State Lighting Reliability: Components to Systems* (Springer, New York, 2012)

3. E.F. Schubert, J.K. Kim, Solid-state light sources getting smart. Science **308**, 1274–1278 (2005)
4. Bardsley Consulting, Navigant Consulting, Inc., Radcliffe Advisors, Inc., SB Consulting, Solid State Lighting Services, Inc., *Solid-State Lighting Research and Development Multi-year Program Plan* (U.S. Department of Energy, Washington DC, 2014)
5. R. Haitz, J.Y. Tsao, Solid-state lighting: 'The case' 10 years after and future prospects. Phys. Status Solidi A Appl. Mater. Sci. **208**, 17–29 (2011)
6. V. Challa et al., Challenges in the qualification of electronic components and systems. IEEE Trans. Device Mater. Reliab. **13**, 26–35 (2013)
7. R. Lingard, *LED Measurement Serious: LED Luminaire Reliability* (U.S. Department of Energy, Washington DC, 2009)
8. M. Pecht, *"Can We Prevent Failures?", Two-Day Course on Application of PHM, Fall 2010 PHM Consortium* (University of Maryland College Park, Maryland, 2010)
9. LeahRae, *Lights of America Fined US$21M over Misleading Bulb Performance Claims* (LED Inside of TRENDFORCE Corp., 2014)
10. MadeinAsia, *Taiwan Market: LED Street Lamp Failure Rates About 8%*. (2011). http://lighting.madeinasia.com/news/Taiwan-Market-LED-Street-Lamp-Failure-Rates-About-8-6305.html
11. M.H. Chang et al., Light emitting diodes reliability review. Microelectron. Reliab. **52**, 762–782 (2012)
12. M. Meneghini et al., A review on the physical mechanisms that limit the reliability of GaN-based LEDs. IEEE Trans. Electron. Device **57**, 108–118 (2010)
13. J.J. Fan et al., Physics-of-failure-based prognostics and health management for high-power white light-emitting diode lighting. IEEE Trans. Device Mater. Reliab. **11**, 407–416 (2011)
14. N. Narendran et al., Performance characteristics of high-power light-emitting diodes. Third Int. Conf. Solid State Light. **5187**, 267–275 (2004)
15. Y. Deshayes, L. Bechou, F. Verdier, Y. Danto, Long-term reliability prediction of 935nm LEDs using failure laws and low acceleration factor ageing tests. Qual. Reliab. Eng. Int. **21**, 571–594 (2005)
16. J.S. Jeong et al., Reliability improvement of InGaN LED backlight module by accelerated life test (ALT) and screen policy of potential leakage LED. Microelectron. Reliab. **48**, 1216–1220 (2008)
17. I. Polavarapu, G. Okogbaa, *An Interval Estimate of Mean-Time-to-Failure for a Product with Reciprocal Weibull Degradation Failure Rate*, Annual Reliability and Maintainability Symposium, 2005 Proceedings, (2005), pp. 261–265
18. C.Y. Peng, S.T. Tseng, Mis-specification analysis of linear degradation models. IEEE Trans. Reliab. **58**, 444–455 (2009)
19. M. Vazquez et al., Degradation of AlInGaP red LEDs under drive current and temperature accelerated life tests. Microelectron. Reliab. **50**, 1559–1562 (2010)
20. Cree, *Cree Xlamp XR Family LED Reliability, CLD-AP26 Rev*. 2 (Cree Inc., 2011)
21. Samsung LED, *Specification for White LED Model: SPHWHTL3D305E6W0F5 Rev. 2* (Samsung, 2011)
22. Nichia, *Specifications for White LED Model: NS6W183BT*, Nichia STS-DA1-1992A, Cat. No. 120524 (Nichia Corporation, 2012)
23. JESD22-A108C, *Temperature, Bias, and Operating Life* (JEDEC Solid State Technology Association, 2005)
24. JESD22-A101B, *Steady State Temperature Humidity Bias Life Test* (JEDEC Solid State Technology Association, 1997)
25. JESD22-B104C, *Mechanical Shock* (JEDEC Solid State Technology Association, 2009)
26. JESD22-A107B, *Salt Atmosphere* (JEDEC Solid State Technology Association, 2004)
27. EIAJ ED-4701/100, *Environmental and Endurance Test Methods for Semiconductor Devices* (*Life Test I*), (Standard of Japan Electronics and Information Technology Industries Association, 2001)

28. Cree, *Cree XLamp XR Family LED Reliability, Application Note: CLD-AP06 Rev 7* (Cree Inc., 2010)
29. Luxeon, *Luxeon K2 Reliability Data RD06* (Lumileds, 2007)
30. OSRAM, *Reliability and Lifetime of LEDs, Application Note* (OSRAM, 2008)
31. NICHIA, *Specifications for White LED, NCSW119T-H3* (NICHIA, 2009)
32. IES-LM-80-08, *Approved Method for Lumen Maintenance Testing of LED Light Source* (Illuminating Engineering Society, New York, 2008)
33. N. Narendran et al., What is useful life for white light LEDs? J. Illum. Eng. Soc. **30**, 57.-+, Win (2001)
34. T. Yanagisawa, T. Kojima, Long-term accelerated current operation of white light-emitting diodes. J. Lumin. **114**, 39–42 (2005)
35. M. Burmen et al., Accelerated estimation of spectral degradation of white GaN-based LEDs. Meas. Sci. Technol. **18**, 230–238 (2007)
36. M. Pecht, R. Jaai, A prognostics and health management roadmap for information and electronics-rich systems. Microelectron. Reliab. **50**, 317–323 (2010)
37. W.B. Wang, M. Pecht, Economic analysis of canary-based prognostics and health management. IEEE Trans. Ind. Electron. **58**, 3077–3089 (2011)
38. M. Pecht, *Prognostics and Health Management of Electronics* (Wiley, New Jersey, 2008)
39. J. Gu, M. Pecht, *Prognostics and Health Management Using Physics-of-Failure*, Annual Reliability and Maintainability Symposium, 2008 Proceedings (2008), pp. 484–490
40. L.A. Escobar, W.Q. Meeker, A review of accelerated test models. Stat. Sci. **21**, 552–577 (2006)
41. H. Cui, *Accelerated Temperature Cycle Test and Coffin-Manson Model for Electronic Packaging*, Annual Reliability and Maintainability Symposium, 2005 Proceedings (2005), pp. 556–560
42. H.S. Choi et al., Prediction of reliability on thermoelectric module through accelerated life test and physics-of-failure. Electron. Mater. Lett. **7**, 271–275 (2011)
43. F.P. McCluskey, M. Pecht, *Rapid Reliability Assessment Using CADMP-II*, 1999 International Conference on Modeling and Simulation of Microsystems (1999), pp. 495–497
44. calcePWA, *Software: A Simulation Failure Assessment Solution of Printed Wiring Assemblies* (University of Maryland, College Park, 2004.) http://www.calce.umd.edu/software/
45. M.J. Cushing et al., Comparison of electronics-reliability assessment approaches. IEEE Trans. Reliab. **42**, 542–546 (1993)
46. P. Gottfried, Comparison of electronics-reliability assessment approaches. IEEE Trans. Reliab. **46**, 2–2 (1997)
47. W. Wang, M. Carr, *A Stochastic Filtering Based Data Driven Approach for Residual Life Prediction and Condition Based Maintenance Decision Making Support*, 2010 Prognostics and System Health Management Conference (2010), pp. 216–225
48. X.S. Si et al., Remaining useful life estimation – a review on the statistical data driven approaches. Eur. J. Oper. Res. **213**, 1–14 (2011)
49. E. Zio, F. Di Maio, A data-driven fuzzy approach for predicting the remaining useful life in dynamic failure scenarios of a nuclear system. Reliab. Eng. Syst. Saf. **95**, 49–57 (2010)
50. J.H. Yan et al., A data-driven neural network approach for remaining useful life prediction. Adv. Des. Manuf. III **450**, 544–547 (2011)
51. Z. Q. Cai, et al., *Research of Failure Prediction Bayesian Network Model*, 2009 I.E. 16th International Conference on Industrial Engineering and Engineering Management, Vols 1 and 2, Proceedings (2009) pp. 2021–2025
52. C.J. Lu, W.Q. Meeker, Using degradation measures to estimate a time-to-failure distribution. Technometrics **35**, 161–174 (1993)
53. S.J. Wu, J. Shao, Reliability analysis using the least squares method in nonlinear mixed-effect degradation models. Stat. Sin. **9**, 855–877 (1999)
54. S.J. Wu, C.T. Chang, Optimal design of degradation tests in presence of cost constraint. Reliab. Eng. Syst. Saf. **76**, 109–115 (2002)

55. H.F. Yu, Designing an accelerated degradation experiment with a reciprocal Weibull degradation rate. J. Stat. Plan. Infer. **136**, 282–297 (2006)
56. A. Patcha, J.M. Park, An overview of anomaly detection techniques: existing solutions and latest technological trends. Comput. Netw. **51**, 3448–3470 (2007)
57. R. De Maesschalck et al., The Mahalanobis distance. Chemom. Intell. Lab. Syst. **50**, 1–18 (2000)
58. G. Niu et al., Health monitoring of electronic products based on Mahalanobis distance and Weibull decision metrics. Microelectron. Reliab. **51**, 279–284 (2011)
59. S. Kumar et al., A health indicator method for degradation detection of electronic products. Microelectron. Reliab. **52**, 439–445 (2012)
60. T. Sutharssan, et al., *Prognostics and Reliability Assessment of Light Emitting Diode Packaging*, 2011 12th International Conference on Electronic Packaging Technology and High Density Packaging (Icept-Hdp) (2011), pp. 938–944
61. Z.G. Tian, M.J. Zuo, *Health Condition Prognostics of Gears Using a Recurrent Neural Network Approach*, Annual Reliability and Maintainability Symposium, 2009 Proceedings (2009) pp. 461–466
62. J.Z. Sikorska et al., Prognostic modelling options for remaining useful life estimation by industry. Mech. Syst. Signal Process. **25**, 1803–1836 (2011)
63. L. Peel, *Data Driven Prognostics Using a Kalman Filter Ensemble of Neural Network Models*, 2008 International Conference on Prognostics and Health Management (Phm) (2008) pp. 65–70
64. J.T. Connor et al., Recurrent neural networks and robust time-series prediction. IEEE Trans. Neural Netw. **5**, 240–254 (1994)
65. Y. Peng et al., Current status of machine prognostics in condition-based maintenance: a review. Int. J. Adv. Manuf. Technol. **50**, 297–313 (2010)
66. S. Zhang, R. Ganesan, Multivariable trend analysis using neural networks for intelligent diagnostics of rotating machinery. J. Eng. Gas Turbines Power Trans. ASME **119**, 378–384 (1997)
67. G. Vachtsevanos, P. Wang, Fault prognosis using dynamic wavelet neural networks. IEEE Syst. Read. Technol. Conf., 857–870 (2001)
68. J. Qu, *Support-Vector-Machine-Based Diagnostics and Prognostics for Rotating Systems*, (Thesis) (University of Alberta, 2011)
69. K.C. Gryllias, I.A. Antoniadis, A Support Vector Machine approach based on physical model training for rolling element bearing fault detection in industrial environments. Eng. Appl. Artif. Intell. **25**, 326–344 (2012)
70. M.E. Tipping, Sparse Bayesian learning and the relevance vector machine. J. Mach. Learn. Res. **1**, 211–244., Sum (2001)
71. Q.C. Jiang et al., Fault detection and diagnosis in chemical processes using sensitive principal component analysis. Ind. Eng. Chem. Res. **52**, 1635–1644 (2013)
72. J. Liang, N. Wang, *Faults Diagnosis in Industrial Reheating Furnace Using Principal Component Analysis*, Proceedings of 2003 International Conference on Neural Networks & Signal Processing, Proceedings, Vols 1 and 2 (2003) pp. 1615–1618
73. M. Daigle, et al., *A Comparison of Filter-based Approaches for Model-based Prognostics*, 2012 I.E. Aerospace Conference (2012)
74. S.K. Yang, T.S. Liu, State estimation for predictive maintenance using Kalman filter. Reliab. Eng. Syst. Saf. **66**, 29–39 (1999)
75. S.K. Yang, An experiment of state estimation for predictive maintenance using Kalman filter on a DC motor. Reliab. Eng. Syst. Saf. **75**, 103–111 (2002)
76. E. Zio, G. Peloni, Particle filtering prognostic estimation of the remaining useful life of nonlinear components. Reliab. Eng. Syst. Saf. **96**, 403–409 (2011)
77. G. Welch, G. Bishop, *An Introduction to the Kalman Filter* (UNC-Chapel Hill, 2006)
78. Q. Miao et al., Remaining useful life prediction of lithium-ion battery with unscented particle filter technique. Microelectron. Reliab. **53**, 805–810 (2013)

79. R. Restaino, W. Zamboni, *Comparing Particle Filter and Extended Kalman Filter for Battery State-of-Charge Estimation*, 38th Annual Conference on IEEE Industrial Electronics Society (Iecon 2012) (2012), pp. 4018–4023
80. S.J. Julier, J.K. Uhlmann, Unscented filtering and nonlinear estimation. Proc. IEEE **92**, 401–422 (2004)
81. S.J. Julier, et al., *A New Approach for Filtering Nonlinear Systems*, Proceedings of the 1995 American Control Conference, vols. 1–6, (1995), pp. 1628–1632
82. E.A. Wan, R. van der Merwe, *The Unscented Kalman Filter for Nonlinear Estimation*, IEEE 2000 Adaptive Systems for Signal Processing, Communications, and Control Symposium – Proceedings (2000), pp. 153–158
83. S. Santhanagopalan, R.E. White, State of charge estimation using an unscented filter for high power lithium ion cells. Int. J. Energy Res. **34**, 152–163 (2010)
84. P. Lall et al., Prognostics health management of electronic systems under mechanical shock and vibration using Kalman filter models and metrics. IEEE Trans. Ind. Electron. **59**, 4301–4314 (2012)
85. S. Jafarzadeh et al., State estimation of induction motor drives using the unscented Kalman filter. IEEE Trans. Ind. Electron. **59**, 4207–4216 (2012)
86. S.F. Cheng, M. Pecht, *A Fusion Prognostics Method for Remaining Useful Life Prediction of Electronic Products*, 2009 I.E. International Conference on Automation Science and Engineering (2009), pp. 102–107
87. J.P. Xu, L. Xu, Health management based on fusion prognostics for avionics systems. J. Syst. Eng. Electron. **22**, 428–436 (2011)
88. S. Vasan, M. Pecht, *Investigation of Stochastic Differential Models and a Recursive Nonlinear Filtering Approach for Fusion-Prognostics*, in Proceeding of Annual Conference of the Prognostics and Health Management Society (2011), pp. 1–3
89. H. Liao, E.A. Elsayed, Reliability inference for field conditions from accelerated degradation testing. Nav. Res. Logist. **53**, 576–587 (2006)
90. S.T. Tsaing, C.Y. Peng, Stochastic diffusion modeling of degradation data. J. Data Sci. **5**, 315–333 (2007)
91. J.J. Fan et al., Lifetime estimation of high-power white LED using degradation-data-driven method. IEEE Trans. Device Mater. Reliab. **12**, 470–477 (2012)
92. IES-TM-21-11, *Projecting Long Term Lumen Maintenance of LED Light Sources* (Illuminating Engineering Society, New York, 2011)
93. IES-LM-79-08, *Electrical and Photometric Measurements of Solid-State Lighting Products* (Illuminating Engineering Society, New York, 2008)
94. ASMT-Jx3x, *Data Sheet: 3W Mini Power LED Light Source* (Avago Technologies, 2012)
95. J.J. Fan et al., Predicting long-term lumen maintenance life of LED light sources using a particle filter-based prognostic approach. Expert Syst. Appl. **42**, 2411–2420 (2015)
96. D.H. Stamatis, *Failure Mode and Effect Analysis: FMEA from Theroy to Execution*, 2nd edn. (ASQ Quality Press, 2003)
97. T. Sutharssan et al., Prognostics and health monitoring of high power LED. Micromachines **3**, 78–100 (2012)
98. ASSIST Recommendation, *LED Life for General Lighting* (Lighting Research Center, Troy, 2005)
99. J.J. Fan, et al., *In-Situ Monitoring and Anomaly Detection for LED Packages Using a Mahalanobis Distance Approach*, 2015 First International Conference on Reliability Systems Engineering (ICRSE) (2015)
100. C. Hua et al., Long-term potential performance degradation analysis method based on dynamical probability model. Expert Syst. Appl. **39**, 4410–4417 (2012)
101. LUXEON, *LM-80 Test Report (DR04)* (PHILIPS, 2011)
102. CREE, *LED components IES LM-80-2008 Testing Results (Revision: 12)* (CREE, 2012)
103. J.P. Zhang et al., Life prediction for white OLED based on LSM under lognormal distribution. Solid State Electron. **75**, 102–106 (2012)

104. J.P. Zhang et al., Life prediction of OLED for constant-stress accelerated degradation tests using luminance decaying model. J. Lumin. **154**, 491–495 (2014)
105. F.K. Wang, Y.C. Lu, Useful lifetime analysis for high-power white LEDs. Microelectron. Reliab. **54**, 1307–1315 (2014)
106. J.J. Fan et al., Prognostics of chromaticity state for phosphor-converted white light emitting diodes using an unscented Kalman filter approach. IEEE Trans. Device Mater. Reliab. **14**, 564–573 (2014)
107. J.J. Fan et al., Prognostics of lumen maintenance for high power white light emitting diodes using a nonlinear filter-based approach. Reliab. Eng. Syst. Saf. **123**, 63–72 (2014)
108. M.S. Arulampalam et al., A tutorial on particle filters for online nonlinear/non-Gaussian Bayesian tracking. IEEE Trans. Signal Process. **50**, 174–188 (2002)
109. W. Caesarendra et al., Machine condition prognosis based on sequential Monte Carlo method. Expert Syst. Appl. **37**, 2412–2420 (2010)
110. M.E. Orchard, G.J. Vachtsevanos, A particle-filtering approach for on-line fault diagnosis and failure prognosis. Trans. Inst. Meas. Control. **31**, 221–246 (2009)
111. C.C. Chen et al., An integrated architecture for fault diagnosis and failure prognosis of complex engineering systems. Expert Syst. Appl. **39**, 9031–9040 (2012)
112. J. Zhao, Z.Y. Li, Particle filter based on particle swarm optimization resampling for vision tracking. Expert Syst. Appl. **37**, 8910–8914 (2010)
113. N. Narendran, Y.M. Gu, Life of LED-based white light sources. J. Disp. Technol. **1**, 167–171 (2005)
114. D. An et al., Prognostics 101: a tutorial for particle filter-based prognostics algorithm using Matlab. Reliab. Eng. Syst. Saf. **115**, 161–169 (2013)
115. T.C. Li et al., Fight sample degeneracy and impoverishment in particle filters: a review of intelligent approaches. Expert Syst. Appl. **41**, 3944–3954 (2014)
116. Y.J. Xing, et al., *Influence of Parameter Initialization on Battery Life Prediction for Online Applications*, 2012 13th International Conference on Electronic Packaging Technology & High Density Packaging (Icept-Hdp 2012) (2012), pp. 1043–1047

Chapter 12
Advances in LED Solder Joint Reliability Testing and Prediction

J. Zhang and Guo Qi Zhang

Abstract Solder reliability in LED assemblies is proven to be very critical for a reliable solid-state lighting system. Evaluation of the reliability in a fast way becomes a cutting edge of the industry, which can greatly diminish the design cycle and hence reduce the time to market. This chapter introduces two methodologies of doing fast reliability qualification of solder joint in LED assemblies: FEM-assisted lifetime estimation modeling and in situ high-precision fatigue damage-based lifetime prediction. These two methods can be also useful for RUL prognostic and quality screening test.

12.1 Introduction

12.1.1 Solder Joints in Solid-State Lighting Package

Solid-state lighting (SSL) is the most promising reliable energy-saving solution for future lighting applications and is based on the semiconductor-based light-emitting diode (LED) [1]. A bare LED die cannot survive without a package. The package not only fulfills optical functions but also contains interconnects, the heat sink, the driver, and other components. The integration of all these items into a single package may result in many reliability issues, such as stress concentrations, interconnect fatigue, material degradation, etc., which decrease the reliability from a systems perspective. Thus, in order to perform a reliability analysis of a SSL system, detailed knowledge of the package configurations and its assembling routine is required. The reliability of LED packages is often addressed at five levels, as shown in Fig. 12.1 [1].

J. Zhang (✉)
Delft University of Technology, Feldmannweg 17, 2628CT, Delft, The Netherlands
e-mail: J.Zhang-1@tudelft.nl

G.Q. Zhang
State Key Laboratory of Solid State Lighting, Institute of Semiconductors, Chinese Academy of Sciences, Beijing, China

State Key Laboratory of Solid State Lighting (Changzhou Base), Changzhou, China

EEMCS Faculty, Delft University of Technology, Delft, The Netherlands
e-mail: g.q.zhang@tudelft.nl

© Springer International Publishing AG 2018
W.D. van Driel et al. (eds.), *Solid State Lighting Reliability Part 2*, Solid State Lighting Technology and Application Series 3, DOI 10.1007/978-3-319-58175-0_12

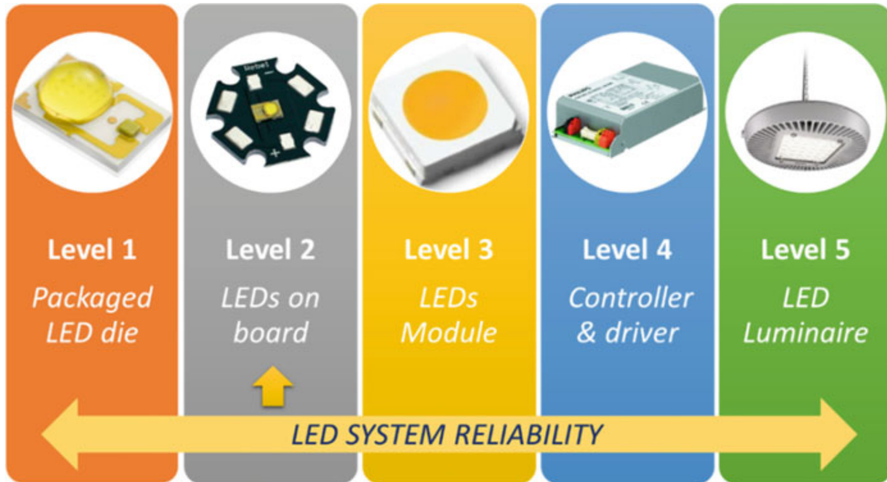

Fig. 12.1 Different level definitions for high-power LED system [1]

The main function of level 2 package is to facilitate the electrical connection and heat dissipation of the level 1 package (LED die on ceramic carrier) mounted on a printed circuit board (PCB) by land grid array (LGA) solder joints. These solder joints endure relatively harsh operating conditions, such as a high temperature, a high current density flow, and thermal stresses induced by the coefficient of thermal expansion mismatch between the chip carrier and the PCB. Hence, the solder joints are commonly regarded as the most vulnerable link of the whole LED system [2]. In this dissertation, the reliability of solder joints used to mount the chip carrier onto the PCB will be addressed in greater detail.

12.1.2 Challenges for Solder Reliability Assessment in SSL System

Although there has been a remarkable growth in the application of LED lighting for luminaires in the market, the technology is certainly not without remaining challenges. The most important consideration for the industry is to assure the long-term reliability, since the specified lifetime of some LED lighting products can be up to 100,000 h. However, these products are expected to be developed in a short time to market in order to retain the competence in this booming industry. Thus, there is always an urgent demand for fast reliability assessment methods of LED products in order to accelerate development cycles without increasing the risk of launching less reliable products.

Accelerated life test (ALT) is a lifetime prediction methodology commonly adopted by the industry over the past decades. The purpose of ALT is to induce field failure under laboratory conditions at a much faster rate than in real-life

conditions, by providing a harsher yet representative environment. Nevertheless, the acceleration factor cannot be set infinitely high, since only those failure modes and mechanisms that can realistically be expected in actual applications should be trigged. Therefore, when testing LED products with very long intended service lifetimes of up to 100,000 h, longer ALT testing time is required. Based on test results from industry [1], to properly test for the main failure mode (creep fatigue), the ALT testing time of solder joint in LED packages can go up to 9000 cycles. Such a test cycle definitely does not meet the industrial target to limit the testing time to 6–12 weeks. Hence new testing methods and ALT protocols are necessary.

Furthermore, the minimally required testing time also depends on the criteria to terminate the test. The most common approach to detect failure during ALTs for solder joints is by forming a daisy chain test structure consisting of a series of joints and monitoring the electrical resistance. However, this method has a relatively low sensitivity to failure, and it involves an arbitrary threshold (exp. 30% resistance increase), which greatly increases the chance of prolonging the testing time beyond the actual onset of joint failure. When the reliability of individual solder joints becomes critical, the daisy chain method is no longer applicable. The alternative way is to conduct regular manual checks, which are much more time- and labor consuming. Therefore, it is crucial to develop an appropriate failure detection technique for ALT of products with long lifetime expectation measuring reliability at the level of individual solder joints.

By increasing the sensitivity and lowering the detection limit for resistance changes, the failure detection method may be used to monitor the damage evolution in individual solder joints. A test method which is capable of monitoring the deformation accumulation phase and the resultant crack initiation and crack propagation phases, in principle, creates the possibility of early termination of the test once enough information is collected to predict final and catastrophic failure. The concept is schematically demonstrated in Fig. 12.2. Currently, no mature technique is available for online damage evolution monitoring in individual solder joints.

Another critical limitation of ALT to be applied to evaluate the solder joint reliability in LED lighting package is the problem of deriving the actual acceleration factor (AF). For conventional high-lead solders, the AF can be determined by the well-established and validated Norris-Landzberg equation (Eq. 12.1):

$$\frac{N_{\text{product}}}{N_{\text{test}}} = \left(\frac{\Delta T_{\text{test}}}{\Delta T_{\text{product}}}\right)^{1.9} \cdot \left(\frac{f_{\text{product}}}{f_{\text{test}}}\right)^{\frac{1}{3}} \cdot \exp\left[\left(\frac{1}{T^{\max}_{\text{product}}} - \frac{1}{T^{\max}_{\text{test}}}\right)\right] \tag{12.1}$$

where the subscripts "test" and "product" denote the accelerated testing and product environments, N is the number of cycles to failure, ΔT is the temperature range, f is the cyclic frequency, and $T^{\max}$ is the maximum temperature for each temperature range. However, such an equation for lead-free solder materials does not exist yet.

On the other hand, even if the Norris-Landzberg equation were available, for products that require long-term reliability of 10–20 years, the extrapolation using Eq. 12.1 based on the assumption of a single and constant failure mechanism to be in place at all times can lead to significant errors. This effect is schematically

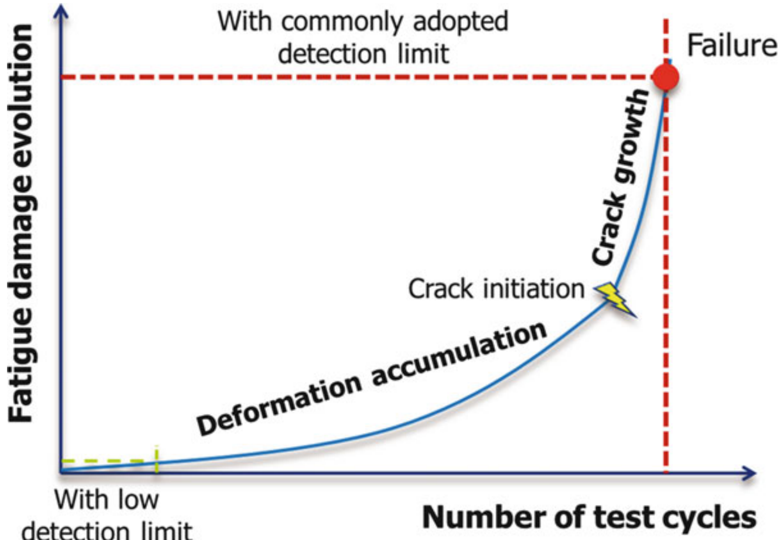

Fig. 12.2 Benefits of precise damage monitor prior to catastrophic failure

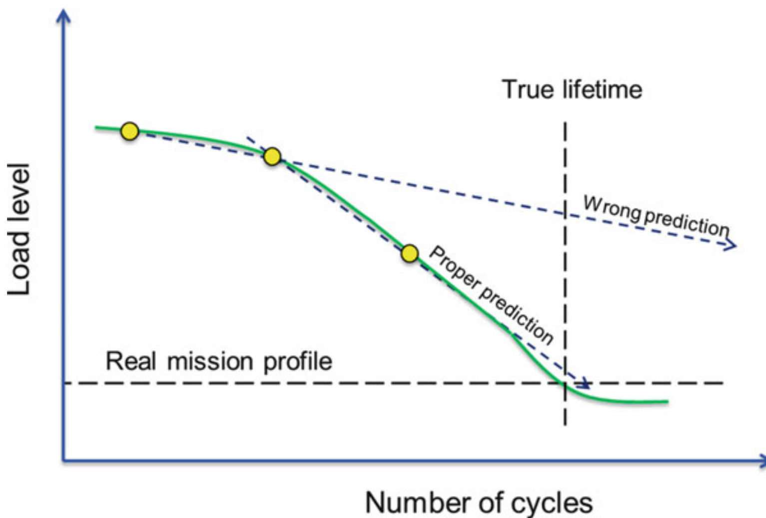

Fig. 12.3 Schematic of load level versus lifetime for a hypothetical product

demonstrated in Fig. 12.1. The question how to accurately correlate the information obtained from ALT to the actual application and its prevailing conditions is not answered yet (Fig. 12.3).

The appeal of the Norris-Landzberg equation is its simplicity and efficiency; however, it has limited possibilities to extrapolate to other configurations and conditions than those for which it was validated. Finite element (FE) calculations relating accelerated test results to service lifetime can be an alternative.

The challenge of performing FE calculations for solder joints in modern LED packages is the introduction of LGA assembly configurations that minimize the solder thermal resistance. This type of solder joint with a high solder contact area to standoff height (SOH) ratio differs significantly from the configuration in conventional and well-studied ball grid array (BGA) assemblies. Many factors related to the reliability of this assembly, such as the geometric effects, are yet unknown. Furthermore, there is a need for a new fatigue model that is compatible with LGA solder configuration, since the guidelines for selecting fatigue critical elements for BGA solder joints [3–5] are unlikely to apply. Thus, it is also of great importance to develop a suitable critical element selection rule particularly for LGA solder joints. Finally, although FEM simulations are no longer very expensive, it would be desirable to have cruder engineering guidelines to quickly estimate the effect of the various geometries and dimensions for new trial LGA configurations.

12.1.3 Challenges for the Prognostic of Remaining Useful Life of Solder Joint in SSL System

Historically, diagnostics and prognostics of remaining useful life (RUL) have often been implemented for critical structural components of complex mechanical systems such as airplanes and nuclear reactors. Electronic equipment played a minor role, and its lifetime was assumed to be much longer than the most critical mechanical components. Currently, however, the functioning of complex products and systems relies more and more on its electronics and therefore on the reliability of solder joints that are embedded in various locations of the system. Consequently, prognosticating the remaining useful life of solder joints is a research area currently attracting lots of attention. The accuracy of life prediction tools has become critically important, due to reliability values now to be expressed in absolute numbers, rather than in relative performance rankings [4]. Much research is currently ongoing to define methods and models to correctly predict RUL of solder joint taking all potential failure modes into consideration [6–9]. In all such studies, there are two prime challenges to be addressed: (i) define and monitor the appropriate damage indicator and (ii) establish a stress and damage model for lifetime prediction.

In older models, an accumulated environmental exposure parameter, such as combinations of time, temperature, and humidity, was used as the indirect damage parameter. These models rely on a phenomenological transient model to recalculate the actual damage from these parameter values [10]. Newer models employ operational parameters, such as voltage, power consumption, or heat dissipation, which are physically related to the damage level, as the damage indicator [9]. The drawback of such a damage parameter is that its value is not uniquely linked to the actual damage accumulation and may induce false alarms or late warnings. Hence, the selection or creation of a suitable physical property to monitor directly the damage evolution is vital for reliable prognostic of RUL for solder joints in LED systems.

To make full use of such a better damage indicator, corresponding new lifetime prediction models should also be established in order to be able to perform really accurate RUL prognostic.

12.2 Fatigue Model Derivation for Solder Joint in LGA Assembly

Nowadays, surface-mount technology (SMT) is seen as a more suitable solution for applications such as solid-state lighting (SSL) and power electronics. In particular, land grid array (LGA) concepts are gaining popularity because of their better heat dissipation and current flow characteristics. But LGA solder joints are not studied as intensively as ball grid array (BGA) solder joints, which are still widely used in various microelectronic applications. Many efforts have been made to derive an accurate fatigue model to evaluate the (thermomechanical) reliability of solder interconnects in BGA assemblies and also predict the resulting lifetime [11].

In a number of countries and regions, conventional lead-based solder has been banned from use in lighting systems. Hence, the reliability of tin-based lead-free solder has become increasingly important. A tin-based alloy, SAC (Sn/Ag/Cu), is considered as one of the best options to replace conventional lead solder. This new type of solder has not been studied as intensively as traditional lead solder. The principal characteristics of this new type of solder alloy are its high creep resistance and its lower ductility compared to lead-containing solder [4, 12–14]. The low ductility results in the commonly adopted strain-based Coffin-Manson fatigue model developed for conventional lead solder reliability studies no longer being applicable, because the strain accumulation per cycle becomes unstable even for low number of cycles [11]. Thus, many researchers currently employ energy-based models to discuss the reliability of SAC solder [4, 12, 15–17]. In most such studies, the crack propagation time is ignored, since (brittle) failure along grain boundaries or near the intermetallic layer is the major fracture mode and forms only a small part of the total lifetime [4, 15, 17].

These energy-based approaches normally involve a finite element analysis (FEA) for calculating the damage evolution per cycle. An indicator based on the volumetric averaged damage per element is then correlated to the corresponding experimental results to establish the final fatigue model. As the damage initiation does not happen all over the interconnect but is localized in some sections of the interconnect, it becomes vital to select the appropriate critical elements in order to derive the most relevant average damage accumulation to the final failure of solder joints. In a BGA assembly, the elements that are in layers within the top 20% of the total standoff height are generally chosen as the most critical elements [5, 18–20], and the predicted lifetime based on this approach shows good agreement with experimental findings for BGA assemblies [21–24].

However, it does not seem appropriate to use the mentioned methods intended for BGA solder joints to select critical elements for LGA solder joints, considering their very large soldering area and their relatively low standoff height (SOH). Therefore, it is necessary to develop a reliable and accurate fatigue prediction model with proper critical element selection method for this new type of solder.

12.2.1 Constitutive Law and Material Models

A complex deformation behavior can be expected when solder joints in an LED package undergo thermal loading due to CTE (coefficient of thermal expansion) mismatch of the various materials in the total package. The deformation behavior is normally associated with many different viscoplastic mechanisms, such as irreversible rate and temperature-dependent inelasticity, strain hardening, dynamic recovery, and even dynamic recrystallization.

To describe this viscoplastic deformation behavior of a solder joint, a partition constitutive model which splits the total deformation to elastic, rate-independent plastic, and creep deformation is used and demonstrated in Eq. 12.2 [25]:

$$\dot{\gamma}_{\text{total}} = \dot{\gamma}_{\text{e}} + \dot{\gamma}_{\text{p}} + \dot{\gamma}_{\text{pc}} + \dot{\gamma}_{\text{sc}} \tag{12.2}$$

where $\dot{\gamma}_{\text{total}}$ is the total strain rate, $\dot{\gamma}_{\text{e}}$ is the elastic strain rate, $\dot{\gamma}_{\text{p}}$ is the rate-independent plastic strain rate, $\dot{\gamma}_{\text{pc}}$ is the primary creep strain rate, and $\dot{\gamma}_{\text{sc}}$ is the secondary creep strain rate. However, under normal thermomechanical loading conditions, solder alloys are often subjected to conditions leading to secondary creep [12, 13, 26–28], for which rate-independent plastic deformation and primary creep deformation is negligible compared to steady-state creep deformation. Therefore, in this chapter, rate-independent and primary creep deformations were assumed to be negligible compared to secondary creep deformation. Thus the partition law can be rewritten as shown in Eq. 12.3.

$$\dot{\gamma} = \dot{\gamma}_{\text{e}} + \dot{\gamma}_{\text{sc}} \tag{12.3}$$

Assuming that the solder joint is isotropic, the linear recoverable, elastic response, Y_e, can be described by Hooke's law. The apparent Young's modulus of SAC solder is temperature and strain rate dependent [14, 29–32]. For ease of inputting the model into finite element software, a temperature-dependent relation of Young's modulus at a typical intermediate strain rate (5.6×10^{-3}) is applied [30]:

$$E = 55.8 - 0.25T \tag{12.4}$$

where E is the Young's modulus in GPa and T is the temperature in °C. For SAC solder, the Poisson's ratio is normally estimated to be in the range of 0.35–0.4 [14, 31, 32]. In this study, a fixed Poisson's ratio of 0.36 is adopted.

The secondary creep deformation is modeled with a Garofalo law, which is shown in Eq. 12.5:

$$\frac{d\gamma_{creep}}{dt} = c_1[\sin h(c_2\sigma)]^n \exp\left(-\frac{Q}{kT}\right) \tag{12.5}$$

where Y_{creep} is the secondary creep strain, Q is the activation energy for secondary creep, k is the Boltzmann constant, and T is the absolute temperature. c_2 reflects the stress level that the power law breaks down. Q, c_1, c_2, and n are material constants that have been derived by Schubert et al. [4] for SAC 405. Material constants values for INNLOT (Sn, $Ag_{3.8}$, $Cu_{0.7}$, $Bi_{3.0}$, $Sb_{1.4}$, $Ni_{0.2}$) solder have been derived by Dudek et al. [33] and were published by Hannach et al. [34]. They are listed in Table 12.1

In this study, the energy-based fatigue model introduced by Dasgupta [35] is applied. This model predicts the occurrence of failure on the basis of the volume-weighted-average stress-strain history. In the model, it is assumed that three aspects contribute to the cyclic fatigue damage: elastic deformation, rate-independent plastic deformation, and rate-dependent creep deformation. The relation is presented in Eq. 12.6:

$$W_{total} = U_e + W_{pl} + W_{cr} \tag{12.6}$$

where W_{total} is the total strain energy density in a particular loading step, U_e is the elastic strain energy density, W_{pl} is the plastic strain energy density, and W_{cr} represents the creep strain energy density. It should be noted that in this paper plastic deformation refers only to the rate-independent plastic deformation. Akay [3] then proposed the fatigue model as shown in Eq. 12.7:

$$N_f = \left(\frac{W_0}{\Delta W_{total}}\right)^k \tag{12.7}$$

where N_f is the characteristic lifetime of solder joint, or the scale parameter of a Weibull plot of the lifetime values, W_0 and k are the fatigue model correlation parameters, and ΔW_{total} is the total strain energy density increase per cycle. Since rate-independent plastic deformation and primary creep deformation are ignored, the expression ΔW_{total} can be given by Eq. 12.8:

Table 12.1 Material constants of solder creep model

	c_1	c_2	n	Q/k
SAC405 [4]	277,984	0.0244	6.41	6496.5
INNLOT [34]	8000	0.05	4	7577.6

$$\Delta W_{\text{total}} = \Delta W_{\text{sc}} \tag{12.8}$$

where ΔW_{sc} is the secondary creep strain energy density increase per cycle. The derivation of ΔW_{total} according to simulation results is demonstrated in the next section. It is worth noting that this model can only determine the crack initiation time. However, for lead-free solders, since fast crack propagation along grain boundaries or near the intermetallic layers is usually expected, it is assumed that the number of propagation cycles is negligible compared to the total number of cycles to failure [4, 15, 17].

12.2.2 Finite Element Modeling

Three different commercially available LED package types were considered, which were referred to as package types A, B, and C. The geometric information of these packaged LED chips was obtained from industrial product data sheets. Figure 12.4 schematically illustrates the cross-section of the type A package.

The other packages studied in this work have a similar structure, although the package materials, size, and the footprint are different. The relevant detailed size and material information of the three packages is listed in Table 12.2

The footprints of the three package types considered are illustrated in Fig. 12.5. The shape of the solder was simplified as being rectangular, and the planar size of the solder was considered to be the same as the size of the copper pads. The size of the PCB is chosen to be equal to that of the real samples from the corresponding accelerated tests performed. More detailed information of the accelerated tests can be found in [36]. Nonlinear viscoplastic finite element analysis was performed using ANSYS™ 13.0. 8-node solid brick elements that can handle large creep

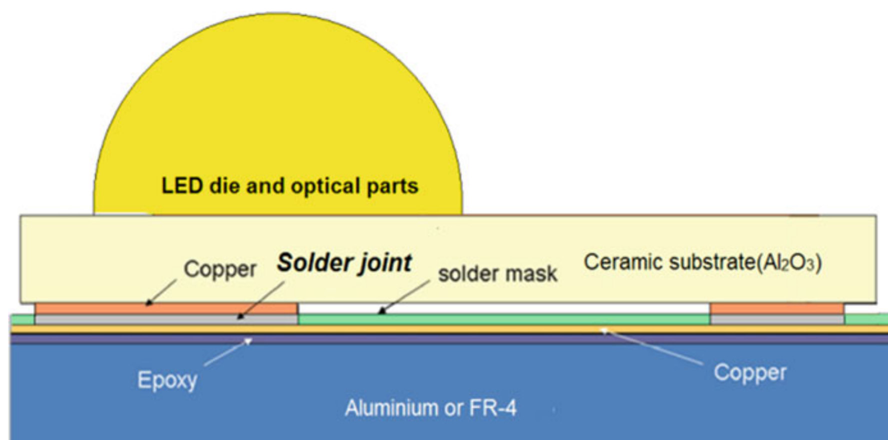

Fig. 12.4 Illustration of a cross-section of the LED package studied [36]

Table 12.2 Detailed size information of the LGA package

Component	Type A		Type B		Type C	
	Area/mm^2	h/mm	Area/mm^2	h/mm	Area/mm^2	h/mm
Die substrate	4.5 × 3	0.44	9 × 7	0.3	10 × 10	0.3
	Alumina		Alumina		Glass	
Copper (big thermal)	2.8 × 1.8	0.035	6.4 × 5.6	0.035	2.7 × 5.3	0.1
					3.7 × 3.7	
Copper (small electrode)	1.2 × 0.8	0.035	6.4 × 0.7	0.1	1.4 × 1.4	0.1
Solder (big thermal)	2.8 × 1.8	0.1	6.4 × 5.6	0.1	2.7 × 5.3	0.1
					3.7 × 3.7	
Solder (small electrode)	1.2 × 0.8	0.1	6.4 × 0.7	0.1	1.4 × 1.4	0.1
Solder mask	6 × 6	0.1	13 × 13	0.1	16 × 16	0.1
Under filled epoxy	6 × 6	0.1	13 × 13	0.1	16 × 16	0.1
Aluminum or FR-4	6 × 6	1.5	13 × 13	1.5	16 × 16	1.5
Solder coverage (SC)	0.52		0.78		0.79	
Thermal to electrical pad Area Ration (AR)	5.2		8.0		NA	

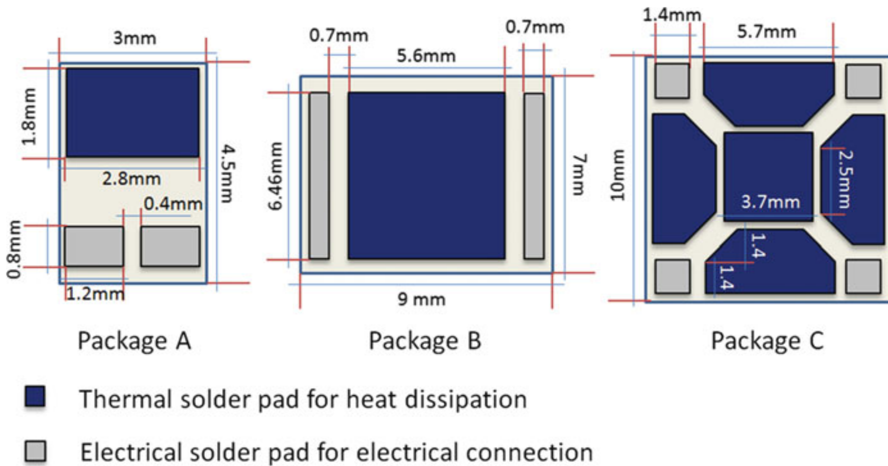

Fig. 12.5 Schematic illustration of footprints of three different packages studied

strains were employed. The deformation of all other components in the system was taken as elastic, and four-node triangle elements were used. As for boundary conditions, the central point of origin (0, 0, 0) was fixed in all directions. In addition, due to symmetry consideration, for the type A package, a half model was simulated, and for types B and C, quarter models were introduced. The material properties are listed in Table 12.3.

Note that the material properties of solder listed here only describes the linear elastic mode. The viscoplastic deformation is presented by the creep model which is

Table 12.3 Material properties of components as applied in FEM model

	CTE(10^{-6} K^{-1})		E_x(GPa)		Poisson's ratio
	x,y	*z*	*x,y*	*z*	
FR-4[10]	18	50	20	10	0.38
MCPCB (Al 6061) [30]	23.6		70		0.33
Deposited copper[6]	16.5		90		0.35
SAC 405[11]	19.7 (373 K)		55.8–0.25 × T[22]		0.36
	21.0 (423 K)				
INNOLOT[26]	23.2 (373 K)		48.5 (218 K)		0.36
	24.8 (423 K)		33 (483 K)		
Solder mask[10]	70		2.0		0.3
Dielectric Epoxy[10]	60		2.4		0.3
Glass substrate	8.5		80		0.22
Al_2O_3 Substrate[10]	7–1		300		0.23

discussed in Sect. 12.2. In addition, since the substrate material FR-4 is a typical anisotropic material, the material properties in different directions are listed. The z direction is the direction normal to the printed circuit board. Since the exact composition of the glass substrate in a type C package is unknown, estimations are made according to Ref. [37].

The thermal load steps considered in the analysis consist of two parts, both shown in Fig. 12.6. (The first part is cooling down from the solidus temperature (217 °C) to room temperature 25 °C.)

A stress-free state within the package at the reflow temperature is assumed, which leads to residual stresses being induced by cooling down from the soldering temperature. Then, three different thermal cyclic loading conditions corresponding to those to be used for accelerated tests and described in Table 12.4 were employed.

It is reported that the accumulated increase in creep strain energy density per cycle is stable after three cycles [38]. Thus, four cycles were performed in the FEM simulation. In total, eight simulations runs with conditions corresponding to the lifetime experiments are conducted. The details, together with the experimentally determined lifetime data [36], are listed in Table 12.5.

To derive the ΔW_{sc} value to be used in the energy-based model, the element (s) with maximum creep strain energy density after four loading cycles should be identified firstly from the FEM analyses. Then, ΔW_{sc} is calculated as the creep strain energy density difference of the most critical elements between the end of the fourth cycle and the end of third cycle using Eqs. 12.9 and 12.10:

$$\bar{\boldsymbol{W}}_{\mathbf{sc}} = \frac{\sum_i \boldsymbol{V}_i \cdot \boldsymbol{W}_i^{\mathbf{cr}}}{\sum_i \boldsymbol{V}_i} \tag{12.9}$$

$$\Delta \boldsymbol{W}_{\mathbf{sc}} = (\bar{\boldsymbol{W}}_{\mathbf{sc}})_{\mathbf{4th}} - (\bar{\boldsymbol{W}}_{\mathbf{sc}})_{\mathbf{3rd}} \tag{12.10}$$

where V_i is the volume of the element in the most critical element set and W_i^{cr} is the creep strain energy density in the corresponding element.

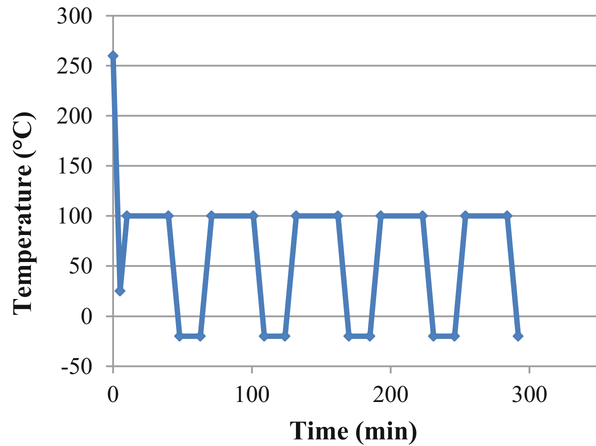

Fig. 12.6 Typical test temperature profile used for lifetime experiments and input into FEM simulation

Table 12.4 Cyclic loading details

	Ramp rate	Hot dwell	Cold dwell	T_{min}(°C)	T_{max}/(°C)
Cycle 1	15 °C/min	30 min	15 min	−20	100
Cycle 2	15 °C/min	30 min	30 min	−40	125
Cycle 3	12.5 °C/min	30 min	30 min	0	125

Table 12.5 Simulation details and corresponding test results [36]

	Package type	Cycle type	Solder material	PCB type	Characteristic lifetime	Standard error (%)
1	A	2	SAC 405	MCPCB	2307	±3.1
2	A	2	SAC 405	FR-4	8014	±2.8
3	A	3	INNOLOT	MCPCB	4291	±3.9
4	A	1	SAC 405	MCPCB	3999	±6.1
5	B	2	SAC 405	MCPCB	1690	±6.6
6	B	3	INNOLOT	MCPCB	2736	±2.7
7	C	1	INNOLOT	FR-4	6913	±10.9
8	C	1	INNOLOT	MCPCB	5665	±5

In order to minimize the edge singularity in the simulation, mesh sensitivity studies were conducted prior to the actual analysis. It was found that a mesh density larger than 1×10^5 element/mm^3 in the critical solder joint, the influence of the mesh density on the total volume of the most critically loaded elements, and the calculated fatigue indicator ΔW_{sc} were limited and remained within 10%. Therefore, 1×10^5 element/mm^3 is determined as the appropriate mesh density for solder materials in the model. The meshed structure is depicted in Fig. 12.7.

In order to find an adequate way of selecting the most relevant elements for LGA assemblies, the distribution of creep energy density for all elements in the actual

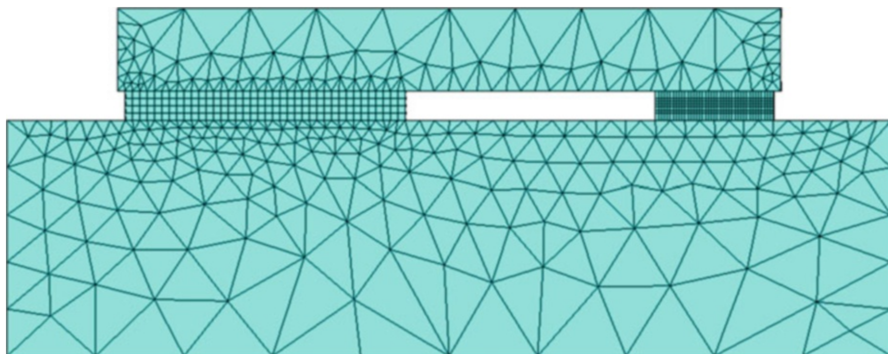

Fig. 12.7 Meshed structure in FEM simulation model

solder joint was investigated for each simulation run. The results were further linked to the aspect ratio of the solder joints, so as to formulate a more suitable critical element selection methodology for a LGA solder assembly.

12.2.3 Model Derivation

The FEM analysis clearly showed that the outer edge corner for the electrical connection is the most critical and dangerous joint location for all cases. Representative contour plots of creep strain energy density for each package are shown in Fig. 12.8.

In addition, the most critical corner in each critical solder joint is identified as that with maximum creep strain energy density and circled with red as shown in Fig. 12.8, which predicts the most probable location of the crack initiation spot. Figure 12.9 shows a cross-sectional micrograph containing the location of the experimentally determined crack initiation point, which is at the outer corner near the ceramic carrier side. The observation confirms the model prediction.

Moreover, Fig. 12.8 shows that most elements in the center of the critical solder joint have low creep energy density, which makes them irrelevant to the fatigue failure initiation. Detailed information regarding the element distribution of creep energy density for each package type at the last sub-step of the simulation is demonstrated in Fig. 12.10. It is clear that only a very limited fraction (less than 10%) of elements that are subjected to a high load level will contribute to fatigue crack initiation. Moreover, as shown in Fig. 12.8, these critical elements are located just at the corner in the neighborhood of the most critical elements. Therefore, a layer averaging procedure as applied to BGA solder joint models is inappropriate. For LGA assembly models, it seems essential to define a suitable energy density threshold and select all the elements that are above this threshold as the critical elements.

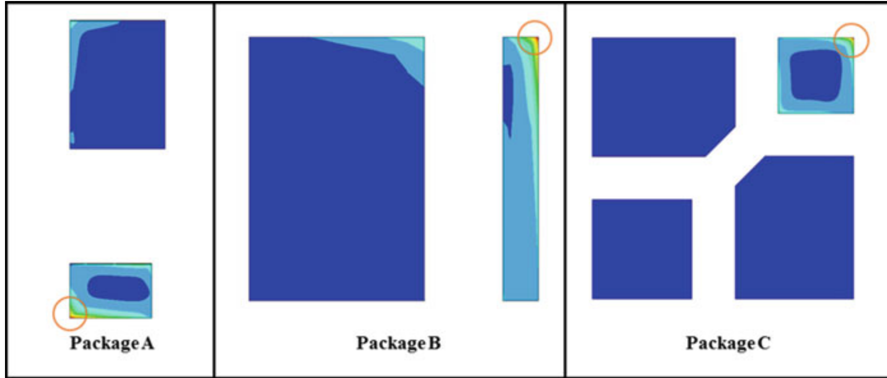

Fig. 12.8 Contour plot of creep energy density distribution of three types of packages after four cycles, half model of *package A* and quarter model for *packages B* and *C*

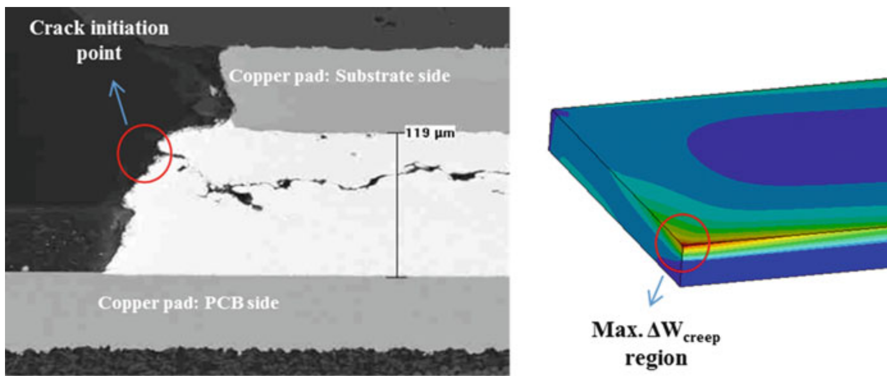

Fig. 12.9 Cross-sectional picture of solder joint at early crack propagation stage

Fig. 12.10 Representative element distribution of creep energy density of critical solder joint for each package type

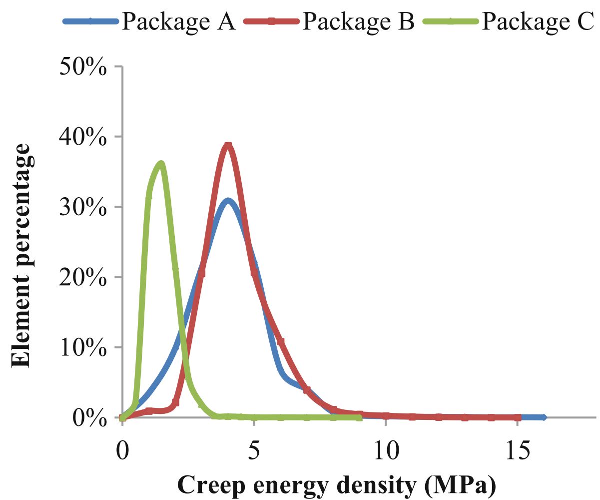

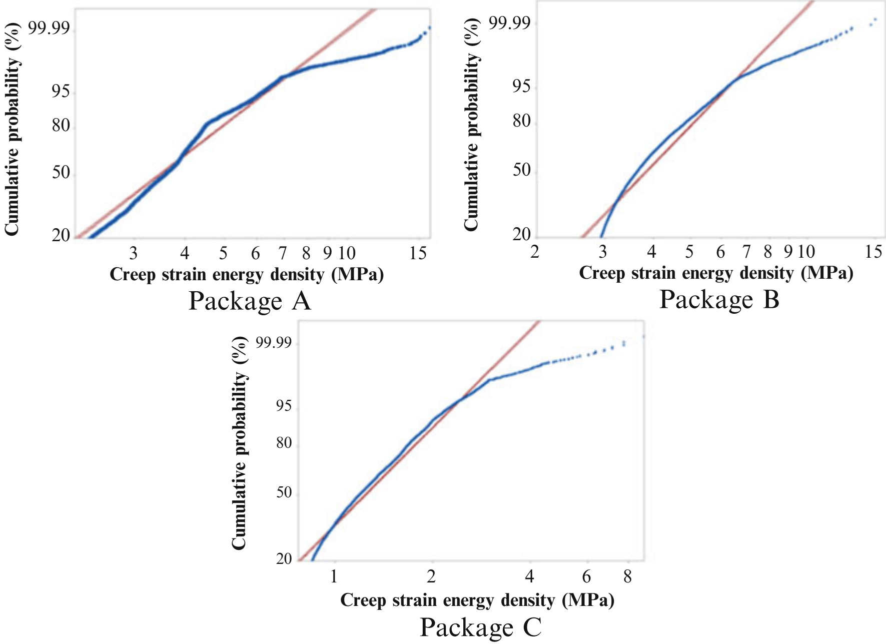

Fig. 12.11 Weibullian plots of creep strain energy density for all three packages

In order to identify the most critical elements, the element distribution of creep energy density is illustrated in Weibullian form as shown in Fig. 12.11 due to its good capability of demonstrating data in both extremes.

It shows that the data plot tends to deviate down from the Weibullian linear regression line at around 97% for each case, which also coincides with simulation results of other scenarios listed in Table 12.5. It implies that those elements that are above the derivation point are very likely to be responsible for the failure. In order to develop a critical selection method that is easy to make robust, although the separation points for all cases are slightly different, adopting a general fixed threshold percentage value seems more appropriate, since it is somewhat arbitrary to determine the separation point. Therefore, elements with top 3% creep strain energy density are considered as critical elements in this study.

Once the threshold is defined, all the elements that have higher creep energy density are selected. However, it may happen that some of the selected elements are located near other corners of the solder joint rather than the most critical one. In that case, those elements have to be excluded. Then, the damage indicator, which is the simulated accumulated creep strain energy density per cycle of the critical elements, is calculated according to the equations that are listed in Sect. 12.2.2.

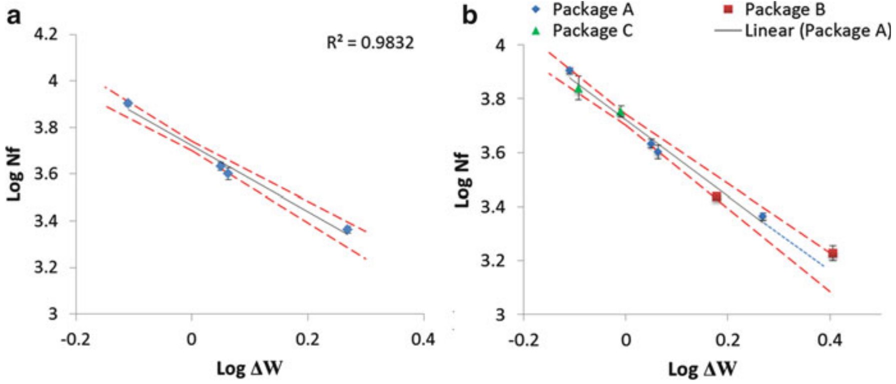

Fig. 12.12 Plot of creep energy accumulation per cycle versus test life cycles: (**a**) data regression of *package A*, (**b**) fit data of *packages B* and *C* to model obtained from package A data [29]

All the calculated damage indicator values ΔW_{creep} are shown in Fig. 12.12. To obtain the calibration parameters in the fatigue model, the simulated accumulated strain energy density per cycle is plotted against its corresponding experimental lifetime in a log-log scale. The results of package A are used to build up the fatigue model. The data and regression line are illustrated in Fig. 12.12a.

The quality of the regression is found to be good according to the R value of 98.3%. The calibration parameters of the fatigue model, W_0 and k, were determined and are presented in Eq. 12.11:

$$N_{\text{f}} = \left(\frac{636}{\Delta W_{\text{total}}}\right)^{1.3} \tag{12.11}$$

The standard error of the calibration parameters $k{\cdot}\log W_0$ and k with 95% confidence interval are calculated as ±9.3% and ±0.53%, respectively. The uncertainty of these two parameters has an impact on the accuracy of the lifetime prediction, which is further illustrated in Fig. 12.12 as the red dashed lines. This confidence interval band indicates that this fatigue model should be only applied to cases with lifetime range from 550 to 14,500 cycles in order to have a prediction with accuracy no worse than ±30%.

Data points of package B and package C are then added to the plot in order to check the feasibility of applying this model to other package geometries. It shows that all the points fit into the regression line quite well within the 95% confidence interval band, which is demonstrated in Fig. 12.12b.

Moreover, the experimental derived number of cycles (NoC) to failure is compared with model predicted lifetime in Table 12.6. It appears that even considering the standard error of both experimental characteristic lifetime and model predicted lifetime, the largest deviation is still below 35%. Since lower deviation is more likely to be found in the real case rather than these extremes, prediction

Table 12.6 Deviation of simulated results from experimental data using the newly developed critical element selection method

	Experimental	Simulated	Largest deviation (%)
Package B and SAC	1690 ± 111	1384 ± 223	35
Package B and INNOLOT	2736 ± 74	2930 ± 252	16
Package C and FR4	6913 ± 754	7190 ± 675	21
Package C and MCPCB	5665 ± 283	5461 ± 564	15

accuracy of ±10–25% is expected (depends on the predicted NoC), which is already sufficient for industrial applications.

In order to check the feasibility of applying the layer critical element selection method (selecting a layer of 20% of the SOH as critical element) for LGA assembly, the same lifetime data are correlated to damage indicator ΔW that is calculated based on this selection approach, which is demonstrated in Fig. 12.13. An energy-based fatigue model for package A is derived following the procedure that has been demonstrated above and listed in Eq. 12.12:

$$N_{\mathrm{f}} = \left(\frac{5 \times 10^{7}}{\Delta W_{\mathrm{total}}}\right)^{0.45} \tag{12.12}$$

The standard error of the calibration parameters $k{\cdot}\log W_0$ and k with a 95% confidence interval in this case are calculated as ±21.2% and ±13.0%, respectively, which are significantly larger than the standard errors (±9.3 and 0.53, respectively) of the fatigue model that employs the new critical element selection method. Moreover, according to the confidence interval band, this model can be only applied to cases with very narrow lifetime range from 1000 to 6400 cycles in order to achieve an accurate lifetime prediction with less than ±30% uncertainty. This range is even narrower than the experimental lifetime range that was correlated for the fatigue model derivation, indicating the irrelevance between the damage indicator and experimental characteristic lifetime. In addition, it seems that the sensitivity of the damage indictor to the experimental lifetime increases with an increasing damage indicator. This suggests that including elements with low energy in the center as critical elements will average out the significant energy accumulation that only occurred in the actual critical elements, especially for cases with lower accumulative creep strain energy.

Furthermore, data points of Package B and Package C are added into Fig. 12.13 as similar as Fig. 12.12b. Although data points from Package C shows good agreement with the regression trend line, Package B hardly follows the prediction model due to its large area to SOH ratio, because the critical element selection method from a certain layer tends to underestimate the fatigue damage accumulation especially when the joint area is large. The largest deviations between the calculated and experimental lifetime for both Package B and Package C are listed in Table 12.7.

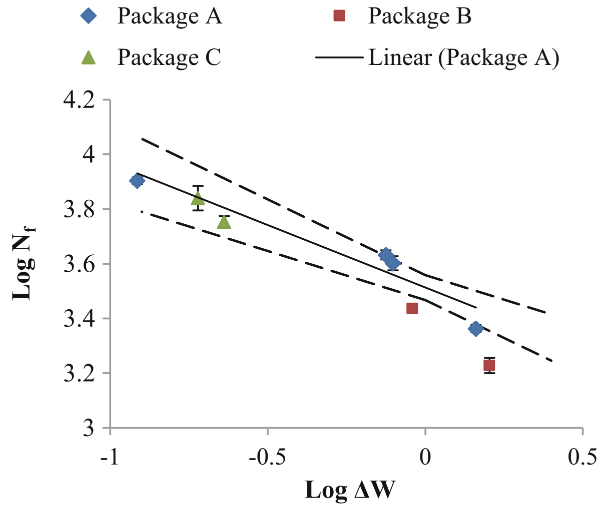

Fig. 12.13 Plot of creep energy accumulation per cycle versus test life cycles calculated with critical element selection method for a BGA

Table 12.7 Deviation of simulated results from experimental data using traditional layer critical element selection method

	Experimental	Simulated	Largest deviation (%)
Package B and SAC	1690 ± 111	2629 ± 428	55
Package B and INNOLOT	2736 ± 74	3401 ± 343	29
Package C and FR4	6913 ± 754	6948 ± 2135	32
Package C and MCPCB	5665 ± 283	6369 ± 1803	34

Significantly high deviations are found, which indicates that it is very risky to trust the lifetime prediction of the LGA assembly derived from a fatigue model that uses the layer critical element selection approach. To sum up, the demonstrated new critical element selection method is in principle more appropriate than the current well-adopted layer selection method to be applied to predict the lifetime of an LGA solder assembly.

Thus, considering the relatively large differences in terms of package size, carrier, PCB materials, solder materials, and solder geometries between the data points plotted, it is concluded that the model is accurate enough to predict the LGA solder lifetime of different package types, solder materials, and solder geometries.

12.3 Geometric Effects of Solder Joint on Board Level Solder Reliability in SSL System

The packaging levels of a SSL system has already been defined in Sect. 12.1. The second level packaging is to mount the light engine to a print circuit board (PCB) by solder joints, so it is also referred as board level assembly. Considering harsh

environments they experienced mainly due to large coefficient of thermal expansion (CTE) mismatch between the light engine materials (mostly ceramics) and the PCB board (in many cases is aluminum), these solder joints in board level assembly tend to be vulnerable [39–43]. Therefore, it is crucial to understand how the influential parameters in board level configuration can affect solder reliability.

Many factors including mission profile, voids, PCB type, solder pad finish, and solder geometry can affect the reliability of LGA solder in the package. Nevertheless, among all the factors, solder geometry seems of vital importance. Several publications discuss the geometric effect on the solder reliability of BGA and other type of assemblies. It is reported that a solder joint with a larger diameter and a larger standoff height is more reliable [44–46]. However, these results cannot be transferred directly to LGA solder joints in LED packages due to their unique solder patterns and a much smaller standoff height. There are limited reliability data available for LGA-type solder joints, but all these studies are for specific configurations and solder types and do not include effects of geometry and cannot be used for lead-free solders [47–49]. Unlike BGA-type solder joints, which have an array of fine-pitched solder joints, the footprint of solder in SSL systems normally consists of three part: two pads for electrical connection and one large pad for heat dissipation [50–52]. Thus, it is no longer appropriate to describe the geometry only using solder diameter and pitch size. In other words, defining new geometric parameters and finding out their effects on the solder reliability are of significant importance, and few publications are available regarding mentioned aspects. It is usually difficult to optimize the geometric parameters once the footprint and solder mask designs are finalized. Therefore, a methodology to assess the reliability of the solder reliability in the design phase rather than in the test phase would reduce the package development cost and time to market. In order to achieve that, it is essential to investigate the influence of different geometric factors in the package on the solder reliability and then to determine an optimized solder geometry.

12.3.1 Modeling and Simulation Details

With the developed fatigue model demonstrated in Sect. 12.2, a series of simulations regarding different solder size and geometry were performed in order to establish a response surface of LGA solder reliability of LED packages in terms of geometric parameters. Package type B described in Sect. 12.2 is selected for an in--depth parameter study. Five parameters (SOH, A, α, β, δ) are selected to represent the geometric parameters of the package, which are illustrated in Fig. 12.14. SOH is the standoff height of the solder joint, A is the chip carrier area, α is the ratio of solder length W over the chip carrier length L, β is the ratio of thermal pad width over chip carrier length L, and δ is an indicator of the fractional area of the electrical pad. The following constraints were applied. The package is considered as symmetric along two axes a and b. See Fig. 12.14. The thermal pad locates always in the middle and has the same length W as the electrical pads. The

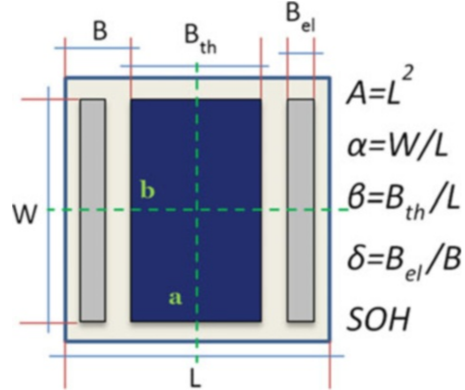

Fig. 12.14 Parameters (SOH, L, α, β, δ) that were defined for reflecting geometric information of LGA solder employed in a DOE analysis

edges of the electrical pads are located 0.2 mm away from the nearest edges of the substrate.

A central composition design was made to establish the response surface model of geometric factors in terms of solder reliability using Minitab 16 software package. Thermal profile cycle 1 defined in Sect. 12.2, INNOLOT (Sn, $Ag_{3.8}$, $Cu_{0.7}$, $Bi_{3.0}$, $Sb_{1.4}$, $Ni_{0.2}$) solder, and Metal Core Printed Circuit Board (MCPCB) were employed for all simulation runs, and only the geometric parameters were varied. The axial high and low points are listed in Table 12.8 together with the resulting 32 simulation runs which are needed for a half factorial design. Six duplicate simulations for central point would have been required for the data of an experimental nature.

However, for fully defined simulations, only one simulation run has to be performed to determine the central point. Once the results were obtained, a sensitivity analysis was performed and optimal geometry of solder joints in this type of package was determined and discussed. It is important to note that this study only consider solder reliability subjected to thermomechanical loading. However, based on this work, further complex investigations considering heat dissipation, electromigration, and cost can be done as well.

12.3.2 Parametric Studies and Response Surface Analysis

The effects of solder geometry on LGA solder joint in SSL application were explored by applying the fatigue model derived in Sect. 12.2 to establish a response surface model of solder reliability in terms of five different predefined geometric parameters. The detailed information of resulted simulation runs and corresponding ΔW_{sc} values for the different thermal cycles are listed in Table 12.8. For each simulation, the critical solder joint was always found to be at the outer corner of the electrical solder joint.

Table 12.8 The range of selected geometric factors, resulted simulation runs and corresponding lifetime results

	L^2(mm^2)		β		α		δ		SOH (urn)		ΔWc_{mep}	N_f
Run	6	70	0.2	0.6	0.6	0.98	0.3	0.8	100	150	(MPa)	(Cycles)
1	38		0.4		0.98		0.55		125		1.492	3018
2	54		0.5		0.885		0.425		112.5		1.939	2140
3	22		0.5		0.885		0.675		112.5		1.233	3876
4	22		0.3		0.885		0.675		137.5		0.995	5132
5	22		0.3		0.695		0.675		112.5		1.102	4487
6	54		0.3		0.695		0.675		1375		1.238	3852
7	38		0.4		0.79		0.3		125		1.477	3059
8	54		0.3		0.695		0.425		112.5		1.854	2270
9	38		0.4		0.6		0.55		125		1.156	4216
10	38		0.6		0.79		0.55		125		1.333	3498
11	38		0.4		0.79		0.55		125		1.378	3350
12	54		0.5		0.885		0.675		137.5		1.357	3416
13	38		0.4		0.79		0.55		125		1.378	3350
14	38		0.4		0.79		0.55		150		1.072	4654
15	22		0.3		0.885		0.425		112.5		1.331	3503
16	22		0.5		0.885		0.425		1375		1.016	4993
17	54		0.5		0.695		0.675		112.5		1.623	2702
18	38		0.4		0.79		0.8		125		1.492	3851
19	38		0.4		0.79		0.55		125		1.939	3350
20	38		0.4		0.79		0.55		125		1.233	3350
21	54		0.5		0.695		0.425		1375		0.995	3448
22	22		0.5		0.695		0.425		112.5		1.102	4269
23	54		0.3		0.885		0.675		112.5		1.238	1864
24	54		0.3		0.885		0.425		1375		1.477	2630
25	38		0.4		0.79		0.55		125		1.854	3350
26	38		0.2		0.79		0.55		125		1.156	3332
27	22		0.5		0.695		0.675		137.5		1.333	6973
28	38		0.4		0.79		0.55		100		1.378	2338
29	6		0.4		0.79		0.55		125		0.424	13,456
30	22		0.3		0.695		0.425		1375		1.378	6416
31	70		0.4		0.79		0.55		125		1.072	2476
32	38		0.4		0.79		0.55		125		1.331	3350

Firstly, a full quadratic model (linear, quadratic, and interactive terms) was applied to the data in order to derive the relation between ΔW_{sc} and the geometric parameters. The model showed a remarkable fit with a R^2 value of 98.4% and an adjusted $R^2{}_{adj}$ value which shows the necessity of terms in the model as 97%. However, the predicted $R^2{}_{pre}$ value is relatively poor compared to the two R^2 values reported above, which indicates that future prediction using this model might result in larger deviations. Thus, to obtain better accuracy, terms with a p-value

Table 12.9 Constants for the final selected response surface model

a_1	a_2	a_3	a_4	a_5	a_6	a_7	a_8	a_9	a_{10}
2.879	0.082	1.061	0.474	−0.372	−0.05	-2.95×10^{-4}	1.762×10^{-4}	−0.0215	2.49×10^{-4}

(indicating the statistically significance of terms) larger than 0.1 are removed from the model. The modified model is shown in Eq. 12.13, and the constants a_1–a_{10} are listed in Table 12.9:

$$\Delta W_{\text{creep}} = (a_1, a_2, a_3 \ldots a_{10}) \times \begin{pmatrix} 1 \\ A \\ \alpha \\ \beta \\ \delta \\ \text{soh} \\ A^2 \\ \text{soh}^2 \\ A \cdot \beta \\ A \cdot \text{soh} \end{pmatrix} \tag{12.13}$$

The predicted R^2_{pre} value for this model increases from 89% to 93% at a relative marginal cost of 0.8% and 0.5% decrease in R^2 and adjusted R^2_{adj} value. Thus, this revised model is considered to be appropriate for modeling LGA solder reliability in terms of different package and solder geometry. Three points on the resulted response surface were randomly selected to validate the model with FEM simulation results. The detailed information of these three points and corresponding results from both response surface model and FEM simulation are listed in Table 12.10. It showed that the largest deviation is only about 10% with regard to solder lifetime.

It is now possible to investigate the effects of the geometric parameters on the LGA solder reliability in SSL system by utilizing the model obtained. As discussed above, the package size plays an important role in solder reliability. Figure 12.15 shows the contour plot of solder lifetime as a function of both carrier size and solder standoff height when all other parameters are kept constant at the middle value of their interval. The position of package B was also indicated in the plot. It is shown that lifetime of solder joint decreases dramatically with increasing carrier size. This is because of the larger stress level generated by the larger carrier size in the solder joint and hence larger creep strain induced. Due to the possibility of redistributing the stress concentrations in the solder height direction, solder joints with larger standoff height in general have longer lifetime. This can also explain why the effect of carrier size on solder joint reliability is more pronounced in case of large standoff height. Therefore, in order to obtain better solder thermomechanical reliability in SSL system, it is suggested that for packages with relatively small package size, increasing the standoff height is increasing the reliability.

Table 12.10 Selected validation data point and deviation from the FEM results

	A	α	β	δ	SOH	Model	FEM	Deviation (%)
Point 1	24.9	0.81	0.49	0.62	120.3	3970	4393	9.6
Point 2	34.1	0.74	0.51	0.70	109.3	3175	3094	2.5
Point 3	54.1	0.70	0.40	0.65	144.5	4161	3830	7.9

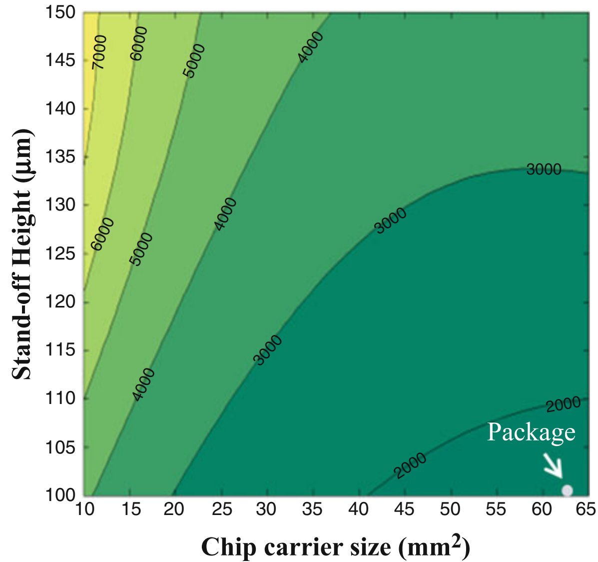

Fig. 12.15 LGA solder life cycles in LED package as a function of A and SOH

As for the effects of other parameters, two new parameters SC and AR were defined to reflect the influence of solder geometry in a more direct way instead of predefined parameters: α, β, and δ. AR is the area ratio between the solder joint for thermal conduction and the solder joint for electrical connections. SC is the solder coverage which is the ratio between solder-covered area on the carrier lower surface and the total area of carrier lower surface. AR and SC are defined in terms of α, β, and δ by Eqs. 12.14 and 12.15:

$$\mathrm{AR} = \frac{B_{\mathrm{th}}}{B_{\mathrm{el}}} = \frac{2 \cdot \beta}{(1-\beta) \cdot \delta} \tag{12.14}$$

$$\mathrm{SC} = \frac{\text{Solder area}}{\text{Carrier area}} = \alpha \cdot \left(\frac{\delta \cdot \mathrm{AR}}{2 + \delta \cdot \mathrm{AR}} + \frac{2}{\mathrm{AR}} \right) \tag{12.15}$$

Solder lifetimes as a function of AR and SC were then derived by substituting above relations to the response surface model as given by Eq. 12.1. Figure 12.16 is a contour plot for various LGA solder life cycle values as a function of SC and AR. The position of package B in the plot is also demonstrated. It shows that solder

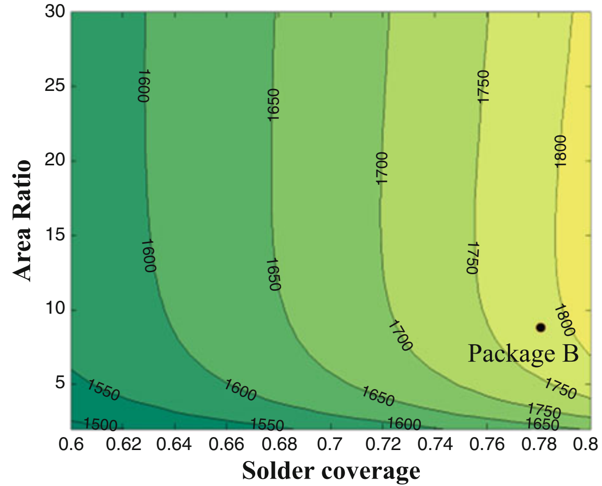

Fig. 12.16 LGA solder life cycles in LED package as a function of AR and SC (at constant $A = 38\ \text{mm}^2$, $\alpha = 0.8$, and SOH = 125 μm)

coverage SC can strongly affect the lifetime. It is observed that the lifetime decays dramatically with SC decreasing.

Figure 12.17 shows the relation between SC and solder lifetime in different AR values at the condition of constant carrier size, α, and SOH as 38 mm^2, 0.8, and 125 μm. It is illustrated that with SC increasing from 0.5 to 0.8, the lifetime increases about 30% for all cases. This is mainly because of a lower stress level induced inside the solder joint by increasing the load handling area. Thus, to achieve better solder reliability, it is possible to enlarge the solder coverage by increasing the solder pad area.

Additionally, according to Figs. 12.16 and 12.17, it appears that AR is an important factor for solder lifetime as well. In the particular case shown in Fig. 12.17, solder lifetime drops with decreasing AR for a fixed value of solder coverage. However, Fig. 12.16 and a further investigation of the lifetime as a function of AR demonstrate that there exists an optimal AR value for optimal solder reliability. The existence of an optimal AR can be explained by considering two competing effects when varying AR. The first effect is the enlargement of thermal solder joint, which means more load will be carried by thermal solder instead of critical solder joint for electrical connection, leading to an increase in lifetime. On the other hand, for larger AR values, the solder joint for electrical connection will become smaller, and hence a higher stress concentration within the solder interconnection is introduced, leading to a decrease in lifetime. This phenomenon is depicted in Fig. 12.18. The small dashed line demonstrates the relation between lifetime and Y when the size of the electrical solder joint is kept constant. When AR increases, the size of the thermal solder joint becomes larger, and therefore, lifetime rises. The dotted line indicates the relation between lifetime and AR when the size of the thermal solder joint is kept constant. In that case, when

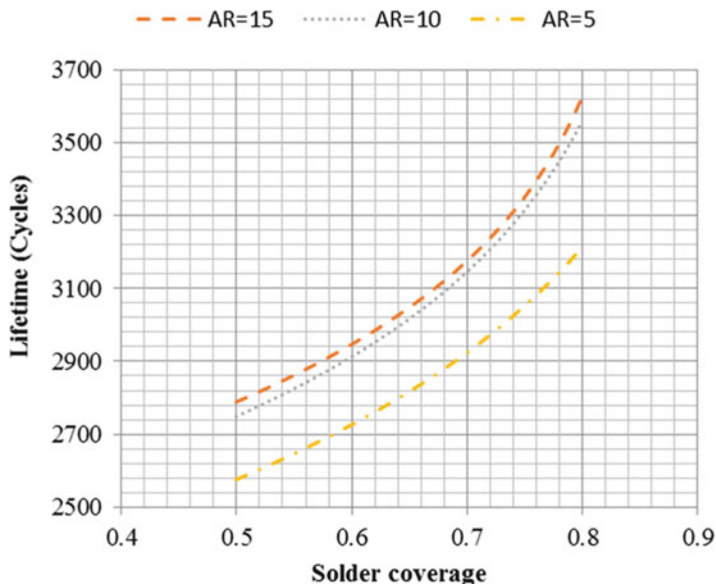

Fig. 12.17 Lifetime as a function of solder coverage in different AR values (at constant $A = 38\ \text{mm}^2$, $\alpha = 0.8$, and SOH = 125 μm)

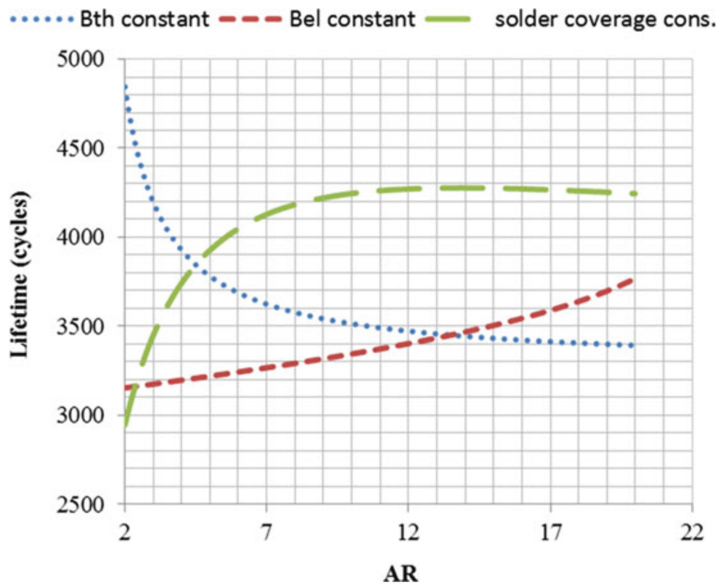

Fig. 12.18 Lifetime as a function of AR at different conditions

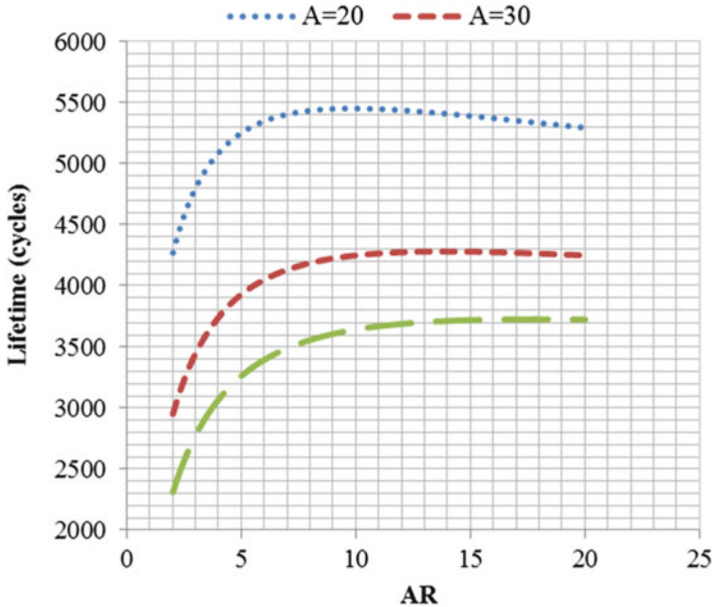

Fig. 12.19 Lifetimes as a function of AR with different carrier size

AR increases, the size of the solder joint for electrical connection becomes smaller and accordingly decreases in solder lifetime. The large dashed line is the next result of these two effects when setting the solder coverage as constant, namely, constant total amount of solder joint in case of constant carrier size A as 38 mm^2 and constant SOH as 125 μm. It is worth noting that when AR increases from 2 to about 14, an increase of lifetime of about 45% is predicted. Such an improvement in lifetime due to AR optimization is significant and almost adds no additional cost to the final product.

Figure 12.19 illustrates the lifetime-AR relation in terms of different carrier size levels. It shows that the optimal AR value decreases with decreasing carrier size. Hence, it is important to investigate the relation between this optimal AR and other geometric parameters. The relation of the optimal AR with different carrier size and solder coverage was determined by setting the first derivative of lifetime versus AR to zero using the response surface model. In that case, the optimal AR as a function of carrier size and solder coverage at constant $\alpha = 0.90$ and SOH = 125 μm was obtained, which was a mathematical expression numerically solved by Mathematica 8.0. Thus, in order to demonstrate this relation, a series of 2000 optimal AR data points were calculated for 50 different carrier sizes (from 15 to 65 mm) and 40 values of solder coverage (from 0.6 to 0.8), and the results are plotted in Fig. 12.20.

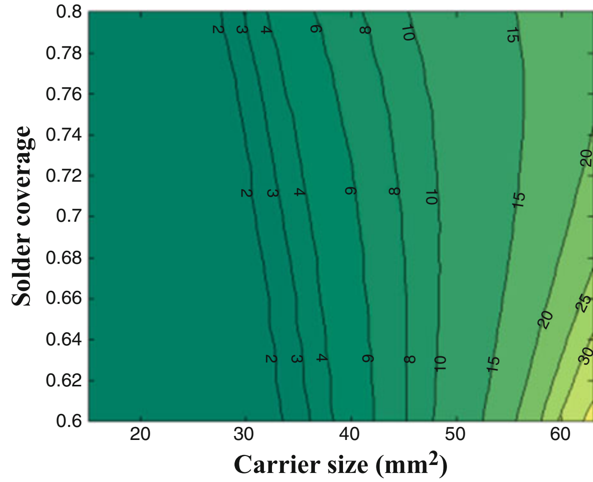

Fig. 12.20 Contour plot of optimal AR as the function of carrier size and solder coverage

Figure 12.20 shows that the maximum optimal AR value occurs when the package has a large carrier size and a low solder coverage value. It can be explained by the fact that when the chip carrier is large and solder coverage is small, it is more effective to allocate more solder material as thermal solder joint, which means increase the AR value. Therefore, more loads are applied to the thermal joints rather than the joint for electrical connection. It also shows that a reduction of the carrier size will result in a decrease of the optimal AR ratio. This is due to the fact that it becomes more important to reduce the stress concentration by enlarging the critical electrical solder joint when chip carrier is small. Similarly, when the carrier size is large, there will be a higher load applied to the solder joint. Therefore it is more effective to increase the thermal solder joint to carry the load for better reliability, especially for low solder coverage values. It is for this reason why the optimal AR value rises dramatically with decreasing solder coverage at large carrier size level. The relations are demonstrated in Fig. 12.21.

In addition, it is clear that a certain chip carrier size value exits, where the optimal AR changes its trend with the solder coverage. When the chip carrier size is large, a higher load level in the solder joint results and the optimal AR value increases with increasing solder coverage. On the contrary, when the chip carrier size is small, the optimal AR value drops with increasing solder coverage value for smaller package. This can be explained by the fact that small carrier size results in relatively small load in the solder joints; hence, avoiding stress concentration in the electrical solder joint becomes more important. In that case, to achieve better solder reliability, it is more efficient to allocate the additional solder materials induced by increasing solder coverage to the electrical solder joint in order to reduce the stress concentration level.

Moreover, when solder coverage is larger, the optimal AR changes more slowly with carrier size. The reason is since the load is already distributed better due to a

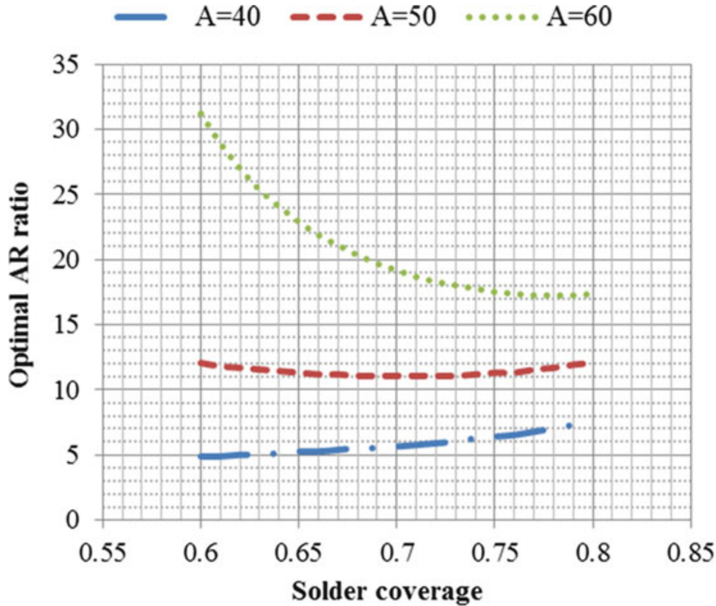

Fig. 12.21 Optimal AR value as function of solder coverage in different carrier size

larger solder area, it is less effective to enhance the reliability by increasing the AR ratio to handle the load even better. Furthermore, when carrier size is small, the optimal AR value varies insignificantly with the solder coverage and carrier size. For smaller package, the relatively small optimal AR value indicates that comparable thermal and electrical pad area will lead to better reliability, because stress concentration in one particular solder joint can be reduced as much as possible. Similar results are found when the same response surface model analysis is conducted for package A. For carrier sizes from 10 to 20 mm^2, it is found that all the optimal AR values indicate that the size of thermal and electrical pads should be comparable.

12.4 In Situ High-Precision Fatigue Damage Monitoring During Accelerated Testing of Solder Joint

Fatigue failures of solder joints are one of the most common failure mechanisms in electronic packages [4, 11, 15, 17, 53]. Accelerated thermomechanical tests have been developed to evaluate solder reliability in terms of solder fatigue failure for many types of packages, such as from small wafer level chip-scale packages (WLCSP) to large-scale land grid array (LGA) packages [54–58]. However, evaluating the reliability of electronic packages in real conditions remains a time-consuming practice [59–65]. Thus, fast reliability methods based on accelerated

thermomechanical test remain highly desirable especially for long-term applications (i.e., solid-state lighting), driven by short product-to-market time and low cost [2].

The testing time is related to the definition of failure indicator, which determines when to terminate the test. Various criteria, such as complete electrical circuit opening, a 50% reduction in measured stress amplitude on a solder joint, a 50% crack propagation across the solder joint, or a 30% increase in the electrical resistance, are often employed [66–72]. However, these failure indicators focus only on the final catastrophic failure and have little power to indicate failure well in advance. It is well known that solder fatigue consists of two consecutive processes: a relatively long viscoplastic deformation accumulation stage and an often shorter resultant fatigue crack initiation and propagation stage [18, 73–75]. Thus, if both types of fatigue damage can be carefully monitored, it seems feasible to define a more appropriate indicator for terminating the accelerated test at a relatively early stage and predict the final failure time based on the monitoring data to substantially save testing time. However, most of the current approaches are not capable of in situ monitoring the fatigue damage in the viscoplastic deformation accumulation stage of individual solder joints in parallel in a real package, not even for typical industrial reliability test with large temperature variations and complex stress and strain states in the joints [39, 76, 77].

Electrical resistance measurement seems a proper way of monitoring the damage in situ and in parallel for multiple solder joints. Liu et al. succeed in monitoring the crack propagation of individual solder joint during accelerated thermomechanical testing using electrical resistance measurement [78, 79]. However, due to an insufficient measurement accuracy and a nonoptimal electrode configuration, the resistance evolution during viscoplastic deformation accumulation could not be captured. Two of the biggest challenges are (i) to select an appropriate damage indicator and (ii) to identify crack initiation according to the selected damage indicator.

Finally, it should be mentioned that a successful definition of a measurable fatigue damage indicator of solder joints will be crucial in the development of more accurate remaining useful life (RUL) prognostic. As electronics have become vital to provide safer, more reliable, and cost-effective systems in applications such as avionic and automotive, the capability of accurate RUL prognostic will create remarkable added value to such industries [7, 10, 80–82].

In this section, a test approach using periodic high-precision electrical measurement that can monitor the fatigue damage evolution in solder joints subjected to temperature cycling is presented. A series of individual SAC 305 (96.5% Sn, 3% Ag, 0.5% Cu) solder joints are tested in a climate chamber for which the temperature is cycled. The electrical resistance of each solder joint is monitored during test using a conventional four-point resistance measurement structure with specially configured electrodes and a built-in temperature sensor per electrode in order to derive the resistance-temperature relation for each cycle of the test. It is found that the temperature coefficient of resistance (TCRc) of a particular solder joint tends to increase continuously with the number of cycles (NoC) due to the development of

fatigue damage. This finding is correlated with the results both from semi-online tomographic analyses and those from FEA simulations. The crack initiation point was estimated from the first derivative of the TCRc-NoC curve. It is shown that in situ fatigue damage monitoring of many solder joints in parallel can indeed be achieved by the use of high-precision electrical measurements.

12.4.1 Geometric Details of Test Sample

A specially designed ceramic print circuit board (PCB) is adopted as a dummy ceramic chip carrier in the test sample assembly. Pictures of the ceramic PCB in top and bottom views are shown in Fig. 12.22.

The alumina ceramic PCB measures 4 mm × 4 mm × 0.6 mm. The trace material on the ceramic PCB is silver-palladium. The large silver-palladium pad on the bottom side measures 3 mm × 3 mm × 0.01 mm with two extension leads. These leads are designed for the four-point electrical resistance measurement setup. In order to connect to the leads, two through board vias and corresponding bond pads were made as also shown in Fig. 12.22. The solder mask defined a soldering area of 2 mm × 2 mm in the center of the large Ag-Pd pad. This ceramic dummy board was mounted on a metal cored printed circuit board (MCPCB) by one single-solder joint made of SAC 305. The MCPCB measures 40 mm × 20 mm × 1.6 mm, and the corresponding copper pad of MCPCB to the large Ag-Pd pad on the bottom side of ceramic board is 3 mm × 3 mm × 0.05 mm. Additionally, a built-in cross-bridge Kelvin resistor (CBKR) structure consisting of a copper trace in a MCPCB was present closely to the solder interconnect as an onboard temperature sensor to be read out via its sheet resistance. During the final assembly, two connectors were soldered onto the sample for electrical resistance monitoring of the solder joint and the onboard temperature measurement. Two columns of holes were drilled at both

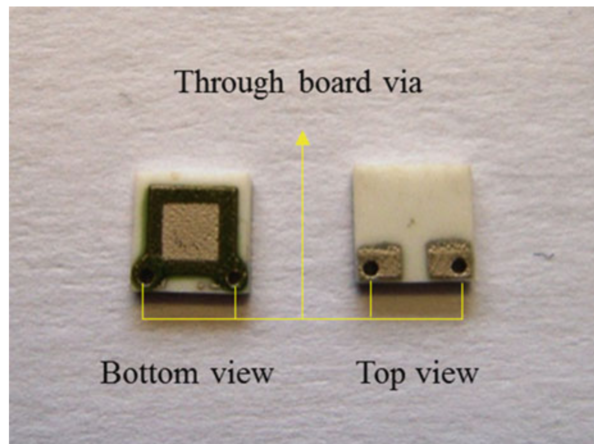

Fig. 12.22 *Bottom* and *top views* of the ceramic PCB dummy

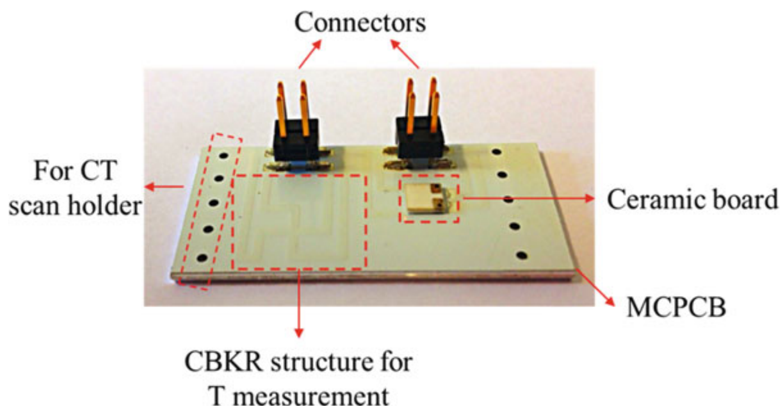

Fig. 12.23 A picture of the test sample assembly

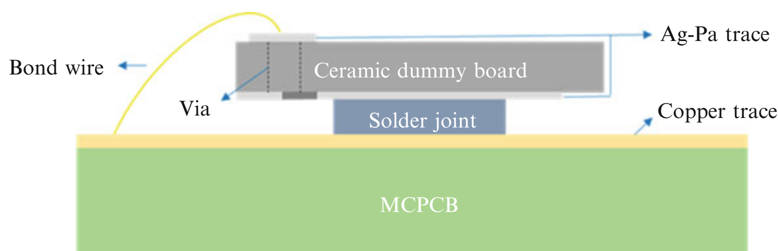

Fig. 12.24 Layout of ceramic package tested (*side view*, not to scale)

sides of the MCPCB to facilitate microtomographic scanning of the sample. A picture of the assembled structure is presented in Fig. 12.23.

Solder interconnects were made using the solder paste screen printing technology followed by the conventional reflow process. The designed standoff height (SOH) of the solder joint was 150 μm, which was achieved by employing a specially designed stencil in the screen printing process and using a metal foil spacer in the reflow process. During the reflow process, the boards were heated from room temperature to 150 °C in about 50 s, followed by a preheat stage to slowly heat up the boards to 200 °C in 120 s. The boards were then heated up to the soldering temperature 260 °C in 20 s with a 30 s dwell time. Afterward, the boards were cooled down with a rate of −7 °C/min. Once the ceramic board was attached to the MCPCB, three bond wires (gold wire, $\Phi = 30$ μm) were made to link each Ag-Pa pad to the corresponding copper pad on the MCPCB. The solder joint is not located in the very center of the MCPCB but 20 mm away from one of the edge. A schematic drawing of the test assembly in side view is depicted in Fig. 12.24.

12.4.2 Temperature Sensor Calibration

In order to measure the onboard temperature during the thermomechanical test, the sheet resistance of the copper trace was monitored because of its good linear temperature dependence given in Eq. 12.16:

$$R_{\mathrm{th}} = \beta_{\mathrm{T}} \cdot T + R_0 \qquad (12.16)$$

where R_{th} is the sheet resistance of copper trace (Ohm), β_{T} is the temperature coefficient of sheet resistance of copper with corresponding thickness (Ohm/ °C), T is temperature (°C), and the R_0 is the sheet resistance at 0 °C (Ohm)

Since the thickness of the copper traces may vary slightly from sample to sample, calibrations for each onboard sensor were made to derive individual resistance-temperature relations for optimal temperature measurement accuracy. Thus, while heating up the samples from room temperature to 70 °C by a hot plate (UC150, Stuart), the sheet resistance of the copper trace is measured five times at each fixed temperature monitored by a surface resistance temperature detector (SA1-4 W-80, class A, Omega), which was glued on top of the CBKR structure. In order to have a better control of the onboard temperature, the sample was covered by a plastic cap. A picture of the calibration setup was shown in Fig. 12.25.

The derived slopes and intercepts of the R-T relation shown in Eq. 12.1 are listed in Table 12.11. The minimum and maximum measurement uncertainties based on the regression analysis and posing 99.9% confidence levels are also listed in Table 12.11.

12.4.3 Thermomechanical Test

Test samples were attached on a quartz boat by high-temperature taps, put into a climate chamber (TPS TENNEY MODEL: TUJR), and thermally cycled from 0 to 125 °C. A picture of the samples in the climate chamber is shown in Fig. 12.26.

The temperature profile imposed in this temperature cycling test is based on the JEDEC standard: JESD22-A-104-B. The ramp rate is 5 °C/min, and the dwell time at high temperature and low temperature were 8 min and 2 min, respectively. Thus, a full cycle should take 1 h.

12.4.4 In Situ DC Electrical Resistance Monitor Setup

The test setup to monitor damage evolution in the solder connects during thermal cycling is depicted in Fig. 12.27.

Four-point resistance measurement was employed to eliminate the effects of contact resistance between the contact and the solder joint, using an electrode

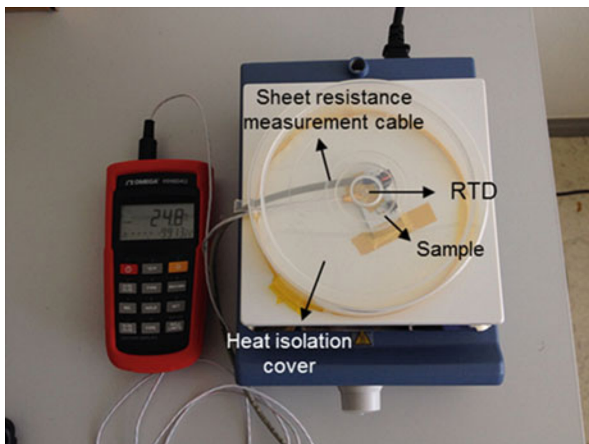

Fig. 12.25 Onboard sensor calibration setup

Table 12.11 Detailed information of linear RT relations adopted

	β (μΩ/°C)	R_0 (μΩ)	T measurement uncertainty (min. and max.)
Sample 1	0.538	112.32	±0.5 and ±0.8 °C
Sample 2	0.544	113.00	±0.4 and ±0.7 °C
Sample 3	0.538	111.82	±0.5 and ±0.8 °C
Sample 4	0.540	111.68	±0.5 and ±0.8 °C

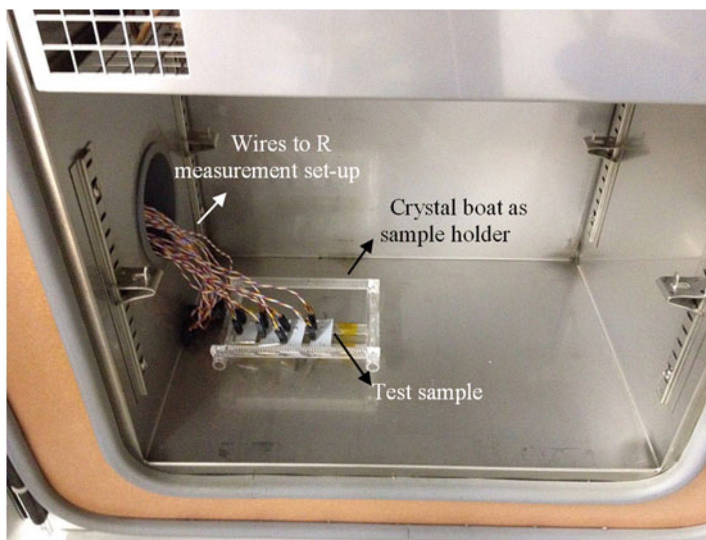

Fig. 12.26 Test samples in the climate chamber

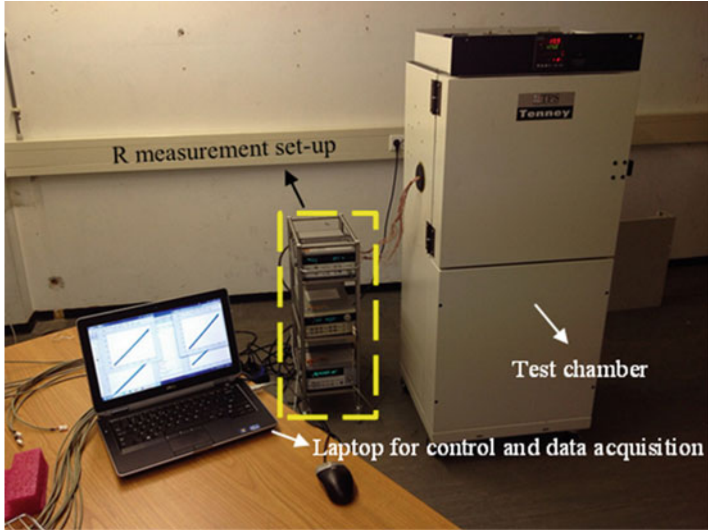

Fig. 12.27 Overview of the test setup

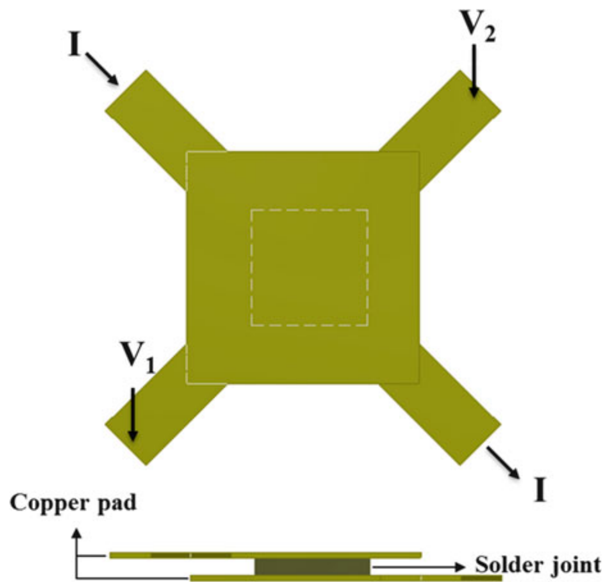

Fig. 12.28 Schematics of the four-point measurement connections, *top* and *side views*

configuration shown schematically in Fig. 12.28 (and presented in detail in the previous chapter). Considering the complexity of the deformation in the solder joint during temperature cycling, knowledge gained in Chap. 5 regarding effects of electrode alignment cannot be easily applied in the current case. However, in order to enhance the sensitivity to the thermal displacements in the joint, the

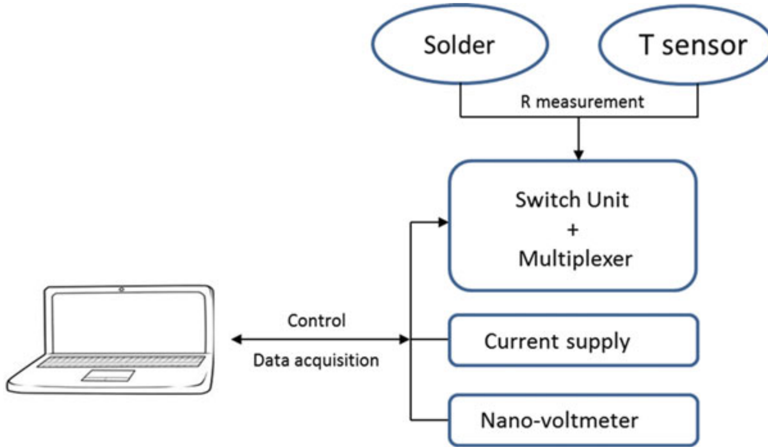

Fig. 12.29 Schematic diagram of the resistance online monitor setup

electrodes were aligned in such a way that the current direction is along the longer side of the rectangle MCPCB, wherein the displacement is more pronounced.

The setup basically consists of three parts: a switch unit module, a resistance and temperature measurement module, and a synchronization module. A schematic diagram of the setup is illustrated in Fig. 12.29. All leads for the resistance measurement of both solder joint and temperature sensor were connected to the switch unit (Agilent 34970A Data acquisition/switch unit equipped with Agilent 34901 multiplexer modules) with multiple channels by well-twisted high-temperature-resistant copper electrical wire. This switch unit together with the resistance and temperature measurement module was connected to a computer to conduct the channel switching, data measurement, online visualization, and final data acquisition using Matlab Instrument toolbox.

Samples were monitored every 60 s in a fixed sequence throughout the temperature cycling test. For each sample, firstly the resistance of the solder joint is measured, while corresponding temperature is derived 1 s after the resistance measurement by the onboard sheet resistance measurement. In order to measure both solder resistance and sheet resistance, four different levels of current (0.1, 0.3, 0.5, and 0.7 A) were forced through the electrode and resulting voltage levels were sensed by Agilent 34420A nanovoltmeter, which has a resolution down to 1 nV. A linear regression was made with the corresponding voltage-current relation, and the slope was derived as the electrical resistance. Using this method, any voltage offset effect is fully eliminated and the influence of the external noise can be also reduced. The temperature value was then calculated based on the linear relations that had been derived and listed in Table 12.11. For each thermal load cycle, the temperature coefficient of resistance of each solder joint was determined, which is taken as an indicator of the fatigue damage evolution in the solder joint.

12.4.5 Micro-tomography Scans of the Solder Assembly

To verify the detection of cracks in the solder joint, ex situ micro-tomography scans were made at several stages of the cyclic loading process. The micro-tomography scans of the dismounted assembly were made using a GE Phoenix Nanotom S machine. A general description of the principle of micro-tomography using standard laboratory instruments can be found in [83]. In the experiments, 30 KeV radiation from a wolfram-molybdenum target was used. During the tomographic measurements, the sample was rotated over 360° at a rate of 5° per min. To maximize the resolution for a given total scan time, two scans were made. This results in a spatial resolution of about 4 μm.

12.4.6 Temperature Coefficient of Resistivity of SAC 305

In order to provide precise input data to the finite element model, the temperature coefficient of resistivity of SAC 305 was experimentally derived separately. A thin bar made out of a casted SAC 305 bulk sample provided by MaTech B.V. was fabricated with great precision by electrical discharge machining. The dimensions of the bar were 70 mm × 1 mm × 1 mm. Two wires were glued on both ends of the bar in order to perform a four-point resistance measurement. A surface RTD sensor (SA1-4W-80, class A, Omega) to be connected to a reading unit HH804 is attached in the middle of the bar to measure the temperature during the testing. Pictures regarding the sample dimensions and the wiring are shown in Fig. 12.30.

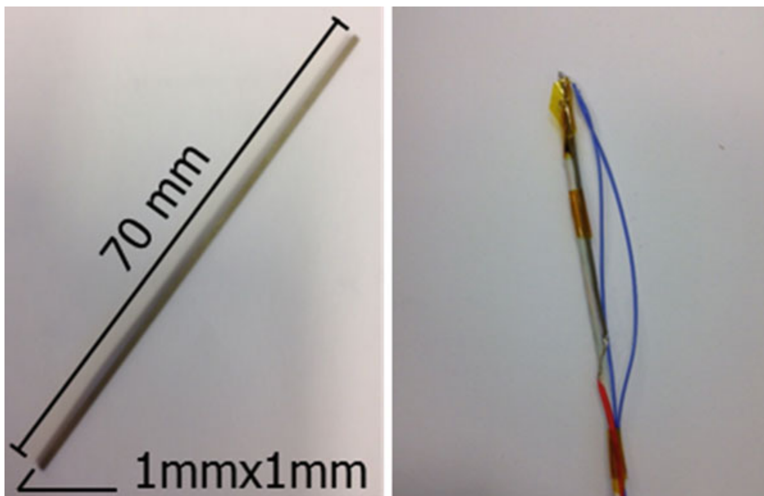

Fig. 12.30 Sample for TCR measurement, dimensions, and wiring

The whole sample was then inserted into an oven to be heated from room temperature to around 80 °C, and meanwhile the resistance was measured by a source meter (Keithley 2400) at seven different temperature levels. For each temperature level, four measurements were taken. The resistivity is calculated by Eq. 12.17 from the resistance measured:

$$\rho = \frac{R \cdot A}{l} \tag{12.17}$$

where ρ is the resistivity of SAC materials; R is the measured resistance; A is the cross-section of area of the bar, which is 1 mm by 1 mm; and l is the length of the bar measured as 70 mm. The test results are listed in Fig. 12.31.

The derived resistivity at 20.8 °C of the solder joint matches the resistivity value at room temperature reported in literature for this material [84]. The temperature coefficient α can be then derived by the linear regression of the ρ-T relation as 4.41×10^{-2} °C^{-1}, a value that is exported into the finite element model. The definition of α is shown in Eq. 12.18:

$$\rho\,(T) = \rho_0 \cdot (1 + \alpha \cdot T) \tag{12.18}$$

where T is temperature in Celsius and ρ_0 is the resistivity at 0 °C.

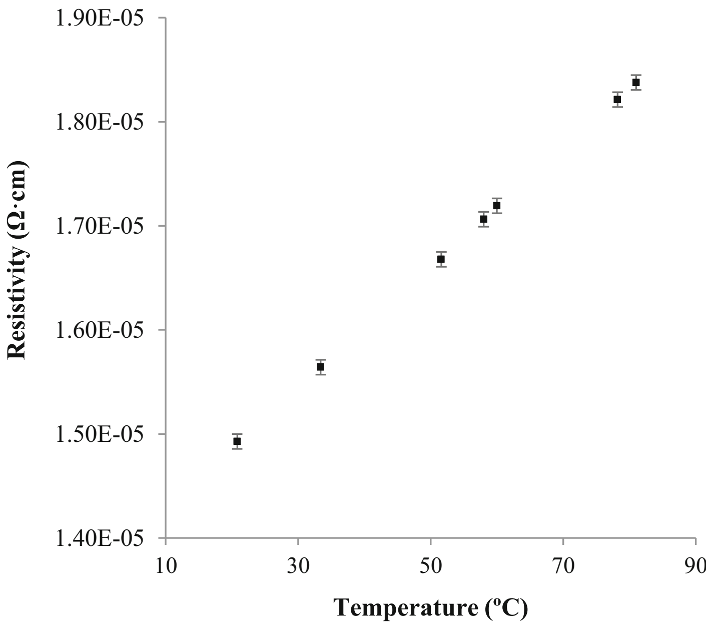

Fig. 12.31 Resistivity as function of temperature for SAC305

12.4.7 Finite Element Model and Simulation Details

To assist in the interpretation of the experimental data to be acquired, a series of FEM simulations was conducted both in ANSYS and Comsol for thermomechanical and electrical-mechanical simulations, respectively.

Thermomechanical simulations were conducted in ANSYS to reveal the complex displacement in the joint and to predict the crack initiation point of this type of package when subjected to the temperature profile described in Sect. 12.4.3. A meshed structure of the FEM model is shown in Fig. 12.32. A half model of the assembly was adopted. In the simulations, four temperature cycles were imposed.

The position of the ceramic on the MCPCB in the model is the same as in the real assembly. In the model, silver-palladium is treated as copper as its thermomechanical properties were not available. The layers in the model from top to down are then ceramic dummy ($4 \times 2 \times 0.6$ mm), upper copper layer ($3 \times 1.5 \times 0.05$ mm), SAC405 solder joint (two cases: $2 \times 1 \times 0.15$ mm and $2 \times 1 \times 0.2$ mm), lower copper layer ($3 \times 1.5 \times 0.05$ mm), dielectric layer in MCPCB ($40 \times 10 \times 0.1$ mm), and Al substrate of MCPCB ($40 \times 10 \times 1.5$ mm), respectively. All material property values can be found in Sect. 12.2. A viscoplastic deformation model for SAC405 solder joint that had been described in Sect. 12.2 was adopted. Considering the scattered solder SOHs in different sample assemblies, simulations were made for two scenarios with SOH as 150 μm and 200 μm, respectively. Additionally, appropriate mesh sensitivity tests were done. It was found that with mesh density larger than 3×10^5 element/mm^3 in the critical solder joint, the influence of the mesh density on the total volume of the most critical elements and the calculated fatigue indicator ΔW_{sc} were limited and within 5%.

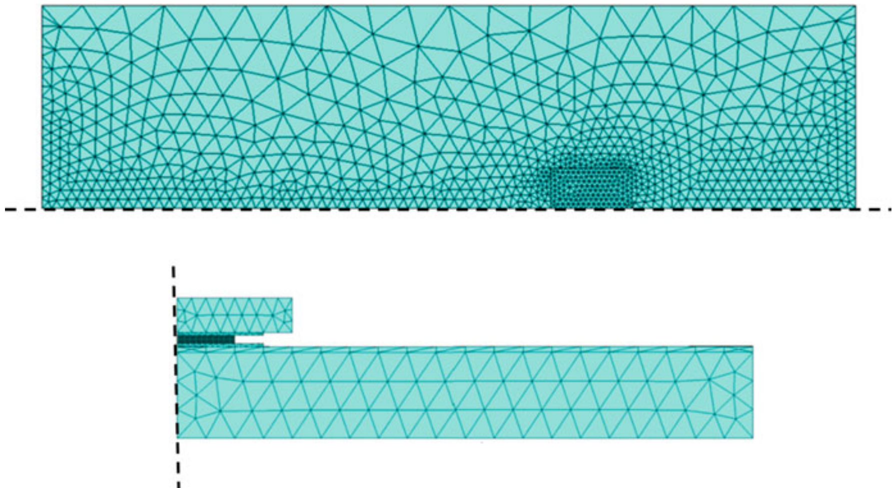

Fig. 12.32 Meshed structure in FEM simulation model: *top* and *right* (not to scale) views

Moreover, in order to investigate the deformation and crack effect on the temperature coefficient of resistance (TCRc) of solder joint, electrical simulations were done to derive TCRc fluctuation as function of deformation and crack size separately. According to ANSYS simulation results, the solder joint becomes more terrace shaped due to the coefficient of thermal expansion (CTE) mismatch of ceramic dummy and the MCPCB substrate. Besides, the upper copper trace tends to tilt along the longer side of the MCPCP with progressive test cycles, which is shown in Fig. 12.33 (demonstrated deformation is not to scale, but with a scale factor of 100).

It is seen that the upper copper trace tend to bend toward the temperature sensor direction, and meanwhile the other side of the trace is departing from the lower trace. Thus, in the electrical simulation, the complex displacement of solder joint is simply implemented by a change in the solder joint shape as explained in Fig. 12.34 together with the meshed structure of the FEM model with 100 μm expansion on each side.

Assuming the volume of the solder joint remains constant and the volume reduction by the trace tilt (shadowed area in Fig. 12.34) is compensated by the terrace slope gain (two triangle area in Fig. 12.34) at both sides of the solder joint, the quantitative indicator of the deformation can be simply selected as expansion b as defined and shown in Fig. 12.34.

Simulations with expansions of 25, 50, 75, and 100 μm were conducted. In order to determine the effect on TCRc, two simulations were made for each TCRc at 20 °C and 80 °C. TCRc changes as a function of deformation were determined. It should be noted that the misalignment of two copper trace is marginal. Therefore, the influence of the copper traces misalignment resulting from thermomechanical

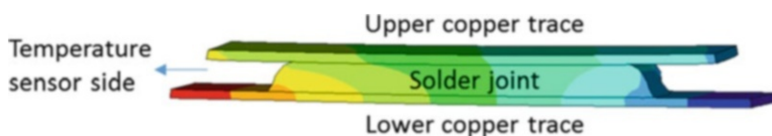

Fig. 12.33 Simulated vector sum displacement of the deformed structure (scale factor of 100) at high dwell temperature after 3 cycles

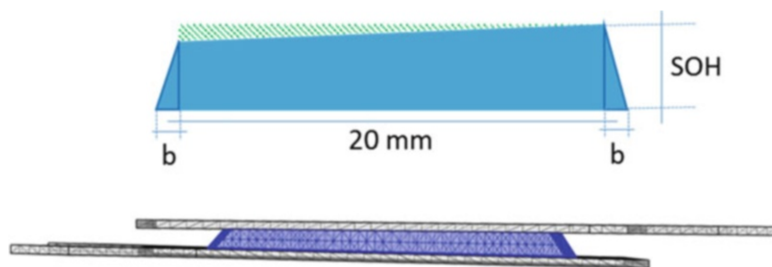

Fig. 12.34 Explanatory drawing about deformation implementation to FEM model and a meshed structure of the model with expansion of 100 μm at both sides

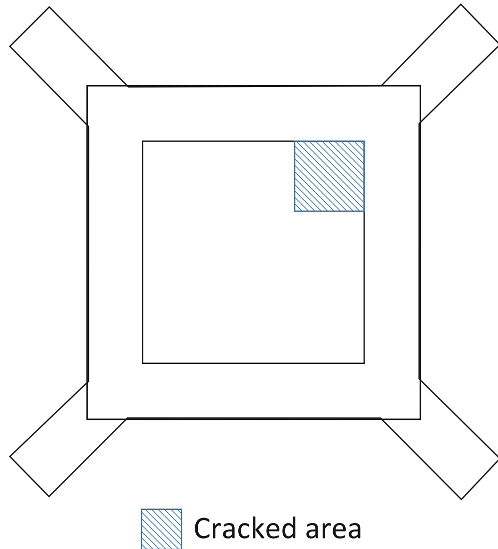

Fig. 12.35 Schematic overview of the model geometry for the 10% crack area case

load was not taken into account in the model. The electrical resistivity of copper at room temperature (20 °C) adopted in the model is 1.68 × 10–8 Ω m and the temperature coefficient of resistivity is 3.86 × 10–3 $°C^{-1}$ [85]. The electrical resistivity of SAC405 employed in the FEM model is 1.23 × 10–7 Ω m [84] and temperature coefficient of resistivity adopted is 4.41 × 10–3 $°C^{-1}$ as derived in previous Sect. 12.4.6. Silver-palladium layer was again treated as copper in the electrical simulation due to the difficulties of finding the temperature coefficient of resistivity of the materials.

In addition, simulations with the nondeformed model geometry were also conducted with different crack sizes as 0%, 10%, 30%, 50%, 70%, and 90%.

A thin square platelike domain with a thickness of 5 μm was removed at the C-sided corner of the solder joint to induce a model crack. The assumed crack was located halfway the solder standoff height. The relation between the crack size and the electrical resistance change was investigated by altering the size of the crack. A schematic drawing of a model with a 10% cracked area is shown in Fig. 12.35.

A relation between the solder TCRc and the internal crack size was determined.

12.4.8 Monitored Fatigue Damage Evolution and Crack Initiation Determination

First of all, it should be noted that no complete failure was observed in any of the samples at the time of writing of this book (at 3481 cycles). In order to demonstrate the damage evolution during these first 3481 cycles, a proper damage indicator

should be selected related to the resistance measurement results. Using the resistance is no long appropriate, as it is highly temperature dependent. Instead, (also taking into account that complete sample failure had not occurred) changes in the temperature coefficient of resistance (TCRc) are taken as an indicator for the damage evolution, as has been done earlier for evaluating material degradation, such as copper interconnect and composite [86, 87]. However, these methods only highlight the microstructural effects or the crack effects on the TCR fluctuation, whereas in current case, it would be crucial to have the viscoplastic deformation monitored by TCRc measurement. Therefore, in this study, the TCRc values were derived by linear regression of all measured resistance-temperature data sets within a particular cycle (about 60 pairs in ramp and also in dwell). The TCRc values of all sample assemblies in the first five cycles are listed in Table 12.12.

Any TCR value is the product of the (volumetric) material response and a geometrical factor (SF) defining the net geometrical contact zone covered by the interconnect (thereby taking into account both viscoplastic shape changes, as well as interfacial and intra-solder cracks, pores, or other spatial defects).

The normalized TCRc at each sequential cycle is calculated by subtracting the initial TCRc listed in Table 12.12 from actual TCRc and then dividing again by the initial TCRc. These normalized TCRc values are plotted as a function of number of cycles in Fig. 12.36. For all solder joints, the initial slowly increasing stage is followed by a stage of a more rapid increase in TCRc with NoC. Most remarkably, for a given joint, the normalized TCRc value at a particular NoC was always equal or higher than that for the previous data point. The absence of scatter along a single

Table 12.12 TCRc of each joint derived at the first five cycles

	Joint 1	Joint 2	Joint 3	Joint 4
TCRc (nΩ/°C)	495.3	502.6	526.7	400.6

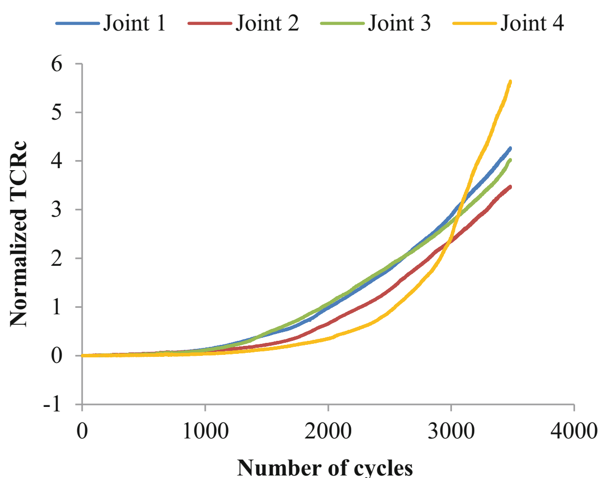

Fig. 12.36 Normalized TCRc plotted against number of cycles

curve is a clear indication of the stability of the installation and the measuring devices, as well as the robustness of the protocol to determine TCRc. Please realize that the total duration of the measurement is about 3600 h (or 5 months!). The figure shows a rather similar behavior for all four joints, with a slightly different behavior for joint 4, which was slow to enter the "fast increase stage," but once the normalized TCRc increased, the rate of increase was higher than that for the three other joints.

We will now try and interpret the change in normalized TCR. Many variations of the solder materials during the temperature cycling test can have an impact on the resistivity fluctuation and further affect the TCR, such as grain growth, precipitant coarsen, IMC layer growth, and recrystallizations. Firstly, since the temperature difference of the cycling test is not extreme and the cooling rate is slow (about 5 °C/min), recrystallization process is less pronounced and localized only in some high-strain spots, which becomes less influential on joint resistivity and can be neglected [88–90]. Furthermore, according to the aging studies on SAC305 solder by Cook et al. [84], Kang et al. [91], and Guo et al. [92], IMC layer growth will be a dominating mechanism to influence the resistivity fluctuation surpassing all changes in the solder matrix, such as grain growth and precipitants coarsen. Since the IMC Cu_6Sn_5 which might form at the interface is a better conductor than the matrix SAC 305, any IMC layer growth will only result in a resistance decrease. However, the experimental results show that the resistance at high temperature (100 ± 1 °C) only increases with number of cycles (see Fig. 12.37), which demonstrates the marginal effect (if present at all) of IMC layer growth. Thus, the captured TCRc growth during ALT is most likely due to SF change rather than changes in the temperature coefficient of resistivity of the material itself.

Therefore, it can be assumed that the solder electrical resistance change during the DLS test can be mainly attributed to the two processes: viscoplastic deformation of the joint and resultant crack formation. Thus, it is reasonable to assume viscoplastic deformation is most likely to be the main cause for the early slow and synchronized TCRc increase stage, and the crack initiation and propagation can be considered as the major reason for the fast solder TCRc increase stage. We can use the FEM model to see the predicted effect of viscoplastic deformation on the TCRc. The predicted effect on the change in normalized TCRc with different expansion displacement is shown in Fig. 12.38.

A slow increasing trend of normalized TCRc with progressive expansion displacement is observed, which confirms our hypothesis. It appears that even the displacement is as large as 100 μm, the resultant TCRc change is only maximum 40%. Additionally, the increasing trend of TCRc according to progressive displacement also turns slower when displacement is accumulated. Therefore, it seems highly unlikely that the measured large change in normalized TCRc achieved (<3) in the late stage of the test can be exclusively attributed to viscoplastic deformation. The only possibility left is the crack effect then.

The effects of crack size on TCRc changes derived from FEM simulations are demonstrated in Fig. 12.39. It appears that TCRc will dramatically increase with progressive crack size to a level that is comparable to or even much larger than that

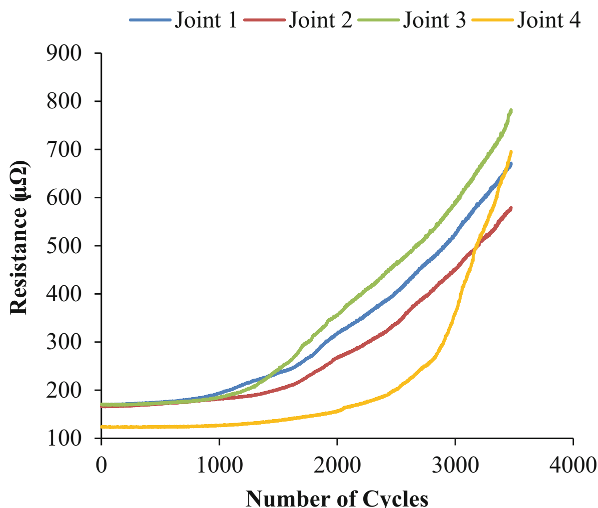

Fig. 12.37 Resistance evolution of each joint at around 100 °C (±1 °C) with NoC

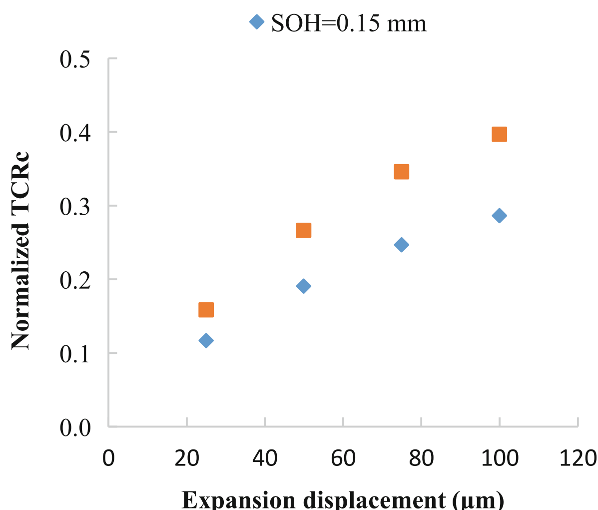

Fig. 12.38 Simulated effects of viscoplastic deformation on TCRc

has been observed experimentally. Furthermore, compared to Fig. 12.39, Fig. 12.38 shows a far more constant rate of increase in TCR with progressive displacement.

Since there were already many discussions on “slow” and “fast” TCRc change related to different root causes for the TCRc increase, it becomes vital to investigate the onset of the crack formation. Thus, the first derivative of the TCRc-NoC curves that reflect the increasing speed of TCRc is plotted against the number of cycles for each joint in Fig. 12.40. The first derivative was derived as the linear regression slope of every 10 points in the TCRc-NoC curve.

The figure shows a steady increase in the slope and in the scatter with increasing NoC. The scatter increase becomes more noticeable in the steeper part of the curve.

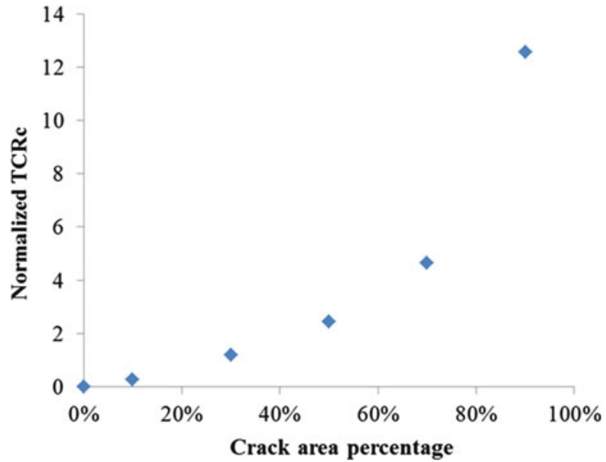

Fig. 12.39 Crack size effect on normalized TCRc derived by FEM simulations

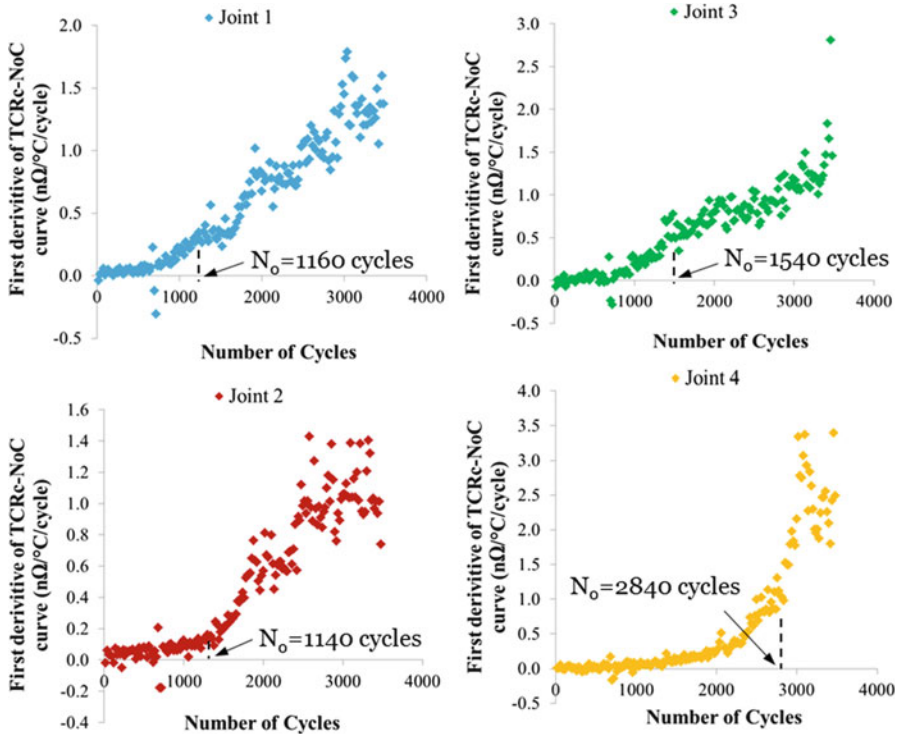

Fig. 12.40 First derivative of the TCRc-NoC curve plotted against the number of cycles and the derivation of the crack initiation cycle

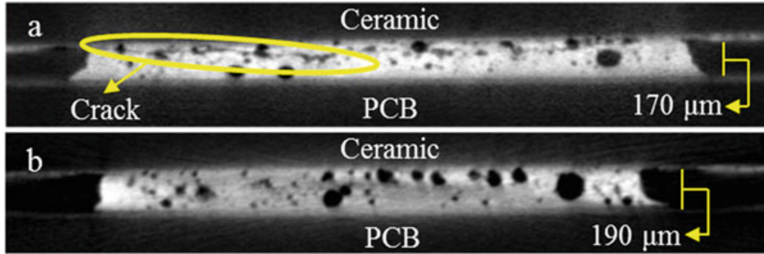

Fig. 12.41 Tomographic pictures of joints 1 (**a**) and 4 (**b**)

This change in scatter in the slope can be attributed to the fact that viscoplastic deformation accumulation in solder joint is a very stable process during temperature cycling test (i.e., causing little scatter when using good equipment and protocols), whereas the later fatigue crack propagation and crack opening and closure are a more stochastic process [3, 4, 19, 25, 93] (i.e., causing more scatter). The crack initiation point now can be identified as the particular test cycle at which a significant variance increase of the TCRc-NoC curve occurs. This has been done by zeroing down the curve average according to high-order polynomial fitting and deriving the variance changing point according to mathematic tool in Matlab 2014a. Details of the method are described in [94]. The predicted crack initiation cycle is shown as N_0 and marked in dashed line in Fig. 12.40.

These predicted crack initiation cycle is verified by tomographic scan results, which were obtained at cycle No. 1425. Considering the high risk of breaking the bond wires, scans were only conducted on joints 1 and 4 for just one time. The TC test was stopped at cycle No.1425, and these two samples were taken out from the chamber to the CT scanner for 3 days. The test was then resumed. The tomographic pictures of joints 1 and 4 are shown in Fig. 12.41. According to the crack initiation cycle predictions, a clear crack should be observable in joint 1, whereas no crack should be found in joint 4 at 1425 cycles, which is in full accordance with the tomographic results. In Fig. 12.41a, a crack initiated in the upper corner can be easily observed. However, no crack can be found in joint 4. Additionally, a relatively large difference in SOH between joints 1 and 4 was observed. As discussed in Chap. 3, variations in SOH can be one of the principal reasons for scatter in the crack initiation point. The observed crack initiation points for solders 1 and 4 are in accordance with the predictions from the FEM model when taking into account this difference in SOH.

The tomographic pictures also confirm simulated shape change of solder joint due to viscoplastic deformation accumulation. A clear terraced shape of joints 1 and 4 can be observed, and also the tilt of the copper trace is also presented. Moreover, another verification from tomographic results is that the simulated normalized TCRc with different cracked area size is quite comparable to the experimental findings for joint 1 at the CT scan cycle. It was revealed by the CT scan that the cracked area in the solder joint at cycle 1425 was about 10%, while the change in normalized TCRc at that stage was 14%. The normalized TCRc in this case derived

from FEM simulation is 12%, which shows good agreement with the experimental results. Additionally, considering the fact that viscoplastic deformation was not taken into account in the simulation, a slightly smaller normalized TCRc derived from simulation result is reasonable.

12.5 Summary

Solder reliability is considered as a vital issue for solid-state lighting product. It is of great importance to develop new methods to realize fast, accurate, and reliable qualification of these long lifetime expected joints, which becomes a vital capability and competitive edge for the industry. In this chapter, it is achieved in two approaches: FEM-based lifetime estimation and in situ high-precision damage monitor-based lifetime prediction.

As for modeling estimation, a series of FEM simulations corresponding to finished accelerated tests are conducted. The simulation results show good agreement with the experimental discoveries and suggest the necessity to develop a new critical element selection approach for LGA solder assemblies. Therefore, a new approach is proposed in this study based on statistical analysis of the element distribution of creep energy density. Adopting this new critical element selection method, a new energy-based fatigue model for predicting LGA solder lifetimes has been established by combining lifetime measurements with corresponding FEM simulations for different material combinations and different LED package configurations.

A RSM analysis is conducted to investigate the influence of geometry on solder reliability in a LED package. It is shown that a smaller carrier size and larger solder standoff height in general will result in better solder reliability. This effect is more pronounced in solder with smaller carrier size and larger standoff height. Additionally, solder reliability declines rapidly with solder coverage decreasing.

The ratio between thermal solder area and electrical solder area AR has a significant influence on solder joint reliability in a SSL system. The optimal AR value is also observed to relate to carrier size and solder coverage. In general, the optimal AR value increases with increasing carrier size, and this phenomenon is more pronounced in package with smaller solder coverage. Nevertheless, the optimal AR value decreases with solder coverage in small carrier size and increases when carrier size is large. It is found that a transition chip carrier size value exits, where the optimal AR changes its trend with the solder coverage value. In addition, when the chip carrier size is relatively small, it is advisable to make the thermal pad and electrical pad comparable. The proposed methodology in this work, a combination of energy-based fatigue modeling and FEM modeling, proves to be very valuable for solder reliability optimization for LED packages. This methodology can also be applied to optimize the solder performance in terms of thermal performance, electrical performance, and cost and combinations thereof.

As for in situ high-precision damage monitoring-based lifetime prediction approach, accelerated temperature cycling test was done to four LED-like board level ceramic packages with in situ periodic high-precision electrical resistance monitoring for each solder joint inside. TCRc fluctuation during the test of the solder joint was correlated to fatigue damage evolution in the joint. A method to identify the crack initiation point based on in situ TCRc monitoring of solder joint is demonstrated and verified by micro-tomographic results and FEM simulation predictions, which can be a quite attractive technique for solder accelerated test, joint quality screening test, and RUL prognostic.

References

1. W.D. van Driel, X.J. Fan, *Solid State Lighting Reliability: Components to Systems* (Springer, New York, 2012)
2. W.D. van Driel, C.A. Yuan, S. Koh, G.Q. Zhang, LED system reliability, in *Thermal, mechanical and multi-physics simulation and experiments in microelectronics and microsystems (EuroSimE)*, 2011 12th international conference on, (2011), pp. 1/5–5/5
3. H.U. Akay, N.H. Paydar, A. Bilgic, Fatigue life predictions for thermally loaded solder joints using a volume-weighted averaging technique. J. Electron. Packag. **119**, 228–235 (1997)
4. A. Schubert, R. Dudek, E. Auerswald, A. Gollbardt, B. Michel, H. Reichl, Fatigue life models for SnAgCu and SnPb solder joints evaluated by experiments and simulation, in Components and Technology Conference, 2003. Proceedings. 53rd (2003), pp. 603–610
5. E. Madenci, I. Guven, B. Kilic, *Fatigue Life Prediction of Solder Joints in Electronic Packages With Ansys* (Kluwer Academic Publishers, 2003).
6. P. Lall, M.N. Islam, N. Singh, J.C. Suhling, R. Darveaux, Model for BGA and CSP reliability in automotive underhood applications. Components Packag. Technol. IEEE Trans. **27**, 585–593 (2004)
7. P. Lall, M.N. Islam, M.K. Rahim, J.C. Suhling, Prognostics and health management of electronic packaging. Components Packag. Technol. IEEE Trans. **29**, 666–677 (2006)
8. N. Patil, D. Das, Y. Chunyan, L. Hua, C. Bailey, M. Pecht, A fusion approach to IGBT power module prognostics, in *Thermal, mechanical and multi-physics simulation and experiments in microelectronics and microsystems*, 2009. EuroSimE 2009. 10th international conference on, (2009), pp. 1–5
9. J. P. Hofmeister, P. Lall, E. Ortiz, D. Goodman, J. Judkins, Real-time detection of solder-joint faults in operational field programmable gate arrays, in *Aerospace Conference*, 2007 IEEE, (2007), pp. 1–9
10. J. Johansson, P. Leisner, Prognostics of thermal fatigue failure of solder joints in avionic equipment. Aerosp. Electron. Syst. Mag. IEEE **27**, 16–24 (2012)
11. W.W. Lee, L.T. Nguyen, G.S. Selvaduray, Solder joint fatigue models: review and applicability to chip scale packages. Microelectron. Reliab. **40**, 231–244 (2000)
12. M. Roellig, R. Dudek, S. Wiese, B. Boehme, B. Wunderle, K.-J. Wolter, et al., Fatigue analysis of miniaturized lead-free solder contacts based on a novel test concept. Microelectron. Reliab. **47**, 187–195 (2007)
13. S. Wiese, F. Feustel, E. Meusel, Characterisation of constitutive behaviour of SnAg, SnAgCu and SnPb solder in flip chip joints. Sensors Actuators A Phys. **99**, 188–193 (2002)
14. F.X. Che, W.H. Zhu, E.S.W. Poh, X.W. Zhang, X.R. Zhang, The study of mechanical properties of Sn–Ag–Cu lead-free solders with different Ag contents and Ni doping under different strain rates and temperatures. J. Alloys Compd. **507**, 215–224 (2010)

15. J.-H. Zhao, V. Gupta, A. Lohia, D. Edwards, Reliability modeling of lead-free solder joints in wafer-level Chip scale packages. J. Electron. Packag. **132**, 011005–011006 (2010)
16. F. X. Che, J. H. L. Pang, B. S. Xiong, X. Luhua, T. H. Low, Lead free solder joint reliability characterization for PBGA, PQFP and TSSOP assemblies, in *Components and Technology Conference*, 2005. Proceedings. 55th, (2005), pp. 916–921 Vol. 1
17. K. Do-Seop, Y. Qiang, T. Shibutani, N. Sadakata, T. Inoue, Effect of void formation on thermal fatigue reliability of lead-free solder joints, in *Thermal and thermomechanical phenomena in electronic systems, 2004*. ITHERM '04. The ninth intersociety conference on, (2004), pp. 325–329 Vol. 2
18. A. Syed, Accumulated creep strain and energy density based thermal fatigue life prediction models for SnAgCu solder joints, in *Components and Technology Conference*, 2004. Proceedings. 54th, (2004), pp. 737–746 Vol. 1
19. R. Dudek, H. Walter, R. Doering, B. Michel, T. Meyer, J. Zapf, et al., Thermomechanical design for reliability of WLPs with compliant interconnects, in *Electronic Packaging technology conference, 2005*. EPTC 2005. Proceedings of 7th, (2005), p. 7 pp
20. F. Xuejun, P. Min, P. K. Bhatti, Effect of finite element modeling techniques on solder joint fatigue life prediction of flip-chip BGA packages, in *Components and Technology Conference, 2006*. Proceedings. 56th, (2006), p. 9 pp
21. X. Li, Z. Wang, Thermo-fatigue life evaluation of SnAgCu solder joints in flip chip assemblies. J. Mater. Process. Technol. **183**, 6–12., 3/5/ (2007)
22. F. X. Che and J. H. L. Pang, Thermal fatigue reliability analysis for PBGA with Sn-3.8Ag-0.7Cu solder joints, in *Electronics packaging technology conference, 2004*. EPTC 2004. Proceedings of 6th, (2004), pp. 787–792
23. V. Vasudevan and F. Xuejun, An acceleration model for lead-free (SAC) solder joint reliability under thermal cycling, in Components and Technology Conference, 2008. ECTC 2008. 58th, (2008), pp. 139–145
24. S. Ridout, C. Bailey, Review of methods to predict solder joint reliability under thermo-mechanical cycling. Fatigue Fract. Eng. Mater. Struct. **30**, 400–412 (2007)
25. R. Dudek, Characterization and modelling of solder joint reliability, Mechanics of Microelectronics. 141, G. Q. Zhang, W. D. Driel, X. J. Fan: Springer Netherlands, 2006, 377–468.
26. R. Dudek, W. Faust, A. Gollhard, B. Michel, A FE-study of solder fatigue compared to microstructural damage evaluation by in-SITU laser scanning and FIB microscopy, in *Thermal and Thermomechanical Phenomena in Electronics Systems, 2006*. ITHERM '06. The tenth intersociety conference on, (2006), pp. 1031–1037
27. R. Darveaux, K. Banerji, Constitutive relations for tin-based solder joints. Components Hybrids. Manuf. Technol. IEEE. Trans. **15**, 1013–1024 (1992)
28. B. Vandevelde, M. Gonzalez, P. Limaye, P. Ratchev, E. Beyne, Thermal cycling reliability of SnAgCu and SnPb solder joints: a comparison for several IC-packages. Microelectron. Reliab. **47**, 259–265 (2007)
29. P. Vianco, J. Rejent, A. Kilgo, Time-independent mechanical and physical properties of the ternary 95.5Sn-3.9Ag-0.6Cu solder. J. Electron. Mater. **32**, 142–151 (2003)
30. J.H.L. Pang, B.S. Xiong, C.C. Neo, X.R. Mang, T.H. Low, Bulk solder and solder joint properties for lead free 95.5Sn-3.8Ag-0.7Cu solder alloy, in Electronic Components and Technology Conference, 2003. Proceedings. 53rd, (2003), pp. 673–679
31. J.-W. Kim, D.-G. Kim, S.-B. Jung, Evaluation of displacement rate effect in shear test of Sn–3Ag–0.5Cu solder bump for flip chip application. Microelectron. Reliab. **46**, 535–542 (2006)
32. M. Amagai, M. Watanabe, M. Omiya, K. Kishimoto, T. Shibuya, Mechanical characterization of Sn–Ag-based lead-free solders. Microelectron. Reliab. **42**, 951–966 (2002)
33. R. Dudek, W. Faust, S. Wiese, M. Rollig, B. Michel, Low-cycle fatigue of Ag-based solders dependent on alloying composition and thermal cycle conditions, in *Electronics Packaging Technology Conference, 2007*. EPTC 2007. 9th, (2007), pp. 14–20
34. T. Hannach, H. Worrack, W. Müller, T. Hauck, Creep in microelectronic solder joints: finite element simulations versus semi-analytical methods. Arch. Appl. Mech. **79**, 605–617 (2009)

35. A. Dasgupta, C. Oyan, D. Barker, M. Pecht, Solder creep-fatigue analysis by an energy-partitioning approach. J. Electron. Packag. **114**, 152–160 (1992)
36. W. D. van Driel, X. J. Fan, (Eds.), Solid state lighting reliability: components to systems (Vol. 1). Springer Science & Business Media, Berlin, Germany,(2012)
37. R. Rawlings, J. Wu, A. Boccaccini, Glass-ceramics: their production from wastes – a review. J. Mater. Sci. **41**, 733–761 (2006)
38. F. Xuejun, P. Min, P. K. Bhatti, Effect of finite element modeling techniques on solder joint fatigue life prediction of flip-chip BGA packages, in *Electronic Components and Technology Conference, 2006*. Proceedings. 56th, (2006), pp. 972–980
39. M.G. Pecht, M.-H. Chang, Failure mechanisms and reliability issues in LEDs, in *Solid State Lighting Reliability*, ed. By W. D. van Driel, X. J. Fan, vol. 1, (Springer, New York, 2013), pp. 43–110
40. T.Y. Tee, H.S. Ng, D. Yap, X. Baraton, Z. Zhong, Board level solder joint reliability modeling and testing of TFBGA packages for telecommunication applications. Microelectron. Reliab. **43**, 1117–1123., 7// (2003)
41. T. Burnette, Z. Johnson, T. Koschmieder, W. Oyler, Underfilled BGAs for ceramic BGA packages and board-level reliability, in *Electronic Components & Technology Conference, 2000*. 2000 Proceedings. 50th, (2000), pp. 1221–1226
42. A. Syed, Reliability of lead-free solder connections for area-array packages, in *IPC SMEMA Council APEX*, (2001)
43. T. Y. Tee, H. S. Ng, Z. Zhong, J. Zhou, Board-level solder joint reliability analysis of thermally enhanced BGAs and LGAs. Adv. Packag. IEEE Transact. **29**, 284–290 (2006)
44. M. Islam, A. Sharif, Y. Chan, Effect of volume in interfacial reaction between eutectic Sn-3.5% Ag-0.5% Cu solder and Cu metallization in microelectronic packaging. J. Electron. Mater. **34**, 143–149 (2005)
45. S.C. Chaparala, B.D. Rogemann, J.M. Pitarresi, B.G. Sammakia, J. Jackson, G. Griffin, et al., Effects of geometry and temperature cycle on the reliability of WLCSP solder joints, in *Thermal and Thermomechanical Phenomena in Electronic Systems, 2004*. ITHERM '04. The Ninth Intersociety Conference on, (2004), pp. 287–295 Vol. 2
46. S.P.V. Nadimpalli, J.K. Spelt, Effect of geometry on the fracture behavior of lead-free solder joints. Eng. Fract. Mech. **78**, 1169–1181 (2011)
47. J. Yang, L. Zhang, I.C. Ume, C. Ghiu, G. White, Board-level solder joint reliability study of land grid array packages for RF application using a laser ultrasound inspection system. J. Electron. Packag. **132**, 021006 (2010)
48. O. Nousiainen, O. Salmela, J. Putaala, T. Kangasvieri, Enhanced thermal fatigue endurance and lifetime prediction of lead-free LGA joints in LTCC modules. Soldering Surf. Mt. Technol. **23**, 104–114 (2011)
49. H. Zhen Xue, L. Xu, W. Ren, W. Bo Ping, T. Reinikamen, Reliability-based design optimization for land grid array solder joints under thermo-mechanical load, in *Thermal and Mechanical Simulation and Experiments in Microelectronics and Microsystems, 2004. EuroSimE 2004*. Proceedings of the 5th International Conference on, (2004), pp. 219–224
50. J.A. Carey, W.D. Collins, B.P. Loh, G.D. Sasser, Surface mountable LED package, ed: Google Patents, (2001)
51. J. Fan, Y. Kam-Chuen, M. Pecht, Lifetime estimation of high-power white led using degradation-data-driven method. Device Mater. Reliab. IEEE Trans. **12**, 470–477 (2012)
52. B.P. Loh, P.S. Andrews, N.W. Medendorp, Light emitting device packages, light emitting diode (LED) packages and related methods, ed: Google Patents, (2011)
53. K. Zeng, K.N. Tu, Six cases of reliability study of Pb-free solder joints in electronic packaging technology. Mater. Sci. Eng. R. Rep. **38**, 55–105., 6/14/ (2002)
54. J. Lau, R. Lee D. Shangguan, *Thermal Fatigue-Life Prediction of Lead-Free Solder Joints*. (n.d.)
55. A. Kujala, T. Reinikainen, W. Ren, Transition to Pb-free manufacturing using land grid array packaging technology, in *Electronic Components and Technology Conference, 2002*. Proceedings. 52nd, (2002), pp. 359–364

56. J.H. Lau, S.W.R. Lee, Effects of build-up printed circuit board thickness on the solder joint reliability of a wafer level chip scale package (WLCSP). Components Packag. Technol. IEEE Trans. **25**, 3–14 (2002)
57. T. Tong Yan, N. Hun Shen, J.L. Diot, G. Frezza, R. Tiziani, G. Santospirito, Comprehensive design analysis of QFN and PowerQFN packages for enhanced board level solder joint reliability, in *Electronic Components and Technology Conference, 2002*. Proceedings. 52nd, (2002), pp. 985–991
58. W.D. Zhuang, P.C. Chang, F.Y. Chou, R.K. Shiue, Effect of solder creep on the reliability of large area die attachment. Microelectron. Reliab. **41**, 2011–2021., 12// (2001)
59. X. Liu, *Processing and Reliability Assessment of Solder Joint Interconnection for Power Chips*, (Virginia Polytechnic Institute and State University, 2001)
60. J.H.L. Pang, D.Y.R. Chong, T.H. Low, Thermal cycling analysis of flip-chip solder joint reliability. Components Packag. Technol. IEEE Trans. **24**, 705–712 (2001)
61. J.H.L. Pang, B.S. Xiong, T.H. Low, Creep and fatigue characterization of lead free 95.5Sn-3.8Ag-0.7Cu solder, in *Electronic Components and Technology Conference, 2004*. Proceedings. 54th, (2004), pp. 1333–1337 Vol. 2
62. A. Perkins and S.K. Sitaraman, Vibration-induced solder joint failure of a Ceramic Column Grid Array (CCGA) package, in *Electronic Components and Technology Conference, 2004*. Proceedings. 54th, (2004), pp. 1271–1278 Vol. 2
63. K. Tunga, K. Kacker, R. V. Pucha, S. K. Sitaraman, Accelerated thermal cycling: is it different for lead-free solder?, in *Electronic Components and Technology Conference, 2004*. Proceedings. 54th, (2004), pp. 1579–1585 Vol. 2
64. R. Pucha, J. Pyland, S.K. Sitaraman, Damage metric-based mapping approaches for developing accelerated thermal cycling guidelines for electronic packages. Int. J. Damage Mech. **10**, 214–234 (2001.) 2001
65. D. Herkommer, M. Reid, J. Punch, In-situ optical creep observation and constitutive modelling of joint-scale SAC solder shear samples, in *Electronics Packaging Technology Conference, 2008*. EPTC 2008. 10th, (2008), pp. 506–515
66. S. Liu, Y. Liu, Modeling and Simulation for Microelectronic Packaging Assembly: Manufacturing, Reliability and Testing. John Wiley & Sons, Hoboken, New Jersey, USA, (2011).
67. S.W. Lee, J.H. Lau, Effect of Chip dimension and substrate thickness on the solder joint reliability of plastic ball grid assrray packages. Circ. World **23**, 16–19 (1997)
68. H. Solomon, The influence of the cycle frequency and wave shape on the fatigue life of leaded Chip carrier printed wiring board interconnections. J. Electron. Packag. **115**, 173–179 (1993)
69. M. Meilunas, A. Primavera, S. O. Dunford, Reliability and failure analysis of lead-free solder joints, in Proceedings of the IPC Annual Meeting, (2002)
70. IPC guidelines for accelerated reliability testing of surface mount solder attachments, in IPC-SM-785, ed. Northbrook: The institute for interconnecting and packaging electronic circuits, (1992)
71. Board level drop test method of components for handheld electronic products, in JESD22-B111, ed: JEDEC Solid state technology association, (2003)
72. N. Duan, T. Bach, J. Shen, R. Rongen, Comparison of in-situ measurement techniques of solder joint reliability under thermo-mechanical stresses. Microelectron. Reliab. **54**, 1753 (2012)
73. J. Lau, S. Erasmus, S. Pan, Effects of voids on bump chip carrier (BCC++) solder joint reliability, in *Electronic Components and Technology Conference, 2002*. Proceedings. 52nd, (2002), pp. 992–1000
74. Z. Qian, A. Dasgupta, P. Haswell, Viscoplastic constitutive properties and energy-partitioning model of lead-free Sn3.9Ag0.6Cu solder alloy, in *Electronic Components and Technology Conference, 2003*. Proceedings. 53rd, (2003), pp. 1862–1868
75. Q. Zhang, *Isothermal Mechanical and Thermo-Mechanical Durability Characterization of Selected Pb-free Solders.*, ed (University of Maryland, College Park, 2004)

76. Q. Haiyu, N.M. Vichare, M.H. Azarian, M. Pecht, Analysis of solder joint failure criteria and measurement techniques in the qualification of electronic products. Components Packag. Technol. IEEE Trans. **31**, 469–477 (2008)
77. H. Xu, T.-K. Lee, C.-U. Kim, Fatigue properties of lead-free solder joints in electronic packaging assembly investigated by isothermal cyclic shear fatigue, in Electronic Components and Technology Conference (ECTC), 2014 I.E. 64th, (2014), pp. 133–138
78. X. Liu, G.-Q. Lu, Effects of solder joint shape and height on thermal fatigue lifetime. Components Packag. Technol. IEEE Trans. **26**, 455–465 (2003)
79. X. Liu, S. Xu, G.-Q. Lu, D.A. Dillard, Effect of substrate flexibility on solder joint reliability. Microelectron. Reliab. **42**, 1883–1891., 12// (2002)
80. N.M. Vichare, M.G. Pecht, Prognostics and health management of electronics. Components Packag. Technol. IEEE Trans. **29**, 222–229 (2006)
81. M. Pecht, Prognostics and Health Management of Electronics in *E*ncyclopedia of Structural Health Monitoring, John Wiley & Sons, Hoboken, New Jersey, USA. (2009)
82. J. Johansson, I. Belov, E. Johnson, P. Leisner, A computational method for evaluating the damage in a solder joint of an electronic package subjected to thermal loads. Eng. Comput. **31**, 467–489 (2014)
83. H. Tsuritani, T. Sayama, K. Uesugi, T. Takayanagi, T. Mori, Nondestructive evaluation of thermal phase growth in solder Ball Microjoints by synchrotron radiation X-ray Microtomography. J. Electron. Packag. **129**, 434–439 (2007)
84. B.A. Cook, I.E. Anderson, J.L. Harringa, S.K. Kang, Isothermal aging of near-eutectic Sn-Ag-Cu solder alloys and its effect on electrical resistivity. J. Electron. Mater. **32**, 1384–1391., 2003/12/01 (2003)
85. W.M. Haynes, *CRC Handbook of Chemistry and Physics*, 95th edn. (Taylor & Francis, Boca Raton, 2014)
86. A. von Glasow, A. H. Fischer, G. Steinlesberger, Using the temperature coefficient of the resistance (TCR) as early reliability indicator for stressvoiding risks in Cu interconnects, in *Reliability Physics Symposium Proceedings, 2003*. 41st Annual. 2003 I.E. International, (2003), pp. 126–131
87. N. Angelidis, Damage Sensing in CFRP Composites Using Electrical Potential Techniques, PhD thesis of Cranfield University, Cranfield, UK (2004)
88. H. T. Chen, T. Mattila, J. Li, X. W. Liu, M. Y. Li, J. K. Kivilahti, Localized recrystallization and cracking behavior of lead-free solder interconnections under thermal cycling, in *Electronic Packaging Technology & High Density Packaging, 2009*. ICEPT-HDP ‘09. International Conference on, (2009), pp. 562–568
89. J.J. Sundelin, S.T. Nurmi, T.K. Lepistö, Recrystallization behaviour of SnAgCu solder joints. Mater. Sci. Eng. A **474**, 201–207., 2/15/ (2008)
90. A.U. Telang, T.R. Bieler, A. Zamiri, F. Pourboghrat, Incremental recrystallization/grain growth driven by elastic strain energy release in a thermomechanically fatigued lead-free solder joint. Acta Mater. **55**, 2265–2277., 4// (2007)
91. S.K. Kang, W.K. Choi, M.J. Yim, D.Y. Shih, Studies of the mechanical and electrical properties of lead-free solder joints. J. Electron. Mater. **31**, 1292–1303., 2002/11/01 (2002)
92. F. Guo, J.G. Lee, T. Hogan, K.N. Subramanian, Electrical conductivity changes in bulk Sn, and eutectic Sn-Ag in bulk and in joints, from aging and thermal shock. J. Mater. Res. **20**, 364–374 (2005)
93. A.R. Syed, Creep crack growth prediction of solder joints during temperature cycling – an engineering approach. J. Electron. Packag. **117**, 116–122 (1995)
94. M. Lavielle, Detection of multiple changes in a sequence of dependent variables. Stoch. Process. Appl. **83**, 79–102., 9/1/ (1999)

Chapter 13
Online Testing Method and System for LED Reliability and Their Applications

Xiaobing Luo and Qi Chen

Abstract Currently, reliability is still a challenging issue for LED products. The testing durations of accelerated life test (ALT) for LED products are still too long (IES LM-80 standard recommends at least 6000 h of estimation time), even longer than their product development periods. For better product development, the reliability estimation time needs to be further shortened. Thus highly accelerated life test (HALT) is proposed and used. In the conventional operating processes of HALT for LEDs, the offline measurement is frequently used, but it has several drawbacks like discontinuity of testing procedure and small data capacity. In this chapter, an online testing system is presented to overcome those shortages of offline measurements. The working principle and operating guideline are described in details. And also a benchmark following IES LM-80 standard is done for the method verification. The error analysis is conducted to assess the efficiency of this online testing system. Finally, two applications using the proposed testing method are given for reference.

13.1 Introduction

The lighting industry has been under revolution ever since the incandescent light bulb was invented by Thomas Edison over 100 years ago. The development targets are toward high efficiency, low cost, no pollution, and long life. For now, light sources mainly include conventional light sources (incandescent light, fluorescent light, etc.) and LED light sources. In contrast, LED light sources have the advantages of high luminous efficiency, long lifetime, no contamination, energy saving, compact size, etc., which results in the increasing trend of replacement of conventional light sources [1–3]. With the development and diversification of people's life, the scale of lighting industry is getting more and more expanded. According to the analysis report of McKinsey, the LED share in general lighting is calculated to be

X. Luo (✉) • Q. Chen
School of Energy and Power Engineering, Huazhong University of Science and Technology, Wuhan, China
e-mail: Luoxb@hust.edu.cn

© Springer International Publishing AG 2018
W.D. van Driel et al. (eds.), *Solid State Lighting Reliability Part 2*, Solid State Lighting Technology and Application Series 3, DOI 10.1007/978-3-319-58175-0_13

almost 70% in 2020 with total revenues of around ERU 100 billion [4]. At present, huge amount of resources are dedicated to solid-state lighting technology, and the product design cycle of LED luminaires is greatly shortened. When a new LED product is developed and prepared for release, reliability estimation must be done, and relative property parameters must be published along with the new product for consumers' reference.

Usually, reliability property can be reflected by specific parameters. For an LED product, its property parameters can be sorted into four categories, i.e., optical parameters (luminous flux, luminous efficiency, spectrum energy intensity, spectral chromaticity coordinates, etc.), thermal parameters (thermal resistance, junction temperature, etc.), electrical parameters (forward voltage, driving current, etc.), and appearance. Among those parameters, luminous flux and junction temperature are most important and reflect the lumen maintenance most directly. The junction temperature variation can lead to the change of luminous flux. Thus, for reliability assessment, the luminous flux degradation over time is mostly concerned. It has been pointed out in literatures [5, 6] that the optical power of LED light source decreases with operation time due to the degradation of relative materials. The attenuation law of LED's lumen maintenance is investigated a lot. Some standards-setting organizations published relative industrial standards to specify the measuring processes of LED's performance parameters [7–9]. One of the most quoted standards is LM-80 which is published by Illuminating Engineering Society of North America (IESNA) [9]. In LM-80, at least 6000 h of testing is required. This testing period is too long for the manufacturers since the product iteration cycle is fast and the test cost can add too much to the final product cost. Under such circumstances, small companies cannot even afford to do such reliability estimation. Actually, they just regard the LED product's lifetime as the nominal 50,000 h which is apparently not true for every LED product due to different materials and technologies used in the production processes. This is impeditive to the standardization of the market. Even if new standard cuts that basic testing duration to half [10], it is still too long concerning the present science and technology developing speed. Therefore, it is of great urge to develop an efficient and effective method to estimate the reliability of LED products.

For highly reliable products like LEDs, the most common mean to estimate their reliability within an acceptable time and limited budget is highly accelerated stress test (HAST). A lot of efforts have been dedicated to investigate LED's reliability problems by using HAST. Meneghesso et al. [11] carried out extensive high-current accelerated aging test and identified failure modes and mechanisms of GaN-based LEDs including phosphor degradation, plastic carbonization, and die attach and wire bonding degradation, resulting in the optical power degradation. Hsu et al. [12] investigated the failure mechanisms of LED modules with various lens shapes under three elevated aging temperatures. The package-related failure modes under thermal-aging test were attributed to the degradation of the plastic lens. Hu et al. [13] studied the mechanism of delamination in LED packages and its effects on thermal characteristics of LEDs experimentally and numerically. The results

showed that the thermomechanical stress plays more important role than the hygro-mechanical stress for the development of delamination in the LED packages.

It can be noticed that all those experimental operations adopted the same testing mode, which can be identified as offline testing method. In this mode, the devices under test (DUTs) are baked in an isothermal chamber for a predefined period and then taken out to normal environment for property parameter recording. After that, they are put back to the harsh environment for aging test again. These steps repeat until the target terminal conditions achieved like optical degradation below 70% or simply destructive failure is reached. This kind of offline testing method can lead to several problems, including as follows:

- Offline measurement neglects the consistence of test conditions, e.g., the degradation status of DUTs may change when they are retested.
- The testing environment is not controllable during the fetching process in terms of temperature, moisture, time variation, etc.
- Time interval of degradation data recording is usually too large (100–300 h) for obtaining enough data within a limited time [14–16]. As a whole, all the uncertainties will add to the measurement inaccuracy in reliability assessment.

Thus, some researchers have been working on developing new testing methods to overcome those shortages. Narendran et al. [17–19] designed a life-test chamber that could keep the ambient temperature constant and also act as a light-integrating box for constant light output measurement. By using several such boxes, the LED's optical property degradation over time can be measured in terms of ambient temperatures and driving currents. Bürmen et al. [20, 21] worked on an automated system for optical quality inspection. The light intensity, average chromaticity, and color variation were obtained for LED reference; the divergence of the optical axis and the viewing angle of the emitting light were measured absolutely. Svilainis [22] proposed a technique for LED measurement in situ, and the far-field pattern could be measured quickly without dismantling the LEDs from the tile. Zhou et al. [23] presented a system which can be used to monitor the quality of LED packaging, and also it can be used to measure photometric, colorimetric, and electrical parameters simultaneously from the electroluminescence of the LEDs in a matter of millisecond. The comparison of these methods is summarized in Table 13.1. By the above methods, the efficiency and precision of detection and measurement for LEDs' properties are improved. Nevertheless, to the best of our knowledge so far, there is no effective method or system to measure the optical parameters in real time for LED's reliability estimation. Such system is essential and needs to be developed.

The development of laser diode (LD) is prior to that of LED. As members of semiconductor family, their principles are more or less similar to each other. Design hints can be obtained from LD society. There are many studies on LD's performance and degradation in reliability characterization by online testing method [24, 25]. It is proved that with accelerated aging test and continuous monitoring, the testing duration can be shortened, and the extrapolation accuracy can be improved.

Table 13.1 Comparison of LED measurement systems

Researchers	Approach	Pros	Cons
Narendran et al. [17–19]	Designed a life-test box	Maintaining ambient temperature	Limited temperature range (35–50 °C)
		Enabling light output measurement (luminous flux, color coordinates)	One sample per box
			Regular calibration
Bürmen et al. [20, 21]	Designed a machine vision system for automatic optical quality inspection of LEDs	Optical property estimation by comparative analysis of the images obtained from the reference and measured LEDs	No temperature adaptability
		Designed for automatic sorting of LEDs	Regular calibration of the reference LED
Svilainis [22]	Developed a system for LED directivity measurement in situ	The far-field pattern can be measured without dismantling the LEDs from the tile	Unable to measure optical properties like luminous flux, power used, color maintenance, etc.
Zhou et al. [23]	Developed an instrument for transient measurement of LED characteristics	Photometric, colorimetric, and electrical parameters can be measured	No temperature adaptability
		Inspect the quality of LED packaging for production line	Regular calibration of the reference LED

In this chapter, an online testing system for LED's reliability estimation is brought up. The built-up and prototype of the whole testing platform are introduced. Optimal design is done to optimize relative setup parameters. Experiments and benchmark according to the IES LM-80 standard are performed to verify the feasibility of this proposed approach. Error analysis is done to exhibit the effectiveness. Finally, two applications using this online testing system are shown for better understanding.

13.2 Online Testing System: Principle and Method

The designed highly accelerated reliability test for LEDs usually contains harsh environment in terms of high temperature or/and high humidity. The biggest shortcoming for offline testing method is that the measurement devices cannot endure the same harsh environment like the specimens, so that we have to switch between the harsh aging condition and normal test condition frequently for aging and recording. As for LEDs, light is the primary parameter, one possible idea comes that we can connect the DUTs under aging condition with data measurement devices under normal test condition through the medium of light.

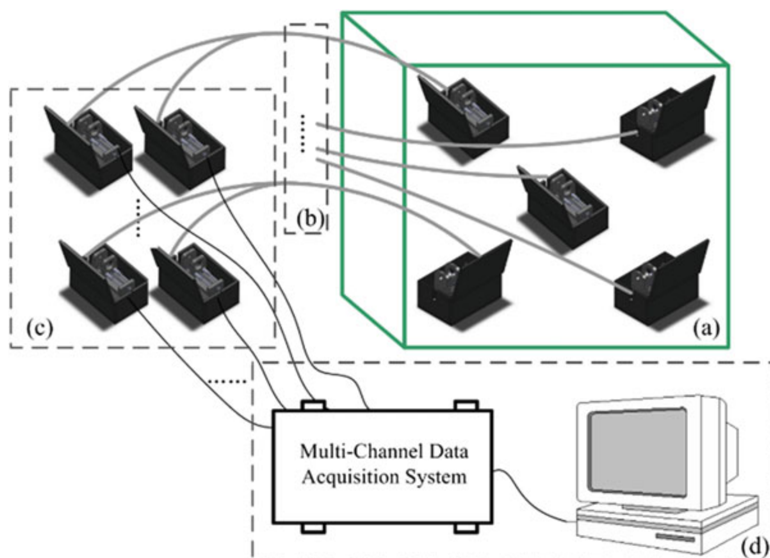

Fig. 13.1 Schematic of the online testing system for LED's optical degradation. (**a**) Light transmission environment enclosure. (**b**) Heat-resistant fiber cable. (**c**) Sensing environment enclosure. (**d**) Multichannel data acquisition system

Figure 13.1 shows the schematic of the proposed online testing system of HAST for LEDs. It is made up of four parts, namely, light transmission environment enclosure, heat-resistant optical fiber cable, sensing environment enclosure, and multichannel data acquisition system. By this system, the light emitted by DUTs can be partially transmitted from the harsh environment to normal environment so that the illuminance and correlated color temperature (CCT) of the light can be measured and recorded. Five output channels are designed to simultaneously measure the optical characteristics of each DUT. The optical parameter data are recorded by the standard optoelectronic detectors using digital photoelectric integral method, which follows the requirements set by CIE127-2007 [26].

More specifically, LED samples are mounted on the light source fixtures, which are placed in accelerated life experimental circumstance. Such harsh environment is usually provided by a thermal chamber or hot-humid chamber. The light from the LEDs goes through the fiber cable and finally reaches the probing surface of the light sensor. The light source and the detector testing fixtures are placed in the lightproof enclosures, respectively, for light isolation from the outside. Some rectangular pores are designed along the inner walls within the lightproof enclosures to maintain identical temperature and humidity with the ambient environment. The distance between the DUTs and the entrance surface of fiber cable is adjustable to meet different light sources.

Figure 13.2 displays the final testing prototype of the present system. As shown in Fig. 13.2a, the armored cable is of Y-type structure, which has the function of single-ended input and double-ended outputs. A bundle of optical fibers are divided

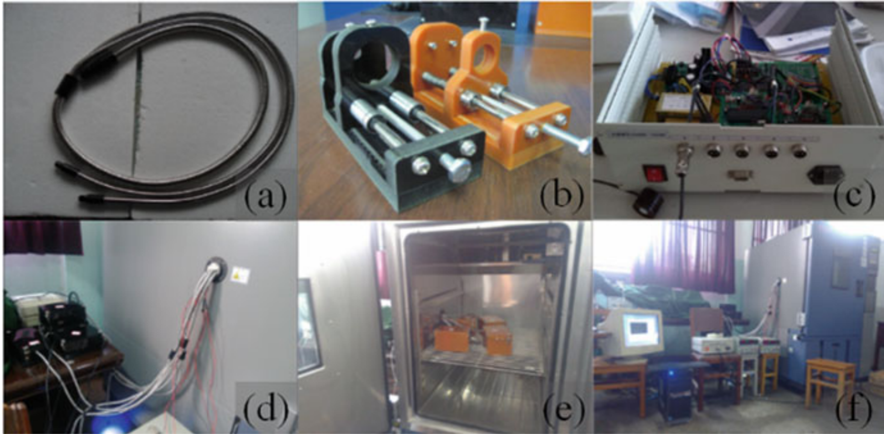

Fig. 13.2 Pictures of the prototype of proposed online testing system. (**a**) Y-type optical fiber cable. (**b**) Manual testing fixtures. (**c**) Multichannel data acquisition system. (**d–f**) Details of the prototype at work

into two parts in quantitative terms. They are butted end to end and are optically aligned by measuring the luminous intensity from one fiber to the other. As for armored cable, the diameters of entrance and exit surfaces are 10 mm and 7 mm, respectively. It is mainly fabricated with heat-resistant materials and can work with a steady performance under temperatures from −40 to 200 °C. Its characteristics and couple efficiency play a key role for the measurement accuracy of this system. The light outputs from the exit surface of the armored cable are acquired by the detectors of illuminometer and colorimeter, respectively. The spectral responsivity of the photometer is mainly determined by the wavelength-selective filter, which represents the relative spectral responsivity of human eye under daylight illumination levels. The spectral responsivity is then determined by the spectral responsivity of the photodiode and the spectral transmittance of the filter [27], which can be calibrated as an entity to account for interreflections between the filter and the detector. The filter is temperature stabilized as it is in contact with the heat sink, so the detector has a good match under the room temperature. It is obvious that only part of the light from the light source can finally reach the detectors. The partial illuminance is proportional to photocurrent, which is modulated to frequency signal by a current-frequency converter (CFC). As for measurement of CCT, its principle is similar to that of the partial illuminance testing. Three independent detectors are provided with different color filters, respectively, so that they can match their spectral responses to the curves of CIE-1931 standard.

To ensure the measurement accuracy, manual testing fixtures are designed for coaxially optical measurement of LED light source, armored cable, and detectors. As shown in Fig. 13.2b, the fixtures mainly consist of the fixed pedestal, device clamp holder, sliding shaft, cross screws, and helical spring. According to the different sizes of armored cable and sensing probe, the fixtures also have two

sizes. The distance between light source and entrance surface of armored cable can be adjusted by cross screws, and the limit is decided by the length of the helical spring.

According to the inverse-square law [28], the measurement errors can be easily caused by small displacement change between the exit surface of fiber cable and the sensing probe. Unevenly stressing can lead to displacement. This means that the stress load on the optical cables and the sensor surfaces can affect test results. The device clamp holder is designed to produce the uniform stress around device when the material is heated or cooled. The heat-resistant bearing is used to reduce relative displacement under the environmental stress.

In this equipment, the optical parameters are collected by the multichannel data acquisition system, as shown in Fig. 13.2c. For each channel, the frequency signal from detector is connected to CFC circuit, respectively, and its value lies in the range of 1–20 kHz. The pulse frequency signal is firstly inputted into a single-limit voltage comparator, and then the timing circuit is triggered by the falling edge of the pulse. When the frequency changes, the pulse is differentiated by an R-C network. The average output current is decided by τ, which is time constant factor, and its value is decided by the R-C network. To improve the measurement accuracy, an operational amplifier is adopted to provide a buffered output and also acts as a two-pole filter so that the average current can be demodulated as voltage signal. The ripple is less than 5 mV peak for all frequencies above 1 kHz. A microcontroller unit of STC11F08XE is used to implement multichannel data collection. System test indicates that the shortest sampling time is about 2 s when the five channels are working simultaneously.

The partial illuminance can be calculated from the following formula:

$$Ev = f(S) \cdot i \tag{13.1}$$

where i is the photocurrent, which is caused by the silicon photodiodes inside the detector. $f\,(S)$ is regarded as the calibration function of detector. Since inputting radiant flux has good linear relationship with photocurrent in the visible region, $f\,(S)$ can be obtained according to the inverse-square law. By changing the distance between the detector and the standard light source of known luminous intensity, the relationship of illuminance between photocurrent variation can be calibrated. The color is divided into three parameters, which can be calibrated with tristimulus theory. The chromaticity coordinates can be measured directly, and thus CCT can be easily obtained.

It must be emphasized that the online testing system must be immobile during the whole testing period. Once the DUTs are substituted, or armored cables are reinstalled, the small variable displacement might lead to large uncertainty, and then the results will be hardly convinced.

13.3 System Optimization

The optical fiber cable is the key part of the online testing system. Its coupling efficiency determines the accuracy of total experimental equipment. When the distance between the DUT and the entrance surface of armored cable is too far, the flux received by detector will be too small to be detected accurately. However, if the distance is too close, the LED sample cannot be approximated to a point light source. In this situation, the light source is area source, and the inverse-square law can no longer be applied. Therefore, the distance needs to be carefully optimized. Besides, the illuminance and the CCT measured by the detectors are critically dependent on the exact measurement conditions [26]. In a word, system optimization should be carried out for good measurement accuracy.

As shown in Fig. 13.3, the optical fiber cable should be idealized for modeling. It is made up of thousands of optical fibers. The optical fibers consist of fiber cores and claddings, and their diameters are 20 μm and 50 μm, respectively. The numerical aperture (NA) of optical fiber is 0.54, and the receiving angle is 65°. LED chip has a standard dimension of 1 mm × 1 mm × 0.1 mm, and its radiation power is 1 W. To simplify the numerical model in this system, the Y-type structure of fiber cable is replaced by the single-end structure. The fibers are bundled with the cylindrical package, and the mechanical axis of the package (which is used to match the center of LED chip in the measurement equipment) should coincide with the optical axis (which is the axis of rotational symmetry of the spatial distribution). The distance between the LED chip and the entrance surface of the optical cable is adjusted along the optical axis. Figure 13.4 displays the characteristics of the partial flux and the partial average intensity distribution as a function of distance. It can be seen that the increased distance leads to the exponential degradation of the normalized relative flux, but the distribution curve flux is still close to Lambertian emission [29, 30]. Comparing the function of distance-flux and that of distance-intensity distribution, the best position for testing distance is selected as 12 mm.

Because the exit and entrance surface of the fiber cable are theoretically perpendicular to the optical axis of LED module, the fiber cable can be considered as

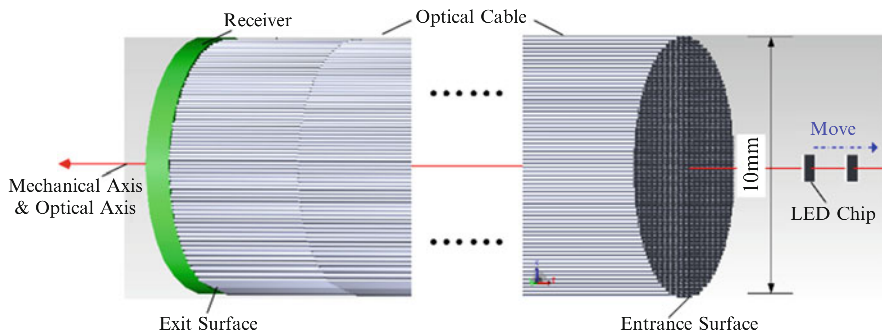

Fig. 13.3 Distance optimization modeling for LED chip, optical fiber cable, and detector

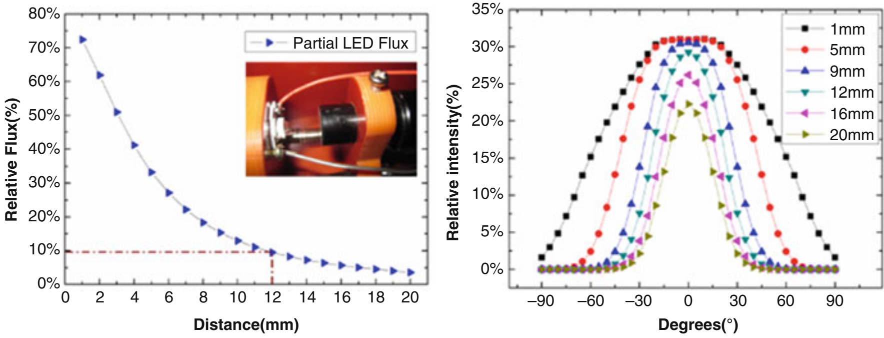

Fig. 13.4 Normalized partial LED flux and partial intensity distribution of entrance surface of optical fiber cable

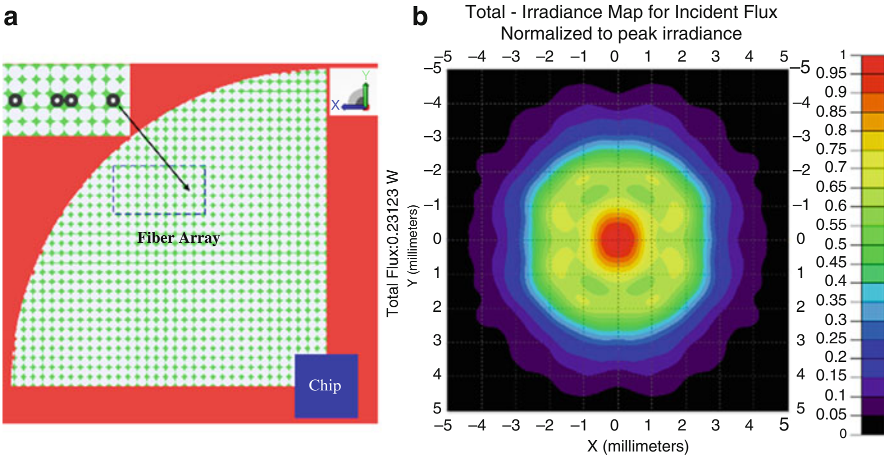

Fig. 13.5 Output simulation of optical fiber cable. (**a**) Composition of optical fiber cable based on microstructures. (**b**) Illuminance chart of exit surface

an optical flat with microstructures, and the surfaces are shown in Fig. 13.5a. For the rotational symmetry structure of cable, the light extraction of exit surface is theoretically proportional to that of the entrance surface. The partial flux is obtained by simulation, as shown in Fig. 13.5b. The normalized output is about 2.31%, and the coupling efficiency of optical fiber cable can be calculated by

$$\eta = \frac{Ev_{\text{exit}}}{Ev_{\text{entrance}}} = 50.5\% \tag{13.2}$$

where Ev_{entrance} and Ev_{exit} are the illuminances of entrance and exit surfaces of the fiber cable, respectively. They are proportional to the area of the receiving surface. It should be noted that the real area of exit surface in the Y-type structure is half of

entrance surface and the simulation result is based on the hypothesis that the light emitted from exit surface is completely accepted by detector. Therefore, the distance between the sensing probe and the fiber cable can be determined by the NA of the exit surface. Because the divergence angle of exit surface obtained by measurement is about 32°, the most suitable distance is calculated to be about 5 mm.

13.4 Experimental Verification and a Benchmark

In LED's reliability estimation, the lumen maintenance or color change over time is mostly concerned. The proposed online testing system is mainly used to measure the optical degradation property of LED packages. In this part, experiments were conducted to validate the presented online testing system. Commercial high-power blue LED packages were used in the investigation. The peak wavelength is about 456 nm under the rated forward current of 350 mA and rated electrical power of 1 W. The LED die was soldered on a copper submount and packaged in a conventional way. According to LM-80 measurement standard, the total flux should be used to evaluate LED's lifetime. To calibrate the relationship between partial illuminance detected by the proposed online testing system and the total flux of the LED die, the sample was operated under various electrical currents, and the total flux was measured by the integrated sphere in the high-accuracy array spectral radiometer (HAAS-2000, Everfine Ltd.) [31]. The response curves were shown in Fig. 13.6. When the current is 350 mA, tested illuminance is about 1385.1 lx, and the total flux is 15.39 lm; the relationship of the two parameters can be represented as

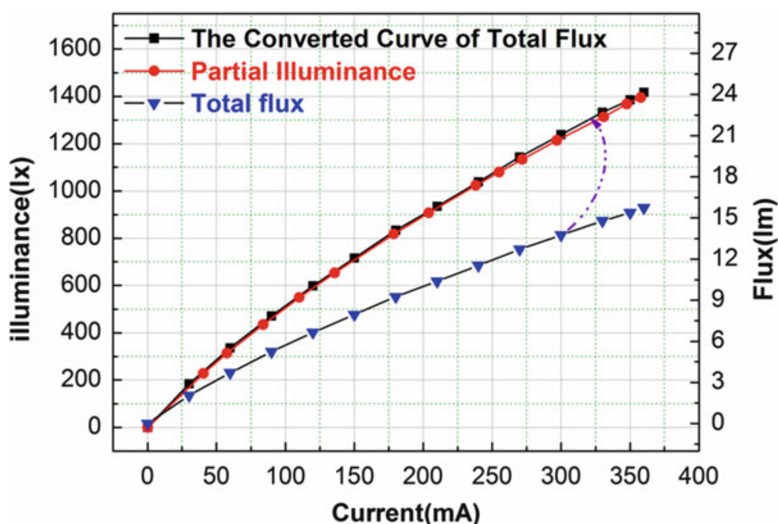

Fig. 13.6 Relationship between the partial illuminance and the total flux under various currents

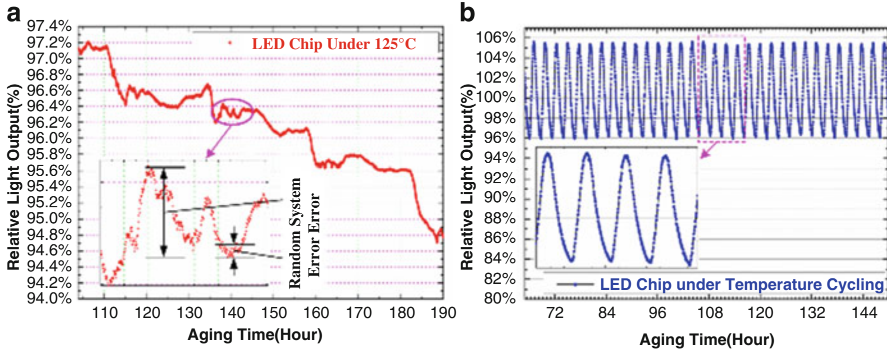

Fig. 13.7 The relative light output in HAST by online testing system. (**a**) Optical degradation in constant temperature of 125 °C. (**b**) Transient response during temperature cycling measurement

$$\beta = \frac{\phi_t}{Ev_d} = \frac{\phi_t \cdot S}{\phi_r} \tag{13.3}$$

where ϕ_t is the total flux, Ev_d is the measured luminance, ϕ_r is the relative flux, and S is the aperture area of detector. According to the tested data, the transfer coefficient β is a constant, whose value is 0.0111. There is a good linear relationship between the measured illuminance and the total flux. The light output efficiency of system reaches 2.2%. Calculating the maximum deviation under the current of 330 mA, the relative error is 1.4%, and the standard deviation is about 0.93%.

In order to analyze the system availability under actual circumstances, five blue LED modules were submitted to HAST with elevated temperature of 125 °C and forward current of 350 mA (1 W operation). The partial illuminance data were collected in a specific interval of 30 s. Figure 13.7a plots the lumen degradation details of the aging process. The light flux was normalized to its initial value. It can be seen that the degradation magnitude of relative illuminance reached 2.5% after about 100 h of aging. From the chart, it can be seen that the data acquisition has good consistency. The inset of Fig. 13.7a shows that the system error is about 0.2% and the random error caused by detector is about 0.02%. The error analysis will be discussed in details in the next section. Apart from the thermal aging, a temperature cycling life test was also conducted using the present online testing system. The high and low temperature sides are 125 °C and −20 °C, respectively, and the cycle period is 2 h. Figure 13.7b displays the testing data of temperature cycling life test. The result indicates a good transient response for relative light output with alternating temperature. By selecting the peak and valley of the curve during the aging time from 100 to 150 h, the measurement uncertainty can be written as

$$\Delta_U = \sqrt{S_{Ev}^2 + \Delta_S^2} \tag{13.4}$$

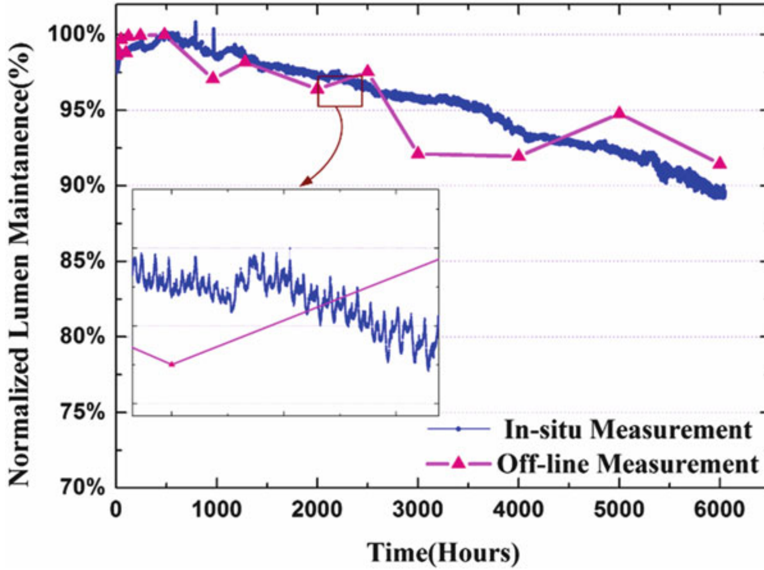

Fig. 13.8 Data collection of the online testing method and offline method according to LM-80 standard

where the standard deviation of S_{Ev} is calculated according to the point of peak value and valley value, which is 1.3%. The system uncertainty Δ_S is regarded as the standard deviation of system. It is calculated that $\Delta_U = 1.6\%$.

To specify the system availability in details, a benchmark was done according to LM-80 standard. Ten commercial white LED modules were selected and worked under an ambient temperature of 55 °C with driving current of 350 mA. The initial junction temperature of these samples was about 105 °C. The illuminance data were collected both by the online method and offline method, respectively. Figure 13.8 reports the results after 6000 h aging. The experimental data were averaged and normalized to the initial values of the original samples. It is found that both optical degradation curves follow the same decay mode. However, compared with the data obtained by offline method, the online method has better continuity and exhibits more degradation details. And also, it seems that smaller measurement uncertainty can be achieved by the online testing method. Obviously, the online testing system is useful for LED's reliability estimation.

13.5 Error Estimation

In this section, the error analysis was carried out to discuss the measuring accuracy of the proposed online testing system under the most common application, which is lifetime projection under accelerated life test. An accelerated aging life test was

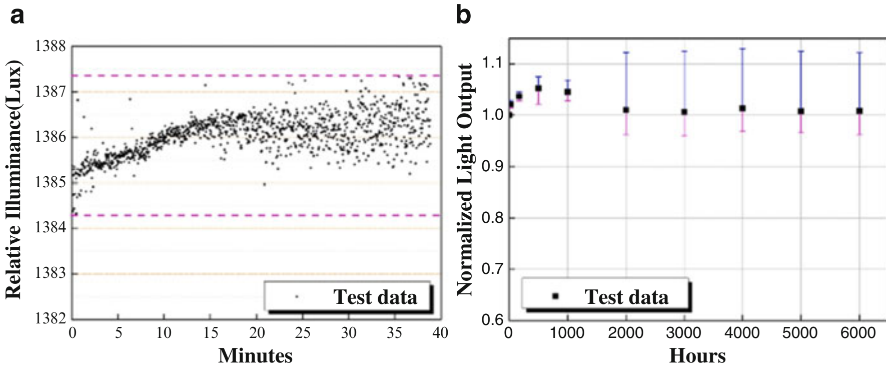

Fig. 13.9 Systematic errors of (**a**) online testing system and (**b**) offline testing method

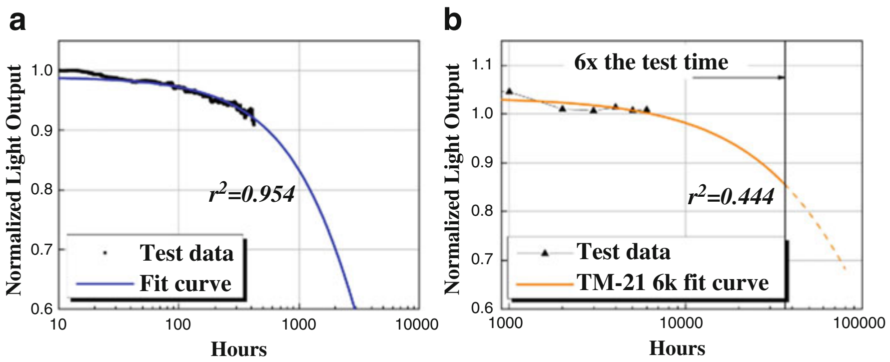

Fig. 13.10 Random errors of (**a**) online testing system and (**b**) offline testing method

conducted by the online testing system. Blue LED modules were placed in an isothermal chamber. The ambient temperature and the forward driving current were set as 125 °C and 350 mA, respectively. The illuminance data were collected at an interval of 30 s. To better explain the measurement accuracy of the online testing system, partial data from LUXEON Rebel IES LM-80 test report was used as a reference [32]. The comparison results were displayed in Figs. 13.9 and 13.10.

The measurement error can be divided into two parts: systematic error and random error. For the first one, it can be calculated by the formula below:

$$e_{sys} = \frac{\Delta_{max}}{F_0} \times 100\% \tag{13.5}$$

where Δ_{max} is the maximum illuminance difference and F_0 is the average illuminance value. As shown in Fig. 13.9a, it can be calculated that $e_{sys} = 0.2\%$ for the online testing system. However, for the offline method, it is found that after 1000 h

of aging, the systematic error increases to be around 16%, as displayed by the error bars of Fig. 13.9b.

The random error can also be identified as the system uncertainty, which can be simply reflected by the standard deviation of the system. For data analysis, the lifetime extrapolation was carried out based on the experimental data obtained by the online testing system and from the literature, respectively. The extrapolation formula recommended by IES TM-21 standard [33] was adopted, which can be expressed as follows:

$$\Phi(t) = B\mathrm{e}^{-\alpha t} \tag{13.6}$$

where t is the operated time, $\Phi(t)$ is the relative light output, B is the initial constant, and α is the degradation rate. The results were reported in Fig. 13.10. It can be calculated that for the online testing system, the standard deviation is 0.21%, and the correlation efficiency is $r^2_{\text{online}} = 0.95$. Comparatively, for the offline method, the standard deviation and the correlation efficiency are 1.02% and 0.444%, respectively. Apparently, a better uncertainty of measurement can be achieved by this online testing system.

13.6 Application I: Effect of Packaging Materials on the Degradation Mechanism of LEDs

For phosphor-converted white LED, its packaging materials mainly consist of silicone encapsulant and phosphor-silicone composite. By using this online testing system, the influence of various packaging materials on the lumen depreciation of LEDs under HAST was studied. Four kinds of LED modules packaged with different materials were submitted to aging conditions, and the partial illuminance data were collected continuously. After a period of aging, different samples exhibited different degradation patterns. Some of the specimens were taken to surface morphology observation under microscope. It was found that the silicone gel could cause defects more easily than phosphor gel, and the phosphor gel would lead to a quick light energy loss during the initial state of the whole aging process. Thus, the improvement for better LED performance can be considered from two aspects. One is to improve the material properties in terms of larger coefficient of thermal expansion (CTE) and stronger adhesion to reduce void production probability; the other is to develop new transparent encapsulant, which should be tough and stable enough in thermal mechanical property.

In order to achieve a good understanding of the degradation mechanism caused by efficiency drop of LED chip or by degradation related to packaging materials, it is necessary to encapsulate specific LED samples in terms of packaging materials so that the degradation of individual components of LED modules can be analyzed separately. In this part, four kinds of LED samples were prepared for experiments,

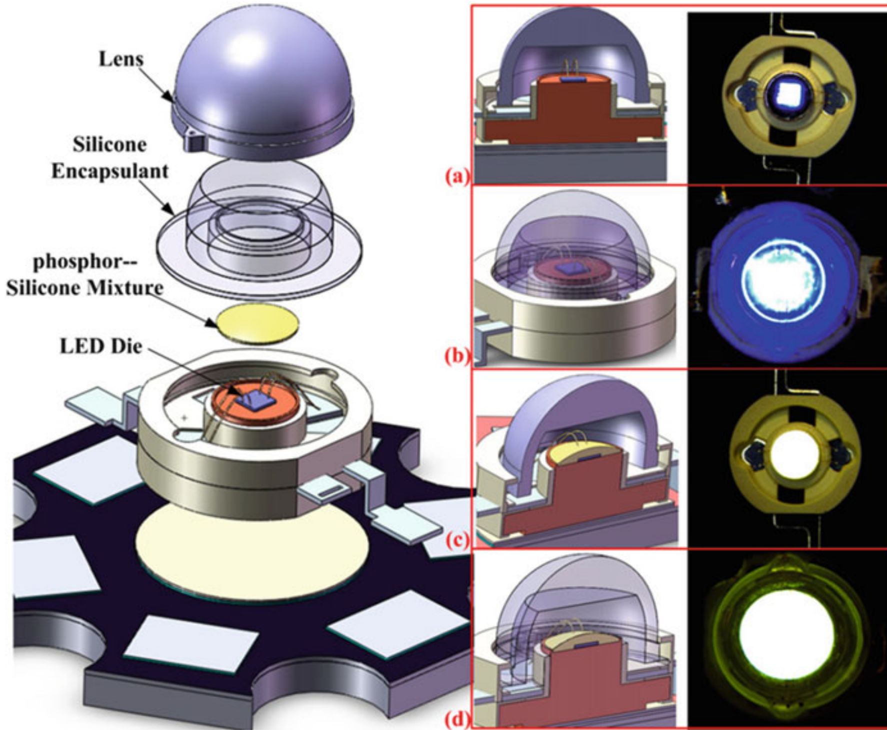

Fig. 13.11 Package compositions of four kinds of LED samples. (**a**) Blue module only based on 1 W LED chip bounding (BTYPE I). (**b**) Blue module based on silicone encapsulated in BTYPE I (BTYPE II). (**c**) White module based on phosphor-silicone composites coated in BTYPE I (WTYPE I). (**d**) Commercial white LED module (WTYPE II)

and their structures are shown in Fig. 13.11. The normal white LED package is mainly composed of several components, including LED chip, die attach, bond wire, lead frame, mounting compound, phosphor-silicone mixture (phosphor gel), silicone encapsulant, adhesive, and optical lens. The blue GaN-based LED chip has the size of 1 mm $\times$ 1 mm $\times$ 0.1 mm and its emitting wavelength is about 455 nm. Figure 13.11a shows the compositions of blue type I (BTYPE I). LED chip was soldered on the copper submount and covered with the lens. This module was vertically mounted on insulate metal aluminum substrate covered by a dielectric layer, whose area and thickness were about 0.03 m^2 and 1 mm, respectively. The adhesive material was thermal grease, whose thermal conductivity was about 50 W/mK. Blue type II (BTYPE II) was fabricated by injecting silicone encapsulant into BTYPE I from the injection port on the optical lens. White type I (WTYPE I) combined BTYPE I with the YAG:Ce phosphor-silicone composite with a mass ratio of 0.114. Finally, white type II (WTYPE II) was fabricated by injecting silicone into the WTYPE I package. The above three kinds of LED structures

Table 13.2 Optoelectronics parameters of four types before aging

Sample	Forward voltage (VF) V	Electrical power (PE) mW	Optical power (PO) mW	Luminous efficiency (EL) lm/W	Wavelength pulse (WLP) nm
BTYPE I	3.275	1145	393.4	12.96	450.9
BTYPE II	3.372	1180	508.6	15.45	449.7
WTYPE I	3.264	1143	324.8	103.42	449.6
WTYPE II	3.296	1153	364.5	105.18	449.6

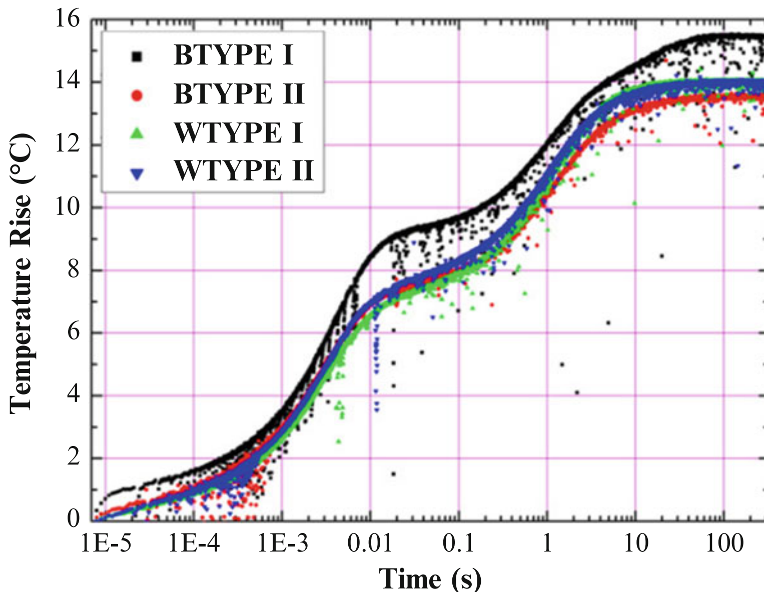

Fig. 13.12 Curves of junction temperature rise of four types of LED samples

were shown in Fig. 13.4b–d, respectively. The samples were fabricated following the commercial packaging technology standard.

The four types of LED modules were operated under the forward driving current of 350 mA, and the voltage range is from 3.2 to 3.4 V. The aging ambient temperature was optimized at 125 °C. The lumen depreciation during the aging process was monitored by the online testing system at an interval of 2 min. The optoelectronics characteristics of the samples were measured by a spectral radiometer before aging. The average values of five individuals for each type were listed in Table 13.2. Besides, considering that the optical degradation of LED modules has a close relationship with the junction temperature, the thermal resistance and junction temperature of LED samples were also measured by Transient Thermal Tester (T3Ster) in the same ambient temperature. The result was displayer in Fig. 13.12. It could be seen that the four curves had a good agreement after thermal

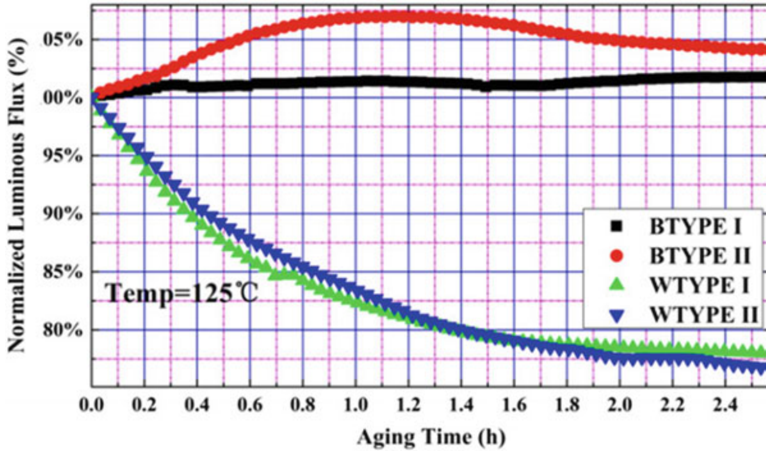

Fig. 13.13 Initial data of normalized luminous flux with four kinds of samples

equilibration. BTYPE I had the highest junction temperature rise of 15.6 °C. This can be well explained as follows. The heat generated by LED chip flows in two directions. The majority goes down through solder, copper slug, thermal grease, and substrate, while the minority goes up through all the packaging materials and finally dissipates in the air. The four kinds of modules had the same downward heat dissipation path. However, the top encapsulant of BTYPE I was filled with air, which had the largest thermal resistance along with the upward heat dissipation path. Thus its junction temperature rise is higher than others'. In general, the maximum difference of junction temperature rise is only 1.8 °C. During this aging experiment, four kinds of samples could be regarded to have the approximately equal operating junction temperature.

Figure 13.13 shows the curves of normalized luminous flux in the early aging stage. The normalized luminous flux shows a rise trend for samples of BTYPE I and BTYPE II. For BTYPE I, the fluctuation is about 1.8%, and the reason counting for this mainly comes from two aspects, which are the increase of cavity density for Mg dopant [34] and the initial annealing effect [19], respectively. Compared with the normalized luminous flux of BTYPE I, that of BTYPE II had a significant increase and reached 108.2% after aging for 70 min. This implied that the external quantum efficiency of the LED sample was improved due to the effect of silicone encapsulant. However, the lumen depreciation of WTYPE I and WTYPE II showed an exponential decline from the beginning, and the optical output was reduced by 25% and 27% within 150 min, respectively. Research implied that phosphor thermal quenching should count for this phenomenon [35, 36]. By comparing the degradation curves from four kinds of samples, it could be found that the phosphor doped in silicone played a decisive role in the early aging process for the lumen depreciation of white LED module.

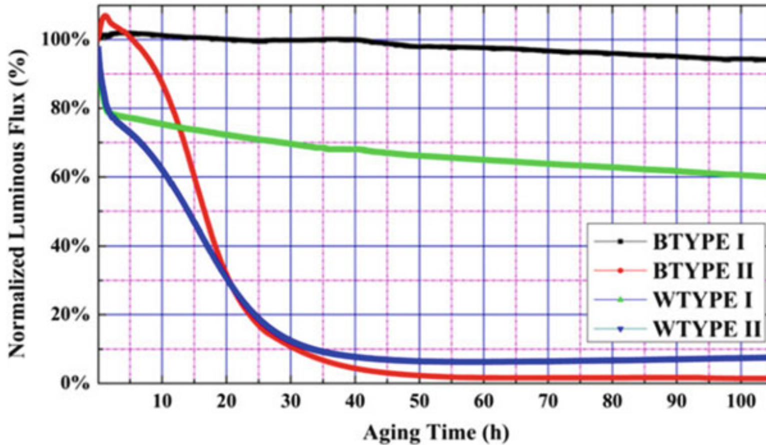

Fig. 13.14 Lumen depreciation curves of samples during aging over 100 h

In order to inspect the degradation influence on the components of LED package, data of the lumen depreciation had been recording. Simultaneously, some individuals were taken out for spot examination after aging for 18 h. Figure 13.14 illustrated the differences of degradation trends for various types of samples in the subsequent aging process. The curve of BTYPE I showed a slow decline trend but stayed changeless as a whole. The light output of BTYPE II experienced a quick drop, whose value exceeded 40% in a moment. The luminous flux of WTYPE I showed the tendency toward stabilization after rapid decline, whose amplitude reached 5.2%. And the luminous flux of WTYPE II was in continuous decay during aging. It was implied that optical degradation in white LED module was influenced by the coupling effect between silicone encapsulant and the phosphor-silicone composites, in which silicone encapsulant degradation played a more important role.

After the aging process, the samples were submitted to microscopy for morphology detection. Figure 13.15 plots the different components of LED module from BTYPE II after aging for 18 h, and Fig. 13.16 shows the surface profiles of samples from other three types. Evidences of carbonization and voids were found in the silicone gel for BTYPE II, as shown in Fig. 13.15a, b. It should be noticed that the carbonization occurs only between the upper surface of LED chip and silicone bulk, not a little along the gold wire. The morphology check for BTYPE II found no abnormalities or encapsulant yellowing in the packaging materials, as shown in Fig. 13.15c, d. For BTYPE I, the LED chip had few flaws upon its surface after aging and still had good I–V characteristics. For WTYPE I, the phosphor-silicone composite showed no carbonization, while that of WTYPE II did. Combined with the degradation curves of all specimens, it can be inferred that phosphor-silicone composite contributes little to the lumen depreciation except for the fast decline at the first 2 h and the failure mechanism of commercial LED modules (almost like WTYPE II) is mainly caused by carbonization of phosphor-silicone composite.

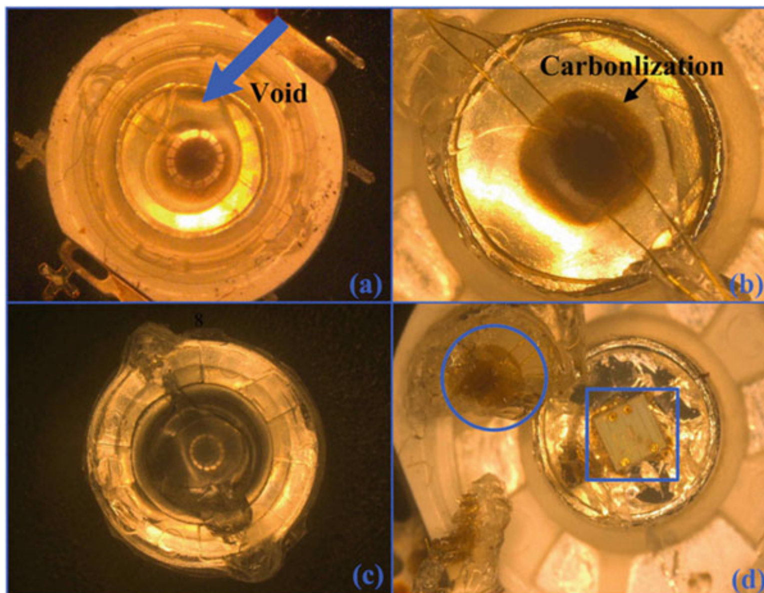

Fig. 13.15 Microscope photos of BTYPE II for different component of LED module at aging test of 18 h with (**a**) view on the void; (**b**) view on the carbonised area; (**c**) top view on the LED and (**d**) zooming into the areas

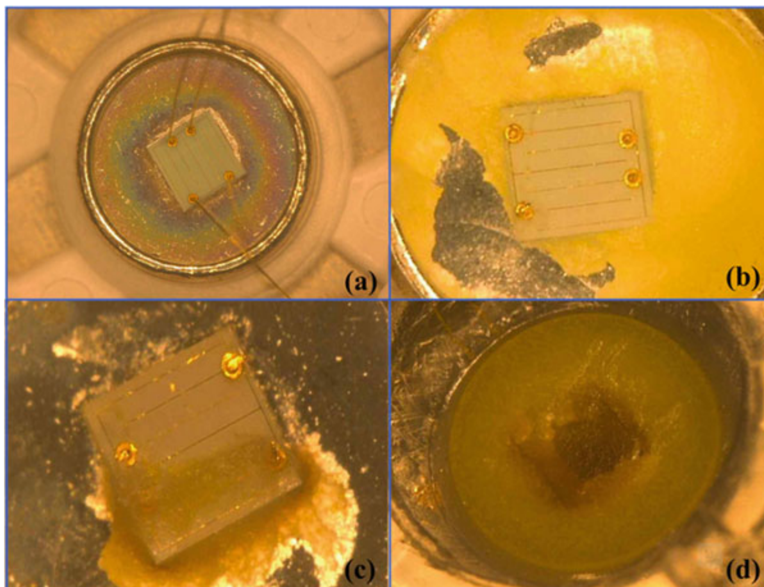

Fig. 13.16 Surface profiles of various samples. (**a**) Chip surface topography of BTYPE I. (**b**) Surface topography of WTYPE I. (**c**) Chip surface topography of WTYPE II. (**d**) Phosphor-silicone composites of WTYPE II

To sum up, through the accelerated degradation test on specific LED packages by online testing system, the degradation mechanism of LEDs related to packaging materials was explored. The results implied that the silicone encapsulant as one of the essential packaging materials could induce claws like voids and carbonization and the degradation of phosphor-silicone composite would lead to a fast light energy loss during the initial stage of high-temperature aging test. Two aspects are recommended for performance improvement. One is to improve the material properties in terms of CTE and strong adhesion to avoid void producing. The other is to develop new transparent encapsulant with sufficiently tough and stable thermal mechanical properties.

13.7 Application II: Effect of Silicone Amount on the Lumen Maintenance of LEDs

In the previous study, the effects of different packaging materials (silicone and phosphor layer) on the reliability of high-power LEDs were studied by HAST. As can be seen from Fig. 13.14, the experimental results implied that the LED samples' lumen maintenance properties might have dependence on the silicone amount in the package. Therefore, in this section, the effect of silicone amount on the lumen maintenance of LEDs under HAST was further studied. Five categories of LED specimens specified by silicone amount were prepared and subjected to an isothermal chamber whose temperature was set at 125 °C. The online testing system was used to monitor and record the light outputs in real time during the experimental process. After 400 h of aging, the largest attenuating range reached 6.17%, and different groups display different degradation behaviors. An exponential decay model was adopted to calculate the decay rate of each lumen maintenance curve. The decay rate differs as the silicone amount inside the package modules changes. This phenomenon is well explained, and Monte Carlo ray-tracing simulations are carried out to validate the explanation. The interaction effect of both silicone amount and temperature is also found, and more researches need to be done for further study.

In the experiment, the key point is to explore the effect of silicone amount. The specimens are selected as blue LED modules, i.e., no phosphor in the packaging materials. By adding various amounts of silicone gel, five types of LED modules are packaged. Figure 13.17 shows the schematic of each type of LED modules. The experimental setups were chosen in accordance to the conditions in the last section. The whole aging process lasted for about 400 h. The online testing system was used to monitor the parameter change during the whole procedure. And the illuminance data of each LED module are measured and recorded continuously as a function of time. Before the aging test, the optoelectronics characteristics of these samples are measured by an integrating sphere. The average values of ten individuals for each sample set are listed in Table 13.3.

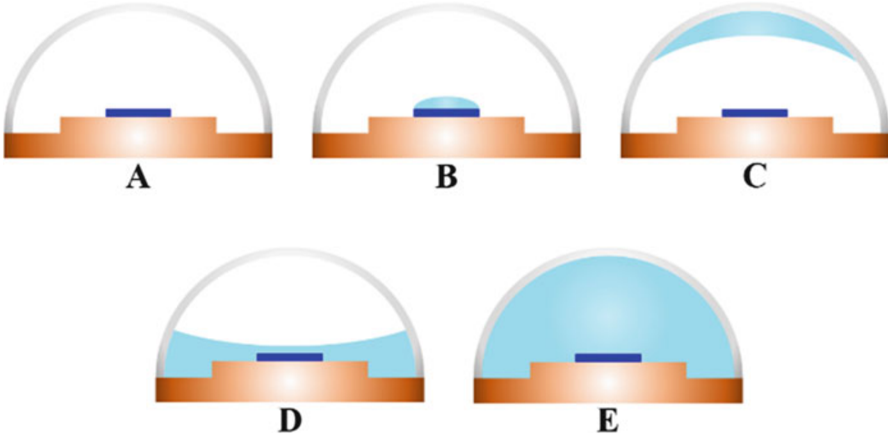

Fig. 13.17 Package details of five types of LED specimens

Table 13.3 Optoelectronics characteristics of five sample sets before aging

Sample set	Forward voltage (VF)	Electrical power (PE)	Optical power (PO)	Luminous efficiency (EL)	Wavelength pulse (WLP)
	V	mW	mW	lm/W	nm
A	3.059	1070	344.9	11.47	455.5
B	3.057	1070	404.8	13.43	455.4
C	3.054	1069	360.3	12.23	455.9
D	3.064	1072	335.2	11.16	455.9
E	3.064	1072	464.6	15.24	455.4

Figure 13.18 plots the relative light power of the five types of LED modules as a function of time under the experimental temperature of 125 °C. The luminous flux is normalized to better show the LED's degradation property. It can be seen that the five types display different depreciation characteristics. The normalized luminous flux shows a fluctuation and increases at the beginning of aging. The reasons counting for this have already been explained in the last section. As time moves on, those influences will decrease and disappear after saturation. The sample data error reflected as normalized light flux fluctuation may be attributed to the uncertainty of the illuminometer probe. After 400 h of aging, the sample set E reaches the maximum attenuating range of 6.17%.

By using the IES TM-21 standard recommended exponential decay model, as listed in formula (13.6), the decay rates of every sample set can be calculated. The data in the fluctuation period during the initial stage is abandoned, and least square method is adopted to get the parameters. The calculation results are listed in Table 13.4. By comparing sample sets A, B, and E, it is known that the decay rate increases as the silicone amount inside the package increases. By contrast, the light output of specimen with no silicone inside the package barely degrades. This is because along with the thermal aging, the silicone transmittance slowly reduces,

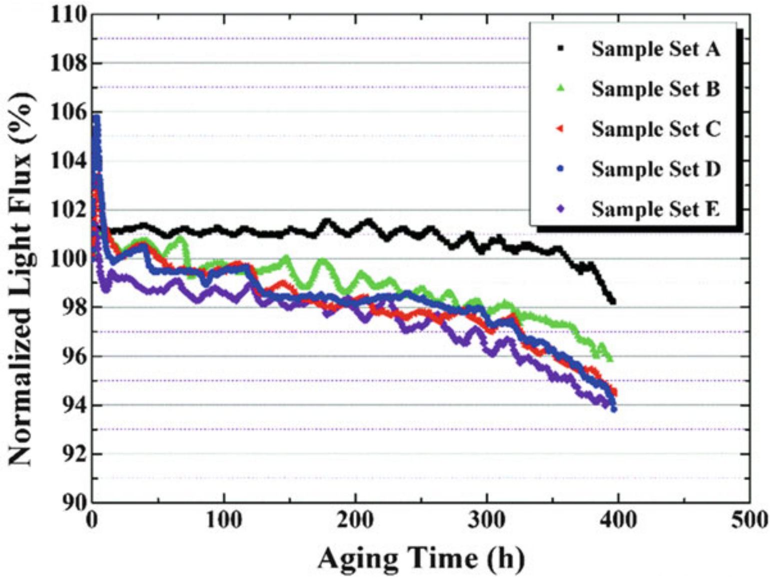

Fig. 13.18 Normalized light flux of five sample sets as a function of aging time

Table 13.4 Curve-fitting results of five sample sets

Sample set	Fitting model: $\Phi(t) = Be^{-\alpha t}$	
	Parameter: α ($\times 10^{-4}$)	Parameter: B
A	0.3694	101.512
B	1.0121	100.878
C	1.4760	101.789
D	1.6610	101.193
E	1.2270	99.926

resulting in more light absorbed by the silicone layer [37]. This influence is greater when there is more silicone gel in the package. However, as for sample sets C and D, it can be seen that their decay rates are larger than that of the sample set E. The reason behind this phenomenon can be described as follows. It is the result of interaction effect of silicone amount and heat dissipation. The transmittance degradation of silicone gel is determined by its temperature. Due to the existence of the air in the packages of sample sets C and D, the thermal resistances of them are larger than that of sample set E. This means that the heat dissipations in sample sets C and D are worse than that in sample set E, resulting in higher temperature, which further accelerates the decreasing of the silicone transmittance inside the packages. Therefore, their decay rates are larger. Comparing these two sample sets along, the decay rate of sample set C is smaller than that of sample set D. It is because the light emitted by LED chip diverges hemispherically and part of it does not pass through the silicone gel. So the influence of silicone degradation for sample set C is somewhat weakened.

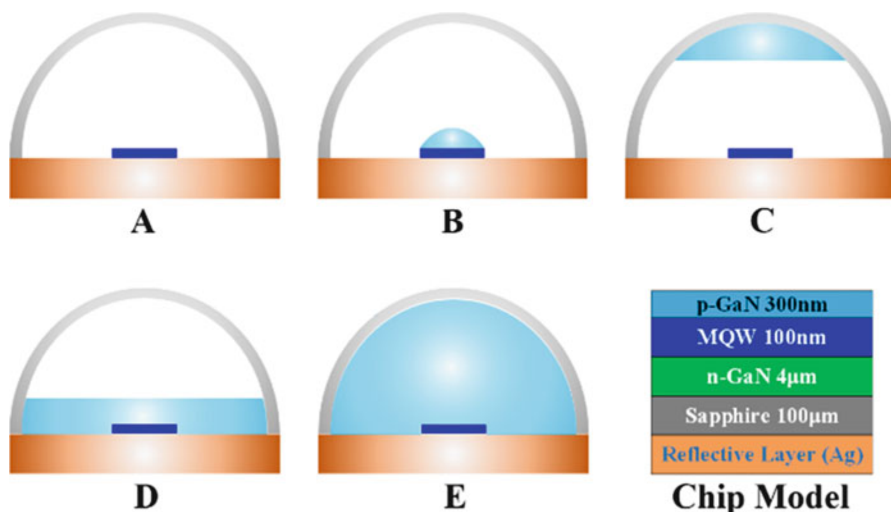

Fig. 13.19 Optical models of various sample sets for simulations

To better illustrate the effect of silicone amount on the lumen maintenance caused by silicone transmittance change, Monte Carlo ray-tracing simulations were conducted. Five models were established in line with the actual LED module packages. Under the premise of guaranteeing the features of every sample set, the models were simplified by replacing the surfaces with planes, as shown in Fig. 13.19. The selection of simulation parameters was decided according to the references [38, 39]. More specifically, the size of the chip was 1 mm $\times$ 1 mm. The luminescence MQW was sandwiched by an n-GaN layer and a p-GaN layer. A sapphire substrate was also taken into consideration. The thicknesses of the layers from top to bottom were 300 nm, 100 nm, 4 μm, and 100 μm, respectively. The top and bottom surfaces of the MQW were set as luminescent surfaces with Lambertian emission. The absorption coefficients and refractive indices for p-GaN, MQW, and n-GaN were 5, 8, and 5 mm^{-1} and 2.45, 2.54, and 2.42, respectively. The surface reflection coefficient of the reflecting layer (Ag) was set as 0.95. By setting the absorption coefficients and refractive indices of the materials, the precise model of GaN-based blue LED chip could be achieved. The silicone transmittance was selected as 98%, 90%, 80%, and 70%, respectively. And the simulation results are shown in Fig. 13.20.

In Fig. 13.20, the x-axis denotes silicone transmittance, and the y-axis is the optical power of LED modules normalized to the light output under silicone transmittance of 98%. It is clear that the light output decreases as the silicone transmittance decreases. The degradation amplitude changes with the silicone amount, which is in good agreement with the experimental results. It is noticed that the sample sets C and D have a great difference in the degradation amplitude, while the silicone amount inside the module packages is almost the same. This is

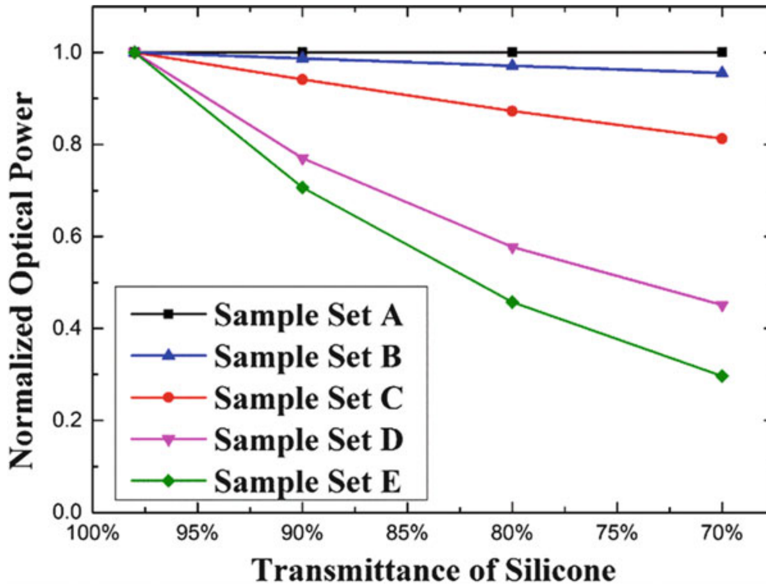

Fig. 13.20 Normalized optical power as a function of silicone transmittance

because the light emitted by the LED chip is hemi-spatially divergent and some of the light does not pass the silicone layer of sample set C. In comparison, in sample set D, every ray emitted from the chip passes through the silicone layer. Thus, the effect of silicone layer on the light output degradation for sample set D is greater than that for sample set C, which is in good agreement with the experimental results. At the same time, the optical power change of sample sets C and D is smaller than that of sample set E, which disagrees with the experimental result. This is because the simulation only considers the effect of silicone amount, while the actual situation is the result of the interaction effect of both silicone amount and temperature, as mentioned before. It implies that the thermal properties of LED packages can also have great influence on the lumen maintenance. Thus, more efforts should be dedicated to related researches.

In summary, the effect of silicone amount on the lumen maintenance of LED was investigated via HAST. Five categories of LED module packages with different silicone amount were prepared and subjected to HAST for aging test for about 400 h. The online testing system was used to record the lumen maintenance of the specimens continuously. The results showed that the decay rates of different sample sets change as the silicone amounts inside the packages change. The silicone transmittance depreciation during aging process was found to account for the effect of silicone amount. And the assumption is validated by Monte Carlo ray-tracing simulations. Also, it was found that the actual situation is the result of the interaction effect of both silicone amount and temperature. More efforts need to be dedicated to related researches for better understanding.

13.8 Summary

In this chapter, an online testing method and a system for LED reliability estimation were introduced. The principle of the proposed online testing system is to connect the DUTs under elevated testing conditions with the parameter recording and monitoring devices under normal conditions through the medium of light, which can be achieved by an optical fiber cable. This online testing method was mainly used in highly accelerated stress test. The advantages of the online testing system over conventional offline method were analyzed. For the prototype, system design and optimization design were carried out to guarantee the availability and measurement accuracy. The distances between light source and entrance surface of fiber cable and between exit surface of fiber cable and the sensing probe were optimized to be 12 mm and 5 mm, respectively. Then an experiment and a benchmark according to LM-80 were carried out for validation of the online testing system. After that, error estimation was conducted in a specific application of lifetime projection under accelerated life test. The systematic error and the measuring uncertainty were calculated to be within 0.2% and within 2%, respectively. This means that the proposed online testing system can be well utilized to monitor the lumen maintenance of LED modules. Finally, two applications using the online testing system were introduced. One is to explore the effect of packaging materials on the lumen depreciation of LEDs. It was found that the silicone encapsulant as one of the essential packaging materials could induce claws like voids and carbonization and the degradation of phosphor-silicone composite would lead to a fast light energy loss during the initial stage of high-temperature aging test. The other is to investigate the effect of silicone amount on the lumen maintenance of LEDs. The results showed that the decay rates of different sample sets change as the silicone amounts inside the packages change and the distribution of silicone encapsulant within the package also has influence on LED's lumen maintenance. The cause is assumed to be the silicone transmittance depreciation under elevated temperature aging, which is validated by well-designed simulations.

As a whole, the proposed online testing system opens a gate for the experimental method for LED reliability estimation. In the foreseeable range, more experiments can be designed to study the LED's reliability properties. These experiments include but are not limited to temperature cycling test, thermal shock test, high-temperature and high-humidity test, thermal step-stress test, etc. Therefore, more researches need to be done for a thorough understanding of LED's reliability issues.

Acknowledgment This work was financially supported by National Science Foundation of China (Grant Nos. 51376070 and 51576078).

References

1. S. Pimputkar, J.S. Speck, S.P. DenBaars, et al., Prospects for LED lighting. Nat. Photonics **3** (4), 180–182 (2009)
2. S. Liu, X.B. Luo, *LED Packaging for Lighting Applications: Design, Manufacturing and Testing* (Wiley, Beijing, 2011)
3. E.F. Schubert, T. Gessmann, J.K. Kim, *Light Emitting Diodes* (Wiley, New York, 2005)
4. T. Baumgartner, F. Wunderlich, A. Jaunich, et al., *Lighting the Way: Perspectives on the Global Lighting Market* (McKinsey, New York, 2012)
5. M. Meneghini, M. Dal Lago, N. Trivellin, et al., Chip and package-related degradation of high power white LEDs. Microelectron. Reliab. **52**(5), 804–812 (2012)
6. S.C. Yang, P. Lin, C.P. Wang, et al., Failure and degradation mechanisms of high-power white light emitting diodes. Microelectron. Reliab. **50**(7), 959–964 (2010)
7. ANSI/UL 8750-2009, *Standard for Light Emitting Diode (LED) Equipment for Use in Lighting Products* (National Electrical Manufacturers Association, Rosslyn, 2009)
8. ANSI/ANSLG C78.377-2011, *Specifications for the Chromaticity of Solid State Lighting Products* (National Electrical Manufacturers Association, Rosslyn, 2011)
9. IESNA LM-80-08, *IES Approved Method for Lumen Maintenance of LED Light Sources* (National Electrical Manufacturers Association, Rosslyn, 2008)
10. IESNA TM-28-14, *Projecting Long-Term Luminous Flux Maintenance of LED Lamps and Luminaires* (National Electrical Manufacturers Association, Rosslyn, 2014)
11. G. Meneghesso, S. Levada, E. Zanoni, et al., Reliability of visible GaN LEDs in plastic package. Microelectron. Reliab. **43**(9–11), 1737–1742 (2003)
12. Y.C. Hsu, Y.K. Lin, M.H. Chen, et al., Failure mechanisms associated with lens shape of high-power LED modules in aging test. IEEE Trans. Electron Devices **55**(2), 689–694 (2008)
13. J. Hu, L. Yang, M.W. Shin, Mechanism and thermal effect of delamination in light-emitting diode packages. Microelectron. J. **38**(2), 157–163 (2007)
14. M. Cai, G. Yang, S. Koh, et al., Accelerated testing method of LED luminaries, in *13th IEEE International Conference on Thermal, Mechanical and Multi-Physics Simulation and Experiments in Microelectronics and Microsystems (EuroSimE)* (2012)
15. S. Koh, C. Yuan, B. Sun, et al., Product level accelerated lifetime test for indoor LED luminaires, in *14th IEEE International Conference on Thermal, Mechanical and Multi-Physics Simulation and Experiments in Microelectronics and Microsystems (EuroSimE)* (2013)
16. Y.H. Yang, Y.F. Su, K.N. Chiang, Acceleration factor analysis of aging test on gallium nitride (GaN)-based high power light-emitting diode (LED), in *14th IEEE Intersociety Conference Thermal and Thermomechanical Phenomena in Electronic Systems (ITherm)*, (2014), pp. 178–181
17. N. Narendran, L. Deng, R.M. Pysar, et al., Performance characteristics of high-power light-emitting diodes, in *48th SPIE Annual Meeting on Optical Science and Technology*, (2004), pp. 267–275
18. N. Narendran, Y. Gu, J.P. Freyssinier, et al., Solid-state lighting: failure analysis of white LEDs. J. Cryst. Growth **268**(3), 449–456 (2004)
19. N. Narendran, Y. Gu, Life of LED-based white light sources. J. Disp. Technol. **1**(1), 167–171 (2005)
20. M. Bürmen, F. Pernuš, B. Likar, Automated optical quality inspection of light emitting diodes. Meas. Sci. Technol. **17**(6), 1372 (2006)
21. M. Bürmen, F. Pernuš, B. Likar, LED light sources: a survey of quality-affecting factors and methods for their assessment. Meas. Sci. Technol. **19**(12), 122002 (2008)
22. L. Svilainis, LED directivity measurement in situ. Measurement **41**(6), 647–654 (2008)
23. S. Zhou, S. Liu, Transient measurement of light-emitting diode characteristic parameters for production lines. Rev. Sci. Instrum. **80**(9), 095102 (2009)
24. L.A. Johnson, Laser diode burn-in and reliability testing. IEEE Commun. Mag. **44**(2), 4–7 (2006)

25. N. Trivellin, M. Meneghini, E. Zanoni, et al., A review on the reliability of GaN-based laser diodes. IEEE Int. Reliab. Phys. Symp. (IRPS), **43**(35), 1–6 (2010)
26. CIE, Publication No. 127, *Measurement of LEDs* (Central Bureau of the CIE, Vienna, 2007)
27. G.P. Eppeldauer, Spectral responsivity-based calibration of photometer and colorimeter standards. J. Mod. Opt. **60**(14), 1124–1135 (2013)
28. I. Moreno, C.C. Sun, Modeling the radiation pattern of LEDs. Opt. Express **16**(3), 1808–1819 (2008)
29. A. Starikov, A.T. Friberg, One-dimensional Lambertian sources and the associated coherent-mode representation. Appl. Opt. **23**(23), 4261–4268 (1984)
30. J.M. González-Leal, Optical functionalities of dielectric material deposits obtained from a Lambertian evaporation source. Opt. Express **15**(9), 5451–5459 (2007)
31. HAAS-2000 high accuracy array spectral-radiometer. [Online]. Available: http://www.everfine.cn
32. Philips Lumileds, DR04: LM-80 Test Report (2011)
33. IESNA TM-21-11, *Projecting Long Term Lumen Maintenance of LED Light Sources* (National Electrical Manufacturers Association, Rosslyn, 2011)
34. J. Hu, L. Yang, M.W. Shin, Electrical, optical and thermal degradation of high power GaN/InGaN light-emitting diodes. J. Phys. D: Appl. Phys. **41**(3), 035107 (2008)
35. M.H. Chang, D. Das, P.V. Varde, et al., Light emitting diodes reliability review. Microelectron. Reliab. **52**(5), 762–782 (2012)
36. R.J. Xie, N. Hirosaki, N. Kimura, et al., 2-phosphor-converted white light-emitting diodes using oxynitride/nitride phosphors. Appl. Phys. Lett. **90**(19), 1101 (2007)
37. J. Huang, D.S. Golubovic, S. Koh, et al., Rapid degradation of mid-power white-light LEDs in saturated moisture conditions. IEEE Trans. Device Mater. Reliab. **15**(4), 478–485 (2015)
38. K. Wang, D. Wu, F. Chen, et al., Angular color uniformity enhancement of white light-emitting diodes integrated with freeform lenses. Opt. Lett. **35**(11), 2010 (1860-1862)
39. Z. Liu, S. Liu, K. Wang, et al., Measurement and numerical studies of optical properties of YAG: Ce phosphor for white light-emitting diode packaging. Appl. Opt. **49**(2), 247–257 (2010)

Chapter 14
Degradation Mechanisms of Mid-power White-Light LEDs

Jianlin Huang, Dušan S. Golubović, Sau Koh, Daoguo Yang, Xiupeng Li, Xuejun Fan, and Guo Qi Zhang

Abstract In this chapter, the optical degradation mechanisms of mid-power white-light LED packages have been studied by using high-temperature operation life test (HTOL), wet-high-temperature operation life (WHTOL) test, and highly accelerated temperature-humidity test (HAST). As a result, it was found that (1) for LED packages aged under HTOL, the major degradation mechanism is different for samples aged at 55 °C and ambient temperature higher than 85 °C, with which lead frame deterioration is the major degradation mechanism at 55 °C, while Ohmic contact deterioration is the major degradation mechanism at 105 °C for the aged

J. Huang (✉)
Beijing Research Center, Delft University of Technology, No.A35, Qinghua East Road, Beijing 100083, China
e-mail: J.Huang-37@tudelft.nl

D.S. Golubović
Philips Lumileds Lighting Company, No.888 Tianlin Road, Shanghai 200233, China
e-mail: Dusan.Golubovic@philips.com

S. Koh
Huawei Technologies Co., Ltd, No. 133, Xuegang North Road, Shenzhen 518129, China

D. Yang
Guilin University of Electronic Technology, No.1 Jinji Road, Guilin, Guangxi 541004, China
e-mail: daoguo_yang@vip.163.com

X. Li
Philips Lighting, No.888 Tianlin Road, Shanghai 200233, China

X. Fan
State Key Laboratory of Solid State Lighting (Changzhou Base), Changzhou, China

Department of Mechanical Engineering, Lamar University, Beaumont, USA
e-mail: xuejun.fan@lamar.edu

G.Q. Zhang
State Key Laboratory of Solid State Lighting, Institute of Semiconductors, Chinese Academy of Sciences, Beijing, China

State Key Laboratory of Solid State Lighting (Changzhou Base), Changzhou, China

EEMCS Faculty, Delft University of Technology, Delft, The Netherlands
e-mail: g.q.zhang@tudelft.nl

© Springer International Publishing AG 2018

W.D. van Driel et al. (eds.), *Solid State Lighting Reliability Part 2*, Solid State Lighting Technology and Application Series 3, DOI 10.1007/978-3-319-58175-0_14

LED packages; (2) for LED packages aged under WHTOL, both deterioration of the Ohmic contacts of the blue chip and yellowing of the package encapsulant are considered as the major degradation mechanisms; (3) and for LED packages aged under HAST, the failure mechanism is considered as the result of blue light over-absorption, which generates very high temperature inside the silicone bulk, resulting in serious carbonization.

14.1 Introduction

Mid-power white-light LED is a relatively new category of LED products that are typically driven within a range of 0.2–1 W. Figure 14.1 shows two kinds of typical mid-power LEDs in the market. Generally, the mid-power LED packages are composed of four components: blue die, lead frames, silicone/phosphor component, and package housing. More specifically, for samples used in our experiments, two pieces of 0.6-mm^2 area blue dies were mounted onto the lead frame by die attach, and gold wires were bonded to connect both blue dies in series and then connect them to lead frames. After wire bonding, silicone mixed with phosphors was dispersed into the package housing and was cured as the encapsulant of the package. Blue lights are converted into white lights after passing through the silicone mixed with phosphors that are dispersed into the package housing. The specified correlated color temperature (CCT) is achieved by carefully tuning the concentration of the phosphors during manufacturing.

Unlike high-power LED packages, mid-power LED packages use plastic package and copper lead frames instead of the traditional ceramic material due to the lower requirement in heat dissipation [1]. Under high temperatures typically experienced by LEDs used for lighting, the very plastic packaging that reduces the cost of the device is also a source of reliability issues, such as color shift and lumen degradation [2, 3]. Recently, driven by demands of cost-down, manufacturers have successfully developed mid-power white-light LEDs which can be powered up to 1.5 W by means of integrating more chips inside one package and overdriving the package with higher forward currents. The trend in smaller package size and more

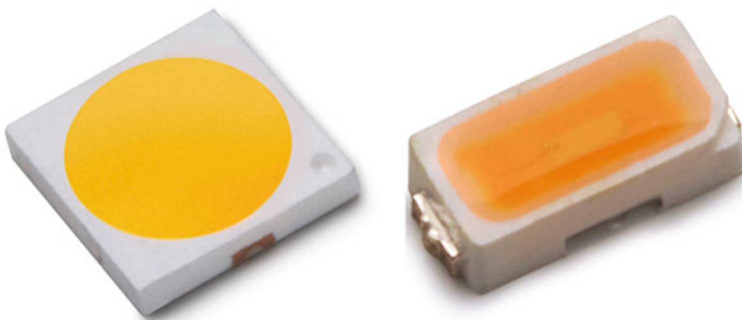

Fig. 14.1 Typical mid-power white-light LEDs

compact integration imposes new challenges in rising LED temperatures in packages. Under high ambient temperature and Joule heating, it has been found that LED packages might suffer from degradation of the Ohmic contacts and semiconductor [4], deterioration of the lead frame's silver coating [5–7], yellowing of encapsulant [8, 9], silicone carbonization [10, 11], as well as phosphor thermal quenching [12].

Besides, LED packages may also suffer from serious reliability issues when operated under environment with a high humidity and high temperature. This is often the case in tropical countries. For instance, LED can be exposed to an average humidity of 83.4% RH and temperature of 125 °C if it is a LED headlight in Singapore's automotive [13]. In order to understand the effects of moistures on the LED products, a few researchers conducted a series of experiments, such as wet-high-temperature operation life (WHTOL) test [14, 15] and highly accelerated temperature and humidity stress test (HAST) [16, 17]. Results showed that the optical degradation of LED packages was mainly due to delamination of packages [18], lights scattering of water particles inside the silicone volume [19], bubble generation in the encapsulant [16], and dissolution of phosphors [20].

These factors could lead to optical degradation of LED packages [21, 22] and finally the shortening of their service lifetime. Reliability issues involved in the mid-power LED packages have been summarized as in Table 14.1 [1, 23]. However, due to complex interactions among multiple failure modes and limited data at the moment, the failure mechanisms are still an opaque issue.

Based on the understanding that optical degradation of LED packages can be accelerated if stressed under the combined effect of humidity and temperature, some studies have been conducted to develop new methodologies to replace the traditionally temperature-only-based test, such as IES LM-80-08 [24]. Fan et al. [1] demonstrated that wet-high-temperature operation life (WHTOL) test could be used for the prediction of LED lumen maintenance with shorter testing time (one third of LM-80-08 test time). More aggressively, Liu et al. [25, 26] presented their results by highly accelerated temperature and humidity stress test (HAST). The authors claimed that this type of accelerated tests could be applied for lifetime

Table 14.1 Optical degradation mechanisms of mid-power LEDs

Failure mode	Failure mechanism	Triggered stress
Chip deterioration	Crystal defects, dopant diffusion, Ohmic contact deterioration	Thermal-mechanical stress, electrical overstress, thermal stress
Encapsulant carbonization/ yellowing	Decrease in transparency	Thermal stress, photodegradation, electrical overstress
Package housing yellowing	Decrease in reflectivity	Thermal stress, photodegradation
Lead frame deterioration	Copper diffusion, metal recrystallization, contamination	Thermal-mechanical stress, hygro-mechanical stress, harmful elements (S, Cl, etc.)
Phosphor degradation	Quantum efficiency by thermal quenching of phosphor	Thermal stress

extrapolation from HAST to WHTOL. However, our previous study [27] indicated that the degradation mechanisms in these two different conditions were much different. It was found that the rapid lumen degradation during HAST was mainly due to serious silicone carbonization [27], while for WHTOL, the degradation was due to chip deterioration and package housing yellowing [28]. Up to now the failure mechanisms of silicone carbonization have not yet fully been understood.

The remaining parts of this chapter are organized as follows.

In Sect. 14.2, the reliability of mid-power white-light LEDs was investigated by high-temperature operation life (HTOL) test. According to the test standard (IES standard LM80-08) [29], the aging duration lasted as long as 6,000 h. After finishing the tests, optical and electrical characteristics of the aged samples were analyzed subsequently. Furthermore, failure analysis of the LED packages was also performed to further study the failure modes and failure mechanisms.

In Sect. 14.3, the optical degradation of mid-power LED packages was studied by wet-high-temperature operation life (WHTOL) test. Optical characteristics, spectrum power degradation, and electrical deterioration were studied. Failure analysis of the degraded samples was also performed to further investigate the degradation mechanisms.

In Sect. 14.4, the failure mechanisms of silicone carbonization occurred during highly accelerated temperature and humidity stress test (HAST) were investigated through the combined experiments, failure analysis, and simulation. A series of experiments as well as failure analysis were performed to separate or eliminate some possible root causes. Blue chip Joule heating, phosphor's self-heating, and blue-color spectrum's over-absorption in silicone were carefully analyzed.

14.2 Optical Degradation Mechanisms Under HTOL

14.2.1 Experiment Setup

In order to reduce effects of sample deviation during testing, 28 pieces of LED packages were prepared for each stressing condition. LED packages were soldered onto metal-core printed circuit boards (MCPCBs). The MCPCBs have a thermal conductivity of 2.2 W/m·K, which guaranteed the reliable heat dissipation during testing.

After the initial measurement, samples were aged by using three climate-aging chambers, which were specially designed for IES LM-80-08 test. The samples were first mounted onto an integrated thermal control system, which regulated the aging temperature during testing. Two thermal couples were used to monitor the test temperature. One was mounted onto the center area of the MCPCB for case temperature monitoring, while the other one was placed several centimeters away from the surface of the MCPCB for ambient temperature monitoring. Based on the feedback of both thermal couples, the case temperature was automatically adjusted

by the integrated thermal control system when the monitored temperature ran out of the specified limit. According to our test condition, the case temperature was maintained within an error of ±2 °C. In addition, the driving current was also monitored. SpikeSafe Test System was used to provide and record the driving current. The variation of the driving current is controlled within ±3% of its setting value. In addition to this, power protection was also predefined. When the driving current is 60% higher/lower than the setting output, the DC supply would be disconnected from the samples and test suspended. This assures no thermal run-away, power outage, surge in current due to unstable power lines if any, and so on. According to the IES standard LM80-08 [24], the samples were aged at temperatures of 55 °C, 85 °C, and 105 °C, combining with two driving currents (i.e., 160 mA and 220 mA), respectively.

On the other hand, thermal resistance was also measured on three pieces of LED packages by using T3ster system. As there is no auxiliary equipment for radiant power measurement, the input electrical power was considered instead of total Joule power by default in the T3ster system. The thermal resistance from LED junction to the solder joints was obtained, i.e., $Rth_{j-s} = 17^{\circ}C/W$. As a result, the highest junction temperature for LED packages aged at 105 °C/160 mA was calculated as in Eq. 14.1:

$$T_j = 105 + 6.4 \times 0.16 \times 17 = 122.4^{\circ}C \tag{14.1}$$

Similarly, the highest junction temperature is calculated as 129 °C for LED packages aged at 105 °C/220 mA. For LEDs aged at other stress conditions, the junction temperatures were confirmed to be less than 125 °C, implying all samples were aged at normal conditions.

After a predefined aging period, the samples were taken out of the aging chambers for optical and electrical measurement. The measurement system is composed of (1) a constant current power supply, which not only provides constant driving currents but also measure the voltage drop of each LED package at the same time; (2) a half-meter integrated sphere, which is used to obtain uniform light distribution; (3) and a spectrometer with 1040 charge-coupled devices (CCDs), which is responsible for light spectrum collection. In order to obtain accurate optical parameters, the system was recalibrated, and discoloration of the MCPCB was compensated prior to each measurement. In addition, three non-stressed samples were measured to monitor the stability of the measurement system. The measurement was executed by driving the LEDs with a mono pulse current, which is finished within 35 ms in order to avoid LED packages self-heating. The measurement current is the same as the stressing current for the LED packages. An acquisition time of 20 ms was provided to ensure enough light exposure. Parameters including forward voltage, and spectrum power, were collected. Figure 14.2 provides pictures of the tested samples, the test equipment, and the measurement system. By using this measurement system, optical and electrical measurement of the samples was performed at a series of predefined time, i.e., 0 h, 48 h, 168 h, 500 h, 1,000 h, 2,000 h, 3,000 h, 4,000 h, 5,000 h, and 6,000 h.

Fig. 14.2 *Bottom left*: samples under aging; *top left*, aging chamber; *right side*, optical and electrical measurement system

After the end of the aging tests, the data were fitted in terms of least square method, based on the hypothesis that the optical output was exponentially degraded along with aging time. Only LED packages with gradual degradation was considered, and those suffered sudden optical degradation were excluded as their degradation mechanisms were different. As a result, the sample size used for data fitting is 26 pieces for the condition of 105 °C/220 mA and 28 pieces for other stress conditions. According to the IES standard TM-21-11 [30], the collected data were first normalized at 0 h for each individual sample tested and then performed an exponential least squares curve fit through the individual values for Eq. 14.2, all fitted data were left-censored by eliminating measurement data obtained before 1,000 h.

$$\Phi(t) = \Phi_0 \cdot \exp(-\alpha t) \tag{14.2}$$

where $\Phi(t)$ is the normalized optical output at time t, Φ_0 is the projected initial constant derived by the least squares curve fit, and α is the decay rate constant which is related to aging stress level.

14.2.2 *Results and Discussion*

14.2.2.1 Optical Degradation Characteristics

The individual lumen values of all samples at different measurement point were normalized to their initial values. As a result, the normalized optical output was found to follow exponential degradation kinetics, as shown in Fig. 14.3. Sharp optical degradation was observed after aging for 1,000 h. The phenomenon was more prominent at stress condition of 105 °C. At this stress condition, 5% of optical degradation has been observed, which is much higher than the normalized optical degradation for LEDs stressed at 55 °C and 85 °C.

The optical degradation does not seem to be temperature sensitive when the case temperature was lower than 85 °C. For LED packages aged at 55 °C and 85 °C, almost the same trend was sustained after aging for 6,000 h, as plotted in Fig. 14.3. In addition, as can be seen from Fig. 14.4, the optical degradation was not current

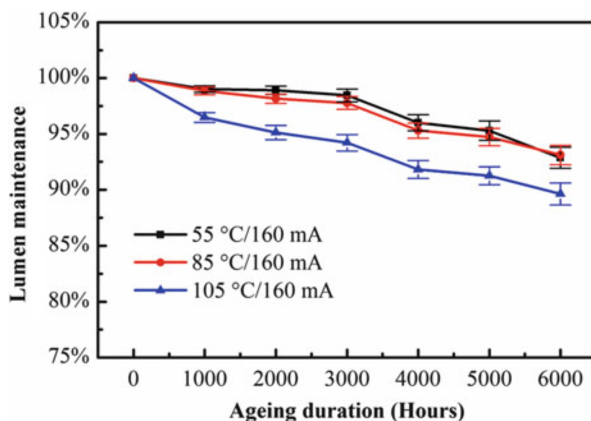

Fig. 14.3 Optical degradation of sample aged at different case temperatures

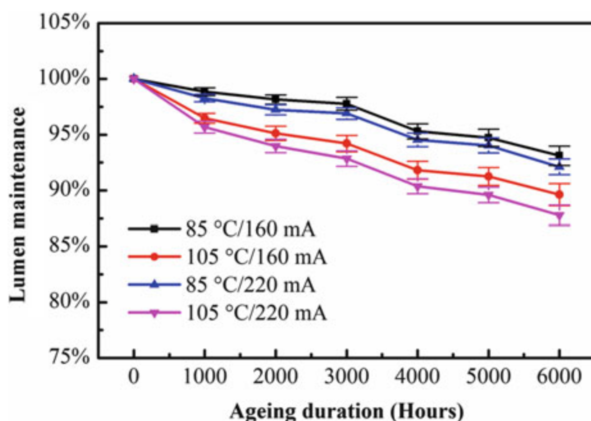

Fig. 14.4 Optical degradation of samples stressed by different driving currents

sensitive neither by comparing optical output of LED packages aged at 85 °C/160 mA and 85 °C/220 mA. The difference of lumen maintenance is due to the initial degradation. However, after aging for 2,000 h, the lumen maintenance shows parallel trends. Similar optical degradation kinetics indicated that the degradation mechanisms were not neither temperature-activating dominant [2] nor current-activating dominant at 55 °C and 85 °C. For LED packages aged at 105 °C, as can be observed in Fig. 14.4, significant difference was observed between 160 and 220 mA, as the standard error bars of the lumen maintenance at each readout point for these stressing conditions did not overlap each other. Due to Joule heating effect, the junction temperatures for LED packages stressed by 105 °C/160 mA and 105 °C/220 mA are close to the maximum junction temperature (125 °C) guaranteed by manufacturer. It can be easily concluded that the LED packages were much more sensitive to current stress when junction temperatures were around the upper limit of the blue chip's capacity.

In order to further understand the optical degradation kinetics, activation energy was calculated in terms of Arrhenius equation. The decay rate constant α was calculated by the least squares curve fit outlined in IES TM-21-11. The correlation to Arrhenius equation is in Eq. 14.3:

$$\alpha = A \cdot \exp\left(-\frac{E_a}{\mathrm{kT}}\right) \tag{14.3}$$

where A is the pre-exponential factor which is related to effects of uncertain stress, k is the Boltzmann constant (8.6173×10^{-5} eV/K), T is the case temperature of the stress condition, and E_a is the activation energy. According to the IES standard TM-21-11, the current effect was considered in terms of thermal effect, as the current effect was mainly transferred to Joule heating. The calculation was performed, respectively, for LED packages with different driving current. Table 14.2 listed the activation energy E_a calculated from different stress conditions.

As presented in Table 14.2, the activation energy was close to 0 eV for LED packages stressed in temperatures ranging from 55 to 85 °C. An activation energy of 0 eV indicates that only temperature effect cannot appropriately describe the degradation kinetics of the LED devices. Except for temperature effect, the effects of other stress, such as humidity, should be carefully accounted for. However, the calculated activation energy has been reached 0.254 eV when LED packages were aged in the range of 85–105 °C (driving current was held at 220 mA). Additional thermal aging tests for the LED packages from the same batch also showed consistent E_a, which was 0.273 eV (samples were aged at 85 °C and 105 °C, respectively, while driving currents were held at 240 mA). This activation energy

Table 14.2 Decay rate constant and corresponding activation energy

Temperature		55–85 °C	85–105 °C
Current	160 mA	0.0005	0.214
	220 mA	0.056	0.254

is similar to that reported value in [31, 32]. However, this activation energy is much lower than that reported in [2], in which the activation energy was calculated as high as 1.5 eV for samples aged at 180 °C and 230 °C, indicating that an accelerating degradation test at such a high temperature (180–230 °C) is not feasible for reliability evaluation of LED packages which are operated at application conditions (solder temperature ranges from 85 to 105 °C).

14.2.2.2 Spectrum Analysis

To investigate and separate the effects of degradation due to chip and package related, first, the silicone encapsulant was carefully removed from the stressed and non-stressed LEDs, and then optical measurement was performed by using an integration sphere system to obtain the LED source degradation directly. The spectra were collected by a spectrometer as described in previous section. Four pieces of non-stressed LED packages and four pieces of stressed LED packages (randomly selected from samples aged at 55 °C/220 mA) were measured respectively.

The total spectrum power of the emission wavelengths ranging from 440 to 460 nm (peak wavelength is 451 nm for the blue lights.) was averaged for both the non-stressed and stressed LED packages, respectively. After that, the average value of the non-stressed LED packages was normalized to 100%, and the percentage of the averaged spectrum power of the stressed LED packages to that of the averaged non-stressed LED packages was plotted in Fig. 14.5. As presented in Fig. 14.5, a decrease of the spectrum power was observed for those stressed LED packages, as compared to that of the non-stressed LED packages, indicating the chip deterioration of the stressed LED packages. The degradation linearly increases with the measurement current. As a consequence, a measurement current of 220 mA induces a degradation value of 4.5%.

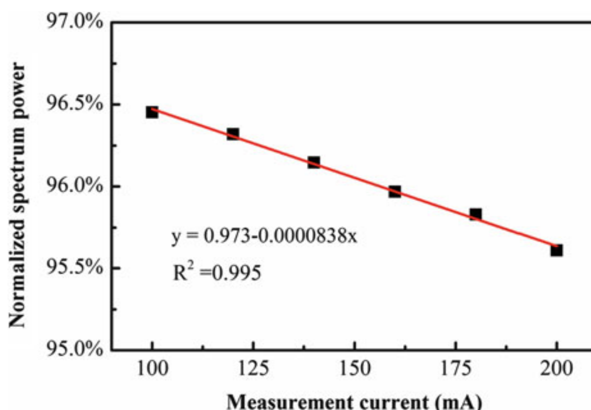

Fig. 14.5 Degradation of blue light intensity vs. measurement current

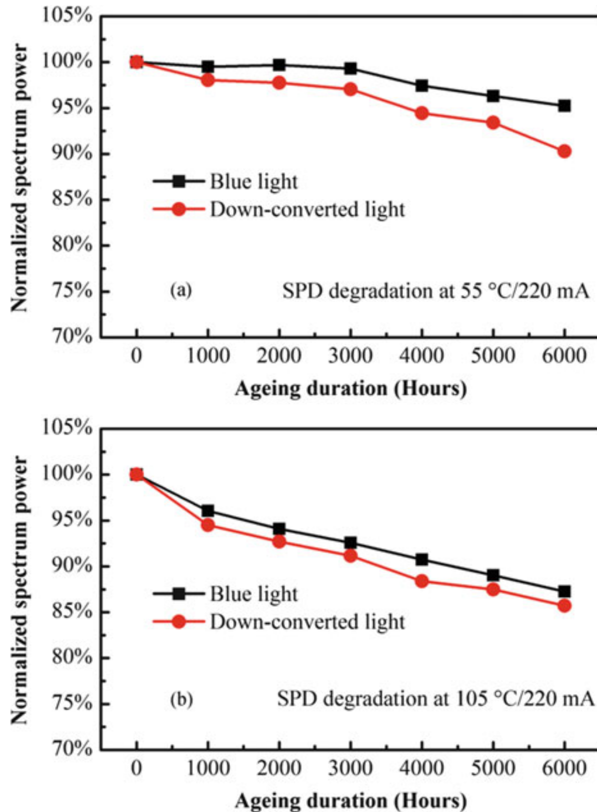

Fig. 14.6 Degradation of light intensity at peak wavelengths

Secondly, the spectra of the stressed LED packages collected at readouts from 0 to 6,000 h were also averaged and normalized. Similar to previous paragraph, the total spectrum power of the emission wavelengths from 440 to 460 nm (peak wavelength is 451 nm for the blue lights.), and down-converted wavelengths from 600 to 620 nm (peak wavelength is 610 nm for the down-converted lights.) obtained at each individual readout, was averaged, respectively, for the individual stress condition. Then, the average values obtained at 0 h was normalized to 100%, and the percentage of the averaged spectrum power obtained at other readouts to that obtained at 0 h was plotted in Fig. 14.6.

As indicated in Fig. 14.6a, for samples aged at 55 °C, it was found that degradation of the blue lights' normalized spectrum power was about 4.7% at 6,000 h, which is quite close to that measured by first removing the silicone of the LED samples. This finding demonstrates that spectra directly collected from the aged LED packages can be used to separate the effects of degradation due to chip and package related.

Based on this conclusion, it is found that the rapid optical degradation for LED packages aged at 105 °C was mainly attributed to the degradation of intensity of the

blue lights, as shown in Fig. 14.6b. In details, blue chip deterioration attributes about 12% and package-related degradation attributes 1.8% to the total lumen degradation. In addition, it is interesting that the package-related degradation has been triggered after 1,000 h, while no more contributions after that, as the difference between the normalized spectrum powers of the blue lights and down-converted lights is almost the same from 1,000 to 6,000 h.

While for LED packages aged at 55 °C, the spectrum degradation showed much more complicated degradation kinetics than that of LED packages aged at 105 °C. It was found that the initial optical degradation was only attributed to the reduction of down-converted light degradation because very little degradation was observed on the blue lights until 2,000 h. A difference of 1.5% was observed between the spectrum power of the blue lights and down-converted lights after aged for 1,000 h, indicating package-related degradation has been triggered. As the percentage amount is quite similar to that of LED packages aged at 105 °C, it is considered that this initial degradation is triggered by stresses rather than temperature. An elevated temperature from 55 to 105 °C did not induce higher package-related degradation at this readout.

By aging the samples from 1,000 to 6,000 h, the degradation of the blue lights and down-converted lights increased from 0.3% to 4.7% and from 2% to 9.7%, respectively, indicating chip deterioration attributes about 4.7% and package-related degradation attributes 5% to the lumen degradation after 6,000 h.

14.2.2.3 Chip Deterioration by I–V Characteristic Analysis

Figure 14.7 shows the I–V characteristics of the non-stressed and stressed LED packages. In Sect. 14.3.2, we have found chip-related deterioration at 55 °C and 105 °C. It has been found that the chip-related degradation of the LED packages is due to either junction deterioration or Ohmic contact deterioration [4, 33]. In order to understand the effects of blue chip degradation to optical performance, the I–V

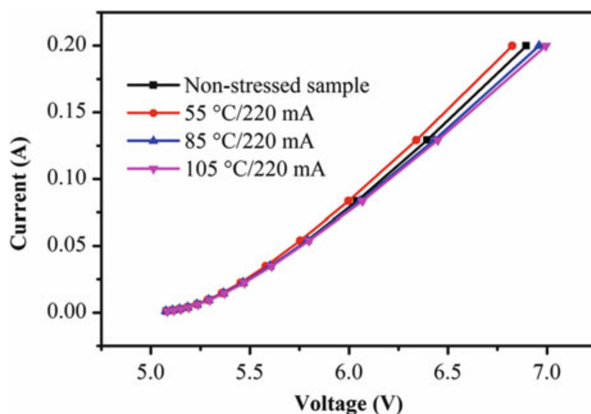

Fig. 14.7 I–V characteristics of LED packages

characteristics was studied in terms of series resistance and ideality factors at high current region (forward current >1 mA) by following equation [34]:

$$I\frac{dV_F}{dI} = R_S I + \frac{nkT}{q} \tag{14.4}$$

where I is the forward current, V_F is the forward voltage, R_S is the series resistance, n is the ideality factor, k is the Boltzmann constant (8.6173×10^{-5} eV/K), T is the measurement temperature, and q is electron charge. The currents vary from 1×10^{-3} to 2×10^{-1} A and corresponding forward voltages were collected for least square fitting.

Notice that the LED packages used in our experiments use two pieces of blue chips that were connected in series. As the equation above can only apply in one single chip, the forward voltage V_F in the equation is only half of the voltage measured from the LED package. This is reasonable because the blue chips are produced by not only using the same materials and processes. They are also classified in the same bin. Furthermore, the blue chips undergo similar stress condition, such as electrical and thermal stress. As a result, the performance and degradation kinetics of the blue chips in one LED package should be similar to each other. The calculated ideality factor and series resistance are shown in Table 14.3.

For the non-stressed LED packages, it is found that the ideality factor n is calculated as 2.16, which is in line with that reported in [35], in which an ideality of 1.5–2.5 was found in GaN-based p-n structures grown on SiC substrates. For the LED with an ideality factor higher than 2.0, Shah et al. [36] proposed a model in which the GaN-based p-n junction diode was modeled by a series of diodes, i.e., the actual GaN p-n junction diode, unipolar heterojunction diodes, and a reverse-biased Schottky diode at the metal/p-type GaN junction. According to Shah's model, the LED in our samples can be modeled by an actual GaN p-n junction diode, which is connected in series with a unipolar heterojunction diodes which are assumed to be very leaky, so that Ohmic rather than rectifying characteristics are exhibited [36].

For samples aged at 55 °C, significant reduction of the ideality factor n was observed as compared with that of the non-stressed samples. At this case temperature, a value of ideality factor around 2.0 was calculated, implying perfect space-charge recombination and p-n junction improvements of the blue chip after aging test [37]. An ideality factor of 2.0 also indicates that Ohmic rather than rectifying characteristics are exhibited in the unipolar heterojunction diodes after aging test. The p-n junction improvement of blue chip was due to annealing effect of the thermal stress, which had been proposed by many researchers [38–40]. In addition,

Table 14.3 Ideality factors and series resistance for samples stressed by 220 mA

Parameter	n	R_S
Non-stressed	2.16	3.40
55 °C	2.01	3.38
85 °C	2.01	3.54
105 °C	1.95	3.71

the series resistance of samples aged at these case temperatures was similar with that of the non-stressed samples, indicating no obvious deterioration of the Ohmic contacts of the blue chip. However, as already verified in the spectrum analysis, the degradation of the spectrum power of the blue chip was found as around 4.5% for LED packages aged at 55 °C after 6,000 h. As no junction deterioration or Ohmic contact deterioration was observed at this condition, the degradation was considered as being induced by either transmittance decrease of the indium tin oxide (ITO), or refractivity deterioration of the multi-layer structure of the chip surface, which needs to be further verified in the future.

On the other hand, for samples aged at 85 °C and 105 °C, significant changes was found on the series resistance R_S, indicating Ohmic contact deterioration was triggered [39]. The increase of the series resistance would affect the emission efficiency of the blue chips, thus rendering the lumen degradation of the LED packages [4]. However, an ideality factor of 1.95–2.01 shows that the LED is in perfect carrier recombination in the space charge region, mediated by recombination centers located near the intrinsic Fermi level [37]. The increase in series resistance is ascribed to the thermally activated metal-metal and metal-semiconductor interdiffusion [41, 42]. A reduction of the active acceptor concentration, due to the interaction between hydrogen and magnesium, can worsen the properties of the anode contact and vary the resistivity and injection properties of the p-layer, thus leading to the measured I–V modifications [43] and optical degradation.

14.2.2.4 Package Degradation Investigation by Physics Analysis

Figure 14.8 shows the appearances of a non-stressed sample and a stressed sample aged at 55 °C and 105 °C. No obvious difference was found between epoxy material compound (EMC) appearance of the non-stressed samples and of samples aged at 55 °C, while slight yellowing was observed on the outer surface of samples aged at 105 °C.

Silicone carbonization was eliminated from the aged samples by observing the silicone surface that attaches to the chip, as indicated in Fig. 14.9. However, silicone yellowing was found by analyzing the element content of the silicone gel near the upper surface of the chip using by means of energy-dispersive X-ray spectroscopy (EDX). As presented in Tables 14.4, 14.5, and 14.6, the atomic % of the element C and O of the silicone residuals, of the LED samples aged at 55 °C and 105 °C, is similar to each other, while it is about 5% higher than that detected from the non-stressed LED samples. Similar atomic % indicates the change of the element C and O is not due to temperature. The change of the element C and O also implies silicone degradation [44], which was considered as a contributor of the initial lumen degradation of the LED packages, as the silicone degradation was only observed at the initial aging duration, as shown in Fig. 14.10.

As presented in Fig. 14.11 are the C-SAM results of LED packages aged at 55 °C. Delamination was not observed neither at the chip/silicone interface nor the

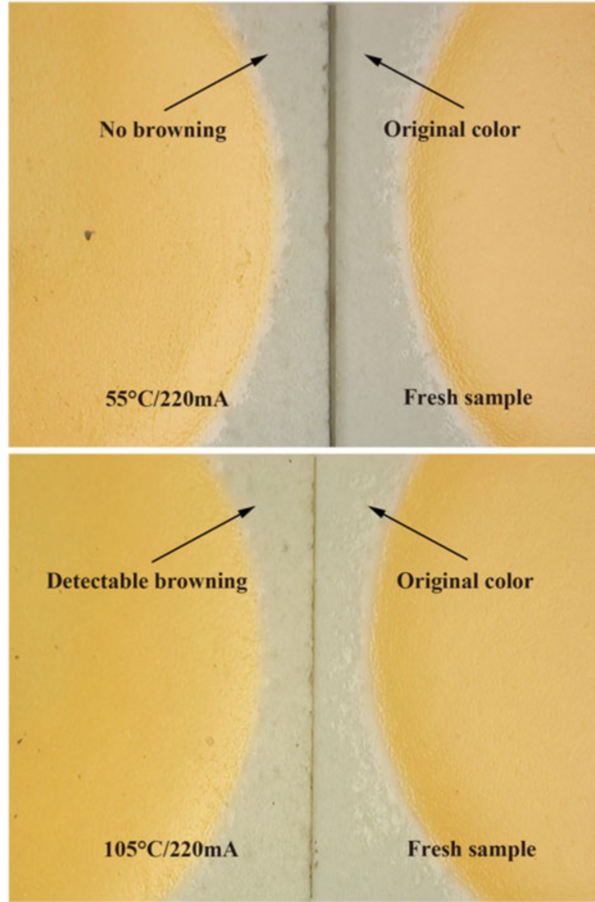

Fig. 14.8 Appearance of samples before aging and after aging for 6,000 h

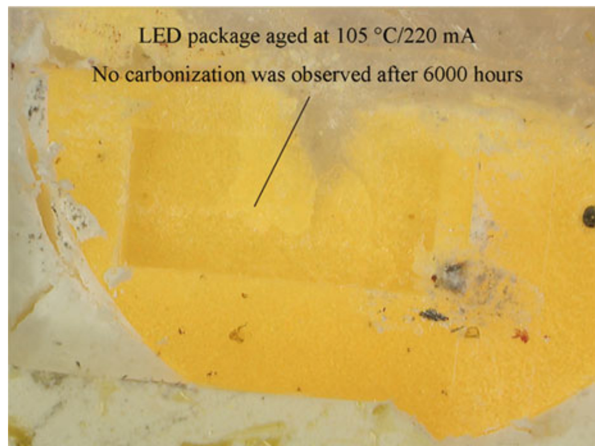

Fig. 14.9 Silicone of LED packages aged at 105 °C/ 220 Ma

Table 14.4 Element content of silicone gel in non-stressed LED packages

Element	Weight %	Atomic %
C K	53.25	67.29
O K	18.24	17.30
Si K	28.51	15.40
Totals	100.00	

Table 14.5 Element content of silicone gel in LED packages aged at 55 °C

Element	Weight %	Atomic %
C K	55.68	66.90
O K	26.58	23.98
Si K	17.74	9.12
Totals	100.00	

Table 14.6 Element content of silicone gel in LED packages aged at 105 °C

Element	Weight %	Atomic %
C K	49.50	63.01
O K	23.11	22.08
Si K	27.39	14.91
Totals	100.00	

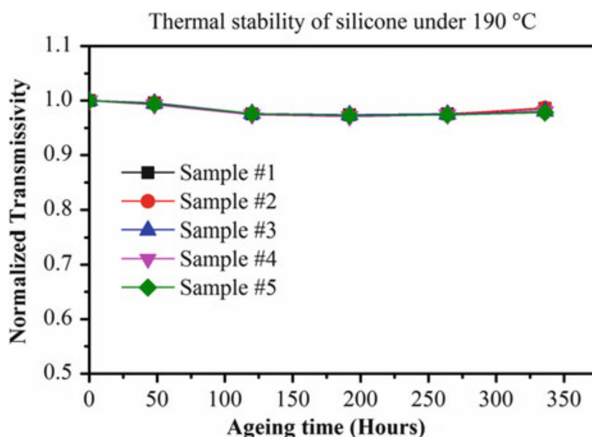

Fig. 14.10 Silicone transmittance vs. aging time in high-temperature storage test

silicone/lead frame interface. Delamination was not observed at the interface of die/die attach gel neither. Similar results were also observed on LED packages aged at 105 °C. However, the picture was not shown here due to content limitation.

Energy-dispersive X-ray spectroscopy (EDX) analysis shows that there are no S, Cl, Br, and I were found on the silver-coating lead frames, thus eliminating chemical contamination as the root cause of the lead frame degradation [6], as indicated in Fig. 14.12. However, shallow pits were observed at the lead frames of samples aged at 55 °C, as shown in Fig. 14.13. It was speculated that, for samples aged at 55 °C, higher relative humidity as compared that at 105 °C leads to an

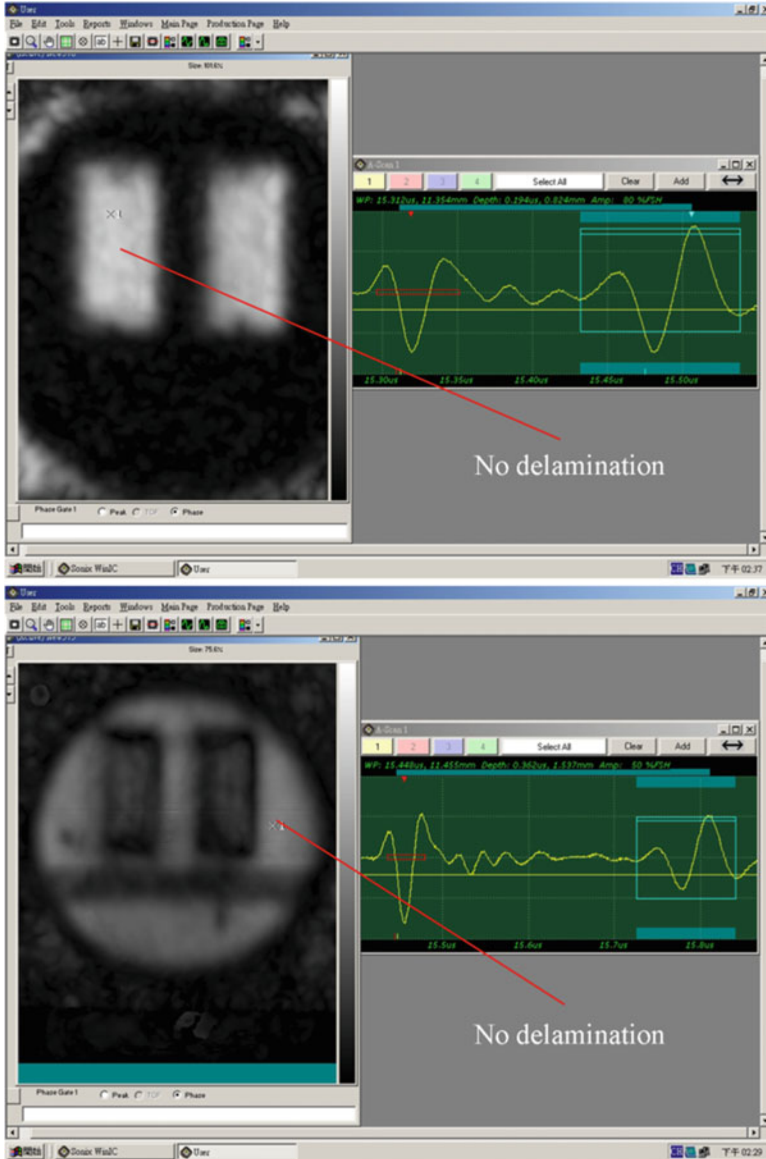

Fig. 14.11 No delamination was found in the aged packages by using C-SAM

osteoporosis structure of the silver coating due to internal stress induced by moisture penetration, resulting in the deterioration of the reflectivity of the lead frames.

Actually, it is found that the relative humidity is still around 13% when case temperature is 55 °C, as shown in Fig. 14.14. Same observation had also been

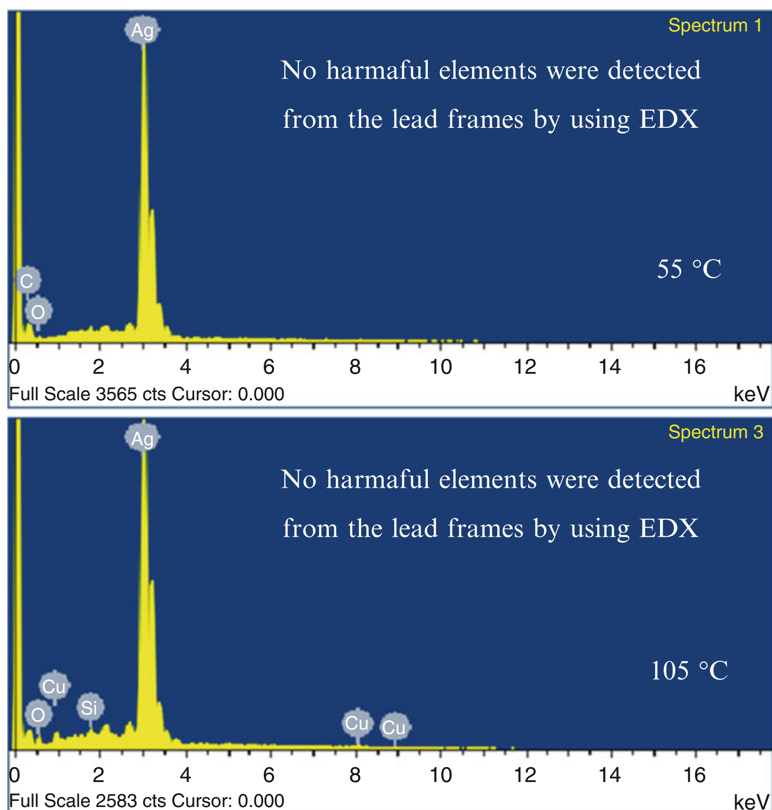

Fig. 14.12 No harmful elements were found by using EDX analysis

observed by Fan et al. [45]. The effect of moisture ingress into the electronic packages, though not LED packages, had been reported as considerable even at a low relative humidity of 10%, as in the case of the aging chamber [46]. For LED packages aged at temperatures at 55 °C, influence of moistures should be carefully taken into account.

The quantum efficiency of the phosphors was not detected due to lack of equipment. However, YAG-(Ce^{3+}) phosphors had been reported to be very stable during thermal aging, thus eliminating any significant nonradioactive quenching processes that existed in the aged samples [47]. On the other hand, Hu et al. [48] reported highly thermal stability of the nitride phosphors after aging for 30 min at 1,000 °C. Moreover, Cheng et al. [49] reported the highly thermal stability of broadband phosphors which were fabricated by sintering the mixture of multiple phosphors (including YAG, LuAG, and nitride) on SiO_2-based glass. All these evidences indicate low possibility of the phosphor degradation in LM-80-08 tests as the highest temperature is only around130 °C in our experiments.

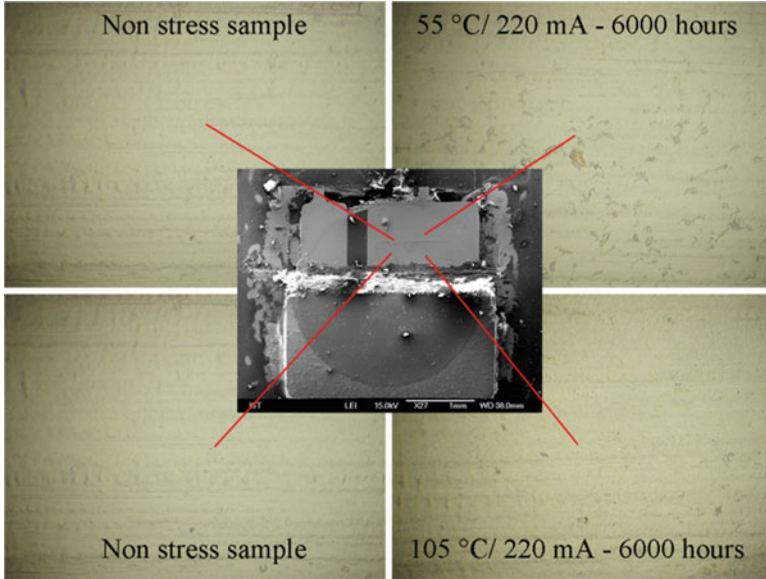

Fig. 14.13 Morphology of the surface of the silver-coating lead frame

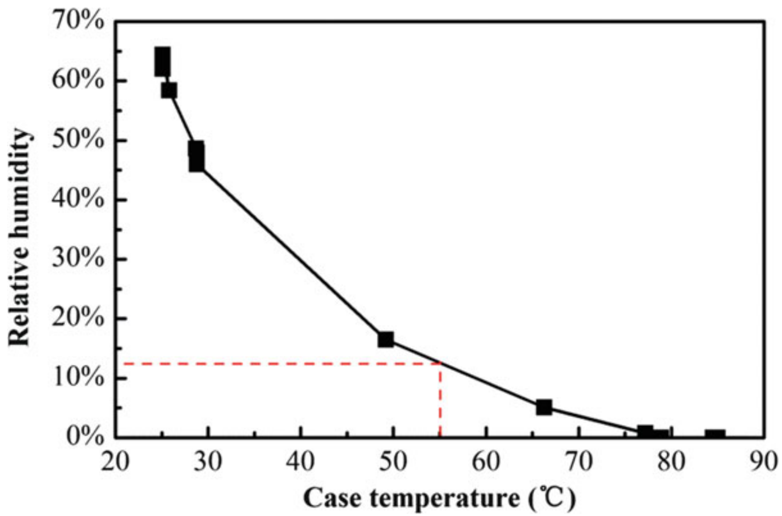

Fig. 14.14 Measured relative humidity versus increase of case temperature

14.3 Optical Degradation Mechanisms Under WHTOL Test

14.3.1 Experiment Setup

Twenty pieces of MP-3030-EMC LED packages (with two blue chips connected in series) were assembled onto an aluminum-based metal-core printed circuit board (MCPCB) by using SAC305 lead-free solder paste. All LED packages were distributed uniformly and connected in series on the MCPCB. At the same time, thermal pad was attached onto a heat sink carefully, on which the MCPCB was then mounted with five screws. This ensures good heat dissipation from LED packages to the heat sink. Total four pieces of MCPCBs were prepared, and only one MCPCB was aged per test condition.

The samples were placed into a climate chamber after finishing the initial optical measurement. During aging test, the ambient temperature and relative humidity of the chambers were maintained at a constant value of 85 °C and 90% RH, 95 °C and 45% RH, and 95 °C and 95% RH, respectively. For convenience, the test was named as WHTOL 85 °C/90% RH for the first test condition, and the same strategy was applied to the rest. After setting the chamber conditions, the LED packages were then stressed by a constant driving current (160 mA per unit). Under these stress conditions, the highest solder temperature of the LED packages was measured as 107 °C, and the junction temperature was calculated as about 130 °C. This means overstressing would be performed in our tests. This is because according to the product specification, the nominal driving current is 120 mA. The specification also defines the maximum driving current as 240 mA at 25 °C (ambient temperature) and 120 mA at 85 °C (ambient temperature), respectively. Furthermore, the maximum junction temperature guaranteed is limited to 125 °C in the specification.

In order to analyze the differences of degradation mechanisms between environments with and without moistures, another group of samples was aged by means of high-temperature operation life (HTOL) test. In this aging test, the stressed current was the same as that in the WHTOL test, and the solder temperature was controlled at 105 °C until the end of the test. Both the solder temperature and driving current are almost the same as that in WHTOL 95 °C/95% RH, so any difference of the degradation kinetics between HTOL 105 °C and WHTOL 95 °C/95% RH could be attributed to the effects of moistures.

The samples were taken out of the climate chambers for optical and electrical measurement at a series of predefined readout points. In order to obtain accurate optical parameters, the system was recalibrated prior to measurement. After that, a Keithley Digital Multimeter was used to light up the LED packages with a constant current. Then a half-meter integrated sphere was used to transfer the lights emitted by the LED packages into diffuse reflection lights in order to obtain uniform light distribution. Then a spectrometer with 1040 CCDs (charge-coupled devices) was turned on to collect the light spectra. The acquisition time was 25 ms to ensure

complete exposure and integration. The complete measurement was finished within 35 ms to avoid LED packages self-heating.

After finishing all aging tests, the data were fitted in terms of least square method, based on the hypothesis that the optical output degrades exponentially during aging. According to the IES standard TM-21-11 [30], collected data were normalized to a value of 100% at 0 h for each individual sample under test; then exponential least squares curve fit was performed through the individual values for Eq. 14.5:

$$\Phi(t) = \Phi_0 \cdot \exp(-\alpha t) \tag{14.5}$$

where $\Phi(t)$ is the normalized optical output at time t, Φ_0 is the projected initial constant derived by the least squares curve fit, and α is the decay rate constant which is related to aging stress level.

Except for analysis of the optical degradation, several degraded samples were also analyzed by means of nondestructive and destructive analysis. I–V characteristics, package materials discoloration, interface delamination, and contamination were carefully detected.

14.3.2 Results

14.3.2.1 Lumen Degradation

According to the IES standard TM-21-11, the individual lumen values of all samples at different measurement points were normalized to their initial values, and then averaged, as mentioned in previous section. The average normalized data were plotted in Fig. 14.15. As a result, the lumen degradation showed very good exponential degradation kinetics in all test conditions, regardless of conditions with or without humidity. The degradation rate became faster as the relative humidity increased to higher percentage. As could be observed from Fig. 14.15, when the relative humidity rose from 0% RH (assume no humidity in HTOL 105 °C) to 45% RH (WHTOL 95 °C/45% RH) and to 95% RH (WHTOL 95 °C/95% RH), the lumen maintenance decreased to 97.7%, 96.3%, and 91.9%, respectively, after 1,000 h. As both the driving current and the solder temperature were similar to each other among all test conditions, the difference of the degradation rate was apparently induced by different relative humidity in the climate chambers.

On the other hand, the lumen degradation mechanisms were explored by using statistics methodology. First of all, the degradation trend was fitted and extrapolated to the time that the LED package’s lumen output reached 90% of its initial value. Here, we defined it as the mean time to 90% lumen maintenance (MTTF 90%). Then the MTTF 90% of each individual sample was collected for probability distribution analysis. The reason that MTTF 90% but not MTTF 70% (as defined in IES TM-21-11) was used for analysis was that the projected MTTF 70% might

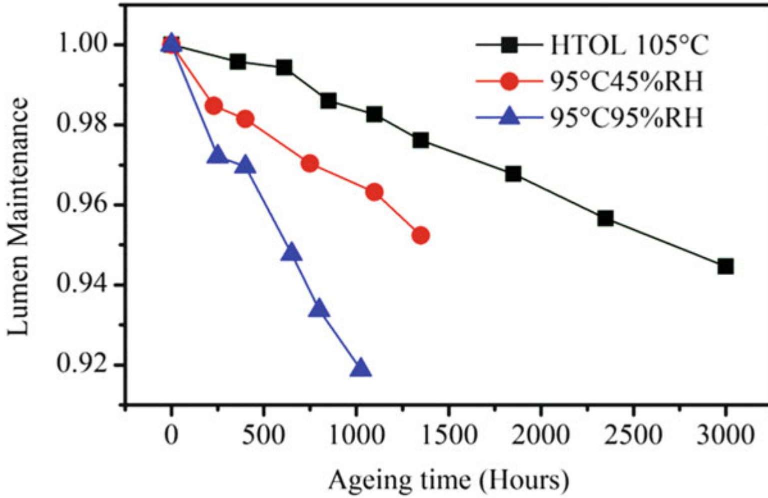

Fig. 14.15 Average lumen degradation of LED packages in different stress conditions

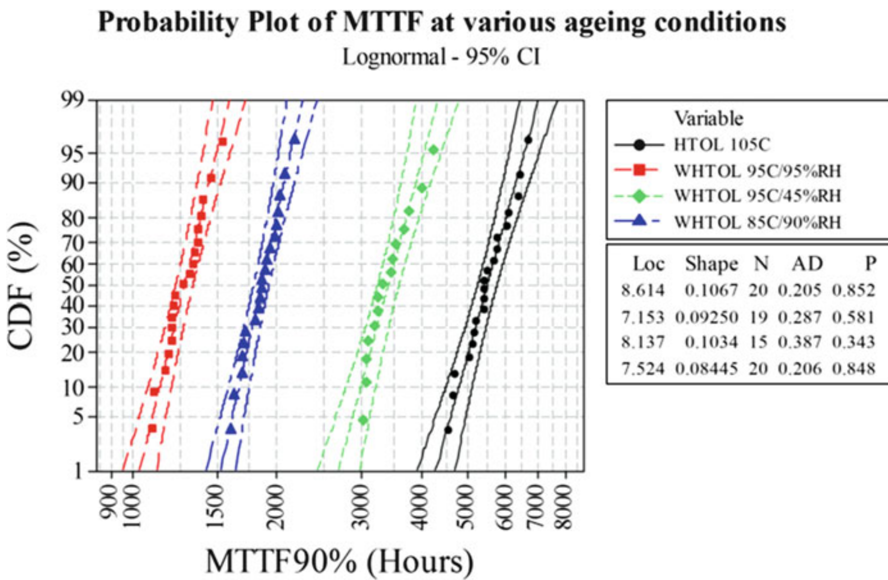

Fig. 14.16 Statistics distribution of the MTTD 90% in all the stress conditions

deviate from the actual degradation path if the aging duration was not as long as needed, for instance, 10,000 h. In our tests, the lumen maintenance was in the range of 90–95%. This ensured accurate lifetime projection to MTTF 90% because 90% was closed to the measured lumen maintenance. The analysis results were plotted in Fig. 14.16. Statistics analysis shows similar degradation mechanisms among all

stress conditions as the shape parameters of the lognormal distributions are very closed to each other [50], indicating that WHTOL test could be applied as an efficient accelerated life test method instead of the IES test standard LM-80-08 [24], which only accounts for effects of temperatures and is very time-consuming for lifetime prediction.

Based on the result of the statistics analysis, Hallberg-Peck's model was used to describe the effect of temperature and humidity combined on LEDs' life as in Eq. 14.6:

$$\mathrm{AF} = \left[\frac{\mathrm{RH}_a}{\mathrm{RH}_u}\right]^n \exp\left[\left(\frac{E_a}{k}\right)\left(\frac{1}{T_u} - \frac{1}{T_a}\right)\right] \tag{14.6}$$

where RH_α is the humidity at testing condition, RH_u is the humidity at usage conditions, n is the humidity factor, E_a is the activation energy, and k is Boltzmann constant.

The activation energy was obtained as 0.47 eV, which was very similar to that reported in [16]. The humidity factor n was also obtained and the value was calculated as 1.21. The humidity factor was smaller than results reported previously by other researchers. For instance, n was calculated as 1.6 in [1], 2.02 in [14], and 2.29 in [17], respectively. The reason is probably because our LED packages were stressed by much higher current than that in [14, 17]. Higher current implies higher temperature inside the packages than temperature outside the packages. Finally, the relative humidity inside the package decreases due to higher saturated vapor pressure inside the LED packages. In addition, higher temperature may drive part of the moistures outside the package due to effects of moisture expansion. All these reasons could reduce the effects of the moisture and, thus, yield a smaller humidity factor. The other reason is that the moisture resistance may differ among different types of LED package.

14.3.2.2 Color Shift

Figure 14.17 shows the average color shift of LED packages in each test condition. The color shift was characterized in terms of $\Delta u' v'$, which is the distance deviating from the color points measured before aging test. As could be observed from the plot, the color shift increased as a parabola along with aging time. All samples showed slight color shift ($\Delta u' v'$ <0.002), with the exception of the samples in WHTOL 95 °C/95% RH. The color shift was similar for samples aged in HTOL 105 °C and WHTOL 95 °C/45% RH, indicating that the package-related degradation mechanisms triggered by moistures were identical when the relative humidity was lower than 45% RH. This conjecture was made under the assumption that only package-related degradation mechanisms induced color shift, which will be discussed in a latter section. On the other hand, a rapid color shift was observed for those samples aged in WHTOL 95 °C/95% RH after 250 h. The color shift went

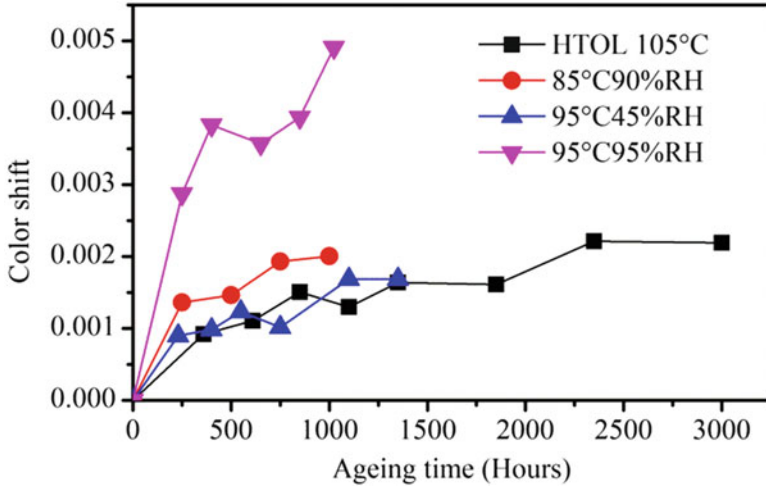

Fig. 14.17 Color shift of LED packages in different stress conditions

up to 0.005 after 1,000 h, indicating that the LED packages were much more sensitive in environment with high humidity and high temperatures than in environment without moisture.

The color shift was further analyzed in terms of light spectrum power degradation. Only samples aged in HTOL 105 °C and WHTOL 95 °C/95% RH were analyzed due to similar color shift kinetics in other stress conditions. As shown in Fig. 14.18a, for LED packages aged in HTOL 105 °C, the normalized spectrum power of blue lights increased at the beginning and then gradually decreased after 500 h. The increase of spectrum power was probably due to transmittance improvements of the silicone plate as silicone was cured continuously until the crosslinking was completed during aging test. The spectrum power of both blue lights and red lights degraded proportionally after 1,500 h (i.e., the same percentage of degradation for the blue lights and red lights), indicating that the chip-related deterioration was dominating in HTOL 105 °C. On the other hand, for LED packages aged in WHTOL 95 °C/95% RH, as presented in Fig. 14.18b, the spectrum power of blue and red lights showed different degradation kinetics. The spectrum power of blue lights decreased rapidly after 400 h. The amount of spectrum power degradation had exceeded that of red lights after 600 h, indicating the blue lights were absorbed significantly during the aging test, probably due to a decrease of reflectivity of the package encapsulant. The rapid degradation of blue lights explained the sharp increase of color shift in WHTOL 95 °C/95% RH.

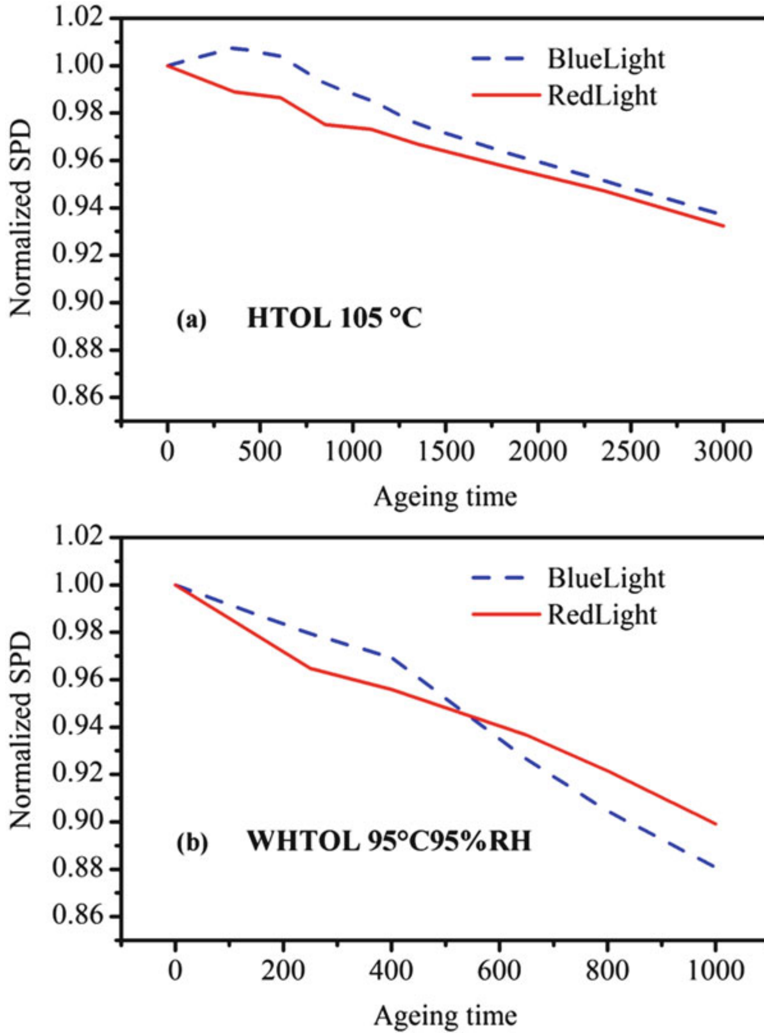

Fig. 14.18 Normalized spectrum power degradation of LED packages in WHTOL 95 °C/95% RH and HTOL 105 °C

14.3.2.3 Electrical Characteristics

Figure 14.19 shows the I–V curves of the non-stressed and stressed LED packages. A right-shift of the curves was observed for LED packages aged in HTOL 105 °C and WHTOL 95 °C/95% RH.

The reverse current measured at −10 V and forward voltage measured at 10 μA were also collected and presented in Table 14.7.

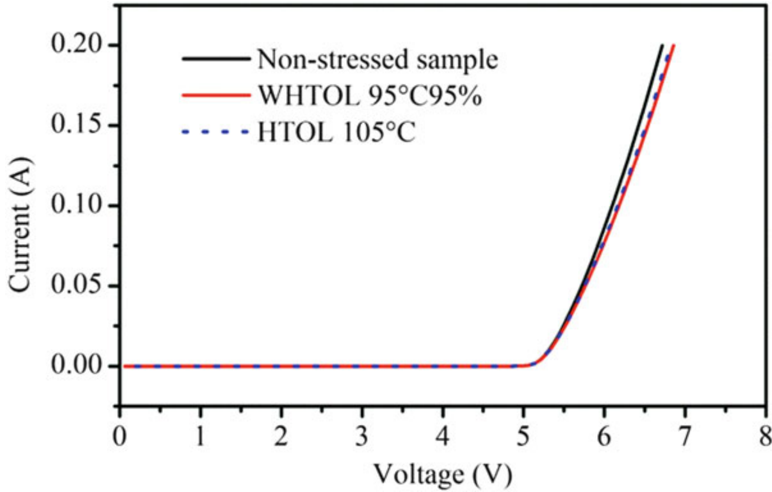

Fig. 14.19 I–V curves of LED packages in HTOL 105 °C and WTHOL 95 °C/95% RH

Table 14.7 Electrical characteristics of the LED packages

Stress condition	Ir at 10 V (A)	Vf at 10 uA (V)
Non stressed	2.0×10^{-08}	4.8
WHTOL 95 °C/95% RH	4.0×10^{-08}	4.8
HTOL 105 °C	6.0×10^{-08}	4.79

It was found that the reverse current I_R, and forward voltage at small driving current, was very similar to that of the non-stressed LED packages. All these parameters demonstrated that no obvious deterioration of the active layer. However, significant changes of the forward voltage were observed in the stressed LED packages, especially for samples aged in WHTOL 95 °C/95% RH, even though the aging duration was much shorter than that in HTOL 105 °C. Similar phenomenon was also reported in recently published papers [50, 51]. It was reported that an increase of the forward voltage (in terms of increase of series resistance) attributed to the first 5% lumen degradation in temperature-humidity conditions even though no deterioration in the p-n junction [50].

The increase of the forward voltage was mainly attributed to the deterioration of the Ohmic contacts. This has been confirmed by measuring the I–V curves at different positions. More specifically, the degraded sample's I–V curves in WHTOL 95 °C/95% RH and HTOL 105 °C were measured at the two ends of the solder joints of the package and the gold pads of the blue chips, respectively. As presented in Fig. 14.20, similar trend of the I–V curves measured at different positions eliminates the possibility of deterioration of the solder joints and wire bonding on the lead frames, thus verifying the deterioration of the Ohmic contacts indirectly. An explanation for deterioration of the Ohmic contact was the thermally activated metal-metal and metal-semiconductor interdiffusion [41, 42]. A reduction of the active acceptor concentration, due to the interaction between hydrogen and

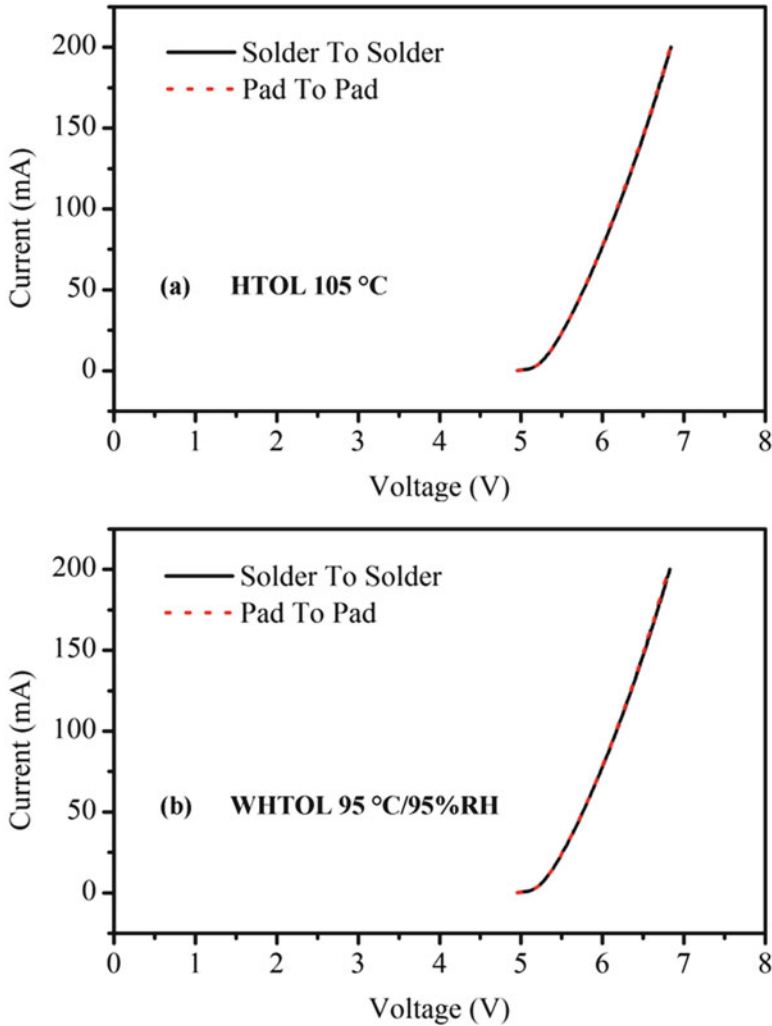

Fig. 14.20 I–V curves measured at different positions

magnesium, can worsen the properties of the anode contact and vary the resistivity and injection properties of the p-layer, thus leading to the measured I–V modifications [43]. However, the reason is not yet clear for the phenomenon that the forward voltage increased more rapidly in WHTOL than in HTOL.

14.3.2.4 Failure Analysis

At first, several degraded LED packages were inspected by optical microscope. In order to clearly emphasize discoloration, a non-stressed sample was used for

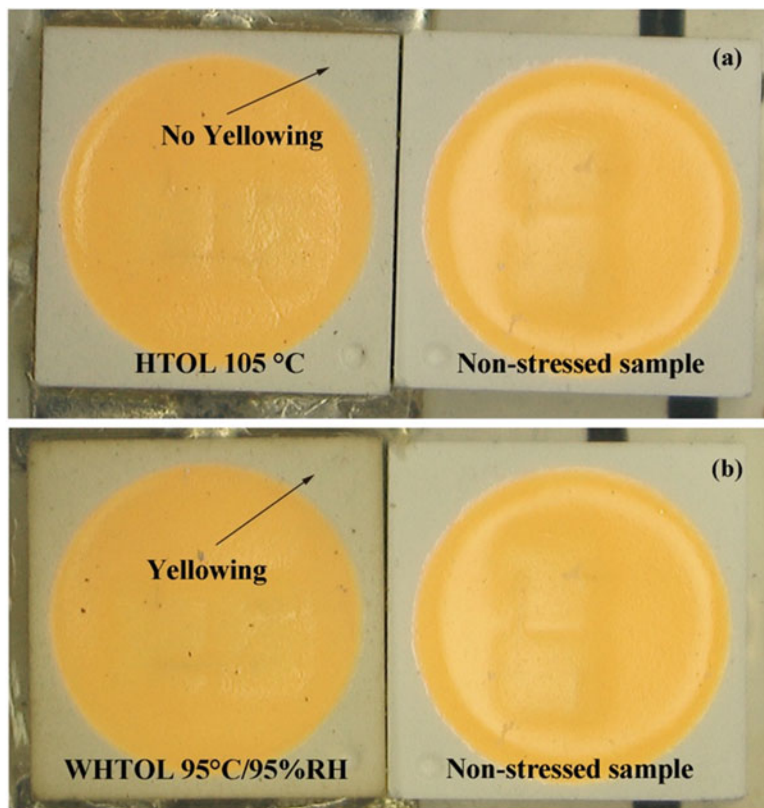

Fig. 14.21 Discoloration of the package encapsulant (EMC)

comparison. Significant yellowing of the EMC encapsulant was found for LED packages aged in WHTOL 95 °C/95% RH. For those samples aged in HTOL 105 °C, only very slight yellowing of the EMC encapsulant was observed, even though a much longer aging duration than samples aged in WHTOL 95 °C/95% RH, as presented in Fig. 14.21. In contrast to LED packages in HTOL 105 °C, it was obvious that moisture significantly affected the stability of the package encapsulant in WHTOL 95 °C/95% RH. Furthermore, small and dense cavities were observed in the inner surface of the package encapsulant, probably due to the dissolution of EMC under combined humidity, temperature, and blue light exposure.

Serious delamination was also observed at the interface of EMC encapsulant and lead frames. Actually, delamination had been frequently reported and considered as the main failure mode by researchers [3, 15, 18, 19, 29]. Due to delamination, foreign materials ingress was found at the interface, as seen in Fig. 14.22. However, no foreign material ingress was observed at the interface of silicone and lead frames, indicating excellent adhesion of the silicone. For LED packages aged in HTOL 105 °C, neither delamination nor foreign material ingress was observed.

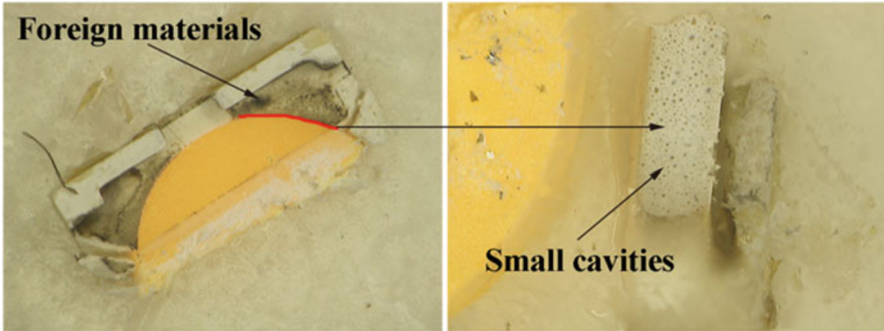

Fig. 14.22 Small cavities were observed at the inner surface of LED encapsulant

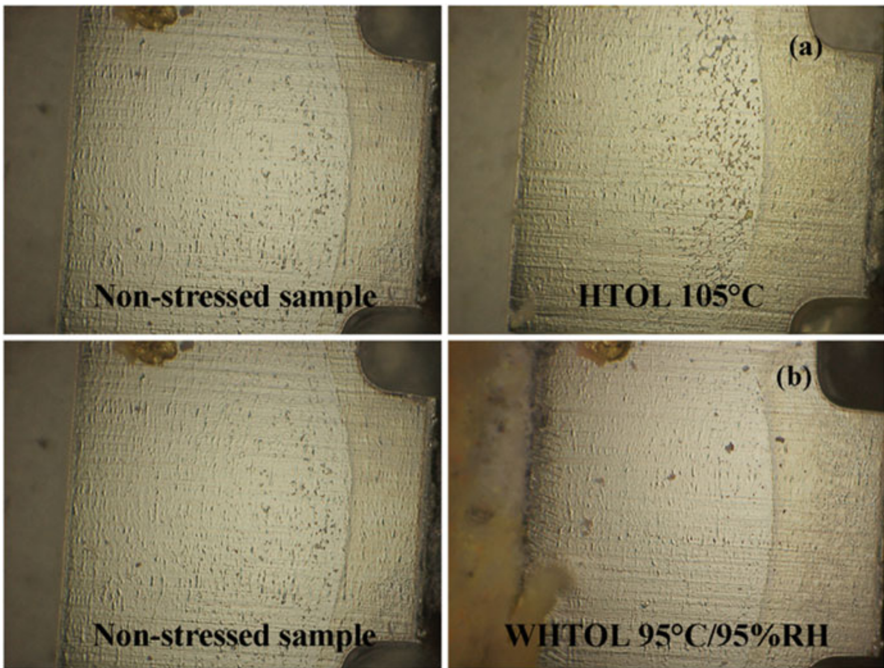

Fig. 14.23 No obvious discoloration on the surface of silver-coating lead frame

On the other hand, the surface of the lead frame was also inspected by optical microscope. No significant blackening was found on the silver coating, as seen in Fig. 14.23. It was further confirmed by XPS (X-ray photoelectron spectroscopy) that the element S did could not be found and the amount of Cl was negligible for the stressed samples in WHTOL 95 °C/95% RH, thus eliminating the contamination of the silver surface as the root cause, as indicated in Table 14.8.

Table 14.8 Lead frame XPS results for WHTOL 95 °C/95% RH

Peak	Position BE (eV)	Atomic mass	Atomic conc %	Mass conc %
Cu 2p-	933.9	63.549	1.71	5.46
O 1 s	531.2	15.999	20.51	16.5
Sn 3d	485.1	118.744	0.37	2.24
Ag 3d	368.4	107.878	4.53	24.59
C 1 s	283.6	12.011	63.99	38.65
Cl 2p	203.2	35.46	0	0
Si 2 s	152.7	28.086	8.89	12.55

14.3.3 Discussion

14.3.3.1 Optical Degradation Mechanisms: Effects of Chip Deterioration

The chip deterioration had been widely reported since LED was invented in 1960s. The degradation mechanisms of chip are very complex. Generation of crystal defects in the multi-quantum wells (MQWs) [52], dopant diffusion from p-GaN layer to active layer [53], electromigration inducing thermal runaway [54], as well as electrical contact metallurgical interdiffusion [55] were the main mechanisms which result in optical degradation during operation. Generally, the chip deterioration could be characterized in terms of leakage current, parasitic resistance, and ideality factor [2].

In order to understand the lumen degradation kinetics due to chip deterioration, one single LED package was driven at a series of temperatures which started from 70 to 100 °C to simulate the efficiency degradation of blue chip during aging test. This is because the efficiency of LED chip reduces as the junction temperature increases. The spectrum power of the blue and red light was then normalized to the value measured at room temperature. As a result, the spectrum power of red light decreased proportionally as well as that of blue lights, as presented in Fig. 14.24. In other words, chip deterioration results in the same degradation trend for blue and red lights. The results demonstrated that the lumen degradation was mainly due to chip deterioration in HTOL 105 °C, as proportional decrease of blue and red light was observed, as shown indicated in Fig. 14.18. As no significant leakage current was detected, the chip deterioration was only attributed to the p-contact deterioration, which induced the increase of the series resistance of the LED packages. The increase of series resistance then resulted in the increase of the junction temperature when LEDs were driven at constant currents. Finally, higher junction temperature rendered optical degradation of the white-light LED packages due to the effect of "efficiency droop" of LED packages [56]. An example of the "efficiency droop" characteristic was illustrated as in Fig. 14.25, which shows linear optical degradation as junction temperature increased.

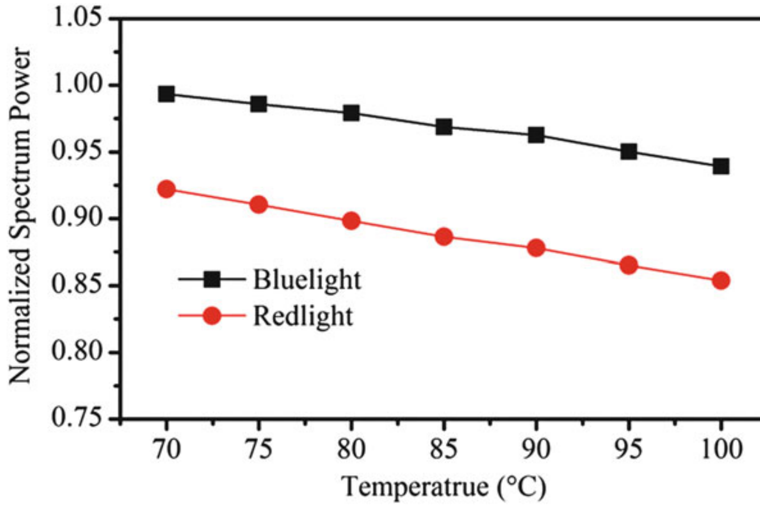

Fig. 14.24 Blue chip degradation kinetics

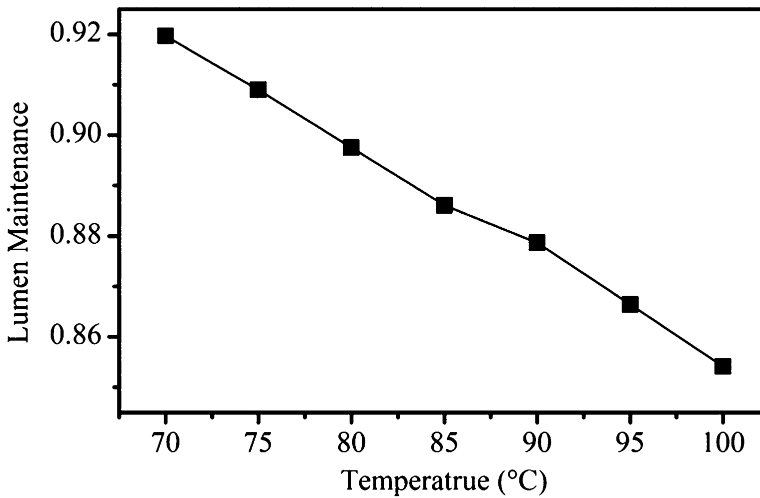

Fig. 14.25 "Efficiency droop" of LED packages due to increase of junction temperature

On the other hand, though many researchers reported that increase of leakage currents in LED packages may result in optical degradation during aging test, the effects were limited only in lower driving current region. For mid-power LED packages driven by high forward currents, only 1% of lumen decay was found even though the leakage current had reached 1 mA, as shown in Fig. 14.26, thus eliminating the effects of leakage current on the light output, as the measured reverse currents were much lower than 1 mA for LED packages aged in HTOL

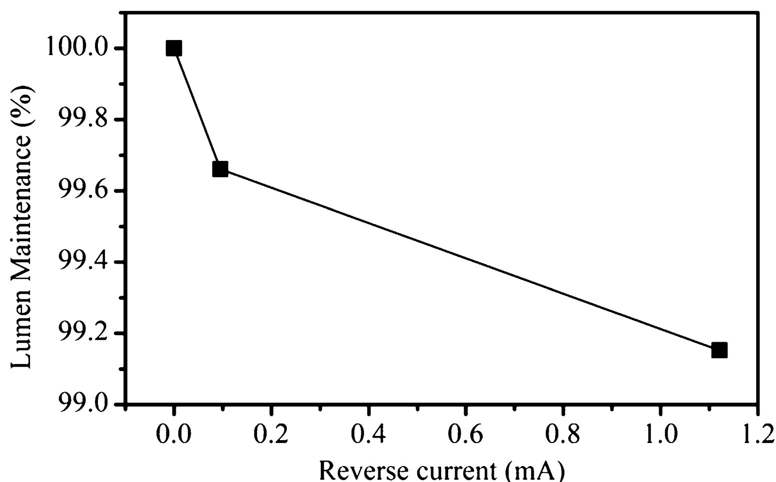

Fig. 14.26 Lumen maintenance vs. reverse current

105 °C and WHTOL 95 °C/95% RH. In Fig. 14.26, the leakage current was obtained by continuously stimulating the LED packages with instantaneous discharge generated through an electrostatic discharge generator.

14.3.3.2 Optical Degradation Mechanisms: Effects of Package Material Degradation

Package material degradation was the other degradation mode which not only influences the lumen maintenance but also color shift. Silicone carbonization, package encapsulant yellowing, and blackening of silver-coating lead frames were considered as the root causes of package-related degradation by researchers. In addition, phosphor dissolution was also reported by a few researchers [20]. However, YAG(Ce^{3+}) phosphors have been reported to be very stable, thus eliminating any significant nonradioactive quenching processes that existed in the aged samples [47]. Water resistance was also determined by measuring the electrical conductivity. The phosphor powders showed no hydrolysis after 30 min. Furthermore, damp heat test showed little $\Delta u'v'$ after 1,000 h, demonstrating the stability of the phosphors used in our LED packages.

In order to understand the optical degradation kinetics due to package materials degradation, highly accelerated temperature and humidity stress test (HAST) and sulfur gas corrosion test were performed separately to stimulate the degradation of silicone plate and silver-coating lead frames. The tests triggered only degradation of silicone or silver surface, while no obvious degradation was stimulated in the rest components. The results showed that degradation of silicone and silver surface mainly affected the light power density of the green/red light, while less impacted

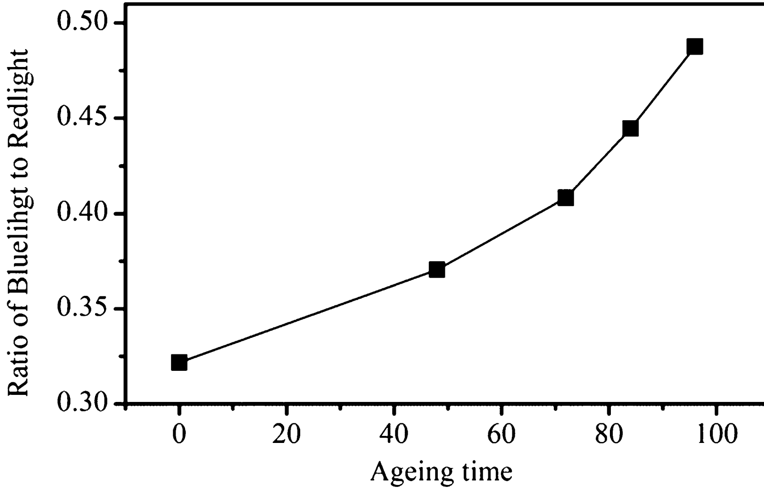

Fig. 14.27 Spectrum power degradation vs. decrease of silicone transmittance

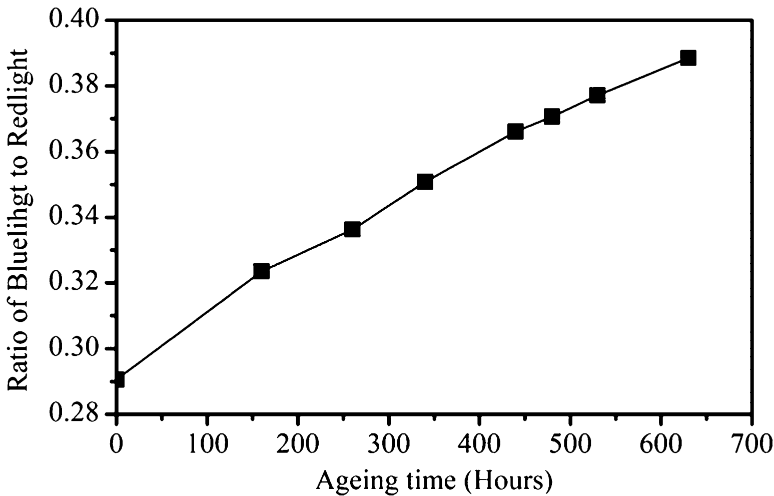

Fig. 14.28 Spectrum power degradation vs. decrease of silver surface reflectivity

the blue light, even though the blue light was more sensitive to the degradation of package materials, as indicated in Figs. 14.27, 14.28, and 14.29.

The phenomenon could be explained by theory of transmission path of light rays in LED packages and the theory of Bouguer-Lambert-Beer law. Because of high absorption coefficient of the phosphors, most of blue light was down-converted to longer wavelength when propagating through the silicone. Based on this fact, blue lights which were finally extracted out of the package were mainly composed of lights which never hit the phosphor particles. On the other hand, the down-

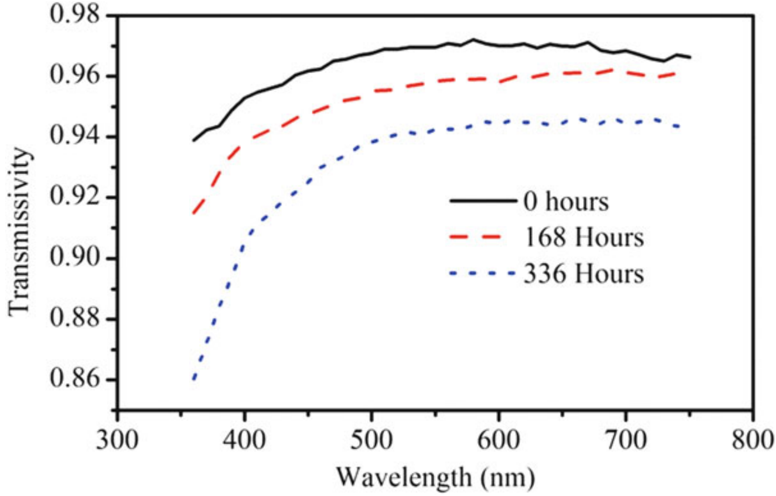

Fig. 14.29 Silicone transmittance vs. light wavelength for samples aged at 170 °C in thermal storage test

converting light were not absorbed by phosphors, because this light was not in the range of the absorption spectrum of the phosphors. As a consequence, the down-converting light would be scattered by phosphor particles and propagated through the silicone plate randomly. The scattering might occur many times before lights finally leave the package. It is, therefore, obvious that converted light went through a much longer path than the blue light before exiting the package.

On the other hand, it is well known that lights propagating through medium follow Bouguer-Lambert-Beer law, which is stated as in Eq. 14.7:

$$\frac{I}{I_0} = e^{-\alpha \cdot L} \tag{14.7}$$

where I_0 and I are the intensity of the incident light and emergent light, L is the distance of transmission path, and α is an exponential constant, which is related to material properties, such as transmittance of silicone plate, reflectivity of package inner surface, absorption efficiency of phosphor particles, and so forth. Suppose the light output degrades from I to I' after a certain period of aging, the degradation rate can be calculated as in Eq. 14.8:

$$\frac{I'}{I} = e^{(a-d)L} \tag{14.8}$$

Based on equation above, it is clear that longer transmission path L of the down-converting light, than that of the blue light, leading to higher degradation rate before outgoing the package.

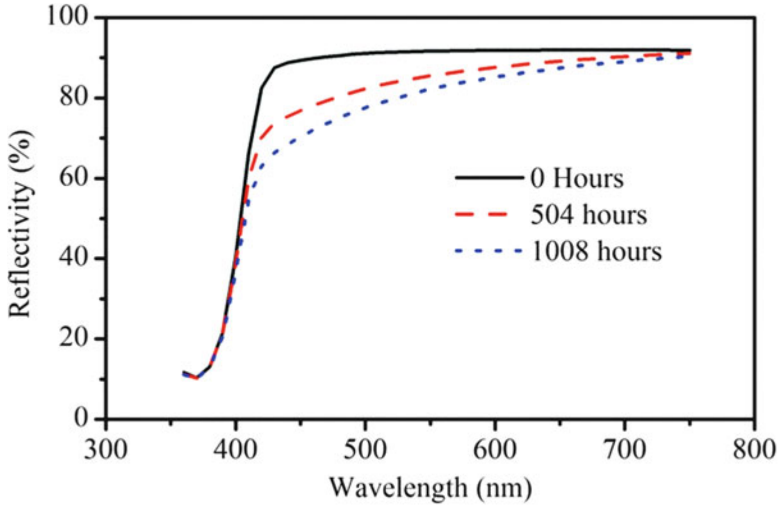

Fig. 14.30 Package encapsulant reflectivity vs. light wavelength for samples aged at 150 °C in high-temperature storage test

Notice that the blue lights degraded faster than the red lights in WHTOL 95 °C/95% RH, thus eliminating the silicone carbonization and silver blackening in the aging test.

Neither deterioration of blue chip nor degradation of silicone and silver-coating lead frames was the root cause which induced faster degradation of the blue light compared to green/red light, so it is clear that the degradation of the package encapsulant induced the rapid degradation of the spectrum power density of the blue lights in WHTOL 95 °C/95% RH. In fact, high-temperature storage test demonstrated that blue light (450 nm) was extremely sensitive to degradation of the package encapsulant, as indicated in Fig. 14.30.

The effects of package encapsulant degradation were explained as follows. Generally, blue lights emitted out of the LED package were mainly composed of lights emitted from the upper surface of the blue chip. However, there was still part of the blue lights that was composed of lights emitted from the side walls of the blue chip. First, these blue lights emitted from the side wall of the chip, and then were reflected by the silver surface, finally were absorbed by either the package encapsulant or the phosphors, or ejected outside the package. As a result, the blue lights emitting outside the package decreased if this part of lights was absorbed seriously by the package encapsulant. However, the rapid degradation of the blue lights was mainly contributed to the large color shift, while performed few effects on the lumen output. In a word, the lumen output was mainly attributed to the degradation of green/red lights, as well as to chip deterioration in WHTOL, as shown in Fig. 14.31.

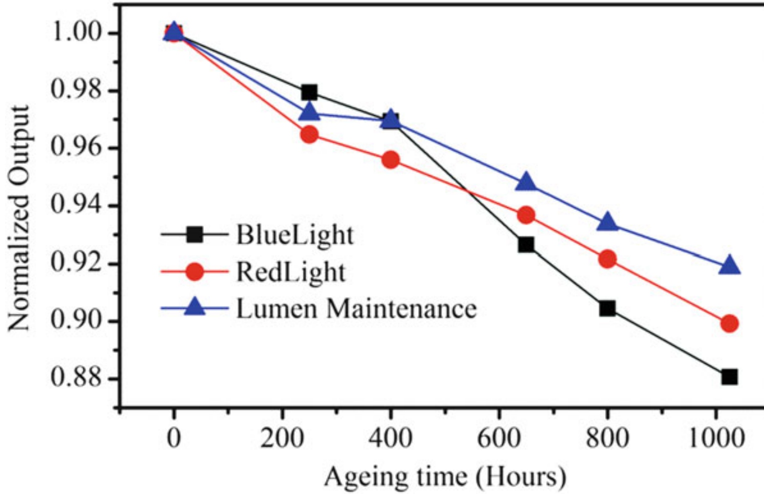

Fig. 14.31 Degradation kinetics of light output and spectrum power density

14.4 Optical Degradation Mechanisms Under HAST

14.4.1 Motivation Example

As reported in our previous study [27], a rapid lumen degradation was observed in LED packages that were stressed by a constant current in HAST within 96 h, even though the ambient temperature was limited to 105 °C. Microscopy observation showed severe carbonization in the bulk silicone, especially at the interface of the upper surface of blue chip. Figure 14.32 shows the cross section of both the LED packages which were stressed with and without driving current, respectively. It was found that silicone carbonization appeared only when the current was applied.

It was speculated that the silicone carbonization was due to either the self-heating of phosphors, or over-absorption of blue lights, which may induce extremely high temperature in silicone volume. To fully understand the failure mechanisms, following studies have been conducted.

14.4.2 High-Temperature Storage

First, high-temperature storage tests were performed in order to explore the thermal characteristics of the silicone. Five pieces of silicone plate, with 30 mm in diameter and 1 mm in thickness, were prepared on quartz glasses. Before aging, the transmissivity of the silicone plates was measured for each sample. Then the silicone plates were placed into a storage chamber and then aged successively according to a

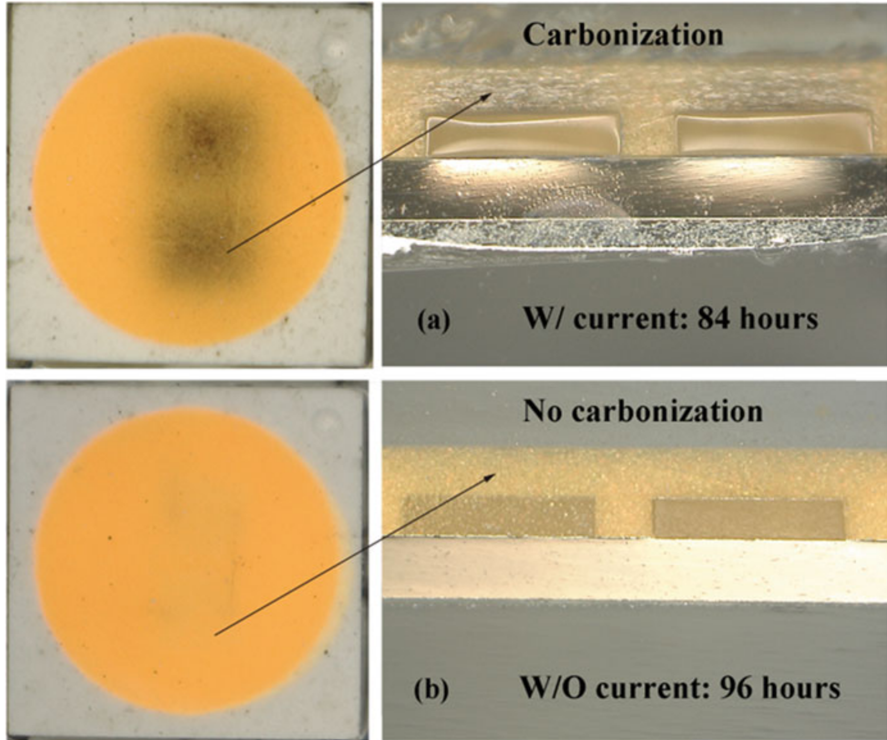

Fig. 14.32 Cross section of the LED packages after aging test

Table 14.9 High-temperature storage of the silicone plates

Temperature (°C)	190	250	300
Duration (hours)	336	24	24

stressing sequence until silicone carbonization was found. The stressing sequence is presented in Table 14.9: initially 336 h at 190 °C, followed by 24 h at 250 °C and finally 24 h at 300 °C, respectively.

It was found that the thermal characteristics of silicone plates were quite stable when aging at 190 °C. No discoloration was observed after 336 h. Furthermore, the normalized transmissivity remained as high as 98% of its initial value, as shown in Fig. 14.33.

However, significant silicone yellowing has been found at the stress sequence of 250 °C, even though the test duration was much shorter than that in 190 °C. The yellowing indicates molecular structure decomposition in silicone plates due to high storage temperature. However, it is far less than carbonization. Figure 14.34 shows the appearance of the silicone plates at end of the stressing sequence of 190 °C and 300 °C, respectively. It is obvious that the silicone plates aged with

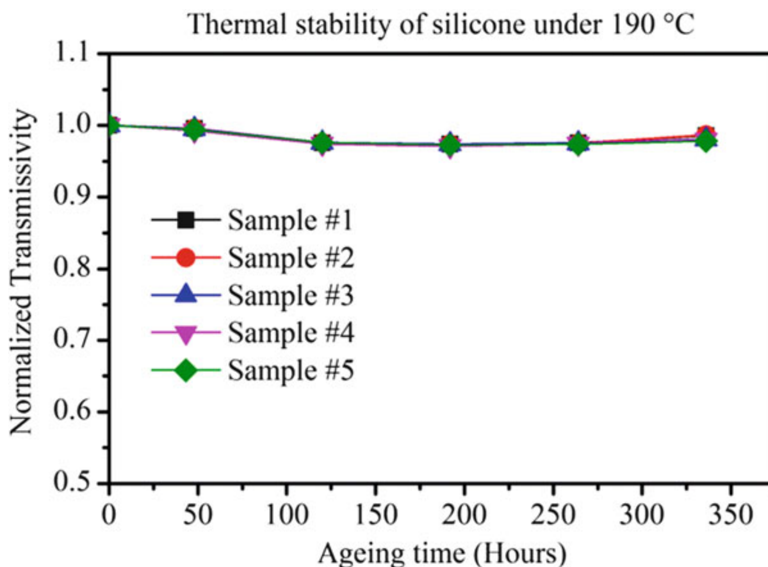

Fig. 14.33 Silicone transmittance vs. ageing time in high-temperature storage test

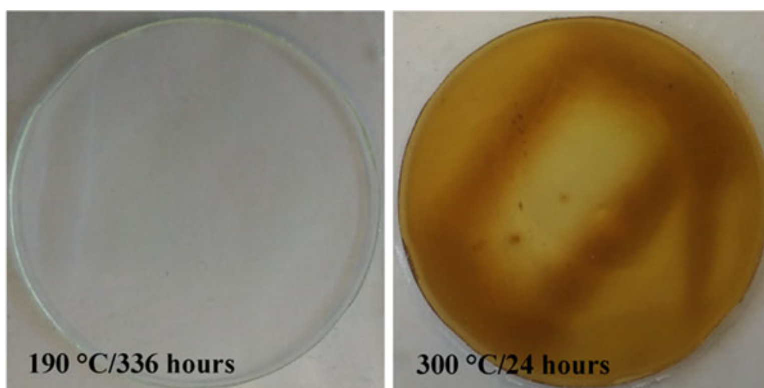

Fig. 14.34 Appearance of silicone plates after storage aging test

higher chamber temperature (300 °C) were blacken rapidly, demonstrating that the silicone carbonization would be triggered only if the temperature inside the silicone volume is higher than 300 °C.

14.4.3 Discussion of the Root Cause of Silicone Carbonization

Some researchers reported that the carbonization of silicone plates was mainly due to a combination of Joule heating and the elevated ambient temperatures [22],

which was often found in high-power white-light LED packages during high-temperature bias test. The most apparent evidence is the blackening of silicone, near the top surface of the blue chip, or near the lead frame [42]. A significant Joule heating due to the high resistances of the Ohmic contacts [57], the n-type and p-type cladding layers [39, 51], and the degradation of heat conduction materials [58, 59] were reported during operation applications [60, 61]. Self-heating induces serious carbonization if the junction temperature is higher than the critical temperature of silicone carbonization.

Another potential carbonization mechanism is the phosphor self-heating [62, 63]. For white-light LEDs, green/red phosphors are applied to down-convert the blue-color spectrum to a longer wavelength, i.e., green/red lights. Unfortunately, not all absorbed blue lights are transferred to green/red lights. Due to non-radiative transfer and Stokes shift, part of the absorbed blue lights is released in terms of heat [64]. The heat accumulation increases rapidly at higher operating ambient temperature [12], because of the thermal quenching characteristic of phosphors [65, 66]. This results from the enhancement of cascade multi-phonon relaxation, a temperature-dependent energy transfer or crossover process [67]. Based on this analysis, some researchers reported a much higher temperature inside silicone than the junction temperature of blue chip. The temperature inside the silicone volume varied from 195 to 316 °C [62, 68–70], depending on the LED products.

In addition to the effects of Joule heating and phosphor self-heating, shorter wavelength irradiation damage is considered as another possible root cause of silicone carbonization. For a practical LED package under the blue light radiation, high temperature, and a small amount of oxygen, epoxy resin will be gradually discolored. This is due to the opening of C-O and C = O bonds, and the dissociative C and O atoms occurring on the die surface. Finally a large amount of carbon or carbon oxide could accumulate on the interface between die and silicone, resulting in a black zone and darkening of the die surface [71].

14.4.3.1 Joule Heating Effects of the LED Packages

A schematic diagram depicting the heat dissipation of the LED packages is shown in Fig. 14.35. Due to low thermal conductivity and large length scale from lateral side, heat dissipation to the ambient through the silicone encapsulant is neglected. Similarly, heat dissipation through the silicone and epoxy material compound (EMC) can also be neglected [58]. As a result, a 1-D schematic of the thermal resistance network from junction to heat sink is shown in Fig. 14.36. Deterioration of any component in the 1-D model can increase thermal accumulation. First, the deterioration of the LED chips was detected. For this purpose, I–V characteristics of the stressed LED packages were measured by using a Keithley Digital Multimeter. The I–V curves of the stressed LED package showed the similar characteristics as compared to the non-stressed sample, demonstrating the excellent electrical performance of the stressed LED chip, as shown in Fig. 14.37. Next, C-mode scanning

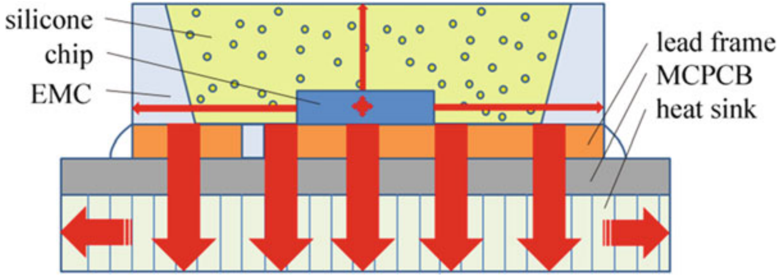

Fig. 14.35 Heat dissipation path of the LED packages

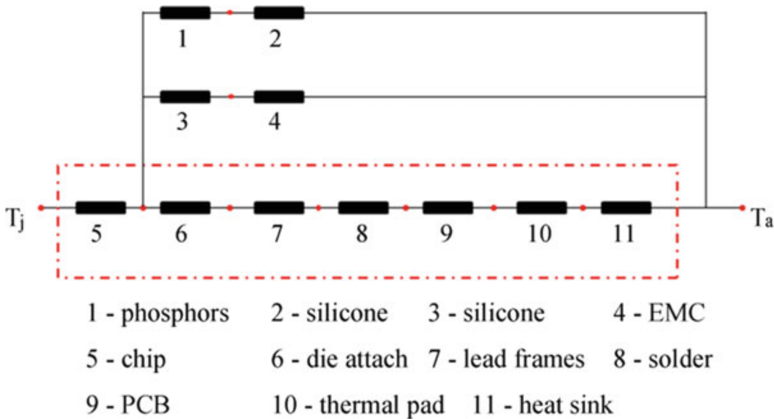

Fig. 14.36 Thermal resistance from junction to heat sink

acoustic microscopy (CSAM) was applied to the stressed/non-stressed samples, as shown in Fig. 14.38. The delamination has been found in the die/silicone interface and lead frame/silicone. This delamination may lead to the increase in the junction temperature of the LEDs. Hence, it is necessary to know the junction temperature of the degraded LEDs. Because all LED packages showed consistent lumen degradation, only one degraded LED was measured. Figure 14.39 shows the differential structure function of thermal resistance measured by using T3ster. The thermal resistance from the junction of the blue chips to MCPCB is about 17 °C/W.

On the other hand, the solder temperature of the aged LED package is monitored during HAST test. An average value of 110 °C was recorded after monitoring for 2 h. Then the junction temperature of the blue chip can calculated as below:

$$T_{\mathrm{j}} = T_{\mathrm{s}} + R_{\mathrm{th}} \cdot P \tag{14.9}$$

where T_{j} is the junction temperature, T_{S} is the solder temperature, R_{th} is the thermal resistance of aged samples, and P is the electrical power. According to the thermal resistance of the tested LED package, the junction temperature was obtained as

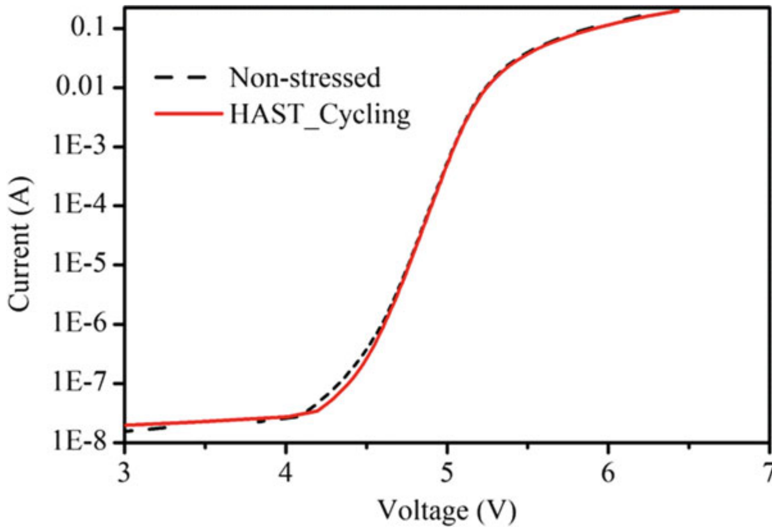

Fig. 14.37 I–V characteristics of the LED packages

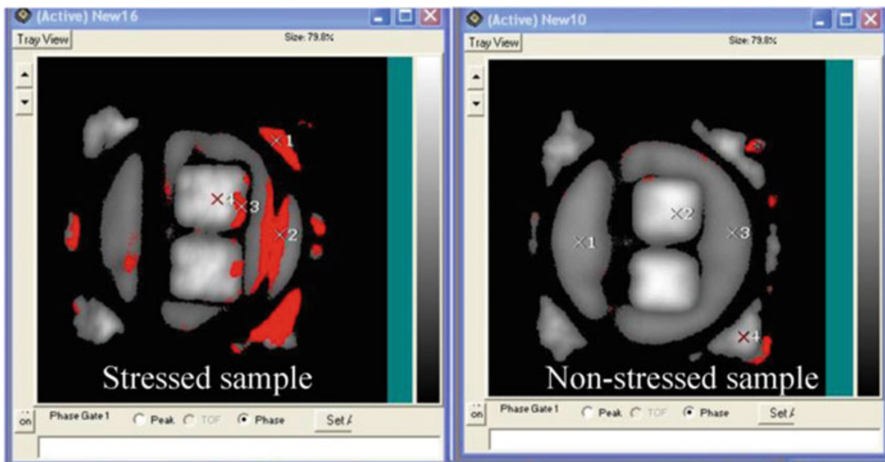

Fig. 14.38 Delamination detection by using CSAM

$T_j = 127$ °C. The junction temperature is much lower than 300 °C, so it can be concluded that the carbonization of silicone is not resulted from high junction temperature.

14.4.3.2 Self-Heating Effects of the Phosphors

To investigate the effect of phosphor self-heating due to thermal quenching, high-temperature operation life (HTOL) test was performed. In this test, the solder

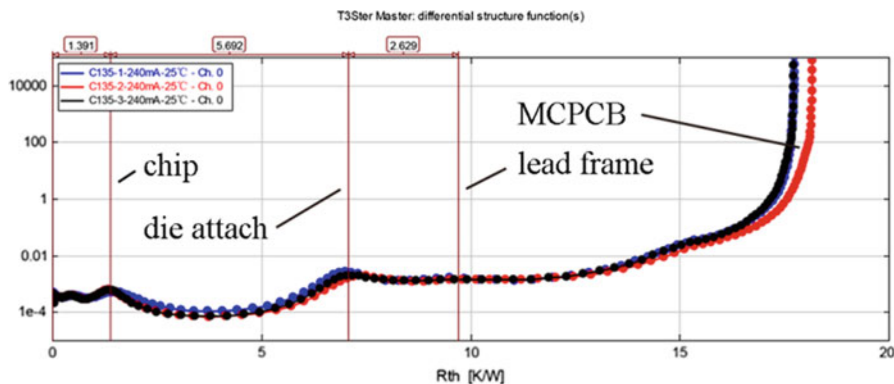

Fig. 14.39 Thermal resistance of the LED packages

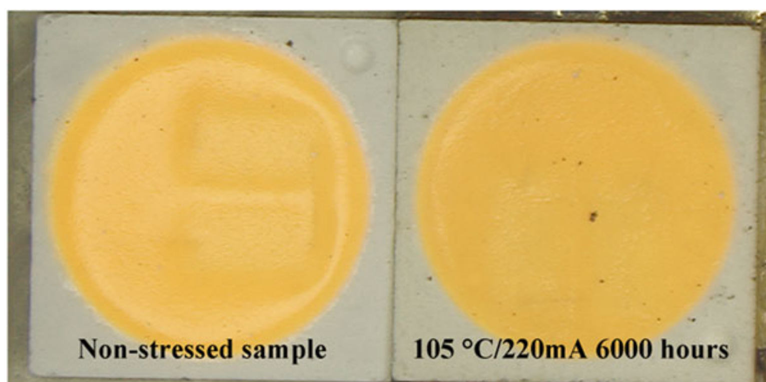

Fig. 14.40 Silicone appearance before and after 6,000 h in HTOL 105 °C

temperature of the LED packages was maintained at 105 °C with a variation of ±2 °C. The solder temperature in HTOL was similar to that of LED packaged aged in HAST. Then the LED packages were stressed with a constant driving current of 220 mA for 6,000 h. The images of silicone appearance before and after 6,000 h in HTOL 105 °C are shown in Fig. 14.40. It is obvious that the self-heating effects of the phosphors cannot result in silicone carbonization. The test also showed good thermal stability of the phosphors in our LED packages.

There has been a concern that hydrolysis may occur in phosphors due to their exposure to high-humidity environment. The hydrolysis lowers the quantum efficiency of the phosphors and finally accelerates the self-heating of the phosphors [64]. To study this effect, we performed the following test. The phosphor powders were first dissolved in deionized waters, and then the electrical conductivity of this solution was measured. The test duration was about 30 min. The results are presented in Table 14.10. The solution showed very stable electrical conductivity after 30 min, indicating there is no hydrolysis in the phosphors.

Table 14.10 Solution conductivity for phosphors dissolved in water

Time (minutes)	0	1	4	7	15	30
Electrical conductivity (μS)	6.4	6.7	6.6	6.6	6.7	6.6

Table 14.11 Color shift due to phosphors degradation in damp heat test

Time (hours)	500		1,000	
Sample number	Δx	Δy	Δx	Δy
1	0.001	−0.002	0.001	−0.001
2	0.001	0	0.001	0
3	0.001	0	0.001	−0.001
4	0.001	0	0.001	−0.001
5	0.001	0	0.001	0

Furthermore, a long-term WHTOL test was also performed to study the hydrolysis stability of phosphors. The phosphor samples were placed into a climate chamber, in which the ambient temperature is 85 °C and the relative humidity is 93%, respectively. The color shift was measured intermediately according to the CIE 1931 color space. The results showed very little color shift appeared after 1,000 h. These data were consistent with what were observed in the HAST test. In fact, for LED packages aged without bias in HAST, a color shift of −0.001 in Δx and 0 in Δy were observed after 96 h. In addition, only 3% lumen decay was found. Both package-level and phosphor material experiments demonstrated that the phosphors did not degrade significantly in high-humidity environment (Table 14.11).

The last concern is that the phosphor self-heating may increase significantly due to blue light over-absorption. As the LED packages are placed in a high-humidity environment, the blue lights emitted from the chip are trapped by water particles inside the silicone volume and thus increase the absorption possibility by the phosphors. As a result, the self-heating of the phosphors may increase with the absorption possibility. It is difficult to verify this hypothesis directly. However, a comparison experiment can be performed to investigate this hypothesis. For this purpose, two groups of LEDs were prepared. One group of LEDs was packaged by silicone dispensed with phosphors and the other group of LEDs was packaged by silicone without phosphors. Both groups of LEDs were stressed with a constant current in the HAST chamber. The results show that the self-heating of the phosphors is not the major mechanism of the silicone carbonization, because the lumen degradation of the LED packages encapsulated without phosphors is much worse than that with phosphors, as presented in Figs. 14.41 and 14.42.

The phenomenon can be explained as follows. For the LEDs packaged with phosphors, because most of the blue lights are absorbed by the phosphors, the blue lights are down-converted to a series of green/red lights which have longer wavelengths. These green/red lights, however, are not easily absorbed by the bulk silicone, as indicated in Fig. 14.43. As a result, the silicone carbonization is expected to be less severe than that in the LEDs packaged without phosphors.

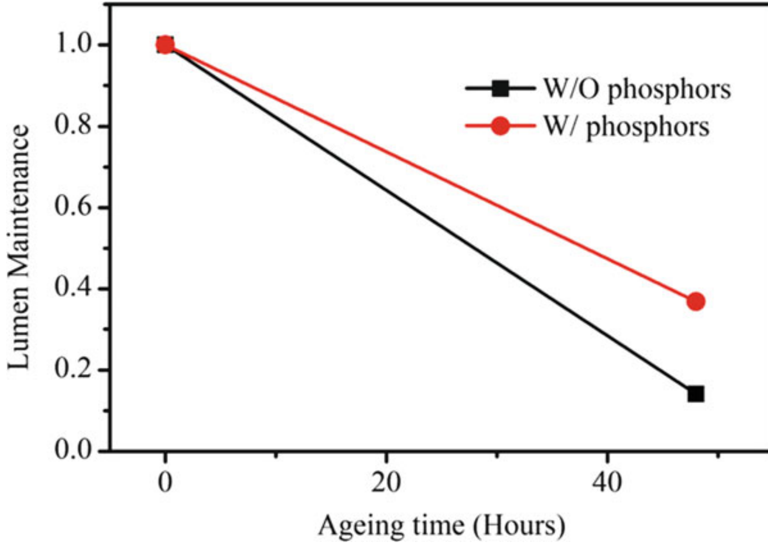

Fig. 14.41 Lumen degradation of LED packages with and without phosphors

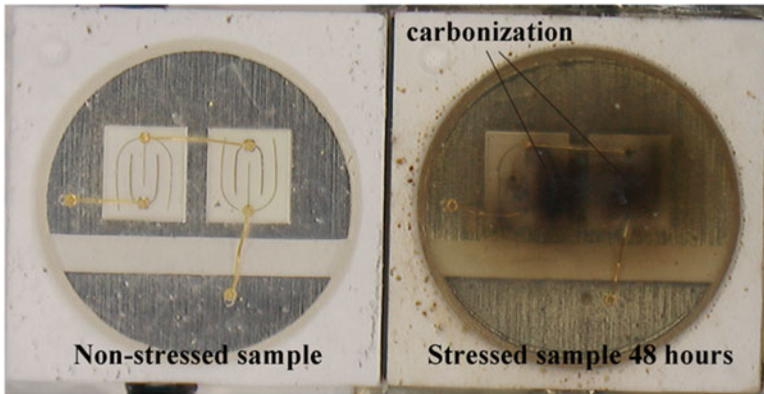

Fig. 14.42 Silicone carbonization was also observed in LED packages without phosphors

On the contrary, for the LEDs packaged without phosphors, the blue lights emitting from the blue chips are either directly absorbed or scattered when propagating through the package. The scattering of the blue lights increases the absorption probability. Higher blue light intensity and higher absorption probability of the blue lights induce more severe silicone carbonization during the aging test, thus resulting in lower lumen maintenance of the LED packages. A detailed description of the degradation mechanism will be provided in following sections.

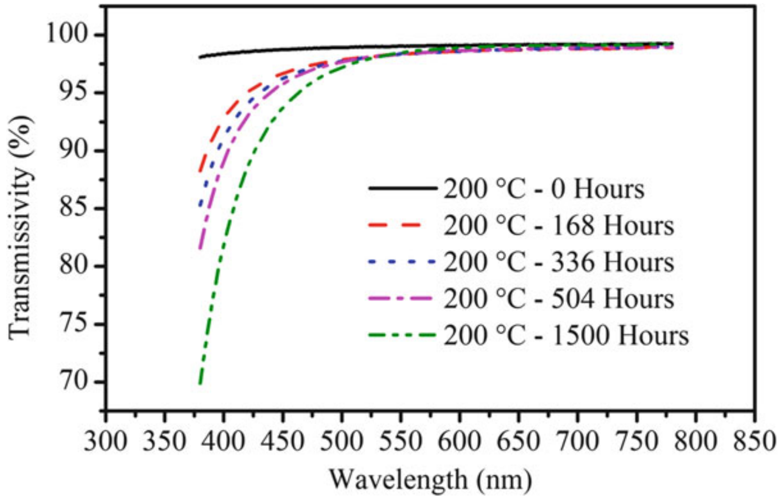

Fig. 14.43 Silicone transmissivity versus light wavelengths

14.4.3.3 Blue Light Over-Absorption by Silicone

Finally the root cause is limited to the over-absorption of blue lights by silicone bulk. This degradation mechanism can be explained as follows. Due to the permeability of silicone, water vapor ingress occurs when LED packages are exposed to high-temperature-humidity environment. When the water vapors reach to the saturated concentration, they are condensed at the pore walls of the silicone bulk due to the adsorption effects. As a result, blue lights emitting from the LED dies are scattered and randomly propagate through the silicone bulk. The scattering may happen many times, until the blue lights are absorbed by the silicone bulk. The absorption of the blue lights increases the temperature inside the silicone volume and finally leads to the carbonization.

It has been found that the light scattering and absorption behavior is very complicated in the phosphor-converted LED packages. Based on the revised Kubelka-Munk and Mie-Lorenz theories, Hu et al. [72] found that the output intensity of both the blue light and down-converted light was significantly affected by the size of the particles mixing in the silicone bulk. This is mainly due to the interaction mechanisms of light scattering and absorption when lights propagate through the silicone encapsulant [73]. On the other hand, a light scattering model was developed to qualitatively describe this phenomenon by Tan et al. [19]. In this model, the entrapped moisture in the silicone volume is modeled as embedded particles which will scatter the emission light from the LED die. The attenuated irradiance by the slab of water particles was obtained as follows:

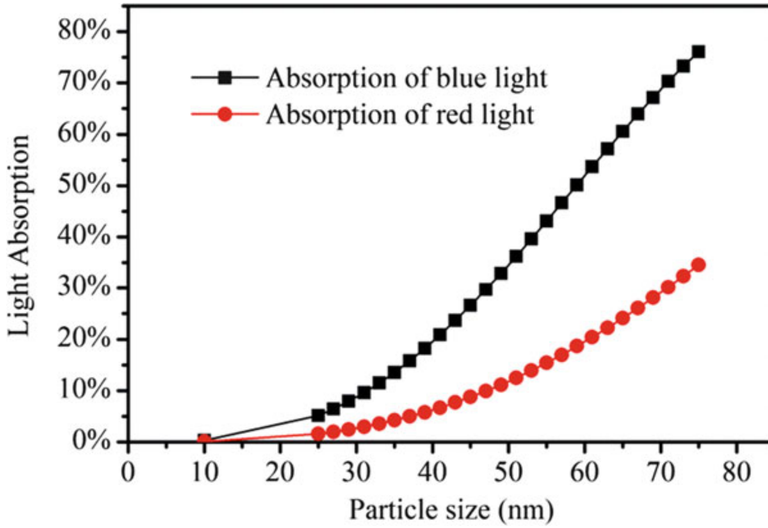

Fig. 14.44 Absorption of emitting lights by silicone volume

$$I_t = I_0 \exp(-\rho \sigma_{scat} t) \tag{14.10}$$

where I_0 is the irradiance of the non-polarized incident light, ρ is the number of particles per unit volume, t is the thickness of the water slab entrapped in the silicone volume, and σ_{scat} is the cross section of light scattering. The cross section of light scattering can be expressed as [74]

$$\sigma_{scat} = \frac{8\pi}{3}\left(2\pi\frac{n_{med}}{\lambda_0}\right)^4 r^6 \left(\frac{(n_{wat}/n_{med})^2 - 1}{(n_{wat}/n_{med})^2 + 2}\right)^2 \tag{14.11}$$

where λ_0 is the vacuum wavelength of the emitting lights, n_{med} is the refractive index of the silicone, n_{wat} is the refractive index of the water particles, and r is the particle radius.

Tan et al. [19] found that the lumen output decreased immediately as the size of the water particles inside the silicone bulk increased. According to [19, 75], the saturated concentration of water particles in polymer materials is only dependent on the relative humidity, while independent of temperature. Hence, the volume fraction of water in silicone is about 0.0753% in saturated water vapors. According to the attenuated irradiance model, the blue light absorption ratio with the pore size of the water particles can be calculated using Eqs. 14.2 and 14.3. Figure 14.44 shows the calculated absorption ratio of emitting lights by silicone volume with the particle size. It indicates that the absorption of the blue lights has been found as high as 40.7%, when the size of the water particles increases to 75 nm. This is reasonable because the pore size of the silicone volume is large enough to accommodate such water particles, as indicated in Fig. 14.45. The pore size measurement

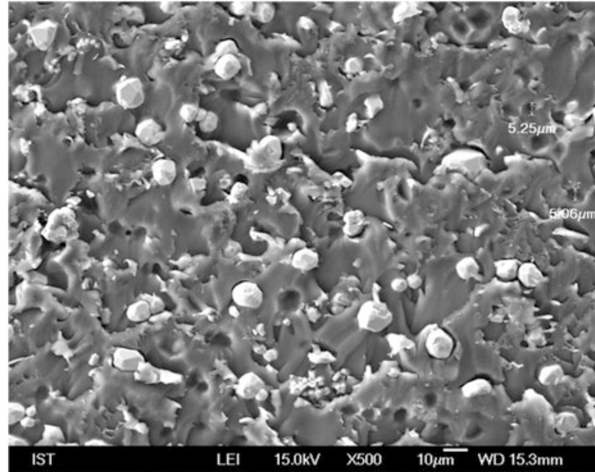

Fig. 14.45 Measured pore sizes in the silicone volume

was performed by using a scanning electron microscope (SEM), from the silicone bulk of one aged LED package.

14.4.3.4 Simulation and Validation

A finite element model is created to simulate the temperature distribution of the LED packages due to blue lights absorption by silicone bulks. For simplicity, the simulation model includes only one LED package, which is mounted onto a metal-core printed circuit board (MCPCB). The simulation model is shown in Fig. 14.46. The detailed dimensions of all components and the thermal conductivity of the materials are listed in Table 14.12.

In this model, the electrical power of the LED package is 1 W, and the radiation efficiency is set as 50% according to the optical measurement data. Two heat sources are created. One is the blue chip, and the other one is the silicone bulk. Only the silicone bulks above the blue chip are considered as heat source, which is in accordance with the area of carbonization observed on the degraded LED packages. The internal heat generation of the chip is calculated as 133 W/mm^3, which corresponds to 0.5 W of the total heat dissipation. The internal heat generation of bulk silicone is 1.1 W/mm^3 when the absorption ratio is 40%. This means that there is about additional 0.2 W heat generated in silicone. In our thermal model, natural convection heat transfer is assumed. The ambient temperature is set as 105 °C, which is in line with the ambient temperature of the HAST chamber.

Figure 14.47 shows the temperature distribution of the silicone volume. It is found that the maximum temperature of the silicone volume is around 125 °C when no blue lights are absorbed, which is in line with the junction temperature measured by T3ster, indicating the validity of our simulation model. However, the maximum temperature increases rapidly with the absorption ratio of the blue lights. In the

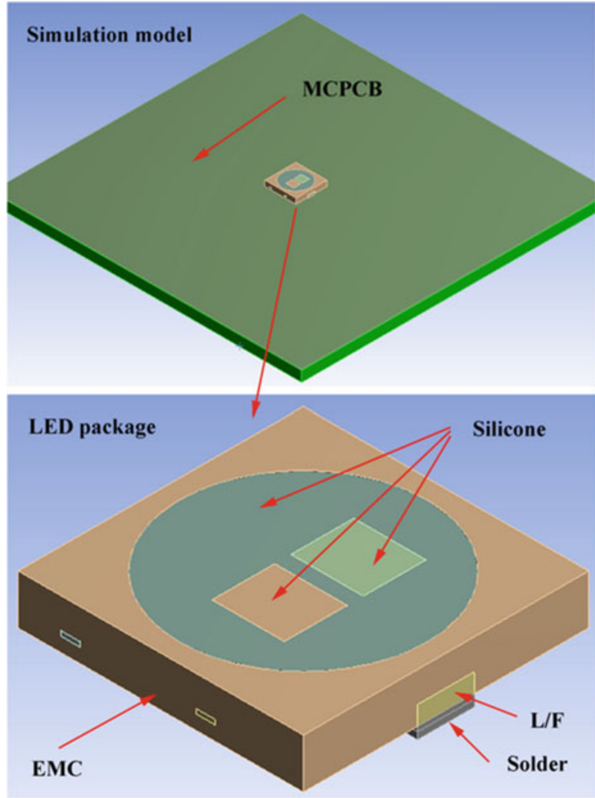

Fig. 14.46 Thermal transferring simulation model

Table 14.12 Component dimension and material thermal conductivity

Component	Material	Dimension (mm × mm × mm)	Thermal conductivity (W/m·K)
Encapsulant	Silicone	φ2.6 × 0.32	0.2
Housing	EMC	3.0 × 3.0 × 0.52	0.36
Chip Active layer	GaN	0.76 × 0.66 × 0.01	140
Chip substrate	Sapphire	0.76 × 0.66 × 0.13	46
Die attach	Silicone	0.76 × 0.66 × 0.002	0.2
Lead frames	Copper	2.2 × 2.6 × 0.2	400
Solder	SAC305	2.2 × 2.6 × 0.05	63.2
Solder pad	Copper	2.2 × 2.6 × 0.07	400
Insulation	Insulation	30 × 30 × 0.08	1.5
MCPCB	Aluminum	30 × 30 × 1.0	237.5

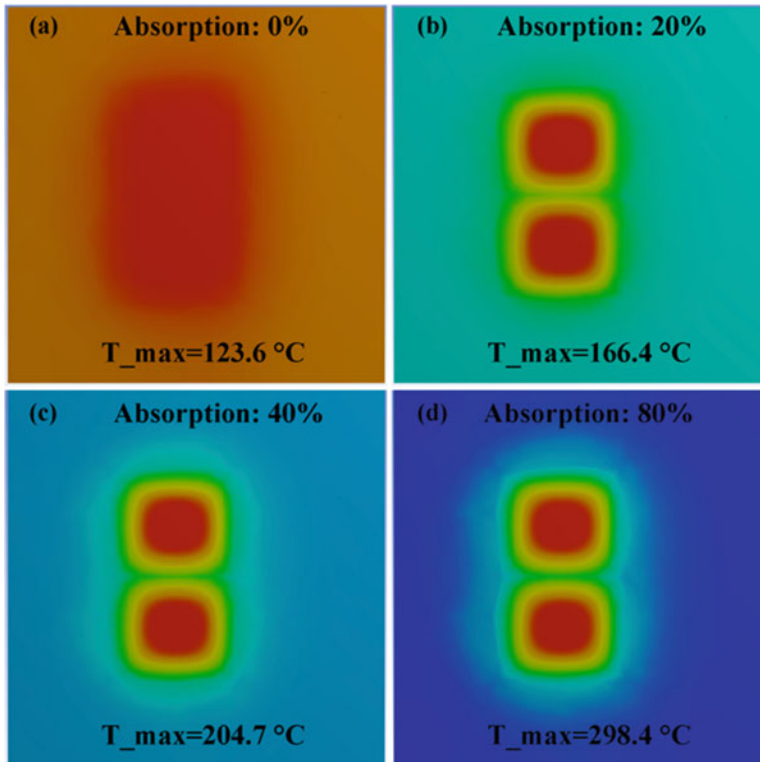

Fig. 14.47 Temperature distribution inside the silicone volume

worst case the temperature is up to 300 °C with the absorption ratio of 80%. It is worth noticing that the internal heat generation in silicone bulk is assumed uniformly distributed. However, the uniform distribution assumption can underestimate the maximum temperature. For silicone materials that are close to the upper surface of the blue chips, the heat generation can be much higher. As a result, the carbonization may occur first in these areas and then spread to other areas. For instance, when internal heat generation is 3 W/mm^3, the maximum temperature will be 366.8 °C. Such high temperature will result in serious carbonization of the silicone. On the other hand, the simulation model did not account for the effect of delamination. The internal temperature of the silicone is expected to be higher than the simulation result if this effect is included.

14.5 Summary

The optical degradation mechanisms of mid-power white-light LED packages were comprehensively investigated by using HTOL, WHTOL, and HAST.

In Sect. 14.2, for LED packages aged by using HTOL, the optical degradation showed neither temperature-sensitive characteristics nor current-sensitive characteristics at low case temperature. Further analysis showed that the optical degradation mechanisms varied at different case temperatures. On the other hand, spectrum analysis showed a combination of the chip-related degradation mechanisms and package-related degradation mechanisms. However, the contribution of both chip-related degradation and package-related degradation varied during the aging test, depending on the case temperatures and aging periods. Further analysis indicated the deterioration of p-contact of the blue chip was the main degradation mechanisms of samples aged at high case temperatures. However, both the chip-related degradation and silver-coating lead frames deterioration were considered as the cause of the optical degradation of samples aged at low case temperatures.

In Sect. 14.3, for LED packages aged by using WHTOL, deterioration of Ohmic contacts of the blue chip and yellowing of the package encapsulant were found. The deterioration of Ohmic contacts was deemed as one of the reasons which inducing lumen degradation. On the other hand, the yellowing of package encapsulant not only influenced the color shift but also the light output, thus inducing rapid lumen degradation for LED packages aged in WHTOL. Though large color shift in WHTOL, statistics analysis demonstrated that WHTOL was an efficient accelerated degradation test instead of IES LM-80-08, which only accounts for effects of temperature and was not enough for reliability requirements of outdoor illumination applications.

In Sect. 14.4, for LED packages aged by using HAST, possible root causes, including Joule heating, phosphors self-heating, and blue light over-absorption by silicone bulk, have been investigated thoroughly. I–V characteristics and thermal resistance of the LEDs are studied to eliminate the Joule heating effect. On the other hand, hydrolysis and water scattering related phosphor degradation are also eliminated. Finally, the failure mechanism is considered as the result of blue light over-absorption, which generates very high temperature inside the silicone bulk, resulting in serious carbonization. It is considered that the blue light over-absorption is strongly dependent on the water particle size. However, the growth of the water particle in saturated moisture environment has not yet been fully understood, which should be further studied in the future.

Acknowledgment The author Jianlin Huang thanks the colleagues of Philips Light Test Center for the optical measurement and testing maintenance. Thanks also to Dr. Haibo Fan, Jinfeng Li, and Longgang Ding for his supports on the experiments.

The author Daoguo Yang would like to thank the National Science Foundation of China for the support (Grant No. 51366003).

References

1. H. Fan, et al., in *Electronic Packaging Technology and High Density Packaging (ICEPT-HDP), 2012 13th International Conference on*, 2012. An effective prediction method for LED lumen maintenance, pp. 1560–1563

2. L. Trevisanello et al., Accelerated life test of high brightness light emitting diodes. Device Mater. Reliab. IEEE Trans. **8**(2), 304–311 (2008)
3. W.D. van Driel, X. Fan, *Solid State Lighting Reliability: Components to Systems*, vol. 1 (Springer Science & Business Media, New York, 2012)
4. M. Meneghini et al., A review on the reliability of GaN-based LEDs. IEEE Trans. Device Mater. Reliab. **8**(2), 323–331 (2008)
5. L. Zhang et al., Study on Ag-plated Cu lead frame and its effect to LED performance under thermal aging. IEEE Trans. Device Mater. Reliab. **14**(4), 1022–1030 (2014)
6. G. Mura et al., Sulfur-contamination of high power white LED. Microelectron. Reliab. **48** (8–9), 1208–1211 (2008)
7. E. Jung, M.S. Kim, H. Kim, Analysis of contributing factors for determining the reliability characteristics of GaN-based white light-emitting diodes with dual degradation kinetics. IEEE Trans. Electron Devices **60**(1), 186–191 (2013)
8. M.Y. Mehr et al., Surface aspects of discolouration in Bisphenol A Polycarbonate (BPA-PC), used as lens in LED-based products. Opt. Mater. **37**, 155–159 (2014)
9. M.Y. Mehr, W. van Driel, G. Zhang, Accelerated life time testing and optical degradation of remote phosphor plates. Microelectron. Reliab. **54**(8), 1544–1548 (2014)
10. P. McCluskey, et al., in *High Temperature Electronics, 1999. HITEN 99. The Third European Conference on*, 1999. Reliability of commercial plastic encapsulated microelectronics at temperatures from 125 C to 300 C, pp. 155–162
11. P. McCluskey et al., Reliable use of commercial technology in high temperature environments. Microelectron. Reliab. **40**(8), 1671–1678 (2000)
12. R.-J. Xie et al., 2-phosphor-converted white light-emitting diodes using oxynitride/nitride phosphors. Appl. Phys. Lett. **90**(19), 191101 (2007)
13. S. Koh, W. Driel, G. Zhang, Thermal and moisture degradation in SSL system, presented at the EuroSimE 2012, Lisbon, 2012
14. E. Nogueira, M. Vázquez, N. Núñez, Evaluation of AlGaInP LEDs reliability based on accelerated tests. Microelectron. Reliab. **49**(9), 1240–1243 (2009)
15. S. Zhou, et al., Evaluation of GaN-based blue light emitting diodes based on temperature/ humidity accelerated tests, presented at the ICEPT-HDP2010, Xi'an, 2010
16. S. Chan et al., Accelerated life test of high power white light emitting diodes based on package failure mechanisms. Microelectron. Reliab. **51**(9), 1806–1809 (2011)
17. E. Nogueira, M. Vázquez, C. Algora, Accelerated life testing in epoxy packaged high luminosity light emitting diodes. J. Electron. Packag. **133**(3), 0345011–0345015 (2011)
18. J. Hu, L. Yang, M. Whan Shin, Mechanism and thermal effect of delamination in light-emitting diode packages. Microelectron. J. **38**(2), 157–163 (2007)
19. C.M. Tan et al., Rapid light output degradation of GaN-based packaged LED in the early stage of humidity test. IEEE Trans. Device Mater. Reliab. **12**(1), 44–48 (2012)
20. C.M. Tan et al., Analysis of humidity effects on the degradation of high-power white LEDs. Microelectron. Reliab. **49**(9), 1226–1230 (2009)
21. D. L. Barton, M. Osinski, P. Perlin, et al., *Life tests and failure mechanisms of GaN/AlGaN/ InGaN light emitting diodes[C]//Reliability Physics Symposium, 1997. 35th Annual Proceedings*, (IEEE International. IEEE, 1997), pp. 276–281
22. D.L. Barton et al., Single-quantum well InGaN green light emitting diode degradation under high electrical stress. Microelectron. Reliab. **39**(8), 1219–1227 (1999)
23. M.-H. Chang et al., Light emitting diodes reliability review. Microelectron. Reliab. **52**(5), 762–782 (2012)
24. *IES Approved Method for Measuring Lumen Maintenance of LED Light Source*, ed. (Illuminating Engineering Society of North America, New York, 2008)
25. L. Liu, J. Yang, G. Wang, in *Electronic Materials and Packaging (EMAP), 2012 14th International Conference on*, 2012. The investigation of LED's reliability through highly accelerated stress testing methods, pp. 1–3
26. C. Hang, et al., in *Electronic Packaging Technology (ICEPT), 2013 14th International Conference on*, 2013. The effects of humidity and temperature aging test on flexible packaging LED module, pp. 1126–1129

27. J. Huang, et al., in *ICEPT*. Investigation of lumen degradation mechanisms of mid-power LED by HAST (Chengdu, 2014), pp. 1437–1441
28. J. Huang, D.S. Golubović, S. Koh, et al., Degradation mechanisms of mid-power white-light LEDs under hightemperature– humidity conditions[J]. IEEE Trans. Device Mat. Reliab. **15**(2), 220–228 (2015)
29. I. LM, *LM-80-08. Approved Method: Measuring Lumen Maintenance of LED Light Sources* (Illuminating Engineering Society of North America, New York, 2008)
30. *Projection Long Term Lumen Maintenance of LED Light Sources*, ed. (Illuminating Engineering Society of North America, New York, 2011)
31. T. Yanagisawa, T. Kojima, Long-term accelerated current operation of white light-emitting diodes. J. Lumin. **114**(1), 39–42 (2005)
32. S. Koh et al., *Product level accelerated lifetime test for indoor LED luminaires. Thermal, Mechanical and Multi-Physics Simulation and Experiments in Microelectronics and Microsystems (EuroSimE)*, 14th International Conference on. IEEE, (2013)
33. L. Liu et al., Efficiency degradation behaviors of current/thermal co-stressed GaN-based blue light emitting diodes with vertical-structure. J. Appl. Phys. **111**(9), 093110 (2012)
34. L. De-gao et al., Relation between ideal factor and lifetime. Chin. J. Liq. Cryst. Display **23**(6), 722–725 (2009)
35. V. Dmitriev, GaN based p-n structures grown on SiC substrates. MRS Internet J. N. S. R. **1**, e29 (1996)
36. J.M. Shah et al., Experimental analysis and theoretical model for anomalously high ideality factors ($n \gg 2.0$) in AlGaN/GaN pn junction diodes. J. Appl. Phys. **94**(4), 2627–2630 (2003)
37. W. Shockley, W. Read Jr., Statistics of the recombinations of holes and electrons. Phys. Rev. **87**(5), 835 (1952)
38. J. Hu, L. Yang, M.W. Shin, Electrical, optical and thermal degradation of high power GaN/InGaN light-emitting diodes. J. Phys. D. Appl. Phys. **41**(3), 035107 (2008)
39. M. Meneghini et al., Reversible degradation of ohmic contacts on p-GaN for application in high-brightness LEDs. IEEE Trans. Electron Devices **54**(12), 3245–3251 (2007)
40. M. Miyachi et al., The activation of Mg in GaN by annealing with minority-carrier injection. Appl. Phys. Lett. **72**(9), 1101 (1998)
41. M. Meneghini et al., High temperature electro-optical degradation of InGaN/GaN HBLEDs. Microelectron. Reliab. **47**(9), 1625–1629 (2007)
42. M. Meneghini et al., A review on the physical mechanisms that limit the reliability of GaN-based LEDs. IEEE Trans. Electron Devices **57**(1), 108–118 (2010)
43. M. Meneghini, et al., in *Electron Devices Meeting, 2005. IEDM Technical Digest. IEEE International*. Failure mechanisms of gallium nitride LEDs related with passivation (2005), pp. 4–1012
44. M.Y. Mehr et al., Photodegradation of bisphenol A polycarbonate under blue light radiation and its effect on optical properties. Opt. Mater. **35**(3), 504–508 (2013)
45. X. Fan, C. Yuan, in *ECTC*. Effect of temperature gradient on moisture diffusion in high power devices and the applications in LED packages (2013), pp. 1466–1470
46. D. S. Peck, in *Reliability Physics Symposium, 1986. 24th Annual*, 1986. Comprehensive model for humidity testing correlation, pp. 44–50
47. B. Ma, J. Kim, Complex-stress accelerated lifetime test for high-power light-emitting diodes. Electron. Lett. **48**(8), 449–450 (2012)
48. Y. Hu et al., High temperature stability of Eu2+-activated nitride red phosphors. J Rare Earth **32**(1), 12–16 (2014)
49. W.-H. Cheng, L.-Y. Chen, W.-C. Cheng, in *SPIE Optical Engineering+ Applications*. High-thermal-stability white light-emitting-diodes employing broadband glass phosphor (2014), pp. 91900N–91900N-10
50. T. Cher Ming, P. Singh, Time evolution degradation physics in high power white LEDs under high temperature-humidity conditions. IEEE Trans. Device Mat. Reliab. **14**(2), 742–750 (2014)

51. E. Jung, H. Kim, Rapid optical degradation of GaN-based light-emitting diodes by a current-crowding-induced self-accelerating thermal process. IEEE Trans. Electron Devices **61**(3), 825–830 (2014)
52. T. Yanagisawa, T. Kojima, Degradation of InGaN blue light-emitting diodes under continuous and low-speed pulse operations. Microelectron. Reliab. **43**(6), 977–980 (2003)
53. M. Pavesi, F. Rossi, E. Zanoni, Effects of extreme dc-ageing and electron-beam irradiation in InGaN/AlGaN/GaN light-emitting diodes. Semicond. Sci. Technol. **21**(2), 138 (2006)
54. O. Ueda, Reliability issues in III–V compound semiconductor devices: optical devices and GaAs-based HBTs. Microelectron. Reliab. **39**(12), 1839–1855 (1999)
55. S.-L. Chuang et al., Kinetic model for degradation of light-emitting diodes. Quantum Electron. IEEE J. **33**(6), 970–979 (1997)
56. L. Liu et al., Efficiency degradation behaviors of current/thermal co-stressed GaN-based blue light emitting diodes with vertical-structure. J. Appl. Phys. **111**(9), 0931101–0931105 (2012)
57. G. Meneghesso et al., Reliability of visible GaN LEDs in plastic package. Microelectron. Reliab. **43**(9–11), 1737–1742 (2003)
58. B. Yan et al., Influence of die attach layer on thermal performance of high power light emitting diodes. IEEE Trans. Compon. Packag. Technol. **33**(4), 722–727 (2010)
59. J. You, Y. He, F. Shi, in *IMPACT*. Thermal management of high power LEDs: impact of die attach materials 2007, pp. 239–242
60. N. Lobo Ploch et al., Effective thermal management in ultraviolet light-emitting diodes with micro-LED arrays. IEEE Trans. Electron. Device **60**(2), 782–786 (2013)
61. M. Khizar, K. Acharya, M.Y.A. Raja, Improved local thermal management of AlGaN-based deep-UV light emitting diodes. Semicond. Sci. Technol. **22**(10), 1081 (2007)
62. X. Luo et al., Phosphor self-heating in phosphor converted light emitting diode packaging. Int. J. Heat Mass Transf. **58**(1–2), 276–281 (2013)
63. M. Meneghini et al., Thermally activated degradation of remote phosphors for application in LED lighting. IEEE Trans. Device Mater. Reliab. **13**(1), 316–318 (2013)
64. R.-J. Xie, N. Hirosaki, Silicon-based oxynitride and nitride phosphors for white LEDs—a review. Sci. Technol. Adv. Mater. **8**(7–8), 588–600 (2007)
65. R. Pązik et al., Thermal quenching mechanisms of the Eu 3+ luminescence in Ca 9 Al (PO 4) 7 obtained by citric route. Mater. Res. Bull. **48**(2), 337–342 (2013)
66. P.F. Smet et al., Thermal quenching at the microscopic level in multi-phase thiosilicate phosphors. Opt. Mater. **35**(11), 1970–1975 (2013)
67. J. Zhang et al., Optical transition and thermal quenching mechanism in CaSnO 3: Eu 3+ phosphors. J. Alloy. Compd. **612**, 204–209 (2014)
68. H. Ye, et al., in *ICEPT-HDP*. Thermal analysis of phosphor in high brightness LED (Guilin, 2012), pp. 1535–1539
69. B. Yan, et al., in *ISAPM*. Influence of phosphor configuration on thermal performance of high power white LED array (Irvine, 2013), pp. 274–289
70. E. Juntunen et al., Effect of phosphor encapsulant on the thermal resistance of a high-power COB LED module. IEEE Trans. Compon. Package. A **3**(7), 1148–1154 (2013)
71. L. Zhou, et al., in *Physical and Failure Analysis of Integrated Circuits, 2009. IPFA 2009. 16th IEEE International Symposium on the*, 2009. Analysis of delamination and darkening in high power LED packaging, pp. 656–660
72. R. Hu et al., Comprehensive study on the transmitted and reflected light through the phosphor layer in light-emitting diode packages. Disp. Technol J. **9**(6), 447–452 (2013)
73. R. Hu et al., Modeling the light extraction efficiency of bi-layer phosphors in white LEDs. Photon. Technol. Lett. IEEE **25**(12), 1141–1144 (2013)
74. A. Cox, A.J. DeWeerd, J. Linden, An experiment to measure Mie and Rayleigh total scattering cross sections. Am. J. Phys. **70**(6), 620–625 (2002)
75. E. Wong, R. Rajoo, Moisture absorption and diffusion characterisation of packaging materials—advanced treatment. Microelectron. Reliab. **43**(12), 2087–2096 (2003)

Chapter 15
Assessing the Reliability of Electrical Drivers Used in LED-Based Lighting Devices

J. Lynn Davis, Karmann Mills, Robert Yaga, Cortina Johnson, and Joe Young

Abstract Electrical components used in LED lighting devices have a significant impact on the reliability of lighting systems. Understanding the reliability of LED drivers requires a knowledge of the intended use of the device including environmental (e.g., temperature, humidity), electrical (i.e., voltage quality and transients), and mechanical (i.e., vibration) stresses that the products would experience. In addition, knowledge of the susceptibility of key electronic components (e.g., capacitors, switching transistors, diodes, ICs, and linear components) to these stresses is also important in understanding overall product reliability. Although this information is difficult to determine for an electronic assembly such as the LED lighting driver, accelerated tests can help provide insights regarding likely failure modes and provide a basis to project reliability and product lifetime. In this chapter we have investigated common failure modes in LED drivers under accelerated testing conditions.

15.1 Introduction

Lighting technologies that use light-emitting diodes (LEDs) as light sources have been shown to provide both excellent energy efficiency and product reliability. To capitalize on the advantages of LED lighting technologies, an electrical driver is usually required to convert an infrastructure mains voltage into the proper voltage and current necessary to drive LEDs. Unfortunately, the reliability of the electrical drivers used in LED lighting often does not match that of LEDs [1]. Consequently, understanding the reliability of the electrical drivers used in LED-based lighting devices is perhaps the most important element in understanding the overall reliability of the lighting system.

J. Lynn Davis (✉) • K. Mills • R. Yaga • C. Johnson • J. Young
RTI International, 3040 Cornwallis Road, PO Box 12194, Research Triangle Park, NC 27709-2194, USA
e-mail: ldavis@rti.org

© Springer International Publishing AG 2018

W.D. van Driel et al. (eds.), *Solid State Lighting Reliability Part 2*, Solid State Lighting Technology and Application Series 3, DOI 10.1007/978-3-319-58175-0_15

15.2 Basics of LED Device Drivers

15.2.1 Common Driver Topologies

The function of the electronic driver used in LED lighting devices is to provide consistent electrical power to the LEDs in the device. Typically, an alternating current (AC) source serves as the electrical mains and provides the input energy for the device, although drivers with direct current (DC) mains can also be found. Within the driver, the mains voltage is converted to a regulated output that is set to either a constant current or a constant voltage. Constant current drivers are the most common because the luminous flux of LEDs is proportional to current; however, constant voltage drivers, in which a series resistor sets the current level, can also be found. Failure to provide a steady electrical power supply to the LEDs can result in a variety of undesirable lighting effects, including flicker (i.e., time-dependent variation in light output) and poor device reliability.

To achieve high electrical efficiency, the most common drivers used with LED devices are switched-mode power supplies (SMPS) [2]. Although linear regulators can be used in a few cases, this driver architecture has generally been discarded by the energy-efficient lighting community due to its high-power dissipation. In contrast, SMPS can readily achieve efficiencies greater than 80% in most designs, and it is even practical to achieve efficiencies above 90% in some custom designs. A key element of the SMPS is an integrated circuit (IC) controller that operates a power transistor. The transistor continually switches at a high frequency between the on and off state, and voltage regulation for the entire device is achieved by controlling the ratio of on to off time for the switching transistor.

Most drivers used for converting power from AC mains to drive current for LEDs are actually composed of five or more electronic circuits as shown in Fig. 15.1.

These circuits include the following:

- Filtering and conditioning of the input AC power
- Rectifying the input AC power to DC power
- Shaping of the DC power to reduce ripple and to provide power factor correction (PFC)
- Operating the switching transistor in the SMPS and regulating output power
- Filtering of the DC output power supplied to the LEDs.

15.2.2 Key Driver Components of LED Device Drivers

The drivers used in LED lighting devices consists of many components, any of which can fail during operation to produce complete device failure (i.e., abrupt or "lights out" failure), reduced performance (e.g., reduction in luminous flux), or

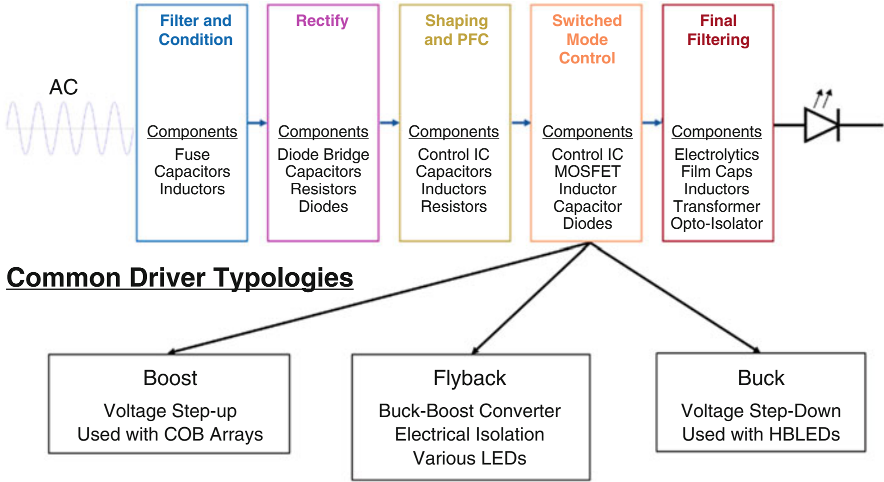

Fig. 15.1 Generalized schematic of the electrical circuits that comprise LED lighting drivers

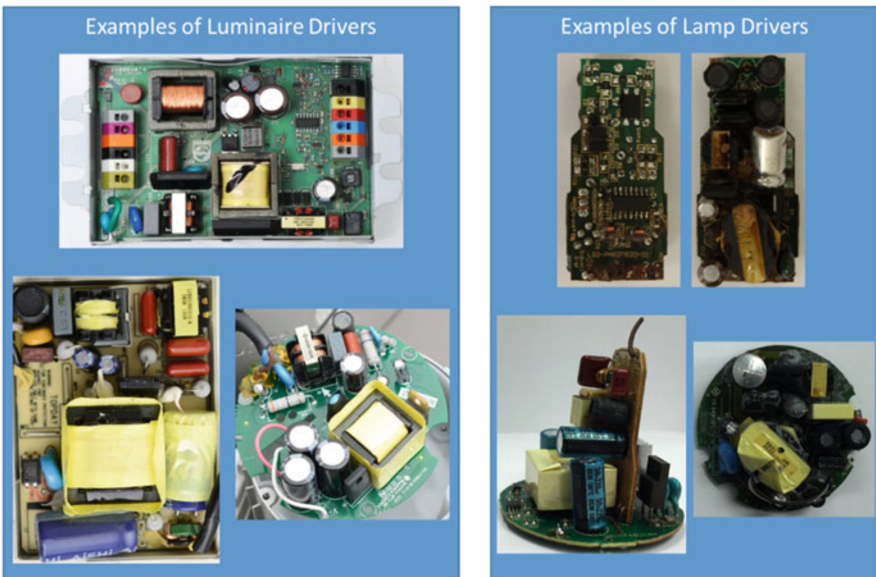

Fig. 15.2 Pictures of common LED device drivers

intermittent failure (e.g., flicker). Some representative examples of common LED device drivers are shown in Fig. 15.2. From a reliability and operational perspective, five common driver components deserve special attention because they have been shown to be potential failure sites [3, 4]. These components are capacitors, inductors, switching transistors, diode bridges and diodes, and resistors.

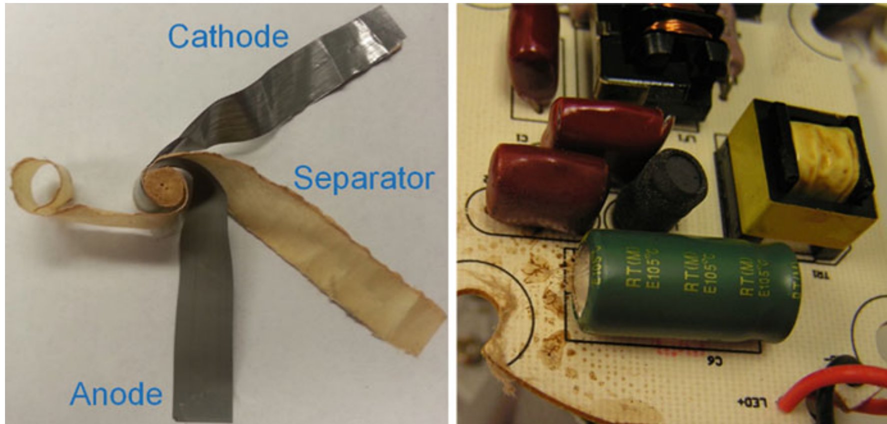

Fig. 15.3 (*Left*) A typical electrolytic capacitor winding. (*Right*) A failed electrolytic capacitor from a LED driver. This capacitor was used to reduce the ripple on the output voltages, which were supplied to the LEDs through the *black* and *red* wires at the *top* of the picture. Failure of the electrolytic capacitor resulted in the opening of the vent on the *top* of the capacitor, releasing pieces of the paper separator (visible as debris around the vent) and electrolyte (visible as *brown* spots on the board)

One of the most common components in an LED lighting device driver is the capacitor, which can be present as surface-mounted chip capacitors, film capacitors, or electrolytic capacitors. Usually multiple capacitors and a mix of capacitor types are found in each driver. Capacitors typically serve several functions in electrical systems including filtering out transients and voltage ripple and serving as an energy storage source. However, the high-charging currents that capacitors draw when a device is first energized cause the short-duration, large inrush currents that are often observed with LED drivers and other nonlinear electronic devices.

Electrolytic capacitors often consist of wound aluminum electrodes, anodized on one side, and immersed in a liquid electrolyte (typically a sodium hydroxide solution) with aluminum dioxide (Al_2O_3) and a separator serving as the dielectric. A picture of a typical electrolytic capacitor is shown in Fig. 15.3. Electrolytic capacitors are often used on LED drivers to filter out transients and ripple voltages especially on the DC output and sometimes to serve a similar function on the AC input. While electrolytic capacitors have the highest energy storage capabilities of the three common capacitor types, their reliability and performance is affected by temperature, voltage spikes, and other stress [5]. To overcome this limitation, manufacturers will typically derate electrolytic capacitors by a factor of two or higher and use them in areas of the circuit where electrical and thermal stresses are minimized.

The failure rate of electrolytic capacitors is usually one or more orders of magnitude higher than film capacitors [6]. A common wear-out mechanism in electrolytic capacitors is the loss of electrolyte either through leakage, degradation, or vaporization leading to an increase in equivalent series resistance (ESR) and a

decrease in capacitance [7]. In extreme cases, the pressure inside the electrolytic capacitor can increase to a high enough level to cause rupture of the device as shown in Fig. 15.3. In addition, transient voltage spikes that exceed the voltage rating of a capacitor, even for a few milliseconds, can produce hot spots within the component that greatly accelerate time to failure [8]. The design of an electrolytic capacitor is also known to impact its reliability with larger capacitors generally having better heat dissipation ability and higher reliability than smaller ones. Although the lifetime of electrolytic capacitors is known to have a strong dependence on temperature, simple accelerated stress tests (ASTs), such as high-temperature storage testing, often have minimal impact on the ESR and capacitance of properly chosen components [9, 10]. Instead, operational lifetime tests, in which the device is operated either continuously or on a power cycle, generally accelerate wear-out failure mechanisms faster due to internal heating from the electrical power.

Film capacitors are compact and highly reliable devices that are increasingly being used in LED driver designs, especially in filtering the AC mains supply. The common film capacitor consists of a wound thin film aluminum layer on a polymer substrate that acts as a separator. After the attachment of the leads with a Schoop's metallization process, the entire jelly roll structure is encapsulated in an epoxy coating. Film capacitors exhibit the ability to "self-heal" if defects form which greatly increases their reliability [11]. As a result, film capacitors exhibit a number of desirable characteristics compared to electrolytic capacitors, including lower ESR, higher surge voltage tolerance, and no polarization [12]. Film capacitors also tend to fail open due to degradation of the metal which interconnects within the capacitor. Although failure of film capacitors is often less common than electrolytic capacitors, they will fail under instances of high temperature, humidity, electrical stress, and mechanical stress [13, 14]. Several examples of failed film capacitors are shown in Fig. 15.4.

Inductors and transformers are other common electrical components found in LED device drivers. These components serve several functions, including combining with capacitors to form LC filters on the driver front end and provide energy storage to power the LEDs in SMPS. In addition, transformers are used in flyback

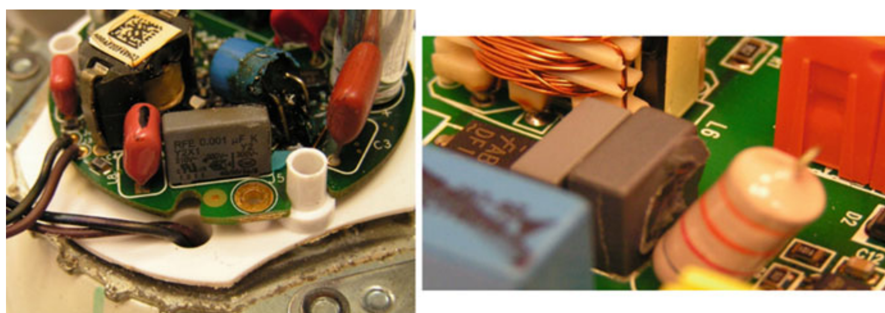

Fig. 15.4 Failed film capacitors from LED drivers

driver topologies to electrically isolate the input AC power from the output DC line. Although failure in inductors and transformers is rare, when it occurs, such failures can usually be traced to either excessive current loads, breakdown of insulating dielectrics, or broken interconnections.

The central element of SMPS drivers is a switching power transistor that is typically a metal oxide semiconductor field effect transistor (MOSFET). Unfortunately, MOSFETs are also a leading cause of failure in SMPS devices unless adequate precautions are taken [15].

The most common failure mode in MOSFET devices is shorting between the collector and emitter terminals, due to several failure mechanisms including gate dielectric breakdown [16, 17], hot carrier injection [18, 19], and increased junction temperatures caused by delamination of the transistor from the lead frame [20, 21]. The primary causes of these failures are either improper thermal management or voltage transients. Consequently, having good thermal management, including adequate heat sinking, and the choice of MOSFET packages with low thermal impedance is critical to reliable operation [4]. In addition, because MOSFETs are sensitive to electrical overstress, choosing components with high forward breakdown voltages, applying sufficient derating factors, and adding additional filtering on the terminal inputs can increase reliability [22].

Other failure modes, such as wire bond breakage, can also occur in MOSFETs, but these are less common. Often MOSFET failures are not readily apparent upon a visual inspection of a failed driver; however, an electrical inspection can usually identify a failed MOSFET, especially if the device failed as a short. An example of a MOSFET with a visible failure is shown in Fig. 15.5. In this instance, shortening of the MOSFET resulted in a large current flow through the device, which melted and distorted the epoxy overmolding material.

A variety of resistors are found in SMPS designs, the most common of which are surface-mounted chip resistors, followed by through-hole resistor technologies. Resistors are used in SMPS designs to control voltage and current levels. Generally resistors will often fail open due to short-term transients that produce current flows

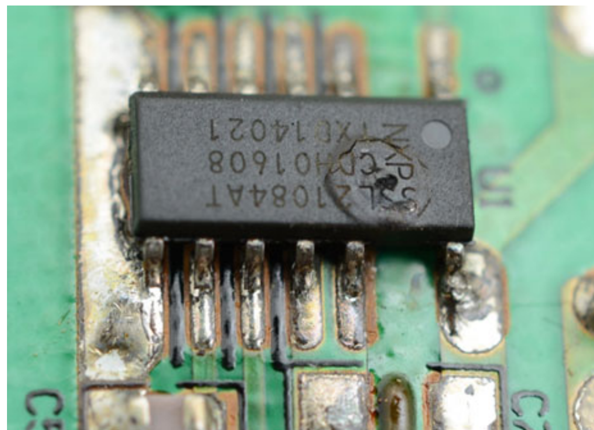

Fig. 15.5 Failed MOSFET from a LED driver. The MOSFET failed short, which caused a large current surge that raised the temperature of the device enough to melt and distort the epoxy overmolding

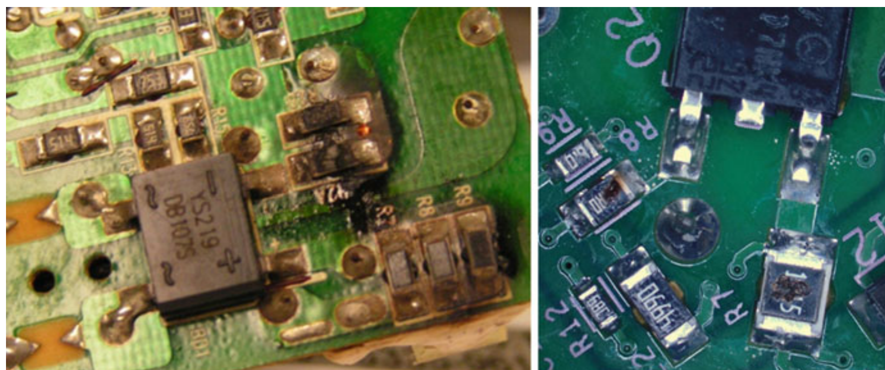

Fig. 15.6 Examples of failed resistors is LED drivers. (*Left*) A current surge exceeding the rating of the chip resistor resulted in a fuse-like increase in resistor impedance until electrical continuity was lost. Significant damage to the resistor is evident. (*Right*) A short-term transient resulted in the failure of the two resistors feeding the MOSFET. The resistors also failed open, but the only visible signs of damage were small *black* marks in the middle of the chip resistor

through the device in excess of the rated capacity. Examples of resistor failures from both normal operational testing and accelerated life testing are given in Fig. 15.6. A variety of root causes can be responsible for resistor failure, including manufacturing defects and failure of regulation components, which cause a cascade failure in which excess current flows through the resistor and other components.

Semiconductor diodes and diode bridges are essential elements of SMPS designs for AC-powered devices. They provide management of current flow and rectification of the electrical voltage from the input mains. As commonly occurs in power electronic components, the reliability of semiconductor diodes and diode bridges is affected by temperature and electrical overstress. The use of proper thermal management techniques, including minimizing the heat buildup in diode and diode bridge packages and applying proper deratings, is important to achieve reliable products.

15.2.3 Common Driver Topologies

Electronic drivers for solid-state lighting (SSL) applications are available in a variety of topologies that vary depending on whether the voltage supplied to the LEDs is higher or low than the AC mains voltage [2]. The buck driver topology is a common low-cost, step-down driver structure, whereas the boost driver topology is a common step-up driver structure. Other driver topologies, such as the boost-buck and flyback, can be either step-up or step-down depending on their configuration. A comparison of these most common driver topologies is given in Table 15.1, and

Table 15.1 Common topologies found in LED drivers

Topology	Output voltage range	Electrical isolation of mains and DC supply	Mode of operation
Buck	Output voltage is <85% of input voltage (i.e., step-down converter)	No	When the switching transistor is closed, energy is stored in the inductor (L1), and the capacitor (C1) powers the LEDs. When the switching transistor is open, L1 in series with LED load provides electrical energy to C1 and LEDs
Boost	Output voltage is greater than input voltage (i.e., step-up)	No	When the switching transistor is closed, energy is stored in inductor (L1), and LEDs are powered by the charged capacitor (C1). When the switching transistor is open, energy stored in L1 flows through the diode and the parallel combination of the LED string and C1
Boost-buck	Can either step-up or step-down the input voltage. Ideal for use with battery	Capacitive isolation between mains and output	When the switch is closed, voltage ramps up on the inductor (L1), and the capacitor (C1) supplies the LEDs. When the switch is open, L1 provides power to operate the LEDs while C1 charges through L1
Flyback	Can either step-up or step-down the input voltage depending on configuration	Yes	When the switch is closed, current flows in the primary side of the isolation transformers, and energy is stored in the transformer magnetic field. During this cycle, the LEDs are powered by the capacitor (C1). When the switch is open, the stored energy in the magnetic field charges C1 and supplies the LEDs

schematics of the most common LED driver topologies are given in Fig. 15.7. In addition to be used individually in single-stage designs, these typologies can be combined to form two-stage drivers. In a common two-stage configuration, a flyback typology is used to provide DC power to a buck converter. The net result is a larger, generally more reliable driver that also possesses a higher power factor.

These driver topologies can also be classified by whether the AC mains and DC output are electrically isolated. Isolated power supplies typically use an isolation transformer, so that the input and output are inductively coupled but electrically isolated. Non-isolated power supplies have the driver input and output electrically connected.

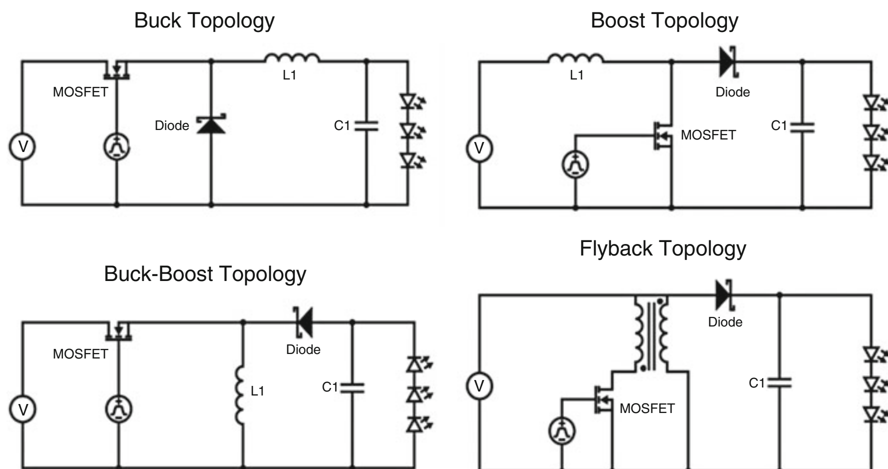

Fig. 15.7 Schematics of the most common driver topologies found in switched-mode power supplies used in LED drivers

15.2.4 Common Electrical Stresses in LED Device Drivers

The quality of the electrical power supplied to the LED driver has a significant impact on reliability because electrical components such as MOSFETs and electrolytic capacitors are particularly sensitive to electrical stresses. This is especially important for nonlinear loads, such as AC mains-powered LED drivers, where large inrush currents can occur when the device is first turned on, and these currents can produce voltage transients, including voltage sags and surges. Likewise, voltage spikes caused by lightning strikes or energizing other nonlinear loads on the same branch circuit can create transients that may affect product reliability. Often forms of surge protection, such as metal oxide varistors (MOVs), are incorporated into LED drivers or supply line branch circuits to minimize the impact of line transients.

The reliability of LED lighting drivers is impacted by the power quality of the electric source and the system compatibility of the driver with the grid. Power quality is the concept of powering and grounding electronic equipment in a manner that is suitable to the operation of that equipment [23]. System compatibility has been defined by the Electric Power Research Institute (EPRI) as “the ability of a device, equipment, or system, generally a load, to function satisfactorily with respect to its power-supply electrical environment without introducing intolerable electrical disturbances to anything in that environment [24].”

Both the magnitude and duration of electrical transients impact the reliability of SSL lighting drivers, and such transients may arise from the utility side or from other devices on the same branch circuit. In addition, wiring and grounding errors within the lighting infrastructure can magnify the impacts of transients. By studying the impacts of transients on driver reliability, EPRI has demonstrated that driver components such as MOSFET transistors, power diodes, and electrolytic capacitors

are particularly susceptible to electrical stress [24]. Surge protection devices (SPDs) are necessary to reduce the transients introduced into the driver.

15.3 Accelerated Stress Tests for Electronics

Because the expected lifetime of most LED drivers is long, ASTs must be used to obtain information about the reliability and lifetime of a design in a greatly condensed timeframe. However, it is essential that the AST methodologies used for SSL luminaires reproduce, as accurately as possible, the cumulative exposure of LED-based products. Typically, AST methods involve, at a minimum, a combination of environmental stressors, such as temperature and relative humidity (RH), and electrical stressors, such as variation in supply voltage and the introduction of transients. Depending on the reliability information being sought, other environmental stressors (e.g., chemical contamination, dust) or mechanical stressors (e.g., vibration) can be added to the test matrix [1].

A variety of AST methods have been developed by the electronics industry and can be applied to the LED drivers. Each of these tests provides some insights into potential failure mechanisms; however, lifetime predictions are possible only when the failure rate is appreciable [1, 25]. These methods can be divided into three broad classifications:

- Rapid tests (or highly accelerated stress test [HAST]) that provide information on possible failure modes in a minimal test period are generally conducted under highly overstressed conditions. Because these tests are often conducted under conditions well beyond the normal operational regime of the device, failure typically occurs much sooner than under normal conditions. Due to the short testing duration, HAST protocols can be a quick and relatively inexpensive approach to obtaining basic information about failure modes. However, establishing a correlation between the findings from these tests and lifetime predictions is difficult, and there is a danger of introducing new failure modes due to the highly overstressed test conditions.
- Screening tests can be used to compare the performance of different products provided an evaluation metric is available for the comparison. Screening tests often use established industry accelerating tests (e.g., elevated ambient, temperature cycling), and the tests are conducted for a predetermined period (e.g., 1,000 h at 150 °C or 1,000 cycles of temperature shock). Changes in measureable parameters that are suggestive of potential failure modes (e.g., increased ripple on output DC voltage, solder joint integrity) can be monitored relative to established pass or fail criteria. Such parameters are measured to determine whether they remain within acceptable limits (i.e., devices that pass the test) or are outside acceptable limits (i.e., devices that did not pass the test). Because screening tests are often performed for a finite duration, test costs can be determined in advance. However, because there is no assurance of failure or

even a significant change in measured parameters, screening tests typically provide limited information about product lifetime and reliability.

- Test-to-failure methods involve operating a sample population in AST experiments until a significant portion of the population, usually greater than 65%, has failed. The primary advantage of test-to-failure methods is that the lifetime and reliability of the product can be calculated if acceptable acceleration factors are known for the test conditions. The primary disadvantage of this approach is that the test period can be very long because testing is concluded only when a sufficient number of failures have occurred. Consequently, test-to-fail protocols can be expensive to run and consume significant resources, but they can provide the best information about device lifetime and reliability.

In choosing practical ASTs, it is usually necessary to further delineate the AST methods by whether the device is intended for indoor or outdoor use. Among the environments to be considered for outdoor luminaires are minimal operating temperatures of at least −20 degrees Celsius (°C) and operation in hot and humid environments. These temperatures could represent conditions found in environmental extremes such as Fairbanks, AK, and Miami, FL, respectively. The maximum operating temperature of both indoor and outdoor luminaires is often dictated by the maximum allowable junction temperature of the LED as listed on the manufacturers' specifications. This value is determined in part by the ambient temperature and the cumulative thermal resistance from the LED junction to ambient. For indoor lighting, an extreme case may be recessed luminaires mounted in ceilings or high bays where ambient temperatures can exceed 100 °C, especially in hot climates such as in Phoenix, AZ. Table 15.2 summarizes representative accelerated test methods that were first developed for the electronics industry and can be applied to LED drivers with appropriate experimental design and test

Table 15.2 Summary of common AST methods used in the electronics industry

Test	Standard test methods	Representative procedures	Minimum test durations
Thermal aging	JEDEC JESD22-A103C	Continuous storage at 150 °C (condition B) or 180 °C (condition C) with possible storage at other temperatures	1,000 h
Biased humidity	JEDEC JESD22-A101-B	Operation of the device at 85 °C and 85% RH under a cyclical bias (typically 1-h duty cycle)	1,000 h
Temperature shock	MIL-STD-202G Method 107G	Cycle temperature between −40 and 125 °C with a 15-min dwell time at each extreme	200 cycles
Electrostatic discharge sensitivity	ANSI/ ESDA/ JEDEC JS-001	A model of electrostatic discharges that mimics discharges from the human body. A capacitor is charged at high voltage and then discharged through a resistor in series with the test device	

method modifications. Modifications to these test methods, such as different temperature and humidity settings, can also be used in AST protocols.

For LED drivers, thermal-aging experiments are mandatory to reproduce the high heat experienced by the device during use and storage/shipping. The extensive literature developed by the electronics industry over the last 30 years clearly demonstrates that temperature can have a significant impact on the reliability of semiconductor devices and other electrical components used in LED drivers. A thermal annealing test, such as JEDEC's JESD22-A103, will allow the examination of high heat on the performance of the entire driver and its electrical components, including the heat load in semiconductors, degradation of die attach materials, and the likelihood of interconnect (e.g., wire bonds, ball bumps) failures. To avoid introducing new failure modes, modifications to this method can be made to accommodate parts of the luminaire that will not experience the full heat load.

Semiconductor packages and other electronic components are often not hermetically sealed, and common encapsulants, such as glass-filled epoxies, can be permeable to moisture. Hence, humidity testing, especially combined with elevated temperatures, can be an effective way to study failure modes of LED drivers [3]. A typical wet high-temperature operational lifetime test (WHTOL), such as JEDEC 22-A101-B, can provide significant information about failure rates often more quickly than can be obtained in testing at higher temperatures. A key element of JEDEC 22.A101-B is testing with a cyclic electrical bias consisting of powering the device on and off at a set duty cycle. Such cyclic biasing allows sufficient cooling during the off cycle for moisture to collect in the semiconductor package, other electronic components, and other surfaces. This will likely intensify the impact of any moisture-related failures mode such as moisture ingress. Because this test is performed with the electrical components energized, it provides a measure of many potential failure modes, including heat, electromigration effects, corrosion, and a chemical attack. However, care must be taken in choosing the temperature and humidity conditions because some components, especially film capacitors, may not be able to withstand high-temperature and high-humidity conditions.

When performing these AST experiments, changes in testing conditions may be used during a given experiment to accelerate the failure rate. For example, during the thermal annealing test, the oven temperature may be increased from 150 to 170 °C during the experiment to increase failure rate. This approach, termed stepped-stress methods, is an established technique for reducing the time of AST experiments to relatively short (<2 months) durations, and there are procedures for analyzing the impact of the change in parametric values on system reliability [25–27]. Although stepped-stress methods can provide insights into potential failure modes, these techniques often can be classified as rapid screening methods. Consequently, it may be difficult to translate the findings from such tests into lifetime and reliability estimates under normal operating conditions.

15.4 Accelerated Testing of Components and Luminaires

Although there is a significant body of knowledge about the behavior of electronic components (e.g., capacitors, MOSFETs) in accelerated tests, there is much less publicly available information about the reliability of these components when integrated into LED drivers. This is likely due in part to the wide variety of driver designs and the absence of industry standards for acceptable driver-level test methods.

One of the first published studies of driver reliability focused on the impacts of degradation of electrolytic capacitors upon ripple in the output DC waveform [28, 29]. In these publications, Han and Narendran demonstrated that degradation of the capacitance and increase in the ESR of the output filter electrolytic capacitors are a leading cause of parametric failure in SMPS designs using flyback topologies. The changes in capacitance and ESR that occur as electrolytic capacitors deteriorate produced greater ripple in the output waveform. The net result was a drop in relative efficiency, which resulted in greater power dissipation in the driver. However, the device continued to operate during the test period; therefore, this may not be considered as a failure if it is viewed in terms of a lighting installation.

One of the first published luminaire-level studies of reliability examined the performance of LED downlights in an HAST. This "hammer test" was developed to cause device failure in a few hundred hours to facilitate the investigation of failure modes [26]. The downlights used in this testing were provided by six different manufacturers, and the drivers in these devices consisted of common topologies, including buck and flyback. No effort was made in this study to correlate reliability and driver topologies. In addition, because this test is highly accelerated, it is not possible to establish a correlation of the findings to lifetime prediction. However, the hammer test was useful in identifying potential failure modes of luminaires that could be studied further.

The hammer test protocol consisted of repetitive loops of different environmental stresses with each loop comprising the following four tests:

- A steady-state WHTOL test for 6 h at 85 °C and 85% RH
- A temperature shock test that consists of 15 h of cycling at −50 °C to greater than 125 °C (air-to-air) with a 30-min dwell at each temperature
- A second steady-state WHTOL test for 6 h at 85 °C and 85% RH
- A high-temperature operational lifetime (HTOL) test that consists of 15 h at 120 °C

Despite the fact that the tested products were designed for indoor use in a constant temperature environment, all samples examined in the hammer test survived more than 100 cycles of temperature shock with nearly half surviving 300 cycles, as shown in Fig. 15.8 [26]. This finding suggests that the reliability of LED luminaires can be high if they are designed properly and that these devices are robust enough to survive for a period of time under conditions outside of their expected design range. The dominant failure modes found in the hammer test were

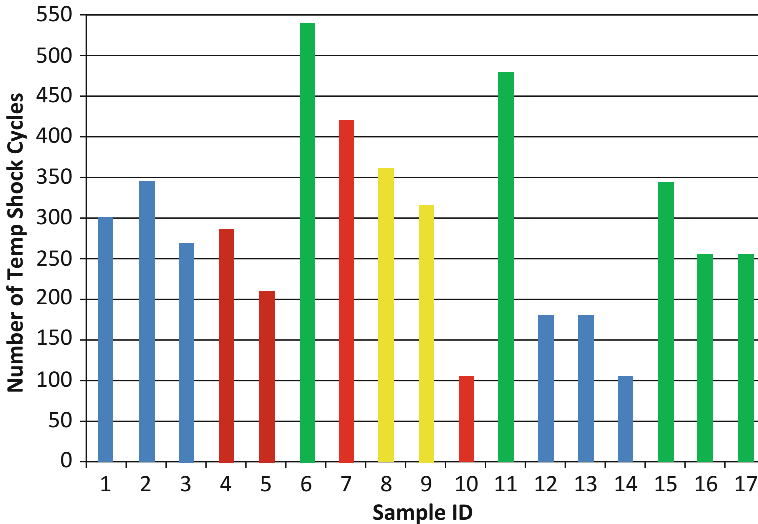

Fig. 15.8 Temperature shock cycles experienced by each luminaire in hammer test. The color of the vertical bars represents the observed failure mode: *blue* PCB failure, *dark red* capacitor, *light red* other components, *yellow* solder interconnects, and *green* still operational at the end of the test

mechanical failures associated with the expansion and contraction of printed circuit boards and solder joints [26]. However, there were several component failures involving capacitors, ICs, and MOSFETs that were found.

Another HAST protocol has been developed by the Pacific Northwest National Laboratory (PNNL) to compare the durability of the Philips L-Prize 60-Watt-equivalent LED lamps with market-proven compact fluorescent lamps (CFLs) [27]. In this study, ten different stress levels consisting of combinations of electrical, thermal, vibration, and humidity stresses were established, and the stress levels were changed in magnitude in each successive step. The experimental plan used in these tests is provided in Table 15.3.

Although the stress level used in portions of this test protocol typically exceeded the intended operational range of the product, these tests provide insights regarding the relative durability of LED and conventional lamps. PNNL found that the electrical performance of all of the L-Prize LED lamps was within acceptable limits at the end of testing, whereas none of the CFLs were operational. This finding demonstrated that the LED lamps performed better than the CFL benchmarks and that these products could survive extreme conditions outside of their intended operational range. However, as noted by PNNL, such HAST protocols cannot be used to quantitatively estimate device reliability or lifetime.

In another report on PAR38 lamps, PNNL used a similar protocol to evaluate the robustness of 40 commercial PAR38 lamp models [30]. The test samples consist of 32 different LED lamp models from different manufacturers and conventional PAR38 lamp technologies consisting of two CFL lamps, one ceramic metal halide lamp, and five halogen lamps. In general, the LED models tested were substantially

Table 15.3 Test plan for each stress level in the stepped-stress method developed by PNNL for testing lamp robustness [27]

Step	Time (min) H = hot C = cold	Hot temperature (°C)	Cold temperature (°C)	Vibration (peak g)	High-temperaturehumidity	Low voltage	High voltage	Total harmonic distortion
1	40 H + 40 C + 40 H	50.0	−20.0	5.0	Yes	114	126	Sine
2	40 H + 40 C + 40 H	56.7	−24.4	8.3	Yes	108	132	Sine
3	40 H + 40 C + 40 H	63.3	−28.9	11.7	Yes	102	138	Sine
4	40 H + 40 C + 40 H	70.0	−33.3	15.0	Yes	96	144	Sine
5	40 H + 40 C + 40 H	76.7	−37.8	18.3	Yes	90	150	Sine
6	40 H + 40 C + 40 H	83.3	−42.2	21.7	Yes	78	162	Sine +10%
7	40 H + 40 C + 40 H	90.0	−46.7	25.0	Yes	66	174	Sine +20%
8	40 H + 40 C + 40 H	96.7	−51.1	28.3	Yes	54	186	Square
9	40 H + 40 C + 40 H	103.3	−55.6	31.7	Yes	42	198	Square
10	40 H + 40 C + 40 H	110	−60.0	35.0	Yes	30	210	Square

more robust than the conventional benchmark lamps. However, there were some variability in the robustness and design maturity of the different LED lamp models, which translated into differences in survivability at the different stress levels of the test.

Another experimental approach for evaluating the reliability of SSL devices is to test identical populations of devices under two or more levels of the same acceleration test. In such studies, a constant setting of one or more environmental stresses (e.g., temperature, humidity) is applied to one population, and a different constant stress level is applied to a second population. Examples of such tests could include HTOL tests of different sample populations at various temperature levels (e.g., 100 °C, 125 °C) or WHTOL tests at different conditions (e.g., 75 °C and 75% RH [i.e., 75/75], 85 °C and 85% RH [85/85]). Constant stress protocols often can be used to develop statistical models provided that both the life distribution (representing the scatter in the population) and the linkage between life and stress (i.e., the acceleration factor) are known or can be determined. A variety of distributions, including the Weibull, lognormal, normal, and exponential distributions [1, 25], are commonly used for analyzing the test data. If the constant stress levels are applied at multiple settings, then acceleration factors can often be determined by using procedures such as the Arrhenius equation for temperature tests or the Peck equation for temperature-humidity tests [25].

As an example of this approach, researchers at RTI International have studied the performance of LED luminaires that contain integrated and stand-alone drivers in temperature-humidity tests [3, 4, 26, 30]. As shown in Fig. 15.9, this AST protocol when combined with an understanding of the physics of failure can lead to models of lifetime performance that can be validated in normal operating conditions. The researchers chose to perform these test on commercial 6-in. downlights because a wide variety of designs are used in commercial products

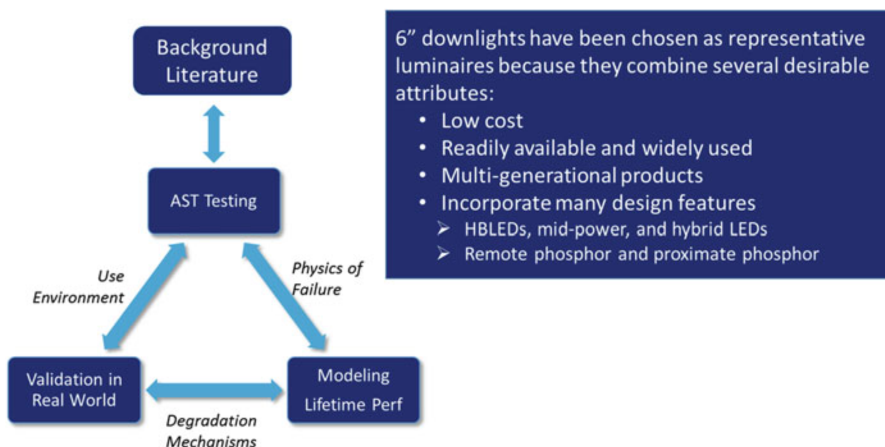

Fig. 15.9 Accelerated lifetime testing method for 6″ downlights

targeting the same applications. The design features that can be found in commercial 6-in. downlights include the following:

- Variation in LED package choice for light engines including the use of high-power LEDs (HP-LED), mid-power LEDs (MP-LED), and chip-on-board (COB) LEDs in different downlights
- A wide variety of driver topologies, including buck, boost, and flyback
- Different optical designs and materials

The testing performed by researchers at RTI included a dozen different commercial products and two main constant temperature-humidity stress environments of 75/75 and 85/85. The size of the test populations of each product in 75/75 and 85/85 was between five and ten samples, and the devices under test (DUTs) were examined after each 250 h intervals. Because the samples were examined after each 250 h increment, failure may occur anytime during this interval so the data are interval censored. The DUTs were considered to have failed when one of the following three criteria was met:

1. The DUT would not turn on when electrical voltage was applied. These devices were classified as abrupt failures.
2. The power consumption of the DUT decreased by more than 20%. These devices were classified as parametric failures.
3. The power factor of the DUT decreased by more than 20%. These devices were classified as parametric failures.

The test results from these 75/75 and 85/85 experiments can be represented in the Weibull probability plot shown in Fig. 15.10. The analysis revealed that separate linear fits can be applied to the test data for both 85/85 and 75/75, and these two lines are approximately parallel with a slope of approximately 1.2. This slope, which is the Weibull shape parameter (β), provides insights regarding the shape of the life distribution and the random failure rate. Because similar β values were observed in the 75/75 and 85/85 testing, this β value can be used to project the expected reliability at other conditions, such as shown in Fig. 15.10.

Although many of the samples in these tests closely followed the Weibull line for the test conditions, some of the early failures deviated from these lines. For example, the failure rate for the first 5% of the samples in 75/75 was higher than that predicted by the Weibull line. Likewise, the first 25% of the failures in 85/85 occurred at a higher rate than accounted for in the Weibull model. These higher failure rates early in the testing are indicative of different latent failure modes possibly due to material, manufacturing, or design defects.

As part of this study, the power consumption of the devices were also measured every 250 h. The data acquired for fives samples of one downlight model tested in 75/75 are shown in Fig. 15.11. The power consumption can be observed to increase steadily for the first 1,000 h of testing, followed by a slower rate of increase up to 1,750 h. This finding is suggestive of increased power dissipation in the driver due to deterioration of electrical components as previously suggested [26, 31]. At the

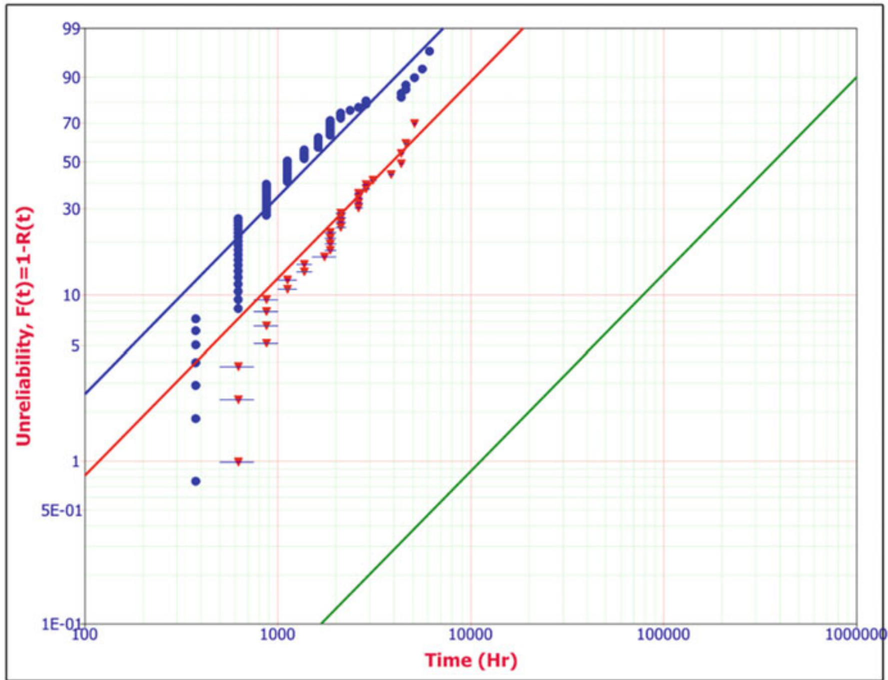

Fig. 15.10 Weibull plot of the reliability of downlight models in WHTOL tests conducted at 85 °C and 85% RH (*blue circle* data points and *blue line*) and 75 °C and 75% RH (*red triangle* data points and *red line*)

measurement taken at 2,000 h, one device displayed a sharp drop in power consumption (and lumen maintenance), which increases the standard deviation. This device was not functional when the next reading was taken, although additional devices began to fail at 2,750 h, thereby increasing the standard deviation again.

To support this hypothesis, an analysis was conducted on the failed DUTs, and the results are presented in Fig. 15.12. The failure analysis protocol, which was previously described [3], consisted of continuity and voltage checks of key components, including MOSFETs, diodes, capacitors, and resistors. In the tests, most of the failed DUTs had a failed MOSFET; fewer failures were found in chip resistors and capacitors. A possible explanation for the multiple failed electrical components in a DUT is that shorting of the MOSFET produced a current surge that caused other components to fail.

Simulations that used an electronic circuit simulators such as SPICE (Simulation Program with Integrated Circuit Emphasis) can also complement experimental findings and enable a deeper understanding of the system-level degradation of LED lighting drivers. Tarashioon et al. have developed a multi-physics reliability simulation for SSL drivers and applied the technique to a buck converter

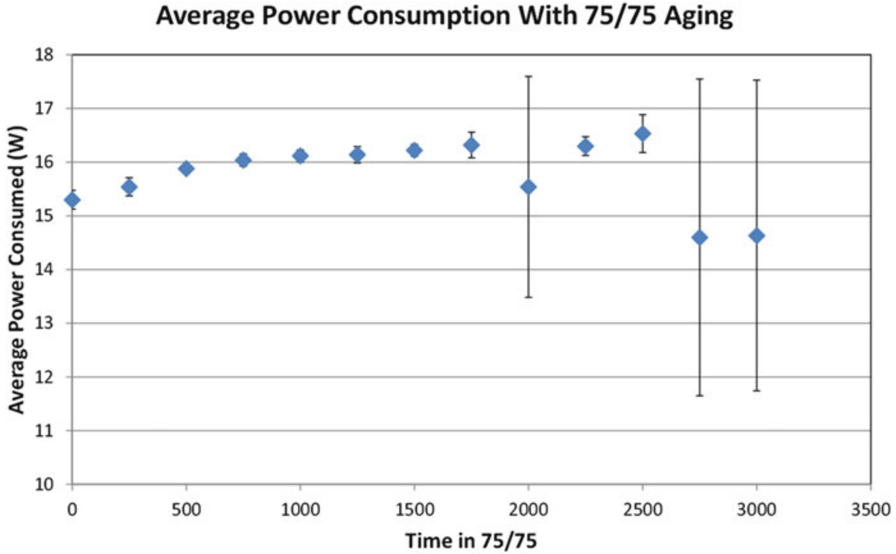

Fig. 15.11 Time-based change in the average power consumption of fives samples of one luminaire model during exposure to 75 °C and 75% RH. The *error bars* signify one deviation

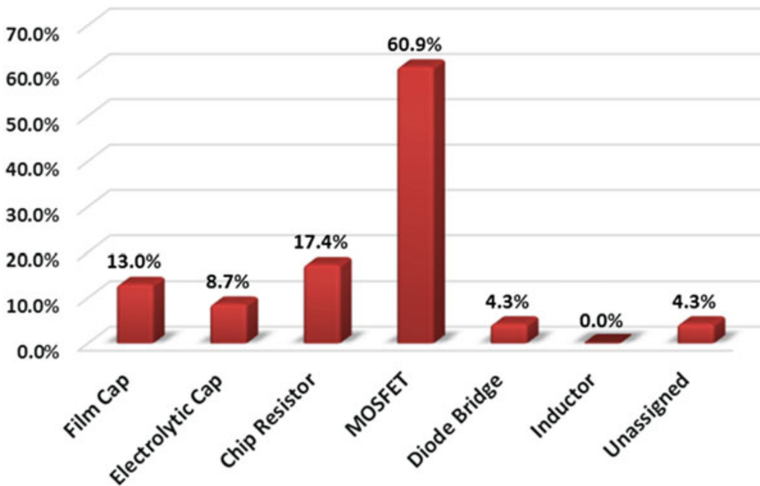

Fig. 15.12 Component failure distribution for downlights in 75/75 test environment. All components identified as having failed are included in this distribution, and some luminaires had multiple components which failed

[17, 32]. A critical element of this reliability simulation involves models of the behavior of electronic components, both individually and when combined into a circuit. These models, built in SPICE, allow for simulation of the circuit under initial conditions and as the electronic components degrade. Key findings of this

analysis is the systematic increase in power consumption and a decrease in efficiency of the buck converter as component degradation occurs. These findings are consistent with the experimental results presented in Fig. 15.11.

15.5 Conclusions

The reliability of electrical components used in LED lighting devices has a significant impact on the reliability of the lighting system. Understanding the reliability of LED drivers requires a knowledge of the intended use of the device including environmental (e.g., temperature, humidity), electrical (i.e., voltage quality and transients), and mechanical (i.e., vibration) stresses that the products would experience. In addition, knowledge of the susceptibility of key electronic components (e.g., capacitors, switching transistors, diodes, ICs, and linear components) to these stresses is also important in understanding overall product reliability. Although this information is difficult to determine for an electronic assembly such as the LED lighting driver, accelerated tests can help provide insights regarding likely failure modes and provide a basis to project reliability and product lifetime.

Acknowledgments This material is based on work supported by the US Department of Energy under Award Number DE-EE0005124.

Disclaimer This report was prepared as an account of work sponsored by an agency of the US Government. Neither the US Government nor any agency thereof, nor any of their employees, makes any warranty, express or implied, or assumes any legal liability or responsibility for the accuracy, completeness, or usefulness of any information, apparatus, product, or process disclosed, or represents that its use would not infringe privately owned rights. Reference herein to any specific commercial product, process, or service by trade name, trademark, manufacturer, or otherwise does not necessarily constitute or imply its endorsement, recommendation, or favoring by the US Government or any agency thereof. The views and opinions of authors expressed herein do not necessarily state or reflect those of the US Government or any agency thereof.

References

1. Next Generation Lighting Industry Alliance and LED Systems Reliability Consortium, *LED Luminaire Lifetime: Recommendations for Testing and Reporting*. Prepared for the U.S. Department of Energy (2014)
2. S. Winder, *Power Supplies for LED Driving* (Elsevier/Newnes, Amsterdam, 2008)
3. S.D. Shepherd, K.C. Mills, R. Yaga, C. Johnson, J.L. Davis, New understandings of failure modes in SSL luminaires. Proc. SPIE **9190**(2014), 919018 (2014). doi:10.1117/12.2062243
4. J.L. Davis, Accelerated life test results for SSL luminaire electronics. Presented at the 2015 U.S. Department of Energy's Solid-State Lighting Research and Development Workshop, San Francisco, CA (2015), http://www.energy.gov/sites/prod/files/2015/02/f19/davis-l_reliability_sanfrancisco2015.pdf

5. A. Lahyani, P. Venet, G. Grellet, P.-J. Viverge, Failure prediction of electrolytic capacitors during operation of a switchmode power supply. IEEE Trans. Power Electron. **13**, 1199 (1998)
6. Reliability Analysis Center, *Reliable Application of Capacitors* (Reliability Analysis Center, Rome, 1996)
7. C.S. Kulkarni, J.R. Celaya, K. Goebel, G. Biswas, Physics based electrolytic capacitor degradation models for prognostic studies under thermal overstress. European Conference of the Prognostics and Health Management Society (2012), p. 1
8. A.M. Iman, D.M. Divan, R.G. Harley, T.G. Habetler, Electrolytic capacitor failure mechanism due to inrush current. Conference Record of the 2007 I.E. Industry Applications Conference, 42nd Annual Meeting of the Industry Applications Conference (2007), pp. 730–736
9. P. Lall, P. Sakalaukus, J.L. Davis, Reliability and failure modes of solid-state lighting electrical drivers subjected to accelerated aging. IEEE Access. **3**, 53 (2015)
10. Y. Zhou, X. Li, X. Ye, G. Zhai, A remaining useful life prediction method based on condition monitoring for LED driver. 2012 Prognostics & System Health Management Conference (PHM-2012 Beijing), MU3086 (2012). doi: 10.1109/PHM.2012.6228797
11. M. Makdessi, Modeling, ageing and health monitoring of metallized films capacitors used in power electronics applications. Journee Scientifique St. Bernard (2012)
12. H. Wang, F. Blaabjerf, Reliability of capacitors for DC-link applications—An overview. 2013 I.E. Energy Conversion Conference and Exposition (ECCE) (2013), pp. 1866–1873
13. F. Lin, X. Dai, Z. Yao, J. Li, Research on electrode-end contact degradation of metallized polypropylene capacitors. IEEE Trans. Magn. **39**(1), 353 (2003)
14. R.W. Brown, Linking corrosion and catastrophic failure in low-power metallized polypropylene capacitors. IEEE Trans. Device Mater. Reliab. **6**(2), 326–333 (2006)
15. S. Yang, A. Bryant, P. Mawby, D. Xiang, L. Ran, P. Tavner, An industry-based survey of reliability in power electronic converters. IEEE. Trans. Ind. Appl. **47**(3), 1441–1451 (2011)
16. N. Valentine, D. Das, B. Sood, M. Pecht, Failure analysis of modern power semiconductor switching devices, in *IMAPS 48th International Symposium on Microelectronics,* Orlando, FL, 27–29 October (2015). doi: http://dx.doi.org/10.4071/isom-2015-THA56
17. X. Li, J. Qin, J.B. Bernstein, Compact modeling of MOSFET Wearout mechanisms for circuit-reliability simulation. IEEE Trans. Device Mater. Reliab. **8**(1), 98–121 (2008)
18. F. Lu, J. Shao, X. Liu, X. Wang, Validation test method of TDDB physics-of-failure models. 2012 Prognostics & System Health Management Conference (PHM-2012 Beijing) (2012), pp. 1–4
19. Z. Zhou, X. Liu, Q. Shi, Y. En, X. Wang, Failure rate calculation for NMOS devices under multiple failure mechanisms. 2013 I.E. International Symposium on the Physical and Failure Analysis of Integrated Circuits (IPFA) (2013), pp. 362–365
20. J.R. Celaya, A. Saxena, C.S. Kulkarni, S. Saha, K. Goebel, Prognostics approach for power MOSFET under thermal-stress aging. 2012 Proceedings of the Reliability and Maintainability Symposium (RAMS) (2012)
21. S. Saha, J.R. Celaya, V. Vashchenko, S. Mahiuddin, K.F. Goebel, Accelerated aging with electrical overstress and prognostics for power MOSFETs. 2011 I.E. EnergyTech (2011)
22. I. Vaalasranta, J. Pippola, L. Frisk, Power MOSFET failure and degradation mechanisms in flyback topology under high temperature and humidity conditions. 2013 9th IEEE International Symposium on Diagnostics for Electric Machines, Power Electronics and Drives (SDEMPED) (2013), pp. 16–22. doi: 10.1109/DEMPED.2013.6645691
23. IEEE, Standard 1100-2005. IEEE Recommended Practice for Powering and Grounding Electronic Equipment (2005)
24. P.F.Keebler, Ingredients for the success of LED lighting. Presented at the U.S. Department of Energy's Solid-State Lighting Research and Development Workshop, Atlanta, GA (2012). January. http://apps1.eere.energy.gov/buildings/publications/pdfs/ssl/keebler_discussion_2012rdworkshop.pdf
25. W.B. Nelson, *Accelerated Testing: Statistical Methods, Test Plans, and Data Analysis* (Wiley Interscience, Wiley, Hoboken, 2004)

26. RTI International, *Hammer Test Findings for Solid-State Lighting Luminaires* (U.S. Department of Energy, 2012), December 2013
27. M.E. Poplawski, M.R. Ledbetter, M.A. Smith, L-Prize: stress testing of the Philips 60W replacement lamp entry (2012), http://www.lightingprize.org/pdfs/lprize_60w-stress-testing.pdf
28. L. Han, N. Narendran, Developing an accelerated life test method for LED drivers. Ninth International Conference on Solid State Lighting. Proceedings of the SPIE **7422**, 742209 (2009)
29. L. Han, N. Narendran, An accelerated test method for predicting the useful life of an LED driver. IEEE Trans. Power Electron. **26**(8), 2249–2257 (2011)
30. J.L. Davis, K. Mills, M. Lamvik, R. Yaga, S.D. Shepherd, J. Bittle, N. Baldasaro E. Solano, G. Bobashev, C. Johnson, A. Evans, System reliability for LED-based products. 2014 15th International Conference on Thermal, Mechanical, and Multi-physics Simulation and Experiments in Microelectronics and Microsystems (EuroSimE), Ghent, Belgium. 7–9 April (2014). doi: 10.1109/EuroSimE.2014.6813879
31. Pacific Northwest National Laboratory, CALiPER Report 20.3: Stress Testing of LED PAR Lamps (2014)
32. S. Tarashioon, W.D. van Driel, G.Q. Zhang, Multi-physics reliability simulation for solid state lighting devices. Microelectron. Reliab. **54**, 1212–1222 (2014)

Chapter 16
Reliability Prediction of Integrated LED Lamps with Electrolytic Capacitor-Less LED Drivers

B. Sun, Xuejun Fan, Willem Dirk van Driel, and Guo Qi Zhang

Abstract This chapter investigates the reliability of the integrated LED lamps with electrolytic capacitor-less LED drivers. Firstly, the impact of the interaction between the degradations of the LED light source and the driver on the lumen depreciation is studied. The electronic-thermal simulation was carried out to obtain the history of temperatures of LED and driver, the driver's output current, and the luminous flux considering the variations of temperature and current throughout the operation life. It is found that the ultimate lamp's lifetime is significantly less than the individual lifetimes of the preselected LED and driver. It is concluded that it is necessary to apply the electronic-thermal simulations to predict the lifetime of LED lamps when driver's lifetime is comparable to the LED's lifetime. Secondly, this chapter focuses on predicting the catastrophic failure of an electrolytic capacitor-free LED driver during the lumen depreciation process. Electronic-thermal simulations are utilized to obtain the lamp's dynamic history of temperature and

B. Sun (✉)
Beijing Research Center, Delft University of Technology, No.A35, Qinghua East Road, Beijing 100083, China
e-mail: sandysun23@gmail.com

X. Fan
State Key Laboratory of Solid State Lighting (Changzhou Base), Changzhou, China

Department of Mechanical Engineering, Lamar University, Beaumont, USA
e-mail: xuejun.fan@lamar.edu

W.D. van Driel (✉)
Philips Lighting, High Tech Campus, Eindhoven, The Netherlands

Delft University of Technology, EEMCS Faculty, Delft, The Netherlands
e-mail: willem.van.driel@philips.com

G.Q. Zhang
State Key Laboratory of Solid State Lighting, Institute of Semiconductors, Chinese Academy of Sciences, Beijing, China

State Key Laboratory of Solid State Lighting (Changzhou Base), Changzhou, China

EEMCS Faculty, Delft University of Technology, Delft, The Netherlands
e-mail: g.q.zhang@tudelft.nl

© Springer International Publishing AG 2018

W.D. van Driel et al. (eds.), *Solid State Lighting Reliability Part 2*, Solid State Lighting Technology and Application Series 3, DOI 10.1007/978-3-319-58175-0_16

electrical current for two distinct modes: constant current mode (CCM) and the constant optical output (CLO) mode, respectively. A fault tree method is applied to calculate the system's MTTF, and the LED's lifetime also is calculated. The CLO mode increases the LED's current exponentially to maintain the constant light output. As a result, junction temperatures of LEDs, MOSFET, and diode rise significantly, leading a shorter lifetime and MTTF. Compare with the current of the MOSFET, the increased junction temperature has larger effects on the failure rate. The MOSFET contributes more to the driver's failure rate than the diode. For the CCM mode, junction temperatures increase slightly and have a little shorter lifetime and MTTF.

16.1 Introduction

Light-emitting diode (LED) has been regarded as one of the most promising lighting solutions due to its energy efficiency, flexible controllability and long life flight source, a driver, control gears, secondary optical parts, and heat dissipation components. The LED light source often has a lifetime as long as 25,000–100,000 h [1, 2], but the LED driver has a shorter life than the light source, in particular, when electrolytic capacitors are utilized [3–5]. Many studies have focused on the degradation analysis of LED only, without taking consideration of the driver degradation [2, 6–10]. For example, an accelerated test method of luminous flux depreciation for LED lamps or luminaires has been developed to reduce the test time within 2000 h at an elevated temperature [2]. Degradations of LEDs in the high-temperature-humidity environment have been studied [6, 7]. The LED color shift caused by optical materials has been investigated [8, 9]. For the degradation of LED drivers, if the driver's lifetime is much shorter than LED's life, the degradation of LED light source may not be significant to the driver's lifetime. With such an assumption, a physics-of-failure (PoF)-based reliability prediction methodology for LED drivers has been developed to estimate the failure rate distribution of an electrolytic capacitor of the given LED driver systems [3].

Electrolytic capacitors are often used [11–18] in commercial LED drivers. In most of the single- and two-stage mainstream commercial LED drivers, electrolytic capacitors are used as energy storages and buffers [11, 12], including buck [14, 15], buck-boost [18], and fly-back drivers [13]. However, the electrolytic capacitor is considered as the weakest component in LED drivers [3–5]. Since electrolytic capacitor's lifetime is much less than that of LED's lifetime, the effect of LED's degradation may not be significant on its driver's reliability [3, 19]. A physics-of-failure (PoF)-based reliability prediction methodology for LED drivers has been developed by the authors to estimate the failure rate distribution of an electrolytic capacitor of the given LED driver systems [3]. In recent years, several electrolytic capacitor-less LED drivers have been presented to improve driver's lifetime, including buck-boost single-ended primary inductor converter (SEPIC) [20], valley-fill SEPIC driver [21], boost-fly-back driver [22] and SEPIC twin-bus buck driver [23]. Moreover, electrolytic capacitor eliminating circuits have also been installed into the mainstream LED drivers, such as power control (PC) converter

[24], two-phase dual asymmetrical half-bridge converter [25], bidirectional buck-boost converter [26], harmonic injection circuits [27], and LC filters [28, 29]. In addition, with the help of new technologies, for instance, resonance-assisted filter [14] and variable on-time control method [15], the lifetime of electrolytic capacitors can also be improved. For an electrolytic capacitor-less LED driver, the LED light source and the driver may have comparable lifetimes [30–32].

When the lifetime of the LED light source is much longer than the driver's, depreciation of the LED light source has little impact on the entire system during the process of the driver's failure. In the case that the LED light source and the driver have similar lifetimes, the lumen depreciation and the driver's failure coexist in the LED lamp and may interact with each other. The question arises that what is the interaction of two simultaneous failure modes: the LED depreciation and the driver's failure, during lamp operation? In this chapter, failures of the LED driver include the catastrophic failure and the degradation which leads to failures of entire system. Thus, there are two combinations: degradations of the LED light source and the driver and LED's depreciation and driver's catastrophic failure.

If degradations of the LED light source and the driver coexist, their interactions become significant factors in determining the lifetime of the LED lamp [33–37]. Both degradations are strongly affected by temperature and time. The LED light source degrades gradually over a long period, which is known as the lumen flux depreciation. During the degradation of the LED light source, its efficacy is reduced; thus, more heat dissipation is expected. On the other hand, when the driver degrades, the electrical current output to the LED light source will decrease over time. Such a process will affect the heat generations of both driver and LEDs. For an integrated lamp, where the LED light source and driver are assembled together, the heat generated by LEDs and the driver will determine the junction temperature of the LED light source as well as the driver's temperature. Such temperatures continuously change over time since LED heat dissipation depends on time, temperature, and current from the driver. In the meantime, the driver's performance also depends on time and temperature. Ultimately the LED's lumen flux depreciation is affected by the degradations of both LED drivers and LED light source. However, there is little systematic research on LED system reliability when LED's degradation and driver's failures coexist during operating conditions.

The catastrophic failure rate of an LED driver depends on its rate of the critical components, such as the MOSFETs and power diodes [34, 38]. The total rate of catastrophic failures determines the mean time to failure (MTTF) for the driver. At the same time, LED experiences degradation that is dependent on driver's output current, LED's junction temperature, and time. Generally, the lifetime of LED is given in terms of the expected operating hours until light output has depreciated to 70% of initial levels. In this sense, there are two distinct concepts of lifetimes involved in an LED system: mean time to failure (e.g., driver) and LED's lifetime in terms of luminous flux depreciation. When these two concepts are far different, it is obvious that they do not interact each other. Many commonly used reliability prediction methods consider the catastrophic failures at constant conditions without the interaction with LED degradation. Few systematic studies have been conducted

to predict the reliability of the LED lamp when the MTTF is comparable to the LED's lifetime.

Intelligent driver and control techniques have been applied to LED systems. For instance, the constant light output (CLO) mode has been implemented in driver design to eliminate the lumen depreciation [39]. In contrast with the constant current mode (CCM), LED drivers in CLO mode usually have optical feedback functions and can adjust their output current to maintain the light output. It has claimed that such technology can eliminate the lumen depreciation during long-term operation. However, the system's reliability with constant light output technology has not yet been studied.

This chapter contains two major sections. In Sect. 16.2, an integrated LED lamp with an electrolytic capacitor-free driver is considered to study the coupling effects of both the LED light source and the driver's degradations on light output. The driver is assumed to have a comparable lifetime with the LED light source. The electronic-thermal simulation was carried out to obtain the history of temperatures of LED and driver, the driver's output current, and the luminous flux considering the variations of temperature and current throughout the operation life. Generally, the useful lifetime of LED lighting products is typically given in terms of the expected operating hours until light output has depreciated to 70% of initial levels [2]. Section 16.3 focuses on predicting the catastrophic failure of an electrolytic capacitor-free LED driver during the lumen depreciation process. The overall catastrophic failure rate of the critical components in this driver is considered as functions of temperature and current. Electronic-thermal simulations are utilized to obtain the lamp's dynamic history of temperature and electrical current for two distinct modes: constant current mode (CCM) and the constant optical output (CLO) mode, respectively. A fault tree method is applied to calculate the system's MTTF, and the LED's lifetime in terms of light output can also be calculated.

This chapter is organized as follows. Section 16.2 considers the coupling effects of degradations of the LED light source and the driver on system's lifetime. In Sect. 16.3, prediction on the catastrophic failure of LED driver during the lumen depreciation process is introduced. Section 16.4 concludes this chapter finally.

16.2 Coupling Effects of Degradations

This section studies the impact of the interaction between the degradations of the LED light source and the driver on the lumen depreciation. As using the electrolytic capacitor-free driver, the driver is assumed to have a comparable lifetime with the LED light source. In this case, degradations of the LED light source and the driver may coexist; their interactions become significant factors in determining the lifetime of the LED lamp [33–37].

The electronic-thermal simulation was carried out to obtain the history of temperatures of LED and driver, the driver's output current, and the luminous flux considering the variations of temperature and current throughout the operation life. Circuit simulations are carried out first to obtain the power distributions and

output current and the voltage to LEDs. Thermal simulations are subsequently performed based on power distribution to obtain the temperature distributions of the LED lamp, in particular, LED junction temperature driver's temperature. Since circuit simulations require the driver's overall temperature and the LEDs' junction temperature, which determine the degradation parameters of the LED light source and the driver, the electronic and thermal simulations are coupled through both degradation models, and therefore, an iteration process among electronic and thermal simulation is required. As a result, the lumen flux depreciation as a function of time can be obtained. Generally, the useful lifetime of LED lighting products is typically given in terms of the expected operating hours until light output has depreciated to 70% of initial levels [2].

16.2.1 Degradation Modelling

16.2.1.1 LED Light Source

The exponential model is applied to describe lumen depreciation in the constant junction temperature T_j and the constant driving current I as follows [2]:

$$\Phi_{\mathrm{lm}}(t) = \Phi(I) \cdot e^{-\beta\left(T_j\right)\cdot t} \tag{16.1}$$

where t is time, Φ_{lm} is the absolute luminous flux at time t, $\Phi(I)$ is the luminous flux before aging, and the depreciation rate β follows the Arrhenius Eq. 16.5:

$$\beta\left(T_j\right) = A_\beta \cdot \mathrm{e}^{-\frac{E_{a,\beta}}{\kappa \cdot T_j}} \tag{16.2}$$

where A_β is the pre-exponential factor and $E_{a,\beta}$ is the activation energy of LED.

$\Phi(I)$ in Eq. 16.1 can be described by the following function [40]:

$$\Phi(I) = \eta(I) \cdot I \cdot V_f \tag{16.3}$$

where V_f is the forward voltage and $\eta(I)$ is the efficacy of the LED light source in current I. V_f is a function of junction temperature and current and will be introduced in the following section. The efficacy η is affected by both temperature droop (T-droop) and current droop (J-droop) [41, 42]. However, in high current status, the T-droop becomes negligible in comparison with the J-droop. Thus, η can be assumed approximately as a function of the J-droop [42]:

$$\eta = \eta_0 \cdot \frac{bn^2}{an + bn^2 + cn^3} \tag{16.4}$$

where η_0 is the basic efficacy, a and c are the linear and the third-order non-radiative recombination rates, b is the radiative recombination rate, and n is the average

carrier density of LED, which is proportional to the current I; hence, the efficacy can be described the following function:

$$\eta(I) = \eta_0 \cdot \frac{B_e I}{A_e + B_e I + C_e I^2} \tag{16.5}$$

where η_0, A_e, B_e, and C_e are dependent on the properties of materials and structure of the LED.

Combined Eqs. 16.1, 16.3, and 16.5, the luminous flux in the ever-changing junction temperature $T_j(t)$ and current $I(t)$ can be described by the following function [43]:

$$\Phi_{\mathrm{lm}}(t) = \eta_0 \cdot \frac{B_e I(t)^2}{A_e + B_e I(t) + C_e I(t)^2} \cdot V_f \cdot e^{-\int_0^x \beta[T_j(x)] \cdot \mathrm{dx}} \tag{16.6}$$

The derivation of Eq. 16.6 is shown in the Appendix A. System conditions, $I(t)$, V_f, and $T_j(t)$, depend on structure and materials' properties of the lamp and circuit and can be determined by the electronic-thermal simulations. The physical characteristics of the selected LED, η_0, A_e, B_e, C_e, A_β, and $E_{a,\beta}$, are invariables and can be extracted by experiments. In this section, η_0, A_e, B_e, and C_e were determined experimentally for the selected LED, and their values are shown in Table 16.2. A_β and $E_{a,\beta}$ will be adjusted through a parametric study in Sect. 16.2.3.3.

16.2.1.2 LED Driver

Literature [33, 34] has shown that the on-state resistance of a MOSFET of an LED driver increases with aging process, leading to the degradation of output current. The study in [36] also indicates that the transistor declines during operation and brings a decreasing output current of the driver. In the present work, the degradation of the driver in terms of the output current is considered. The effective value of the output current I can be represented by the following equation:

$$I(t) = \frac{V_{\mathrm{ref}}}{R_{\mathrm{ref}}} \tag{16.7}$$

where V_{ref} is a constant reference voltage and R_{ref} is the overall current control resistance. Research in [44] has shown that the resistance of current control device degrades linearly with time. Thus, a linear degradation model for the overall current control resistance R_{ref} is assumed:

$$R_{\mathrm{ref}}(t) = R_0 \cdot [1 + A(T_D) \cdot t] \tag{16.8}$$

where R_0 is the initial resistance, T_D is the average driver temperature, and the degradation rate A follows the Arrhenius equation:

$$A(T_D) = A_0 \cdot e^{-\frac{E_{a,D}}{\kappa \cdot T_D}} \tag{16.9}$$

where A_0 is the basic degradation rate and $E_{a,D}$ is the overall activation energy of LED driver. If the driver temperature T_D changes continuously in time t, Eq. 16.8 can be deduced to an integration form, as follows:

$$R_{\mathrm{ref}}[t, T_D(t)] = R_0 \cdot \int_0^t \{1 + A[T_D(x)] \cdot x\} \cdot \mathrm{dx} \tag{16.10}$$

where the driver temperature $T_D(t)$ is a system condition and can be determined by electronic-thermal simulations. Among the physical characteristics of the selected driver, R_0 can be determined by the initial current of the LED light source, $E_{a,D}$ and A_0, which control the driver degradation, and will be adjusted through a parametric study in Sect. 16.2.3.3.

16.2.2 Simulation Methodology

16.2.2.1 Electronic Simulations

In the present study, electronic simulations are carried out to analyze circuit behaviors of an entire LED lamp. The current, voltage, and power dissipation of each component can be calculated. The LTSPICE is selected as the electronic simulation platform. An electrolytic capacitor-free buck-boost converter, as shown in Fig. 16.1, is selected as LED driver. This type of LED driver is one of the most commonly used drivers that can achieve high efficiency, wide voltage range, and low distortion of line current in lighting applications [31]. In this section, the driver's switching frequency is 300 kHz, the input voltage range is 9–20 Vdc, the rated output current is 400 mA, the duty cycle is 25%, and the rated output power is 6.0 W. Device models in the driver, which are provided by a public database [45], have been validated and verified.

A temperature-dependent model for the LED light source is considered in circuit analysis. In this model, the performance of the LED light source can be described by the following equation [40]:

$$V_f[I(t), T_j(t)] = N \cdot \kappa \cdot T_j(t) \cdot \ln\left[\frac{I(t)}{I_s} + 1\right] + R_s \cdot I(t) \tag{16.11}$$

where N is the ideality factor, I_s is the saturation current, and R_s is the equivalent series resistance of the LED light source. Literature [46] suggests that the electronic characteristics of LEDs after seasoning is not affected by aging time but strongly affected by junction temperature T_j. Thus, the R_s, I_s, and N are considered as the

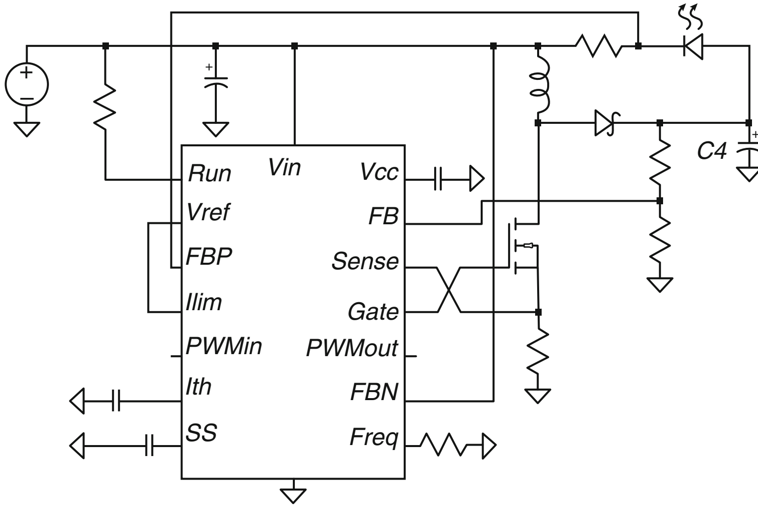

Fig. 16.1 The electrolytic capacitor-free buck-boost LED driver

functions of junction temperature T_j as following, according to literature [40, 47, 48]:

$$R_s\left[T_j(t)\right] = R_{s0} \cdot \left[1 + A_s \cdot T_j(t)\right] \tag{16.12}$$

$$I_s\left[T_j(t)\right] = I_{s0} \cdot T_j^2(t) \cdot e^{-\frac{A_I}{T_j(t)}} \tag{16.13}$$

$$N\left[T_j(t)\right] = \frac{T_j(t)}{A_N \cdot T_j(t) + B_N} \tag{16.14}$$

The power distribution of the entire circuit can be obtained by circuit simulations. The thermal power of the LED light source P_L is the difference between input power and optical power of the LED light source:

$$P_L(t) = I(t) \cdot V_f\left[I(t), T_j(t)\right] - C \cdot \Phi_{\mathrm{lm}}(t) \tag{16.15}$$

where C is the ratio of optical power and luminous flux.

The thermal power of the driver P_D is the sum of heat from all components in the driver. Thus, P_D equals to the difference between total input power and total output power of the driver:

$$P_D(t) = P_{\mathrm{in}}(t) - I(t) \cdot V_f\left[I(t), T_j(t)\right] \tag{16.16}$$

where P_{in} is the total input power.

16.2.2.2 Thermal Simulations

This chapter selects a commercial available LED light bulb as the carrier for the study. Figure 16.2 displays the lamp's structure, in which the geometrical information and material properties can refer to the literature [49–52]. In such lamps, the LED light source and driver are assembled together; thus, the heat generated by both the LED light source and the driver determine the junction temperature of the LED light source as well as the driver's temperature. As a result, system level finite element modeling is required to obtain accurate temperatures. The entire lamp operates at room temperature (298 K) with natural convection condition.

In the thermal finite element model, the driver and its potting materials as a whole are considered as a volume with a thermal conductivity of the potting material. The driver temperature, T_D, is defined as the maximum temperature of the volume. As the input of thermal simulations, the thermal power of the LED light source and the driver, P_L and P_D, are calculated by the electronic simulations. By performing the thermal simulations, T_j and T_D can be obtained which are significant to the degradations and electronic characteristics of the entire system.

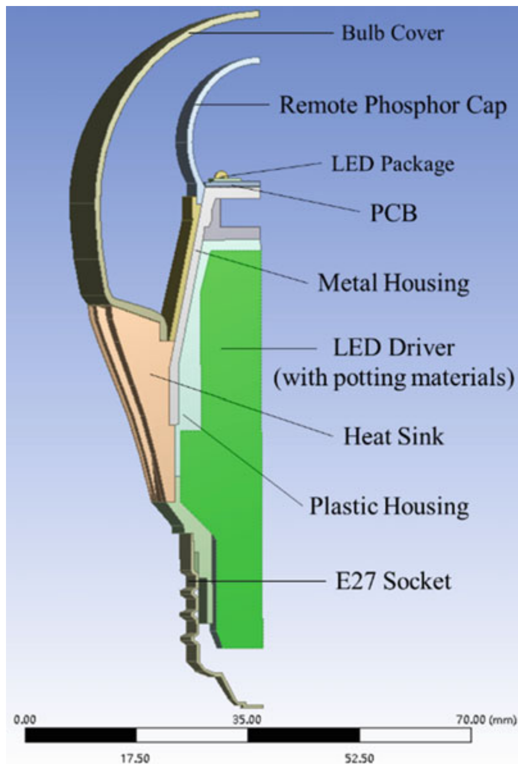

Fig. 16.2 The model of the selected (**a**) LED lamp

16.2.2.3 Simulation Methodology

Figure 16.3 illustrates the flowchart of the electronic-thermal simulation methodology in our present study. The simulation process begins with the initial guess of T_j and T_D and the LED's initial forward voltage V_f, from which the degradation models in Eqs. 16.6 and 16.10 can be applied to obtain the luminous flux Φ_{lm} and the current I. Then the electronic simulations are performed to update V_f and obtain the power dissipations by Eqs. 16.11, 16.15, and 16.16. Subsequently, the thermal simulations are performed to update T_j and T_D. Such a simulation process loop is performed iteratively until the error between values of T_j in two consecutive steps is less than 0.1 °C, as shown in Fig. 16.3. Then light output can be calculated using Eq. 16.6. Generally, the useful lifetime for LED lighting products are typically given in terms of the expected operating hours until light output has depreciated to 70% of initial levels [2]. If this threshold is not reached, the aging time t advances to a small increment Δt. Since the temperatures update T_j and T_D are not known at $t + \Delta t$, the above iteration process repeats. When time $t = t_{\mathrm{F}}$, and the Φ_{lm} has depreciated to 70% of initial value, the simulation stops, and t_{F} is considered as

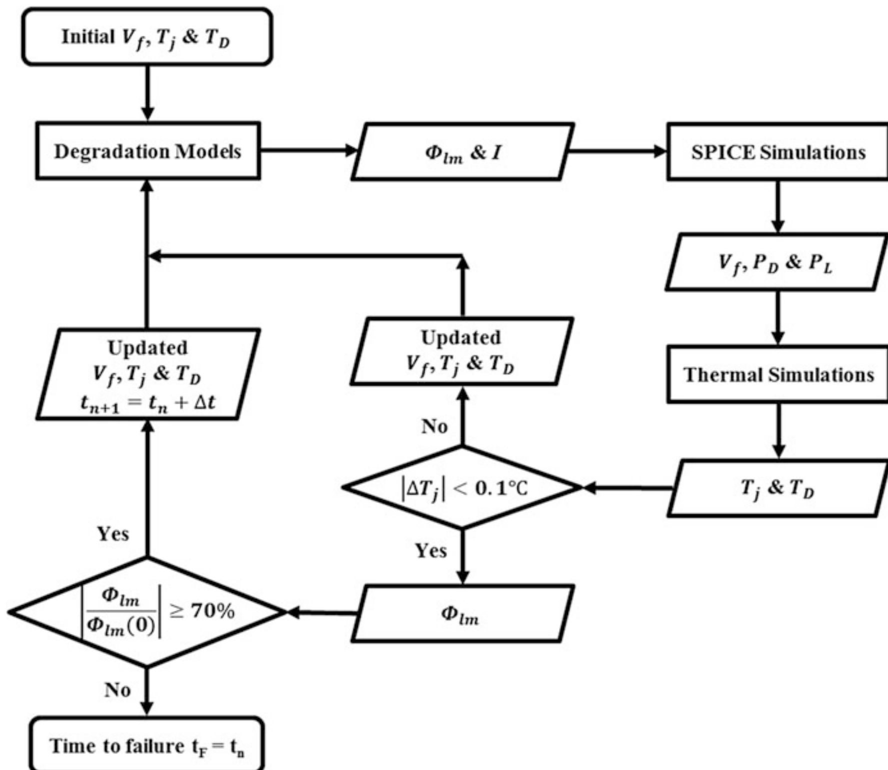

Fig. 16.3 Flowchart of the electronic-thermal simulation methodology

the lifetime of the LED system. Through the simulation iteration, the LED current, the LED junction temperature, the driver's temperature, and the luminous flux can be obtained as function of time.

16.2.3 Results and Discussions

16.2.3.1 Parameter Extraction of LED Models

The physical parameters of the lumen depreciation model and the electronic model of the LED light source, C, η_0, A_e, B_e, C_e, R_{s0}, A_s, I_{s0}, A_I, A_n, and B_n, need to be determined experimentally. Hence, selected high-power LED packages were tested in eight junction temperature levels, from 293 to 363 K. Each sample was placed on a thermal plate inside a 50 cm integrating sphere system. Then, the transient electronic and optical characteristics of each sample, including current, forward voltage, luminous flux, and efficacy, are measured at different junction temperature levels. For each junction temperature, the transient current of each sample sweeps from 200 to 350 mA. As shown in Fig. 16.4, the measured I–V characteristics were fitted by Eqs. 16.11, 16.12, 16.13, and 16.14, whereas the efficacy was fitted by Eq. 16.5 by the least square method, obtaining these physical parameters of the LED models. Table 16.1 summarizes the averaged values of the model parameters. The details of tests and parameter extractions can refer to the Literature [43].

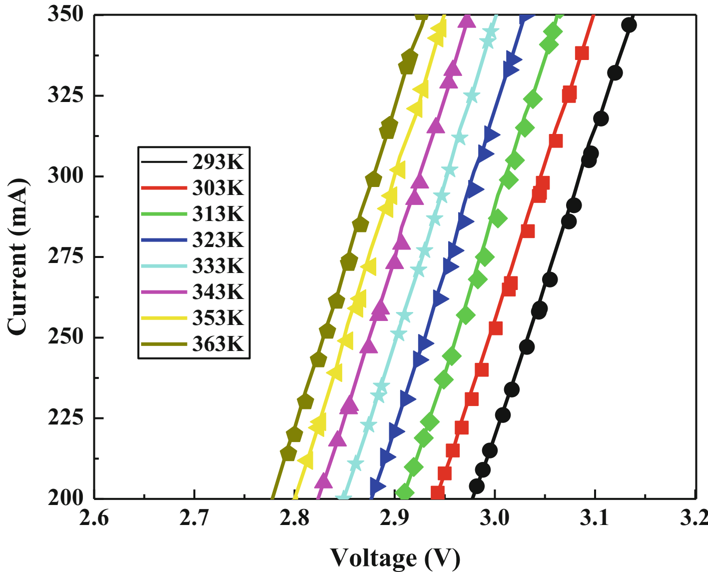

Fig. 16.4 Test results of the selected LED

Table 16.1 Physical parameters of the LED light source

R_{s0}	A_s	I_{s0}	A_I
5.914×10^{-1}	6.699×10^{-4}	4.786×10^{5}	1.274×10^{-1}
A_n	B_n	**C**	η_0
1.240	$-2.882\ 10^{2}$	4.087×10^{-3}	1.456×10^{2}
A_e	B_e	C_e	
0.999	$1.406\ 10^{3}$	2.138×10^{3}	

Table 16.2 Temperature distributions

	Predicted initial temperature (K)	Targeted temperature (K)
T_j	352	358
T_D	318	328

16.2.3.2 Lamp's Initial Temperature Distributions

It is important to know the initial temperature distributions within the lamp under operating conditions. The electronic-thermal simulations were carried out to obtain the power distributions and the ensuing initial temperature distributions. Table 16.2 lists the results of initial T_j and T_D, LED junction temperature and driver overall temperature. Table 16.2 also gives the targeted temperatures of T_j and T_D for the selected lamp. It can be seen that the predicted initial temperatures are within the design specifications. The proposed simulation method provides a useful verification tool for LED lamp design.

Due to the degradations of the LED and driver over time, both T_j and T_D will change continuously with time, which ultimately will affect the LED light output. These results will be presented and discussed in subsection 16.2.3.4.

Based on the predicted initial temperatures, the LED light source and driver can be preselected to meet the lifetime requirement. For example, LED may be selected to have 25,000 h lifetime in the predicted initial LED temperature. This means that the selected LED will have luminous flux above 70% of initial levels before 25,000 h. Similarly, the driver may also be preselected to have 25,000 h lifetime at the predicted initial driver temperature. This implies that the output current from the driver will not decrease to the certain level of the initial value (e.g., 10% of output current) before 25,000 h.

The question now is what is the lamp's ultimate lifetime in terms of luminous flux if the LED and driver's lifetimes are both 25,000 h? In the following, three scenarios are defined to study the problem.

16.2.3.3 Definition of Different Scenarios

Usually, LED's lifetime is defined at the targeted constant temperature and constant current. In the present study, as shown above, the LED is selected to have a lifetime

Table 16.3 Designed scenarios

Case	LED	Driver
Scenario 1	25,000 h lifetime at the constant initial T_j (L25K)	No degradation
Scenario 2	No degradation	25,000 h lifetime at the constant initial T_D (D25K)
Scenario 3	25,000 h lifetime at the constant initial T_j (L25K)	25,000 h lifetime at the constant initial T_D (D25K)

of 25,000 h at the initial temperature of operation, denoted as "L25K" throughout the subsequent analysis. Similarly, "D25K" indicates the 25,000 h lifetime for the selected driver at the initial temperature T_D of lamp operation. Table 16.3 lists the three scenarios to be analyzed. Scenario 1 considers LED light source degradation only with the selection of L25K LEDs. Scenario 2 considers the driver degradation only with the selection of a D25K driver. The Scenario 3 considers both of the degradations from LED and driver simultaneously. It should be noted that there are different choices of LEDs to reach L25K lifetime, with a combination of the activation energy $E_{a,\beta}$ and the pre-exponential factor A_β in Eq. 16.2. Nonetheless, unless specified, the values of $E_{a,\beta} = 0.3\text{eV}$ and $A_\beta = 2.8293 \times 10^{-1}$ are used throughout the Sect. 16.2.

16.2.3.4 Results and Discussions

LED Current

Figure 16.5 shows the relative LED current with respect to the initial value in each scenario as a function of operation time. As expected, the LED current maintains at its initial value for Scenario 1 as the driver's degradation is not considered. Since the selected driver is a constant current driver, the lumen depreciation has a negligible effect on the driver's output current. For Scenario 2 where only driver's degradation is considered, the LED current drops 10% at 25,000 h. When two degradations are considered, the LED current drops a little more, about 11% at 25,000 h.

LED Junction Temperature

Figure 16.6 shows the LED junction temperature as a function of operation time in each scenario. The LED junction temperature increases significantly in 25,000 h for Scenario 1. This is because when LED experiences the lumen depreciation, more heat is generated by the LED, leading to the temperature rise. However, the LED junction temperature decreases for Scenario 2 when the driver's degradation is considered only. This is because that driver's current degrades over time, as seen in

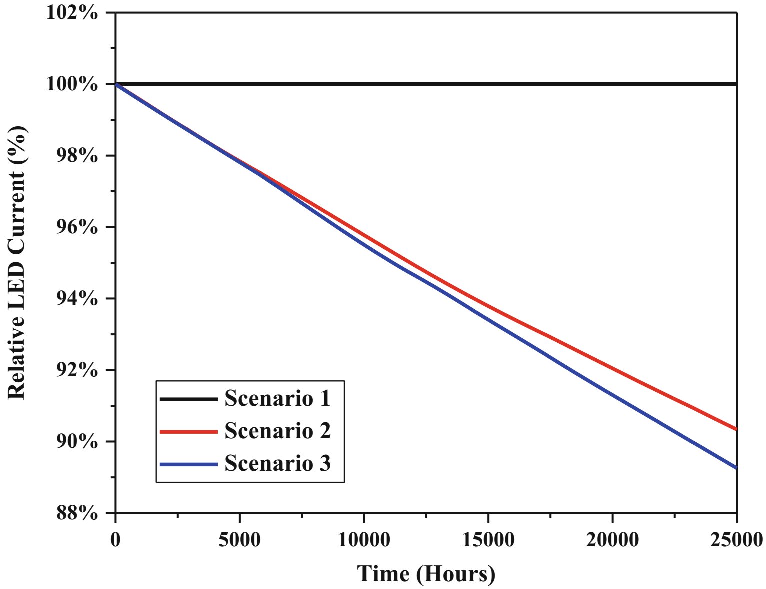

Fig. 16.5 The LED current of each scenario

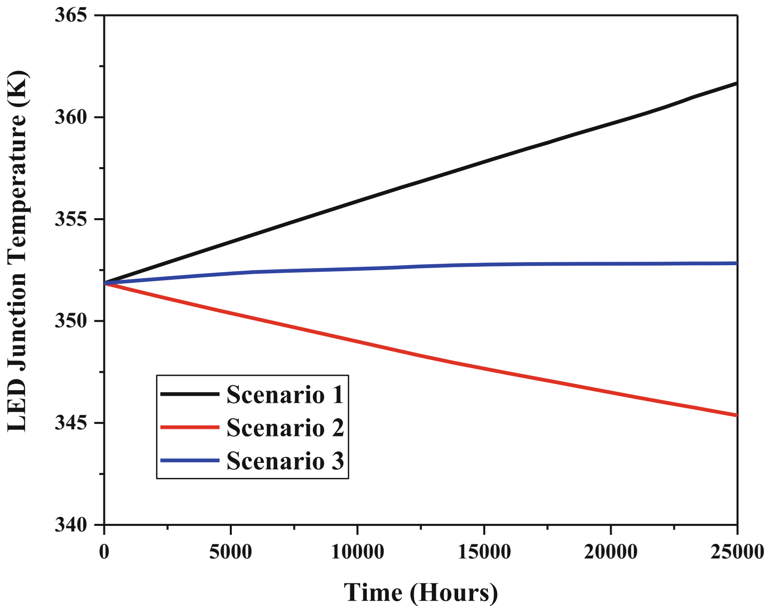

Fig. 16.6 The LED junction temperature of each scenario

Fig. 16.5; thus, less power is consumed by LEDs. It is found that the two degradations have competing effects on the junction temperatures of the LED in a lamp. As a result, Fig. 16.6 shows that LED's junction temperature does not change much for

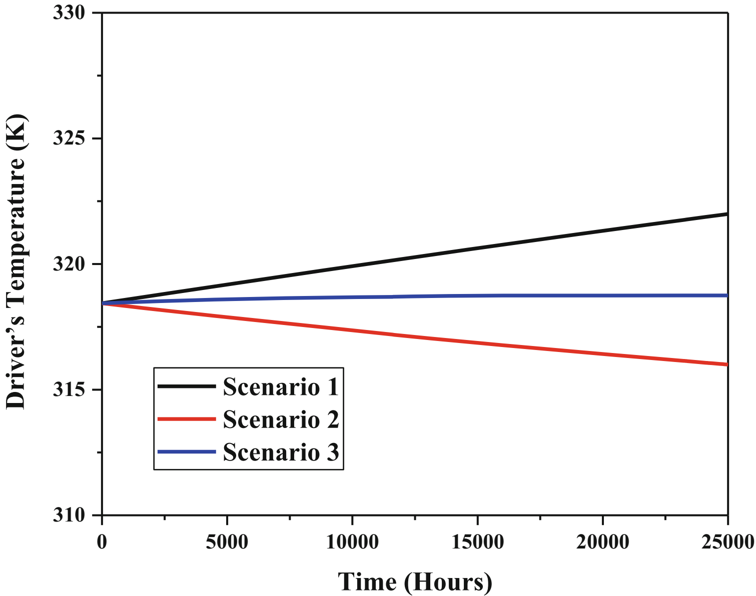

Fig. 16.7 The driver's temperature of each scenario

Scenario 3. When both degradations are considered, the LED junction temperature increases slightly initially and then decreases over time, but in a very narrow range. Overall LED temperature maintains a relatively constant value throughout 25,000 h. It should be noted that the actual LED junction temperature is not a simple superposition of Scenarios 1 and 2 but through the coupled electronic-thermal simulation.

Driver's Temperature

Figure 16.7 shows the driver's temperature as a function of operation time in each scenario. The driver's temperature increases about 3.5 K in 25,000 h for Scenario 1 and decreases about 3 K in the same time period for Scenario 2. As a result, the driver's temperature does not change much for Scenario 3. It is noted that the driver's temperature change is not as much as the LED junction temperature change for Scenarios 1 and 2.

Lumen Maintenance and Lifetime

Figure 16.8 shows the lumen maintenance of each scenario. For Scenario 1, the lumen maintenance drops to 70% in about 21,500 h. This means that even the LED is preselected as 25,000 h lifetime at the initial temperature, it's actual lifetime is

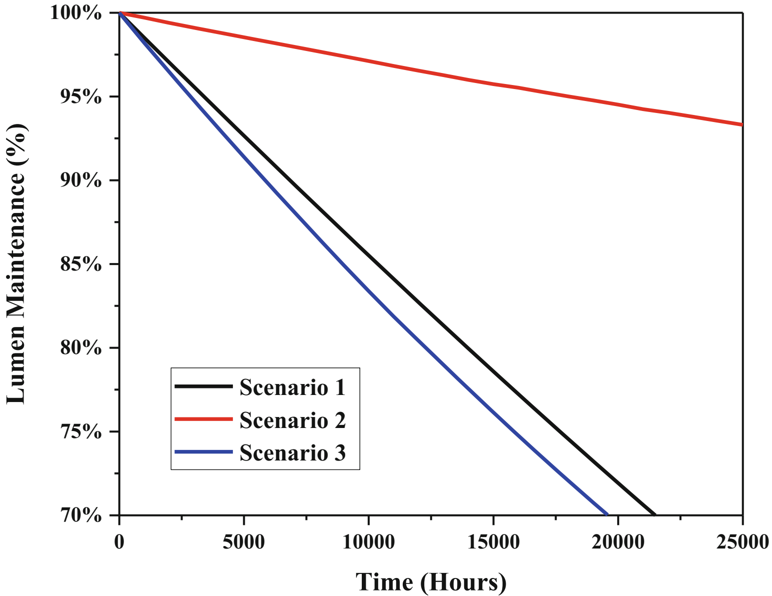

Fig. 16.8 The Lumen maintenance and for each scenario

Table 16.4 Lifetime of each combination

Combination	Lifetime
L25K D15K	18,400 h
L25K D25K	19,600 h
L25K D35K	20,100 h

reduced to 86% due to junction temperature rise. For Scenario 2, the lumen depreciation in 25,000 h is just about 7% due to the driver's degradation. In this case where LED assumes no degradation, the lumen depreciation occurs due to the reduction of both current and temperature.

For Scenario 3, the lamp's actual lifetime is about 19,600 h under the combined effect of degradations of both the LED light source and the driver, which is about 22% reduction of the initial lifetime.

The simulation results shown above illustrate only one case where the LED's lifetime (in terms of lumen depreciation) is same as the driver's lifetime (in terms of output current degradation). However, the presented methodology can be applied to any combinations of driver's and LED's lifetimes to obtain the ultimate lifetime of the lamp. Table 16.4 shows the lamp's actual lifetime for three different combinations of driver/LED lifetime selections. The D15K, D25K, and D35K represent the driver's lifetime of 25,000, 35,000, 15,000 h, respectively, while LED's lifetime remains 25,000 h (L25K). Obviously, the lamp's actual lifetime increases with the driver's lifetime but is not proportional to it. The lifetime of each combination should be differently predicted.

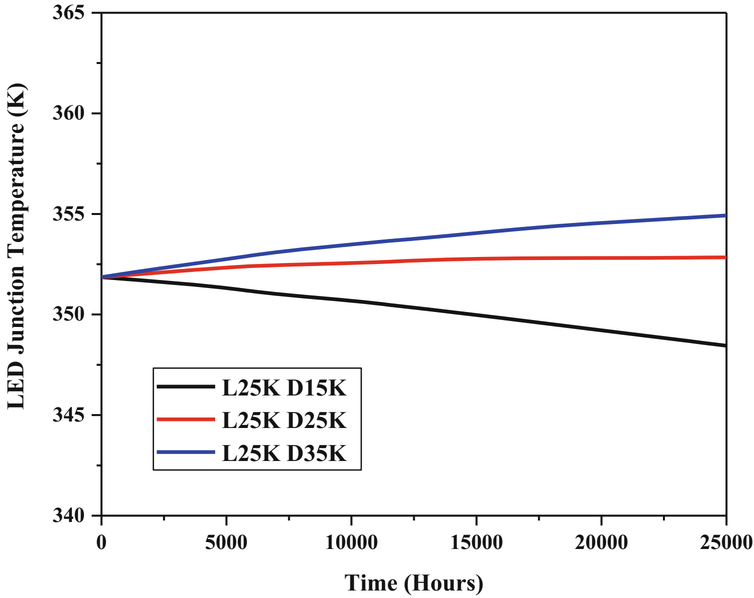

Fig. 16.9 The LED junction temperature of each combination

Figure 16.9 shows the LED junction temperature of each combination. Unlike the L25K/D25K, the LED junction temperature of the L25K/D35K case rises and the junction temperature of the L25K/D15K case falls throughout the operation time. Under effects of the interaction between degradations of the LED and the driver, these combinations have respective junction temperature curves. Thus, it is necessary to calculate the junction temperature differently by the proposed electronic-thermal simulations.

16.3 The Catastrophic Failure Under Lumen Depreciation

This section focuses on predicting the catastrophic failure of an electrolytic capacitor-free LED driver during the lumen depreciation process. The overall catastrophic failure rate of the critical components in this driver is considered as functions of temperature and current. Similar to interactions of degradations discussed in Sect. 16.2, electronic-thermal simulations are utilized to obtain the lamp's dynamic history of temperature and electrical current for two distinct modes: constant current mode (CCM) and the constant optical output (CLO) mode, respectively. A fault tree method is applied to calculate the system's MTTF, and the LED's lifetime in terms of light output can also be calculated.

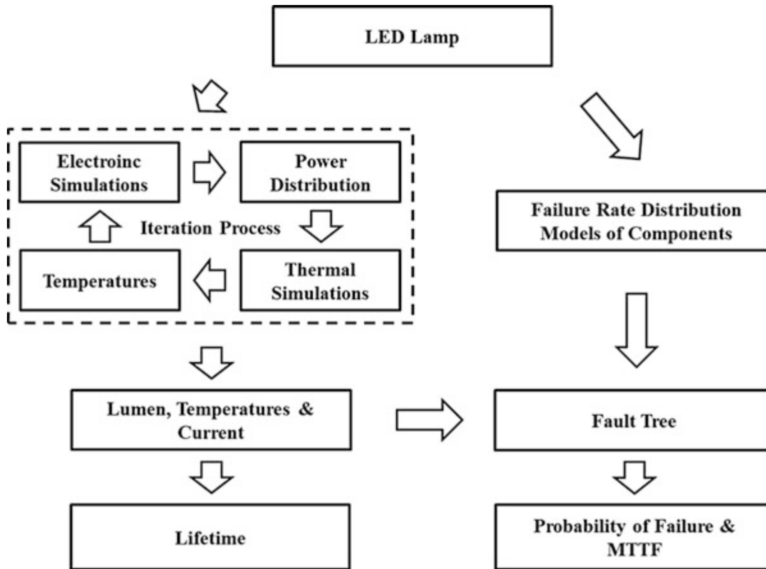

Fig. 16.10 General methodology of the proposed approach

16.3.1 General Methodology

Figure 16.10 displays the general methodology that integrates the electronic thermal simulation with the fault tree method to obtain both the LED's lifetime and driver's probability of failure and MTTF. For a given LED system, such as an LED lamp and the selected driver, electronic models are applied to obtain the power distributions of each component including LEDs. Based on the system's structure and materials, thermal simulations that combine both system-level thermal modeling and compact models are conducted. An iteration process is necessary at each operation time point to determine the state of temperature for the given system under operating condition. Details of the electronic thermal simulations can be found in the literature [3, 19]. Through the electronic thermal simulation, the junction temperature of the LED light source, current of the driver, and the lumen output can be obtained. Based on the failure rate distribution models of the critical components and the results of temperature and current, the fault tree model can be applied to obtain the driver's probability of failure and MTTF.

16.3.2 Modelling

16.3.2.1 Driver Circuit

Figure 16.11 displays the circuit of the driver. A fly-back LED driver with LC filter is selected. The LC filter can store energy as capacitors; thus, it is considered as one

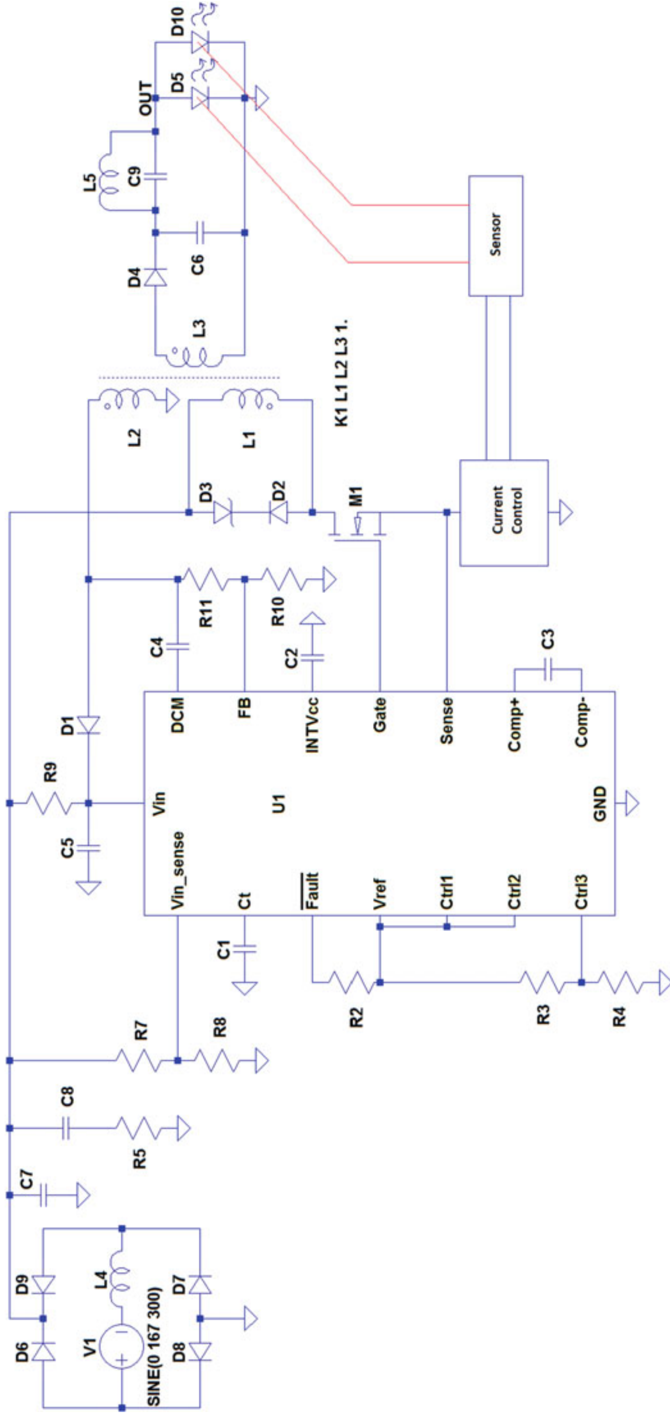

Fig. 16.11 Fly-back LED driver with LC filter

of the most cost-effective electrolytic capacitor elimination methods [28, 29]. In this circuit, the models of all components are well validated and verified by manufacturers [45]. An ideal feedback sensor and a current control unit are added, making this driver have two operation modes: the constant current mode (CCM) and the constant light output mode (CLO). In the constant current mode, the current from the driver to the LED light source remains unchanged. The current can be adjusted to achieve invariant light output in CLO mode.

16.3.2.2 Model of LED Light Source

This section uses same LED models as Sect. 16.2. Since, the CLO mode may increase the LED's junction temperature significantly. Thus, in this section, it limits the maximum junction temperature of LEDs. When its junction temperature exceeds the maximum limit T_{MAX}, the LED is supposed to be burned and give zero luminous flux. When the LED junction temperature within its limitation, the luminous flux is a function of the ever-changing junction temperature $T_j(t)$ and current $I_{\mathrm{LED}}(t)$ as discussed in Sect. 16.2. As a result, the luminous flux $\Phi_{\mathrm{lm}}(t)$ described by Eq. 16.6 can be replaced by the following function:

$$\Phi_{\mathrm{lm}}(t) = \begin{cases} \eta_0 \cdot \dfrac{B_e I_{\mathrm{LED}}(t)^2}{A_e + B_e I_{\mathrm{LED}}(t) + C_e I_{\mathrm{LED}}(t)^2} \cdot V_f \cdot e^{-\int_0^t \beta\left[T_j(x)\right] \cdot \mathrm{dx}} & \left(T_j < T_{\mathrm{MAX}}\right) \\ 0 & \left(T_j \geq T_{\mathrm{MAX}}\right) \end{cases} \tag{16.17}$$

In this section, $T_{\mathrm{MAX}} = 423$ K.

16.3.2.3 Thermal Model

Since there are several heat source, system level thermal simulations are required to obtain accurate temperatures. This section uses same thermal models of the LED lamp as Sect. 16.2. Thermal simulations in this section consist of two parts. Firstly, the finite element thermal analysis is carried out to calculate the LEDs' junction temperature T_{LED} and the driver's overall temperature T_D as Sect. 16.2. Then, the thermal compact model of each critical component in the driver is used to find their junction temperature:

$$T_{j,i} = T_D + R_{\mathrm{th},i} \cdot P_{\mathrm{th},i} \tag{16.18}$$

where $T_{j,i}$ is the junction temperature of the component, $R_{\mathrm{th},i}$ is the thermal resistance from junction to surface of the component which is usually provided

by components' datasheets, and $P_{\text{th},i}$ is the thermal power of the component which can be obtained by electronic simulations.

16.3.3 Fault Tree and Failure Rate Models

As a carrier of the proposed method, this section considers the catastrophic failures of the MOSFET M1 and the diode D4 in the circuit shown in Fig. 16.11. Thus, the catastrophic failure of the driver can be described by a fault tree shown in Fig. 16.12.

Assuming that the failures of the MOSFET and the diode are independent to each other, the probability density of the catastrophic failure of the LED driver can be described by the following function:

$$f_{\text{Driver}}(t) = f_M(t) + f_D(t) - f_M(t) \cdot f_D(t) \tag{16.19}$$

where f_{Driver} is the failure probability density of the LED driver at time t, f_M is the failure probability density of the MOSFET, and f_D is the failure probability density of the diode.

The failure probability density of a MOSFET can be described by the inverse power law [53]:

$$f_M(t) = f_M[I_M(t), T_M(t)] = f_{M0} \cdot \left[\frac{I_M(t)}{I_{\text{rated}}}\right]^p \cdot e^{-\frac{E_{a,M}}{k}\left[\frac{1}{T_M(t)} - \frac{1}{T_A}\right]} \tag{16.20}$$

where $I_M(t)$ is the average current of the MOSFET at time t, $T_M(t)$ is junction temperature of the MOSFET at time t, f_{M0} is the failure probability density of the MOSFET in rated current I_{rated} and typical ambient temperature $T_A = 298$ K, p is the current accelerated coefficient, and $E_{a,M}$ is the activation energy of the MOSFET.

Similar to the MOSFET, the failure probability density of a diode can be described by the [53]:

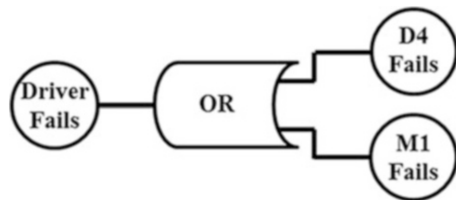

Fig. 16.12 The fault tree of the LED driver

$$f_D(t) = f_D[T_{\mathrm{Di}}(t)] = f_{D0} \cdot \mathrm{e}^{-\frac{E_{a,D}}{k}\left[\frac{1}{T_{\mathrm{Di}}(t)} - \frac{1}{T_A}\right]} \tag{16.21}$$

where f_D is the failure probability density of the diode, $T_{\mathrm{Di}}(t)$ is junction temperature of the diode at time t, f_{D0} is the rated failure probability density of the diode in typical ambient temperature $T_A = 298$ K, and $E_{a,D}$ is the activation energy of the diode.

The conditions $I_M(t)$, $T_M(t)$, and $T_{\mathrm{Di}}(t)$ at each operation time point can be obtained by the electronic-thermal simulations, and thus, the failure probability densities f_M, f_D, and f_{Driver} at each time point can be calculated by Eqs. 16.8, 16.9, and 16.10. Then, the mean time to failure (MTTF) of the LED driver can be calculated by the following equation:

$$\mathrm{MTTF} = t_{\mathrm{MAX}} / \int_0^{t_{\mathrm{MAX}}} f_{\mathrm{driver}}(t) \cdot \mathrm{dt} \tag{16.22}$$

where t_{MAX} is the total operation duration.

16.3.4 Case Studies and Results

16.3.4.1 Selection of LED and Driver

To estimate the actual lifetime and the MTTF of the investigated LED lamp, the LED light source is preselected with the activation energy and pre-factor of $E_{a,\beta} = 0.3$eV and $A_\beta = 0.2829$, according to our previous test results [43]. According to the electronic thermal simulation at the initial state during operation, the LED's junction temperature in the lamp is about 351 K. Based on the parameters defined above, the LED's lifetime is 25,000 h in terms of lumen depreciation at the constant 351 K with a current of 400 mA, by Eqs. 16.1 and 16.2. It means that the lumen maintenance is above 70% of its initial value in 25,000 h if the LED temperature maintains at 351 K, and it's current of 400 mA does not change during operation.

For LED driver, the empirical values of model parameters for the MOSFET M1 and diode D4 in the circuit are selected as from the literature [54] p of 2.0 and as $E_{a,M}$ and $E_{a,D}$ of 0.7 eV, respectively. Without any lumen degradation, the driver's average temperature in the lamp is defined as the initial driver temperature $T_D(0)$, and the junction temperatures of M1 and D4 in $T_D(0)$ are called initial junction temperatures of M1 and D4, $T_M(0)$, and $T_{\mathrm{Di}}(0)$. According to simulation results, the values of $T_D(0)$, $T_M(0)$, and $T_{\mathrm{Di}}(0)$ are about 342 K, 363 K, and 350 K respectively. To ensure the MTTF of the driver before lumen depreciation equals to the lifetime, it supposes $f_{M0} = 2.31 \times 10^{-7}$, $f_{D0} = 1.54 \times 10^{-7}$. As a result, the MTTF of M1 in $T_M(0)$ is about 32,000 h; the MTTF of D4 in $T_{\mathrm{Di}}(0)$ is about 109,000 h, according to Eqs. 16.9 and 16.10. This means that the driver's MTTF is about 25,000 h in $T_D(0)$,

and MOEFET's current I_M does not change during operation, according to the fault tree model to used.

Both of the lifetime and MTTF are 25,000 h without the lumen degradation. However, since the junction temperature in the lamp during operation will change over time, to be shown in details later, the actual LED's lifetime will be different from the preselected lifetime. Since values of T_D, $T_M(0)$, and $T_{\mathrm{Di}}(0)$ change over time during operation, and the failure rate of the M1 also depends on the current I_M, the actual MTTF of the driver will also different from the preselected MTTF. The details of the results will be discussed below.

16.3.4.2 Results and Discussions

Constant Light Output (CLO) Mode

Figure 16.13 displays the LED current curve at the CLO mode. The LED's current increases exponentially, e.g., from the initial 400 to 730 mA in 14,000 h. Such an increase in current mainly compensates the luminous flux degradation of the LED to maintain the constant light output.

Figure 16.14 displays the LED junction temperature as a function of time. Due to the increased current, the LED's temperature increases greatly. At 14,000 h, the junction temperature of the LED light source increases about 75 K and exceeds 423 K.

Figure 16.15 shows the history of the junction temperatures of M1 and D4 at the CLO mode. In 14,000 h, the junction temperatures of M1 increases from 363 to 429 K, and the junction temperatures of D4 rises from 350 to 408 K.

Figure 16.16 shows the cumulative failure rate of M1 in different conditions of the CLO mode. In the constant temperature and current of the M1, the cumulative failure rate is about 43% at 14,000 h. If only considers increasing of M1's junction temperature, the failure rate accumulates to 100% around 12,000 h. If only considers M1's current increasing, the cumulative failure rate is about 86% at 14,000 h. If considers both of junction temperature and current of M1 in CLO mode, the failure rate of M1 accumulates to 100% in about 10,000 h. The failure rate of M1 is increased greatly in the junction temperature and current of M1. Compare with the current, the increased junction temperature has larger effects on the failure rate, due to the high activation energy.

Figure 16.17 displays cumulative failure rate of the driver in different conditions of CLO mode. In the ever-increasing temperature and current obtained by proposed models, the failure rate of the driver accumulates to 100% in about 9,300 h. In the constant temperature and current, the failure rate accumulates about 56% linearly in 14,000 h. As discussed above, failure rates of driver's components are greatly increased by driver's temperature and M1's current. Thus, the driver in CLO mode has a shorter MTTF than in constant conditions.

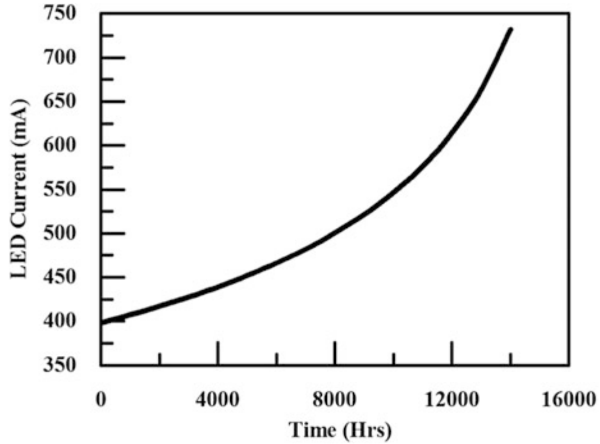

Fig. 16.13 The LED current curve of the CLO mode

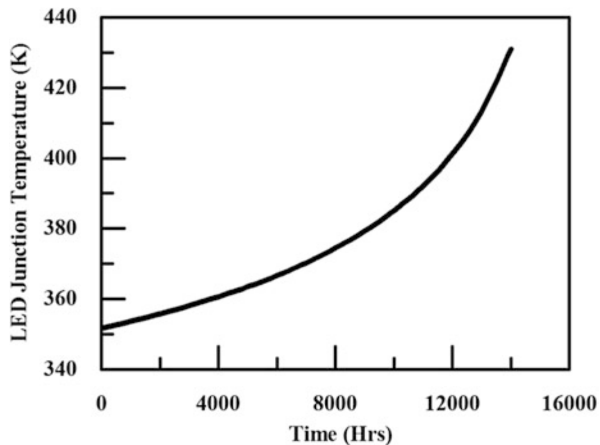

Fig. 16.14 The LED junction temperature of the CLO mode

Constant Current Mode (CCM)

Figure 16.18 displays the LED junction temperature in CCM mode. After 25,000 h, the junction temperature of the LED increases about 10 K. As the degradation process of the LED light source, more thermal power is generated, leading temperature increasing of the entire lamp. Although the increment is less than the CLO mode, the increased LED junction temperature still have a significant impact on the lamp's lifetime.

Figure 16.19 displays the normalized luminous flux of CCM mode. The lifetime of the LED lamp in this mode is around 21,500 h. The elevated junction temperature accelerates the degradation of the LED light source. Thus, the lifetime in CCM is about 14% shorter than in the constant temperature and current.

Figure 16.20 shows the history of the junction temperatures of M1 and D4 at the CCM mode. The junction temperature of M1 increases from 363 to 366 K, and D4's

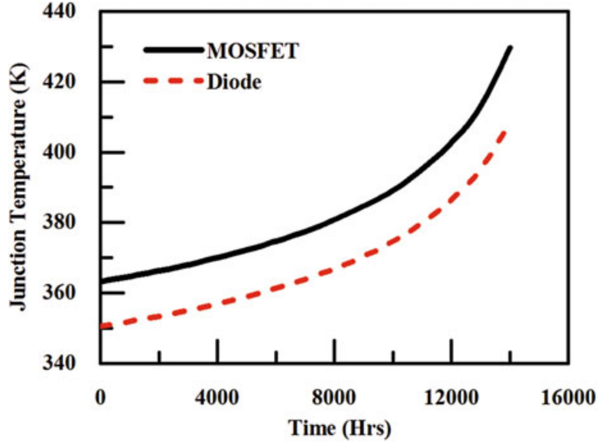

Fig. 16.15 The junction temperature of M1 and D4 of the CLO mode

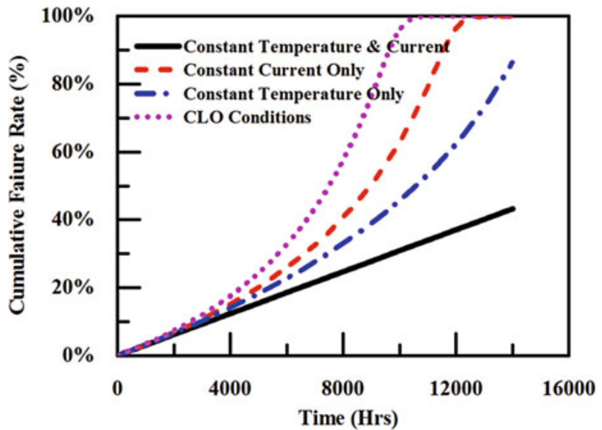

Fig. 16.16 Cumulative failure rates of M1 in the CLO mode

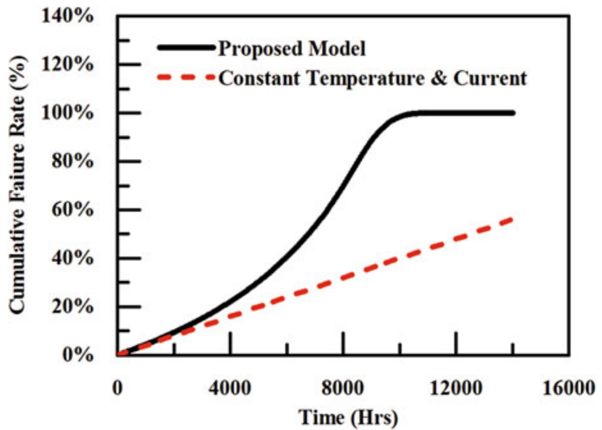

Fig. 16.17 Cumulative failure rates of the driver in CLO mode

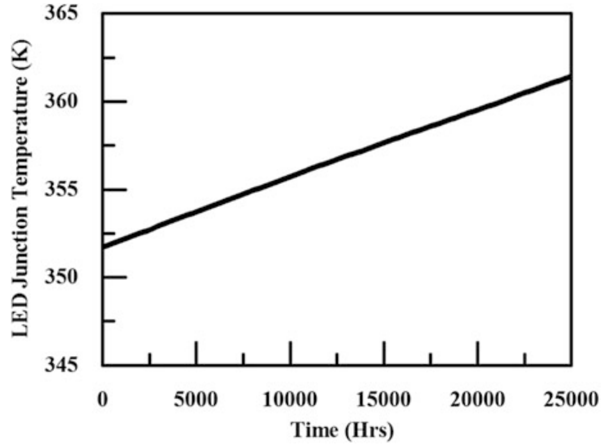

Fig. 16.18 The LED junction temperature of the CCM mode

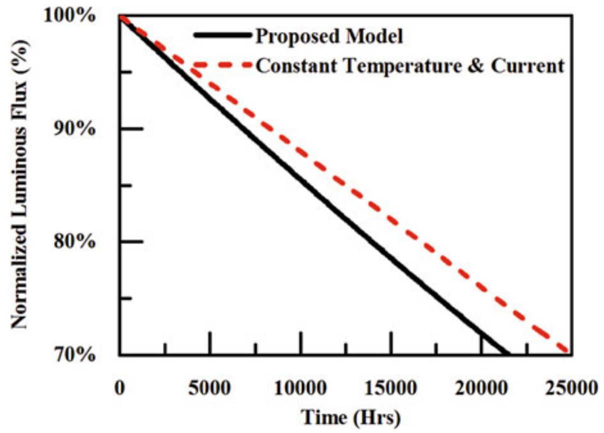

Fig. 16.19 Normalized luminous flux of the CCM mode

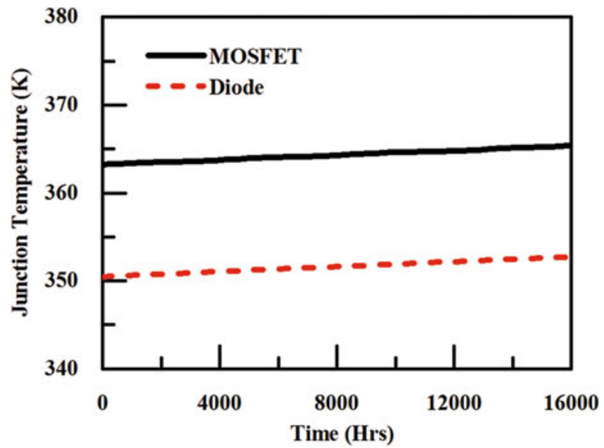

Fig. 16.20 The junction temperatures of M1 and D4 in the CCM mode

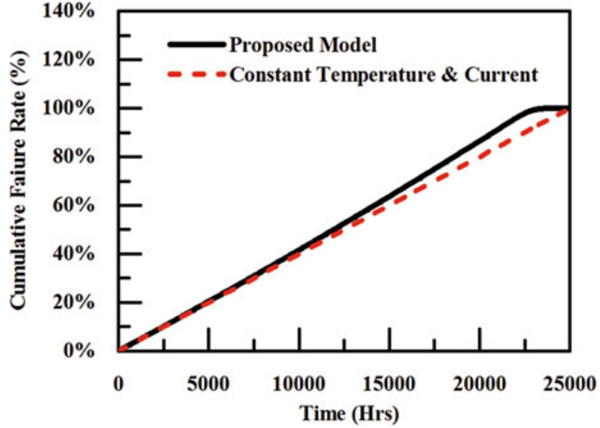

Fig. 16.21 Cumulative failure rates of the driver in the CCM mode

Table 16.5 Lists lifetimes, MTTFs, and temperatures of each mode

Case	Lifetime (H)	T_j (K)	MTTF (H)	T_D (K)
Initial status	25,000	351	25,000	342
CLO	14,000	Varying	9,300	Varying
CCM	21,500	Varying	22,900	Varying

junction temperature rises from 350 to 354 K in 25,000 h. Compared with the CLO mode, the junction temperature of M1 and D4 increases slightly.

Figure 16.21 displays cumulative failure rate of the driver in different conditions of CCM mode. In the ever-increasing temperature and current obtained by proposed models, the failure rate of the driver accumulates to 100% in about 22,900 h. In the constant temperature and current, the cumulative failure rate is about 100% at 25,000 h. As discussed above, failure rates of driver's components are slightly increased by driver's temperature. Thus, the driver in CCM mode has a little shorter MTTF than in constant conditions (Table 16.5).

In CLO mode, the lifetime is about 14,000 h since the LED junction temperature exceeds its maximum value, and the MTTF is about 9,300 h. The light output compensation brings the increased current and temperatures and, thus, a shorter lifetime and MTTF. Thus, the constant light output mode eliminates lumen depreciation at the expense of the reliability of the LED lamp. Such technologies are not suitable to improve the reliability of LED lamps. Due to the higher activation energy of the driver, the MTTF is more temperature sensitive than the lifetime. The MTTF becomes much shorter than the lifetime, and the catastrophic failure may occur before the lumen depreciation. In reliability optimization, it should put a priority on the catastrophic failure of the driver.

In CCM mode, the lifetime is about 21,500 h, and the MTTF is about 22,900 h. As the discussion above, the ever-increasing LED junction temperature accelerates the degradation process of the LED light source and brings high failure rate of the driver. Moreover, the lifetime and the MTTF in this mode are comparable. It means

that both of the catastrophic failure and the lumen depreciation may occur. In reliability optimization, both of these two failure modes should be considered.

16.4 Conclusions

Section 16.2 investigates the impact of the interaction between the degradations of the LED and driver on the lifetime of an integrated LED lamp. The electronic-thermal simulation was carried out to obtain performance of the LED. Three scenarios were simulated first:

- Scenario 1 considers the LED light source degradation only, with the selection of 25,000 h LED's lifetime. In this case, LED current stays almost at its initial value due to the non-degradation driver applied. However, the LED junction temperature and the driver's temperature increase over time. As a result, the lamp's lifetime is reduced to 21,500 h, about 86% of the targeted lifetime.
- Scenario 2 considers the driver's degradation only, with a selection of 25,000 h lifetime of driver in terms of output current. Since LED's degradation is not take into consideration in this case, the LED's junction temperature and the driver's temperature decrease over operation time, as less electric current is applied. As a result, the lumen output is depreciated at only 7% in about 25,000 h. It implies that when the driver's lifetime is comparable to the LED's lifetime, the LED's degradation must be taken into considerations.
- Scenario 3 investigates the ultimate lifetime of the LED lamp when both degradations from LED and driver simultaneously occur. It has been found that the LED's junction temperature and the driver's temperature do not change much in 25,000 h. However, the lamp's lifetime in terms of lumen output has been reduced to 19,600 h.

Furthermore, the different combinations of driver/LED lifetime selections were studied, with the driver's lifetime as 25,000, 35,000, 15,000 h, respectively, while LED's lifetime remains 25,000 h. It has been found that the lifetime and the LED junction temperature of each combination need to be predicted case by case by the electronic-thermal simulations.

Section 16.3 focuses on predicting the catastrophic failure of an electrolytic capacitor-free LED driver during the lumen depreciation process. A commercial LED bulb and a fly-back converter with an LC filter are used in the present study. Electronic-thermal simulations are utilized to obtain the lamp's dynamic history of temperature and electrical current for two distinct modes: constant current mode (CCM) and the constant optical output (CLO) mode, respectively. A fault tree method is applied to calculate the system's MTTF, and the LED's lifetime also is calculated.

- The CLO mode increases exponentially the LED's current to maintain the constant light output. As a result, junction temperatures of LEDs, MOSFET,

and diode rise about 75 K, 50 K, and 50 K, respectively. As a result, the lifetime decreases to 14,000 h, and the MTTF drops about 9870 h. Thus, the constant light output mode eliminates lumen depreciation at the expense of the reliability of the LED lamp. Such technologies are not suitable to improve the reliability of LED lamps. Compare with current of MOSFET, the increased junction temperature has larger effects on the failure rate. The MOSFET contributes more to the driver's failure rate than the diode. Since the MTTF is shorter than the lifetime, the catastrophic failure of the driver may occur before the lumen depreciation. In reliability optimization, it should put a priority on the catastrophic failure of the driver.

- For the CCM mode, the current keeps unchanged; junction temperatures of the LED, the MOSFET, and the diode rise about 10 K, 4 K, and 4 K respectively, leading the lifetime drops to about 21,500 h; and the MTTF drops to about 22,600 h. Similar to the CLO mode, MOSFET also contributes more to the driver's failure rate than the diode. Since the lifetime and the MTTF in this mode are comparable, both of the catastrophic failure and the lumen depreciation may occur. In reliability optimization, both of these two failure modes should be considered.

From abovementioned results and discussions, it is concluded that it is necessary to apply the electronic-thermal simulations to predict the reliability of LED lamps when driver's lifetime is comparable to the LED's lifetime. This chapter presents a methodology to accurately predict the ultimate lamp's lifetime. Such a methodology will be very useful in designing LED product by selecting different drivers and LED light sources.

References

1. J. Fan, K.C. Yung, M. Pecht, Prognostics of lumen maintenance for high power white light emitting diodes using a nonlinear filter-based approach. Reliab. Eng. Syst. Saf. **123**, 63–72 (2014)
2. C. Qian, X.J. Fan, J. Fan, C.A. Yuan, G.Q. Zhang, An accelerated test method of luminous flux depreciation for LED luminaires and lamps. Reliab. Eng. Syst. Saf. **147**, 84–92 (2015)
3. B. Sun, X.J. Fan, C. Qian, G.Q. Zhang, PoF-simulation-assisted reliability prediction for electrolytic capacitor in LED drivers. IEEE Trans. Ind. Electron., in press **63**, 6726–6735 (2016)
4. B. Sun, X. J. Fan, C. A. Yuan, C. Qian, G. Q. Zhang, A degradation model of aluminum electrolytic capacitors for LED drivers, in *2015 16th International Conference on Thermal, Mechanical and Multi-Physics Simulation and Experiments in Microelectronics and Microsystems (EuroSimE),* (2015), pp. 1–4
5. S. Koh, C. Yuan, B. Sun, B. Li, X. J. Fan, G. Q. Zhang, Product level accelerated lifetime test for indoor LED luminaires, in *2013 14th International Conference on Thermal, Mechanical and Multi-Physics Simulation and Experiments in Microelectronics and Microsystems (EuroSimE)*, (2013), pp. 1–6

6. J. Huang, S.W. Koh, D. Yang, X. Li, X.J. Fan, G.Q. Zhang, *Degradation Mechanisms of Mid-power White-light LEDs under High Temperature-Humidity Conditions*. IEEE Trans. Device Mat. Reliab. **15**, 1–1 (2015)
7. J. Huang, D.S. Golubović, S.W. Koh, D. Yang, X. Li, X.J. Fan, G.Q. Zhang, Rapid degradation of mid-power white-light LEDs in saturated moisture conditions. IEEE Trans. Device Mater. Reliab. **15**, 478–485 (2015)
8. G. Lu, W.D. van Driel, X.J. Fan, M.Y. Mehr, J. Fan, K. Jansen, G.Q. Zhang, Degradation of microcellular PET reflective materials used in LED-based products. Opt. Mater. **49**, 79–84 (2015)
9. G. Lu, M.Y. Mehr, W. van Driel, X.J. Fan, J. Fan, K. Jansen, G.Q. Zhang, Color shift investigations for LED secondary optical designs: comparison between BPA-PC and PMMA. Opt. Mater. **45**, 37–41 (2015)
10. J. Fan, C. Qian, K.C. Yung, X.J. Fan, G.Q. Zhang, M. Pecht, Optimal design of life testing for high-brightness white LEDs using the six sigma DMAIC approach. IEEE Trans. Device Mater. Reliab. **15**, 576–587 (2015)
11. R. Pinto, M.R. Cosetin, A. Campos, M.A. Dalla Costa, R.N. do Prado, Compact emergency lamp using power LEDs. IEEE Trans. Ind. Electron. **59**, 1728–1738 (2012)
12. S.R. Hui, S.N. Li, X.H. Tao, W. Chen, W. Ng, A novel passive offline LED driver with long lifetime. IEEE Trans. Power Electron. **25**, 2665–2672 (2010)
13. D.G. Lamar, M. Arias, A. Rodriguez, A. Fernandez, M.M. Hernando, J. Sebastián, Design-oriented analysis and performance evaluation of a low-cost high-brightness LED driver based on flyback power factor corrector. IEEE Trans. Ind. Electron. **60**, 2614–2626 (2013)
14. X. Qu, S.C. Wong, C.K. Tse, Resonance-assisted buck converter for offline driving of power LED replacement lamps. IEEE Trans. Power Electron. **26**, 532–540 (2011)
15. X. Wu, J. Yang, J. Zhang, Z. Qian, Variable on-time (VOT)-controlled critical conduction mode buck PFC converter for high-input AC/DC HB-LED lighting applications. IEEE Trans. Power Electron. **27**, 4530–4539 (2012)
16. P.S. Almeida, D. Camponogara, M. Dalla Costa, H. Braga, J.M. Alonso, Matching LED and driver life spans: a review of different techniques. IEEE Ind. Electron. Mag. **9**, 36–47 (2015)
17. C. Branas, F.J. Azcondo, J.M. Alonso, Solid-state lighting: a system review. IEEE Ind. Electron. Mag. **7**, 6–14 (2013)
18. J.M. Alonso, J. Viña, D.G. Vaquero, G. Martínez, R. Osorio, Analysis and design of the integrated double buck–boost converter as a high-power-factor driver for power-LED lamps. IEEE Trans. Ind. Electron. **59**, 1689–1697 (2012)
19. B. Sun, X. J. Fan, W. D. van Driel, H. Ye, J. Fan, C. Qian, G. Q. Zhang, *A Novel Lifetime Prediction for Integrated LED Lamps by Electronic-Thermal Simulation*, IEEE Transactions on Industrial Electronics, Submitted 2016
20. P. S. Almeida, G. M. Soares, D. P. Pinto, H. A. Braga, Integrated SEPIC buck-boost converter as an off-line LED driver without electrolytic capacitors, in *IECON 2012-38th Annual Conference of IEEE Industrial Electronics Society*, (2012), pp. 4551–4556
21. H. Ma, J.S. Lai, Q. Feng, W. Yu, C. Zheng, Z. Zhao, A novel valley-fill SEPIC-derived power supply without electrolytic capacitor for LED lighting application. IEEE Trans. Power Electron. **27**, 3057–3071 (2012)
22. Z. Bo, Y. Xu, X. Ming, C. Qiaoliang, W. Zhaoan, Design of boost-flyback single-sage PFC converter for LED power supply without electrolytic capacitor for energy-storage, in *. 2009 I. E. 6th International Power Electronics and Motion Control Conference, IPEMC'09*, (2009), pp. 1668–1671
23. H. Ma, W. Yu, C. Zheng, J. S. Lai, Q. Feng, B. Y. Chen, A universal-input high-power-factor PFC pre-regulator without electrolytic capacitor for PWM dimming LED lighting application, in *2011 I.E. Energy Conversion Congress and Exposition (ECCE)*, (2011), pp. 2288–2295
24. D. Camponogara, D. Ribeiro Vargas, M. Dalla Costa, J.M. Alonso, J. Garcia, T. Marchesan, Capacitance reduction with an optimized converter connection applied to LED drivers. Ind. Electron. IEEE Trans. **62**, 184–192 (2015)

25. C. Wong, Y. Lai, K. Loo, C. K. Tse, Elimination of electrolytic capacitor in LED power supplies by two-phase driving approach, in *2014 16th European Conference on Power Electronics and Applications* (*EPE'14-ECCE Europe*), (2014), pp. 1–9
26. K.W. Lee, Y.H. Hsieh, T.J. Liang, A current ripple cancellation circuit for electrolytic capacitor-less AC-DC LED driver, in *2013 Twenty-Eighth Annual IEEE Applied Power Electronics Conference and Exposition (APEC)*, (2013), pp. 1058–1061
27. L. Gu, X. Ruan, M. Xu, K. Yao, Means of eliminating electrolytic capacitor in AC/DC power supplies for LED lightings. IEEE Trans. Power Electron. **24**, 1399–1408 (2009)
28. B. Wang, X. Ruan, K. Yao, M. Xu, A method of reducing the peak-to-average ratio of LED current for electrolytic capacitor-less AC–DC drivers. IEEE Trans. Power Electron. **25**, 592–601 (2010)
29. X. Ruan, B. Wang, K. Yao, S. Wang, Optimum injected current harmonics to minimize peak-to-average ratio of LED current for electrolytic capacitor-less AC–DC drivers. IEEE Trans. Power Electron. **26**, 1820–1825 (2011)
30. S. Dietrich, S. Strache, R. Wunderlich, S. Heinen, Get the LED out: experimental validation of a capacitor-free single-inductor, multiple-output LED driver topology. Industrial Electronics Magazine, IEEE **9**, 24–35 (2015)
31. P. Fang, Y. F. Liu, An electrolytic capacitor-free single stage Buck-Boost LED driver and its integrated solution, in *2014 Twenty-Ninth Annual IEEE Applied Power Electronics Conference and Exposition (APEC)*, (2014), pp. 1394–1401
32. J.C. Lam, P.K. Jain, A high power factor, electrolytic capacitor-less AC-input LED driver topology with high frequency pulsating output current. IEEE Trans. Power Electron. **30**, 943–955 (2015)
33. S. Lan, C.M. Tan, K. Wu, Reliability study of LED driver–a case study of black box testing. Microelectron. Reliab. **52**, 1940–1944 (2012)
34. S. Lan, C.M. Tan, K. Wu, Methodology of reliability enhancement for high power LED driver. Microelectron. Reliab. **54**, 1150–1159 (2014)
35. D. Ang, C. Ling, On the time-dependent degradation of LDD n-MOSFETs under hot-carrier stress. Microelectron. Reliab. **39**, 1311–1322 (1999)
36. X. Shao, *Research on Reliability Assessment Method of The LED Driver Power Supply* (Master of Engineering, School of Electrical Engineering, Harbin Institute of Technology, Harbin, 2012)
37. Z.Y. Zhou Yue-ge, L. Xiang, Z. Guofu, Performance reliability assessment of LED drivers for lighting. Electri c Machines and Control **18**, 2014.09 (2014)
38. R. Wu, F. Blaabjerg, H. Wang, M. Liserre, Overview of catastrophic failures of freewheeling diodes in power electronic circuits. Microelectron. Reliab. **53**, 1788–1792 (2013)
39. Constant Light Output (CLO)., Available: http://www.lightingproducts.philips.com/our-brands/philips-controls/constant-light-output-clo.html (2014)
40. E.F. Schubert, T. Gessmann, J.K. Kim, *Light Emitting Diodes* (Wiley Online Library, Hoboken, 2005)
41. D.S. Meyaard, Q. Shan, J. Cho, E.F. Schubert, S.-H. Han, M.-H. Kim, C. Sone, S.J. Oh, J.K. Kim, Temperature dependent efficiency droop in GaInN light-emitting diodes with different current densities. Appl. Phys. Lett. **100**, 081106 (2012)
42. J. Piprek, Efficiency droop in nitride-based light-emitting diodes. Phys. Status Solidi A **207**, 2217–2225 (2010)
43. B. Sun, X. J. Fan, W. V. Driel, T. Michel, J. Zhou, G. Q. Zhang, Lumen decay prediction in LED lamps, *Presented at the IEEE International Conference on Thermal, Mechanical and Multi-Physics Simulation and Experiments in Microelectronics and Microsystems, Montpellier*, 2016
44. S. Tarashioon, W. van Driel, G.Q. Zhang, Multi-physics reliability simulation for solid state lighting drivers. Microelectron. Reliab. **54**, 1212–1222 (2014)
45. Linear Technology Corporation., LTwiki. Available: http://ltwiki.org/?title=Main_Page (2014)

46. B. Hamon, B. Bataillou, A. Gasse, G. Feuillet, N-contacts degradation analysis of white flip chip LEDs during reliability tests, in *2014 I.E. International Reliability Physics Symposium*, (2014), pp. FA. 1.1–FA. 1.6
47. H.T. Chen, S.-C. Tan, S. Hui, Color variation reduction of GaN-based white light-emitting diodes via peak-wavelength stabilization. Power Electron. IEEE Trans. **29**, 3709–3719 (2014)
48. M. Hudait, S. Krupanidhi, Doping dependence of the barrier height and ideality factor of Au/n-GaAs Schottky diodes at low temperatures. Phys. B **307**, 125–137 (2001)
49. X. Perpina, R. Werkhoven, M. Vellvehi, X. Jorda, J. Kunen, J. Jakovenk, P. Bancken, P. Bolt, LED driver thermal design considerations for solid-state lighting technologies, in *2012 13th International Conference on Thermal, Mechanical and Multi-Physics Simulation and Experiments in Microelectronics and Microsystems (EuroSimE)*, 2012, pp. 1/5–5/5
50. Y. Huaiyu, K.S. Wee, W. Jia, H.W. Van Zeijl, Dynamic thermal simulation of high brightness LEDs with unsteady driver power output, in *2012 13th International Conference on Thermal, Mechanical and Multi-Physics Simulation and Experiments in Microelectronics and Microsystems (EuroSimE)*, 2012, pp. 1/5–5/5
51. J. Jakovenko, R. Werkhoven, J. Formanek, J. Kunen, Thermal simulation and validation of 8W LED Lamp, in *2011 12th International Conference on Thermal, Mechanical and Multi-Physics Simulation and Experiments in Microelectronics and Microsystems (EuroSimE)*, 2011, pp. 1/4–4/4
52. J. Jakovenko, J. Formánek, V. Janíček, M. Husák, R. Werkhoven, High power solid state retrofit lamp thermal characterization and modeling. Radioengineering **21**, 231–238 (2012)
53. T. Santini, S. Morand, M. Fouladirad, L.V. Phung, F. Miller, B. Foucher, A. Grall, B. Allard, Accelerated degradation data of SiC MOSFETs for lifetime and remaining useful life assessment. Microelectron. Reliab. **54**, 1718–1723 (2014)
54. M.S. Handbook, *MIL-HDBK-217F: Reliability Prediction of Electronic Equipment* (US Department of Defense, Washington, DC, 1995)

Chapter 17
Statistical Analysis of Lumen Depreciation for LED Packages

M. Schuld, Willem Dirk van Driel, and B. Jacobs

Abstract Commercial claims for LED-based products in terms of lumen maintenance are fully based on TM-21 extrapolations using LM-80 data. This chapter indicates that there may be a risk in doing this as TM-21 only relies on the behavior of the average LED degradation, instead of taking into account the degradation of all individual LEDs. Therefore, we propose a more profound statistical approach in order to make the appropriate step from TM-21 extrapolation to lumen maintenance on a product level. This is needed as some commercial claims are based on 10 years of warranty and some service bids provide periods of 20–25 years of operation. This chapter reviews the different approaches currently available to perform lumen maintenance extrapolations.

17.1 Introduction

Solid-state lighting (SSL) refers to a type of lighting that uses semiconductor light-emitting diodes (LEDs), organic or polymer light-emitting diodes (OLED/PLED) as sources of illumination rather than electrical filaments, plasma (used in arc lamps such as fluorescent lamps), or a gas. SSL applications are now at the doorstep of massive market entry into our offices and homes. This penetration is mainly due to the promise of an increased reliability with an energy saving opportunity: a low-cost reliable solution [1].

M. Schuld (✉)
CQM, Eindhoven, The Netherlands
e-mail: marc.schuld@cqm.nl

W.D. van Driel (✉)
Philips Lighting, High Tech Campus, Eindhoven, The Netherlands

Delft University of Technology, EEMCS Faculty, Delft, The Netherlands
e-mail: willem.van.driel@philips.com

B. Jacobs
Delft University of Technology, EEMCS Faculty, Delft, The Netherlands
e-mail: boudewijn.jacobs@philips.com

© Springer International Publishing AG 2018

W.D. van Driel et al. (eds.), *Solid State Lighting Reliability Part 2*, Solid State Lighting Technology and Application Series 3, DOI 10.1007/978-3-319-58175-0_17

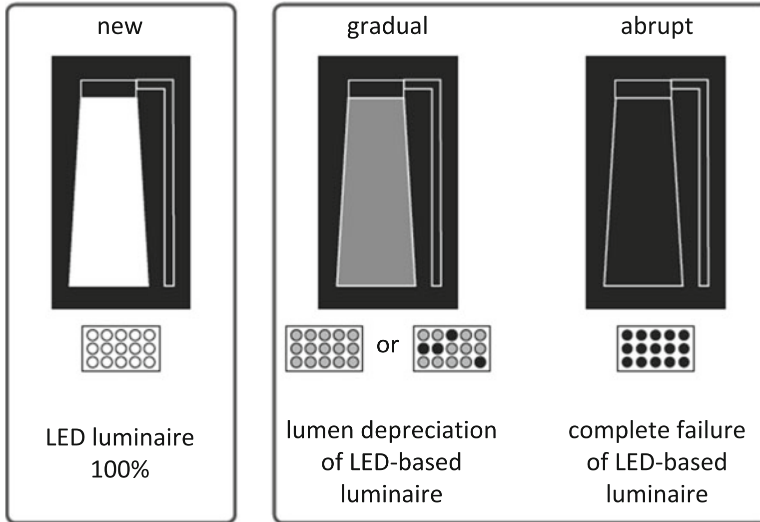

Fig. 17.1 Over time performance of an LED-based system

On system level, there are two relevant "over time" performance values to be considered: gradual and abrupt light output degradation; see Fig. 17.1. Gradual light output degradation relates to the lumen maintenance of a luminaire over time. It tells you how much of the initial lumen output of the luminaire is maintained after a certain period of time. The lumen depreciation can be a combination of degradation of optical elements used, individual LEDs giving less light and individual LEDs giving no light at all. Abrupt light output degradation describes the situation where the LED-based luminaire no longer gives any light at all because the system, or a critical component therein, has failed.

Per today, commercial claims for LED-based products in terms of lumen maintenance are fully based on LM-80 data[1] [2] and TM-21 extrapolations [3–5]. IES LM-80-08 is an approved method for measuring lumen maintenance of LED lighting sources. The IES standard TM-21-11 provides a guideline for lifetime prediction of LED devices. It uses an average normalized lumen maintenance data coming from LM-80 measurements and performs nonlinear regression for lifetime modeling. It cannot capture the dynamic and random variation of the degradation process of LED devices. The lumen maintenance life is defined as the time when the maintained percentages of the initial light output fall below a failure threshold. There may be a risk in doing this as TM-21 only relies on the behavior of the average LED degradation, instead of taking into account the degradation of all

[1]The LM-80 test is a Department of Energy (DOE)-approved method for measuring lumen depreciation of solid-state light packages, arrays, or modules. LM-80 requires testing to be conducted at least 6000 h at representative operating temperatures and currents, with luminous flux and colour properties collected at a minimum of every 1000 h.

individual LEDs. A more profound statistical analysis is required to make the step from TM-21 extrapolation to lumen maintenance on a product level. For that, we have analyzed several LM-80 data sets from a statistical point of view.

17.2 Problem Formulation

Lumen maintenance is the basis for commercial claims of LED-based products [6–8]. As such, it is extremely vital to perform projections that are statistically sound and correct. Being an industry agreement, TM-21 flaws in this respect, and alternative approaches are needed. Such an alternative approach should encompass the following nature:

- Use all the raw data, per setting, per LED, and per time point.
- Provide statistically sound results in terms of prediction stability.
- Provide a true value for the lumen life of the LED technology.

Paragraph 3 describes the current agreed methods and provides an alternative statistical approach.

17.3 Statistical Methods

17.3.1 Current Agreed Methods

Per today, all LED suppliers deliver LM-80 data sets typically at three currents and three temperatures. A typical data set is depicted in Fig. 17.2 [6]. This relative data is then used for the TM-21 extrapolation tool to create a prediction that is listed in Fig. 17.3. The result is truncated using the so-called 6× rule, where one can only claim a value that is six times the LM-80 time (e.g., with 6 kh test time, one can only claim 36 kh lumen maintenance).

Within the TM-21 committee, an initial approach to the problem of projecting lumen maintenance life was the consideration of multiple mathematical models [4, 5]. These ranged from 1-parameter exponential decay until 3-parameter multi-exponential decay.

Note that there is a risk in accepting lifetimes that are predicted far beyond the LM-80 testing time because of the significant effect of measurement errors and lack of numerical convergence of estimators. Note that it may have an effect the other way round as well: impact of lack of numerical convergence and additional (not identified) degradation mechanisms that are expected to be more dominant.

Within TM-21, being an industry agreement, finally, the simplest possible form was chosen as

2.0 TEST CONDITION 1: 55 °C 0.200 A

TABLE 2.1 - LUMEN MAINTENANCE RESULTS
TEST CONDITION 1: 55 °C 0.200 A

Photometric test drive current: 0.200 A
Photometric test ambient temperature: 25 ± 2 °C
Failures observed: none

Load board ID	Device number	Zero hour measurements: Flux (lm)	Zero hour measurements: V_F (V)	Lumen Maintenance (%): 168	500	1000	2000	3000	4000	5000	6000	7000	8000	9000
A80000008945 7031C	1	515.10	25.79	100.4	100.5	99.9	99.7	100.0	99.9	99.9	99.2	99.1	98.9	98.1
	2	518.67	26.40	99.9	99.9	99.4	99.1	99.3	99.2	98.9	98.5	98.4	98.3	97.6
	3	518.57	25.75	100.1	100.3	99.8	99.6	100.1	100.0	100.0	99.4	99.3	99.2	98.5
	4	511.77	26.23	100.7	100.9	100.3	100.3	100.7	100.8	100.7	100.3	100.1	100.0	99.1
	5	517.49	26.12	99.9	99.9	99.4	99.0	99.7	99.8	99.7	99.2	99.0	99.2	98.4
	6	516.60	27.17	100.2	100.2	99.6	99.6	99.9	99.8	99.8	99.2	99.1	99.0	97.7
	7	522.52	27.56	100.3	100.4	100.0	99.9	100.3	100.3	100.3	99.4	98.8	97.7	96.0
	8	512.03	26.30	100.4	100.4	99.8	99.7	100.1	100.0	99.9	99.3	99.1	99.1	98.5
	9	516.71	25.83	100.5	100.3	99.9	99.8	100.2	100.1	100.1	99.6	99.6	99.5	98.5
	10	516.33	25.70	100.3	100.3	99.8	99.9	100.4	100.4	100.5	99.9	99.7	99.5	98.6
	11	520.62	25.94	100.2	100.1	99.6	99.5	99.9	99.9	99.9	99.4	99.3	99.2	98.4
	12	515.88	26.51	100.1	100.1	99.6	99.6	100.2	100.2	100.3	99.7	99.6	99.3	98.5
F6000000B9E7D031C	1	524.22	26.27	100.0	100.2	99.6	99.7	99.8	99.8	99.6	99.0	98.9	98.7	97.8
	2	516.25	27.44	99.9	100.0	99.4	99.5	99.6	99.4	99.4	98.6	98.2	97.4	95.8
	3	514.76	26.05	99.3	99.3	98.8	98.8	98.8	98.7	98.5	97.7	97.9	97.7	96.8
	4	515.71	25.99	99.5	99.7	99.1	99.1	99.3	99.2	99.2	98.8	99.0	99.0	98.3
	5	517.33	25.99	99.9	100.1	99.6	99.8	100.0	99.8	99.9	99.3	99.4	99.3	98.4
	6	512.51	25.96	99.9	100.0	99.8	100.1	100.4	100.3	100.3	99.8	99.8	99.4	98.0
	7	514.99	25.59	99.8	99.8	99.1	99.2	99.1	99.1	98.9	98.4	98.6	98.5	97.6
	8	514.99	26.45	99.9	100.1	99.7	99.9	100.0	100.1	100.0	99.6	99.6	99.3	98.2
	9	520.72	25.88	99.7	99.9	99.4	99.7	99.8	99.7	99.7	99.2	99.3	99.3	98.6
	10	517.69	25.52	99.8	100.1	99.6	99.8	99.9	99.9	99.9	99.5	99.6	99.6	98.9
	11	507.07	26.24	100.5	100.9	100.6	100.7	101.1	101.0	101.0	100.5	100.5	100.4	99.3
	12	522.09	25.92	99.8	100.0	99.4	99.5	99.8	99.7	99.6	99.1	99.1	99.1	98.2
			n	24	24	24	24	24	24	24	24	24	24	24
			mean	100.0	100.1	99.6	99.6	99.9	99.9	99.8	99.3	99.2	99.0	98.1
			median	100.0	100.1	99.6	99.7	100.0	99.9	99.9	99.3	99.2	99.2	98.4
			std. dev.	0.3	0.3	0.4	0.4	0.5	0.5	0.6	0.6	0.6	0.7	0.9
			min	99.3	99.3	98.8	98.8	98.8	98.7	98.5	97.7	97.9	97.4	95.8
			max	100.7	100.9	100.6	100.7	101.1	101.0	101.0	100.5	100.5	100.4	99.3

Fig. 17.2 Typical LM-80 data set showing lumen decay per LED as function of measurement time [6]

$$\Theta(t) = \exp\left(-\alpha t^{\beta}\right) \tag{17.1}$$

where:

- t is time in hour.
- $\Theta(t)$ is the averaged normalized luminous flux output at time t.
- α is the decay rate constant derived by a least squares curve fit.
- β is the shape parameter.

For each separate temperature and/or current L_{70}, that is $\Theta = 0.7$, can then be calculated using averaged normalized luminous flux output:

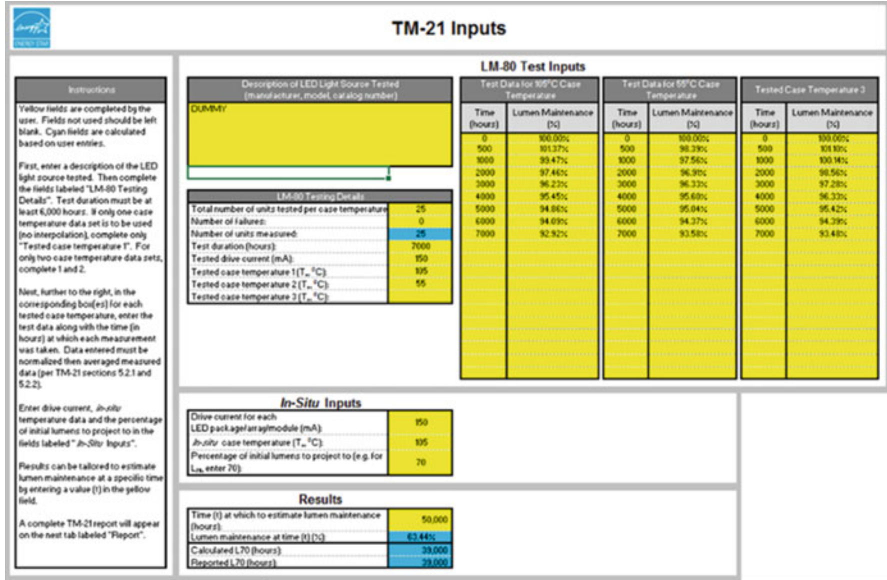

Fig. 17.3 TM-21 report example

$$L_{70} = (-\ln(0.7)/\alpha)^{1/\beta} \tag{17.2}$$

Estimates of (α, β) can be easily obtained by applying the least squares method. Temperature acceleration, within the measured temperatures, is allowed and supposed to follow the Arrhenius equation:

$$\alpha = C\ \exp\left(\frac{-E_a}{k_B T_s}\right) \tag{17.3}$$

where:

- C is a pre-exponential factor.
- E_a is the activation energy (in eV).
- T_s is the in situ absolute temperature (in K).
- k_B is the Boltzmann's constant ($8.617385 \times 10-5\,\mathrm{eV}/K$).

This model for α can be easily extended by using the inverse power law model that takes into account the effect of current:

$$\alpha = C\ \exp\left(\frac{-E_a}{k_B T_s}\right) I^n \tag{17.4}$$

where:

- I is the current.
- n is a life-stressor slope.

If applicable the interaction between temperature and current can be added easily.

The TM-21 method has become quite a standard way of working within the lighting industry. In the issue of LEDs Magazine from December 2014, Hansen and Davis [9] used the approach to assess LM-80 data across a variety of packaged LEDs in an effort to determine the effects of different LED platform designs and materials on performance, light quality metrics, and cost.

Alternative approaches are rare as only few other publications are built upon the TM-21 method. An exemption is the VDE standard VDE-AR-E2715-1 [10] currently published in Germany only. Here, the authors describe the so-called border function method (in German: Grenzfunction). This border function (BF) method is based on the assumption that an exponential model is a conservative estimation (worst-case scenario) of the actual long-term luminous flux maintenance as it is expected that most LED packages will show a long-term luminous flux maintenance which is better than the assumed exponential function. Fan et al. from the CALCE institute of technology [11] have used the degradation-data-driven method (DDDM) which is based on the general degradation path model. They use it to predict the reliability of high-power LEDs through analyzing the lumen maintenance data collected from the IES LM-80-08 lumen maintenance test standard. Their method is capable of getting much more reliability information out of the data (e.g., mean time to failure, confidence interval, reliability function). In an accompanying paper, Fan et al. [12] describe a particle filter-based (PF-based) prognostic approach based on both sequential Monte Carlo (SMC) and Bayesian techniques. These techniques are used to predict the lumen maintenance life of LED light sources. Also here the alternative approach achieves better prediction performance, with an error of less than 5% in predicting the long-term lumen maintenance life of LED light sources. Lall et al. [13] follow up on this approach by using Bayesian probabilistic models for the assessment of the onset of degradation in solid-state luminaires. The failure threshold decay rate has been calculated using an Arrhenius model, neglecting the effects of current density and humidity. The statistical approach is quite valid but also seen as complicated. Quan et al. [14] describe an in situ method to monitor the lumen degradation of LED packages. They conclude that the luminous flux of the LEDs shows a steady and slow depreciation, but no proper statistical analysis was performed on their measured data. Huang et al. [15–17] investigated the degradation mechanisms of mid-power white-light LEDs. In their studies, a modified Wiener process was employed for the modeling of the LED devices' degradation, following the earlier work of Tsai et al. [18]. Using this method, the dynamic, random variation, as well as the nonlinear degradation behaviors of the LED devices, was described. They applied the Hallberg-Peck's model to describe the effects of temperature and humidity on LED degradation thereby ignoring the crucial effects of the current density on this degradation. Other studies devote lumen decay to silicone degradation and/or crack formation [19, 20]. In these investigation, silicone degradation was quantitatively evaluated

using finite element analysis and used to estimate the LED package lifetime depending on the operation conditions. Buffolo et al. [21] present the results of a reliability investigation performed on four different groups of commercially available mid-power white LEDs. Their data gathered all along the 4000 h of stress accumulated suggest the presence of multiple degradation mechanisms that may limit the useful lifespan of the LED packages. This study lacks a proper statistical analysis of the experimental data, nor proposes an alternative method.

17.3.2 Alternative for Model Fitting

An alternative approach is to study the "degradation" data of each LED individually. It means that for each individual LED, a model as stated in Eq. 17.1 is fitted. Then, we can predict L70 values for each LED and turn degradation values into failure times. The question is whether the differences between predicted lifetimes are due to production variation (and measurement spread) only, or due to operating variation, such as temperature and current as well. Such an experiment is called an accelerated degradation test (ADT). In order to conduct an ADT efficiently, there are several aspects that need to be considered. These aspects are termination time, the number of stress factors, the number of stresses, the choice of stress levels, and the sample size for each stress level. For instance, Nelson [22] and Meeker and Escobar [23] addressed those aspects.

Besides the mentioned aspects, one of the most important questions arising from a degradation experiment is how many hours (or cycles) an accelerated degradation experiment should last for gathering proper data to allow one to make inference about the product lifetime under the normal use condition. In this chapter we focus on the convergence of the quantile estimators (such as B10 or B50) to decide whether we are able to make this inference. Therefore, determination of the termination time cannot be decided upfront. Yu and Tseng [24] proposed to combine the outcomes of an ADT with a known accelerated life test (ALT) model. They showed that the termination time of a degradation experiment has a huge impact on the precision of estimating a product's lifetime. It appeared that the mean time to failure (MTTF) estimates oscillate severely at the beginning; however, as the termination time t_i (with $i = 1,2,\ldots n$) increases, more degradation data are collected, the MTTF estimate converges. It is obvious that B10 and B50 behave similarly. Our intuitive approach to determine the termination time for an LM-80 experiment is based on the work of Yu and Tseng [24]. In this paragraph we will explain the mentioned approach.

The approach for determining the termination time for an ADT has three steps:

1. Use the degradation paths to estimate the lifetimes of LEDs under specific temperatures and currents up to the testing time t_i. So for each LED the parameters (α, β) of Eq. 17.1 need to be estimated, such that L_{70} can be calculated.

2. Find a suitable life-stress model and use a maximum likelihood (ML) procedure to estimate B10 (50) under certain use conditions (T, I). Lognormal and Weibull distributions are both appropriate models to fit the (estimated) lifetime data. Check the distribution assumptions by making probability plots, and study the patterns of the parallel lines (for different values of T and I).
3. Investigate the behavior of B10 (50) for different times t_i ($i = 1,2,..n$), and propose an appropriate termination time. B10 (or B50) at time t_i often oscillates severely at the beginning but will converge in time. Yu and Tseng [24] mention three types of convergence patterns: monotonically increasing to a value, monotonically decreasing to a value, and slightly oscillating around a value. To derive an appropriate termination time, they also propose an algorithm that considers the relative rate of change of the asymptotic mean lifetime by using the 3-period moving average. In this study we focus mainly on the question whether we have sufficient testing data in time to show convergence at all using the mentioned LM-80 data.

In the next paragraph, we will demonstrate this alternative method for several LM-80 data sets coming from high-power (HP) and mid-power (MP) LEDs.

17.4 Analysis of the Selected Use Cases

17.4.1 Mid-power and High-Power LED Technology

In order to assess the applicability of our proposed statistical approach, we have gathered five use cases of long-term lumen maintenance data. These are:

- Case 1a: HP LED technology, 14 kh LM-80 data at four currents and four temperatures
- Case 1b: HP LED technology, 10 kh LM-80 data at three currents and four temperatures
- Case 2a: MP LED technology, 10 kh LM-80 data at three currents and three temperatures
- Case 2b: MP LED technology, 8 kh LM-80 data at three currents and three temperatures
- Case 2c: MP LED technology, 12 kh LM-80 data at three currents and three temperatures

For cases 1a and 1b, the target application settings are 85 °C and a forward current of 1A. For cases 2a, 2b, and 2c, the target application settings are also 85 °C but using a forward current of 150 mA.

All five data sets are subjected to the alternative method. For that, all data points with a sufficient level of degradation are used. Figure 17.4 shows the predicted B50L70 values as function of the LM-80 measurement time (or degradation time). The following is observed:

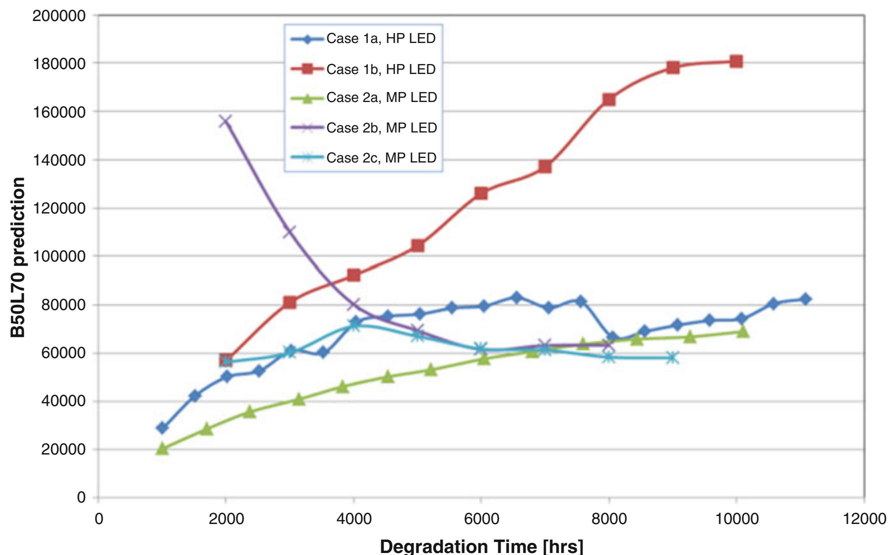

Fig. 17.4 Predicted B50L70 as function of the LM-80 measurement time for the five use cases

- Case 1a: The predicted B50L70 value gradually increases as function of time to reach almost stable values around 80 kh.
- Case 1b: The predicted B50L70 value keeps on increasing, and a stable value is not insight yet. A value of 180 kh seems to be reached, but the curve itself could start decreasing after that.
- Case 2a: The predicted B50L70 value keeps on increasing; stable value seems to hit 65 kh.
- Case 2b: The predicted B50L70 value gradually decreases as function of time to reach a stable value around 60 kh.
- Case 2c: The predicted B50L70 value first increases after which it gradually decreases as function of time to reach a stable value around 60 kh.

From a test termination point of view, cases 1a, 2b, and 2c have reached stable values for the model parameters (and thus B50), implying that the LM-80 tests can be stopped. For 1b and 2a however, stable values are not reached yet, meaning the test cannot be stopped.

Table 17.1 gives all the predicted acceleration model parameters following Eqs. 17.3 and 17.4. The activation energy is in the range 0.1–0.4 eV, which is believed to be the correct values for this failure mode. The standard deviation is quite reasonable. The effect of the current, parameter n, is quite different, and a large spread is found. A negative value indicates that with a higher current, the degradation is worse. A positive value is not reasonable (higher current improves the degradation level).

Table 17.1 Resulting fitted parameters following Eqs. 17.3 and 17.4. σ is the standard deviation assuming that ln(t) has a normal distribution. Note the positive value of n for case 2a

Case	*C*	*n*	*Ea*	*σ*
1a	7.82	−0.50	0.11	0.35
1b	9.98	−0.19	0.07	0.93
2a	0.55	0.15	0.34	0.27
2b	1.92	−2.89	0.11	0.25
2c	4.52	−0.72	0.16	0.68

Table 17.2 Comparison of the proposed statistical method with the existing TM-21 method for B50L70 values

Case	Reference	TM-21 prediction [h]	Proposed method [h]	Difference [%]
1a	1A, 85C	85,000	83,005	−2
1b	1A, 105C	142,000	161,669	14
2a	150 mA, 85C	65,000	68,981	6
2b	150 mA, 85C	63,000	63,227	0
2c	150 mA, 85C	45,000	51,355	14

The fitted parameters listed in Table 17.1 uniquely describe the lumen maintenance performance for the five LED packages under any application condition.

With the fitted parameters available, Table 17.2 depicts the comparison of the proposed statistical method with the TM-21 prediction. In general the deviation is found to be in the order of 0–14%. The main reason for this deviation is due to the fact that TM-21 only predicts the B50L70 values based on extrapolating the given test data. It does not take the other conditions into account, whereas the proposed method searches for congruency in the full data set using all tested conditions. We believe that the comparison is quite reasonable from an engineering point of view.

17.4.2 *Deep Dive into High-Power LED Technology*

Year to date the high-power LED technology is reaching a maturity level where all supplier uses the same kind of materials, i.e., very stable silicones (both for the optical system and the die attach), ceramic carriers, and gold wire bonding. As such, we expect that the lumen degradation would be quite identical between the different suppliers of this technology. At least if we can ignore the decay of the epitaxial, which is quite likely at moderate operation conditions. We have taken all the available LM80 data and analyzed that accordingly. The following data is available:

- LED 1
  - 9 kh LM-80 data at four currents and three temperatures (full matrix)
  - Measurement times: 0, 24, 168, 500, 1000, 2000, 3000, 4000, 5000, 6000, 7000, 8000, 9000 h
  - Total set of $300 \times 11 = 3300$ read points for analysis

- LED 2
  - 14 kh LM-80 data at four currents and four temperatures (partial matrix)
  - Measurement times: 0, 168, 1008, 1512, 2016, 2520, 3024, 3528, 4032, 4536, 5040, 5544, 6048, 6552, 7056, 7560, 8064, 8568, 9072, 9576, 10,080, 10,584, 11,088, 11,592, 12,096, 12,600, 13,104, 13,608, 14,112
  - Total set of 3,880 read points for analysis
- LED 3
  - 7 kh LM-80 data at three currents and two temperatures (partial matrix)
  - Measurement times: 0, 168, 1008, 1512, 2016, 2520, 3024, 3528, 4032, 4536, 5040 , 5544, 6048, 6552, 7056
  - Total set of 1300 read points for analysis
- LED 4
  - 10 kh LM-80 data at five currents and four temperatures (partial matrix)
  - Measurement times: 0, 1000, 2000, 3000, 4000, 5000, 6000, 7000, 8000, 10,000
  - Total set of 2277 read points for analysis

In total these are over 10k data points, spread out over long testing times, and to be analyzed by our proposed statistical method. The target application settings are 85 °C and a forward current of 1A, the same as in the previous case. But we concentrate on L80 values instead of L70. Figure 17.5 shows the predicted B50L80

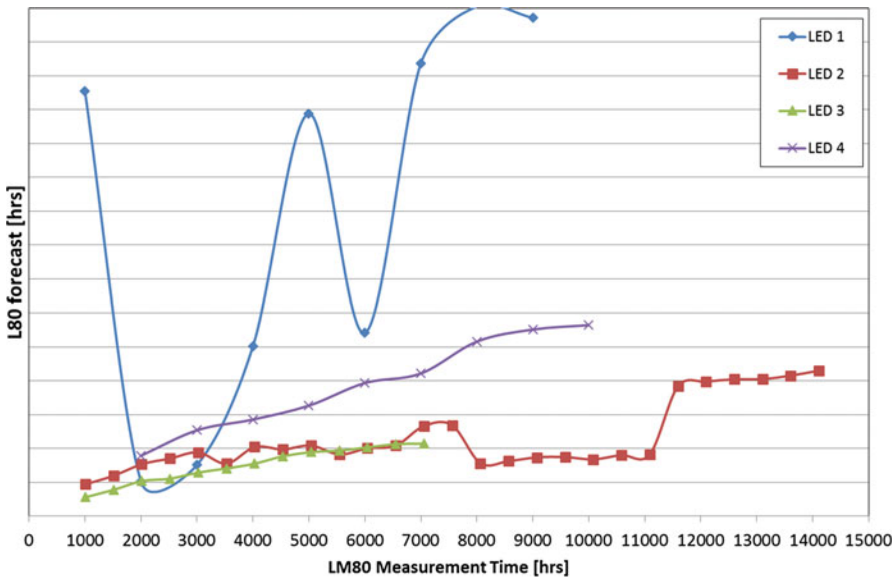

Fig. 17.5 Predicted B50L80 as function of the LM-80 measurement time for the four LEDs

values as function of the LM-80 measurement time (or degradation time). The following is observed:

- LED 1: The predicted B50L80 value fluctuates as function of time and reaches no stable values.
- LED 2: The predicted B50L80 value keeps on increasing, and a dip is seen in the period of 8,000–11,000 h, probably due to a measurement error (most likely a reference that is drifting).
- LED 3: The predicted B50L80 value keeps on increasing. Test time seems to be too short in order to judge the value until convergence.
- LED 4: The predicted B50L80 value keeps on increasing and apparently could level off. Also here, test time is too short to judge the converged value.

These results indicated that test time should be long enough and some level of degradation is to be detected in order to get a proper prediction of the long-term behavior.

As mentioned before, we believe that the high-power LED technology reached a certain level of maturity that allows us to put all the data into one set. Using the developed approach, we can then derive the B50L80 of this technology. Figure 17.6 shows the result of this exercise. Here we removed the prediction at 11,000 h as it showed a significant dip in the curve. The curve shows the increasing fingerprint of the other four LEDs in Fig. 17.5. For this generic curve, the fitted parameters are listed in Table 17.3. The activation energy Ea is in line with earlier findings [25, 26]. With these fitted parameters, the generic lumen maintenance behavior

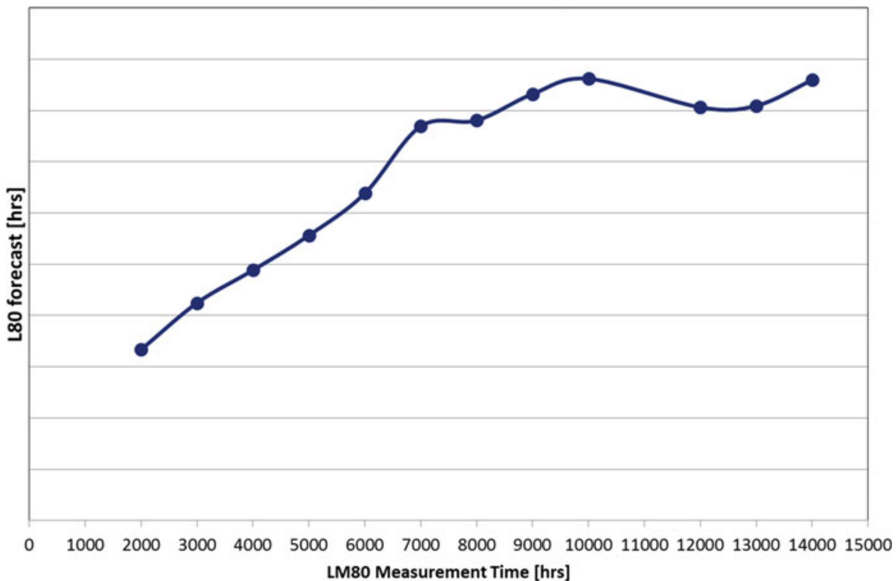

Fig. 17.6 Predicted B50L80 as function of the LM-80 measurement time when taken all the data is one set for high-power LED performance

Table 17.3 Resulting fitted parameters following Eqs. 17.3 and 17.4. σ is the standard deviation assuming that ln(t) has a normal distribution

Case	C	n	Ea	σ
HP LED	8.4	−0.8	0.1	0.3

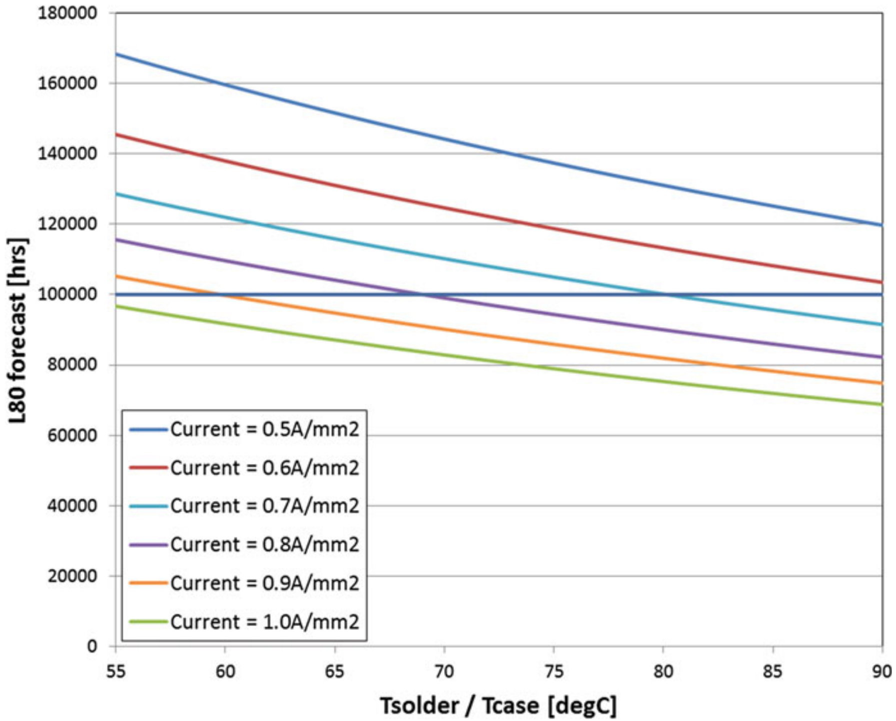

Fig. 17.7 Forward current density isolines for generic high-power LED lumen maintenance behavior using the fitted parameters $C = 8.4$, $n = -0.8$, $Ea = 0.10$ eV, and $\sigma = 0.3$

for high-power LEDs can be modeled following Eqs. 17.3 and 17.4. And accordingly, isolines can be given.

Figure 17.7 plots B50L80 isolines as function of the forward current density and the case/solder temperature using the fitted generic high-power LED model. A target line around 100 kh is given to indicate the current market demand in outdoor environments. Here we can also argue if values beyond 100 kh are possible or if truncation is required. However, this is not the topic of this chapter. The isolines indicate that the lumen maintenance performance decreases as function of temperature and current density. In the reference application of 85 °C and forward current of 1A, we find an L80 value of 72 kh. Actually, Fig. 17.7 can be seen as a look-up table for designs where one can target the requested L80 performance in terms of temperature and current.

17.5 Conclusions and Discussion

In this chapter we describe the different approaches currently available to perform lumen maintenance extrapolations for LEDs. We proposed an alternative statistical approach to estimate lumen depreciation of LEDs. In order to demonstrate this approach, we have analyzed five LM-80 data sets from a statistical point of view. A reasonable comparison with the existing TM-21 extrapolated values was found. We also analyzed several long-term LM80 high-power LED data to calculate a generic lumen maintenance model. Such a generic model allows the creation of isolines that may serve as a design guide. The analysis of these data sets shows the strength of the described method as the resulting unique fitted parameters describe the lumen maintenance of the LED over a long period. In principle there is also no need for a limitation based on the so-called $6\times$ rule from TM-21.

Other than the approach as described in Sect. 17.3.2, different – more complex – stochastic models are used to describe the degradation path. As stated, the big challenge is to get accurate estimates of a product's lifetime. The performance of an ADT, obviously, strongly depends on the appropriateness of the modeling of its degradation path. A typical degradation path consists of mean degradation curve and its error term (measurement error). There are two approaches available in the literature. First, the mixed effect model is one of the most popular approaches in degradation analysis. In order to describe the unit-to-unit variations of the test units, the unknown parameters of the mean degradation path are described in terms of the mixed (or random) effects. Often the mixed effect formulations do not take the time-dependent error structure into consideration. Therefore, the stochastic process formulation or Gauss-Markov method can be an alternative approach to model the product's degradation path. Dealing with those more complex models, to find the maximum likelihood estimates (MLEs) of the unknown parameters, the mixed effect model is computationally intensive. STATA (see: http://www.stata.com) or R (https://www.r-project.org) can be used. However, on-hand procedures do not always guarantee that the precise parameter estimations can be obtained. Besides the mixed and Gauss-Markov approaches, the application of Bayesian methods may be promising. Bayes allows a reliability engineer to incorporate one's prior knowledge about the unknown parameters of the model into data analysis to provide important improvements in precision. Based on previous experiments, an engineer may specify priors for the effects of temperature and/or current. As generally well known, such priors are key components in a Bayesian model specification and should be chosen carefully.

Acknowledgments The research leading to these results has received funding from the European Unions' Seventh Framework Program (FP7/2007-2013) for DEWI Dependable Embedded Wireless Infrastructure Joint Undertaking under grant agreement 621353 and from specific national programs and/or funding authorities.

References

1. W.D. van Driel, X.J. Fan, *Solid State Lighting Reliability: Components to Systems*, ISBN 978-1-4614-3066-7, (Springer, 2012), 617 pages
2. IES LM-80-08. Approved Method: Measuring Lumen Maintenance of LED Light Sources, Illuminating Engineering Society of North America, (2008)
3. IES TM-21-11, *IES Approved Method for Measuring Lumen Maintenance of LED Light Source* (Illuminating Engineering Society of North America, New York, 2008)
4. H.A. Qiao, T.C. Pulsipher, J.E. Hathaway, E.E. Richman, E. Radkov, A statistical method to analyze LED lumen depreciation and project useful LED product life, IES Annual Conference, Toronto, 9 Nov 2010
5. IES Conference, Development of a standard method for projecting lumen maintenance of LED products (TM- 21), Illuminating Engineering Society of North America, (2007)
6. R. Hechfellner, S. Landau, Understanding LED performance, Led light. (2009)
7. USA Department of Energy, Lifetime and reliability, fact sheet available at: ssl.energy.gov
8. Next Generation Lighting Industry Alliance and LED Systems Reliability Consortium (2014) *LED Luminaire Lifetime: Recommendations for Testing and Reporting. Pre-pared for the U.S. Department of Energy*. September 2014. Available at: http://energy. gov/sites/prod/files/2015/01/f19/led_luminaire_lifetime_guide_sept2014.pdf
9. M. Hansen, L. Davis, *Using LM-80 Measurement Methodology to Determine the True Value of Packaged Leds*, Leds Magazine, 9 Dec 2014
10. VDE-AR-E 2715-1, Measurement and prediction of reduction in luminous flux of LEDs, German Standard, November 2012
11. J. Fan, K.-C. Yung, M. Pecht, Lifetime estimation of high-power white LED using degradation-data-driven method. IEEE Trans. Device Mater. Reliab. **12**(2), 470–477 (2012)
12. J. Fan, K.-C. Yung, M. Pecht, Predicting long-term lumen maintenance life of LED light sources using a particle filter-based prognostic approach. Expert Syst. Appl. **42**(5), 2411–2420 (2015)
13. P. Lall, J. Wei, P. Sakalaukus, Bayesian models for life prediction and fault-mode classification in solid state lamps, in *16th International Conference on Thermal, Mechanical and Multi-Physics Simulation and Experiments in Microelectronics and Microsystems*, (2015)
14. C. Quan, X. Luo, C. Qi, K. Wang, L. Sheng, L. Jingyana, Research on lumen depreciation related to LED packages by in-situ measurement method. Microelectron. Reliab. **55**, 2269–2275 (2015)
15. J.L. Huang, D.S. Golubović, S. Koh, D.G. Yang, X.P. Li, X.J. Fan, G.Q. Zhang, Degradation mechanisms of mid-power white-light LEDs under high temperature-humidity conditions. IEEE Trans. Device Mater. Reliab. **15**(2), 220–228 (2015)
16. J.L. Huang, D.S. Golubović, S. Koh, D.G. Yang, X.P. Li, X.J. Fan, G.Q. Zhang, Degradation modeling of mid-power white-light LEDs by using Wiener process, Opt Express. **23** (15) (2015). doi:10.1364/OE.23.00A966
17. J.L. Huang, D.S. Golubović, S. Koh, D.G. Yang, X.P. Li, X.J. Fan, G.Q. Zhang, Optical degradation mechanisms of mid-power white-light LEDs in LM-80-08 tests. Microelectron. Reliab. **55**(12, Part B), 2654–2662 (2015)
18. T.-R. Tsai, C.-W. Lin, Y.-L. Sung, P.-T. Chou, C.-L. Chen, Y. Lio, Inference from lumen degradation data under Wiener diffusion process. IEEE Trans. Reliab. **61**, 710–718 (2012)
19. S. Watzke, P. Altieri-Weimar, Degradation of silicone in white LEDs during device operation: a finite element approach to product reliability prediction, in *15th International Conference on Thermal, Mechanical and Multi-Physics Simulation and Experiments in Microelectronics and Microsystems*, (EuroSimE, 2014). doi: 978-1-4799-4790-4/14
20. S.-U. Zhang, Quantification of silicone degradation for LED packages using finite element analysis. Microelectron. Reliab. **55**, 2678–2684 (2015)

21. M. Buffolo, C. De Santi, M. Meneghini, D. Rigon, G. Meneghesso, E. Zanoni, Long-term degradation mechanisms of mid-power LEDs for lighting applications. Microelectron. Reliab. **55**, 1754–1758 (2015)
22. W.B. Nelson, Accelerated testing: statistical models, test plans, and data analysis, 624, (2004). ISBN: 978-0-471-69736-7
23. Meeker, Escobar, A review of accelerated test models. Stat. Sci. **21**(4), 552–577 (2006)
24. H.-F. Yu, S.-T. Tseng, On-line procedure for terminating an accelerated degradation test. Stat. Sin. **8**, 207–220 (1998)
25. T. Yanagisawa, T. Kojima, Long-term accelerated current operation of white light emitting diodes. J. Lumin. **114**, 39 (2005)
26. S. Koh, C. Yuan, B. Sun, B. Li, X. Fan, G. Zhang, Product level accelerated lifetime test for indoor led luminaires, in *14th International Conference on Thermal, Mechanical and Multi-Physics Simulation and Experiments in Microelectronics and Microsystems* (EuroSimE, 2013), pp. 1–6

Chapter 18
Long-Term Reliability Prediction of LED Packages Using Numerical Simulation

Sung-Uk Zhang

Abstract Solid-state lightings (SSL) rapidly penetrate the global illumination market because of the energy efficiency and the reliability. The energy efficiency can be easily evaluated, but the reliability is not convenient to be estimated. SSL is based on semiconductor and brings new manufacturing process and new materials, which introduces a series of new and unknown failure modes. Using several reliability tests, the reliabilities of LED packages are evaluated. However, the general experiments are mostly time-consuming and expensive. In this chapter, two failure modes caused by the corresponding reliability tests are focused, which are wire bond breakage for the thermal shock cycle test and silicone degradation for high temperature operating life test (HTOL). As these failure modes belong to long-term reliability issues for LED packages, solving these issues is crucial in term of time to market (TTM). Two failure modes were quantified by using finite element analysis. For the wire bond failure, a wire bond lifetime model was developed to predict the number of cycles to failure during thermal shock tests. For the silicone degradation, a lumen depreciation model was suggested to estimate the lumen depreciation for HTOL. Using two models, long-term reliability of LED packages could be predicted using numerical simulation without time-consuming experiments.

18.1 Introduction

Solid-state lightings (SSL) rapidly penetrate the global illumination market because of the energy efficiency and the reliability. The energy efficiency can be easily evaluated, but the reliability is not convenient to be estimated. SSL is based on semiconductor and brings new manufacturing process and new materials, which introduces a series of new and unknown failure modes. Caers and Zhao [1] have

S.-U. Zhang (✉)
Samsung Electronics Co., Ltd., 1, Samsung-ro, Giheung-gu, Youngin-si, Geonggi-do 446-711, South Korea

Dong-Eui University, Pusan, South Korea
e-mail: zsunguk@deu.ac.kr

© Springer International Publishing AG 2018

W.D. van Driel et al. (eds.), *Solid State Lighting Reliability Part 2*, Solid State Lighting Technology and Application Series 3, DOI 10.1007/978-3-319-58175-0_18

reported failure modes from device level to system level. The failure modes are categorized into catastrophic failures and degradation failures. The catastrophic failures include die cracking, electrical opens, electrical shorts, delamination damage from ESD, driver failures, and so on. The degradation failures consist of degradation of the lens and the encapsulant, yellowing of the lens and of the encapsulant, increase of the contact resistance, and degradation of the phosphors. These failures brought reliability issues for LEDs. Pecht and Chang [2] have reviewed failure mechanisms and reliability issues in LEDs. In order to evaluate the reliability, several qualification tests are performed by LED manufacturers, which are categorized into operating life tests and environmental tests. The operating life tests include room temperature life test (RTOL), high temperature operating life test (HTOL), low temperature life test (LTOL), wet high temperature operating life test (WHTOL), and so on. On the other hand, thermal shock test, mechanical shock test, and temperature humidity storage tests belong to the environmental tests. Among several reliability tests, the operating life tests and the thermal shock test are time-consuming and expensive. Currently LED manufacturers need efficient ways to evaluate these reliability issues. In this chapter, two failure modes caused by the corresponding reliability tests are focused, which are wire bond breakage for the thermal shock cycle test [3] and silicone degradation for HTOL [4]. Figure 18.1 shows wire neck breakage after performing the thermal shock test. This wire bond failure is one of metal fatigue failures.

Figure 18.2 shows lens cracks of LED package caused by an operating life test. These lens cracks result from silicone degradation. Both failure modes belong to long-term reliability issues so that alternative approach is required instead of general measurements.

This chapter introduces one efficient way to evaluate long-term reliability of LED packages. The way is to predict the reliability by using numerical simulation. This chapter is divided into three sections. The first is related to the wire bond breakage. For numerical estimation, a wire bonding lifetime model for the thermal shock test was developed so that the number of cycles to failure could be predicted by using numerical simulation. The model was based on the Coffin-Manson fatigue

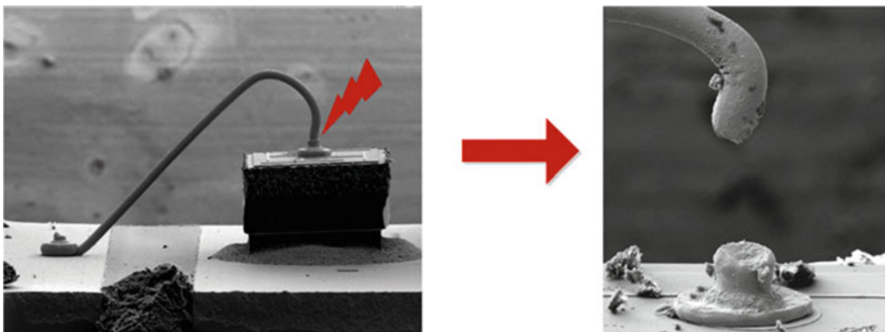

Fig. 18.1 Wire neck breakage caused by thermal shock tests

Fig. 18.2 Lens cracks of LED package caused by an operating life test

law, which was calibrated from failure data of the thermal shock tests and computed plastic strain. In order to calculate the plastic strain under the test conditions, the finite element method (FEM) was performed. The second section describes the silicone degradation in LEDs. Assuming that the degree of the silicone degradation is strongly related to creep strain rate of the siloxane, silicone degradation during the operating life test of LEDs was quantitatively evaluated using numerical simulation. In order to compute creep strain rate of the silicone, the linear visco-elastic property of the silicone was measured and used for the FE thermal-mechanical simulation. The creep strain rate of the silicone polymer was computed in a predefined volume of interest (VOI). Furthermore, the correlation between the computed creep strain rates and lumen depreciation could be established, which lead to a lumen depreciation model using the viscosity effect of the silicone. Based on this model, the tendency of the lumen maintenance for LED packages could be estimated using numerical analysis without time-consuming tests. The conclusion and further works are presented in the final section.

18.2 Fatigue Life Evaluation of Wire Bonds During a Thermal Shock Cycle Test

Previous researchers have studied thermal fatigue lifetime evaluation of wire bonds for IGBT modules, RF LDMOS, power modules, and silicon power semiconductors [3–10]. Ciappa and Fichtner [5] needed to evaluate a failure rate of IGBT over 30-year operation. Hager et al. [6] demanded to evaluate lifetimes between 10 and 30 years under harsh conditions for IGBT. Bielen et al. [7] demanded RF LDMOS to be able to undergo more than 10,000 cycles to failure. Although LED packages have a similar problem in terms of time-consuming tests, the failure mode of the

LED package is different from the others. The failure of the LED package belongs to low-cycle fatigue failure. On the other hand, the failures of other electronic packages are categorized into high-cycle fatigue failure. In the LED package, gold bonding wires are surrounded by silicone encapsulant which has a higher thermal coefficient of expansion than the gold has. Moreover, the material property of the silicone for LED packages is highly dependent upon temperature. Elastic modulus of the silicone at low temperature is usually much higher than one of the silicone at high temperatures. The low temperature condition induces large plastic strain accumulated in the wire. The cumulated plastic strain becomes a main cause for the wire bonding breakage.

This section describes a wire bonding lifetime model for the thermal shock test in order to estimate the number of cycles to failure by using numerical simulation. The section has two subsections. The first subsection includes the way to establish the model based on the Coffin-Manson fatigue law. The second subsection explains a design example using the wire bonding lifetime model.

18.2.1 Wire Bonding Lifetime Model

During the thermal shock test, one of the major failure modes for LED packages is wire neck breakage occurred by thermal stresses. The wire neck breakage belongs to low-cycle fatigue as the number of cycles to failure occurs less than 10,000 thermal cycles and the load frequency is less than 10 (Hz). Hence, the wire bonding lifetime model was based on Coffin-Manson fatigue law. The model is shown as follows:

$$N_{\mathrm{f}} = a\left(\Delta\varepsilon_{\mathrm{p}}\right)^{b} \tag{18.1}$$

where N_{f} is the mean number of cycles to failure and $\Delta\varepsilon_{\mathrm{p}}$ is the increment of volume averaging accumulated plastic strain between the first thermal cycle to the second thermal cycle. We assumed that residual stresses inside the wire could be neglected during manufacturing processes. a and b are coefficients which are calibrated by using linear regression. N_{f} is analyzed by Weibull analysis based on failure data of the thermal shock tests. $\Delta\varepsilon_{\mathrm{p}}$ is computed by using the finite element analysis corresponding to prescribed test conditions.

18.2.1.1 Experiments

Thermal shock cycling was performed in the range of −45 °C–125 °C. Each cycle lasted 30 min. Each dwell time at high and low temperatures consumed 15 min. The LED packages were placed inside a thermal shock chamber and cycled according to prescribed conditions. On-off tests were performed to check failures for LED

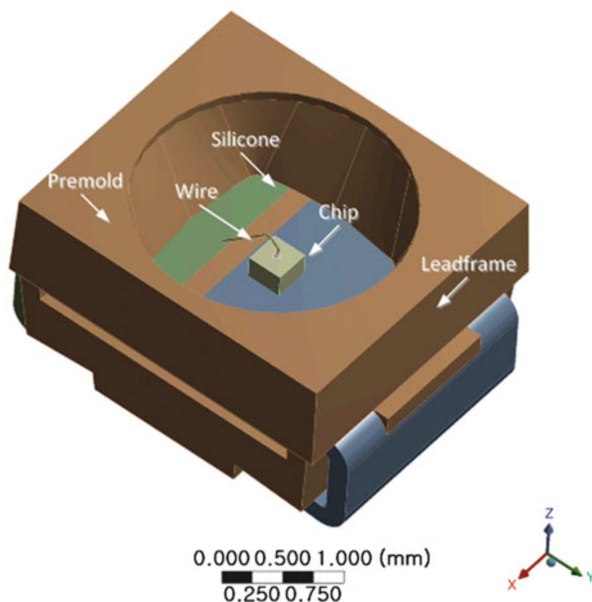

Fig. 18.3 Schematic of a LED package

packages. The failure data were further analyzed by Weibull analysis software (Minitab) to determine the number of cycles to failure. N_f is defined as a mean value of the number of cycles when the failure rate is 1%.

Figure 18.3 shows the schematic of a LED package. The LED package is composed of reflector, silicone encapsulant, a wire, a LED chip, and lead frames. As the wire with a low coefficient of thermal extension (CTE) is surrounded with the silicone encapsulant with a high CTE, thermal deformation of the encapsulant induces plastic strains in the wire. The CTE of the silicone is about 2 × 10–4 (°C^{-1}); however the CTE of the wire is approximately 1.4 × 10–5 (°C^{-1}). The plastic strains are largely accumulated in the wire neck, which results in the wire neck breakage.

Several thermal shock tests were conducted on various packages which varied according to their sizes, encapsulants, diameters of wires, and wire loops. Among them, we selected proper data points which had high correlation coefficients to Weibull distribution. The data points were used for linear regression. The criterion of the correlation coefficient was defined as 0.95. Table 18.1 lists the test data points. The data point is denoted as DP.

Elastic moduli of silicone encapsulants used for LED packages were measured by using the dynamic mechanical analyzer (DMA). Figure 18.3 shows that the elastic moduli vary with temperature. The graph shows that the silicone A has slightly higher elastic modulus than the other at low temperatures.

Table 18.1 LED package and test condition for thermal shock tests

Number of DP	Size	Kind of silicone	Wire diameter (μm)	Wire height (μm)	Wire length (μm)	Wire loop
1	Large	A	25.0	190	1,000	L1
2	Large	A	25.0	230	1,000	L1
3	Large	A	25.0	190	1,000	L2
4	Large	A	25.0	230	1,000	L2
5	Small	B	30.0	200	650	L2
6	Small	B	30.0	300	650	L2
7	Small	B	30.0	200	920	L2
8	Small	B	30.0	300	920	L2
9	Medium	A	25.0	280	1,100	L3

18.2.1.2 Finite Element Model

The above data points were simulated in finite element models to calculate the accumulated plastic strains during each temperature cycle. The models were subjected to quasi-static thermal loading. Each LED package includes wires. Small PKGs, medium PKGs, and large PKGs have one, three, and six wires.

In order to reduce geometry discrepancy between manufactured wire shapes and finite element models, a scanning electron microscope (SEM) was used to acquire the wire shape in detail. Figure 18.4a, b show the SEM picture and the finite element model corresponding to the picture. The finite element model did not include the shape of second bonding precisely because the stitch was not our volume of interest (VOI).

The VOI was the wire neck as shown in Figs. 18.5 and 18.6, which is defined as a heat-affected zone of the wire with a height of 30 μm.

In the VOI the accumulated plastic strain was computed by employing volume averaging technique as follows:

$$\bar{\varepsilon}_{\mathrm{p}} = \frac{\sum_{e} \left(\varepsilon_{\mathrm{p}}^{e}\right) \times V_{e}}{\sum_{e} V_{e}} \tag{18.2}$$

where $\bar{\varepsilon}_{\mathrm{p}}$ is the volume averaging plastic strain, e is the element number, and V_{e} and $\varepsilon_{\mathrm{p}}^{e}$ are the volume and the accumulated plastic strain of the eth element. The element size in the VOI was 5 μm for all data points. The volume averaging technique was applied in order to reduce a numerical error in the VOI.

The computation of accumulated plastic strain was based on following assumptions. The wire had bilinear kinematic hardening behavior. Elastic modulus and tangent modulus of the wire were 55 GPa and 318 MPa. Yield stress of the wire was 167 MPa.

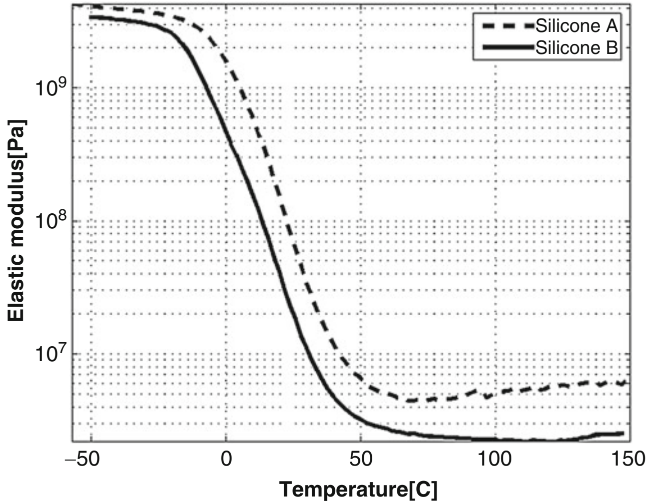

Fig. 18.4 Elastic moduli of silicones in changes of temperature

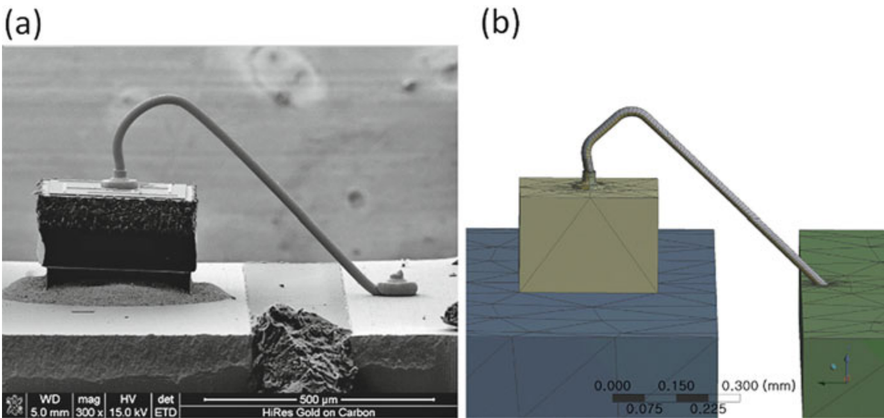

Fig. 18.5 Wire shape (**a**) SEM picture (**b**) finite element model

18.2.1.3 Calibrated Model

Under above assumptions, plastic strains in VOI were computed for each data point. Figure 18.7 shows finite element results for DP5. The maximum plastic strain occurs in the VOI. Figure 18.7b, c represent the exaggerated deformations at −45 °C and 125 °C.

Figure 18.8 shows that the accumulated plastic strain increases as time increase for eight design points. The plastic strains have stepwise increases because larger plastic strains are cumulated at low temperatures.

Fig. 18.6 Volume of interest for finite element computation

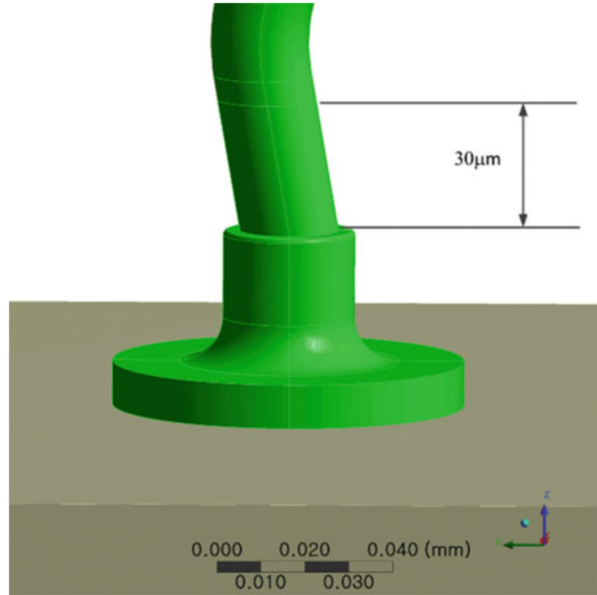

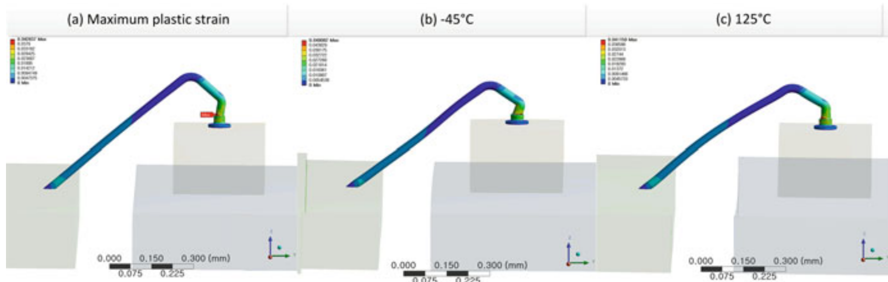

Fig. 18.7 Equivalent plastic strain distribution, (**a**) location of the maximum plastic strain, (**b**) exaggerated deformation at −45 °C, (**c**) exaggerated deformation at 125 °C

According to Fig. 18.8, the plastic strain increment between 30 and 60 min could be computed as shown in Table 18.2. DP3 has the largest increment, and DP5 has the smallest one among the design points.

Using numerical and experimental results of the selected four design points, regression analysis could be performed. Coefficients of the wire bonding lifetime model were obtained as follows:

$$N_{\mathrm{f}} = 6.98\left(\Delta\varepsilon_{\mathrm{p}}\right)^{-1.2} \tag{18.3}$$

The R-squared value was 99.8%, which presents how well data points fit a line or a curve. Comparatively, Matsunaga and Uegai [8] developed a high-cycle fatigue lifetime model for aluminum wires in a power module. The number of cycles to

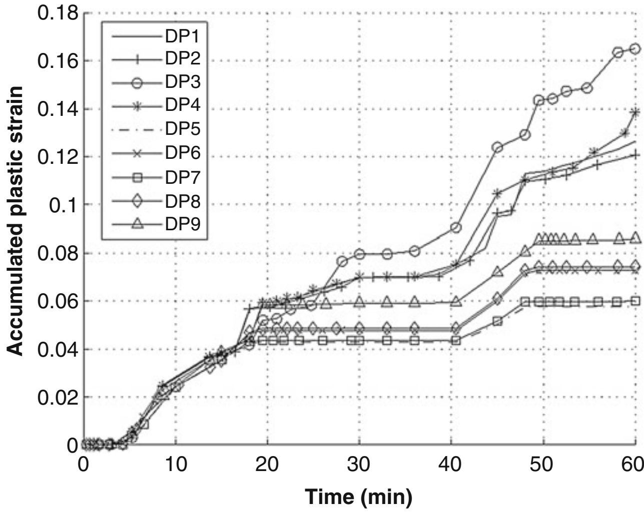

Fig. 18.8 Accumulated plastic strain vs. time

Table 18.2 Plastic strain during the second cycle for each data point

Data point	$\Delta\varepsilon_p$
1	0.05678
2	0.05115
3	0.06857
4	0.03511
5	0.01491
6	0.02508
7	0.01639
8	0.02578
9	0.02679

failure was dependent on the thermal cycling swing range. The coefficients of *a* and *b* were $1.63 \times 1{,}013$ and -4.5. Those coefficients vary with wire materials and input parameters.

In order to evaluate our lifetime model, the other results were used to compare with the lifetime model as shown in Fig. 18.9. The discrepancy between DP6 and the wire bonding lifetime model is the largest among them. Nf estimated by the lifetime model was 582. The error may be caused by differences in geometry and material property of encapsulants. The encapsulant highly affects the wire bonding lifetime. The volume of the encapsulant in our FE model may be different from one of the real package. Moreover, we assumed the silicone encapsulant in the FE model was pure silicone. However, the real silicone encapsulant contains phosphors so that the material properties may be different. The effect of the material property of the encapsulant will be further work.

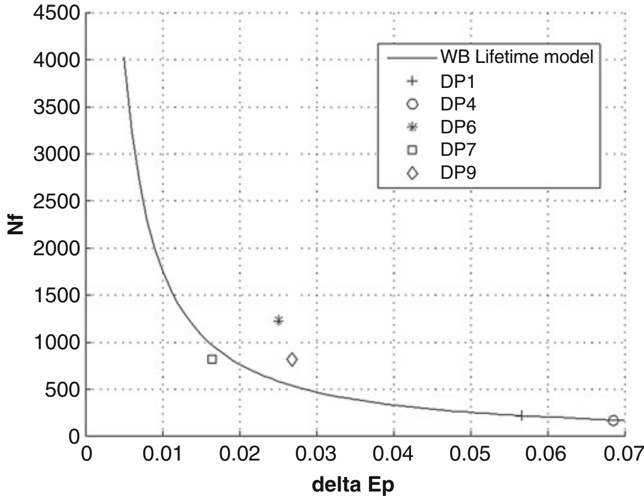

Fig. 18.9 Wire bonding lifetime model

18.2.2 A LED Package Design Example Using the Wire Bond Lifetime Model

As SSL brings new manufacturing process and new materials, material selection is important for LED manufacturers. One of new developing materials is a premold. Sometimes several material vendors provide their products. One of the major considerations could be the wire bond reliability for LED packages.

For this problem, this wire bond lifetime model was adopted, and the response surface methodology (RSM) was used to study the relationship between mechanical properties of premold materials and N_f. Design parameters for the mechanical properties were defined as elastic modulus, coefficient of thermal expansion (CTE), and Poisson's ratio. The range of each parameter was determined as shown in Table 18.3 [4], which was defined by reference material properties of epoxy mold compound (EMC), polyphthalamide (PPA), and polycyclohexylenedimethylene terephthalate (PCT).

Using the above ranges, a Box-Behnken design generates the set of the required treatment combinations, which included 13 treatment combinations created by Minitab. The response surface model had an R-squared value of 98.97%. Using the response surface model, contour plots are shown in Fig. 18.10, which graphically shows the most sensitive parameter for the N_f is CTE. When CTE is more than 80 ppm/K, Nf could not be more than 950 cycles.

Fourteen candidate materials were evaluated using the response surface model and the wire bonding lifetime model as shown in Fig. 18.11. Among them, the wire bond reliability of the LED package including Material#7 would be worst during thermal shock tests. The best case would be Material#13.

Table 18.3 Parameter ranges for the mechanical property of a premold material

	CTE (ppm/K) [min, max]	Elastic modulus (GPa) [min, max]	Poisson's ratio (mm/mm) [min, max]
Design parameters	[12,94]	[4.2,18]	[0.2,0.35]

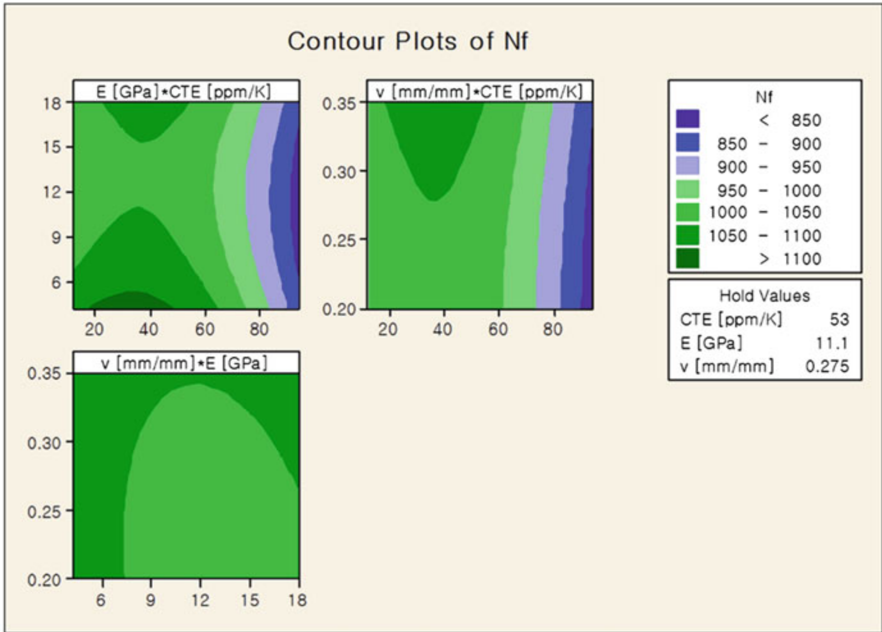

Fig. 18.10 Contour plots of Nf using the response surface model

18.3 Quantification of Silicone Degradation During HTOL

Silicone polymers are used for encapsulant and lens for LED devices because of their high transparency, manufacturability, stable thermomechanical properties, and controlled refractive index [11]. Among several kinds of silicones used for LED devices, the most common one is polydimethylsiloxane (PDMS) which can have a wide range of refractive indices from 1.40 to 1.57. The common linear PDMS is based on Me2SiO2/2 with refractive indices between 1.40 and 1.42. If some methyl groups along the polymer chain are substituted with phenyl groups, the refractive index can increase up to 1.57. The controlled refractive index becomes a great merit in terms of light extraction efficiency. The light extraction efficiency is a portion of the external quantum efficiency of LEDs. The total external quantum efficiency, η_{EQE}, is given by

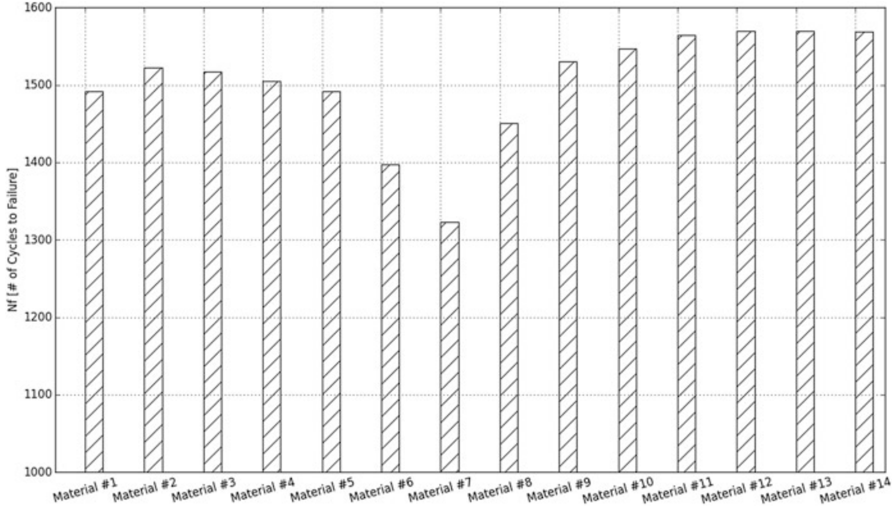

Fig. 18.11 Number of cycles to failure for 14 premold materials

$$\eta_{\mathrm{EQE}} = \eta_{\mathrm{inj}} \times \eta_{\mathrm{rad}} \times \eta_{\mathrm{extraction}} \tag{18.4}$$

where η_{inj} is current injection efficiency, η_{rad} is radiative efficiency, and $\eta_{\mathrm{extraction}}$ is the light extraction efficiency [12, 13]. The GaN-based LED has the high refractive index (RI) of 2.45. If RI of the interface materials such as PDMS is close to 2.45, mismatch of the refractive indices could be reduced so that the light extraction efficiency can be enhanced. However, a trade-off exists between the refractive index and thermal stability for the operating life tests.

Silicone degradation is one of the major causes for degradation of LEDs. Two silicone degradation mechanisms are suggested by Camino et al. [14]. The first mechanism is that the formation of cyclic oligomers is generated under the low temperature (400 °C) and slow heating condition. The second mechanism is that methane and oligomers are formed under the high temperature (800 °C) and fast heating condition. In addition, these mechanisms lead to a weight and volume shrinkage, which are investigated by differential scanning calorimetry [15]. Considering operating temperature of LEDs, the thermal degradation mechanism is close to the first mechanism. But the degradation mechanism of LEDs is too slow to be revealed because typical temperature of LEDs is controlled around 150 °C. The volume shrinkage of PDMA at the temperature is hardly observed within 100 h aging [7]. Based on the phenomenon of degradation of material properties, Watzke and Altieri-Weimar [7] developed a degradation material model for the silicone crack. Using a coupled thermo-optical model and FE thermomechanical model, they estimated time to failure of LEDs.

In this study, a key assumption was made, that is, the degree of the silicone degradation is strongly related to creep strain rate of the siloxane. The creep behavior is deformation of a solid material under a sustained load with time

[17]. The time-dependent material behavior of the creep like polymers is often referred to as viscoelasticity. The creep generally increases in materials as their temperature is close to their melting point. Based on the assumption, silicone degradation during this lifetime test of LEDs was quantitatively evaluated using finite element analysis. In order to compute creep strain rate of the silicone, the linear viscoelastic property of the silicone was measured and used for the FE thermal-mechanical simulation. The creep strain rate of the silicone polymer was computed in a predefined volume of interest (VOI). Furthermore, the correlation between the computed creep strain rates and lumen depreciation could be established, which lead to a lumen depreciation model using the viscosity effect of the silicone. Based on this model, the tendency of the lumen maintenance for LED packages could be estimated using numerical analysis without time-consuming tests.

18.3.1 Linear Viscoelastic Model of PDMS

PDMS has a viscoelastic property, which is used as lens or encapsulant for LED packages. The mechanical property of PDMS has a direct influence on results of finite element analysis because PDMS is our VOI. Similarly the linear viscoelastic property for finite element analysis has been used in the IC devices and packages. Van Driel et al. [18] adopted the linear viscoelastic property for the molding compound and die/attach materials to order to predict thermally induced deformations of electrical packages during packaging and testing processes. However, the linear viscoelastic material models for finite element analysis are not simple to be established. Jansen et al. and Sadeghinia et al. [19, 20] investigated changes in the viscoelastic behavior of an epoxy molding compound during the curing process. The material models depend highly on degree of cure. In this study, the curing effects for the viscoelastic behavior were neglected. This will be further work.

The material properties of PDMS were measured using dynamic mechanical analyzer (DMA). Isothermal modulus-frequency response and isofrequency modulus-temperature response were observed [21]. An example for isothermal modulus-frequency response is shown in Fig. 18.12. The x axis and y axis represent frequency and storage modulus. The storage modulus varies with frequency and temperature. Figure 18.12 shows that the storage modulus of PDMS increases as the frequency increases. On the other hand, the storage modulus decreases as the temperature increases. The other example for isofrequency modulus-temperature response is shown in Fig. 18.13. The x axis means temperature. The storage modulus dramatically decreases as the temperature increases. The highest slope in the graph is defined as glass transition region. When PDMS exists below the glass transition region, PDMS becomes hard and brittle like glass. Otherwise, PDMS becomes soft and flexible like rubber.

A constitutive equation of PDMS is based on a generalized Maxwell model which is the linear model for viscoelasticity. Figure 18.14 graphically shows a

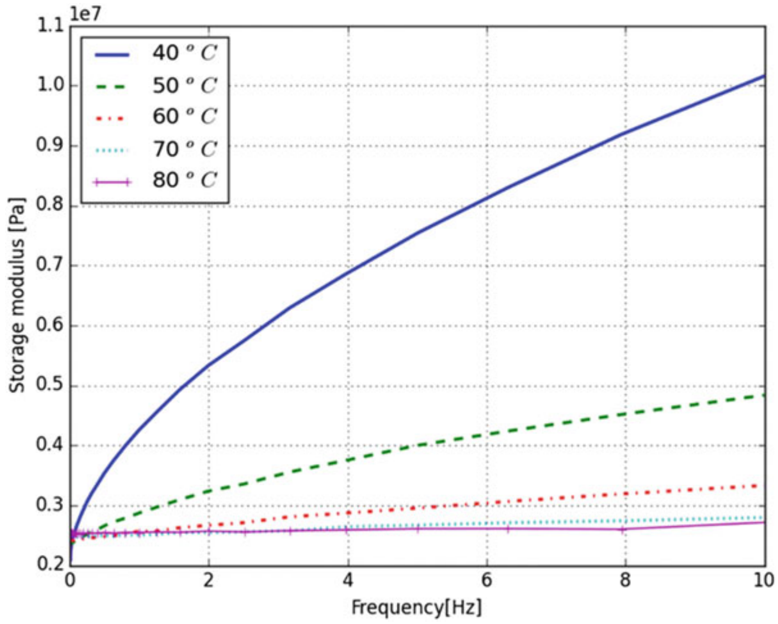

Fig. 18.12 Isothermal modulus-frequency response

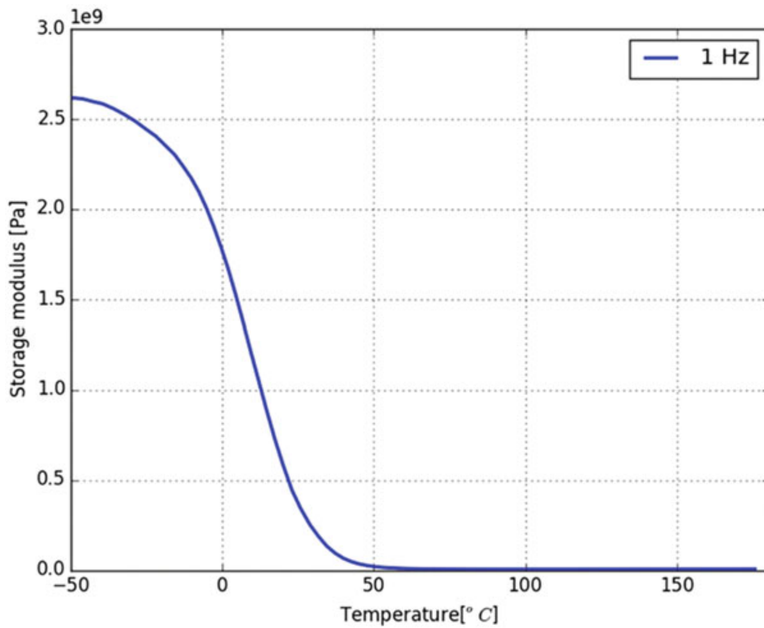

Fig. 18.13 Isofrequency modulus-temperature response

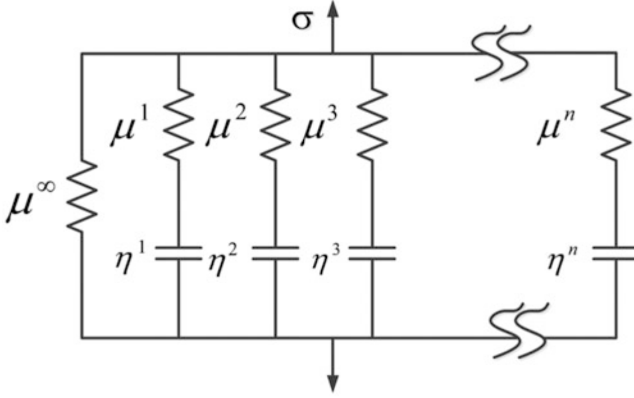

Fig. 18.14 Generalized Maxwell model in one dimension

one-dimensional form of a generalized Maxwell solid that is made up of a single spring element in parallel with a number of Maxwell elements. Each Maxwell element has a spring and a dashpot in series. μ denotes the spring stiffness and η represents the dashpot viscosity. The spring stiffness could be extracted from the isofrequency modulus-temperature response. The dashpot viscosity could be obtained from the isothermal modulus-frequency response and the isofrequency modulus-temperature response.

In three dimensions, the constitutive equation for the generalized Maxwell model is expressed as follows:

$$\sigma = \int_0^t 2G(t-\tau)\frac{de}{d\tau}d\tau + I\int_0^t K(t-\tau)\frac{d\Delta}{d\tau}d\tau \tag{18.5}$$

where σ is Cauchy stress, e is deviatoric strain, Δ is volumetric strain, and $G(t)$ and $K(t)$ are the Prony series shear and bulk relaxation moduli that are given by

$$G(t) = G_0\left[\alpha_\infty^G + \sum_{i=1}^{n}\alpha_i^G \exp\left(\frac{-t}{\tau_i^G}\right)\right] \tag{18.6}$$

$$K(t) = K_0\left[\alpha_\infty^K + \sum_{i=1}^{n}\alpha_i^K \exp\left(\frac{-t}{\tau_i^K}\right)\right] \tag{18.7}$$

where G_o and K_o are relaxation moduli when $t = 0$. α_i and τ_i are relative moduli and relaxation time [22]. These coefficients are calibrated using two measured responses from DMA. Moreover, the time-temperature superposition principle is applied in order to observe temperature-dependent behavior of the constitutive relations.

18.3.2 Finite Element Analysis

The volume of interest (VOI) is a portion of the silicone encapsulant made of PDMS. An LED package and the VOI are shown in Fig. 18.15. The VOI has 0.02 mm depth from the outer surface of the LED package. An assumption was made that the VOI is one of the most sensitive locations for lumen depreciation during the lifetime test. All rays generated from a LED chip must pass through the VOI to be detected. If the silicone degradation in the VOI gets worse as creep strains increase, the density of dimethyl siloxane groups of PDMS decreases. Turek et al. [23] investigated the effect of mechanical stress on the refractive index and the coefficient of absorption of PDMS. They discovered that changes of the refractive index of PDMS and coefficient of absorption of PDMS result from a change of the density of dimethyl siloxane groups. Changes of the optical and mechanical properties of PDMS could result to reduce the light extraction efficiency.

In order to compute a numerical quantity induced by viscosity effects in the VOI, the finite element analysis (FEA) was performed. Except for the encapsulant, the other materials were assumed to be linear elastic. As the analysis belongs to the weak-coupling analysis, steady-state thermal analysis was performed under the operation condition, and sequentially static structural analysis was completed to compute thermal stresses and strains for the VOI as shown in Fig. 18.16. In this study, the creep strains were defined as an increment of equivalent elastic strain in change of time as shown in Fig. 18.17. In the VOI, the creep strain was computed by employing volume averaging technique as follows:

$$\overline{\varepsilon}_{\text{creep}} = \frac{\sum_{e} \left(\varepsilon_{\text{creep}}^{e} \right) \times V_e}{\sum_{e} V_e} \tag{18.8}$$

where $\overline{\varepsilon}_{\text{creep}}$ is the volume averaging creep strain, e is the element number, and V_e and $\varepsilon_{\text{creep}}^{e}$ are the volume and the creep strain of the eth element. The element size in the VOI was 100 μm. The volume averaging technique was applied in order to reduce a numerical error in the VOI. Moreover, the creep strain rate was denoted as an increase of the volume averaging creep strain within a predefined period.

18.3.3 Lumen Depreciation Model

In LED lighting, evaluating lumen maintenance or lumen depreciation is a time-consuming task. If a LED package generates 100 lumens in the initial time, the package produces 70 lumens at 30,000 h. In this case, it is defined that the lumen maintenance and the lumen depreciation are 70% and 30% at 30,000 h. The criteria of lumen depreciation at certain time vary with a customer's requirement and

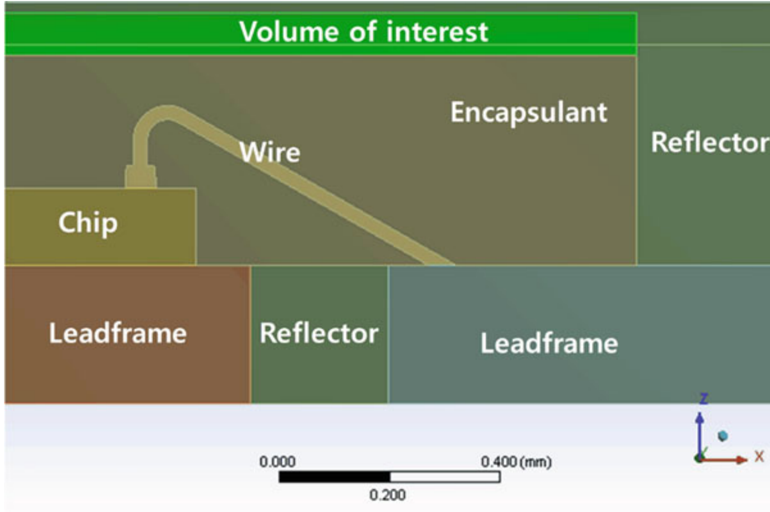

Fig. 18.15 Volume of interest for the LED packages

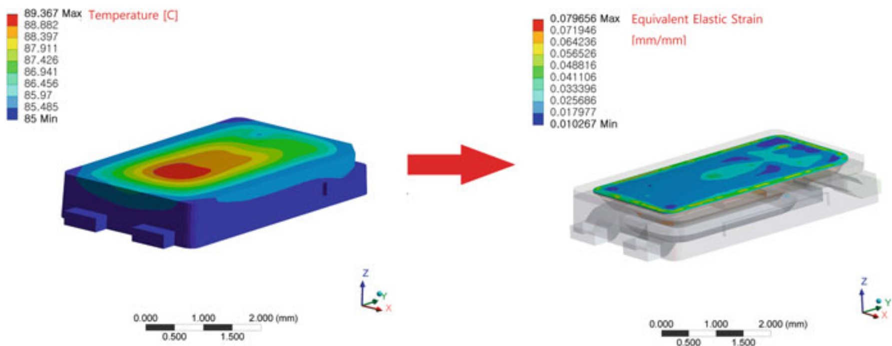

Fig. 18.16 Weak-coupling analysis using FEA

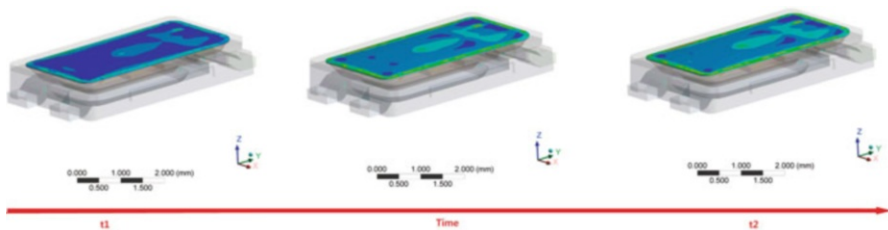

Fig. 18.17 An increment of equivalent elastic strain in change of time for VOI

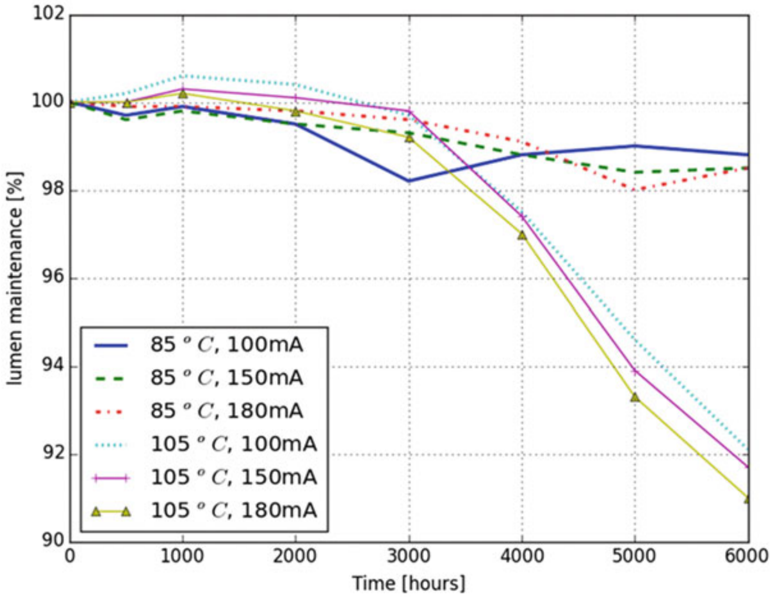

Fig. 18.18 LM-80 tests for six cases

applications. Generally, US Department of Energy (DOE) guides the LM-80 test method and the LM-80 test criteria for LED light sources, arrays, and modules. In this study, LED packages are focused and investigated. Six test conditions were prepared for the LM-80 test method, which varied with ambient temperatures and electrical currents for LED chips. Figure 18.18 shows the LM-80 test results for six test conditions. The ambient temperatures were 85 °C and 105 °C. The electrical currents were 100 mA, 150 mA, and 180 mA. Using these results, the amounts of lumen depreciation could be calculated.

Under above assumption for the lumen degradation, a correlation between the computed strain rate in the VOI and the lumen depreciation at 5,000 h was established according to ambient temperatures. When the ambient temperature is 85 °C or 105 °C, the R-square value is 0.91 or 0.96. Figures 18.19 and 18.20 show curve fittings.

Using the linear regression curves, lumen depreciation estimation models were defined as

$$\begin{aligned} \mathrm{LD}[\%] &= 4.083 \times 10^{44} \left(\Delta\bar{\varepsilon}_{\mathrm{creep}}/\Delta t\right)^{15.62} \quad T_{\mathrm{a}} = 85C^{o} \\ \mathrm{LD}[\%] &= 7.277 \times 10^{40} \left(\Delta\bar{\varepsilon}_{\mathrm{creep}}/\Delta t\right)^{14.68} \quad T_{\mathrm{a}} = 105C^{o} \end{aligned} \tag{18.9}$$

where LD is the lumen depreciation at 5,000 h and $\Delta\bar{\varepsilon}_{\mathrm{creep}}/\Delta t$ is defined as the volume averaged creep strain rate of the VOI, and T_a is the ambient temperature. Currently the models are limited in only one PDMS material. In order to generalize

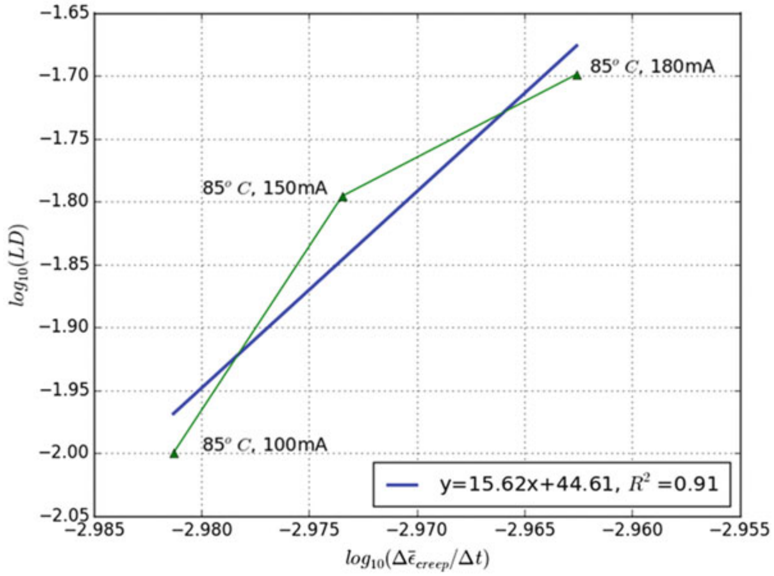

Fig. 18.19 Curve fitting when the ambient temperature is 85 °C

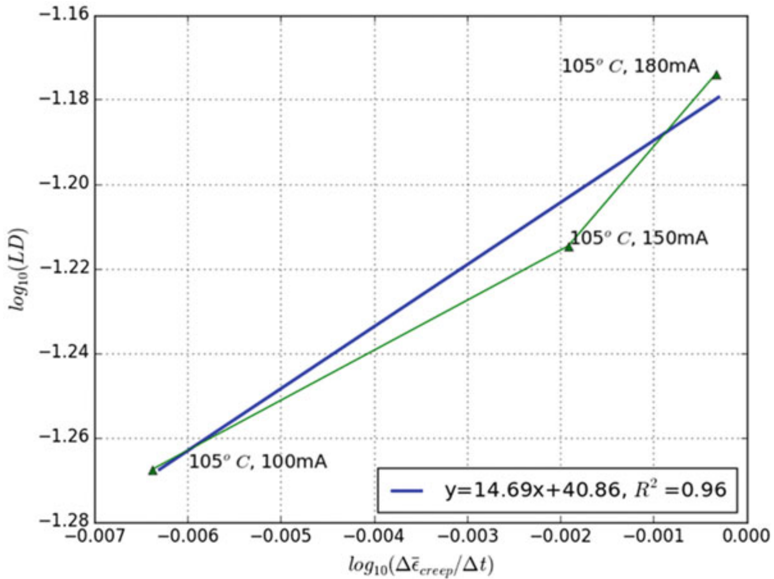

Fig. 18.20 Curve fitting when the ambient temperature is 105 °C

Table 18.4 Parameter ranges for the mechanical property of a reflector material

	CTE (ppm/K) [min, max]	Elastic modulus (GPa) [min, max]	Thermal conductivity (W/m-K) [min, max]
Design parameters	[12, 94]	[4.2, 18]	[0.37, 3.1]

this model, more experimental data are necessary in the change of PDMS materials and LM-80 test conditions. This will be further work.

18.3.4 A LED Package Design Example Using the Lumen Depreciation Model

The same problem in the Subsect. 2.2 could be considered in terms of the lumen depreciation. This lumen estimation model may be helpful for the LED manufacturers because the reliability of the silicone could be quantified without time-consuming experiments.

For this problem, the response surface methodology (RSM) was used to study the relationship between mechanical properties of reflector materials (or premold) and computed strain rates. Design parameters for the mechanical properties were defined as elastic modulus, coefficient of thermal expansion (CTE), and thermal conductivity. The range of each parameter was determined as shown in Table 18.4.

These ranges were used in a Box-Behnken design to generate the set of the required treatment combinations. The Box-Behnken design was generated by Minitab, which included 13 treatment combinations in order to create a response surface model for three parameters. The response surface model had an R-squared value of 99.99%. Using the response surface model, contour plots are shown in Fig. 18.21, which graphically shows the most sensitive parameter for the strain rate in the VOI is CTE. As CTE increases within the given range, the strain rate decreases.

Fourteen candidate materials were evaluated using the response surface model and the lumen estimation model as shown in Fig. 18.22. Among them, LED packages including Material#7 would be expected to have the best reliability during HTOL.

18.4 Conclusions

In this chapter, two methodologies have been developed to quantitatively evaluate fatigue life of wire bond and silicone degradation for LED packages using finite element analysis. For the wire bonding lifetime model, the volume averaging accumulated plastic strain was computed in the VOI. The computed values and

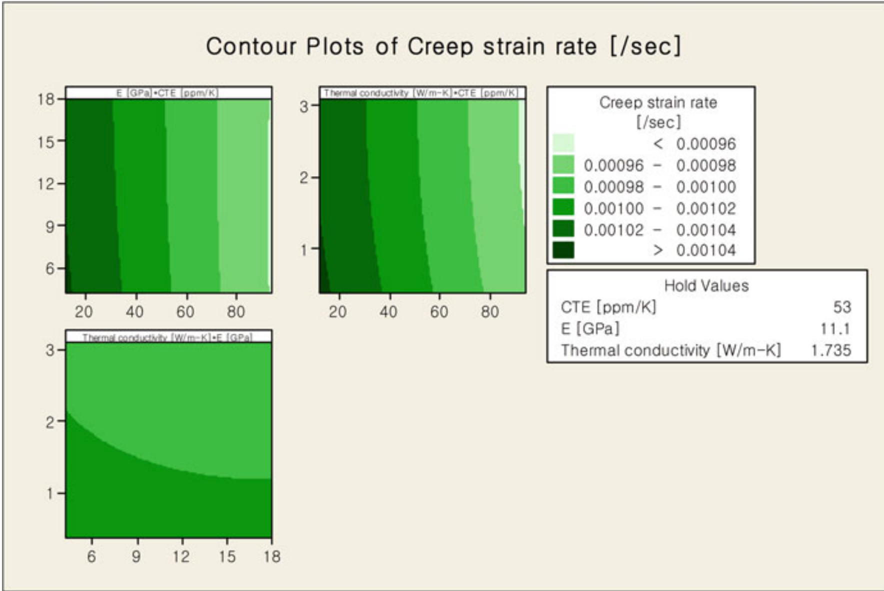

Fig. 18.21 Contour plots of strain rate using the response surface model

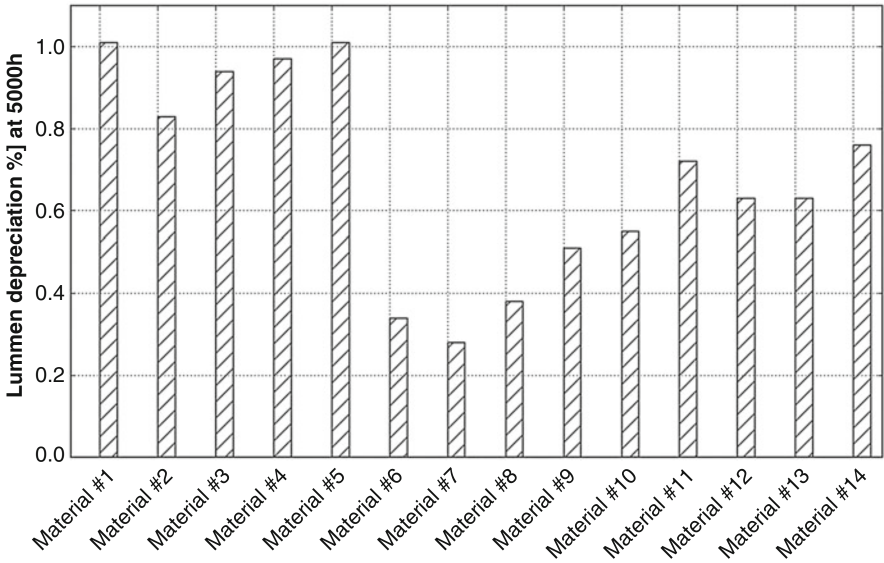

Fig. 18.22 Lumen depreciation using 14 reflector materials

the fatigue data were used to calibrate the model. For the silicone degradation, the strain rate induced by viscosity effects was computed in the VOI. Using the values, the lumen depreciation model was developed. Both models could be used to help LED manufacturers to make an engineering decision without time-consuming reliability tests. Currently the chapter focused two failure modes for corresponding reliability tests. In order to solve long-term reliability issues for LED packages, more numerical models for related failure modes would be necessary for LED manufacturers in order to reduce time to market (TTM).

References

1. J.F.J.M. Caers, X.J. Zhao, *Solid State Lighting Reliability*, ed. by W.D. van Driel, X.J. Fan. Failure modes and failure analysis (Springer, New York, 2013), pp. 111–184
2. M.G. Pecht, M.-H. Chang, *Solid State Lighting Reliability*, ed. by W.D. van Driel, X.J. Fan. Failure mechanisms and reliability issues in LEDs (Springer, New York, 2013), pp. 43–110
3. S.-U. Zhang, B.W. Lee, Fatigue life evaluation of wire bonds in LED packages using numerical analysis. Microelectron. Reliab. **54**, 2853–2859 (2014)
4. S.-U. Zhang, Quantification of silicone degradation for LED packages using finite element analysis. Microelectron. Reliab. (2015). doi: 10.106/j.microrel.2015.09.006
5. M. Ciappa, W. Fichtner, in *IEEE 38th IRPS*. Lifetime prediction of IGBT modules for traction applications (2000), p. 210–216
6. C. Hager, A. Stuck, Y. Tronel, R. Zehringer, W. Fichtner, in *12th ISPSO*. Comparison between finite-element and analytical calculations for the lifetime estimation of bond wires in IGBT modules (2000), p. 291–294
7. J. Bielen, J.J. Gommans, F. Theunis, *EuroSimE*. Prediction of high cycle fatigue in aluminum bond wires: a physics of failure approach combining experiments and multi-physics simulations (2006), p. 1–7
8. T. Matsunaga, Y. Uegai, in *1st ESTC*. Thermal fatigue life evaluation of aluminum wire bonds (2006), p. 726–731
9. L. Merkle, T. Kaden, M. Sonner, A. Gademann, J. Turki, C. Dresbach, M. Petzold, in *2nd ESTC*. Mechanical fatigue properties of heavy aluminum wire bonds for power applications (2008), p. 1363–1368
10. M.L. Spencer, R.D. Lorenz, in *IEEE IAS*. Analysis and in-situ measurement of thermal-mechanical strain in active silicon power semiconductors (2008), p. 1–7
11. M. Bahadur, A.W. Norris, A. Zarisfi, J.S. Alger and C.C. Windiate, in *6th International Conference on Solid State Lighting*. Silicone materials for LED packaging (2006)
12. Y. Ee, P. Kumnorkaew, R.A. Arif, H. Tong, J.F. Gilchrist, N. Tansu, Light extraction efficiency enhancement of InGaN quantum wells light-emitting diodes with polydimethylsiloxane concave microstructures. Opt. Express **17**, 13747–13757 (2009)
13. P. Zhao, H. Zhao, Analysis of light extraction efficiency enhancement for thin-film-flip-chip InGaN quantum wells light-emitting diodes with GaN micro-domes. Opt. Express **20**(105), A765–A776 (2012)
14. G. Camino, S.M. Lomakin, M. Lazzari, Polydimethylsiloxane thermal degradation. Part 2. The degradation mechanisms. Polymer **43**, 2011–2015 (2002)
15. G. Camino, S.M. Lomakin, M. Lazzari, Polydimethylsiloxane thermal degradation. Part 1. Kinetic aspects. Polymer **42**, 2395–2402 (2001)
16. S. Watzke, P. Altieri-Weimar, in *15th EuroSimE*. Degradation of silicone in white LEDs during device operation: a finite element approach to product reliability prediction (2014), p 1–5

17. A.P. Boresi, R.J. Schmidt, *Advanced mechanics of materials*, 6th edn. (Wiley, New York, 2002)
18. W.D. van Driel, G.Q. Zhang, J.H.J. Janssen, L.J. Ernst, F. Su, K.S. Chian, S. Yi, Prediction and verification of process induced warpage of electronic packages. Microelectron. Reliab. **43**, 765–774 (2003)
19. K.M.B. Jansen, C. Qian, L.J. Ernst, C. Bohm, A. Kessler, H. Preu, M. Stecher, Modeling and characterization of molding compound properties during cure. Microelectron. Reliab. **49**, 872–876 (2009)
20. M. Sadeghinia, K.M.B. Jansen, L.J. Ernst, Characterization of the viscoelastic properties of an epoxy molding compound during cure. Microelectron. Reliab. **52**, 1711–1718 (2012)
21. L.E. Nielsen, R.F. Landel, *Mechanical Properties of Polymers and Composites*, 2nd edn. (CRC press, Boca Raton, 1994)
22. ANSYS InC, ANSYS mechanical APDL Theory Reference: ANSYS Release 15.0, 2014
23. I. Turek, N. Tarjanyi, I. Martincek, D. Kacik, Effect of mechanical stress on optical properties of polydimethylsiloxane. Opt. Mater. **36**, 965–970 (2014)

Chapter 19
Corrosion Sensitivity of LED Packages

B.J.C. Jacobs, C. van der Marel, Willem Dirk van Driel, S.J. Lu, and X.P. Li

Abstract The penetration of solid state lighting applications is due to the promise of a low-cost reliable solution by means of application of low- and mid-power LEDs. These LED packages are manufactured by making use of new processes and materials which in principle introduces a series of known and unknown failure modes. Corrosion is a specific failure mode which limits the lifetime, and hence manufacturers realize that their package integrity needs to be improved. This chapter describes the sensitivity to corrosion of LED packages. In the first part, an introduction to chemical incompatibility is given. In the second part, different sources of corrosion are distinguished. The construction of LED packages and their vulnerability to corrosion is described in the third part. In the fourth part of this chapter, testing methods are reviewed and their effectiveness to simulate real-life conditions. A series of experimental setups is used to explore the behavior of LED packages in contaminated environments. A combined experimental–theoretical approach is used to describe the performance in certain conditions of pollution. This will be covered in the fifth part. The last part describes a list of classes of chemicals, often found in electronics and construction materials for luminaires that may affect LED performance and for this reason should be avoided for the design of SSL solutions.

B.J.C. Jacobs (✉) • C. van der Marel
Philips Lighting, High Tech Campus, Eindhoven, The Netherlands
e-mail: boudewijn.jacobs@philips.com; cees.van.der.marel@philips.com

W.D. van Driel (✉)
Philips Lighting, High Tech Campus, Eindhoven, The Netherlands

Delft University of Technology, EEMCS Faculty, Delft, The Netherlands
e-mail: willem.van.driel@philips.com

S.J. Lu • X.P. Li
Philips Lighting, Innovation Campus, Shanghai, China
e-mail: alan.sj.lu@philips.com; xiupeng.li@philips.com

© Springer International Publishing AG 2018

W.D. van Driel et al. (eds.), *Solid State Lighting Reliability Part 2*, Solid State Lighting Technology and Application Series 3, DOI 10.1007/978-3-319-58175-0_19

19.1 Introduction

SSL applications are now at the doorstep of massive market entry into our offices and homes. This penetration is mainly due to the promise of an increased reliability with an energy-saving opportunity: a low-cost reliable solution by means of application of low- and mid-power LEDs. These LED packages are manufactured making use of new processes and materials which will introduce a series of known and unknown failure modes [1–3]. Semiconductor failure modes are well described [4], but their relation to the quality and reliability of light is not well known. Corrosion of LED packages is a specific failure mode which presently limits their lifetime. While most failure modes of high-power LED packages are being understood [5, 6], these packages are quite robust against corrosion. However, LED package manufacturers realize that the package integrity of low- and mid-power LEDs needs to be improved to achieve comparable lifetimes. LED package performance strongly relies on its lumen depreciation in which the light source gradually but slowly degrades over time [7]. Besides lumen depreciation LED packages may degrade by a shift in color [8–10]. The presence of sulfur- and halogen-containing chemical compounds as well as chemically incompatible volatile organic compounds (VOCs) in LED-based solid state lighting designs may impair the performance and strongly reduce its lifetime. Even if measures are taken to avoid harmful substances in the proximity of electronic components, in general customers still experience corrosion issues. Gradually, manufacturers are gathering field experiences with this new failure mode and developing more robust LED packages. They acknowledge that the robustness against corrosion of low- and mid-power LED package needs to be improved to reach lifetimes similar to high-power LED packages.

Epoxy-based adhesives, elastomers, coatings, and potting compounds are examples of materials frequently used in the construction of luminaires. These products may also face degradation influencing the system lifetime [11, 12]. Additionally they often contain incompatible chemicals leading to a rapid decrease in luminous flux and noticeable shift in chromaticity on LED package level. In extreme cases the chemicals may even lead to a short or open electrical contact. In addition to chemical contamination due to outgassing, consideration must also be given to the environment in which the LED-based lighting solution will be installed and operated. While some degradation mechanisms of mid-power LED packages are described [13, 14], this chapter focusses on the influence of aggressive environments such as corrosive atmospheres, coastal climates, and chemical industry which negatively affect low- and mid-power LED light source behavior and service life.

19.2 Sources of Corrosion

Since LEDs are part of a system, they can be exposed to different environmental conditions. Presence of sulfur, halogens, and VOCs in the air may affect the reliability of LED components of the system. We may distinguish different sources of corrosion, as illustrated in the figure below (Fig. 19.1).

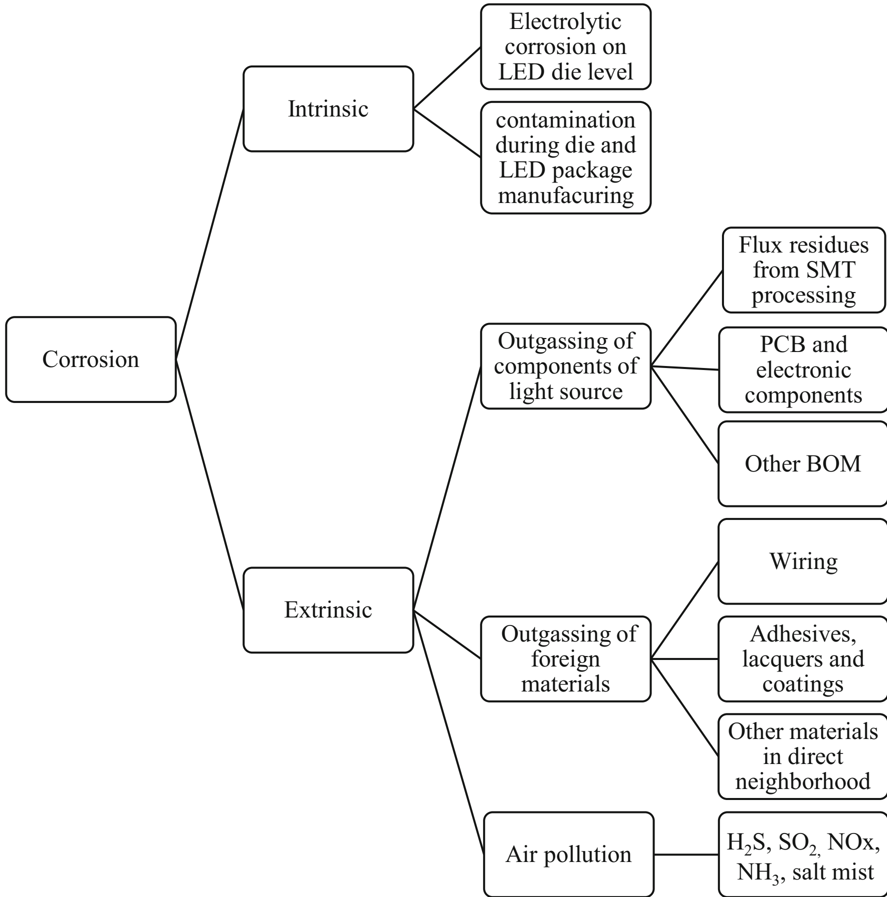

Fig. 19.1 Overview of different sources for LED corrosion

19.2.1 Intrinsic Corrosion

Intrinsic corrosion effects are found on different levels inside a LED package. Due to the permeability of the silicone resin for moisture, oxidizing substances, and corrosive gasses, the conducting ITO layer on LED die level may dissolve by electrolytic corrosion. As a consequence, metallic indium is separated and migrates through the LED mesa edge passivation layer leading to electrical shortage of LED p-n junction. One could question if this corrosion mechanism should be classified as an intrinsic or an extrinsic corrosion effect. For some LED packages however, the thickness of the passivation layer seems to be too thin to provide sufficient level of mesa surface protection which makes the surface of the LED mesa edge initially vulnerable to organic acids from the environment and causes local surface leakage channels with ongoing electrolytic reaction. For these specific LEDs, this failure

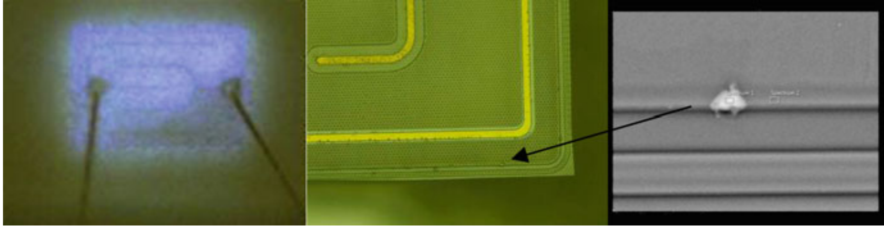

Fig. 19.2 Example of a de-capped MP LED package showing migration of metallic particles at mesa edges

mechanism is observed during exposure to normal humid environmental conditions and could for this reason be classified as intrinsic corrosion. As a result of long continuous surface leakage current flow, chemical reduction of ITO, and agglomeration of indium metallic residuals at the mesa edges, a low-ohmic leakage channel is created which causes a high leakage current. Hence LEDs fail to light up at a certain state of dimming during normal life. In Fig. 19.2, a mid-power (MP) LED package is shown with a leaky chip. During driving a clear dark corner on the bottom right of the chip can be observed. On the exact location, a bright dot at the mesa edge is found. The defects could easily be found with SEM. In almost all cases, the defects mainly consist of indium.

Another example of intrinsic corrosion is found to be caused by chemical residues on the lead frame due to the manufacturing process, either by transport and handling of the lead frames before silicone dispense or by the use of materials, tools, equipment, or process consumables containing typical chlorine or sulfur. Although chlorine may be present on the lead frame as contaminant during manufacturing, causing silver tarnish, it may not be able to detect presence of chlorine after a period of operation since chlorine gradually leaves the LED package as gaseous hydrogen chloride by diffusion. In the figure below, the lumen maintenance of a MP LED package is shown during a steady-state wet high-temperature operation test. Initially, chlorine was present at the surface of the Ag-mirror; the amount of chlorine can be expressed by the ratio of the surface concentrations of chlorine (Cl) over silver (Ag) (surface concentrations are concentrations in the upper few nm). In this case the initial concentration ratio Cl/Ag was larger than 10%. The figure shows that the products suffering from intrinsic corrosion do not follow a time-single-exponential lumen decay (dashed line) but tend to depreciate significantly faster after some time (solid line) (Fig. 19.3).

Also contaminated materials inside the LED, such as phosphors, silicone, or adhesives, could cause intrinsic corrosion. And PCB material, in particular CEM type, generally contains some small amounts of bromide. If, for instance, by diffusion, bromide reaches the silver-coated lead frame, it will lead to the formation of silver bromide, decreasing the reflectivity of the internal reflector and hence reducing the LED package lifetime.

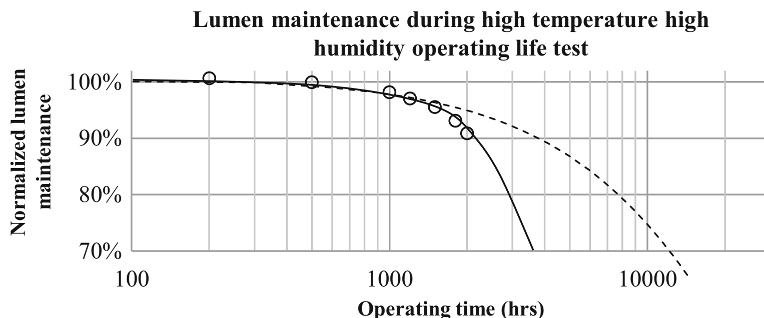

Fig. 19.3 Normalized lumen maintenance during high temperature and high humidity operating life test. The *dashed line* represents normal lumen maintenance behavior, while the *dots* and *solid trend line* represent behavior of MP LED packaging showing early wear-out by intrinsic chlorine corrosion

Even at room temperature, remnants of flux desorb significantly organic components like nitrogen-containing fatty acids. By consequence, a leaking path between flux remnants and the silver mirror in LED modules must be avoided.

19.2.2 Extrinsic Corrosion

Extrinsic corrosion can be split up by:

- Outgassing of components that are used in the product itself
- Outgassing of materials used in the direct environment of the lamp or luminaire
- Climatic air pollution

In general application guides from manufacturers of LED packages and LED-based lighting solutions describe the effect of extrinsic corrosion and give guidance to protect the product from this failure mode [15].

19.2.2.1 Corrosion by Components of Light Source

Due to the proximity of various components and materials in a system, the environmental chemical conditions of LEDs are often originating from the system itself. Especially at higher temperatures, aggressive substances like H_2S, halogens, as well as volatile organic compounds (VOCs) evaporating from materials like foam pads, rubber sealing, anti-vibration pads, or thermal conductive pads will affect the degradation of luminous flux in LEDs. Below results from gas chromatography mass spectroscopy measurements are shown during baking of a commercial available electronic transformer component. As can be seen from the figure, the release of bromide-, chlorine-, and sulfur-containing compounds is minimized to approximately zero, indicating that harmful corrosion effects could by minimized by baking this component for a certain time period (Fig. 19.4).

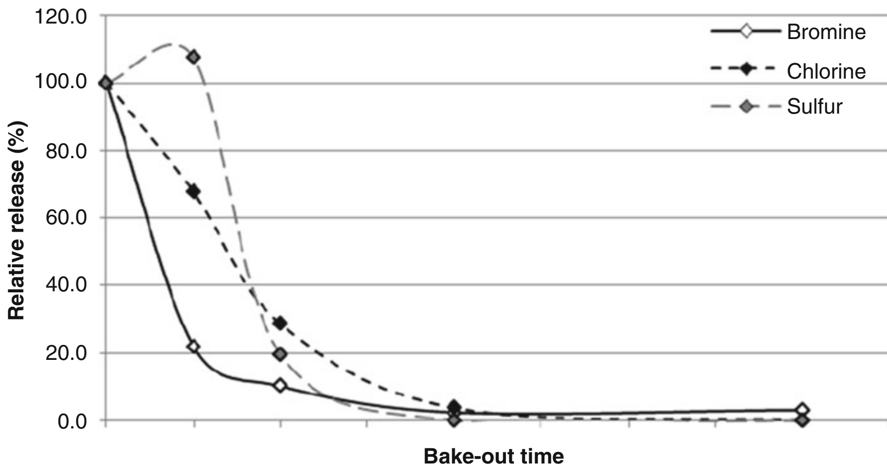

Fig. 19.4 The release of bromine, chlorine, and sulfur as function of bake-out time of an electronic transformer; the release is negligible after some time

19.2.2.2 Corrosion by Outgassing of Materials from the Environment

Local environmental contamination can be caused by materials that are used in the close neighborhood of the lighting system. Ceiling panels treated with a fungicide often contain iodine which negatively affects the reliability of LED packages in the system. LED manufacturers generally maintain a list of chemicals in their application guides and product description sheets that are often found in electronics and construction materials for luminaires that should be avoided. In § 19.6 more information on harmful chemicals can be read.

19.2.2.3 Corrosion by Air Pollution

Air pollutants as sulfur dioxide (SO_2), nitrogen dioxide (NO_2), hydrogen sulfide (H_2S), chlorine (Cl_2), and ammonia (NH_3) which are present in air promote corrosion of metals and need to be taken into consideration in the evaluation of corrosion resistance of products that are especially sensitive to corrosion failures such as electronic devices. Exposure tests in the presence of such air pollutants are therefore frequently used in the qualification of electronic products to determine the corrosion resistance.

Corrosion by air pollution is critical in case light sources are used in areas with moderate or high activities of industry or traffic. Air pollution is mainly caused by industry, traffic, power stations, heating systems, and waste disposal facilities. Moisture-rich environments are extra vulnerable.

19.3 Sensitivity to Corrosion by LED Package Design

In the interest of both protecting the LED chip and maximizing the light that is coupled out, all LED packages feature some form of encapsulation. Silicones are frequently used for transparent encapsulation. The silicone is added with phosphor as light converter material.

Silicones possess a high optical transparency, favorable mechanical properties, and thermal and radiation stability but are to some extent permeable for gases. Some VOCs and chemicals react with silicone and produce discoloration and surface damage. Other VOCs do not chemically react with the silicone material directly but diffuse into the silicone and oxidize during the presence of heat or light. Since silicone permeability increases with temperature, more VOCs may diffuse into and/or evaporate out from the silicone at elevated temperatures [15].

A typical high-power (HP) LED package contains a high brightness LED chip on a ceramic substrate. The ceramic substrate provides mechanical support and thermally connects the LED chip to a heat pad on the bottom of the substrate. An electrical interconnect layer connects the LED chip to a cathode and anode on the bottom of the substrate. In contrast to HP LED packages, low-power (LP) and mid-power LED packages consist of a silver-coated lead frame with polycyclohexylenedimethylene terephthalates (PCT), polyphthalamide (PPA), or epoxy molding compound (EMC)-based housing. Here, a LED die is glued to the lead frame and electrically connected to the lead frame with bond wires. The LED is casted with a silicone-based encapsulation to protect the die and wire bond. Refer to Fig. 19.5.

19.3.1 Package Integrity

In general, the sensitivity for corrosion of a LED package depends mainly upon the package integrity of the LED package. The figure below shows a cross section of a MP LED package (Fig. 19.6).

Possible passages of sulfur, halogens, and VOCs to reach the silver-coated lead frame are:

- Through the silicone (A)
- Interface mold compound and silicone (B)
- Interface mold compound and metal lead frame interface (C)

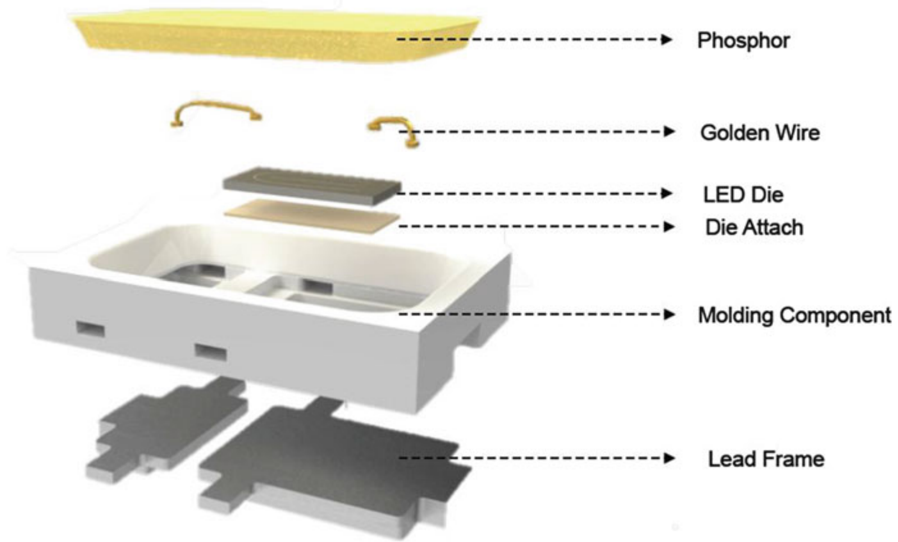

Fig. 19.5 Typical construction of a low- and mid-power LED package

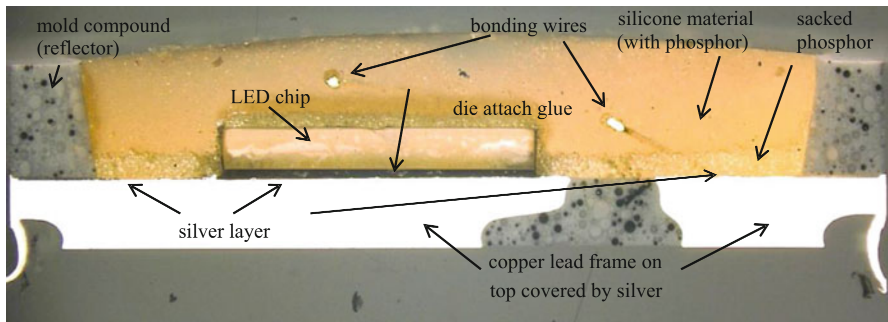

Fig. 19.6 Cross section of a typical mid-power LED package

An example of a passage along the mold compound and silicone (B) can be seen on the picture below. Clearly a gap is visible enabling corrosive gasses to penetrate into the package and attacking the silver layer very easily (Fig. 19.7).

Besides ingress of sulfur and halogens at locations of interlayer delamination and through the silicone, also diffusion of VOCs at the same locations should be considered.

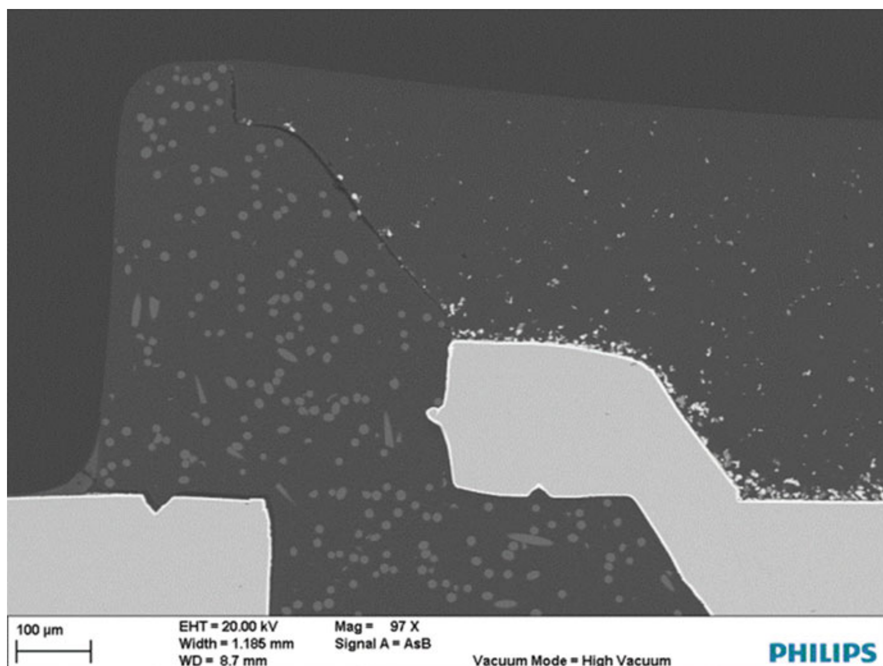

Fig. 19.7 Electron micrograph of a MP LED package cross section showing a clear passage to the lead frame by delamination along the mold compound and silicone

19.3.2 Corrosion-Sensitive Materials

Silver, being an excellent reflecting material, is used as a reflector on top of the lead frame to increase the amount of emitting light from the package. Silver is known to corrode quite easily, a phenomenon that is called tarnish. It is known that sulfur and halogens act as a catalyzer for this corrosion. Tarnish is the result of an oxidation reaction between a metal and some chemical in its environment. Unlike rust, which continues to eat away the underlying metal even after it has covered the metal's surface, tarnish continues to grow at a slower rate as soon as one mono-atomic layer has been formed. It forms a gray-black-colored patina, a layer of already-oxidized metal compound, known as silver sulfide (Ag_2S) that protects the remaining metal below it by excluding the oxidizing agent, preventing it from making further contact with the fresh metal. It forms when elemental silver (Ag) is exposed to hydrogen sulfide (H_2S), the gas responsible for the familiar "rotten egg smell" of organic sulfur compounds. When the two chemicals meet and also oxygen is present, they react. The sulfur breaks away from its two hydrogens to form two new covalent bonds with silver atoms. This makes silver sulfide (Ag_2S) and releases water (H_2O). Silver tarnish is caused by sulfur compounds, but oxygen or other oxidant compounds are necessary for the reaction to happen. The balanced equation is written below:

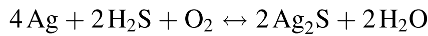

$$4\,Ag + 2\,H_2S + O_2 \leftrightarrow 2\,Ag_2S + 2\,H_2O$$

Silver can also be tarnished by exposure to chlorine (Cl_2). Other potentially harmful photosensitive compounds are iodine (I_2 or organic I –> AgI), bromide (Br_2 or organic Br –> AgBr), as well as organic acids (R-C=O-OH –> R-C=O-O-Ag).

These silver compounds all give rise – even *without* irradiation with light – to a cyclic reaction and corrosion of the silver-plated lead frame.

Below a picture is shown of a series of MP LED packages which suffered severe silver tarnish by H_2S. The high permeability of the silicone encapsulation allows H_2S gas to diffuse to the silver, even in a nonoperational state. The leakage of the lead frame is in this case not the primary cause of Ag-tarnish since for this particular LED package, H_2S reaches the silver surface much faster through the silicone than through the lead frame. The mechanically de-capped LED packages on the right clearly show that silver particles are migrated into the silicone (Fig. 19.8).

Corrosion of the silver plating of the lead frame may finally result in the destruction of the electrical contact between lead frame and the die by a lifting ball or wedge bond. Below a SEM picture of a wedge bond is shown of samples suffering from corrosion. On the wire clear traces of silver migration are visible (Fig. 19.9)

Manufacturers are constantly developing less sensitive LED packages by applying protective layers and less permeable silicones or are changing over to high-reflective mold compounds or application of gold finish instead of silver. As an example, the graph below shows the normalized lumen maintenance of a LED package containing a silver (solid line)- and gold (dashed line)-plated lead frame, respectively, during a binary gas exposure test showing a large improvement in lumen maintenance for the latter product (Fig. 19.10).

19.3.3 Hitting Probability on Surface

Lumen decay by corrosion of a LED package depends mainly upon the package integrity, the use of corrosive sensitive metals in the LED package, and their contribution to the reflectiveness of these metals to the total light output.

By determining the hitting probability on surface (HPOS) of the lead frame, one can determine its sensitivity for corrosion by design. The HPOS value represents the average probability that an emitted photon from the chip (epi-die) hits a particular surface area before it leaves the package. In Fig. 19.11 the left columns show the HPOS on the side wall reflector (plastic PPA/PCT/EMC), while the right columns give information about the HPOS on the silver-coated lead frame. Please note that the mentioned HPOS value is not valid for each commercially available

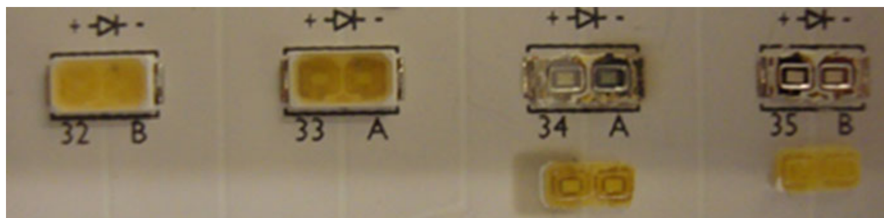

Fig. 19.8 Picture of MP LED packages with silver tarnish in which silver particles are migrated into the silicone

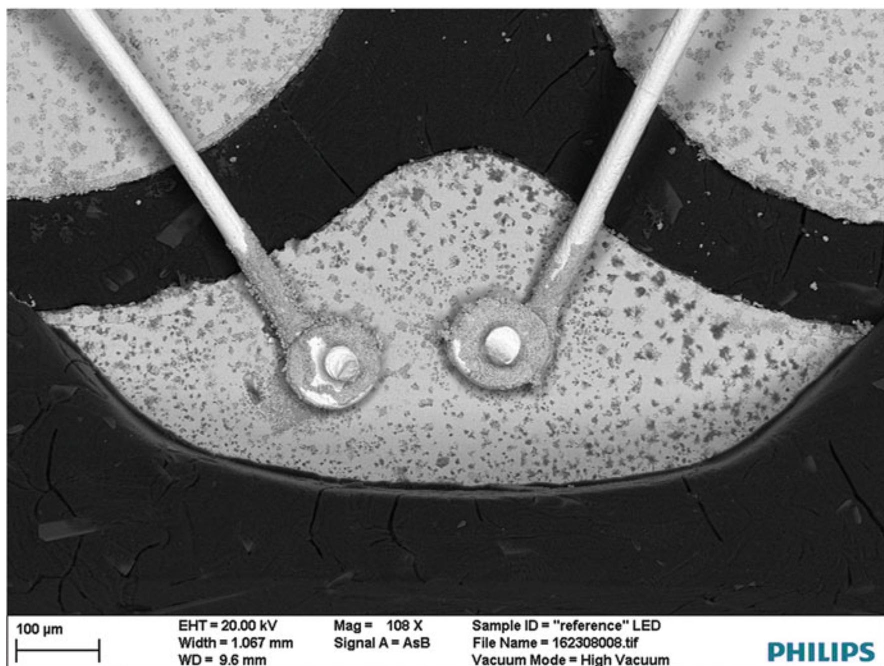

Fig. 19.9 Picture of a MP LED package showing silver migration effect on the wire bonds. The part of the gold wires close to the wire bond is covered with silver (*dark gray*)

LED package for the mentioned typical package sizes since the LED package design for a specific package size may differ per LED manufacturer.

From the figure above, one can conclude that, by design, the probability that the emitted light from the die for a specific 5630-package will hit the reflector is only very limited compared to the probability that the emitted light will hit the silver surface. This package is therefore very sensitive for the decrease in reflectivity of the silver layer but is less sensitive for the decrease in reflectivity of the plastic reflector. When comparing this package to 3014-size packages, one may conclude that this latter package suffers severe influence of photons hitting the reflector.

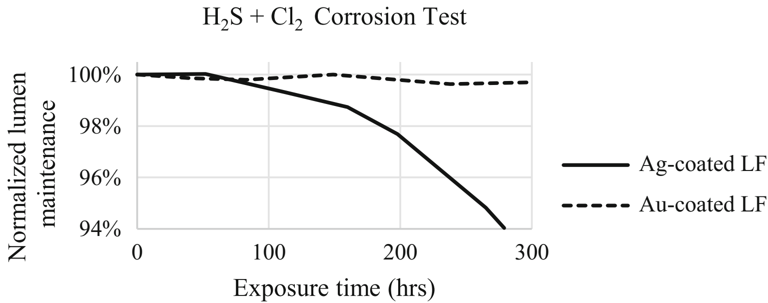

Fig. 19.10 Normalized lumen maintenance of a MP LED package with silver- (*solid line*) and gold (*dashed line*)-plated lead frame during a binary corrosion test

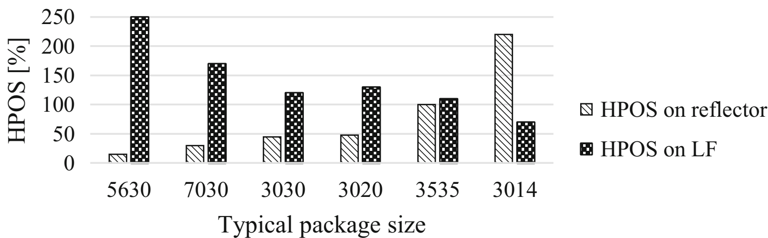

Fig. 19.11 Hitting probability on surface of the side reflector and lead frame of some typical MP LED package sizes

During qualification tests, it was observed that the dominant failure mode of this 3014-size package was indeed discoloring of the plastic material causing lumen decay and color change, while at the 5630-package, the observed lumen decay and color change was mainly caused by change of the reflectivity of the silver mirror.

19.4 Corrosion Test Methods

19.4.1 Standard Test Methods

Corrosion tests have been developed in the 1980s by researchers at Battelle Labs, Telcordia, and IBM by using gas tests to accelerate atmospheric corrosion and its effect on electronic applications [16]. A gas test is a laboratory test in which the temperature, relative humidity, concentration of gaseous pollutants, and other critical variables such as volume exchange rate and airflow rate are carefully defined, monitored, and controlled. The purpose of this test is to simulate corrosion phenomena due to atmospheric exposure. In early 1990s, professional organizations, including American Society for Testing and Material (ASTM), Electronic Industries Association (EIA), International Electro technical Commission (IEC),

Table 19.1 Mixed flowing gas test methods developed by IEC 60068-2-60 Part 2 [16]

Parameter	Method 1	Method 2	Method 3	Method 4
H_2S (10^{-9} vol/vol)	100 ± 20	10 ± 5	100 ± 20	10 ± 5
NO_2 (10^{-9} vol/vol)	–	10 ± 5	20 ± 5	10 ± 5
Cl_2 (10^{-9} vol/vol)	–	200 ± 50	200 ± 50	200 ± 20
SO_2 (10^{-9} vol/vol)	500 ± 100	–	–	200 ± 20
Temperature (°C)	25 ± 1	30 ± 1	30 ± 1	25 ± 1
R.H. (%)	75 ± 3	70 ± 3	75 ± 3	75 ± 3

and Telcordia, began to standardize these test methods and published corresponding documents as guidelines. The operational environments for electronic equipment in the atmosphere are divided into four classes, from least corrosive (Class I) to most corrosive (Class IV). Some examples of standard gas test methods are test methods developed by Battelle Labs, IBM, EIA-364-TP65A, Telcordia GR-63-CORE, and IEC 60068-2-60 Part 2. For the latter mentioned test method, the testing conditions are given in Table 19.1.

There is strong need to review existing mixed gas test specifications to determine their relevancy for silver-based corrosion mechanisms in relation to LED applications, specifically in a reducing sulfur environment. Understanding the relevancy of the test specifications and the potential need for modification requires a review of conditions in the field and an understanding of how the physics of the corrosion process changes with variation in these parameters.

Future versions of silver-oriented gas testing may wish to eliminate SO_2 gases and increase H_2S gas concentrations to potential maximum levels encountered in heavy traffic or industry-specific harsh environments. Single flowing gas at a well-defined concentration of H_2S, temperature, and relative humidity is the most common way to determine the corrosion sensitivity for low- and mid-power LED packages. Qualification tests, like IEC 62861, typically refer to the standard corrosion test method IEC 60068-2-43. Its derative standard JIS C 60068-2-43 (former JIS C 0092) differs from the IEC 60068-2-43 standard by describing an additional accelerated test condition at 40 °C at a relative humidity of 80%. Standard test method IEC 60068-2-42 is less favorable as gas test for LED packages since this test method does not include exposure to H_2S and for the additional reason that tests in which MP LEDs are exposed to SO_2 showed that the luminous flux is not influenced by exposure of this gas at concentration levels up to 25 ppm (Table 19.2).

Eventually salt mist tests according to IEC 60068-2-11 or IEC 60068-2-52 are proposed as an accelerated laboratory corrosion test simulating the effects of seacoast atmosphere on devices and package elements. Apart from electrochemical corrosive effects in metallic materials, these tests may be used to indicate deterioration of some nonmetallic materials by assimilation of salts.

Table 19.2 Single flowing gas test conditions of different standard corrosion test methods

Parameter	IEC 60068–2-42	IEC 60068–2-43	JIS C 60068–2-43	
H_2S (10^{-6} vol/vol)	–	10–15	10–15	
SO_2 (10^{-6} vol/vol)	25 ± 2	–	–	
Temperature (°C)	25 ± 2	25 ± 2	25 ± 2	40 ± 2
R.H. (%)	75 ± 5	75 ± 5	75 ± 5	80 ± 5
Duration (days)	4, 10, 21	4, 10, 21	4, 10, 21	

19.4.2 Accelerated Test Methods

Large efforts have been made to develop accelerated corrosion tests for the purpose of product qualification. As a result of this work, a broad spectrum of methods now exists of which some are also available as international standards, as mentioned above. However, some of those tests are intended only for checking the comparative quality of a metallic material with or without corrosion protection, while others may even be useful for predicting or estimating the long-term performance of a product with metallic materials when exposed to corrosive stress representing in-service conditions. Corrosion effects may appear at air volume fractions of pollutants less than 10^{-9}. The conduct of air pollutant corrosion tests, therefore, requires special test equipment.

For qualification of new materials and products with respect to corrosion resistance, accelerated corrosion tests generally need to be adapted during product design work. The higher the degree of acceleration of a corrosion test, the more favorable the accelerated corrosion test will be in keeping the required testing time short. On the other hand, a too large acceleration of the corrosion process may give rise to deviations from the naturally occurring corrosion processes. This makes clear the main problem in designing meaningful accelerated corrosion tests for product qualification. Identifying the most relevant method for testing the corrosion sensitivity of LED-based lighting solutions requires knowledge that usually goes beyond what you can get from a single standard.

In general, any accelerated model needs to be validated with test and real field data. For corrosion lifetime modeling, one should be very careful to assume a certain chemical reaction or physical diffusion process. Examining products from the field and comparing the corrosion rate with testing data should be done only in case the similarity of the failure mechanisms is proven. By closely studying the appearance of the surface of the corroded silver layer by means of SEM, one could verify the consistency of the layer structure and hence confirm or suspect similarity. The figure below presents micrographs of the silver-plated lead frame of mechanically de-capped LED packages. The left picture shows the corroded structure of a product after a corrosion qualification test, while at the right picture, the corroded mirror surface of a product from the field is presented. Here, the difference in structure of the corroded surfaces is unmistakable in which similarity of the failure mechanism should be questioned (Fig. 19.12).

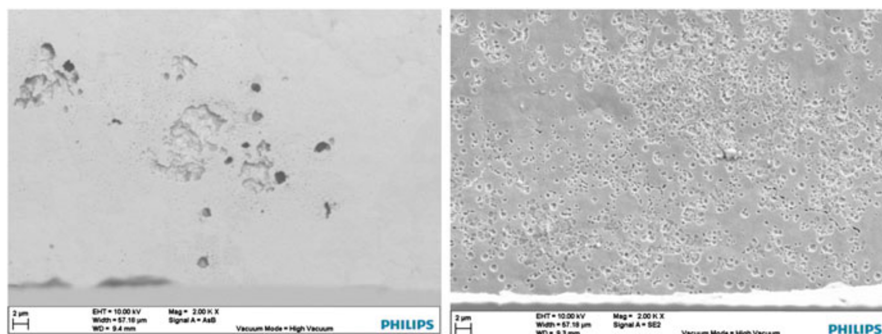

Fig. 19.12 SEM electron micrographs of chemically de-capped packages. Note the difference in appearance of the corroded mirror surfaces

In order to be able to conduct corrosion tests with a wide variety of concentrations and (combination of) types of sulfurous gasses, halogens, VOCs, or other gasses, LED manufacturers often develop nonstandard and specific testing methods for reasons of lifetime prediction and process optimization. By using power supplies and timers, also operational tests can be conducted and the influence of operational mode to corrosion sensitivity examined.

19.5 Test Results

Corrosion tests have been conducted to gain more insight in the sensitivity for corrosion of typical low-power and mid-power LED packages. At predefined time intervals, the product performance has been measured to be able to study time-dependent product changes. In this paragraph results of corrosion tests are summarized.

19.5.1 Sulfur Testing

Sulfur hydrogen (H_2S) is the main contributor for silver tarnish from sulfur-containing gasses. Below the test results are shown of several MP LED packages during a single gas test according to IEC 60068-2-43 with a volume concentration of approximately 15 ppm of H_2S in which the differences in corrosion sensitivity is obvious (Fig. 19.13).

From the test results, it has been found that the lumen maintenance can be best described by means of a time exponential curve fit function

$$\frac{\mathrm{dL}}{\mathrm{dt}} = -\lambda \cdot L$$

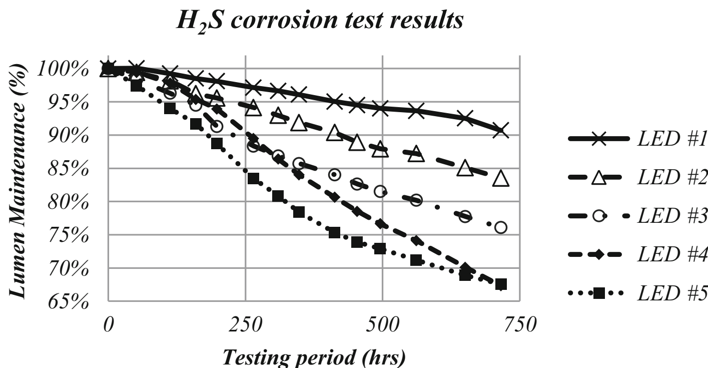

Fig. 19.13 Normalized lumen maintenance of five different LED packages during a non-operational single gas test at 15 ppm H_2S according to IEC 60068-2-43

where L is the normalized lumen output, t time, and λ (lambda) the exponential decay constant. The solution to this equation is

$$L(t) = B \cdot e^{-\alpha t}$$

Here $L(t)$ is the lumen output at time t, B is the initial lumen output, i.e., the lumen output at time $t = 0$, and α represents the decay constant.

To gain insight into the influence of the concentration of a corrosive gas to the level of silver tarnish, several additional corrosive gas tests have been conducted at different concentration levels. For every LED package and at each concentration level, the emission spectrum is being measured and lumen maintenance and color consistency calculated. This provides important information about the acceleration factor of a specific corrosion test to the conditions in which the LED package is being exposed in its application. In the figure below, the projected average lifetime L70 is shown at several stress levels of H_2S for a group of MP LED packages with different levels of corrosion sensitivity. Two outliers are visible representing a package containing an Ag-protective layer (Fig. 19.14).

Next to the concentration level of the corrosive gas, also the ambient temperature and the relative humidity influence the corrosion rate. It has been found that their relationship can be drawn by Peck's and Arrhenius' equation [17, 18], respectively.

Finally the package integrity for corrosion of LED packages is influenced by long-term storage or exposure to thermal shock or high humidity in which even the best virgin LED packages lose their robustness against corrosion. Hence this may be a concern for either products requesting long lifetime specifications or lighting applications in harsh environments.

High-power LED packages are less sensitive for H_2S exposure since the silver plating in the EPI is protected by a passivation layer during the wafer process. Corrosion tests on HP LEDs according to IEC 60068-2-43 showed negligible lumen depreciation levels after 21 days of exposure. However, when silver plating in HP LEDs is applied to increase internal reflectivity and hence optical efficacy, these

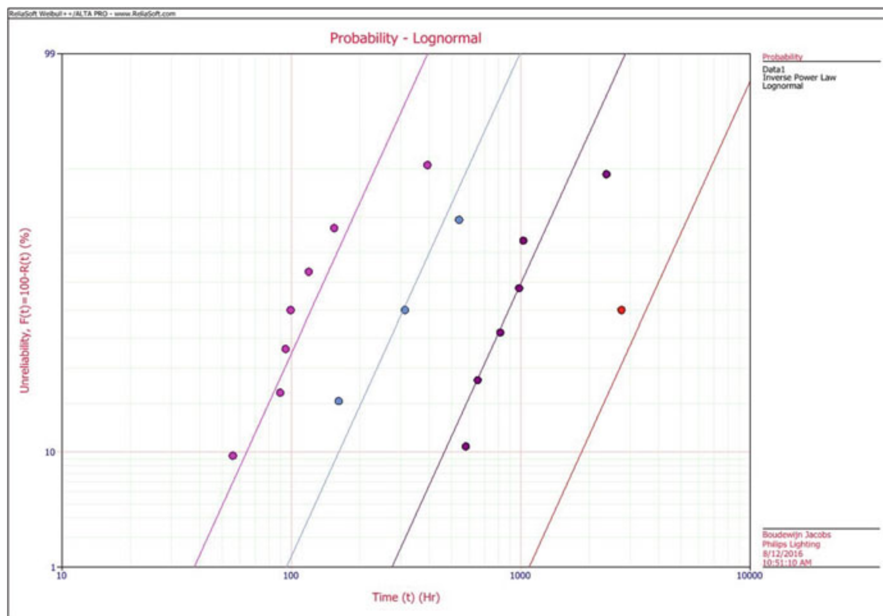

Fig. 19.14 Lifetime of typical MP LED packages at different concentrations of H_2S in air. The *dots* represent the probability of failure toward L70 at a certain time and concentration. H_2S concentration increases from *right* (*red dot*) to *left* (*purple dot*)

layers remain sensitive to corrosion as can be seen from the figure below. As stated earlier in this chapter, corrosion of the silver layer causes lumen maintenance issues and reduced adhesion of the wire bond attached to the corrosive surface potentially leading to high-ohmic or open electrical contacts. An example of a HP LEDs in which the silver layer has been corroded by H_2S is shown below (Fig. 19.15).

19.5.2 Testing with Halogen Gasses

Besides executing single gas exposure tests, also mixed gas test according to IEC 60068-2-60 is often used as qualification tests for new packages. The halogens or halogen elements are a group in the periodic table consisting of four chemically related elements: fluorine (F), chlorine (Cl), bromide (Br), and iodine (I). Binary tests may be useful to determine any cross talk or acceleration effect of corrosive gasses.

19.5.3 Testing with VOCs

LED manufacturers of high-power LEDs clearly mention the effects of exposure to chemically incompatible volatile organic compounds in their data sheet or

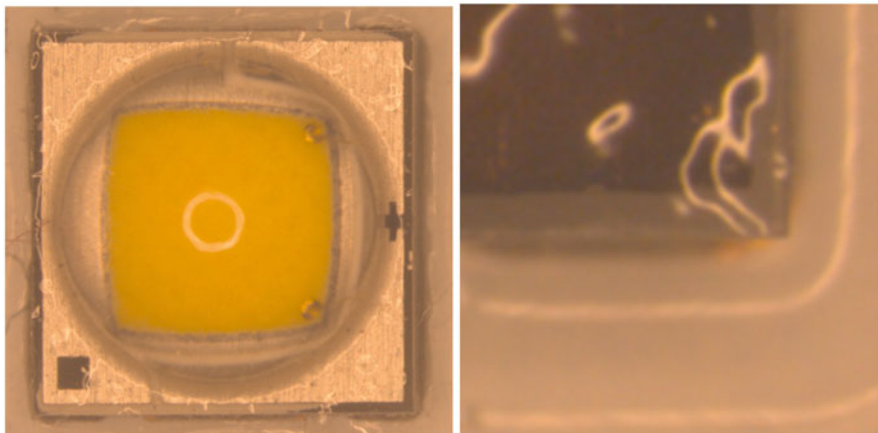

Fig. 19.15 An example of a HP LED package in which the silver-coated reflective layer has been corroded by H_2S (*left* picture = virgin, *right* picture = after corrosion testing)

separately published application notes concerning product packaging considerations and provide a list of commonly used chemicals that should be avoided as they may react with the silicone material to avoid discoloration and surface damage [15, 19–21]. For low- and mid-power LED packages, the effect of exposure to volatile organic compounds to the lifetime is however not widely explored. To investigate if specific commonly used organic compounds give rise to "darkening" of a MP LED package, several exposure tests have been conducted.

Below the results on maintenance tests of four different types of mid-power LEDs are shown after 100 h and 250 h of operating and nonoperational exposure testing to a typical VOC class.

From the figure below, we can see that for the selected class of VOC the lumen maintenance of LED type #4 does no seem to be affected whilst LED type 3 seems most vulnerable of all tested LED types, but in operational mode only (Fig. 19.16). On samples D16 and D17 the area underneath the LED die is clearly blackened suspecting interaction with the die attach glue. Hence it is believed that the generation of blue light seems necessary to trigger oxidation.

19.6 Harmful Chemicals

A list of classes of chemicals, often found in electronics and construction materials for luminaires that should be avoided, is provided in the table below. Although some LED manufacturers provide exhaustive lists of harmful chemical [19–21], please note that it is impossible to determine all chemicals that may affect LED performance.

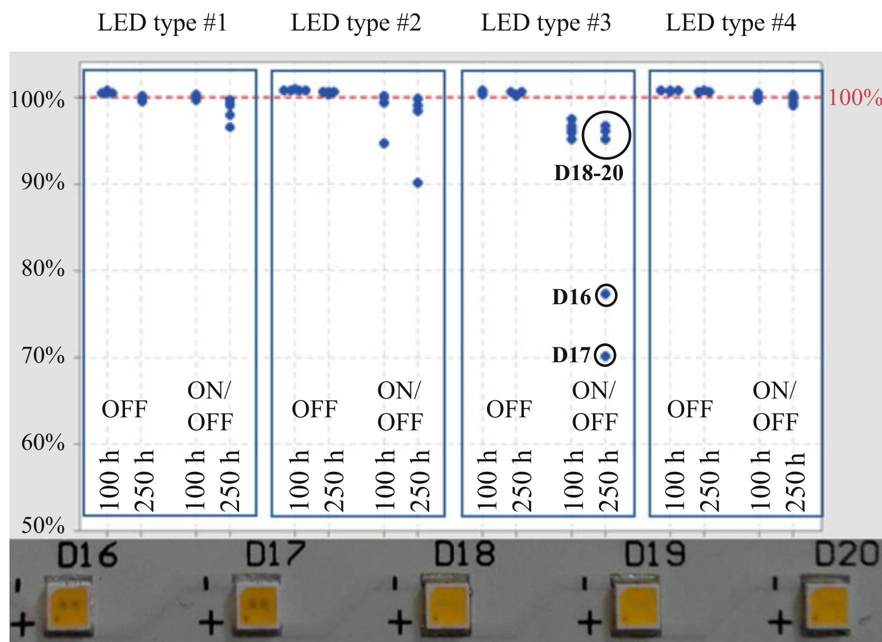

Fig. 19.16 Normalized lumen maintenance results during VOC exposure tests on several MP LED packages

Table 19.3 List of classes of chemicals hazardous for LED-based products [19–21]

Class	Typical hazardous compounds
Acids	Hydrochloric acid, nitric acid, phosphoric acid, sulfuric acid, phthalic acid
Hydroxides	Amines, potassium hydroxide, sodium hydroxide
Low molecular mass organics	Acetate, acetone, acrylate, aldehydes, dienes, ether, ethyl acetate, formaldehyde
Organic and aromatic solvents	Benzene, benzotriazole, butyl acetate, chloroform, chloromethane, glycol, ketones such as MEK, MIBK, toluene and xylene
Petroleum oils	Cleaning or oil-assisted cleaning oil, diesel, petroleum
Phthalic acid-based plasticizers	DOP, DEP, DNHP, DIP
Sulfur- and halogen-containing chemical compounds	H_2S and thiol-containing organic compounds, halogens like chlorine, fluor, bromide and iodine

In addition to chemical contamination due to outgassing, consideration must also be given to the environment in which the final product will be installed and operated. All possible environmental conditions therefore have to be taken into account when designing a LED luminaire (Table 19.3).

19.7 Conclusion

In this chapter, the sensitivity for corrosion of LED packages been discussed. Different sources for corrosion can be distinguished in which examples of both intrinsic and extrinsic corrosion are presented. The sensitivity for corrosion of a LED package mainly depends upon the package integrity and the use of corrosive materials inside the package. Possible passages for corrosive gases have been illustrated as well as the application of corrosion-sensitive materials inside the LED package. By design, LED packages become more sensitive for silver tarnish in case of a high probability of emitted photons hitting the lead frame before leaving the package.

From the standard single and mixed flowing gas test methods, the accelerated test conditions as mentioned in IEC 60068-2-43 and JIS C 60068-2-43 seem most appropriate to determine the sensitivity for corrosion for a low- and mid-power LED package. However, investigation of the morphology of the corroded surface may be necessary to verify consistency in the crystal formation to be able to reproduce the failure mechanism similar to the actual environment. Although HP LEDs are less sensitive for corrosion, an example of a high-power LED package bearing silver corrosion is shown.

From gas exposure tests, the relationship between the concentration of H_2S and the lifetime of the LED package has been shown. VOC tests showed that specific mid-power LED packages are more vulnerable for exposure to organic compounds than other and that in some cases the generation of blue light is necessary to trigger oxidation.

As a general guideline, a list of classes of chemicals is mentioned that should be avoided as they may affect LED performance.

References

1. M.H. Chang, D. Das, P.V. Varde, M. Pecht, Light emitting diodes reliability review. Microelectron. Reliab. **52**, 762–782 (2012)
2. S.D. Shepherd, K.C. Mills, R. Yaga, C. Johnson, J.L. Davis, in *Proceedings of the SPIE 9190*. New understandings of failure modes in SSL luminaires (2014)
3. R. Tuttle, *LED System Lifetime and Reliability: LED Components,* presented at Strategies in Light, Las Vegas 2015
4. JEP122F, *Failure Mechanisms and Models for Semiconductor Devices*, JEDEC Solid State Technology Association, South Arlington 2010
5. S. Watzke, P. Altieri-Weimar, in 2014 15th International Conference on Thermal, Mechanical, and Multi-physics Simulation and Experiments in Microelectronics and Microsystems. Degradation of silicone in white LEDs during device operation: a finite element approach to product reliability prediction (IEEE EuroSimE, Ghent, 2014)
6. M. Buffolo, C. De Santi, M. Meneghini, D. Rigon, G. Meneghesso, E. Zanoni, Long-term degradation mechanisms of mid-power LEDs for lighting applications. Microelectron. Reliab. **55**, 1754–1758 (2015)

7. W.D. van Driel, X.J. Fan, *Solid State Lighting Reliability: Components to Systems* (Springer, 2012), 617 pages, ISBN 978-1-4614-3066-7
8. J.L. Davis, K. Mills, M. Lamvik, R. Yaga, S.D. Shepherd, J. Bittle, N. Baldasaro, E. Solano, G. Bobashev, C. Johnson, A. Evans, in *Proceedings of the 2014 15th International Conference on Thermal, Mechanical, and Multi-physics Simulation and Experiments in Microelectronics and Microsystems*. System reliability for LED-based products (IEEE EuroSimE, Ghent, 2014)
9. J.L. Davis, Solid-state lighting luminaire reliability, presentation at Delft University, Delft, 2014
10. J.L. Davis, Color shift in LEDs and SSL luminaires, presentation at the 2014 DOE Solid-State Lighting Manufacturing R&D Workshop, San Diego, 2014
11. M.Y. Mehr, W.D. van Driel, G.Q. Zhang, Accelerated life time testing and optical degradation of remote phosphor plates. Microelectron. Reliab. **54**, 1544 (2014)
12. G. Lu, M. Yazdan Mehr, W.D. van Driel, X. Fan, J. Fan, K.M.B. Jansen, G.Q. Zhang, Color shift investigations for LED secondary optical designs- comparison between BPA-PC and PMMA. Opt. Mater. **45**, 37–41 (2015)
13. Huang J, Golubović DS, Koh S, Yang D, Li X, Fan X, Zhang GQ, Rapid degradation of mid-power white-light LEDs in saturated moisture conditions. IEEE Trans. Device Mater. Reliab. 99 (2015)
14. J. Huang, D.S. Golubović, S. Koh, D. Yang, X. Li, X. Fan, G.Q. Zhang, Degradation modeling of mid-power white-light LEDs by using wiener process. Opt. Express **23**, A966–A978 (2015)
15. Philips Lumileds, *Luxeon Rebel Platform Assembly and Handling Information,* Application Brief 20150330 (n.d.)
16. http://www.calce.umd.edu/TSFA/MFG.pdf, *Mixed Flowing Gas Testing Introduction and CALCE MFG Capability*
17. F. Jensen, *Electronic Component Reliability* (Wiley, 1995), ISBN 0-471-95296-6
18. W. B. Nelson, *Accelerated Testing: Statistical Models, Test Plans, and Data Analysis* (Wiley Series in Probability and Statistics) (1990), ISBN 0-471-52277-5
19. Osram, Preventing LED Failures caused by corrosive Materials, Application Note (2013), http://www.osram-os.com/Graphics/XPic1/00088375_0.pdf/Preventing
20. Samsung Electronics LED Business, Chemical guide of LED component (2013), http://www.samsung.com/global/business/businessimages/ led/file/product/lighting/201408/Application_Note_Chemical_Guide_for_LED_Component_Rev.1.3.pdf
21. Cree, Cree XLamp LEDs Chemical Compatibility, Support document CLD-AP63 rev 0A (2012), http://www.cree.com/led-components/media/documents/XLamp_Chemical_Comp.pdf

Chapter 20
Reliability Management of a Light-Emitting Diode for Automotive Applications

C. Jung and Th. Zahner

Abstract In the last years, the automotive industry are using more and more light-emitting diodes (LEDs) in automotive interior and exterior applications such as dashboards, ambient lighting, rear-turn indicator, daytime running light and head-lamps. Safety applications like drowsy driver warning or night vision systems are meanwhile already established in the midsize premium car segment. Not only visible LEDs but also infrared (IR) emitting LEDs and visible laser components are demanded from the market for new innovative light designs. Especially the design of headlamps and rear lights is established as distinctive feature for car set maker. The focus in this chapter is to give an overview about the reliability management for automotive LEDs and explain the benefits for automotive industry to get full support from LED manufacturer.

20.1 Introduction

Besides enabling novel lighting design features, LEDs are also economical priced, and even under the harsh environmental conditions that cars, trucks and motorcycles are subjected to, LEDs are expected to survive the coldest winters and the hottest summers and tolerate the associated temperature, humidity, vibration and other environmental impacts.

The ability of a LED to survive such extreme conditions depends on the materials and processes used to develop the LED, as well as on the know-how and experience of the LED manufacturer. In addition to it, the aim of the LED suppliers is to offer reliability support during the entire life cycle of a LED starting from product development via product release through to product and process change management, principally shown in Fig. 20.1.

The LED reliability starts with the product development phase where the borders of the LED design, material and process are evaluated during the project launch process. One of the most important steps is the validation of the LED reliability by

C. Jung (✉) • T. Zahner
OSRAM Opto Semiconductors GmbH, Leibnizstr. 4, 93055 Regensburg, Germany
e-mail: Christian.Jung@osram-os.com; Thomas.Zahner@osram-os.com

© Springer International Publishing AG 2018

W.D. van Driel et al. (eds.), *Solid State Lighting Reliability Part 2*, Solid State Lighting Technology and Application Series 3, DOI 10.1007/978-3-319-58175-0_20

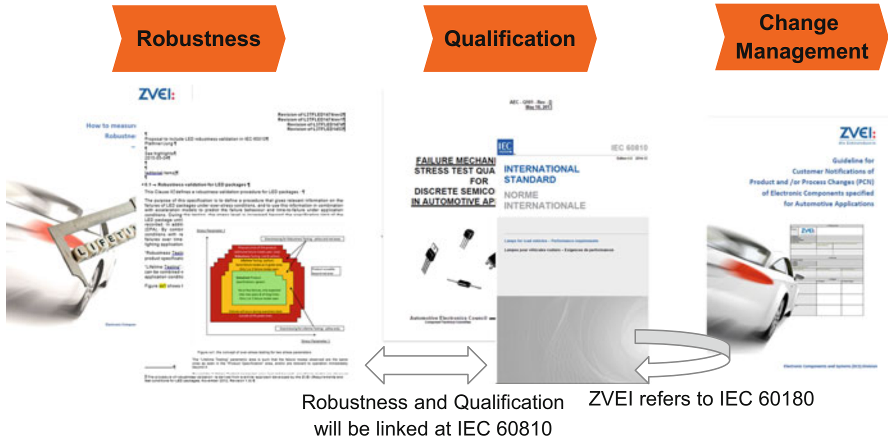

Fig. 20.1 Reliability cycle of a LED for automotive application

performing accelerated reliability life tests. The target of these tests is to gain all relevant information on possible degradation mechanisms of a LED package under overstress conditions. Accelerated stress tests are performed exceeding the specification of the product datasheet in order to detect significant deviations of LED key parameters (e.g. light, forward voltage or colour shift) or simply to provoke catastrophic failures. In combination with the appropriate acceleration model, it is possible to predict the failure behaviour and time to failure under application conditions. In the first section of this chapter, the principle of acceleration life testing and the strategic benefit for the automotive industry are explained briefly.

The LED reliability mainly covers the process of LED automotive qualification testing. The second section of this chapter explains why the automotive industry still requires a LED product qualification and provides an update on the current status of automotive standard. The process flow of LED qualification testing by referencing to the IEC 60810 [1] is explained in detail, and a guidance to the user will be given.

Due to extensive and expensive tests for car maker, the design-in period of new LED technologies in automotive applications is very long compared to other industries. Therefore the typical use of LEDs in automotive applications is about 5 years. For this reason, it is important that any improvement or change to the product or process will be communicated by the LED manufacturer to relevant parties by process or product change notification (PCN). The change management process is regulated by the German Electrical and Electronic Manufacturer's Association (ZVEI) and is direct linked to the automotive qualification acc. to IEC 60810 in case if the retesting of the LED package is required.

[1]IEC 60810, Lamps for road vehicles – Performance requirements, Chap. 8 "Requirements and test conditions for LED packages".

20.2 Accelerated Life Testing

The aim of accelerated life testing is to test the performance of a new product in a short time in order to realize that the product is operated at a high stress conditions, which are much higher than the usual operation conditions. Especially for products with a short development time and high lifetimes at application conditions such kind of tests are necessary to prove product capabilities. Usually these tests are carried out with a small number of samples.

Although this may seem simple, one has to understand the physics of the product to select the right stress conditions (see Fig. 20.2).

First of all one has to find the possible stress test conditions for an accelerated life testing beyond the applications' conditions. Besides experience this can be done by looking at the material properties and limits used to build up the product. Experiments may be required to derive these limits. Once these limits and failure modes are understood, one has to do a physical failure analysis in order to see that the application also under accelerated stress conditions shows the same failure mode. If one exhibits a different failure mode, the overstress conditions are reached.

As an example Fig. 20.3 shows experimental test results of a high-power LED. Here the test at 55 °C at 1,5A and the 85 °C at 1,5A conditions are considered to be application like conditions, whereas the test at 125 °C at 1,5A is an accelerated test. After that an acceleration factor

$$A_{\mathrm{f}} = \frac{t_{\text{low stress}}}{t_{\text{high stress}}} \tag{20.1}$$

between different stress conditions can be determined from the data (green and red arrow) to estimate the degradation curves at lower stress conditions.

Based on several acceleration factors between different stress levels, an acceleration function can be derived. The **acceleration function $A_{\mathbf{f}}$** allows the calculation of the acceleration factor between any low stress and high stress condition and

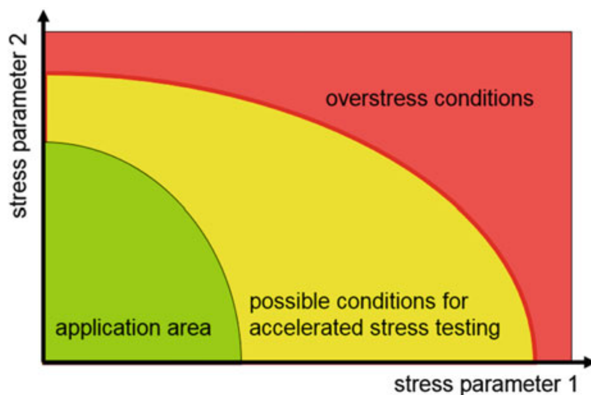

Fig. 20.2 Concept of accelerated testing for two stress parameters showing the different areas of LED operation

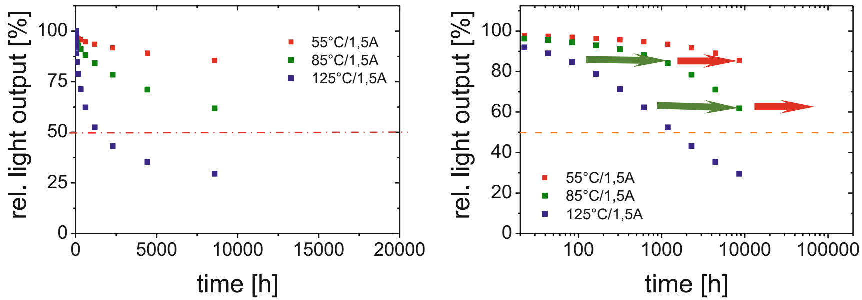

Fig. 20.3 High temperature operating life (HTOL) testing data of a high-power LED at different stress conditions in a linear and a logarithmic time scale

is an essential ingredient in any lifetime model. For a given type of stress (e.g. temperature), a specific function is chosen that depends on the relevant **stress variables** (e.g. junction temperature and forward current). The acceleration function contains parameters (e.g. activation energy) that need to be determined experimentally. These parameters reflect the specific ageing mechanism of a given LED.

Quite often temperature-accelerated tests can be described by the commonly used and relatively simple but relatively realistic Arrhenius equation. However for LED light output degradation specifically the junction temperature T_J is the temperature which is important not the ambient temperature or the temperature at the LED package:

$$A_f = \exp\left(\frac{E_A}{k_B} \cdot \left(\frac{1}{T_J} - \frac{1}{T_{J0}}\right)\right) \tag{20.2}$$

Where E_A is the activation energy and κ_B the Boltzmann's constant, T_J is the junction temperature at low stress (in Kelvin), and T_{J0} is the junction temperature at high stress (in Kelvin).

Accelerated life testing is performed in the early phases of the development process. It is a good method determining possible failure mechanism or limits of a new product. Besides that it allows to set up lifetime models on the recorded data basis. In the end it reduces significantly the development time (time to market) and costs for reliable products.

20.3 Automotive Qualification Process

20.3.1 Motivation

Not all LEDs in the market are suitable for automotive applications. In order to differentiate automotive-qualified LEDs from all other LEDs, it is common practice

to require automotive LEDs to pass a very specific set of tests. The tests are designed to verify the outer boundaries of the product specification but testing within the specification limits. A LED package is considered "automotive qualified" on component level at laboratory environment if the tested devices fulfil the requirements under the defined criteria, i.e. a "test-to-pass" approach. The testing of LEDs to these environmental conditions requires highly specialized equipment, making the procedure relatively expensive and time-consuming. The market has accepted that standardized test methods are needed to enable the LED manufacturers to optimize the test procedures and, at the same time, to ensure the LED customers can have high confidence in the test results.

The United States Council for Automotive Research (USCAR) committee started work on a test procedure for the overstress testing of LEDs [1], i.e. testing the LED beyond the specification limits to provoke failures (test to failure). This overstress testing is required to get information about the failure mechanism of the product and is including the accelerated testing approach presented in Sect. 20.1.

20.3.2 Automotive Qualification Standards AEC Q101/IEC 60810

LEDs were tested according to the standard established by the Automotive Electronics Council, AEC Q 101 – "Stress Test Qualification for Automotive Grade Discrete Semiconductors" [2]. Some of the tests defined at AEC Q101 are not suitable for LED components, and the stress conditions in terms of temperature range, environmental conditions and forward current regime differ from discrete semiconductor devices. LEDs are considered to have long life times and a very low failure rate in the sub ppm regime. Also the typical ageing mechanism of LEDs is different compared to silicone-based discrete semiconductors. For LEDs the most significant degradation mode is the continuous depreciation of light over time, whereas for discrete semiconductor devices the catastrophic failure is the limiting factor. OSRAM Opto Semiconductors found that AEC Q101 is appropriate for silicone-based semiconductors, but it does not deal with the specifics of light-emitting III–V semiconductors.

To focus on the issue of qualification of light-emitting semiconductors, an initiative was started at the International Electrotechnical Commission (IEC) to develop an international standard for the qualification testing of LEDs for automotive applications. The expanding functionality in automotive lighting applications, like adaptive driving beam, increases the necessity for such standards. Even though AEC Q101 has recently been updated (from the C-version to the D-version) [2], there are still many significant differences between testing of LEDs and silicon semiconductors devices. The IEC standard addresses the specific issues that are relevant for LED.

The basis for the IEC work for defining the qualification tests of LEDs for automotive applications was the document published by the Automotive Electronics Council, AEC Q101. Especially the referenced Joint Electron Device Engineering Council (JEDEC) test standards were also used by the IEC committee for defining the test procedures.

The LED qualification test is already published as a new part of the existing standard IEC 60810:2014 Ed. 4 “Lamps for Road Vehicles – Performance Requirements” [3]. The related part for LED components qualification can be found in Sect. 20.4.8. “Requirements and test conditions for LED packages.”

Although many aspects could be taken over from the AEC Q101 testing experience for silicone semiconductors, many LED specific definitions and criteria had to be defined at IEC level.

20.3.3 Why Do We Need LED Qualification?

The qualification defines the final release of a LED package within the product launch process at LED manufacturers and validates the minimum requirements for automotive exterior and interior applications and makes it visible to the customer. Since existing automotive qualification standards as AEC Q101 Rev. D and IEC 60810 give a clear guideline to LED manufacturer how to perform the reliability tests, car makers (OEM) and set makers (Tier 1) achieve a comprehensive and comparable set of benchmarking data from their LED suppliers. This is one reason why car makers and set maker strongly request from their LED suppliers a complete automotive product qualification, even if the boundaries of the LED have been investigated thoroughly by performing accelerated testing during the robustness validation within the product launch process.

Another reason definitely is that different automotive lighting applications may have different requirements. For example, a LED for a headlamp application which is close to the engine compartment will be exposed to very high temperatures, whereas a LED used for a rear turn indicator may not be exposed to such high temperatures.

Figure 20.4 explains briefly how a LED qualification can help OEMs and set maker to choose the right LED with the required performance. The red and blue square shows a schematic specification range for two LED types. This specification is validated by qualification tests at the corner points. The two star symbols represent the requirements (mission profiles) for two different automotive applications, A and B. It can be seen that LED type 1 is suitable only for application A, whereas LED type 2 is suitable for applications A and B.

The qualification testing is intended to validate the specification range for an automotive product. If the test conditions are chosen to represent the corner points of the specification range, and if all tests are passed, then it can be assumed with a particular confidence level that the LED is suitable for automotive applications that lie within the product specification.

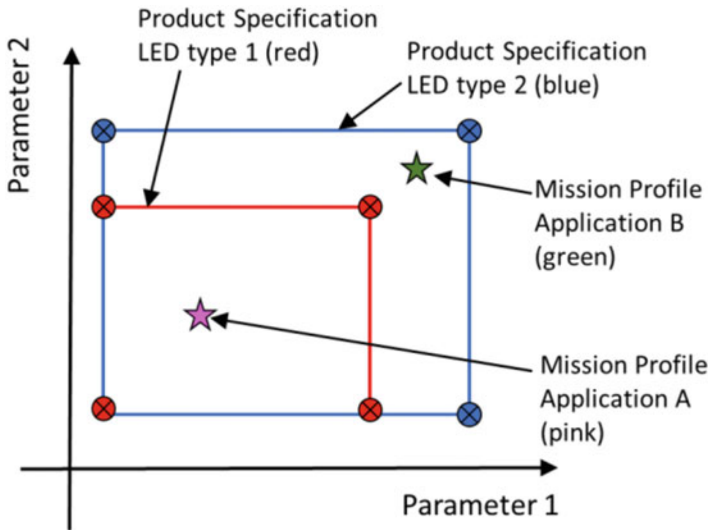

Fig. 20.4 Schematic representation of two LED product specification and two application mission profiles depicted as *pink* and *green star* symbols

20.4 LED Qualification Testing According to IEC 60810

In this section the minimum requirements for automotive qualification according to the IEC 60810 will be described, and additionally some background information about the performed tests are given. This section will only provide a short guidance through the IEC standard and therefore cannot offer insights into all tests and test conditions in detail.

The purpose of the LED package qualification is to make sure that a LED passes the minimum stress requirements and is expected to have a certain level of reliability in automotive lighting applications. The IEC 60810 standard is valid for visible and infrared LEDs but does not currently cover detectors/photodiodes or laser diode packages. The chart in Fig. 20.5 shows the exemplary process flow of the automotive qualification testing.

In the following sections, the qualification process flow in Fig. 20.5 will be briefly explained with practical guidance for its use.

20.4.1 Sample Selection and Family Definition of LED Packages

It is understood that all samples for qualification testing must be produced on mass production tooling according to production processes at the LED manufacturer site and no laboratory samples shall be used. The qualification samples are supposed to

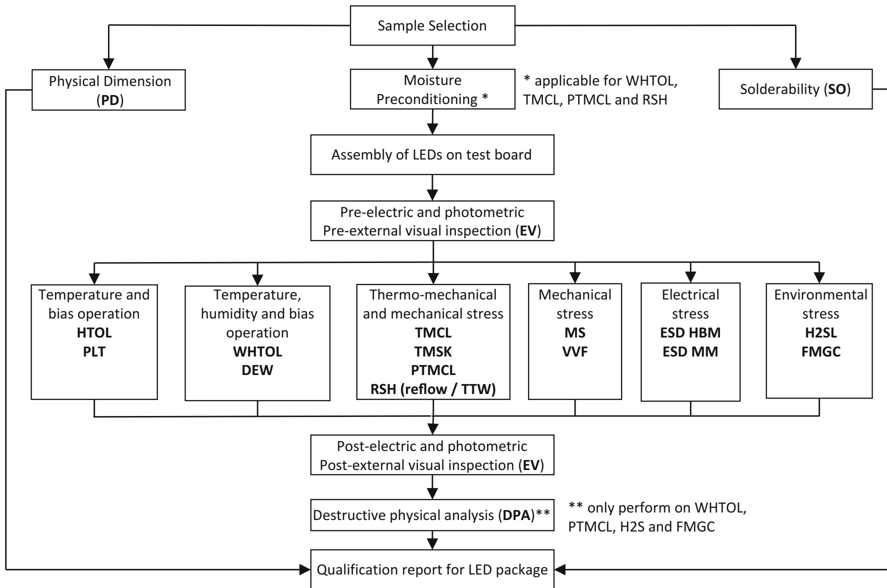

Fig. 20.5 Schematic process flow of the automotive qualification testing according to the IEC 60810 standard, Chap. 8

reflect the final released product status with final design and materials. Further changes on product and/or process have to be reported according to the ZVEI guideline for customer notification for automotive applications which is described in detail in Sect. 20.3 of this chapter.

Unless specified otherwise in total a sample size of minimum 78 LED packages from 3 different batches with 26 pieces each shall be used. The number is guided by the AEC Q101 Rev. C requirement of 77 pcs and must be divisible by three. Based on the statistics, the sample size of 3×26 is not suitable to detect a failure rate in a 10 parts per million (ppm) regime, but it provides the safety for failures of <0.2 % with 90 % confidence level and prevents imminent production downtime at set maker assembly lines.

In order to reduce the effort at qualification testing, a family approach is offered, but the current official version of IEC 60810 edition 4.0 gives no explicit guidance for such a family approach. At the moment international automotive experts of the GTB [2] working group of light sources discuss a first proposal. In the next step, this family approach will be submitted to the IEC SC 34A work group to start the comment draft for voting (CDV). This new proposal of a family classifies major key characteristics of the LED package such as:

[2]**G**roupe de **T**ravail "**B**ruxelles 1952".

- Package material (e.g. premould, ceramic, epoxy, etc.) and design
- Casting material (e.g. silicone, epoxy)/lens material/window on top
- Conversion technology (e.g. layer transfer; sedimentation volume conversion)
- Interconnect die attach (e.g. glued, bonded)/wire bond
- Chip technology (e.g. InAlGaP, InAlGaN, InAlGaAs, Sapphire, etc.) regardless of colour

LEDs belong to a family if all major key characteristics are the same. If there is any deviation in the key characteristics, the results of the qualification cannot be transferred.

A transfer of qualification test results is theoretically possible in case that:

- Phosphor CCT is the same or has better performance.
- Chip size/number of chips in LED package is the same, current density is the same or smaller and the current density is scalable by size of active area.

For a family qualification the selected three batches shall represent the whole variety of the LED product family.

20.4.2 Moisture Preconditioning and Assembly of LED Packages

To ensure safe handling, the LEDs may need to be assembled on suitable printed circuit boards (PCB), e.g. FR4 or metal-core PCBs. Even if bulk handling is feasible at some stress tests without bias operation, it is strongly recommended to mount the LEDs on a PCB to ensure the complete traceability during testing and to avoid handling damage during pre- and post-electrical measurement and visual inspection.

The choice of the test board and the interconnect material and process depends on the stress test and the stress conditions. As an example, a metal-core PCBs is typically used for testing at high temperatures and high forward currents and secures a sufficient heat dissipation to the heat sink. The circuit layout of the boards should be optimized to achieve the best thermal management and avoid heating between the LEDs on the board, see Fig. 20.6.

The arrangement of the LEDs in Fig. 20.6 is determined by considering the thermal path for heat dissipation in the PCB material and is optimized to prevent thermal crosstalk between the LEDs during electrical operation. If the stress temperature exceeds 125 °C, it is recommended to use metal-core boards without solder resist coating since this coating can discolour (changing the reflectivity of the PCB) during the test and influence the luminous flux or radiant power measurement leading to a false interpretation of light degradation. Particularly for humidity and environmental tests, the contact pins on the PCB should be Au plated to avoid corrosion, since any corrosion on the contact pins aggravate the electrical contacting during the readout measurement.

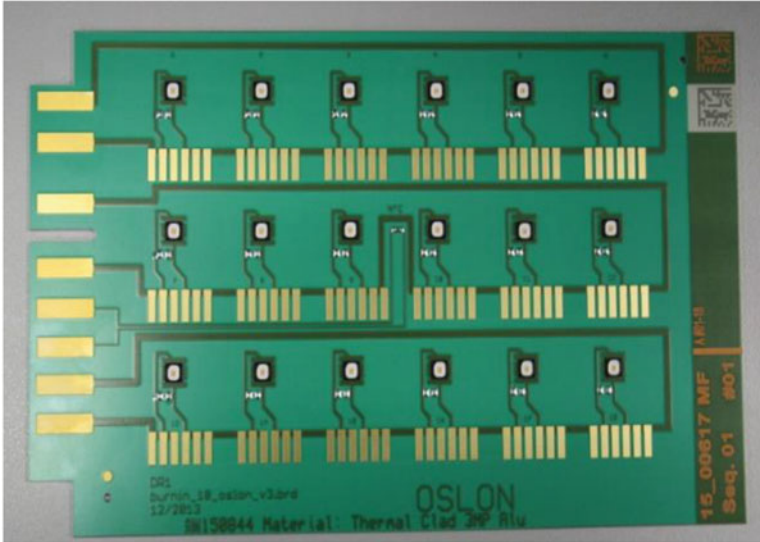

Fig. 20.6 Standard metal-core PCB with optimized layout for improved thermal management designed for HTOL tests (Provided by OSRAM Opto Semiconductors GmbH)

Prior to the assembly and stress test, a moisture preconditioning of the SMD LED packages shall be performed. The objective of the preconditioning is to classify the LED packages according to the moisture levels specified in JEDEC J-STD-020D.1 [4]. The moisture level defines the period between opening the humidity-sealed dry pack bag and reflow soldering process. For a typical preconditioning the LED packages will be stored 168 h at 85 °C/85 % relative humidity, which corresponds to 1 year floor life at 30 °C/60 % relative humidity. During humidity storage a certain amount of moisture will be absorbed by the SMD LED packages. The fast temperature ramp up from reflow soldering, will vaporize the moisture in the package abruptly and can pre-damage the LED encapsulation or weaken the adhesion between resin material and housing material. This material delamination could cause failures during the subsequent reliability stress testing when moisture or other corrosive gases creep into the package. Critical stress tests requiring a preconditioning process include the temperature cycle (TMCL), the wet high temperature operating life (WHTOL), the power temperature cycle (PTMCL) and the reflow to solder heat (RSH-reflow or RSH-TTW).

20.4.3 Thermal Management

An appropriate thermal management is essential to achieve a reliable and good performance of LED packages, especially for high-power LEDs. Thus, the automotive qualification of LED packages contains the characterization of the thermal

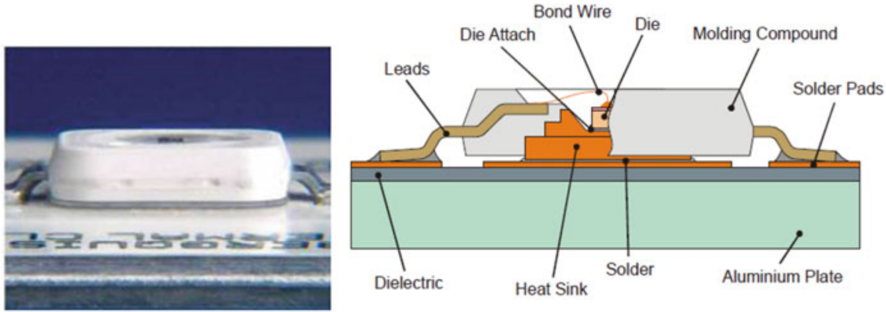

Fig. 20.7 Exemplary LED structure of a premould high-power SMD package [4]. The *right side* shows the schematic drawing and the individual components of the LED and the PCB

resistance (R_{th}). Knowing the R_{th} of the LED in the test set up allows to calculate the corresponding junction temperature (T_J). The junction temperature T_J specifies the stress level on the LED component independently of the test apparatus and makes the results of different LED manufacturers transparent and comparable. In addition many ageing phenomenon are attributed to the junction temperature.

In practice, the internal thermal resistance of a LED depends on the geometry, used materials, die attach technology and chip size. Whereas the external thermal resistance is influenced by the application-specific resistance and considers the heat flow from the internal heat spreader of the LED to the surrounding environment. Figure 20.7 shows the exemplary LED structure mounted on a metal-core PCB.

The overall thermal resistance can be divided into the parts covering the LED component, the substrate technology and the used external cooling system. A general sketch of the thermal resistance series of a high-power LED package is illustrated in Fig. 20.8.

The thermal resistance board to ambient $R_{th\ BA}$ is considering the heat transfer from the PCB substrate to the ambient environment. The thermal resistance solder point to board $R_{th\ SB}$ characterizes the heat transfer from the LED through the PCB and is strongly influenced by various factors, e.g. solder pad design, PCB material, board layout, stencil layout, solder paste and solder paste height. Therefore both thermal resistance values $R_{th\ SB}$ and $R_{th\ BA}$ vary from the application set up and test configuration at the testing labs. In practice, however, the junction to solder point thermal resistance $R_{th,\ JS}$ will be used to determine the junction temperature T_J of the LED at the corresponding stress test condition using Eq. 20.3:

$$T_J = T_S + R_{th\ JS} \cdot P_{el} \tag{20.3}$$

$R_{th\ JS}$ is independent from the used PCB and the environmental conditions. The solder point temperature T_S is defined as the temperature of the solder joint under or near to the heat spreader and can be measured by using a thermocouple [5].

The temperature increase ΔT of the LED during operation is caused by the power dissipation from electrical input power to thermal output power by heating

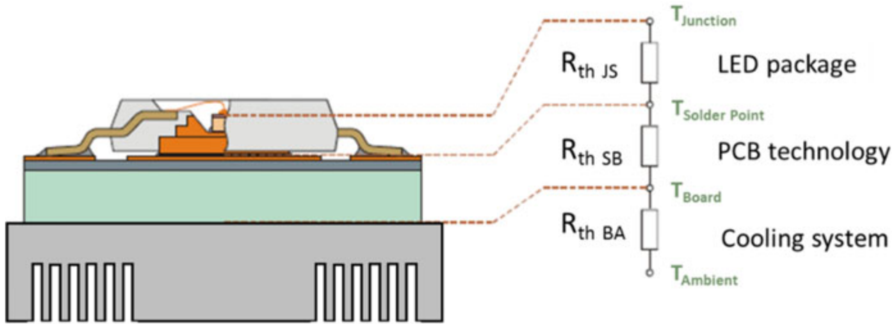

Fig. 20.8 Thermal resistance series configuration of a high-power LED component, substrate technology and external cooling system

the device. Assuming that the complete electrical power will be transformed into heat, the thermal resistance results in $P_{heat} = P_{el}$.

For high-efficient LEDs, we have to take into account that not the complete electrical power is converted into heat and a certain portion is coupled out as optical power P_{opt}. The resulting real thermal resistance R_{th} real is defined as

$$R_{th\ \ real} = \frac{\Delta T}{P_{heat}} = \frac{\Delta T}{\left(P_{el} - P_{opt}\right)} = \frac{\Delta T}{P_{el} \cdot \left(1 - \eta_{LED}\right)} \tag{20.4}$$

where η_{LED} is the optical efficiency of the LED

$$\eta_{LED} = \frac{P_{opt}}{P_{el}} \tag{20.5}$$

Through the use of $R_{th\ real}$, it will be ensured that the maximum permissible junction temperature will not be exceeded for all modes of stress operation. Details how to measure the thermal resistance of LED packages and how to calculate the real thermal resistance $R_{th\ real}$ are given in [6]. The thermal resistance can fluctuate due to process variations, e.g. glue thickness at die attach process, thus the specification of the typical $R_{th\ (typ)}$ and the maximum thermal resistance $R_{th\ (max)}$ are required. Specifying only the electrical values does not reflect the real thermal resistance of today's high-efficient high-power LEDs since a larger portion of the electrical input power will be converted into light (see Eq. 20.5), instead of heat, and needs to be considered for the thermal resistance calculation. Thus, the real thermal resistance $R_{th\ real(typ)}$ and $R_{th\ real(max)}$ describe the actual thermal performance of a LED and should be specified therefore in the product data sheets.

20.4.4 Sample Lot and Production Requirements

A reasonable sampling ensures that LED packages which are selected for testing fulfil the product specifications at the nominal drive current before the stress test. The nominal drive current is specified by the LED manufacturer and is typically the drive current for the LED binning in the product datasheet.

As reference all LEDs are measured at the nominal drive current prior to and after the stress test and at each additional readout in between. The following electro-optical parameters represent the minimum requirement for LED characterization:

- Luminous flux [lm] or radiant power [W] or intensity [*lm*/*sr*], [*W*/*sr*]
- Forward voltage [V]
- Chromaticity or colour coordinates $C_{X,}$ C_Y or dominant wavelength λ_{dom} or peak wavelength λ_{peak}

Depending on the device under test (DUT), the appropriate measuring unit has to be used. As a recommendation all LED parameters above should be measured additional at stress current, and the complete spectrum should be recorded as well. Especially for LEDs using a conversion technology (e.g. white or colour-on-demand LEDs), the spectrum provides more information regarding ageing of the conversion material. The visual inspection of the construction, marking and workmanship prior to, in between and after the stress test ensure that all LEDs comply with the production specification and will document any abnormalities in appearance during the tests.

20.4.5 Qualification Stress Tests

The section contains a brief overview about the applicable reliability stress tests for automotive qualification. Particularly, the testing of a high-power LED requires highly specialized test equipment. The Fig. 20.9 shows an example of the inside view into a test chamber where high-power LEDs are stressed under high temperature and high current operation conditions.

The temperature of the used heat sink is actively controlled, which allows to run the LEDs exactly at the stress conditions. To ensure a sufficient heat transfer from the metal-core PCB to the heat sink, the boards are mechanically clamped. During the stress test, the technical parameters, the heat sink temperature and the ambient temperature of the oven are regularly monitored. The air circulation inside the chamber is minimized. Usually strong air circulation or air flow will influence the ambient temperature around the LEDs and cause passive cooling.

For thermo-mechanical stress tests, the standard offers the choice between different stress conditions. The LED manufacturer can choose the conditions which are closest to the product specification in the data sheet. In general it will

Fig. 20.9 View inside of thermal chamber for high temperature and high current stress tests of high-power LED packages

be assumed that passing harsher stress conditions implies the more relaxed condition is also fulfilled. The choice of the conditions must be documented in the official communication sheet or qualification report.

The IEC 60810 standard typically gives references to applied JEDEC and IEC standards. Further details on test conditions and execution are given in the referenced standards and are not part of this chapter. As shown in the qualification process flow in Fig. 20.5, the stress tests can be differentiated in six main categories as follows:

1. *Temperature and bias operation*

   HTOL – **H**igh **T**emperature **O**perating **L**ife test acc. to JESD22-A108D
   PLT – **P**ulse **L**ife **T**est acc. to JESD22-A108D

2. *Temperature, humidity and bias operation*

   WHTOL – Wet High Temperature Operating Life acc. to JESD22-A101C
   DEW – Dew test in accordance to BMW group standard GS 95011-4

3. *Thermo-mechanical and mechanical stress*

   TMCL – Temperature Cycle acc. to JESD22-A104D
   TMSK – Thermal shock acc. to JESD22-A106D
   PTMCL – Power Temperature Cycle acc. to JESD22-A105C
   RSH-reflow – Resistance Soldering Heat acc. to JESD22-A113F or alternative ANSI/IPC/ECA J-STD-002C
   RSH-TTW – Resistance Soldering Heat acc. to JESD22-B106D

4. *Mechanical stress*

   MS – Mechanical Shock acc. to JESD22-B110B
   VVF – Vibrations Variable Frequency acc. to JESD22

5. *Electrical stress*

ESD-HBM – Electrostatic Discharge, Human Body Model acc.to ANSI/ESDA/JEDEC JS-001-2012
ESD-MM – Electrostatic Discharge, Machine Model acc. to JESD22 A115C

6. *Environmental stress*

H2S – Hydrogen Sulphide test acc. to IEC 60068-2-43
FMGC – Flow Mixed Gas Corrosion acc. to IEC 60068-2-60, Method 4

The concept of these automotive qualification stress tests is to verify the reliability of the LEDs in terms of continuous degradation and/or sudden event or catastrophic failures. As known, different stress tests and conditions are responsible for various ageing mechanisms or failure modes. In the following a closer look on the particular stress categories and a short outline on the most expected degradation mechanism are given.

20.4.5.1 Temperature and Bias Operation

The high temperature operating life (**HTOL**) stress tests are mainly performed in order to detect continuous luminous flux ageing caused by the package material degradation (e.g. emitter chip, housing, resin, lenses). Figure 20.10 shows an example for typical result of the luminous flux maintenance of 26 LEDs that are stressed under HTOL conditions. The chart demonstrates that all tested LEDs exhibit a luminous intensity maintenance higher than 90 % after 1000 h.

For pulse life test (**PLT**), the focus is mainly to validate the current load capacity of the current spreaders (e.g. bond pad, current spreader layout) on the emitter chip under high current pulsed operation. The most expected stress-induced failure mechanism is a burn-off at the current spreader caused by local high current densities – also called electrical overstress failure (EOS). A typical EOS failure is shown in Fig. 20.11. Possible root cause for a burn-off is most likely an insufficient layout of the current spreader or process fluctuations in the frontend wafer process at photolithography or top metallization.

20.4.5.2 Temperature, Humidity and Bias Operation

Both humidity tests, wet high temperature operating life (**WHTOL**) and dew test (**DEW**), will be performed under biased operation. Especially for the WHTOL, the current bias at the minimum and maximum rated drive current with 30 min on and 30 min off sequence allows humidity to creep into the package. The aim is to validate possible failure modes like, e.g. delamination between resin and housing material, passivation of chip, die attach interface between chip and lead frame and migration inside the LED cavity. If the LED is operating continuously at high current, the area around the chip is heated, and the humidity vaporizes such that humidity will not attack the chip or the die attach interface. It is generally

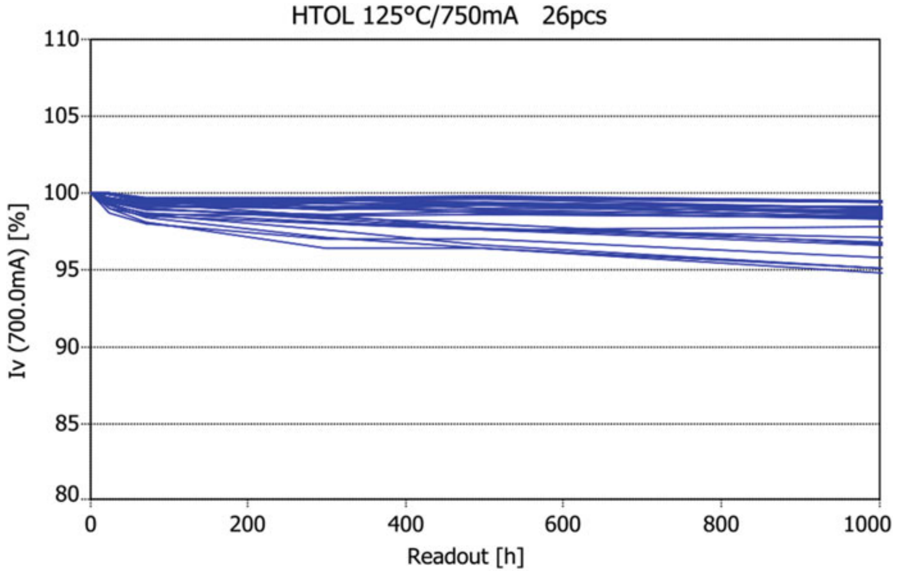

Fig. 20.10 Example for luminous intensity test results over time for HTOL testing

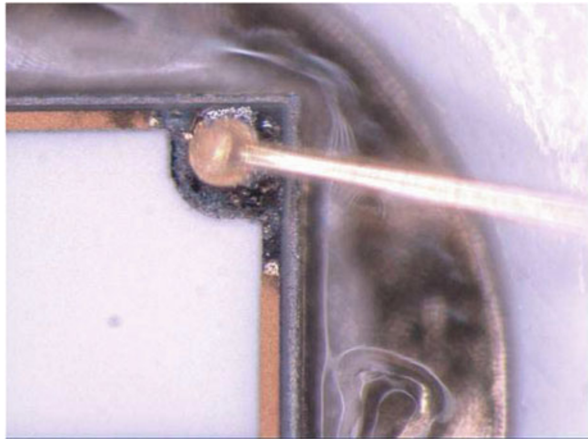

Fig. 20.11 The microscope pictures show a burnt bond pad and current spreader on the chip surface caused by electrical overstress (EOS)

understood that the DEW test is the more severe test compared to damp heat cycle stress, which is also documented in the beginning of IEC 60810. At the dew phase, water can deposit as a water droplet on the LED surface casting. In case of delamination or openings in the package, the water can directly become embedded into the package cavities. Thus, the main risk for this stress test is a catastrophic failure related to lifted glue or lifted die, where the interface between lead frame and glue or glue and chip backside opens. Another imaginable failure mode is the corrosion of aluminium layers in the epitaxial structure caused by a crack in the

passivation layer or insufficient passivation of the chip surface. Such a failure mode is primary attributable to chip technologies using aluminium-based materials systems such AlInGaP and AlGaAs. Finally both humidity tests are suitable to validate if a LED package and the chip passivation are resistant against humidity corrosion and migration effects.

20.4.5.3 Thermo-mechanical Stress

Thermo-mechanical stress on the LED is primarily induced by repeating extreme temperature changes. In combination with the different thermal expansion coefficients of the materials used in the LED package, these temperature cycles raise a strong thermo-mechanical stress. The standard temperature cycle (**TMCL**) test is performed using an air-filled, tempered chamber, and the DUT is cycled between temperature extremes of, e.g. −40 °C to 125 °C. The standard condition for the TMCL is the two-chamber test where the DUT is physically transitioned from a chamber with the low temperature condition to a chamber with the high temperature condition. It applies a higher stress to the LED, since lower transfer time causes a higher temperature gradient than for single chamber condition. The transfer time between both temperature extremes is around 10 s. Often a two-chamber TMCL is also called air-to-air thermal shock. A single chamber set up is typically used when testing interconnections for solder joint fatigue to avoid big transient thermal gradients. The thermal shock (**TMSK**) is very similar to the two-chamber TMCL test, but more severe, because the temperature change is realized by immersing the LEDs in tempered liquids. The transfer time from hot to cold area shall not exceed 10 s. For many LED packages, this liquid-to-liquid shock condition is the harsher stress compared to the two-chamber TMCL and is therefore regarded as overstress for most LEDs.

The power temperature cycle (**PTMCL**) is one of the most important reliability tests for the automotive industry, because it simulates the worst-case stress conditions encountered under real automotive applications. The aim of this test is to determine the ability of the LED to withstand alternate exposure at high and low temperature extremes, similar like for TMCL, with periodically on/off electrical operation. The transition time between the temperature extremes depends on the temperature difference and is comparable with the one chamber TMCL test. The power- and temperature cycle profile for the PTMCL according to the JEDEC standard [6, 7, 8] is illustrated in Fig. 20.12.

Another way to expose thermo-mechanical stress to a LED is the reflow or TTW (“through the wave”) soldering process. Furthermore we will focus on the reflow soldering for SMD devices. The purpose of the **RSH-reflow** is to evaluate the performance of the LED under stress due to the soldering heat during the reflow process. The standard temperature profile is 260 °C peak temperature in a nitrogen atmosphere, because some LED packages may show some discoloration of the housing without nitrogen. Details of the reflow soldering profile are specified in the product data sheets of the LED manufacturer.

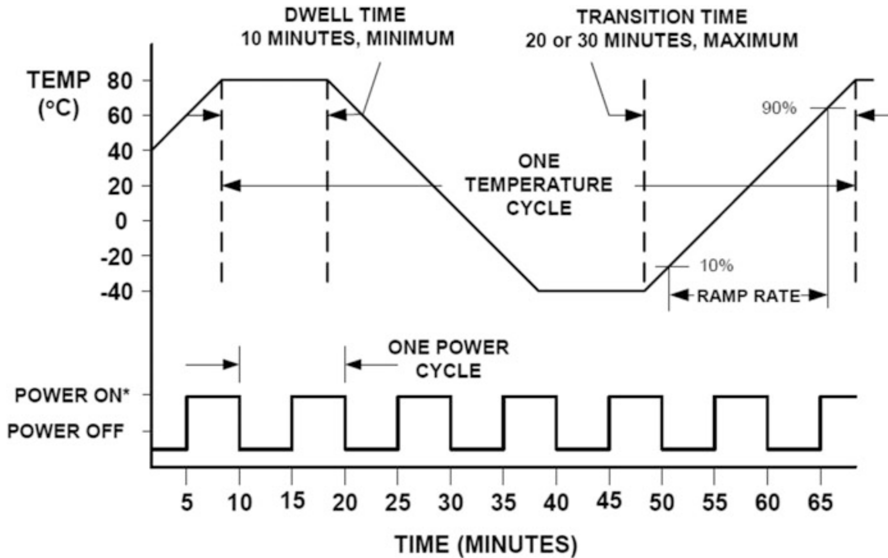

Fig. 20.12 Typical power- and temperature cycle condition for PTMCL testing [acc. to JEDEC JESD22-A105C]

Generic observed failure modes from thermo-mechanical stress are broken wires, lifted die, cracks in the package or emitter chip, delamination and cracks in the solder joint. Solder joint cracks are not subject of this LED package qualification testing, since many assembly parameters (e.g. solder paste, solder height, stencil design, PCB material, etc.) influence the result in the TMCL, PTMCL or TMSK tests. Hence, failures in the LED to board interconnection which are not attributable to the LED package will not be considered but shall be reported as part of the official qualification report. The most common package level failures are broken wires, and these are observed most often during thermal cycling tests. Fluctuations at the wire bond process, abnormal wire loop or kinks in the wire are often identified as root cause.

In some rare cases, broken wire or lifted die/glue induces intermittent operation during the thermo-mechanical stress tests. This intermittent operation is difficult to detect if pulsed measurement is performed at the readout characterization. The phenomenon can be described as follows: at room temperature the epoxy or silicone resin constringe and the open gap are closed. During continuous bias operation, the LED package heats up and the gap expands. The LED shows now open contact, no light up and the temperature decreases. The gap will close again, the LED lights up and it starts from the beginning. In order to validate that the LED is not intermittent, the IEC standard requires to perform a destructive physical analysis to verify that die attach and wire are not damaged to ensure a higher confidence level to the electrical performed measurement results. Figure 20.13 shows a SEM picture of a broken bond wire close to the ball bond area on the chip surface after chemical decapsulation of resin.

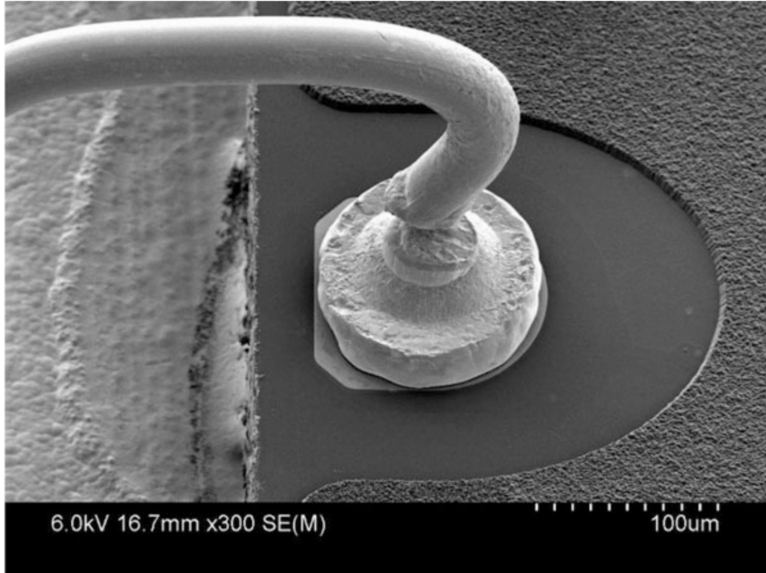

Fig. 20.13 DPA analysis reveals broken wire after PTMCL testing

20.4.5.4 Mechanical Stress

The mechanical shock (**MS**) is intended to determine the suitability that the LED is subjected to severe shocks as a consequence of abrupt applied mechanical forces or changes in motion, caused by wrong handling, transportation or field application. The purpose of vibration variable frequency (**VVF**) test is to evaluate the effect of vibration on LED components at high frequency range. This test particularly validates the reliability of LEDs placed close to the car engine and are exposed to incessant vibrations, e.g. LEDs used in headlamps or front side indicator. Both MS and VVF are destructive tests and in principal suitable for large LED components with a high mass. Generic observed failures are the drop of lenses, glass windows or phosphor conversion layers and any damage of the LED package or ceramic substrate.

20.4.5.5 Electrical Stress

The ESD human-body-model (**ESD HBM**) test is performed to determine the robustness against electrostatic discharge during manual handling by a person without any ESD protection. According to the ANSI/ESDA/JEDEC JS-001-2014 standard, the ESD HBM sensitivity of LED component should be classified. The ESD machine-model (**ESD MM**) test simulates the electronic discharge during

handling of the LED by a machine (e.g. pick and place equipment) without any ESD protection. The applied electrical energy at ESD MM is several times higher as for ESD HBM at same voltage level, since at ESD MM testing no pre-resistor and a higher capacitor are used. Concerning the circuit layout at ESD MM, the applied energy depends on the internal resistance of the DUTs and can differ from LED package to LED package.

The HBM model represents the discharge by manual handling by an individual person delivered to the LED. A discharge similar to HBM can also occur from charged conductive part of an assembly tool, such as a nozzle or fixture. This type of discharge is covered by the machine model. But even so a transfer of electrical charge can cause an ESD event. A LED can become charged, for example, when sliding down in the bowl feeder at testing and taping. This event is known as charged device model (**CDM**). The ESD CDM has not been considered for this IEC 60810 qualification approach, since typical single emitter LED packages have a too small surface to carry sufficiently high electric charge to damage the chip or the electrical pathway in the LED. Whereas large LED packages such as chip on board (**COB**) or large multi-chip modules have typically tray handling with less risk for an ESD CDM failure.

20.4.5.6 Environmental Stress

IEC 60810 focuses on corrosive impact from extreme environment conditions found in some automotive applications. The purpose of the environmental stress test is to ensure that a LED exposed to a cocktail of corrosive gases will not show any degradation or functional damage after a defined period of time. Even though the direct contact to harmful substances should be avoided in proximity of electronic components, an increasing number of application scenarios exposing LEDs to corrosive environments have been detected during the last years. For example, sulphur components, which, e.g. are evaporated from rubber-like materials, corrode the silver plating of the lead frame. This results in a destruction of the electrical interface between lead frame and wire or die bond. During the hydrogen sulphide test **(H2S)**, the LED is exposed to a micro climate containing a high sulphur concentration. The permanent presence of such a micro climate causes a diffusion of the sulphur components through the silicone encapsulation and into the LED package. Humidity conditions, temperature and light are able to accelerate this corrosion process. Detailed studies show that corrosion becomes visible at a concentration of greater than 100 ppb. From investigations it can be concluded that the concentration in a rubber-like material is several times higher in the range of 10 ppm. Thus, for the environmental test, a condition of 40 °C/90 % relative humidity and 15 ppm H_2S concentration is applied.

The flow-mixed gas corrosion (**FMGC**) test reflects the corrosive stress in case that the LED is exposed to a chemical cocktail of several harmful gases like NO_2,

Cl_2, SO_2 and H_2S. Both tests are accepted by automotive LED manufacturers and set makers as suitable and sufficient to ensure corrosion stability for LED packages.

20.4.6 Miscellaneous Requirements

Not all tests in the IEC 60810 are directly addressed as reliability tests, but nevertheless they need to be done to ensure the production quality. Measuring the physical dimension (**PD**) verifies the mechanical package outlines from the product data sheet based on production fluctuations at, e.g. trim and form and moulding process for the LED housing. Deviations in the physical dimension could lead to assembly problems due to narrow application specification, e.g. close spacing between LEDs or height tolerances to secondary optics.

The solderability (**SO**) test examines the assembly at the board level. In the current version of the IEC 60810, this test is not defined, and hence it is up to the LED manufacturer to ensure this workability on board level. The actual review of IEC 60810 addresses this topic, and the IEC 60068-2-58 is in discussion to be used for evaluation of the solderability of lead-free solder alloys applicable for SMD LED packages and low temperature soldering (e.g. Sn-Bi, 170–201 °C).

20.4.7 Failure Criteria

The qualification is a test-to-pass approach, and all LEDs have to pass the tests, otherwise the LED or LED family is considered to have failed the qualification. At this point it should be emphasized that the term “failure” does not necessarily mean that all devices in the test are going to fail catastrophically. In most cases the term “failure” belongs to a continuously change in the electro-optical LED characteristics (e.g. light, forward voltage, colour shift), where the parameter value fails according to a predefined application criteria. For the forward voltage V_F and the colour coordinates C_X, C_Y, the criterions are fixed, whereas the failure criterions of ± 20 % or ± 30 % light decay are free of choice by the LED manufacturer. A light decay of ± 50 % from the initial value typically reflects the requirements for some interior applications (e.g. dashboard or instrument clusters).

In case LEDs have failed the acceptance criteria of the qualification test, the root cause has to be determined by an internal 8D process. This means corrective actions have to be defined assuring that the failure mechanism is understood and contained. In order to verify that all defined corrective and preventive actions are effective, the failed qualification tests have to be repeated successfully.

If a LED package is physically damaged due to mishandling or electrically by ESD, the failure can be discounted but has to be reported as part of the data submission. Failures at interconnect of test board and LED package caused by pick and place or/and assembly process (e.g. wrong orientation, tilted or distorted

LED) or on the test board (e.g. corrosion of contact pads, damaged electrical pathway) are not attributable to a LED package failure and are not taken into account.

Failures like broken wire or lifted die/glue might not be detectable in the electrical or optical parameter at room temperature. Thus, a simple light/no-light check at different temperatures is suggested to validate the stability of the LED after thermo-mechanical stress testing. In addition, a destructive analysis (**DPA**) shall be performed on random samples of two good units after completion of PTMCL, WHTOL, H2S and FMGC test. The aim of this destructive analysis is to demonstrate that the materials, the design and the workmanship withstand the various stresses and no methodical failure are occurred. The DPA requires to perform a visual inspection on the decapsulated packages. Details for the DPA can be found in the normative Annex J of the IEC 60810. For the IEC review, the ELMAPS experts propose furthermore to validate the corrosion stability by performing an additional cross-sectional cut through chip/die attach area/lead frame interconnect. Such a cross-sectional investigation can reveal more details as to whether a visible discolouration could cause a serious failure at electrical interconnects or if it only affects cosmetic appearance.

A destructive analysis is not always needed, and in some cases a non-destructive analysis like X-ray or microscope could provide adequate results as well.

20.4.8 USCAR-33 Requirement

In addition to the automotive qualification, the USCAR Lighting Group determined there was a need to create a common set of requirements that focus on LED use for exterior automotive lighting applications.

By publishing the SAE/USCAR-33 “Specification for testing automotive LED modules”, USCAR created a standard to help the US Auto OEMs in the rapid adoption of LED lighting. This document is written to encompass testing a complete LED module including any drive electronics and also includes a section on LED component overstress testing.

The idea behind the LED overstress testing is to determine the failure limits of the LED device. Many of the tests are written to go beyond the manufactures’ specifications in both temperature (such as $+15\ ^{\circ}\mathrm{C}$ above maximum T_{J}) and forward current (130 % of maximum), while the part is tested in various environments. The duration of each test is specified at 1500 h or when 50 % or more of the test population has failed. These rigorous requirements work to ensure that all the components and the complete module are suitable for use in harsh automotive exterior application environments.

20.5 Conclusion and Next Steps

The new IEC 60810 standard is customized for optoelectronic devices used in advanced exterior and interior automotive applications with main focus on visible and IR LED packages. Future work of the LED expert group is to consolidate the automotive requirements also for laser diode packages, IR photodetectors and sensors in order to achieve a comprehensive automotive qualification standard. Primary focus is on the development of a qualification standard for visible and IR laser diode packages, since the market of laser-powered headlights is increasing significantly in the premium car segment. The work has been already started on in the relevant groups at ELMAPS and IEC.

The IEC 60810 and the AEC Q101 ensure only the qualification of the LED component at standardized laboratory condition and shall demonstrate the principle capability of the LED packages for automotive applications. Furthermore additional investigations and validations on application system level or car maker side are required.

20.6 Summary and Outlook

With the IEC 60810 [2] and the ZVEI guideline for product and process notification [9], two powerful tools for validation of automotive requirements for LEDs are already available and in practical use. The benefit for the automotive industry is to get an aligned procedure linking the reliability requirements and the change management process of optoelectronic devices including LEDs, IR sensors, laser diode packages, etc. Still missing is an international guideline for systematic accelerated testing or robustness investigation of III/V optoelectronic semiconductors. The aim of such an approach would be to provide a guided method for testing beyond the specification limits of a LED product and evaluate the degradation mechanism as a function of overstress. In combination with well-known modelling approaches like Arrhenius, Eyring, Peck, Norris-Landzberg and Coffin-Manson, it is possible to project the degradation (or number of failures) during “application” operation. The robustness validation provides a higher confidence level and helps to improve the worldwide quality standards in automotive applications.

This work has started in the relevant standardization groups to prepare a guideline for robustness validation of LED packages.

References

1. SAE/USCAR-33, *Specification for Testing Automotive LED Modules, Section 7* (SAE international, New York, 2013)
2. AEC-Q101-Rev-D, *Failure Mechanism Based Stress Test Qualification for Discrete Semiconductors in Automotive Applications* (Automotive Electronics Council, New York, 2013)

3. IEC 60810:2014 Ed. 4.0, Lamps for road vehicles – Performance requirements, in *Chapter 8 "Requirements and Test Conditions for LED Packages"*, Ed. 4.0 (IEC standardisation body, London, 2014)
4. IPC/JEDEC J-STD-020D.1, *Moisture/Reflow Sensitivity Classification for Nonhermetic Solid State Surface Mount Devices* (IPC/JEDEC standardisation body, New York, 2008)
5. OSRAM Opto Semiconductors GmbH, *Application Note "Temperature Measurement with Thermocouples"* (OSRAM, Munich, 2004)
6. JEDEC Standard JESD51-51, *Implementation of the Electrical Test Method for the Measurement of Real Thermal Resistance and Impedance of Light-Emitting Diodes with Exposed Cooling* (JEDEC standardisation body, New York, 2012)
7. OSRAM Opto Semiconductors GmbH, Application Note, *Preventing LED Failures caused by corrosive Materials* (OSRAM, Munich, 2013)
8. JEDEC Standard JESD22-A105C, *Power and Temperature Cycling* (JEDEC standardisation body, New York, 2004)
9. *ZVEI Guideline for Customer Notifications of Product and/or Process Changes (PCN) of Electronic Components specified for Automotive Applications*, 4th revised Ed., Rev. 3 (ZVEI standardisation body, Frankfurt, 2016)

Chapter 21
Lightning Effects on LED-Based Luminaires

Adedotun Agbemuko, Johannes van Meurs, and Willem Dirk van Driel

Abstract This chapter gives an extensive overview into the nature of the environment that luminaires and thus LEDs are subjected to during the event of a lightning stroke. Direct lightning stroke almost always results in instant damage for low-voltage connected devices, except in "extraordinary circumstances" where random components may survive. This is usually not a subject for debate and is not the subject of this monograph. Indirect consequences of lightning strokes, however, can be effectively mitigated as described. This chapter also delves into a realistic expected overvoltage levels for two typical systems, overhead lines and insulated cables, as obtained from lightning studies on a power network supplying power to LED devices and thus justifies the recommendations by several standards. In addition, it shows the importance of an often neglected device—MOV in mitigating attendant surges due to lightning to a level that can be withstood by LEDs and associated devices.

21.1 Introduction

Despite the advances and rapid improvements in the state-of-art of light-emitting diodes (LEDs), these devices are still sensitive and vulnerable to overvoltages; particularly the effect of overvoltages (otherwise termed surges) due to lightning—direct stroke and indirect strokes. It is known that low-voltage devices (in general)

A. Agbemuko (✉)
Delft University of Technology, EEMCS Faculty, Delft, The Netherlands

Institut de Recerca en Energia de Catalunya (IREC), Barcelona, Spain
e-mail: aagbemuko@irec.cat

J. van Meurs
Philips Lighting, HTC48, 5656 AE Eindhoven, The Netherlands
e-mail: jos.van.meurs@philips.com

W.D. van Driel
Philips Lighting, High Tech Campus, Eindhoven, The Netherlands

Delft University of Technology, EEMCS Faculty, Delft, The Netherlands
e-mail: willem.van.driel@philips.com

© Springer International Publishing AG 2018

W.D. van Driel et al. (eds.), *Solid State Lighting Reliability Part 2*, Solid State Lighting Technology and Application Series 3, DOI 10.1007/978-3-319-58175-0_21

inclusive LEDs cannot survive a direct lightning stroke, except in *extraordinary circumstances*.

The magnitude of overvoltages due to such direct stroke is outrageously high that LEDs are damaged so fast beyond recognition, to a state where it becomes remotely difficult to ascertain the true sequence of event that lead to damage. A conservative lightning current magnitude of 10 kA within the vicinity of a luminaire housing LED devices with impedance of 50–100 W can produce an overvoltage as high as 1 MV!

As a result of this, protection against direct strokes for LED-based luminaires is not feasible technically and economically as this would defeat the benefits of an otherwise cheap device, and this is usually not a subject for debate.

A more common source of overvoltages that can be effectively mitigated with proper circuit layout, architecture, and extra measures is overvoltages due to indirect strokes, specifically those that are the consequences of lightning strokes. Main route of lightning-induced surges to LEDs is via the power network to which the LEDs are connected [1].

It should be noted early on that direct strokes in the context of this monograph are lightning strikes that hit a structure carrying a luminaire (luminaire in this text is assumed to be LED based) or stroke to the luminaire itself. On the other hand, strokes to ground in the vicinity of a luminaire cannot be termed a direct stroke in this context since the only means of propagation to the luminaire is via electromagnetic induction and/or via grounding lines which per se is indirect; albeit it is a direct stroke to ground [1]. Indirect lightning strikes are of course attendant of lightning strokes, but either some distance away from the position of luminaire or due to the apparent connection of luminaires and/or support structures. In fact, lightning stroke between two clouds tens of kilometres from ground could cause overvoltages in luminaires depending on the medium of power distribution overhead lines (OHL) or cables (overhead and underground) [2, 3]. This is usually referred to as the capacitive mode of propagation or more scientifically electrostatic mode of propagation as it deals with the movement of charges.

21.2 Mechanism of Lightning Propagation

The first step in identifying ways to mitigate surges due this natural and highly unpredictable phenomenon is to ascertain its mode of propagation. There are several known mechanism in which lightning surges could propagate through to the terminals of luminaires.

1. Induced overvoltages: This is the most common means of lightning propagation in power networks connecting luminaires to source of power. It is the main mechanism of indirect strokes. Electromagnetic fields attendant of a lightning current induce voltage in nearby structures, including houses, conductors, and underground cables. Magnitude of overvoltages is inversely proportional to the distance between points of stroke and location or structure housing LED

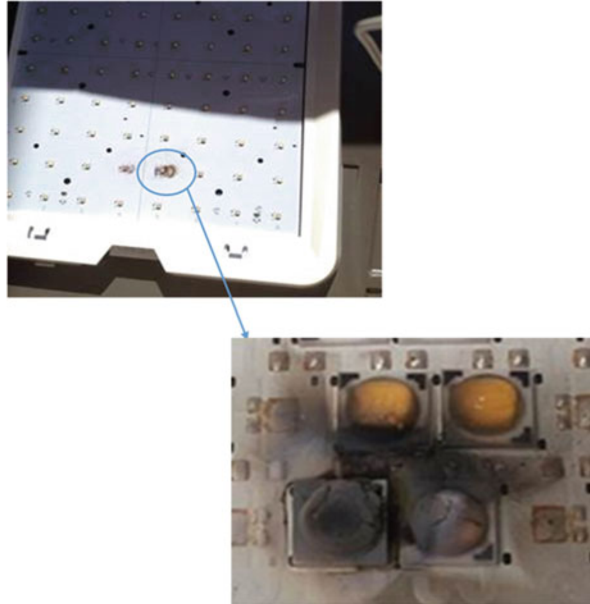

Fig. 21.1 Damaged LED device

devices [4]. At low system voltages (as is the case of luminaires and other LED-based devices), this may result in a few kilovolts (kV) with differential mode coupling (DM) and tens of kilovolts for common mode (CM) with consequent surge current in the region of tens of kilo amps for CM [2, 4, 5]. In the same vein, induced overvoltages can go from the medium-voltage (MV) system to low-voltage system (LV). Above 66 kV system-level voltages, this mechanism is not an issue as induced voltages may well be below the basic insulation level (BIL). But for LV systems, this is the main cause of damages and insulation breakdown. Figure 21.1 depicts the damages to the LEDs of a luminaire as observed in the field.

2. Ground overvoltages: This is due to strokes to ground within the vicinity of luminaires. Transfer to the power network thus depends on the mode of grounding. This mode of propagation is the source of the well-known ground potential rise (GPR) [4–6].
3. Line charging: This is more of a relatively understudied mode of propagation. This is mainly prevalent in OHL systems. Lightning studies on cable systems—overhead and underground cables—show that this method is not prevalent for cables. Generally speaking, it is widely agreed that clouds are mostly (but not always) negatively charged which induces opposite charges on ground and OHLs [7]. This is referred to as line charging. In the event that lightning discharge between two charged clouds occurs, these induced positive charges are no longer bounded as they initially were predischarge and will be forced to move. Hence, these charges move swiftly in lines resulting to overvoltages in devices connected to such lines. A good solution to this is the use of overhead insulated cables, but cost of installation may be a valid drawback.

21.3 Effects of Lightning on LEDs and Basic Mitigation Method

21.3.1 Effects of Lightning

In most cases, the ultimate effect of lightning on LEDs is instant damage. However, depending on the duration of the lightning stroke itself, partial damage may also be observed. In such a case, damages are usually to the devices closest to entrance point of a surge, while others at some distance remain healthy as the duration of stroke was too short to propagate. Nevertheless, the healthy devices may at some point in time malfunction due to the impact and stress induced by surge. Figure 21.1 depicts one of such possible damage observed in the field.

21.3.2 Basic Mitigation

Sources of surges in a practical systems include surges from supply sources, stroke within the vicinity of luminaires but not a direct hit, and lightning strokes between two clouds as already mentioned.

Metal-oxide varistor (MOV) is one of the most important and basic device for mitigation of surges. The importance of these devices is often neglected. To say the least, the life of a luminaire is a function of the life of the MOV connected to its terminals. Once an MOV has degraded to a point where it can no longer operate, it is just a matter of time before transient surges cause damage to luminaires. This is to underscore the significance of MOVs.

Another important design consideration for luminaires is the withstand strength. MOVs are not capable single-handedly to completely mitigate surges; luminaires (LEDs inclusive) must also take some responsibilities. MOVs are responsible for clamping down overvoltages to safe levels (but not in all cases). The voltage level that remains after an MOV clamps down on a surge depends on the magnitude of the overvoltage that arrives at the terminals of the MOV. Therefore, luminaires must be able to withstand whatever residual voltages remain after MOV clamps down on the surge. As an illustration, if an overvoltage of 30 kV impinges on the terminals of a luminaire where an MOV is situated, a properly installed MOV could clamp down this voltage to 1 kV or less. Thus, luminaire including all connected devices must be able to withstand 1 kV without damage. As a rule of thumb, luminaires should be designed to withstand a minimum voltage level which could be determined by lightning studies simulations or by resorting to recommended values in standards [8, 9].

21.4 Lightning Studies on Outdoor LED-Based Luminaires

21.4.1 Modelling in ATP-EMTP

The Alternative Transients Program (ATP) is a version of the famed Electromagnetic Transients Program for digital simulation of transient phenomena. ATP is widely regarded as the most widely used transient analysis program for simulation of electric power systems transients. ATP is a free of charge software program with extensive modelling capabilities and other computational capabilities. As described, it belongs to a family of EMTP-based programs. EMTP was initially developed in the public domain at the Bonneville Power Administration (BPA) of Portland, Oregon, before the commercialization of the program [11].

ATP program operates by predicting important parameters within an electric power network in time domain, prior to a application of a source of disturbance. ATP has an advantage of having many built-in models including transformers, electrical machines, surge arresters, transmission lines and cables, etc. Therefore, all that is required is data to make these models work. Frequency-domain computations and analysis can also be carried out using harmonic frequency scan technique.

Finally, algorithms are available for plotting of parameters and variables as a function of both time and also in the frequency domain1. Interested readers are referred to the reference manual of ATP, for more extensive information on the capabilities of ATP program [11].

21.4.2 Studies and Simulation

This section gives an overview of expected voltage levels that imping on luminaires when there are no MOVs to mitigate and why MOVs are indispensable devices. Result of simulation of lightning surge propagation in a low-voltage lighting power network for 15 poles in a series in an OHL configuration using an electromagnetic transients (EMT)-based program—Alternative Transients program (ATP)—in time domain is shown.

Typically, most systems to be simulated can be divided into subsystems for which models are already available for each subject to availability of other information required to make a model appropriate for simulation. Subsystem include, but not limited to, surge arrester, line, cable, and transformers, while support structures can be made up of components sufficient to model their behaviour under lightning surge. Internal model details and parameters are not the subject of this chapter and are not discussed further.

Figure 21.2 shows a typical low-voltage OHL system in ATP-EMTP program. Each line cable component (LCC) represents line segment between two support structures approximately 50 m distance apart. The distance is entered internally in

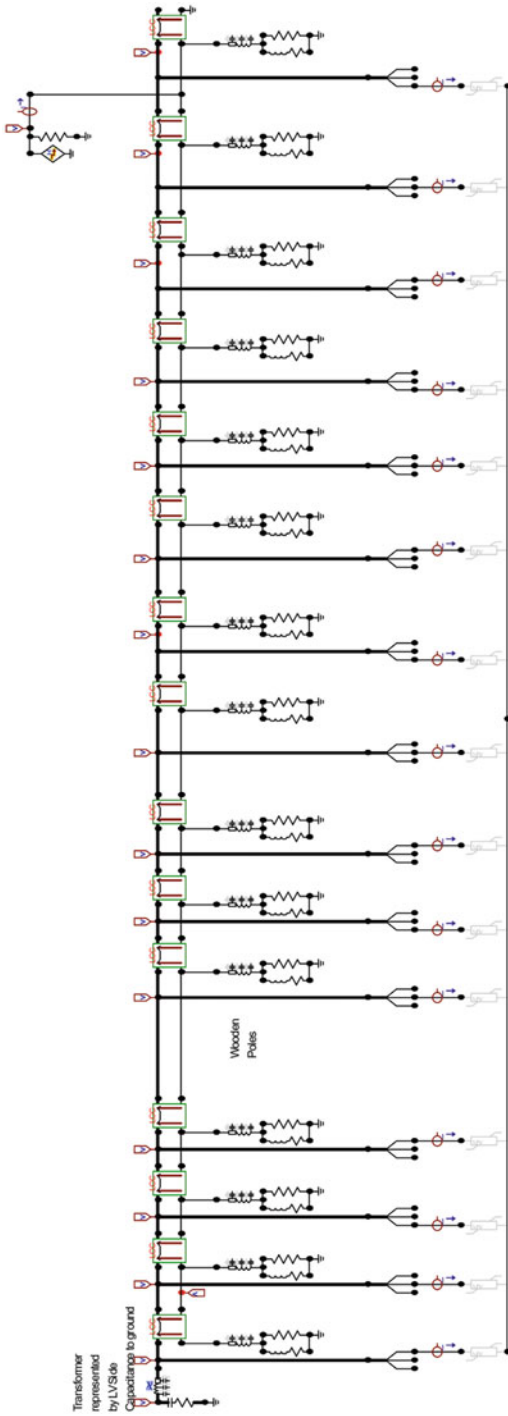

Fig. 21.2 Typical low-voltage OHL system in ATP-EMTP

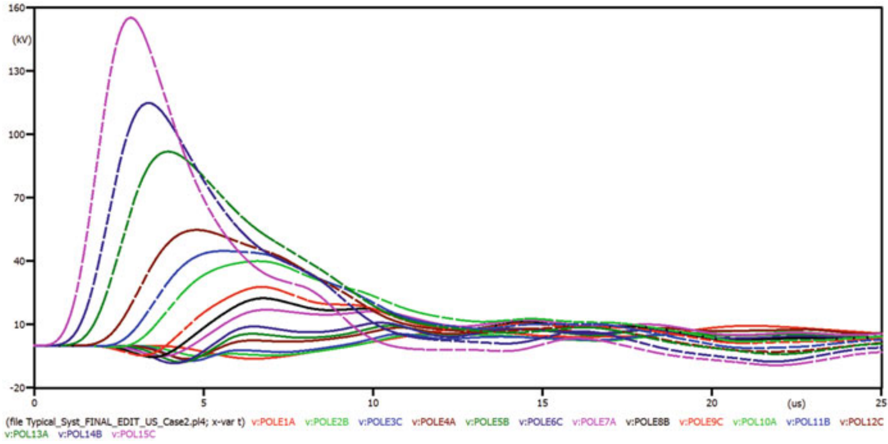

Fig. 21.3 Expected overvoltages for a typical OHL system

the LCC model. Below each LCC component is the MOV that provides a path dissipation of the energy contents of lightning. The high-voltage transformer is suitable represented by the low-voltage capacitance to ground, and this is sufficient for this scenario. Each parallel combination of inductor and resistor between each LCC component and MOV simulates the inductance and resistance of the supporting structure. All these, coupled with the lightning source, simulate the phenomena.

Location of lightning source in this scenario is at the end of a series of pole. It should be noted that the location of source affects how the waves travel. For simulation of a lightning stroke at midpoint of a series, the source should be located midpoint of the series.

Results give a generic overview of lightning-induced voltages carried out on a power network. These results are intended to show the influence, role of MOVs, and to show that increasing the rating of MOVs does not necessarily make a difference as is usually the first decision (except in regions prevalent with lightning strikes). Results provide an insight into the nature of the environment LEDs are exposed to during the event of lightning.

Figure 21.3 shows a graphical view of expected voltages based on a lightning current impulse of 10 kA 8/20s within the vicinity of an OHL system. This is a conservative lightning current stroke. In areas with prevalent strikes, lightning current of at 30 kA is possible, but currents above 30 kA are rare [7] and almost result in instant damage to luminaires as a whole. This highlights the importance of MOVs in reducing this overvoltages to levels that can be withstood by LEDs. As depicted in the plot (Fig. 21.3), overvoltages present an unfavourable environment during the event of lightning. This shows the need to pay attention to and improve the design of MOVs. As a matter of fact, MOVs will degrade overtime irrespective of how good it is, but improving designs to be able to operate for as long as necessary is imperative. As already pointed out, lifetime of LEDs under transient conditions is dependent on the lifetime of an MOV.

Figure 21.3 shows the results of a lightning studies simulated on an outdoor power network (OHL) supplying power to 15 luminaires attached to support structures. The above figure assumes there is no MOV to clamp down on overvoltages. A lightning stroke to ground within the vicinity of the 15th pole in the series was simulated. Highest voltage was observed at the terminals of the 15th pole at 150 kV which attenuated to approximately 5.5 kV at the far end. For such a system, luminaires attached to poles 1, 2, and 3 (being the farthest from point of stroke) have the best chance of survival without an MOV. Luminaires on poles 10–15 are likely to be completely damaged. This shows the kind of unfavourable environment LEDs are subjected to during a lightning strike.

21.5 Influence of System Type on Expected Overvoltage Levels

An important design consideration so often ignored is the choice of power distribution system type—OHL systems, insulated cable systems, and hybrid combination of OHL and cable systems (insulated cable systems may include underground and overhead cables). In certain areas of the world, there may not be a freedom of choice on what system to utilize for lighting applications. In other cases, the choice of what system to utilize borders around cost, technical factors, ease of construction, convenience, aesthetics, environmental impact, and so on.

A comparative modelling analysis carried out on an OHL system and an overhead insulated cable system showed the dramatic difference in overvoltages. Figure 21.3 shows the simulation for an OHL system as already analyzed. At the vicinity of strike, the peak voltage stood at approximately 150 kV and at the farthest point (from point of strike) in the series, peak voltage stood at approximately 10 kV. For such a case, any one pole without an MOV or improper operation of the MOV will incur some level of damage. The only components that can survive are those random components with high withstand strength.

As already described in Sect. 21.4, in most cases, the lowest peak voltage is not necessary at the farthest point, and for this case, the lowest voltage is actually at the third pole in the series at 5.5 kV; this has also being confirmed by reports from technicians in the field where a couple of poles between point of strike and farthest pole survived, but not the farthest pole or poles. Thus farthest point is only taken as a logical reference point. Reasons for this is beyond the scope of this monograph but is related to the wave reflection at exit points of the travelling wave [10].

Figure 21.4 shows the overvoltage profile of an insulated overhead cable system with the same number of poles, injected lightning current level, and similar conditions. At the point of strike, the peak overvoltage stood at approximately 17 kV, almost eight times less than that for a similar OHL system (non-insulated). In the same vein, the peak voltage at the farthest point (to point of strike) stood at a meagre 1.5 kV (negative) which the luminaire itself should withstand without an

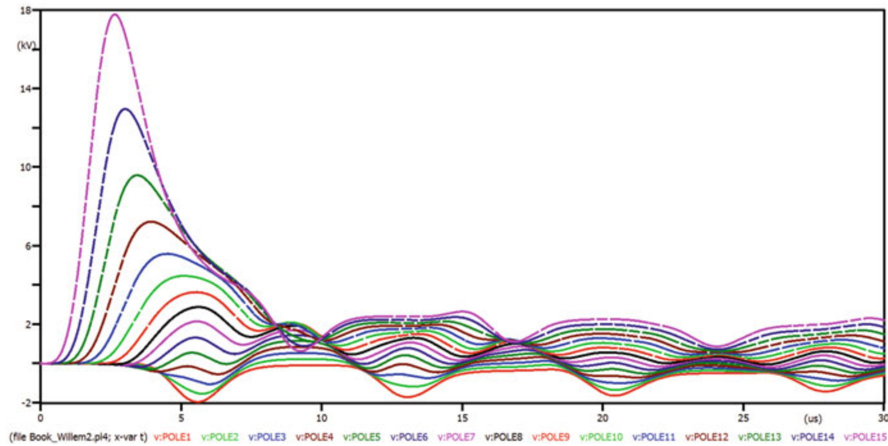

Fig. 21.4 Expected overvoltages for a typical insulated overhead cable system

MOV present. In such a case, with an MOV, overvoltages are effectively reduced to negligible levels. Even at 17 kV, there are several components of the luminaire that would survive the overvoltage without an MOV to reduce the burden.

Both cases compared above represent conditions whereby lightning strikes at one end of the series. In principle, there are infinitely possible points of strike along a series of support structures, and this is only a conservative choice. Strike could occur at midpoint of the series in which case simulation that shows voltages on both sides of this point will have more or less equal magnitude but different polarities depending on the actual conditions. The plots presented though represent models of actual configurations, but results are based on ideal models and only serve to give an insight into the whole problem and what to expect.

This is particularly important during the design stages of both LEDs and the luminaires itself to know what to expect when MOVs operate as expected, do not operate as expected, or do not operate at all. It could be observed that when MOVs operate as expected, the burden is dramatically reduced and represents a best case scenario. Withstand strength can be improved at the design stage given a minimum as obtained from simulation studies while assuming the MOVs do operate as expected. Little can be done at low-voltage levels if the MOVs do not operate. Therefore, the most imperative for such case is to minimize the damage.

Notwithstanding, there is an obvious dissimilarity between both systems. Observing the tail end of the graphical plots in Figs. 21.3 and 21.4, Fig. 21.4 shows tail-end oscillation compared to Fig. 21.3. This oscillation is peculiar to insulated cables due to the extra capacitance added to the system. A challenge that may be presented by such sustained oscillation is the energy content. Though both the voltages and currents are very low, the lengthy time duration of the oscillations may result to considerable high energy content that may or may not play a role. In such cases, standards may be referred to for more insight and considerations on mitigation [8, 9].

21.6 Conclusions

Lightning is a natural phenomenon that can neither be prevented nor avoided. Notwithstanding, its effect can be mitigated with the proper installation and coordination of protective devices in a way that ensures maximum protection. The effects of lightning cannot be completely mitigated, but can be reduced to a level that luminaires (and thus LEDs) can withstand for a short period of time (within the range of 50 ms a few milliseconds). For direct lightning strokes on luminaires and low-voltage devices, based on experimental data on current measured from direct strokes [1, 2], there is no cost-effective method to protect against such. Therefore, for luminaires, the goal is to protect against indirect effects of lightning.

In most cases, if standards are properly adhered to in the design and installation of both luminaire and the host power network, most of the damages incurred will be reduced. However, in less developed and developing regions in the world, standards and codes are seldom complied with, most especially with the installation and commissioning of power networks which would be eventual hosts to luminaires and LED devices. The most easily preventable source of surges is that which originates from the power supply, for example, surges that propagate from the supply transformer. If transformer were to be properly installed following recommendations from international standards and codes, this should never occur as relevant standards do specify that transformers should be protected on both sides with respective protective devices. If done accordingly, surges from the supply side will at best be clamped to such a low level that protective devices in luminaires need do nothing.

Finally, a few things are important to the long-term reliability of installed luminaires:

1. The minimum voltage level that luminaires should be able to withstand after MOVs must have clamped down on a propagating surge. Whatever the method to determine what such voltage level is, a statistical method is recommended. ANSI standard [8, 9] recommends a minimum of 6 kV for outdoor application. Simulation studies confirmed this as a great rule of thumb. It may be more or less depending on experiences obtained from the field.
2. There is a correlation between the life of an MOV and the life of a luminaire in the field. Point (1) assumes that is MOV is in fact healthy. If it is not, installed luminaire may not survive. The design of MOVs needs to be improved to ensure they can stay healthy for at least 10 years. Without MOVs, luminaires have very little chance of surviving a surge with amplitude greater than 10 kV which experience show is a conservative value for a surge. MOVs over the years have not changed much, and more attention should be given to their reliability over a minimum period. The moment an MOV can no longer operate, it’s just a matter of time before the luminaire it is protecting is damaged.

References

1. I. Tsunayoshi, O. Syuichi, S. Yoshiki, O. Shigemitsu, A field study of lightning overvoltages in low-voltage distribution lines, in *Electrical Engineering in Japan* (John Wiley & Sons, Inc., 2013)
2. M. Costea, The effects of lightning induced overvoltages on low voltage power networks, in *IEEE Power Tech. Conference Bucharest* (IEEE, 2009)
3. V. Cooray, V. Scuka, Lightning-induced overvoltages in power lines: validity of various approximations made in overvoltage calculations, in *IEEE Transactions on Electromagnetic Compatibility* (IEEE, 1998)
4. S. Sekioka, K. Aiba, S. Okabe, Lightning overvoltages on low voltage circuit caused by ground potential rise, in *International Conference on Power Systems Transients (IPST) in Kyoto, Japan* (IEEE, 2009)
5. M-System, Japan, Lightning and Surge Protection, Available via http://www.m-system.co.jp/mssenglish/service/emmrester.pdf (2015)
6. H. Schmitt, W. Winter, Simulation of lightning overvoltages in electrical power systems, in *International Conference on Power Systems Transients* (2001)
7. F.H. Kreuger, *Industrial High Voltage* (Delft University Press, Delft, 1991)
8. IEEE Power Engineering Society, *IEEE Guide on the Surge Environment in low voltage (1000 V and less) AC Power Circuit*. IEEE Std C62.41.1TM-2002 (2002)
9. IEEE Power Engineering Society, IEEE Recommended practice on characterization of surges in low-voltage (1000 V and less) AC Power circuits. IEEE Std C62.41.2TM-2002 (2002)
10. L. van der Sluis, *Transients in Power Systems* (Wiley, New York, 2001)
11. L'aszl'o Prikler, H.K. Høidalen, ATPDRAW Version 5.6 User Manual

Chapter 22
The Next Frontier: Reliability of Complex Systems

D. Schenkelaars, Willem Dirk van Driel, and R. Duijve

Abstract Traditional lighting is focused on the prevention of hardware failures. With the trend toward controlled and connected systems, other components will start playing an equal role in the reliability of it. Here reliability need to be replaced by availability, and other modeling approaches are to be taken into account. Software reliability can only be covered by growth models, with the Goel-Okumoto as a promising candidate. System prognostics and health management is the next step to service the connected complex systems in the most effective way possible. In this chapter we highlight the next frontiers that will need to be taken in order to move the traditional lighting catastrophic failure thinking into a thinking more toward new ways how system (degraded) functions can fail or be compromised.

22.1 Introduction

Nowadays the lighting industry experiences an exponential increasing impact of digitization and connectivity of its lighting systems [1]. The impact is far beyond the impact on single products but extends to an ever larger amount of connected systems. Continuously, more intelligent interfacing with the technical environment and with different kind of users is being built-in by using more and different kinds of sensors, (wireless) communication, and interacting or interfacing devices. Figure 22.1 gives two examples toward these controlled and connected systems, just to highlight the scale of it.

When the number of components and their interactions significantly increase, so-called large or complex systems are formed. The commonly used description of a large or complex system is given as [2, 3]:

D. Schenkelaars (✉) • R. Duijve
Philips Lighting, HTC45, 5656 AE, Eindhoven, The Netherlands
e-mail: dick.schenkelaars@philips.com; r.duijve@philips.com

W.D. van Driel
Philips Lighting, High Tech Campus, Eindhoven, The Netherlands

Delft University of Technology, EEMCS Faculty, Delft, The Netherlands
e-mail: willem.van.driel@philips.com

© Springer International Publishing AG 2018

W.D. van Driel et al. (eds.), *Solid State Lighting Reliability Part 2*, Solid State Lighting Technology and Application Series 3, DOI 10.1007/978-3-319-58175-0_22

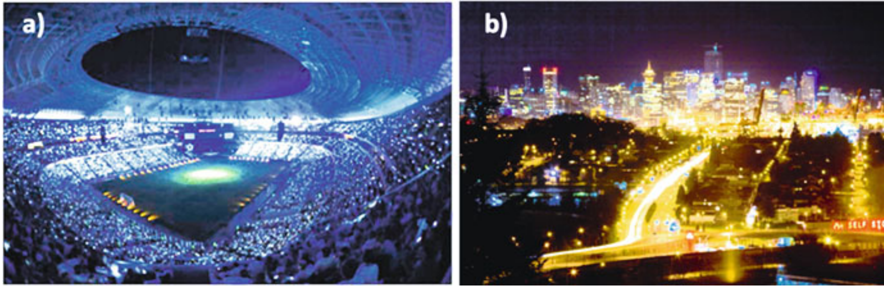

Fig. 22.1 Two examples of controlled and connected systems, with (**a**) >1000 connected luminaires on one theater system and (**b**) >10,000 connected street luminaires in one city

> A complex system: *a system composed of interconnected parts that as a whole exhibit one or more properties (behavior among the possible properties) not obvious from the properties of the individual parts.*

With the increasing amount of complexity, it is imperative that the reliability of such systems will enter a next frontier. In this chapter we will discuss the current state of the art and challenges that are to be confronted in order to tackle this.

22.2 All Components Matter

The functions in a complex lighting product can be listed as four basic properties [1, 3] being the (i) traditional lighting unit and its components, (ii) the software needed for processing data, (iii) a monitoring function for getting this data, and (iv) the communication to, for example, the user or the product. Examples of these functions are listed below:

(i) Lighting unit components

- Hardware: electronics, LED, PCBs, optics, plastics, solders
- Connectors – indoor & outdoor – , rigid and flexible
- Other mechanical connectors (e.g. screws, clips)
- Moving parts
- Fans, SynJet, and motor drives (air cooling)
- Wires
- Batteries
- Sealants

(ii) Processing and storage

- Software
- Data storage

Table 22.1 Complexity level versus reliability fingerprint

System complexity	High-level reliability fingerprint
Lighting unit components	Catastrophic failures of sub-components, relative well known
Controlled systems	More functions, more complex failure modes, software failure as component
Connected lighting systems	Degradation of system features and/or nuisance incidents with poor predictability, strong impact of software, availability, and customer experience

(iii) Monitoring

- Sensors – indoor and outdoor
- IoT – Internet of Things

(iv) Communication

- Sensors – indoor and outdoor
- Wireless/wired connectivity (including data integrity)
- IoT – Internet of Things

When processing and monitoring is added, one creates a so-called controlled lighting system. By adding the communication part, the system further evolves into a connected lighting system. Obviously, the system complexity increases in these three steps, simply because more components are added (see the above definition). Each of these systems has its own fingerprint when it concerns reliability, see Table 22.1 for a high-level view. On the lowest level of complexity, catastrophic failure of the sub-components determine the reliability and lifetime of the system. When the system is controlled, more complex failure modes may occur, and software failure is added to the equation. In the highest possible level of complexity, a fully connected and controlled lighting system, it becomes more difficult to predict the reliability performance, and here it is availability that come into play. In order to capture the systems availability, it is essential to introduce data analytics. In the following paragraphs, we will discuss these topics in more details.

22.3 Complex Systems: Availability Rather Than Reliability

System availability is the degree to which a system is operational and accessible, when required for use [4]. It can be defined as the part of a system that is functional (over time) following the below equation:

$$A = 1 - \frac{\#\ \text{of failing components}}{\text{total}\ \#\ \text{components}} \tag{22.1}$$

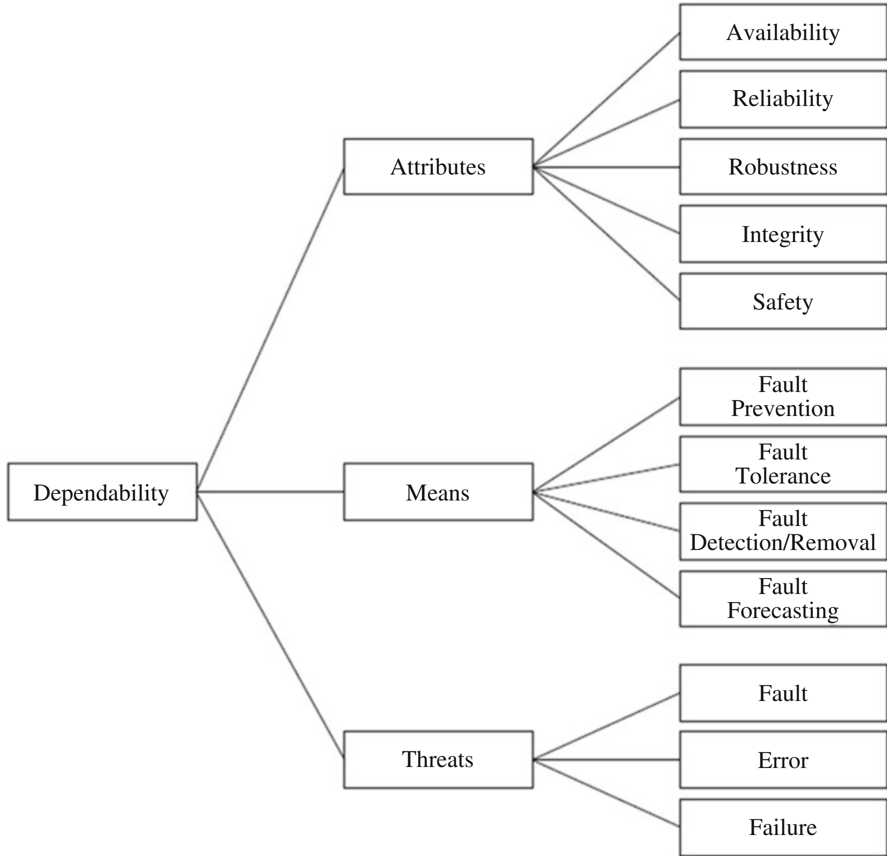

Fig. 22.2 The dependability tree: a measure of system's availability, reliability, and maintainability

When parts of a system are independent, availability does not scale with system size. In general, a high reliability will always lead to a high availability, but a system with low reliability can still have a very high availability. Reliability and availability belong to the attributes of the system dependability as well as integrity and safety as shown in Fig. 22.2 (input used from [5]). Dependability then is the ability of a system to avoid failures that are more frequent and more severe than acceptable. A dependable system is having all its required properties and does not show failures.

Typically for a networked and connected lighting system, this availability differs from the classical definition of system availability where system availability is defined as the fraction of time that a system provides the service for which it is specified. Where for one light point, reliability states the probability for survival after a specific period over time, for thousands of light points connected together this claim as isolated statement is not useful anymore. When thousands of light points are connected, it makes no sense to define system, or network failure, as failure of just one single light point in the system. It makes more sense to define

light point availability, indicating the fraction of light points operating in the controlled network over time. Where the formal system availability depends on planning and duration of repair, the availability of light points can be referred as "without repair" or "including repair." Repair here should be seen as system maintenance. In connected lighting systems, the availability of light points not only depends on the lighting units reliability but also on the reliability of sensors, controllers, communication devices, gateways, routers, and any other component that is in the system. Also it will depend on the robustness of software and on the system architecture which can determine how "deep" a hardware unit failure or software fault impacts the lighting system.

22.4 Testing and Validation

The creation of testing tools starts with a proper understanding of ways to quantify and predict the reliability of these systems in various complex operating environments. There are different ways of testing the system, e.g.:

- *System Testing*: The process of testing an integrated hardware and software system to verify that the system meets its specified requirements. It is conducted by the testing teams in both development and target environment.
- *Scalability Testing*: Part of the battery of nonfunctional tests which tests a software application for measuring its capability to scale up – be it the user load supported, the number of transactions, the data volume, etc. It is conducted by the performance engineer.
- *Performance Testing*: Functional testing conducted to evaluate the compliance of a system or component with specified performance requirements. It is usually conducted by the performance engineer.
- *Compatibility Testing*: Testing technique that validates how well software performs in a particular hardware/software/operating system/network environment. It is performed by the testing teams.
- *Operational Testing*: Testing technique conducted to evaluate a system or component in its operational environment. Usually it is performed by testing teams.
- *Model-Based Testing*: The application of model-based design for designing and executing the necessary artifacts to perform software testing. It is usually performed by testing teams.
- *Acceptance Testing*: Formal testing conducted to determine whether or not a system satisfies its acceptance criteria and to enable the customer to determine whether or not to accept the system. It is usually performed by the customer.
- *Inter-systems Testing*: Testing technique that focuses on testing the application to ensure that interconnection between application functions correctly. It is usually done by the testing teams.

Testing is an essential part of any complex system that combines hardware with software and connectivity. The test effort becomes harder with an increase of the system complexity and with the number of variations that can be out in the field.

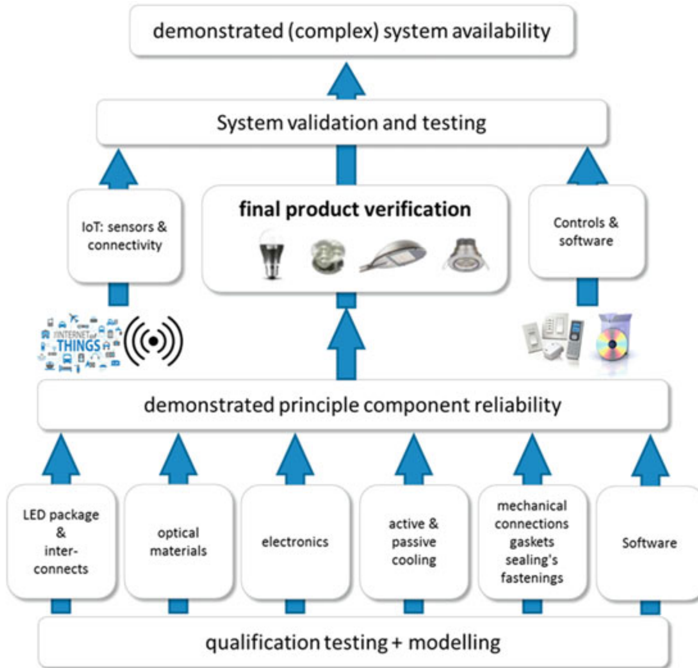

Fig. 22.3 Adding to the complexity in lighting systems: controls, software, sensors, and connectivity

Particularly if distributed connected systems reconfigure themselves in runtime, this poses challenges. For example, in identifying the proper key performance indicators (KPI) and collecting the respective critical to quality (CTQ) variables that carry the information which will allow the system to perform according to specification.

Following the approach from IEC62861, the work to create a so-called guide to principal component reliability testing for LED light sources and LED luminaires (see also Chap. 1 and [6]), new components have to be added that cover the complexity of the connected lighting system. Figure 22.3 schematically shows the added components, controls, software, and connectivity (including sensors). Testing and validation on the highest possible system level is based on the demonstrated behavior of its components. Note that also software should be seen as a component and release as such.

22.5 Software Reliability

There are many differences between the reliability and testing concepts and techniques of hardware and software. Software reliability or robustness is the probability of failure-free software operation for a specified period of time and environment

[7]. In this sense, software failures are considered a primary cause of product reliability problems, and hence a reasonable KPI for testing the software reliability is the number of software failures left in the system [8].

A software failure mode and effect analysis (FMEA) can determine the software failure modes that are likely to cause failure events [9–11]. It determines what single or multiple point failures could produce these top-level events. Software FMEAs are useful when designing or testing the error handling part of your software. Software FMEAs are also needed in order to develop inspection criteria for requirements, design, and code that are geared toward the appropriate failure modes. Design reviews are more effective when you know in advance the types of failure modes that are most likely.

Unlike hardware failures, software systems do not degrade over time, unless modified and software failures are not caused by faulty components, wear-out, or physical environment stresses such as temperature and vibration [7]. Software failures are caused by latent software defects that were introduced into the software as it was being developed but were not detected and removed before the software was released to customers. The best approach to achieving higher software reliability is to reduce the likelihood that latent defects are in released software. Unfortunately, even with the most highly skilled software engineers following industry best practices, the introduction of software defects is inevitable due to the inherent complexities of the software functionality and its execution environment.

A comparison of software and hardware reliability is useful in developing software reliability models. Table 22.2 (input used from [8]) shows the differences and similarities between the two.

Software reliability growth models (SRGM) are mathematical functions that describe fault detection and removal phenomenon [7, 8]. Some realistic issues such as imperfect debugging and learning phenomenon of software developers are incorporated in software reliability assessment. Among all SRGMs, a large class of stochastic reliability models is based on a nonhomogeneous Poisson process. These models are known as NHPP reliability models and have been widely used to track reliability improvement during software testing. Another popular class is the class of general order statistics, or GOS models. Goel-Okumoto is the most well-known NHPP model. Due to the important role that this model has played on the software reliability modeling history, it is often called “the” NHPP model. The mean value function is given by below formula:

$$m(t) = a\left(1 - e^{-bt}\right) \tag{22.2}$$

for all $t \geq 0$, where $a > 0$ and $b > 0$. The parameter a is the expected number of failures to be eventually detected while b is the rate at which each individual failure will be detected during testing. Following the sequence of software testing and

Table 22.2 Comparison between hardware and software reliability

Hardware	Software
Hardware failures are induced by component wear-out or stress invoked by thermal cycling, surges, ESD etc.	Software failures are not introduced by wear-out or stress. Software failures may be due to errors, ambiguities, oversights, or misinterpretation of the specification that the software is supposed to satisfy, carelessness or incompetence in writing code, inadequate testing, incorrect or unexpected usage of the software, or other unforeseen problems
Early failures	Software reliability is not a function of time
Constant failure rate (FIT)	No wear-out
End-of-life failures	Software will not change in time
Environmental conditions can be specified (indoor/outdoor, global area)	Errors will be induced by environments or contexts unforeseen in the design
Failure rate has a bathtub curve	Without considering program evolution, failure rate is statistically nonincreasing
Material deterioration can cause failures even though the system is not used	Failures never occur if the software is not used
Failures are caused by material deterioration, random failures, design errors, misuse, and environment	Failures are caused by incorrect logic, incorrect statements, or incorrect input data. This is similar to design errors of a complex hardware system
Hardware reliability can be improved by better design, better material, applying redundancy, and accelerated life testing	Software reliability can be improved by increasing the testing effort and by correcting detected faults
Hardware repairs restore the original condition	Software repairs establish a new piece of software
Hardware failures are usually preceded by warnings	Software failures are rarely preceded by warnings
Hardware might fail due to unforeseen application conditions	Software might (also) fail due to unforeseen application conditions

faults found, one can derive the maturity growth of the software by following this approach; Fig. 22.4 see for an example.

22.6 Reliability and Data Analytics

Traditional lighting is shifting toward connected lighting, and as a result companies are also enabled to shift more toward an information-based environment [12]. The use of information from connected sources can be described as a revolution named big data. With big data, data analytics from live connections of "intelligent" systems can be used to determine the system prognostics. Due to these changes in technology, the next generation of product data will be much richer in information [13, 14]. Reliability and availability will become enablers for product designs. Big

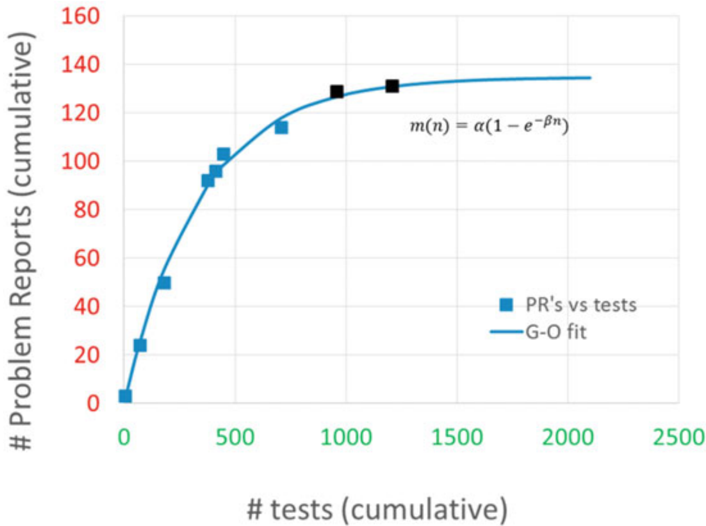

Fig. 22.4 Example of a maturity growth analysis for assessing the software reliability

data will bring detailed understanding of failure mechanisms, usage scenarios, technology, and optimal designs. For example, products can be outfitted with sensors that can be used to capture information about how and when and under what environmental and operating conditions products are being used. But the data can also be used for pure reliability analysis. Examples are signal-detection algorithms to detect unsafe operating conditions or precursors to system failure that can be used to protect a system by shutting it down or by reducing load to safe levels. And on top of this, there can be a need to predict the remaining life of the system (or the remaining life of its most important life-limiting components). This topic is named as prognostics and health monitoring (PHM). PHM refers to the process of predicting the future reliability or determining the remaining useful lifetime of a product by assessing the extent of deviation or degradation of a product from its expected normal operating conditions [15]. Today, we predict failure rates on system level following classical reliability approaches, where standardized testing and experimental failure analysis are used in order to obtain conservative bounds from the failure models. However, except in the case of reliability "incidents," there is only limited feedback with which we can judge the effectiveness of our reliability approach. Prognostics and monitoring is not just about creating a more reliable product: it is about creating a more predictable product based on real-world usage conditions. Data analytics is a necessary part of this but, in itself, is not sufficient. In order to add value, product insights need to be leveraged into the technologies that are used in order to differentiate from others. Prognostics and monitoring is not about troubleshooting reliability issues; rather, it is a new control point enabled by the transition to a lighting services business. It is the combination of data and deep physical (and technological) insight that will give a unique "right to win" in the

lighting industry. The future possibilities for using big connected data in reliability applications are unbounded. Lifetime models that are based on this data have the potential to explain much more variability in field data than has been possible before.

22.7 Final Remarks

The discussion and thinking so far in the lighting industry is focused on hardware failures. But controlled and/or connected lighting systems contain much more components; they encompass a level of complexity that goes beyond the traditional hardware thinking. Processing, monitoring, and communication functions are added with software playing an increasingly important role. Correspondingly, system reliability and availability will be increasingly dependent on the reliability of software. On top of this, the requirement of prognostics and health management is inevitable to be able to maintain and service the connected complex systems in the most effective way possible.

References

1. D. Schenkelaars, W.D. van Driel, M. Klompenhouwer, I. Flinsenberg, R. Duijve, Towards Prognostics & Health Management in Lighting Applications, European Conference Of The Prognostics And Health Management Society 2016, open access journal, available at: http://www.phmsociety.org/node/2090/, Volume 7, Page count: 7, (2016)
2. C. Joslyn L. Rocha. Towards semiotic agent-based models of socio-technical organizations, Proc. AI, Simulation and Planning in High Autonomy Systems (AIS 2000) Conference, Tucson, Arizona, (2000), pp. 70–79
3. X.J. Fan, W.D. van Driel, *Solid State Lighting Reliability: Components to Systems* (Springer, New York, 2012)
4. P.Jaramillo, A. Pruteanu, W.D. van Driel, J-P. Linnartz, Tools and methods for validation and verification, in *Runtime Reconfiguration in Networked Embedded Systems: Design and Testing Practices*, eds. by Zoltan Papp, George Exarchakos, ISBN 978-981-10-0714-9, (Springer, Springer Science+Business Media Singapore, March 2016)
5. B. Randell, C. Landwehr, A. Avizienis, J.-C. Laprie, I.E.E.E. Trans, Dependable Secure Comput.1, 11 (2004).
6. PT 62861 Principal Component Reliability Testing for LED-based Products, Working Groups TC 34/SC 34A/PT 62861, available at http://www.iec.ch/dyn/www/f?p=103:14:0::::FSP_ORG_ID,FSP_LANG_ID:9683,25. Last assess on 11/18/2016
7. H. Pham, *Software Reliability* (U.S. Government Printing Office, 2000), http://books.google.nl/books?id=TI0Sj6er8UEC
8. W.D. van Driel, M. Schuld, R. Wijgers, W.E.J. van Kooten, Software reliability and its interaction with hardware reliability. 2014 15th International Conference on Thermal, Mechanical and Multi-Physics Simulation and Experiments in Microelectronics and Microsystems (EuroSimE); 04/2014
9. A.M. Neufelder, *Ensuring Software Reliability* (Marcel Dekker, New York, 1993)

10. A.M. Neufelder, Lance Fiondella, Lou Gullo, Taz Daughtrey, IEEE 1633 Standard for Recommended Practice on Software Reliability" RAMS Conference January, 2015
11. J.A. McCall, W. Randell, J. Dunham, *Software Reliability, Measurement, and Testing,* (Rome Laboratory, RL-TR-92-52, 1992)
12. S. Ismail, *Exponential Organizations: Why New Organizations Are Ten Times Better, Faster, and Cheaper Than Yours (and What to do About It)* (Diversion Books, EAN: 9781626814233, New York, 2014)
13. W.Q. Meeker Y. Hong, Reliability Meets Big Data: Opportunities and Challenges (2013), Statistics Preprints. Paper 82. http://lib.dr.iastate.edu/stat_las_preprints/82
14. W.Q. Meeker, L.A. Escobar, *Statistical Methods for Reliability Data* (Wiley, New York, 1998)
15. M.G. Pecht, *Prognostics and Health Management of Electronics* (Wiley, Hoboken, 2008)

Index

A

Accelerated degradation tests (ADTs), 83
Accelerated life tests (ALTs), 142, 241, 243, 302
  acceleration factors, 551
  development process, 552
  high stress conditions, 551
  HTOL testing data, 552
  outcomes, 551
  selection, right stress conditions, 551
  stress parameters, 551
  stress test conditions, 551
  temperature, 552
Accelerated stress tests (ASTs)
  constant failure rate, 449
  constant stress protocols, 448
  design features, 449
  downlight models, 450
  DUTs, 449, 450
  electrolytic capacitors, 445
  environmental stressors, 442
  failure mechanisms, 442
  failure rate, 449
  hammer test, 445
  HAST, 445, 446
  methods, 443
  populations, 448
  power consumption, 449, 450
  rapid tests/HAST, 442
  screening tests, 442
  semiconductor packages and electronic components, 444
  simulations, 450, 451
  stepped-stress methods, 444
  stress level, stepped-stress method, 446, 447
  temperature shock cycles, 446
  temperature-humidity tests, 448
  temperatures, 443
  test-to-failure methods, 443
  thermal-aging experiments, 444
  Weibull probability plot, 449
Acceleration model parameters, 495
Advanced methods
  lumen maintenance, 83–85
  temperature-driven accelerated method (*see* Temperature-driven accelerated test)
Advanced methods, 97–109
  SPD (*see* Spectral power distribution (SPD))
Alliance for Solid-State Illumination Systems and Technologies (ASSIST), 131, 278
Artificial neural network (ANN), 267
ASTs. *See* Accelerated stress tests (ASTs)
ATP-EMTP, 577
Automotive qualification process, LEDs
  AEC Q101/IEC 60810, 553–554
  manufacturers, 554
  motivation, 552–553
  OEMs, 554
  product specification, 555
  requirements, 554
  suppliers, 554

B

Binder, 151–153
Blue light exposure
  blue chip and yellow phosphor, 119

© Springer International Publishing AG 2018

W.D. van Driel et al. (eds.), *Solid State Lighting Reliability Part 2*, Solid State Lighting Technology and Application Series 3, DOI 10.1007/978-3-319-58175-0

Blue light exposure (*cont.*)
intensity, 132
Philips modules, 132
spatial nonuniformity, 122
stress, 129

C

Calibrated model
accumulated plastic strain vs. time, 511
evaluation, lifetime model, 511
finite element, 509
high-cycle fatigue lifetime model, 510
plastic strain distribution, 510
plastic strain, second cycle, 511
Canonical variated analysis (CVA), 264
Centroid wavelength, 198
Cerium-doped lutetium aluminum garnet (Ce:LuAG), 223
Cerium-doped yttrium aluminum garnet (Ce:YAG), 223
Chemical mechanical polishing (CMP), 56, 69
Chromaticity
diagrams, 180–183
lighting products, 183
Chromaticity maintenance, 236–247
applications, 222
CCT, 223
contaminants, 235–236
efficacy, 221
experimental studies, 226–228
luminaire design effects, 247–250
optical material (*see* Optical materials)
package substrates, 233
phosphors, 223, 224, 233–235
shift mechanisms, 229–230
structures, 232–233
Chromaticity shift modes (CSMs), 229, 230, 250
CMP. *See* Chemical mechanical polishing (CMP)
Coefficient of thermal expansion (CTE), 339
Color quality
characteristics, 179
light source, 180
object color specification, 180
Planckian locus, 179
preference and perception, 193–195
specifications, 189–191
Color rendering
light source, 188–189
Color rendering index (CRI), 116, 132, 180, 191–193
Color shift
acceleration and prediction, 217–218
after aging, 217
before aging, 215, 216
aging temperature, 205
color coordinates, 207
discoloration, 205
downlight before and after aging, 213
FTIR analysis, 205
LED-based luminaire, 202, 208
color shift investigation, 210
cycle of reflections, 212
extraction, 212
LED package, 211
light flux, 211
light paths, 211
luminous flux maintenance, 202
materials and methods, 202–204
package level color shift, 202
simulation, 214
transmission spectra, 206
Color shifting, 127–131
Complex systems
controlled and connected systems, 586
data analytics, 592–594
functions, 586
vs. reliability fingerprint, 587
software reliability, 590–592
testing and validation, 589–590
Constitutive Law, 307–309
Controlled and connected systems, 586
Cool White Remote Phosphor Sample, 145–148
Correlated color temperature (CCT), 179, 184, 185, 223
Corrosion
accelerated test methods, 540–541
chemical contamination, 545
chemicals hazardous, 545
different sources, 529
epoxy-based adhesives, elastomers, coatings, and potting compounds, 528
extrinsic (*see* Extrinsic corrosion)
gas exposure tests, 546
intrinsic, 529, 530
lumen depreciation, 528
manufacturers, 528
semiconductor failure modes, 528
sensitivity
HP LED packages, 533
HPOS, 536
LED packages, 533

materials, 535–537
package integrity, 533–534
silicones, 533
silver tarnish, 546
SSL applications, 528
standard test methods, 538–540
test outcomes
Halogen Gasses, 543
sulfur testing, 541–543
VOCs, 543–544
Crack initiation, 303, 309, 313, 329
Cross-bridge Kelvin resistor (CBKR), 330

D
Data acquisition (DAQ) module, 161
Data-driven (DD) methods
learning approach
algorithms, 266
supervised learning, 266–268
unsupervised learning, 269, 270
reliability of systems, 264
statistical approach
degradation path model, 265
MD, 265, 266
Degradation mechanisms, mid-power LED packages
blue lights, 382
chip deterioration, 409, 410
components, 382
correlated color temperature, 382
C-SAM, 393
EDX analysis, 395
effects, package material, 411–414
electronic packages, 397
HAST
blue light over-absorption by silicone, 424–426
carbonization of silicone plates, 417
high-temperature storage tests, 415
Joule heating effects, 418–420
self-heating effects of the phosphors, 420–423
simulation and validation, 426–428
HTOL
aging tests, 386
characteristics, 387–389
MCPCB, 384
measurement, 384
optical and electrical measurement, 385
SpikeSafe Test System, 385
stress conditions, 385
IES LM-80-08, 383
I–V characteristics, 391–393
manufacturers, 382
non-stressed sample, 393
Ohmic contacts and semiconductor, 383
optical, 383
outcomes
color shift, LED packages, 402, 403
electrical characteristics, 404–406
failure analysis, 406–408
Lumen, 400–402
phosphors, 397
plastic package and copper lead frames, 382
reliability issues, 383
silicone carbonization, 384, 393
spectrum analysis, 389–391
wet-high-temperature operation life, 383
white-light, 382
WHTOL test, 384
aging test, 399
hypothesis, 400
measures, 399
MP-3030-EMC LED packages, 399
nondestructive and destructive analysis, 400
optical and electrical measurement, 399
WHTOL test, 399
Degradation, InGaN-based optoelectronic devices
air gap, 36
cracking, 27–29
defects
energy levels, 16
non-radiative losses, 16–17
optical performance, 15
Shockley-Read-Hall (SRH) theory, 16
shunt current, 17–18
silicon and magnesium, 15
design variation, 34
diffusion processes
bias current, 22, 23
cathodoluminescence maps, 19–21
current and temperature, 18
electron-hole pairs, 21
emission spectrum, 19
Fick's second law, 19
intensity profile, 20
junction temperatures, 21
laser diodes (LD), 19
mechanisms, 23
optical performances, 19
reliability tests, 21
threshold current, 22
yellow luminescence (YL), 20

Degradation (*cont.*)
electric field, 36
electroluminescence, 36
electromigration, 25–27
EOS, 37–38
IDCBL, 36
MOS capacitor, 36
ohmic contacts, 23–25
p-AlGaN EBL thickness, 36
polarity discharges, 35
reversed bias, 38–41
superlattice approach, 35
Devices under tests (DUTs), 258, 449, 450
Die attach
AuSn and Ag paste, 176
ceramic substrate, 163
epitaxial layer, 163
transient behavior, 174
DOE Energy Star Program, 202
Dominant domain, 169–170
Dominant wavelength, 196
DTI resistance, 173–175
DUTs. *See* Devices under test (DUTs)
Duv, 185–186

E
EDX. *See* Energy-dispersive X-ray spectroscopy (EDX)
Electrical overstress (EOS), 37, 38
Electrical overstress failure (EOS), 563
Electron beam-induced current (EBIC), 26
Electrostatic discharge (ESD), 39, 41
electroluminescence, 35
electronic devices, 29
emission microscopy, 33, 34
EOS, 37
failure mechanism, LED, 30
"hot spots", 33
InGaN MQW LEDs, 32
internal capacitance, 31, 32
SEM mapping, 32
V-pits, 30, 31
V-shaped defects, 30
Encapsulant/lens, 124–127
Energy-based fatigue model, 308, 317, 346
Energy-dispersive X-ray spectroscopy (EDX), 26, 27, 39
EOS. *See* Electrical overstress (EOS)
Epoxy resin, 123
ESD. *See* Electrostatic discharge (ESD)
Extrinsic corrosion
air pollutants, 532
components of light source, 531
outgassing materials, 532

F
Failure mode and effect analysis (FMEA), 591
Failures
batch-to-batch variability
batch, lot, wafer, and die definitions, 53
lot-to-lot, wafer-to-wafer, and within-wafer variabilities, 54
burn-in test, 64, 72
current modeling and investigations, 50
defects
die, 69, 71
epitaxial layers, 68
failure mechanisms, 67
hot spots, 67, 68
localization, 67
detection methods, 61
device lifetime, 50
electrical characterizations and model, 62–63
electrical signatures, 66–67
experiment, 64–66
failure rate *vs.* time, 51
hard defects
process improvement, 59–60
process recipe error, 60–61
weak population distribution, 59
LED production process, 50
LED reliability and lifetime prediction, 49
lower lifetime, 71–72
main population and weak population, 51, 52
material defects, 51
soft defects
chemicals, 57
CMP, 56
crystal growth, 58–59
lithography misalignment, 57
standard metrology limitations, 58
wafer substrate, 56
tool-to-tool variability, 54
weak components, 72
Fatigue model derivation, 306–318
FEM. *See* Finite element modeling (FEM)
Finite element analysis (FEA), 306
Finite element method (FEM), 10, 309–313, 505, 508
Flow-mixed gas corrosion (FMGC) test, 568

G
Gauss-Markov method, 500

H
Hammer Tests, 8
HAST. *See* Highly accelerated stress test (HAST)
High temperature operating life test (HTOL), 504
High-brightness LEDs (HB LEDs), 116
Highly accelerated stress test (HAST), 8, 132, 133, 383, 442, 445, 446
High-precision damage monitor
  crack initiation determination, 340–346
  electrical resistance measurement, 329
  finite element model, 338–340
  geometric details, 330–331
  temperature coefficient, 336–337
  temperature sensor calibration, 332, 333
  testing time, 329

I
IES-TM-21 Projecting Method, 281, 282
Illuminating Engineering Society (IES), 133, 259
In situ DC electrical resistance, 332–335
International Commission on Illumination (CIE), 179
Intrinsic corrosion, 529–531
Inverse approach
  numerical simulation, 171
  steady-state temperature, 171
  thermal conductivities, 172
Ion-damaged current-blocking layer (IDCBL), 36

L
Land grid array (LGA), 302, 306
Least-squares regression (LSR) approach, 278
LED device drivers
  capacitors, 436
  common topologies, 439–440
  components, 434, 435
  constant current, 434
  electrical stresses, 441–442
  electrolytic capacitors, 436
  electronic circuits, 434
  electronic components, 452
  film capacitors, 437
  inductors and transformers, 437
  MOSFETs, 438
  resistors, 438, 439
  semiconductor diodes, 439
  SMPS, 434, 438
LED package reliability, 505, 506, 513–522
  failure modes, 504
  finite element analysis, 522
  LED manufacturers, 524
  lens cracks, 504, 505
  manufacturers, 504
  operating life tests, 504
  prediction, 504
  quantification, Silicone degradation (*see* Silicone degradation, HTOL)
  silicone polymer, 505
  solid-state lightings, 503
  TTM, 524
  wire bonds
    elastic modulus, 506
    gold bonding wires, 506
    lifetime model (*see* Wire bonding lifetime model)
    thermal fatigue lifetime evaluation, 505
  wire neck breakage, thermal shock tests, 504
LED penetration
  failure modes, 5
  LED packages and arrays, 4
  levels, 3
  light-emitting diodes, 3
  power consumption, 4
  products, 2
  projections, 3
  submarkets, 3
LED qualification testing, IEC 60810
  characteristics, LED package, 556
  electro-optical parameters, 561
  exemplary process flow, 555
  family approach, 556
  minimum stress requirements, 555
  moisture preconditioning and assembly of LED packages, 557–558
  product specifications, 561
  sample size, 556
  samples selection, 555
  schematic process flow, 556
  stress tests
    categories, 562, 563
    concept, 563
    electrical, 567–568
    environmental, 568
    failures, 570
    high temperature and high current, 562
    high-power LEDs, 561
    JEDEC and IEC standards, 562
    measures, physical dimension (**PD**), 569
    mechanical, 567

LED qualification testing (*cont.*)
reliability, 561
solderability (**SO**) test, 569
temperature and bias operation, 563, 564
temperature, humidity and bias operation, 563–565
test-to-pass approach, 569
thermo-mechanical stress, 565–567
USCAR-33 requirement, 570
thermal management, 558–560
transfer, 557
visual inspection, 561
LED Systems Reliability Consortium (LSRC), 5
Light intensity
acceleration factor, 135
reference temperature, 135
remote phosphor, 135, 136
Light-emitting diodes (LEDs), 180
accelerated life testing (*see* Accelerated life testing, LEDs)
AEC Q101, 571
automotive applications, 550
automotive qualification process (*see* Automotive qualification process, LEDs)
automotive qualification testing, 550
capacitance, 160
catastrophic failures, 550
contaminations, 121
CRI, 117
degradation mechanism, 550, 571
design features, 549
device failures, 120
discoloration, 122–124
efficacy, 117
environmental benefit, 116
equipment, 160
failure mechanisms, 119–120
GaAsP semiconductor, 116
hybrid analytical/numerical model, 160, 166–168
interface delamination, 121–122
junction temperature, 159
LED product, 571
light sources, 116
material and process, 549
optoelectronic devices, 571
packaging high-power LEDs, 120
packaging materials, 120
product development phase, 549
qualification testing, IEC 60810 (*see* LED qualification testing, IEC 60810)
qualitative measurements, 116
reliability models, 133–136
reliability performance, 131–132
structural function, 160
thermal resistance, 159
ZVEI guideline, 571
Lighting systems, 577
Lighting technologies, 433
Lightning effects, 577–581
direct stroke, 574
effects, 575, 576
long-term reliability, 582
luminaire (*see* Luminaires)
mode of propagation, 574, 575
MOV, 576
overvoltage levels (*see* Overvoltages)
Lightning studies, 577–580
Linear Viscoelastic Model of PDMS, 515, 517
Liquid crystal displays (LCD), 117
LM-80 measurement time, 494
Lumen degradation, Mid-power and high-power LED technology, 496
Lumen depreciation model
creep strain rate, 520
curve fittings, 520
customer's requirement and applications, 518
evaluation, 518
LED package design, 522, 523
LM-80 tests, 520
Lumen maintenance
ADTs, 83
degradation model, 85
high temperature-humidity tests, 83
mixed effect model, 84
time-based, 84
Luminaire design
lenses and reflectors, 248
PMMA lens, 248
simulated/virtual approach, 248
Luminaires
ATP-EMTP, 577
studies and simulation, 577–580
Luminous efficacy, 195
Luminous efficacy of radiation (LER), 180
Luminous flux, 235, 236, 238, 239, 244, 247, 248, 250

M

Mahalanobis distance (MD), 265, 266
Material Models, 307–309
Metal oxide semiconductor field effect transistor (MOSFET), 438, 439, 441, 445, 446, 450
Metal-oxide varistor (MOV), 576
Microcellular PET, 207–210
Micro-tomography Scans, 336

Mid-power and high-power LED technology
analysis, L80 data, 497
analysis, LM80 data, 496
B50L80, 497, 498
B50L80 isolines, 499
fitted parameters, 496, 499
LM-80 measurement time, 494
long-term lumen maintenance data, 494
lumen degradation, 496
lumen maintenance behavior, 499
materials, 496
predicted acceleration model parameters, 495
predicted B50L70 values, 494
TM-21 method, B50L70 values, 496
MIL-HDBK-217, 263

N
NHPP, 591

O
Online testing method and system
advantages, 377
aging process, 363
calibration function of detector, 359
data collection, 364
data of temperature cycling life test, 363
DUTs, 355
effect of silicone, 372–376
error estimation, 364–366
GaN-based LEDs, 354
HAST, 354, 357, 363
illuminance and correlated color temperature (CCT), 357
laser diode (LD), 355
LED light sources, 353
LED measurement systems, 356
LED packages, 362
LED product, 354
LED reliability estimation, 377
LED's optical degradation, 357
LED's optical property degradation, 355
lumen maintenance, 362
luminous flux, 354
maintenance of LED modules, 377
measurement, 358
offline testing method, 356
optical parameters, 359
optical power, LED, 354
optimization, 360–362
packaging materials
blue type I (BTYPE I), 367
BTYPE II, 371
CTE, 366
degradation mechanism, 366
LED modules, 366
LED samples, 368
morphology detection, 370
normalized luminous flux, 369
optoelectronics parameters, 368
package compositions, 367
phosphor-converted white LED, 366
samples, 370
surface profiles of samples, 370, 371
parameters, 354
partial illuminance and the total flux, 362
performance parameters, 354
prototype, 358
reliability of LED products, 354
solid-state lighting technology, 354
Y-type structure, 357
Optical materials
ALTs, 241, 243
lens aging, 238–240
PET, 238
PMMA, 238
polyolefin-TiO_2, 246, 247
reflectors, 243–244
Overvoltages
ATP-EMTP, 578
cable systems, 580
comparative modelling analysis, 580
insulated overhead cable system, 581
OHL, 580
Oxidation
corrosion, 120
polycarbonate, 124
polymer, 121

P
Peak wavelength, 198
PECVD. *See* Plasma-enhanced chemical vapor deposition (PECVD)
Phosphor-converted white LED packages
Anomaly Detection, 275–277
electricity to light, 256
environmental testing, 258, 259
failure mechanisms, 257
FMMEA, 274, 275
IES-TM-21 Projecting Method, 281, 282
JEDEC, 258
JEITA, 258
LED lamps, 256

Phosphor-converted white LED packages (*cont.*)
LSR method, 278, 280
manufacturers, 258
method testing, 288, 290–292
method training, 287, 288
parameter identification, 274, 275
PF, 283, 285, 286
physics-of-failure-based, 257
product qualification, 260
qualification test, 257
short-term and cost-effective qualification, 278
test vehicle, 272, 273
theory and methodology, 272–277
TVs and commercial displays, 256
Physics-of-failure (PoF) methods
Arrhenius model, 262
Black's model, 262
Coffin-Manson model, 262, 264
Eyring model, 262
PHM methodology, 261
product's life, 260
steps, 261
Plasma-enhanced chemical vapor deposition (PECVD), 24, 25
Polycarbonate, 124
Polyethylene terephthalate (PET), 238
Polymethyl methacrylate (PMMA), 238
Power temperature cycle (PTMCL), 558, 565
Principle component analysis (PCA), 264
Printed circuit board (PCB), 302
Probabilistic neural networks (PNN), 264
Prognostics and health management (PHM)
categorisation, 260
electronic products, 260
Prognostics and health monitoring (PHM), 593
Program Change Review Board (PCRB), 59, 60

R

Reliability prediction of integrated LED lamps
catastrophic failure, lumen depreciation
CCM mode, 478, 480, 481, 483
CLO mode, 458, 477, 482
Driver Circuit, 472–474
electronic thermal simulation, 472
fault tree and failure rate models, 475–476
LED Light Source, 474
thermal models, 474
commercial LED bulb and a fly-back converter, 482
constant current mode (CCM), 458
coupling effects
degradations, 458
electronic simulations, 461, 462
electronic-thermal simulation, 458
LED light source, 459–461
simulation methodology, 464–465
thermal simulations, 459, 463
D25K driver, 467
degradation analysis, 456
designed scenarios, 467
driver's temperature, 469
electrolytic capacitor-free driver, 458
electrolytic capacitors, 456
electronic-thermal simulation, 458, 482, 483
high-temperature-humidity environment, 456
initial temperature distributions, 466
interaction, 482
L25K LEDs, 467
LED current, 467
LED junction temperature, 467, 468, 482
light source, 457
lumen flux depreciation, 457
lumen maintenance and lifetime, 469–471
luminous flux depreciation, 457
MOSFETs and power diodes, 457
parameter extraction, 465, 466
power control (PC) converter, 456
SEPIC, 456
Reliability test
catastrophic and degradation failures, 78
categories, LED lighting products, 82
combined and direct exponential extrapolation techniques, 80
illuminance applications, 79
LM-80-08 and LM-80-15, 79
luminous flux maintenance, 81
numerous applications, 78
program requirements, 81
TM-28-14, 80
Remaining life, 260, 261
Remaining useful life (RUL), 260, 278
Remote phosphor, 136
CCT values, 142
testing, 144, 145
Remote phosphor disk (RPD), 142, 143
Remote phosphor structures, 153–155
Response Surface Analysis, 320–328

S

Sequential Monte Carlo (SMC) method, 281
Silicone degradation, HTOL, 518–522

causes, 514
creep strain rate, siloxane, 514
finite element analysis, 518, 519
GaN-based LED, 514
LED devices, 513
Linear Viscoelastic Model of PDMS, 515–517
lumen depreciation (*see* Lumen Depreciation Model)
PDMS, 513
Silver mirror
in LED modules, 531
reflectivity, 538
Single Color LEDs, 196–198
Single-ended primary inductor converter (SEPIC), 456
SMPS. *See* Switched-mode power supplies (SMPS)
Software reliability
FMEA, 591
vs. hardware, 592
SRGM, 591
Software reliability growth models (SRGM), 591
Solder creep
material constants, 308
Solder fatigue
consecutive processes, 329
types of packages, 328
Solder reliability in LED assemblies
model derivation, 313–318
modeling and simulation, 319–321
parametric studies, 320–328
prognostics of remaining useful life (RUL), 305
SSL, 301–305
Solid-state lighting (SSL), 2, 116, 141, 179, 301, 487, 503
acceleration, 8, 9
announcements, 2
automatic coupling, 11
big data, 11
components, 12
energy-saving opportunity, 2
failure modes, 5–7
FEM techniques, 10
Hammer Tests, 8
LED penetration (*see* LED penetration)
lighting companies, 2
mechanisms, 11
multiscale modeling, 10
principal component reliability testing, 9
processes and materials, 12
product reliability, 9
services, 11, 12
system components, 1
Spectral power distribution (SPD), 133
Asym2sig function, 99, 100
asymmetric Gaussian function, 99
chromaticity lifetime qualification, 97
degradation prediction, 105–110
Gaussian function, 99
luminous flux, 102
parameters, 103, 106
photometric and colorimetric parameters, 98
sensitivity study, 105
similarity-based metric, 98
SSL. *See* Solid-state lighting (SSL)
Standardization. *See* Reliability test
Statistics
alternative approach, model fitting, 493, 494
current agreed methods
6× rule, 489, 500
Arrhenius model, 492
DDDM, 492
estimation, 491
Hallberg-Peck's model, 492
inverse power law model, 491
LM-80 data, 489, 490
lumen maintenance life of LED light, 492
luminous flux output, 490
mid-power white-light LEDs, 492
non-linear degradation behaviors, LED devices, 492
TM-21 extrapolation tool, 489
TM-21 method, 492
TM-21 report, 491
degradation analysis, 500
LM-80, 488
lumen maintenance, 488
lumen maintenance extrapolations, LEDs, 500
mid-power and high-power LED technology, 494–496
performance, LED-based system, 488
problem formulation, 489
SSL applications, 487
stochastic process formulation, 500
TM-21, 488
Support vector machine (SVM), 267, 268
Surface-mount technology (SMT), 306
Switched-mode power supplies (SMPS), 434, 437–439, 445

System availability, 587, 589
System reliability, 587, 589

T
Tarnish
 causes, 535
 H_2S, 536
 oxidation reaction, 535
 silver, 530, 537, 541
TDDB. *See* Time-dependent dielectric breakdown (TDDB)
Temperature coefficient of resistance (TCRc), 329, 339
Temperature-driven accelerated test
 accelerated time, 90–92
 boundary curve, 86–88
 parameters determination, 89–90
 two-stage process, 88
 verification, 92–97
Temperature sensor calibration, 332, 333
Test vehicle, 273
Thermal interface, 159
Thermal resistance
 die-attach, 160
 thermal capacitance, 160
 transient behavior, 160
Thermomechanical test, 332
Time-dependent dielectric breakdown (TDDB), 40
TLM. *See* Transmission line method (TLM)
Transient junction temperature
 measurement, 161–166
 power dissipation, 160
 resistance, 160
 steady-state temperature, 171
 transient voltage behavior, 165
 voltage behavior, 161
Transmission line method (TLM), 24, 25

V
Viscoplastic deformation, 307, 310, 329, 338

W
Wafer level chip-scale packages (WLCSP), 328
Warm White Remote Phosphor Samples, 148–151
Wet High-Temperature Operational Lifetime (WHTOL) Test, 143, 504, 558
White light chromaticity, 186–187
White light LEDs, 119
Wire bonding lifetime model
 Box-Behnken design, 512
 Calibrated Model, 509–511
 Coffin-Manson fatigue law, 506
 correlation coefficient, 507
 design parameters, 512
 elastic moduli of silicone, 507, 509
 Finite Element Model, 508
 LED manufacturers, 512
 LED package and test condition, 508
 residual stresses, 506
 response surface methodology (RSM), 512
 schematic LED package, 507
 thermal shock cycling, 506
 thermal shock tests, 506, 507
 wire neck breakage, 506